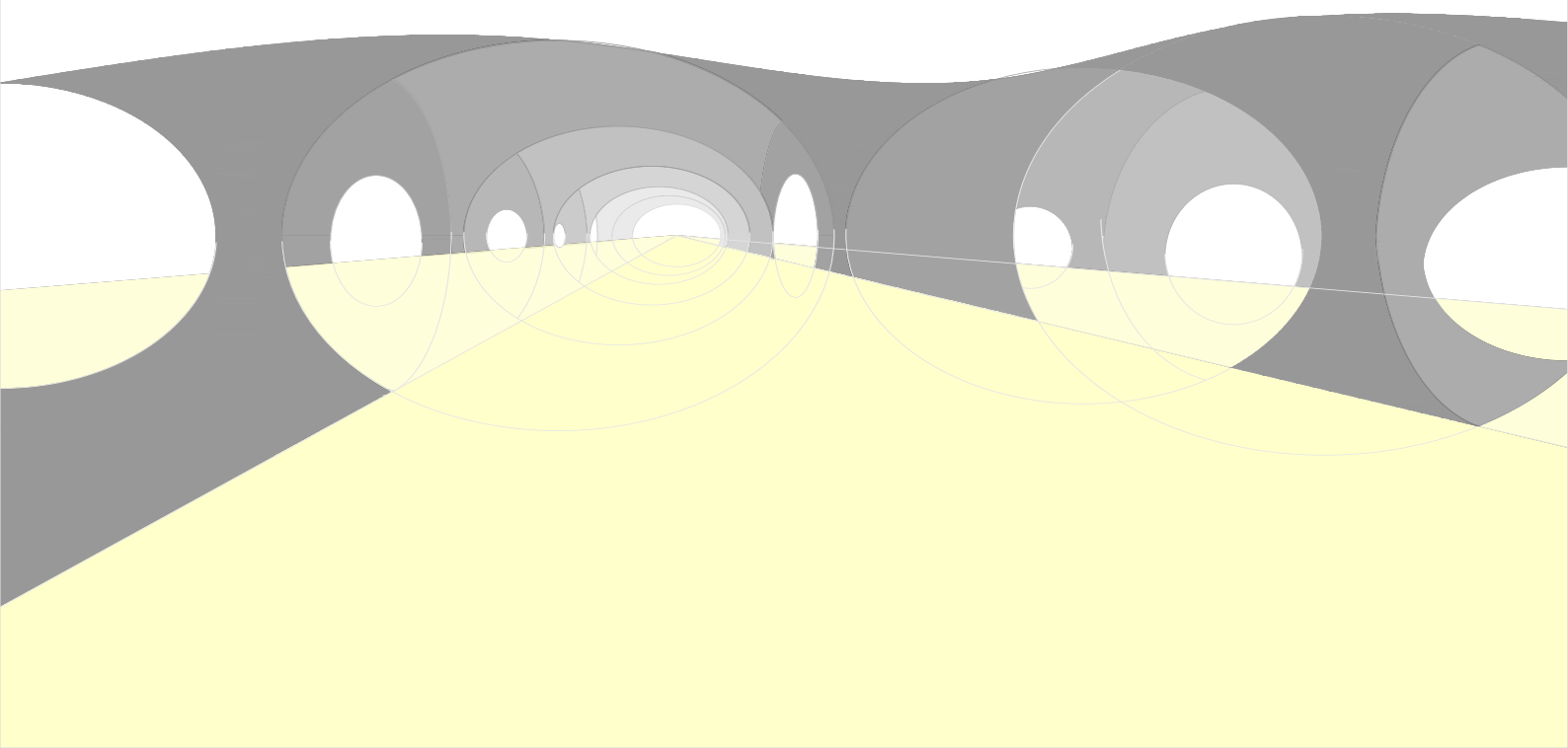


 DinEst 2024  
12-13 SEPTIEMBRE  
SEVILLA



# Proceedings of the DinEst: 3rd Conference on Structural Dynamics

Editors. . . . .	2
Sponsors and collaborators. . . . .	3
Organization. . . . .	4
Preface. . . . .	7
Plenary keynote lectures. . . . .	8
Lectures. . . . .	12
Materials characterization session. . . . .	13
Manuel Buitrago, Juan C. Reyes-Suárez and José M. Adam. Robust timber-to-timber connections for buildings to avoid disproportionate collapse. . . . .	14
Álvaro Magdaleno, Álvaro Iglesias-Pordomingo, Lara del Val, Emiliano Pereira and Antolín Lorenzana. Physical properties tracking of a laboratory-scaled two-story building model. . . . .	23
Manuel Aenlle, Héctor Cifuentes and Pelayo Fernández. Modulus of elasticity of concrete at different temperatures by means of modal analysis. . . . .	25
Antonio Manuel Merino Lechuga, David Suescum Morales, David Cantador Fernández, Ágata González Caro, Enrique Fernández Ledesma, José Ramón Jiménez Romero and José María Fernández Rodríguez. Mechanical behaviour of precast concrete pavers curing in CO2 environment. . . . .	26
Manuel Aenlle, Carlos Cima and F. Pelayo. Damping of laminated glass plates. Comparison of numerical model and experimental results. . . . .	28
Railway dynamics session. . . . .	38
Álvaro Brazales, Javier F. Aceituno, Rosario Chamorro and José L. Escalona. Simplified railroad track models with periodically variable parameters for MBD simulation of railway vehicles. . . . .	39
Lutz Auersch. Vibrations of multi-span structures like floors, rail and road bridges. . . . .	41
Antonio Martínez de la Concha, David Suescum Morales and Héctor Cifuentes Bulté. Influence of deep foundations in a deck slab high-speed railway bridge: a theoretical study. . . . .	60
José M Goicolea, Nicola Tarque, Andrea Tapia, Alfredo Cámara and Khanh Nguyen Gia. A study of the contribution of bending, torsion and distortion for the dynamic response of current structural types in high-speed railway bridges. . . . .	84
Josep Chordà-Monsonís, Juan Carlos Sánchez-Quesada, Emma Moliner, Antonio Romero, Pedro Galvín and María de los Dolores Martínez-Rodrigo. Influence of the soil-structure coupling on the dynamic behaviour of a portal frame railway bridge. . . . .	85
Robert Arcos, Yazdan Shafieyoon, Arnau Clot, Kenny F. Conto and Jordi Romeu. Investigation of different methodologies for simulating the ground-borne vibration response of buildings due to underground railway traffic. . . . .	101
Jose Escalona, Rosario Chamorro, Álvaro Brazales and Javier F. Aceituno. Application of the moving modes method to the dynamics of infinitely long flexible tracks with discrete supports. . . . .	102
R. Velázquez-Mata, A. Romero, A. Tadeu, M.D. Martínez-Rodrigo, E. Moliner and P. Galvín. Effectiveness of acoustic barriers for mitigating train traffic noise. . . . .	104
Rafael Jesús Luque, Pedro Reyes, Montserrat Simarro, Sergio Postigo and Juan Jesús Castillo. Optical data collection device for predicting wear on rigid catenary with results on Málaga metro infrastructures. . . . .	106



Hassan Liravi, Arnau Clot, Robert Arcos and Jordi Romeu. Modelling railway-induced vibrations using a 2.5D hybrid SBM-MFS methodology. . . . .	116
Juan Sánchez-Quesada, Emmanuela Moliner, Antonio Romero, Pedro Galvín and María Martínez-Rodrigo. Assessing the dynamic response of skewed railway bridges through detailed modelling. . . . .	117
María Dolores Martínez-Rodrigo, Pedro Galvín, José M. Goicolea, Antonio Martínez de la Concha, Emma Moliner, Javier Naranjo, Carlos Rodrigo, Antonio Romero and Nicola Tarque. InBridge4EU project for bridge dynamics: towards interoperability in the European railway network. . . . .	124
Analytical and computational dynamics session. . . . .	128
Mauricio Larrodé Diaz and Alejandro Rincón Casado. Vibratory analytical-computational model of a neonatal incubator. . . . .	129
Ángel Vidal, María Macías, Manuel Castillo and Álvaro Serrano. Validation of CFD simulation with fluid-structure interaction by means of aeroelastic tests in physical wind tunnels. . . . .	131
José Manuel Torres Serrano, Sandro Andrés Martínez and Rafael Jiménez Rodríguez. Advanced numerical modelling for nonlinear dynamic soil-structure interaction. . . . .	133
Belén Vecino Muñoz, Luis Chillitupa Palomino, Javier Naranjo, Carlos Martín de la Concha Renedo, Iván Muñoz Díaz and Jaime H. García Palacios. Simplified procedure to track the tension force: numerical validation. . . . .	134
José Miguel Martínez Valle. A simple and efficient 3D finite element for dynamic analysis of shell structures. . . . .	142
Mikel Merino-Olagüe, Aitor Plaza and Xabier Iriarte. Dynamic mode decomposition method for model order reduction of a non-linear elastic beam. . . . .	143
Sergio Sánchez Gómez, Shagun Agarwal and Oriol Colomés. Analytical and numerical modelling of non-linear dynamic behaviour of a flexible cable subject to motion. . . . .	158
Nicola Tarque, José María Goicolea and Leonel Lipa. Predicting collapse mechanisms in masonry buildings through the use of rigid body dynamics. . . . .	163
Jacob D.R. Bordón, Guillermo M. Álamo, Luis A. Padrón, Juan J. Aznárez and Orlando Maeso. MultiFEBE: open-source package for mixed-dimensional boundary element – finite element models for coupled linear mechanics. . . . .	171
Javier González Carbajal, Alejandro Rincón Casado, Daniel García Vallejo and Jaime Domínguez. Steady-State oscillation analysis: nonlinear solutions for a rotating cantilever beam. . . . .	173
Bridge dynamics and vibration control session. . . . .	175
Juan Camilo Reyes, Manuel Buitrago, Brais Barros, Santiago López and José M. Adam. Dynamic evaluation of a scaled-down bridge subjected to sudden member losses. . . . .	176
Carlos Rodrigo Villar, María Dolores Martínez Rodrigo, David Hernández Figueirido, Víctor Roda Casanova and Joaquín Luis Sancho Bru. Dynamic characterization and vibration serviceability assessment of an ultra-high strength concrete footbridge using numerical and experimental techniques. . . . .	185
María Macías Infantes, Ángel Vidal, Manuel Castillo and Álvaro Serrano. A combined CFD-FEM approach to study wind-induced vibrations in a real cable stayed bridge. . . . .	188
Seismic engineering and soil-structure dynamic interaction session. . . . .	190
Alejandro E. Martínez-Castro, Antonio L. Sánchez-López-Cuervo and Rafael Gallego. A multi-task learning approach for dynamic stiffness of foundations in poroelastic layered media. . . . .	191
José Luis Ordóñez, Arturo Fontán and Luis Romera. Post-seismic dynamic properties study and damage validation of a steel arch bridge with an intermediate deck. . . . .	193
Carlos Romero-Sánchez and Luis A. Padrón. Dynamic structural response of four-legged jacket-supported offshore wind turbine considering the effect of wind and seismic ground motion directionality. . . . .	196
Beatriz Zapico Blanco, Antonia Sillero Ruz and Enrique Vázquez Vicente. Seismic vulnerability of a 1950s-1960s representative social housing type in Málaga (Spain). . . . .	198
Beatriz Zapico Blanco and Carlos Baena Arrabal. Seismic vulnerability assessment of social housing units in Ayamonte (southern Spain). . . . .	210

Laura Navas-Sánchez, Maribel Jiménez-Martínez, Lisandra Hernández, Beatriz González-Rodrigo and Orlando Hernández-Rubio. Select. FC: methodology, calibration, APP and database to assess and select fragility curves for seismic risk studies. . . . .	221
Carlos Merino, Patricio García, Pedro Negrette and José Manuel Torres. Seismic assessment of a UNESCO world heritage site. The great mosque in Córdoba. . . . .	230
Berna Istegün, Pelayo Fernández, Natalia García-Fernández and Manuel Aenlle. Dynamic analysis of a 6th floor concrete prefabricated building. . . . .	242
Hugo Pillajo, Luis Romera and Ruth Gutiérrez. Experimental and numerical seismic evaluation of connection systems between reduced-section beams and steel-concrete composite columns. . . . .	246
Beatriz Zapico Blanco and Bruno Tello Fernández. Seismic vulnerability preliminary assessment of social housing in Cádiz (Spain). . . . .	248
Wouter Kroon, Rita Esposito, Satya Sharma, Enrique Vázquez and Beatriz Zapico Blanco. Seismic vulnerability assessment of the arch-structure in the historical city of Medina Azahara	263
Cristina Medina, Jacob D.R. Bordón, Luis A. Padrón, Juan C. Galván, Juan J. Aznárez and Orlando Maeso. Kinematic interaction factors for bucket foundations in homogeneous soils using multiFEBE. . . . .	269
Sergio Sánchez Gómez, Athanasios Tsetas and Andrei Metrikine. Experimental investigation of pile installation settings under coupled axial-torsional excitation. . . . .	271
A. José Hernández-Carrillo Venegas. Seismic analysis of the access viaducts in the fourth bridge over the panamá canal project. . . . .	272
Julio Rodríguez-Sánchez, Antonio Jesús Díaz-Moreno, Jose Martin Romero and Ignacio Hinojosa Sánchez-Barbudo. Seismic aspects in the project of lines 2 and 4 of the Lima metro	288
Monitoring, damage detection, system identification and model updating session. . . . .	301
Guillermo Fernández Ordóñez, Ismael García García, Alfonso Gómez Bravo, Pedro Gil Jiménez and Tomislav Jarak. Experimental methodology for monitoring physical magnitudes of slender structures using wearable devices. . . . .	302
César Peláez Rodríguez, Álvaro Magdaleno, Álvaro Iglesias-Pordomingo, Jorge Pérez-Aracil, Sancho Salcedo-Sanz and Antolín Lorenzana. Detecting structural damage in slender constructions using a hybrid system of supervised learning algorithms and model updating for analyzing raw dynamic data. . . . .	304
Natalia García-Fernández, Pelayo Fernández, Manuel Aenlle and Carmelo Gentile. Application of T-mass and T-stiffness correlation techniques on real structures. . . . .	306
Javier C. Cámara-Molina, Antonio Romero, Pedro Galvín, María Dolores Martínez-Rodrigo, Emma Moliner and Pilar Marín. Modelling and design optimisation of a magnetoelastic vibration energy harvester for railway bridges. . . . .	310
Natalia García-Fernández, Pelayo Fernández and Manuel Aenlle. A model updating method based on t-mass and t-stiffness correlation techniques. . . . .	311
Álvaro Iglesias Pordomingo, César Peláez Rodríguez, Guillermo Fernández Ordóñez, José María García Terán and Álvaro Magdaleno González. Developing a modal identification technique to perform an experimental modal analysis based on CNN and deep learning. . .	329
Mario Solís, Qiaoyu Ma and Pedro Galvín. Approaches for damage detection and quantification in beams from wavelet analysis of incremental mode shapes. . . . .	331
Alejandro Cebada, Mario López and Manuel Aenlle. Fatigue damage on a floating breakwater - a case study. . . . .	340
Manuel Aenlle, Natalia García-Fernández and F. Pelayo. The concept of ROTMAC in structural dynamics. . . . .	341
Aitor Baldomir, Arturo N. Fontán, Luis E. Romera, Marta Pérez Escacho and Carlos J. Bajo Pavía. Dynamic behaviour of transmission towers through experimental testing and numerical modelling. . . . .	354
Antolín Lorenzana, Juan José Villacorta, Roberto Diego Martínez, Mariano Cacho and Alberto Izquierdo. Operation of an interactive vibration monitoring system ad-hoc designed for tracking historic façades during conservation works. . . . .	357
Pelayo Fernández, Natalia García-Fernández, Miguel Muñiz Calvente and Manuel Aenlle. Fatigue monitoring of structures as a SHM technique. . . . .	359

Antonio Romero, J.D. Clavijo-Vázquez, Rocío Velázquez-Mata, Javier Cámara-Molina, M.A. Mengual-Pintos and Pedro Galvín. Autonomous monitoring systems for long-term predictive maintenance of a metro bridge. . . . .	363
Javier Álvarez Pozo, Blas González, Lucija Barišic, Javier Fernando Jiménez-Alonso and Andrés Sáez. Thermal digital twin for monitoring an asphalt road based on a physics. . . .	365
Asier Legaz, Iñigo Vilella, Miroslav Zivanovic, Xabier Iriarte, Aitor Plaza and Alfonso Carlosena. Operational modal analysis of an entire wind farm.. . . .	373
Javier Naranjo, Javier F. Jiménez-Alonso, José M. Soria and Iván M. Díaz. Fatigue life cycle assessment of external post-tensioning systems considering corrosion effects. . . . .	375
Carlos M.C. Renedo, Iván M. Díaz, Jaime H. García Palacios, Belén Vecino and Luis Chillitupa Palomino. Current challenges on vibration-based NDT and continuous monitoring of external post-tensioning tendons in bridges. . . . .	377

# **PROCEEDINGS OF THE DINEST: 3RD CONFERENCE ON STRUCTURAL DYNAMICS**

---

**3rd Conference on Structural Dynamics (DinEst 2024)**  
**Seville, September 2024**

**Editors**

Antonio Martínez de la Concha  
Antonio Romero Ordóñez  
Beatriz Zapico Blanco  
Daniel García Vallejo  
Esther Puertas García  
Héctor Cifuentes Bulté  
Javier C. Cámara Molina  
Mario Solís Muñiz  
Pedro Galvín Barrera  
Rafael Gallego Sevilla  
Rocío Velázquez Mata  
Rosario Chamorro Moreno

## Sponsors



## Collaborators

**EASD**  
European Association  
for Structural Dynamics



DinEst 2024 would like to acknowledge the financial support provided by the Universidad de Sevilla under the grant SOL2024-28805 (VII Plan Propio de Investigación y Transferencia - US 2024).

**3rd Conference on Structural Dynamics (DinEst 2024)**  
**Seville, September 2024**  
**Organization**

**Scientific committee**

Alberto Fraile de Lerma, Universidad Politécnica de Madrid, Spain  
Alejandro E. Martínez-Castro, Universidad de Granada, Spain  
Amadeo Benavent Climent, Universidad Politécnica de Madrid, Spain  
Antolín Lorenzana, Universidad de Valladolid, Spain  
Antonio Romero Ordóñez, Universidad de Sevilla, Spain  
Beatriz Zapico Blanco, Escuela Técnica Superior de Arquitectura, Universidad de Sevilla, Spain  
Carlos Zanuy Sánchez, Universidad Politécnica de Madrid, Spain  
Daniel Cantero, Norwegian University of Science and Technology, Norway  
Daniel García Vallejo, Universidad de Sevilla, Spain  
M. Dolores G. Pulido, Universidad Politécnica de Madrid y Consejo Superior de Investigaciones Científicas, Spain  
Felipe Gabaldón Castillo, Universidad Politécnica de Madrid, Spain  
Francisco López Almansa, Universitat Politècnica de Catalunya, Spain  
Francisco Martínez Cutillas, Universidad Politécnica de Madrid, Spain  
Gia Khanh Nguyen, Universidad Politécnica de Madrid, Spain  
Guillermo Rus, Universidad de Granada, Spain  
Ignacio Romero Olleros, Universidad Politécnica de Madrid, Spain  
Iván Muñoz Díaz, Universidad Politécnica de Madrid, Spain  
Jaime Domínguez Abascal, Universidad de Sevilla, Spain  
Jaime H. García Palacios, Universidad Politécnica de Madrid, Spain  
Javier Cara Cañas, Universidad Politécnica de Madrid, Spain  
Joaquín Martí Rodríguez, Universidad Politécnica de Madrid, Spain  
Jordi Romeu, Universitat Politècnica de Catalunya, Spain  
José Domínguez Abascal, Universidad de Sevilla, Spain  
José Manuel Soria, Universidad Politécnica de Madrid, Spain  
Jose Maria Goicolea, Universidad Politécnica de Madrid, Spain  
Juan Carlos García Orden, Universidad Politécnica de Madrid, Spain  
Juana Mayo, Universidad de Sevilla, Spain  
Luis A. Padrón, Universidad de Las Palmas de Gran Canaria, Spain  
Manuel Aenlle López, Universidad de Oviedo, Spain  
María Dolores Martínez Rodrigo, Universitat Jaume I, Spain  
María Jesús Elejabarrieta, Universidad de Deusto, Spain  
Mario López Gallego, Universidad de Oviedo, Spain  
Mario Solís Muñiz, Universidad de Sevilla, Spain  
Miguel Muñiz Calvente, Universidad de Oviedo, Spain  
Orlando Maeso, Universidad de Las Palmas de Gran Canaria, Spain  
Pedro Galvín Barrera, Universidad de Sevilla, Spain  
Pedro Museros Romero, Universitat Politècnica de València, Spain  
Pelayo Fernández Fernández, Universidad de Oviedo, Spain  
Ricardo Perera Velamazán, Universidad Politécnica de Madrid, Spain  
Robert Arcos, Universitat Politècnica de Catalunya, Spain  
Salvador Ivorra Chorro, Universidad de Alicante, Spain

**3rd Conference on Structural Dynamics (DinEst 2024)**  
**Seville, September 2024**  
**Organization**

**Local committee**

Antonio Martínez de la Concha  
Antonio Romero Ordóñez  
Beatriz Zapico Blanco  
Daniel García Vallejo  
Esther Puertas García  
Héctor Cifuentes Bulté  
Javier C. Cámara Molina  
Mario Solís Muñiz  
Pedro Galvín Barrera  
Rafael Gallego Sevilla  
Rocío Velázquez Mata  
Rosario Chamorro Moreno



**3rd Conference on Structural Dynamics (DinEst 2024)**  
**Seville, September 2024**  
**Organization**

Front page: Antonia Sillero Ruz

**3rd Conference on Structural Dynamics (DinEst 2024)**  
**Seville, September 2024**  
**Preface**

Seville, September 10th, 2024.

Structural dynamics is a technological and research field with growing importance. Since structures are being built slenderer, studying their dynamic behaviour becomes more relevant. On the other hand, society requires a greater safety guarantee against dynamic actions such as seismic, aerodynamic, and traffic, or accidental situations such as explosions and impacts.

During the Eurodyn 2017 conference in Rome, it was agreed to promote this structural dynamics conference (DinEst), to bring together researchers and professionals in the field to share ideas and project results, as well as to promote and encourage collaborations between different research groups and with companies in the sector. Two previous editions of DinEst have been successfully held: in 2018 at the Universidad Politécnica de Madrid in 2018, and in 2021 at the Universidad de Oviedo (Gijón).

From the organizing committee, we would like to welcome all participants and put ourselves at your disposal to develop this third edition of DinEst in Seville. We thank the Escuela Técnica Superior de Ingeniería and the Universidad de Sevilla for their collaboration and support.

The conference covers all major aspects of Structural Dynamics with focus on the following topics: materials characterization, railway dynamics, analytical and computational dynamics, bridge dynamics and vibration control, seismic engineering and soil-structure dynamic interaction, monitoring, damage detection, system identification, and model updating.

We also hope that the conference will also be useful in promoting a Spanish candidature for the organization of the Eurodyn Conference with the support of the European Association for Structural Dynamics (EASD).

In addition to the interesting papers presented by researchers, technical specialists, and students, the conference comprehends keynote lectures by Professor Guido De Roeck (KU Leuven), Professor Andrei Metrikine (Delft University of Technology) and Patricio García (ARUP). The organizing committee is grateful for the kindness, willingness, and commitment of the invited researchers to the Spanish structural dynamics engineering community.

The organizing committee also deeply acknowledges the support of our colleague and mentor José Domínguez for the organization of this conference. Pepón was an example for us to follow.

We warmly thank all the contributors, authors, speakers, and sponsors of DinEst and wish this conference offers you fruitful discussion and a pleasant time in Seville.

Prof. Pedro Galvín  
Continuum Mechanics and Structural Analysis  
Universidad de Sevilla

**3rd Conference on Structural Dynamics (DinEst 2024)**  
**Seville, September 2024**  
**Plenary keynote lectures**

**Guido De Roeck**

**Vibration based structural health monitoring: strengths and weaknesses.**

About keynote speaker

Guido De Roeck is Emeritus Professor of the Faculty of Engineering Science, KU Leuven, Belgium, where he is also the Head of the Structural Mechanics Section. He leads multiple research activities ranging a spectrum of domains, including static and dynamic analysis of mechanical structures, damage detection by vibration monitoring, dynamic system identification, soil-structure interaction, nonlinear constitutive soil models, fracture mechanics of composite materials, fuzzy finite element method, and so on.

Several members of the Spanish engineering community have visited the Structural Mechanics Section of the KU Leuven, a world reference in dynamics of structures, where they have improved their knowledge and expertise given the excellent quality of its research and team. The Spanish engineering community is very grateful to this research group.

**Andrei Metrikine**

**Dynamics and vibroacoustics of the monopile foundations for offshore wind turbines.**

About keynote speaker

Andrei is Antoni van Leeuwenhoek Professor at the Faculty of Civil Engineering and Geosciences of the Technical University of Delft. Currently he is Chair of the Department of Engineering Structures and Head of Section of Offshore Engineering within the Department of Hydraulic Engineering. Andrei also holds the position of Editor-in-Chief of the Journal of Sound and Vibration. Andrei graduated in radio-physics from the State University of Nizhniy Novgorod, Russia in 1989 and received his PhD and DSc in 1992 and 1998 in St.Petersburg, Russia. In 1994-1998 he held a number of post-doctoral positions, including one at the Institute for Mechanics of the Hannover University, Germany awarded by the Alexander von Humboldt foundation. Since 1999 Andrei is employed by TU Delft.

Andrei's research interests focus on vibrations of and waves in structures that are in contact with solids and fluids and on the dynamics of complex materials. The main application areas of his research include:

Dynamics of offshore wind turbines with the focus on foundations

Dynamics of high-speed trains and railway lines

Dynamics of flexible offshore structures

In terms of fundamentals of vibrations of structures and associated waves in the surrounding media Andrei is most interested in the nonlinear synchronization phenomena (VIV, human-induced vibrations of bridges, ice-induced vibrations), wave-induced instabilities (dynamics of high-speed trains) and multi-physics interactions, including electro- and magneto-elasticity. His research interests also extend to the areas of structural acoustics and pile driving by means of shakers operating at high frequencies.

Andrei is also a professional teacher. Especially he enjoys being a supervisor of MSc graduation theses. To-date, he was involved as university supervisor and chair in nearly 400 theses.

**Patricio García**

**Structural assessments after the earthquakes in Türkiye.**

About keynote speaker

Over his more than ten years of professional experience, Patricio has worked seismic and non-seismic in projects in all of their phases; from the conceptual schematic design and the subsequent full development of the construction drawings to the administration of engineering services during construction. He has work for different companies in Spain and the US.

Project experience

Post-Earthquake Rapid Seismic Damage Assessments of Buildings Gaziantep area, Türkiye.

Seismic assessment of residential buildings, the Netherlands.

Seismic assessment and upgrading of the Nestlé Portugal Headquarter, Lisbon, Portugal.

Atrio. Bogota, Colombia.

New Bus Station and Transit Hub La Rinconada, Caracas, Venezuela.

New Football National Stadium, Caracas, Venezuela.

King Abdulaziz International Airport (KAIA). Jeddah, Saudi Arabia.

IBC. Bucharest, Romania.

Bispebjerg Somatic Hospital, Copenhagen (on going).

BBK Headquarters. Bilbao, Spain.

Health and Wellness Facilities. Doha, Qatar.

BBVA Headquarters. Madrid, Spain.

Iberdrola Steel Roof 'Flying Carpet'. San Agustín de Guadalix, Spain.

New Valencia CF Stadium Towers. Valencia, Spain.

Trafford Center. Torremolinos, Spain.

Say  
hi



Say  
human  
intelligence

Say hi to a new era  
in technology  
and engineering.

Say hi to a future  
powered by human  
talent.

Say hi to a better  
world.

Say hi Ayesa



**3rd Conference on Structural Dynamics (DinEst 2024)**  
**Seville, September 2024**  
**Materials characterization session**



## ROBUST TIMBER-TO-TIMBER CONNECTIONS FOR BUILDINGS TO AVOID DISPROPORTIONATE COLLAPSE

Manuel Buitrago<sup>1\*</sup>, Juan C. Reyes-Suárez<sup>2</sup> and Jose M. Adam<sup>3</sup>

ICITECH, Universitat Politècnica de València  
Camino de Vera s/n, 46022 Valencia, Spain  
<sup>1</sup>e-mail: [mabuimo1@upv.es](mailto:mabuimo1@upv.es)

ICITECH, Universitat Politècnica de València  
Camino de Vera s/n, 46022 Valencia, Spain  
<sup>2</sup>e-mail: [jcreysul@upv.es](mailto:jcreysul@upv.es)

ICITECH, Universitat Politècnica de València  
Camino de Vera s/n, 46022 Valencia, Spain  
<sup>3</sup>e-mail: [joadmar@upv.es](mailto:joadmar@upv.es)

**Keywords:** Timber, Glulam, Laminated Timber, Robustness, Connections, Buildings, Progressive Collapse.

**Abstract.** *Timber buildings are considered the construction of the future given the environmental advantages that this type of construction has over concrete or steel structures. This main advantage is followed by the outstanding characteristics of energy efficiency, thermal and acoustic comfort, lightness and even fire resistance, as well as the economic and temporal advantages of industrialised construction. The use of timber also requires little energy or water, and is 100% renewable. This reality and current promotion of timber structures contrasts drastically, however, with the scarce amount of research carried out in the field of structural robustness in relation to that of other materials (i.e. concrete or steel). This contrast is especially relevant nowadays, as extreme events (e.g. storms, floods, vehicle impacts, explosions or terrorist attacks) that usually cause sudden local-initial failures in structures become more frequent and unpredictable due to climate change and emerging conflicts. In this context, state-of-the-art structural design standards and guidelines indicate that structures should have sufficient structural continuity. This will prevent the propagation of failures because the structure will be able to activate alternative load paths in case of sudden failure of any element. In the case of timber structures, continuity and efficient activation of alternative load paths are considered critical because of the way in which the connections between elements are made and their limited rotation capacity. The main novelty of this study lies in the design of robust timber-timber connections that have subsequently been validated in tests at a 1/3 scale of building subassemblies. The tests have been carried out for two new types of connections, which have also been subsequently modified to improve the structural robustness against sudden column failures.*

## 1 INTRODUCTION

Timber structures are increasingly used in the building sector thanks to their special characteristics in terms of sustainability, energy efficiency, and thermal and acoustic comfort. [1]. Also noteworthy are its resistance qualities, fire resistance, lightness, and those inherent to industrialized construction, such as advantages in costs and execution times. [2]. Increasingly, it is considered to be the construction type of structure of the future and is already an alternative to the classic solutions of concrete or steel structures [3]. In fact, the number of multi-story buildings constructed in the U.S. with timber increased by 50% between July 2020 and December 2021 [4]. Globally, the world timber construction market is expected to grow at an annual rate of 13.6% between 2021 and 2028 [5–7]. Countries where timber has traditionally been used (e.g. Sweden) already have more than 20% of their buildings constructed with this type of structure [8].

Wooden structures are not exempt from collapse. Fröhwald Hansson [9] analyzed the causes and failure modes of up to 127 structures. The most relevant cases occurred in the Siemens Arena (Denmark, 2003), in an exhibition hall (Finland, 2003) or in the Bad Reichenhall Ice Arena (Germany, 2006) [10,11]. Local or initial failures in timber structures can trigger a disproportionate propagation of failure to a global collapse of the structural system.

Progressive collapse of a structure is defined as the disproportionate failure that occurs after an initial or local failure of a small part of the structure that propagates to global failure or failure of a large part of the structure [12]. This initial failure is caused by an event E (e.g. design error, extreme weather, terrorist attack, hurricane) with a certain probability of occurrence. This event is responsible for producing the initial failure I and, in turn, this initial failure can propagate disproportionately. When acting on a structure, strategies can be adopted to reduce the probability of E occurring (e.g. bollards against impacts), or the probability of although E is occurring trying to avoid I (e.g. design of key elements), or the probability that, although E and I occur, the failure does not propagate disproportionately [13,14]. The latter group includes structural robustness methods, understood as the insensitivity of a structure to the local failure of one of its elements, thus allowing this failure not to propagate. Currently, there are two methods for achieving robust structures: prescriptive tying force rules or alternative load paths. Tying consists of providing structural continuity in all directions and between all elements. On the other hand, the alternative load paths method consists of designing the structural system against sudden removals of a load-bearing element in any position (e.g. columns or walls). [15]. Timber structures require robust structural details to avoid the propagation of failures in the form of disproportionate collapse.

The current increasing use of timber constructions contrasts drastically with the number of research studies carried out on the subject of progressive collapse, with respect to those existing with concrete or steel. This shows that there is still a lot of work to be done in the field of timber, where the number of publications is really scarce. To date, few experimental tests have been carried out in this area [16–22], with clear limitations in terms of: connections considered between elements, construction typologies studied, three-dimensional behavior, and alternative load paths mobilized. Therefore, there is still a long way to go, especially in the cases of modular structures, CLT-platform type structures, and post-and-beam structures [23,24]. There is a clear need to make progress in this area, primarily through experimental tests, in order to bring the structural robustness of wood structures up to the level of concrete or steel structures.

This is the objective of the Enroot research project, which consists of improving the robustness of timber structures through the design and evaluation of improved inter-element connections to meet structural robustness requirements. This paper presents the preliminary results of

two tests carried out on scaled building subassemblies, where two different types of connections between timber elements were used to improve the robustness of this type of structure.

After this introduction, Section 2 shows the design of the complete building from which the subassemblies for the test and the design of the connections are extracted. Section 3 describes the test setup and the monitoring used. Section 4 presents the preliminary results obtained, and Section 5 draws the main conclusions of the study and future lines of work.

## 2 DESIGN OF THE BUILDING, SUBASSEMBLY, AND CONNECTIONS

The research approach, based on the testing of robust connections, started with the design of a complete building. The overall dimensions of the building under consideration are  $38.5 \times 32\text{m}$ , with 7 spans of  $5.5\text{m}$  in the long direction and 4 spans of  $8\text{m}$  in the short direction. The height between floors is  $4\text{m}$  for the first floor and  $3.6\text{m}$  for the remaining five floors. Figure 1 shows a plan and a 3D view of the designed building. The loads adopted for the design of the structure were  $2.5\text{kN/m}^2$  as dead load and  $5\text{kN/m}^2$  as live load. The timber used for columns and beams was Glulam GL24h type, available in the Spanish market.

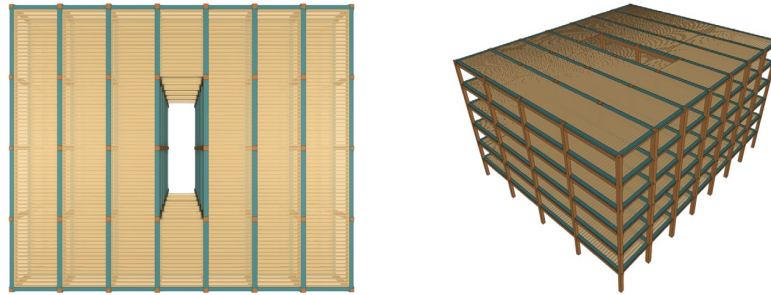


Figure 1: Plan and 3D views of the designed building.

The robust connection test was performed on a substructure taken from the complete building. Due to space and budget constraints, this substructure was scaled up, employing a scale factor of  $1/3$ . Figure 2 shows a sketch of the subassembly representing a part of the whole building composed of three columns ( $170 \times 360\text{mm}$ ) and two first-floor beams ( $170 \times 340\text{mm}$ ), where the central column is removed to simulate the failure scenario, and the lateral columns are fixed representing the continuity of the building. The setup of the subassembly test has been widely used in the past for robustness assessment of concrete, steel, and timber structures [17–20,25,26].

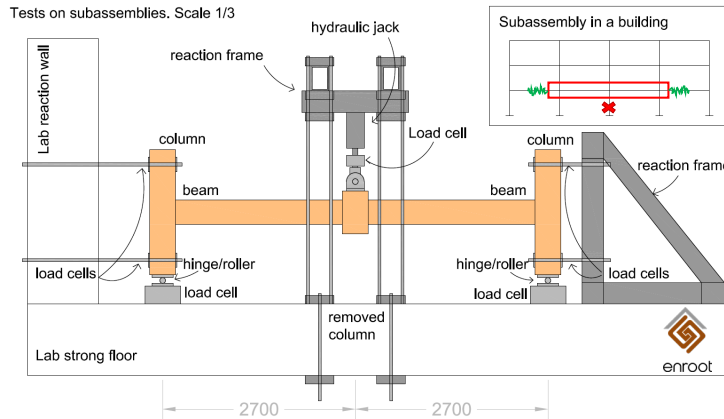


Figure 2: Sketch of the designed subassembly.

After defining the subassembly, two different connections already available in the market were considered, together with two different proposals for a robustness strengthening of the connections for existing buildings. In this paper, only the tests considering the two available connections in the market are presented. These connections are purposely designed for seismic loading and with robustness criteria, allowing some free rotations at the beginning and working as a fixed connection once the free rotation limit is reached. Thus, the connections can be considered as perfectly pinned connections for small rotations (around 2.2 degrees), and as perfectly rigid connections for greater rotations.

Figure 3 and Figure 4 show the two connections considered. Connection #1 is composed of small straight screws on the side of the column (diameter 10mm and length 80mm), while connection #2 is composed of greater 45°-inclined screws on the side of the column (diameter 9mm and length 180mm). Both solutions have the same 45°-inclined screws on the side of the beam.

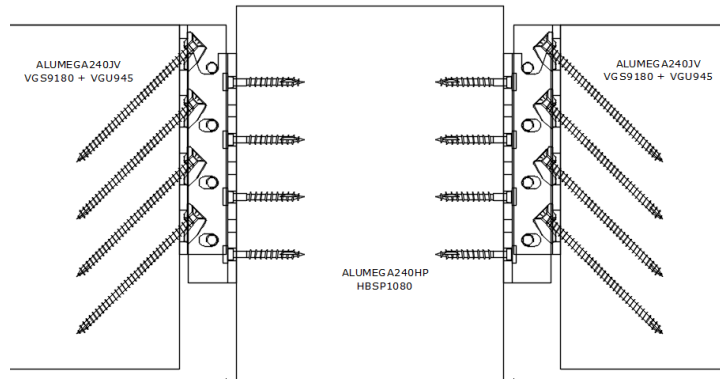


Figure 3: Connection #1 used for Test 1.

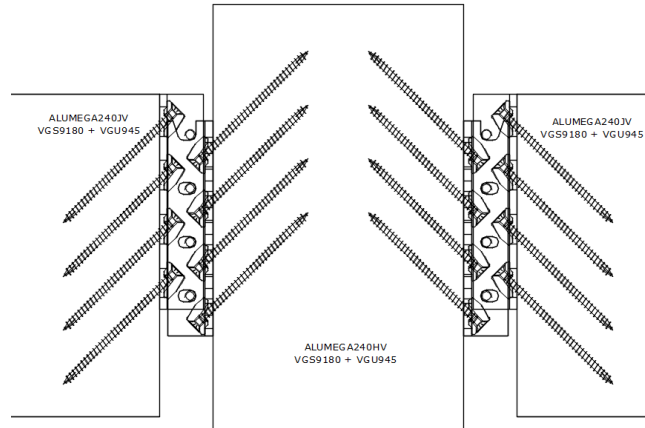


Figure 4: Connection #2 used for Test 2.

### 3 SETUP OF THE TEST AND MONITORING

Figure 5 shows the setup of the test and the monitoring. The test setup follows the designed subassembly defined in Figure 2. Regarding monitoring, each test was highly monitored, with the following sensors:

- 3 load cells located at the hydraulic jack and the hinged supports.
- 3 steel strain gauges located in each of the restrains (12 in total) located at both sides of the subassemblies, as a measure of the load carried out by these elements (WU, WD, EU, ED).

- 2 additional steel strain gauges to control and compensate temperature effects.
- 2 LVDTs located in each of the restrains (8 in total) located at both sides of the sub-assemblies, as a measure of the total absolute vertical and horizontal displacements of the restrains to quantify the total stiffness of the restrains.
- 7 inclinometers distributed along the beams and columns to quantify rotations.
- 7 cable sensors (displacement sensors) distributed along the beams to quantify the deformed shape.

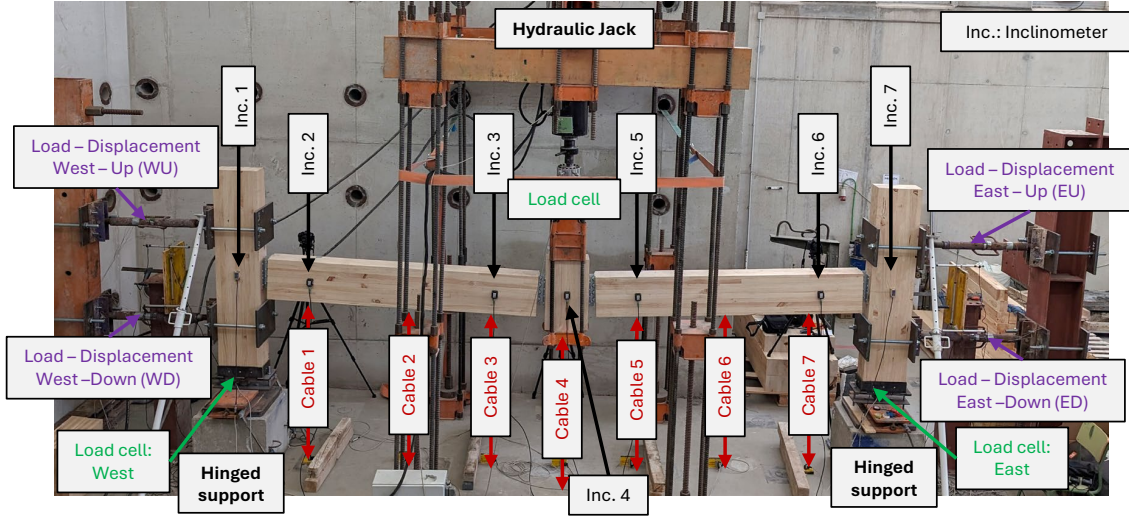


Figure 5: Setup of the test and monitoring.

Tests involved the application of a pseudo-static loading, with displacement control, at a speed of 0.07mm/s. This load was monolithically applied until the failure of the specimen. This manuscript presents the preliminary results of the two first tests carried out with the different described connections.

#### 4 PRELIMINARY RESULTS

Figure 6 shows the force-displacement curves measured with the load cell located next to the hydraulic jack and the displacement registered by the cable 4 sensor. It can be seen that the global response of the two subassemblies is quite similar, almost identical, in terms of stiffness, load and ductility. However, Test 1 had an earlier failure due to the failure of the timber of the central column. As it has been shown in Figure 3, the short straight screws used in this connection demanded the column in pure tension perpendicular to the grain.

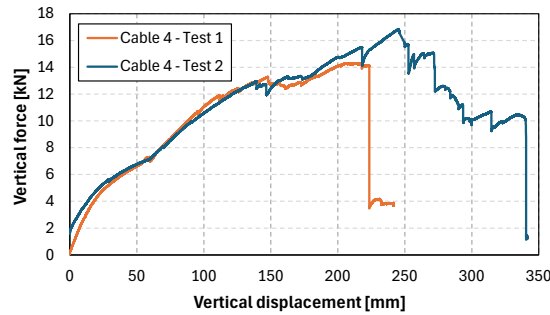


Figure 6: Vertical force-displacement curves.

Figure 7 shows the distribution of the vertical load to the hinged supports versus the vertical displacement measured by Cable 4 sensor. A quite symmetrical distribution was found, at least for Test 2. Those supports that carried more load were coincident with those stiffer at the beginning (e.g. East in Test 1). Once the failure was achieved in the part that carries more load (i.e. East in Test 1 or West in Test 2), the load distribution started to change to the other support, increasing its load.

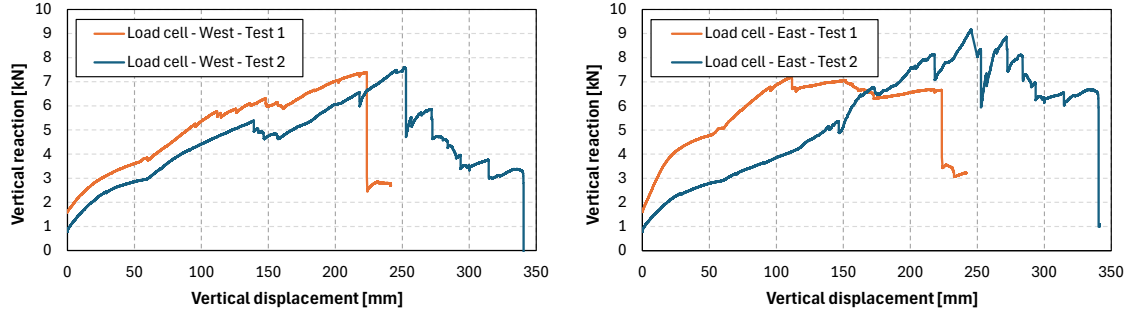


Figure 7: Distribution of the vertical load to the hinged supports.

Figure 8 shows the horizontal reactions and bending moments versus vertical displacement (Cable 4 sensor). The horizontal reaction was evaluated as the mean of the up and down axial loads carried out by the external horizontal restrains at the west and east sides. Bending moments, however, were evaluated as the difference between these axial loads and the computed mean value, multiplied by the lever arm (i.e. 0.8m). Regarding the horizontal reaction (Figures 8a and 8b), it can be seen that negative values are generally computed, representing that catenary action was activated during the test. This catenary action was more activated in the case of Test 2 with connection #2. Regarding bending moments, both tests showed a similar response, with higher flexural action at the East support.

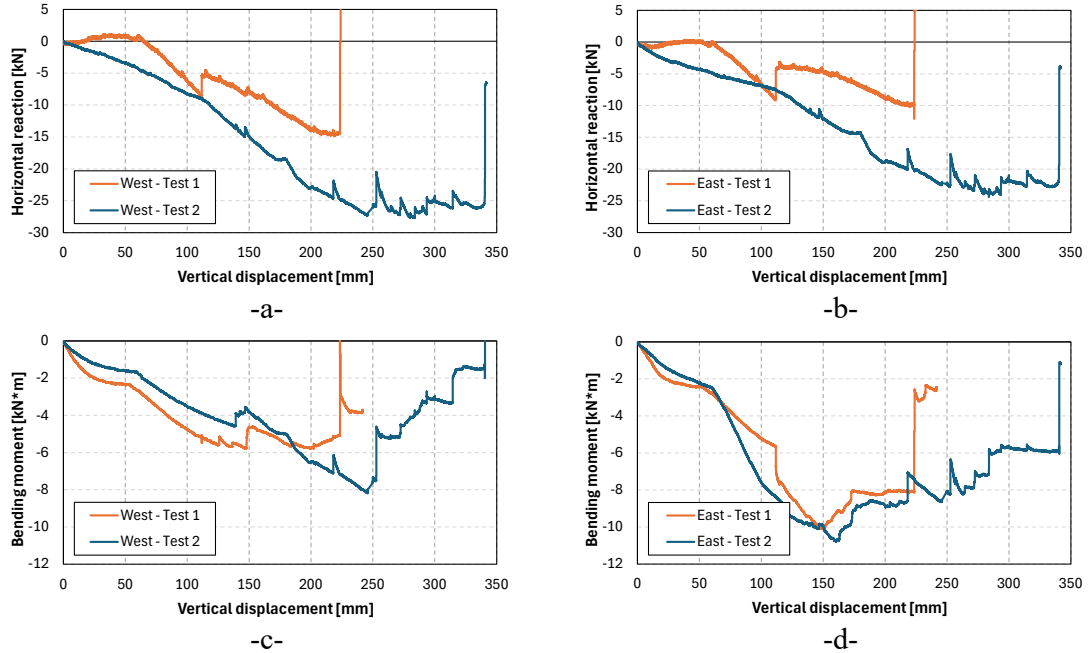


Figure 8: Catenary and flexural actions evaluation. Negative reaction forces mean tension, while negative bending moments mean hogging moments.



The mode of failure was different for the different Tests. Whereas Test 1 response was limited by the premature failure of the timber of the central column (see Figure 9, left), Test 2 achieved the total failure of the connection. It can be noted that the global behavior of both types of connections was similar. Actually, the connection used for Test 1 was also seriously damaged, as shown in Figure 9, indicating that if the timber had not failed, a similar mode of failure with similar loads would have been obtained. However, it is also important to highlight that introducing straight short screws promoted a pure tension demand perpendicular to the grain of the central column, promoting in this was the premature failure of this element.



Figure 9: Mode of failure identified for each Test.

## 5 CONCLUSIONS AND FUTURE WORK

This paper presents the preliminary results of two tests carried out on scaled building sub-structures using two different types of connections intended to improve the robustness of timber structures. From the results obtained it can be concluded that, although the two connections evaluated had similar results, connection #2 performed better, since it did not demand the central column to tensile forces perpendicular to the grain and the failure mode occurred at a slightly higher load and never limited by the strength of the timber.

Future work is intended to analyze the results obtained in greater depth, as well as to test new solutions to improve the robustness of the connections using strengthening solutions that can be applied to existing buildings.

## ACKNOWLEDGEMENTS

This article is part of a project (Enroot) that has received funding from the Generalitat Valenciana – Conselleria de Innovación, Universidades, Ciencia y Sociedad Digital under the GE 2023 call (CIGE/2022/120). The authors would also like to express their gratitude for funding received under the postdoctoral Grant IJC2020-042642-I funded by MCIN/AEI/10.13039/501100011033 and by the “European Union NextGenerationEU/PRTR”. The authors are also grateful to the Rotho Blaas SRL company for their invaluable cooperation.

## REFERENCES

- [1] Arriaga F. Estado actual de la construcción con madera en España. Quad d'Estructures - Asoc Consult Estructuras 2020.
- [2] Think Wood. 4 Things to Know about Mass Timber 2022.
- [3] Herranz-Molina JM. De la ciudad de hormigón, a la ciudad de madera. Raíces - Madera y Construcción 2022.
- [4] Niiler E. Wooden Skyscrapers Are on the Rise. Wall Str J 2022.
- [5] Grand View Research. Cross Laminated Timber Market Size Report, 2021-2028. 2020.
- [6] Grand View Research. Timber Construction Connectors Market Report, 2021-2028. 2020.
- [7] Grand View Research. Glue Laminated Timber Market Size, Share, Industry Report, 2018-2025. 2016.
- [8] Leszczyszyn E, Heräjärvi H, Verkasalo E, Garcia-Jaca J, Araya-Letelier G, Lanvin J-D, et al. The Future of Wood Construction: Opportunities and Barriers Based on Surveys in Europe and Chile. Sustainability 2022;14:4358. <https://doi.org/10.3390/su14074358>.
- [9] Frühlwald Hansson E. Analysis of structural failures in timber structures: Typical causes for failure and failure modes. Eng Struct 2011;33:2978–82. <https://doi.org/10.1016/J.ENGSTRUCT.2011.02.045>.
- [10] Hansson M, Larsen HJ. Recent failures in glulam structures and their causes. Eng Fail Anal 2005;12:808–18. <https://doi.org/10.1016/J.ENGFAILANAL.2004.12.020>.
- [11] Munch-Andersen J, Dietsch P. Robustness of large-span timber roof structures — Two examples. Eng Struct 2011;33:3113–7. <https://doi.org/10.1016/J.ENGSTRUCT.2011.03.015>.
- [12] Starossek U. Typology of progressive collapse. Eng Struct 2007;29:2302–7. <https://doi.org/10.1016/J.ENGSTRUCT.2006.11.025>.
- [13] The Institution of Structural Engineers. Practical guide to structural robustness and disproportionate collapse in buildings. 1st ed. London: The Institution of Structural Engineers; 2010.
- [14] EN 1991-1-7. Eurocode 1: Actions on structures - Part 1-7: General actions - Accidental actions; 2006.
- [15] Adam JM, Parisi F, Sagaseta J, Lu X. Research and practice on progressive collapse and robustness of building structures in the 21st century. Eng Struct 2018;173:122–49.



<https://doi.org/10.1016/j.engstruct.2018.06.082>.

- [16] Lyu CH, Gilbert BP, Guan H, Karampour H, Gunalan S. Finite element modelling of the progressive collapse of post-and-beam mass timber building substructures under edge and corner column removal scenarios. *J Build Eng* 2022;49:104012. <https://doi.org/10.1016/J.JOBE.2022.104012>.
- [17] Lyu CH, Gilbert BP, Guan H, Underhill ID, Gunalan S, Karampour H. Experimental study on the quasi-static progressive collapse response of post-and-beam mass timber buildings under an edge column removal scenario. *Eng Struct* 2021;228:111425. <https://doi.org/10.1016/J.ENGSTRUCT.2020.111425>.
- [18] Lyu CH, Gilbert BP, Guan H, Underhill ID, Gunalan S, Karampour H. Experimental study on the quasi-static progressive collapse response of post-and-beam mass timber buildings under corner column removal scenarios. *Eng Struct* 2021;242:112497. <https://doi.org/10.1016/J.ENGSTRUCT.2021.112497>.
- [19] Lyu CH, Gilbert BP, Guan H, Underhill ID, Gunalan S, Karampour H, et al. Experimental collapse response of post-and-beam mass timber frames under a quasi-static column removal scenario. *Eng Struct* 2020;213:110562. <https://doi.org/10.1016/J.ENGSTRUCT.2020.110562>.
- [20] Cheng X, Gilbert BP, Guan H, Underhill ID, Karampour H. Experimental dynamic collapse response of post-and-beam mass timber frames under a sudden column removal scenario. *Eng Struct* 2021;233:111918. <https://doi.org/10.1016/J.ENGSTRUCT.2021.111918>.
- [21] Hua Y, Chun Q. Influence of Pu-zuo on progressive collapse behavior of ancient southern Chinese timber buildings built in the Song and Yuan dynasties: Experimental Research. *Eng Fail Anal* 2022;137:106405. <https://doi.org/10.1016/j.engfailanal.2022.106405>.
- [22] Grantham R, Enjily V. UK design guidance for multi-storey timber frame buildings. 8th World Conf. Timber Eng., 2004, p. 6.
- [23] Huber JAJ, Ekevad M, Girhammar UA, Berg S. Structural robustness and timber buildings—a review. *Wood Mater Sci Eng* 2019;14:107–28. <https://doi.org/10.1080/17480272.2018.1446052>.
- [24] Elkady N, Augusthus Nelson L, Weekes L, Makoond N, Buitrago M. Progressive collapse: past, present, future and beyond. *Structures* 2024;62:106131. <https://doi.org/10.1016/j.istruc.2024.106131>.
- [25] Meng B, Zhong W, Hao J, Song X. Improving anti-collapse performance of steel frame with RBS connection. *J Constr Steel Res* 2020;170:106119. <https://doi.org/10.1016/j.jcsr.2020.106119>.
- [26] Kai Q, Li B. Dynamic performance of RC beam-column substructures under the scenario of the loss of a corner column-Experimental results. *Eng Struct* 2012;42:154–67. <https://doi.org/10.1016/j.engstruct.2012.04.016>.

## PHYSICAL PROPERTIES TRACKING OF A LABORATORY-SCALED TWO-STOREY BUILDING MODEL

Alvaro Magdaleno<sup>1\*</sup>, Alvaro Iglesias-Pordomingo<sup>1</sup>, Lara del Val<sup>1</sup>, Emiliano Pereira<sup>2</sup>  
and Antolin Lorenzana<sup>1</sup>

<sup>1</sup> ITAP. Universidad de Valladolid  
Paseo del Cauce, 59, 47011 Valladolid  
e-mail: {alvaro.magdaleno, alvaro.iglesias, lara.val, antolin.lorenzana}@uva.es

<sup>2</sup> Department of Signal Processing and Communications. Universidad de Alcalá  
Ctra. Madrid-Barcelona, km 33.600, 28805 Alcalá de Henares  
e-mail: emiliano.pereira@uah.es

**Keywords:** Modal identification, physical properties, two-storey building, structural health monitoring

**Abstract.** Structural health monitoring is a topic that has gained much interest in the last decades. It is devoted to mitigating the effects of the natural ageing of structures among other aims. Data acquisition systems are deployed on structures and ambient vibration data is stored and processed to assess the actual structural state and foresee potential issues [1, 2]. Natural frequencies are one of the most commonly estimated properties and, by means of a variety of algorithms, which usually involve computational models, damage can be detected [3, 4].

In this work, a methodology is proposed to track the evolution of the physical properties of a two-storey structural model that represents a slender shear building. As shown in Figure 1a, it is composed of two rigid, thick plates that represent the floors connected via several thin aluminium sheets that represent the columns. This element disposal restrains the movement of the model to one vertical plane. In addition, these materials confer the resulting model a set of interesting dynamic properties, such as low damping and low natural frequencies, which are very adequate for the purposes of this work. The modal properties of this model are estimated through operational modal analysis (OMA) techniques. The acceleration of both storeys is measured by means of two accelerometers one on each floor connected to a data acquisition system. This system automatically records a set of data every hour and records it in a computer. In parallel, a Python script runs periodically to check the presence of new data files and process them. This script is responsible for pre-processing the data, performing the operational modal analysis to estimate the modal properties of the model, tracking its physical properties and storing the results in an online time-series database (TSDB).

The OMA algorithm used in this work is the well-known covariance-driven stochastic subspace identification method (SSI-cov), that provides accurate estimates of natural frequencies, damping ratios and unscaled mode shapes. By means of these modal properties, an estimation of the evolution of the physical properties is obtained. To do so, first the structure is assimilated to a specific model such as the one shown in Figure 1b. This model is composed of two degrees of freedom, so two concentrated masses ( $m_1$  and  $m_2$ ), two spring constants ( $k_1$  and  $k_2$ ) and two

damping coefficients ( $c_1$  and  $c_2$ ) need to be determined. The algorithm, however, does not provide with the specific values of the physical properties. Instead, for each measurement, the variation of each property is calculated with respect to the previous one and tracked over time. The variation ratio of the six properties (which equals to 1 if that property does not change from one measurement to the next) is finally stored in an online database, which is easily queried via web. Finally, several scenarios are presented to show the usefulness of the tracking algorithm. In these scenarios, both masses and stiffness coefficients are alternatively modified. These modifications are tracked, and the obtained variations compared to the true values.

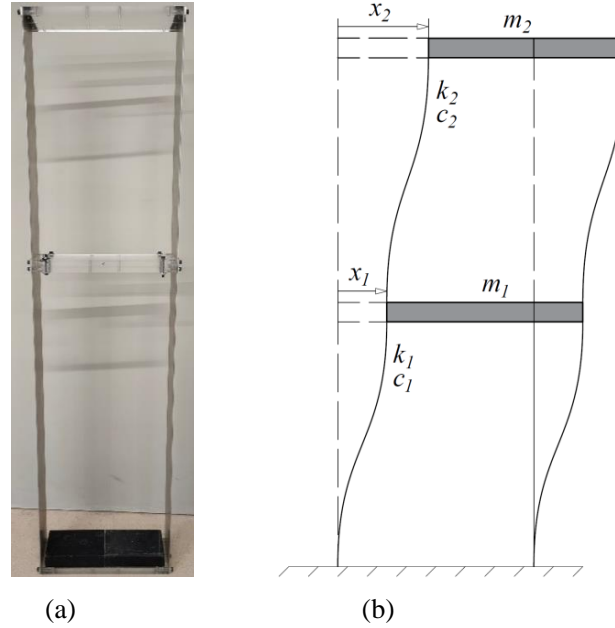


**Figure 1.** (a) Picture of the structural model and (b) its conceptual model

### Acknowledgements

The authors wish to acknowledge to the AEI, Spanish Government (10.13039/501100011033), and to “ERDF A way of making Europe”, for the partial support through the grant PID2022-140117NB-I00.

### References

- [1] Zhang, C.W. et al. (2022) Vibration feature extraction using signal processing techniques for structural health monitoring: A review. *Mechanical Systems and Signal Processing*, 177, 109175. DOI: 10.1016/j.ymssp.2022.109175
- [2] Deng, Z.H., Huang, M.S., Wan, N. and Zhang, J.W. (2023) The current development of Structural Health Monitoring for bridges: a review. *Buildings*, 13(6), 1360. DOI: 10.3390/buildings13061360
- [3] Burgos, D.A.T. et al. (2020) Damage identification in Structural Health Monitoring: A brief review from its implementation to the use of data-driven applications. *Sensors*, 20(3), 733. DOI: 10.3390/s20030733
- [4] Palma, P. and Steiger, R. (2020) Structural health monitoring of timber structures – Review of available methods and case studies. *Construction and Building Materials*, 248, 118528. DOI: 10.1016/j.conbuildmat.2020.118528

## MODULUS OF ELASTICITY OF CONCRETE AT DIFFERENT TEMPERATURES BY MEANS OF MODAL ANALYSIS

Manuel Aenlle<sup>1</sup>, Héctor Cifuentes<sup>2,\*</sup> and Pelayo Fernández<sup>1</sup>

<sup>1</sup> Department of Construction and Fabrication Engineering. University of Oviedo, Spain  
e-mail: {aenlle, fernandezpelayo}@uniovi.es

<sup>2</sup> Department of Continuum Mechanics and Structural Analysis. School of Engineering. University of Seville, Spain  
e-mail: bulte@us.es

**Keywords:** Concrete, Modulus of elasticity, Temperature, Modal analysis

**Abstract.** *Concrete is one of the most widely used materials in structures today, and in many applications, it operates at temperatures different from ambient. However, the mechanical strength of concrete, and consequently the modulus of elasticity, decreases as the temperature increases. Some of the drawbacks of concrete can be mitigated by incorporating short fibers. Reinforcing concrete with fibers creates a more homogeneous material whose tensile strength and fatigue resistance are greater than those of concrete without fibers. The modulus of elasticity of concrete can be determined from a compression test defined in the standard UNE-EN 12390-13. According to this test, to obtain the modulus of elasticity, it is necessary to measure deformations, usually with strain gauges attached to the specimen. However, the process of attaching the gauges at high temperatures presents serious difficulties. An alternative to avoid this issue is to use dynamic tests. In this work, the tangent modulus of elasticity of concrete has been determined in the temperature range of 20°C-300°C through dynamic tests on specimens with dimensions of 44x10x10 cm. Three different types of concrete were tested:*

- *Concrete without fibers.*
- *Concrete reinforced with black macro polypropylene fibers.*
- *Concrete reinforced with white micro polypropylene fibers.*

## MECHANICAL BEHAVIOUR OF PRECAST CONCRETE PAVERS CURING IN CO<sub>2</sub> ENVIRONMENT

**A.M. Merino-Lechuga<sup>1\*</sup>, D. Suescum-Morales<sup>1</sup>, D. Cantador-Fernandez<sup>2</sup>, A. González-Caro<sup>2</sup>, E. Fernández-Ledesma<sup>1</sup>, J.R. Jiménez<sup>1</sup> and J.M. Fernández-Rodríguez<sup>2</sup>**

<sup>1</sup> Departamento de Ingeniería Rural, Construcciones Civiles y Proyectos de Ingeniería.  
E.P.S. de Belmez (Univ. de Córdoba) Av. De la Universidad S/N, Belmez, 14240 Córdoba, Spain.  
e-mail: {ammlechuga, p02sumod, efledesma, jrjimenez}@uco.es

<sup>2</sup> Departamento de Química Inorgánica e Ingeniería Química.  
E.P.S. de Belmez (Univ. de Córdoba) Av. De la Universidad S/N, Belmez, 14240 Córdoba, Spain.  
e-mail: {um1feroj, q32gocaa, p12cafed}@uco.es

**Keywords:** construction and demolition waste; CO<sub>2</sub> curing; CO<sub>2</sub> uptake; accelerated carbonation

### Abstract.

Since the mid-19th century, the boom in the economy and industry has grown exponentially. This has led to an increase in pollution due to rising Greenhouse Gas (GHG) emissions and the accumulation of waste, leading to an increasingly imminent future scarcity of raw materials and natural resources.

Carbon dioxide (CO<sub>2</sub>) is one of the primary greenhouse gases, accounting for up to 55% of Greenhouse Gas (GHG) emissions. The manufacturing of construction materials generates approximately 73% of CO<sub>2</sub> emissions, with Portland cement production contributing to 41% of this figure. Hence, there is scientific and social alarm regarding the carbon footprint of construction materials and their influence on climate change. Carbonation of concrete is a natural process whereby CO<sub>2</sub> from the environment penetrates the material, primarily through pores and microcracks. Once inside, carbon dioxide reacts with calcium hydroxide (Ca(OH)<sub>2</sub>) and/or CSH, yielding calcium carbonates (CaCO<sub>3</sub>) and silica gel. Consequently, construction materials act as carbon sinks.

This research investigated the effect of accelerated carbonation on the physical, mechanical, and chemical properties of two types of non-structural vibrated concrete pavers (conventional and draining) made from natural aggregates and two types of recycled aggregates from construction and demolition waste (CDW). Natural aggregates were replaced by recycled aggregates using a volumetric substitution method, and the CO<sub>2</sub> capture capacity was calculated. Two curing environments were utilized: a carbonation chamber with 5% CO<sub>2</sub> and a standard climatic

chamber with atmospheric CO<sub>2</sub> concentration. Additionally, the effect of curing times of 1, 3, 7, 14, and 28 days on concrete properties was analyzed. Accelerated carbonation increased the apparent dry density, reduced water-accessible porosity, improved compressive strength, and decreased setting time to achieve greater mechanical strength. The maximum CO<sub>2</sub> capture ratio was achieved with the use of recycled concrete aggregate (52.52 kg/t) in the draining paver. Accelerated carbonation conditions led to a 525% increase in carbon capture compared to curing under atmospheric conditions. Accelerated carbonation of cement-based products containing recycled aggregates from construction and demolition waste is a promising technology for CO<sub>2</sub> capture and utilization, offering a means to mitigate the effects of climate change and promote the new paradigm of circular economy.

## DAMPING OF LAMINATED GLASS PLATES. COMPARISON OF NUMERICAL AND EXPERIMENTAL RESULTS

M. Aenlle<sup>1\*</sup>, Carlos Cima<sup>2</sup>, and F. Pelayo<sup>2</sup>

<sup>1</sup> Dept. Construction and Manufacturing Engineering  
Campus de Gijón. s/n. Universidad de Oviedo, Gijón. 33203  
e-mail: [aenlle@uniovi.es](mailto:aenlle@uniovi.es)

<sup>2</sup> Dept. Construction and Manufacturing Engineering  
Campus de Gijón. s/n. Universidad de Oviedo, Gijón. 33203  
{F. Pelayo} e-mail: [fernandezpelayo@uniovi.es](mailto:fernandezpelayo@uniovi.es)

**Keywords:** Laminated glass. Operational Modal Analysis. Effective Thickness. Viscoelasticity

**Abstract.** *Laminated glass beams and plates are sandwich elements which show a viscoelastic behavior. In recent years, the concept of dynamic effective thickness has been proposed to estimate the modal parameters of laminated glass elements. However, when the analytical predictions are compared with the experimental results, a good accuracy is obtained in the natural frequencies, whereas large discrepancies are obtained in the loss factors. In this paper, the natural frequencies and loss factors of two laminated glass plates are predicted from the frequency response function (FRF) obtained with a numerical model, using the half-power bandwidth method. The numerical predictions are compared with the analytical results obtained with the dynamic effective thickness concept and with the experimental modal parameters estimated with operational modal analysis.*

### 1 INTRODUCTION

Laminated glass plates are sandwich layered materials, which consist of two or more plies of monolithic glass (Fig. 1) with one or more interlayers of a polymeric material [1,2]. Polyvinyl butyral (PVB) is the most widely used interlayer material, which is available in thicknesses of 0.38 mm or a multiple of this value (0.76 mm, 1.12 mm, and 1.52 mm). All polymeric interlayers are viscoelastic in nature [1,2], i.e. their mechanical properties are frequency (or time), and temperature dependent, and consequently laminated glass elements exhibit a viscoelastic behavior. Glass mechanical behavior is usually modeled as linear-elastic (prior to glass breakage), whereas polymeric interlayers are commonly characterized as linear viscoelastic.

Several analytical models were proposed in the past to predict the modal parameters of sandwich plates with viscoelastic core. Nashif et al. [3] proposed to extend the Ross, Kerwin, and Ungar (RKU) [4], developed for beams, to the two-dimensional case of rectangular laminated glass plates. Mead [5] and Mead and Yaman [6] proposed a model to predict the vibration

response of a rectangular sandwich plate, consisting of two glass layers with same thickness and one viscoelastic interlayer, subject to a harmonic line force which varies sinusoidally across the plate.

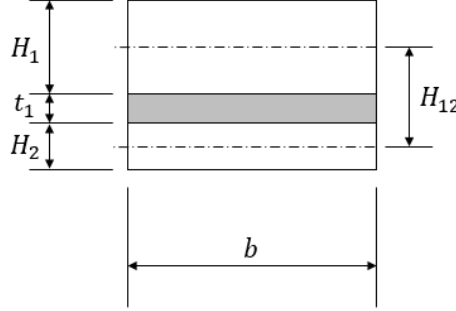


Figure 1. Detail of the section of a laminated glass beam composed of two glass layers and one polymeric interlayer.

Gallupi and Royer-Carfagni [7] developed a model to calculate the static response of laminated glass plates with three glass layers and two polymeric interlayers. Pelayo and Aenlle [8], applying the correspondence principle [1, 2] to the static stiffness formulated by Galuppi and Royer Carfagni [7], derived a dynamic effective stiffness, which was used to predict the modal parameters of laminated glass plates.

Due to the fact that laminated glass plates exhibit a viscoelastic behavior, the wavenumbers  $k^* = k_R + ik_I$  are complex. The complex wavenumbers are needed when analytical equations are used to predict the natural frequencies and the loss factors. The complex wavenumber can be obtained from the sixth-order differential equation that governs the flexural wave motion of a rectangular constrained-layer sandwich, but this calculation is tedious and complicated. In order to simplify the estimation of modal parameters, we can assume  $k_R = 0$  and the components  $k_I$  can be taken from the literature or obtained from an undamped numerical model.

This methodology has been successfully used in the literature [8,9] to predict the natural frequencies of laminated glass beams and plates. With respect to the loss factors, large errors can be obtained because of the assumption  $k_R = 0$ . In this paper, the natural frequencies and loss factors of two laminated glass plates are predicted from the frequency response function (FRF) obtained with a numerical model, using the half-power bandwidth method. The numerical predictions are compared with the analytical results obtained with the dynamic effective thickness concept and with the experimental modal parameters estimated with operational modal analysis.

## 2 THEORY

Galuppi and Royer-Carfagni [7] derived a model to predict the static response of a rectangular laminated glass plate with dimensions  $a \times b$ , composed of two glass layers and one interlayer, and subject to a uniform pressure and with different boundary configurations at the borders. Assuming linear elastic materials, the following expression for the static stiffness was obtained:



$$D_{S2} = D_{T2} \left( 1 + \frac{Y_{P2}}{1 + \frac{\psi_{P2} a^2}{g_{P2}}} \right) \quad (1)$$

Where the subindices 's', 'p', and '2', indicate static, plate and two glass layers, respectively. and:

$D_{T2} = \frac{E}{12(1-\nu^2)} (H_1^3 + H_2^3)$	Stiffness of glass layers
$Y_{P2} \frac{12H_{12}^2 H_1 H_2}{(H_1^3 + H_2^3)(H_1 + H_2)}$	Geometrical parameter
$\psi_{P2}$	Geometrical parameter
$g_{P2} \frac{G_t(1-\nu^2)(H_1 + H_2)a^2}{EH_1 H_2 t_1}$	Geometrical and material parameter
$G_t$	Shear modulus for the polymeric interlayer
$E$	Young's modulus of glass layers
$\nu$	Poisson ratio of glass layers
$H_i$	Thickness the 'i-th' glass layer
$t_1$	Thickness of the interlayer
$H_{12} = t_1 + \left( \frac{H_1 + H_2}{2} \right)$	Distance between neutral axis of glass layers
$a$	Dimension of a rectangular plate

Using the secant stiffness approximation [7, 10] the static stiffness is given by:

$$D^{SSS}(t, T)_{S2} = D_{T2} \left( 1 + \frac{Y_{P2}}{1 + \frac{\psi_{P2} a^2}{g_{P2}(t, T)}} \right) \quad (2)$$

Where t and T indicate time and temperature, respectively, and  $\psi_{P2}$  is a parameter dependent on loading and boundary conditions [7].

Applying the correspondence principle [1,2] to eq. (1), the following expression for the effective complex flexural stiffness of a laminated glass plate, with two glass layers and one polymeric interlayer, is derived.

$$D^*(\omega, T)_2 = D_{T2} \left( 1 + \frac{Y_{P2}}{1 - \frac{k^{*2} a^2}{g_{P2}^*(\omega, T)}} \right) \quad (3)$$

Where  $\omega$  indicates frequency, and  $g_{P2}^*(\omega, T)$  is given by:

$$g_{P2}^*(\omega, T) = \frac{G_t(\omega, T)(1-\nu^2)}{E} \frac{(H_1 + H_2)a^2}{H_1 H_2 t} \quad (4)$$

This expression coincides with that developed by Mead and Yaman [6] for a symmetric ( $H_1 = H_2$ ) rectangular sandwich plate with viscoelastic core.

The natural frequencies and the loss factors can be estimated with the expression:

$$\omega^{*2} = \omega^2(1 + i \cdot \eta) = (k^*)^4 \frac{D^*(\omega, T)_2}{\rho_G(H_1 + H_2) + \rho_t t_1} \quad (5)$$

Where  $\rho_G$  and  $\rho_t$  are the mass-density of the glass and the polymeric layers, respectively.

Parameter  $k_R$  is difficult to obtain analytically, and no values are reported in the literature. We can simplify eqs. (3) and (5) considering  $k_R = 0$ , i.e.  $k^* = ik_I$ , and they become:

$$D^*(\omega, T)_2 = D_{T2} \left( 1 + \frac{Y_{P2}}{1 + \frac{k_I^2 a^2}{g_{P2}^*(\omega, T)}} \right) \quad (6)$$

and:

$$\omega^{*2} = \omega^2(1 + i \cdot \eta) = k_I^4 \frac{D^*(\omega, T)_2}{\rho_G(H_1 + H_2) + \rho_t t_1} \quad (7)$$

### 3 EXPERIMENTAL RESULTS

A rectangular laminated glass plate of dimensions  $a = 1400 \text{ mm}$  and  $b = 1000 \text{ mm}$ , glass thicknesses  $H_1 = 7.82 \text{ mm}$  and  $H_2 = 7.83 \text{ mm}$ , and a polyvinyl butyral (PVB) core thickness  $t_1 = 0.76 \text{ mm}$ , was tested at room temperature  $T = 20^\circ \text{C}$  using operational modal analysis (OMA). The plate was pinned supported at the four corners using four wooden balls with a diameter of 50 mm. The plate was excited applying many small hits with an impact hammer on the plate surface randomly in time and space. The responses of the plate were measured using 16 accelerometers with a sensitivity of 100 mv/g, uniformly distributed (Figure 2). The responses were recorded for approximately 5 minutes with a sampling frequency of 1632 Hz and using a 16 channel Compact DAQ acquisition system by National instruments. The first 8 modes were estimated using the frequency domain decomposition (FDD) [12]. The results are presented in Tables 1(natural frequencies) and Table 3 (loss factors).

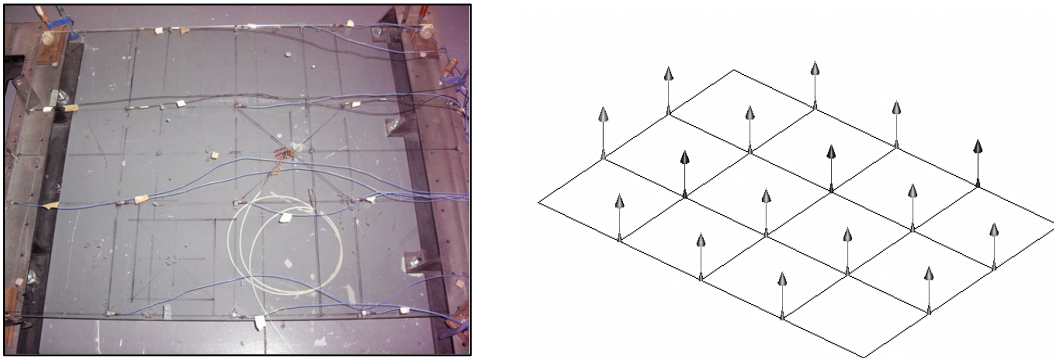


Figure 2. Test setup of the OMA tests.

#### 4 NUMERICAL SIMULATIONS

A numerical model of the plate was also assembled in ABAQUS and the modal parameters (natural frequencies and damping ratios) at temperatures  $T = 20^\circ\text{C}$ ,  $25^\circ\text{C}$ , and  $30^\circ\text{C}$ , respectively, were estimated from the numerical frequency response function (FRF) (Fig. 3) using the half-power bandwidth method.

The following material properties were considered for the glass: Young's modulus  $E = 72000 \text{ MPa}$  Poisson's ratio  $\nu = 0.22$  and mass-density  $\rho_G = 2500 \text{ kg/m}^3$ . With respect to the PVB core, a mass-density  $\rho_t = 1030 \text{ kg/m}^3$  and complex shear modulus  $G_2^*(\omega, T)$  determined in previous works [13, 14] were considered in the simulations.

The numerical natural frequencies are presented in Table 1 and the loss factors in Table 3. The numerical model, a detail of the mesh, and the mode shapes are shown in Fig. 4.

#### 5 ANALYTICAL RESULTS

The modal parameters at temperatures  $T = 20^\circ\text{C}$ ,  $25^\circ\text{C}$ , and  $30^\circ\text{C}$ , were also estimated using eq. (7), where the wavenumbers  $k_I$  (see Table 5) were estimated using a monolithic glass FE model with the same dimensions, total thickness, and boundary conditions, as the laminated glass plate.

The analytical modal parameters are presented in Tables 1 (natural frequencies) and Table 3 (loss factors), respectively.

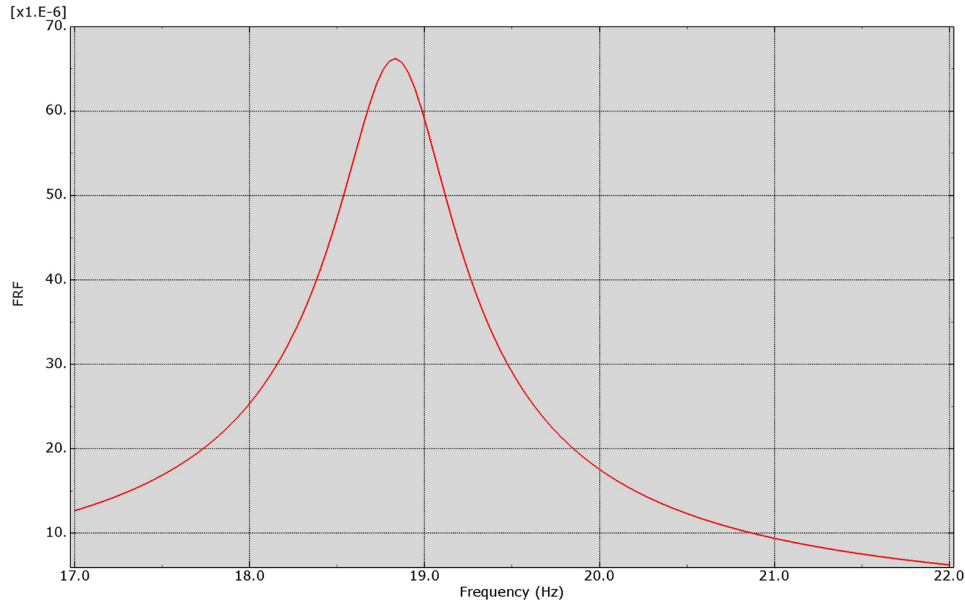


Figure 3. Detail of the FRF (magnitude) corresponding to the first mode at  $25^\circ\text{C}$ .

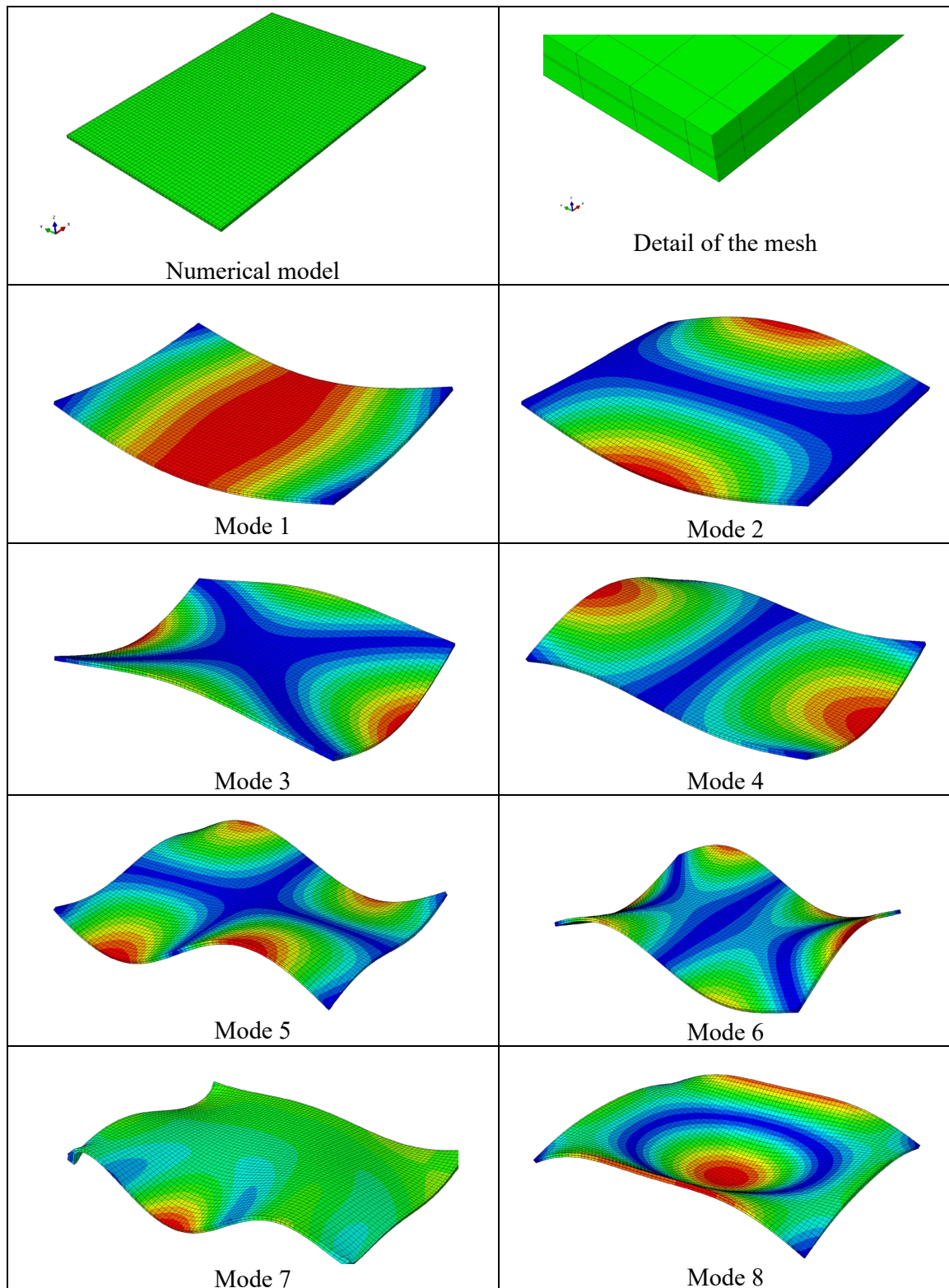


Figure 4. Numerical model and mode shapes.

## 6 DISCUSSION

The errors between the experimental, numerical and analytical natural frequencies are shown in Table 2. It can be observed that the errors are less than 8%, which indicates that both the analytical and the numerical models predict with a good accuracy the natural frequencies. However, less error is obtained with the numerical model.

The discrepancies between the numerical and the analytical predictions increases with increasing temperature.

Mode	20°C			25°C		30°C	
	Experimental	FEM	Eq. (7)	FEM	Eq. (7)	FEM	Eq. (7)
1	18.71	19.09	19.36	18.83	19.262	18.46	19.124
2	42.61	43.87	45.60	42.87	45.242	41.406	44.622
3	48.91	51.65	53.18	50.41	52.709	48.907	51.887
4	66.07	66.51	66.42	65.85	65.731	64.818	64.518
5	102.91	107.03	109.56	103.65	107.894	99.463	105.241
6	120.9	120.14	119.45	118.63	117.576	116.329	114.573
7	131.62	135.01	137.33	131.93	134.919	127.681	131.273
8	167.11	176.37	179.45	171.88	175.837	166.01	170.549

Table 1: Natural frequencies (Hz) of the laminated glass plate at 20°C, 25°C and 30°C.

Mode	20°C			25°C	30°C
	Exp-FEM	Exp-Eq. (7)	FEM-Eq. (7)	FEM-Eq. (7)	FEM-Eq. (7)
1	2,03	3,47	-1.41	2,30	3,60
2	2,95	7,03	-3.94	5,55	7,77
3	5,60	8,73	-2.96	4,55	6,09
4	0,66	0,54	0.14	-0,18	-0,46
5	4,00	6,46	-2.36	4,10	5,81
6	-0,63	-1,20	0.57	-0,89	-1,51
7	2,57	4,34	-1.72	2,27	2,81
8	5,54	7,39	-1.75	2,30	2,73

Table 2: Errors between the natural frequencies estimated by OMA (Exp.) and the predictions obtained with a numerical model (FEM) and with Eq. (7)

Mode	20°C			25°C		30°C	
	Experimental	FEM	Eq. (7)	FEM	Eq. (7)	FEM	Eq. (7)
1	0.0224	0.0184	0.0078	0.0229	0.0161	0.0768	0.0372
2	0.0365	0.0354	0.0132	0.034	0.0249	0.092	0.0469
3	0.0423	0.0360	0.0143	0.0328	0.0265	0.107	0.0499
4	0.0157	0.0143	0.0158	0.0163	0.0291	0.044	0.0554
5	0.0270	0.0321	0.0190	0.0364	0.0372	0.101	0.0723
6	0.0127	0.0153	0.0196	0.0234	0.0391	0.0563	0.0757
7	0.0310	0.0263	0.0207	0.0314	0.0425	0.0833	0.0812
8	0.0393	0.0293	0.0231	0.036	0.0480	0.11	0.0914

Table 3: Loss factors of the laminated glass plate at 20°C, 25°C and 30°C.

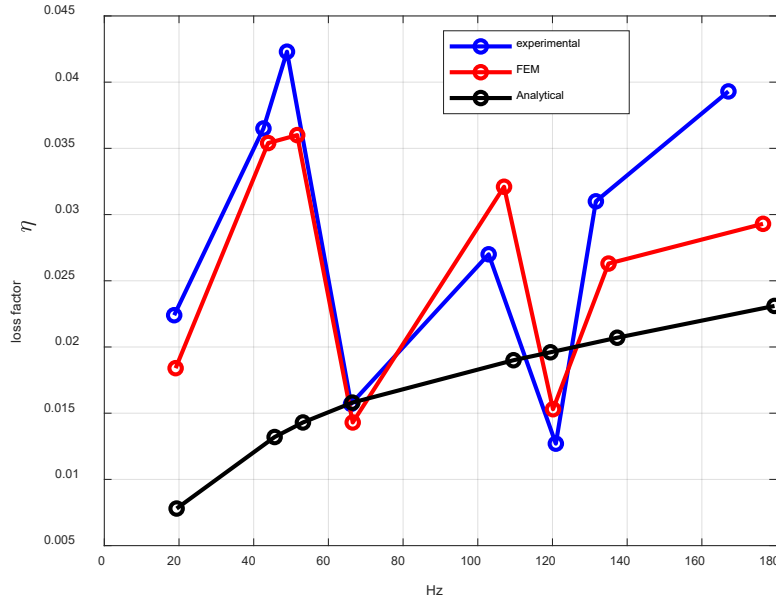


Figure 5. Numerical and analytical loss factors at 20°C.

The errors in the loss factors are presented in Table 4. It can be observed that the discrepancies between the experimental and the numerical values are less than 20%. On the other hand, errors of 65% have been obtained between the experimental values and the analytical predictions, which indicates that the numerical model predicts the loss factors with a better accuracy.

Due to the assumption  $k_R = 0$ , Eq. (7) predicts the loss factors increasing as increasing frequency (Fig. 5). On the other hand, the numerical model is more accurate and predicts the trend obtained experimentally (Fig. 5).

Mode	20°C			25°C	30°C
	Exp-FEM	Exp-Eq (6)	FEM-Eq6()	FEM-Eq (6)	FEM-Eq (6)
1	-17.86	-65.00	57.61	-58.18	-51.60
2	-3.01	-63.88	62.71	-57.03	-48.99
3	-14.89	-66.25	60.28	-56.80	-53.34
4	-8.92	0.61	-10.49	18.83	25.86
5	18.74	-29.56	40.81	-34.32	-28.41
6	20.47	54.49	-28.10	31.54	34.44
7	-15.16	-33.36	21.29	-12.61	-2.55
8	-25.45	-41.15	21.16	-16.58	-16.91

Table 4: Errors between the loss factors estimated by OMA (Exp.) and the predictions obtained with a numerical model (FEM) and with Eq. (7).

Using the natural frequencies and the loss factors obtained with the numerical model in Eq. (7) the complex wavenumbers presented in Table 5 were estimated. It can be observed that the imaginary components  $k_i$  are similar to those obtained from the monolithic model and decrease slightly as increasing temperature. Moreover,  $k_i$  increases with increasing frequency.

With respect to  $k_R$ , it increases as increasing temperature, but the trend in frequency is different to that exhibited by  $k_I$  (Fig. 6.)

Mode	$k_I$ monolithic model	$k^* = k_R + ik_I$ 20°C	$k^* = k_R + ik_I$ 25°C	$k^* = k_R + ik_I$ 30°C
1	2.157	0.0057 + 2.1423i	0.0122 + 2.1331i	0.0215 + 2.1207i
2	3.320	0.0185 + 3.2562i	0.0276 + 3.2318i	0.0380 + 3.1983i
3	3.588	0.0196 + 3.5355i	0.0316 + 3.5088i	0.0522 + 3.4847i
4	4.014	0.0015 + 4.0160i	0.0048 + 4.0170i	0.0120 + 4.0223i
5	5.172	0.0172 + 5.1116i	0.0265 + 5.0680i	0.0407 + 5.0269i
6	5.406	0.0060 + 5.4206i	0.0135 + 5.4300i	0.0288 + 5.4259i
7	5.804	0.0085 + 5.7533i	0.0100 + 5.7373i	0.0149 + 5.7205i
8	6.656	0.0108 + 6.5974i	0.0185 + 6.5792i	0.0342 + 6.5667i

Table 5: Complex wavenumbers estimated using Eq. (7) and the natural frequencies and loss factors obtained from the numerical model (FEM).

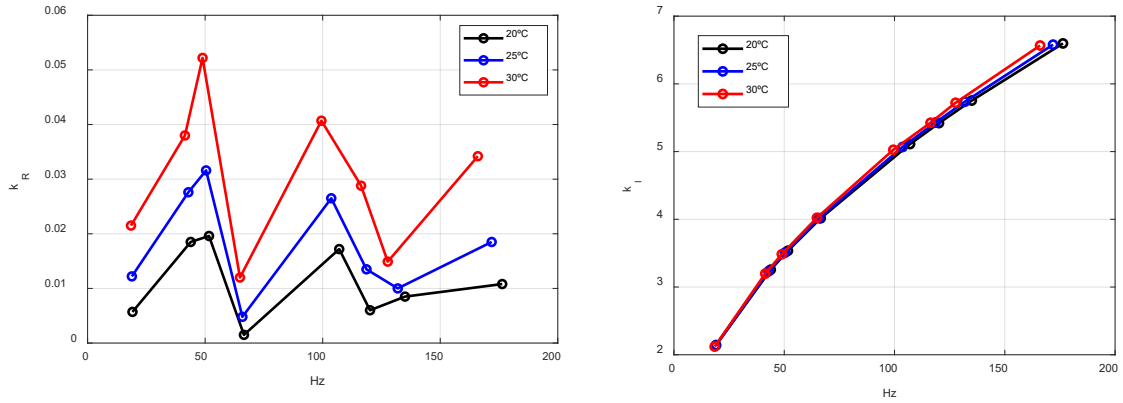


Figure 6. Real and imaginary components of the wavenumber estimated from the numerical model, using Eq. (7)

## 7 CONCLUSIONS

- The natural frequencies and loss factors of a rectangular laminated glass plate at 20°C, 25°C and 30°C have been estimated by operational modal analysis, using a numerical model, and using an analytical equation.
- The natural frequencies and the loss factors of the numerical model were estimated from the FRF obtained with a steady-state dynamic analysis using a harmonic excitation.
- A good agreement has been obtained in natural frequencies, the discrepancies between the experimental values and those predicted analytically and numerically being less than 20%.
- With respect to the loss factors, the numerical model predicts with a better accuracy the experimental results, the errors being less than 20%.
- The analytical model predicts loss factors increasing as increasing frequency. This trend is different to that exhibited in the experiments and different to that obtained from the numerical model.

## ACKNOWLEDGEMENTS

The authors would like to express their gratitude to the Spanish Ministry of Science and Innovation for the financial support through the project BIA2014-53774-R

## REFERENCES

- [1] Ferry, J.D., *Viscoelastic Properties of Polymers*, Third ed., John Wiley & Sons, Ltd., New York. 1980.[
- [2] Lakes, R., *Viscoelastic solids*. CRC Press, New York, (2009).
- [3] Nashif, A.D., Jones, D.I.G., and Henderson, J.P., *Vibration Damping*. John Willey and Sons, New York. 1985.
- [4] Ross, D., Ungar, E.E., and Kerwin, E.M., *Damping of Plate Flexural Vibrations by Means of Viscoelastic Laminate*, Structural Damping, ASME, 1959; p. 49-88.
- [5] Mead, D.J., The damping properties of elastically supported sandwich plates. *Journal of sound and vibration*. 24(3), 275-295, 1972.
- [6] Mead, D.J., Yaman, Y. The harmonic response of rectangular sandwich plates with multiple stiffening: A flexural wave analysis. *Journal of Sound and Vibration*, 145(3), 409-428, 1991.
- [7] Galuppi, L., and Royer-Carfagni, G.F., *Laminated Beams with Viscoelastic Interlayer*, Int J Solids Struct, 2012;49(18):2637-2645.
- [8] M. López-Aenlle, F. Pelayo, Dynamic effective thickness in laminated-glass beams and plates. *Composite: Part B*, 67, 332-347, 2014.
- [9] F. Pelayo, M. López-Aenlle. Natural frequencies and damping ratios of multi-layered laminated glass beams using a dynamic effective thickness. *Journal of Sandwich Structures and Materials*. 21(2):439-63. 2019.
- [10] Galuppi, L., and Royer-Carfagni, G.F., The Effective Thickness of Laminated Glass Plates, *J Mech Mater Structures*, 2012;7(4):375-400.
- [11] Pelayo, F., López-Aenlle, M., Brincker, R. and Fernández-Canteli, A., Artificial Excitation in Operational Modal Analysis, In Proc. Of the 3<sup>rd</sup> International Operational Modal Analysis Conference (IOMAC). Portonovo, Ancona. 2009, Paper 223.
- [12] Brincker, R., Ventura, C. *Introduction to Operational Modal Analysis*. Wiley, 2015.
- [13] Pelayo F, Lamela-Rey MJ, Muniz-Calvente M, López-Aenlle M, Álvarez-Vázquez A, Fernández-Canteli A. Study of the time-temperature-dependent behavior of PVB: Application to laminated glass elements. *Thin Wall Struct*. 2017; 119:324-31.
- [14] M. López-Aenlle, F. Pelayo, A. Fernández-Canteli, M. García Prieto. The effective-thickness concept in laminated-glass elements under static loading. *Engineering Structures*. 56:1092-102. 2013.



**3rd Conference on Structural Dynamics (DinEst 2024)**  
**Seville, September 2024**  
**Railway dynamics session**

# SIMPLIFIED RAILROAD TRACK MODELS WITH PERIODICALLY VARIABLE PARAMETERS FOR MBD SIMULATION OF RAILWAY VEHICLES

Á. Brazales<sup>1\*</sup>, J. F. Aceituno<sup>1</sup>, R. Chamorro<sup>2</sup> and J. L. Escalona<sup>2</sup>

<sup>1</sup>Mechanical and Mining Engineering Department, University of Jaén  
Campus Científico-Tecnológico s/n, 23700 Linares, Spain  
e-mail: {brazales, jaceitun} @ujaen.es

<sup>2</sup> Mechanical and Material Engineering Department, University of Seville  
Camino de los descubrimientos s/n, 41092 Seville, Spain  
e-mail: {rchamorro, escalona} @us.es

**Keywords:** track flexibility, receptance, periodic orbit, multibody simulations.

**Abstract.** *This work presents a simplified 2-dimensional railroad track model with periodic variable parameters to be used in computational multibody simulations of railway vehicles. Because the modelling of railroad track flexibility is a challenging task due to the rail length, sleeper supports and both ballast and sub-ballast heterogeneous properties, the aim of this work is to evaluate vehicle-track interaction using a simple track model that accounts for the sleeper spacing by periodically modifying the model mechanical properties.*

*The 2D flexible track models proposed in this work consist of a set of concentrated masses, which represent the rails of the track, and planar elements, that aim to model the sleepers, connected to each other by a set of spring-dashpot elements, which represent the railpads and fastening elements and ballast and sub-ballast layers (see Fig. 1 where a simple and vertical track model is depicted). This simplified track model travels within the wheelset -one model per wheelset- and periodically changes the values of its mechanical parameters within the track, with the period being equal to the sleeper spacing. Thus, the parametric excitation due to the variation of dynamic stiffness of the discretely supported track is being considered.*

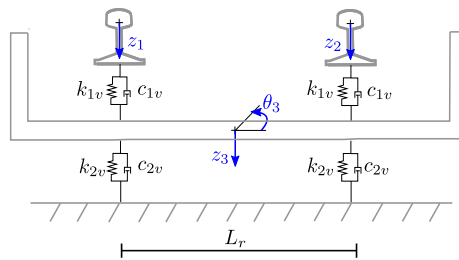
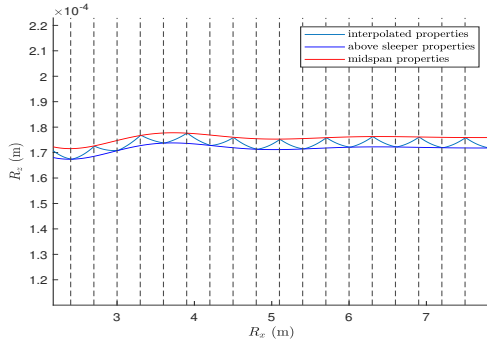


Figure 1: 4-DOF simplified track model

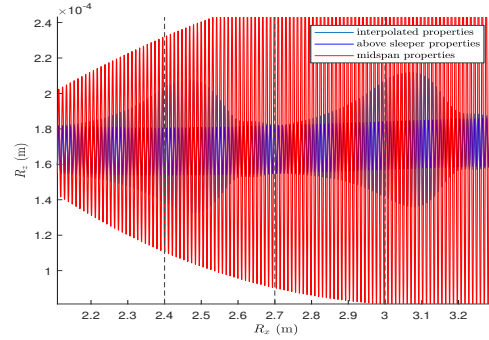
The major advantage of these simplified track models is that the receptance matrix and the time derivate of their state vector can be obtained by a systematic and straightforward procedure in terms of their mass, stiffness and damping matrices. In the same way, a systematic procedure to increase the degrees of freedom of these models or to include lateral sets of spring-dashpot elements to account for the flexibility of the railway track in both vertical and lateral directions can be followed. However, due to the fact that these track models are viewed from a cross-sectional perspective in longitudinal direction, the main drawback of these models is that they cannot take into account the longitudinal dynamics of the railroad track.

The matching between models is achieved by solving a constrained optimization problem (constraints are included based on numerical and physical requirements), where the objective function is the mean squared error between receptances or periodic orbits in the absence of irregularities computed in different points; above sleeper and midspan are the most representative locations. In those points where receptances or vertical/lateral displacements related to the periodic orbits are not computed, mechanical parameters need to be interpolated. If periodic orbits are taken into consideration to solve the constrained optimization problem, the mechanical parameters of simplified track models will not only change with position, but also with the forward velocity of the wheelset. In this work, a FEM model of a discretely supported track is used to compute both reference receptances and periodic orbits to be fitted.

In Fig. 3 numerical results from multibody simulations where simplified track models are coupled to a railway vehicle with two bogies and four wheelsets running at 10 m/s forward velocity and 0.6 m sleeper spacing are shown. In this case, only above sleeper and midspan properties are considered and a linear interpolation between both is applied.



(a) Track with no irregularities



(b) Track with irregularities to excite the pinned-pinned frequency

Figure 3: Wheelset vertical displacement due to railway track flexibility using track models with constant and periodically variable parameters. Red: constant parameters fitted at midspan receptance. Blue: constant parameters fitted above sleeper receptance. Black: Periodically-variable parameters.

## VIBRATIONS OF MULTI-SPAN STRUCTURES LIKE FLOORS, RAIL AND ROAD BRIDGES

Lutz Auersch<sup>1</sup>

<sup>1</sup>Federal Institute of Material Research and Testing  
12200 Berlin, Germany  
e-mail: lutz.auersch-saworski@bam.de

**Keywords:** Railway bridge, Train passage, Resonance, Multiple spans, Mode shape spectrum.

**Abstract.** *Resonances of rail bridges due to the passage of trains have been mainly investigated for single-span bridges. When multi-span bridges are to be considered, it is of interest if stronger resonance amplifications must be taken into account. Measurements of several multi-span structures have been evaluated for natural frequencies and mode shapes. An integral rail bridge with three different spans shows a separated local resonance of the longest main span and clearly higher natural frequencies of the shorter side spans. A two-span continuous beam on the test area of the Federal Institute of Material Research and Testing showed a regular pattern of natural frequencies where always a pair of frequencies is found with a certain frequency ratio. The corresponding mode shapes are the out-of-phase and in-phase combinations of the first, second, third ... bending mode. A seven-span road bridge has been monitored for one of the almost equally long spans. Similar mode shapes have been observed for different, clearly separated natural frequencies. Three modal analyses measurement campaigns have been performed on the whole bridge. The combined mode shapes of the seven spans have been clearly identified where different combinations of spans are dominating in the different mode shapes. Equal weakly coupled spans have been analysed for a large wooden floor in a castle. A cluster of natural frequencies has been observed and a special method to extract the mode shapes has been developed and tested. The consequences of multi-span bridges for rail traffic will be discussed. If  $n$  simply supported bridge spans have no coupling,  $n$  equal modes with amplitude  $A/n$  exist and their superposition would yield the same resonance as for a single bridge. Real simply supported bridges have always a weak coupling due to the track or the common piers. Therefore, the natural frequencies differ a little and they cannot be in resonance at the same time for the same train passage so that the resonance amplification cannot be as strong as for the single bridge. This rule holds also for the average amplitude of the time history of the bridge passage which is an adequate quantity to judge for the bridge behaviour. The maximum amplitude of the time histories of different bridge points are quite random and could exceed the values of a single bridge. The meaning of such criteria is questioned and frequency domain analyses are suggested for a clearer bridge analysis and understanding.*

## 1 INTRODUCTION

The research on bridges at the Federal Institute of Material Research and Testing (BAM) has been initiated by Rohrmann [1], and many bridges have been measured and monitored mainly under the aspect of damage detection [2]. Floor resonances are a main concern when railway-induced vibrations are analysed [3], and many floors have been measured during the last 40 years [4]. The experience with bridges and floors can be used for the topic of resonances of rail bridges. This contribution focusses on multi-span bridges and their special effects compared to single span bridges. What are the typical resonance frequencies (resonance frequency patterns) and what are the typical mode shapes? Are multi-span rail bridges more dangerous or less dangerous than single span bridges? Can a multi-span bridge analysed by looking at only one span? The typical resonance frequencies and mode shapes are analysed by beam models for floor beams. Eight measurement examples follow, two beams/floors, four road bridges, and two rail bridges. The rail bridges are further discussed in frequency domain by characteristic spectra of the train, the mode shape (modal force) and the transfer function of the bridge. The bridge examples are analysed as single spans at first. Then these examples are extended to two-, three-, and multi-span bridges.

## 2 THEORY OF MULTI-SPAN STRUCTURES

The principal behaviour of multi-span floors and bridges can be analysed by one-dimensional beam models. The differential equation for the displacements  $u$  of a beam

$$EI u'''' + \mu u'' = 0 \quad \text{or in frequency domain } \omega \quad EI u'''' + \mu \omega^2 u = 0 \quad (1)$$

with bending stiffness  $EI$  and mass per length  $\mu$  has four solutions

$$u = A_1 \cos ax + A_2 \sin ax + A_3 \exp(+ax) + A_4 \exp(-ax), \quad (2)$$

if the parameter  $a$  is fitted to the differential equation

$$a = \sqrt[4]{EI/\mu\omega^2}. \quad (3)$$

The constants  $A_i$  are fitted to the boundary conditions at the supports.

At first, the full coupling of identical floors is considered. The assembly of all floors yields a continuous beam with continuous rotations at the supports. This is demonstrated for 5 m span concrete floors in Figure 1. For coupled floors, the support conditions depend on the vibrations of the adjacent floors. If two floors vibrate in anti-phase, the mid support is “hinged” (Fig. 1a), whereas the mid support is “clamped” if the floors are in phase (Fig. 1c). Therefore, the two coupled floors have two eigenfrequencies (Fig. 1e), the hinged-hinged and the higher hinged-clamped eigenfrequency of a single floor. In case of many coupled floors, more than one eigenfrequency exist. The eigenfrequencies are in a frequency band between the hinged-hinged and the clamped-clamped eigenfrequency of a single floor (Fig. 1f). Generally, all floors participate to all eigenmodes (Fig. 1b,d).

As a difference to this strong coupling of floors, a weak coupling of simply supported floors is analysed by inserting rotational springs at the supports. Thus two adjacent floors can have discontinuous rotations. The resulting spectra and a mode shape is demonstrated in Figures 1g,h for the same floor model as before. The fourth mode of the 6-bay floor clearly shows the additional rotations due to the weaker coupling (Fig. 1g). The different eigenfrequencies of the weakly coupled floors (Fig. 1h) are in a narrower frequency range compared to the strong coupling.

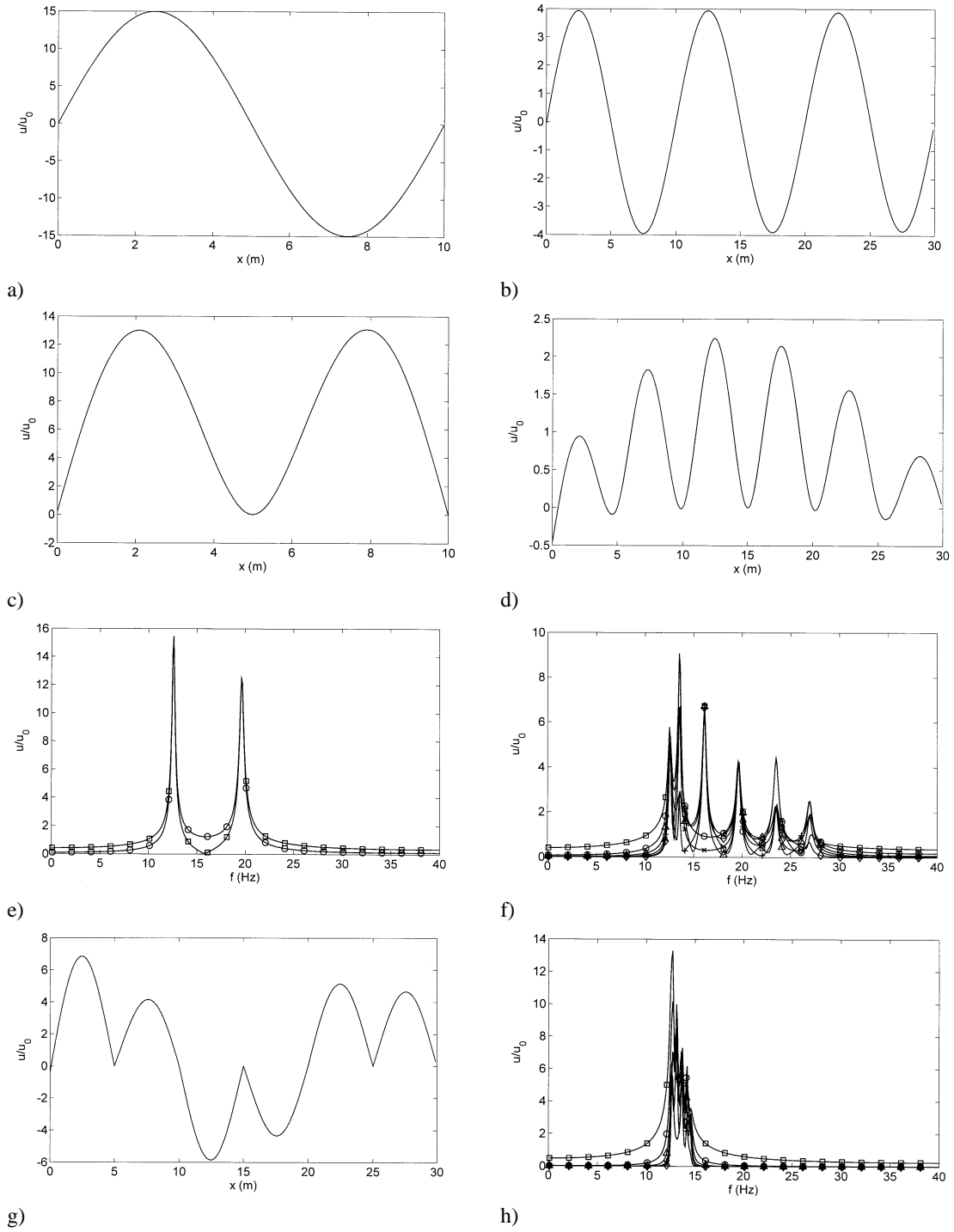


Figure 1: Coupled floor beams of 5 m length, 0.2 m thickness, concrete, a,c,e) 2-span continuous, b,d,f) 6-span continuous, g,h) 6-span weakly coupled by rotational springs, a-d,g) vibration modes, and e,f,h) spectra.

### 3 OBSERVATIONS AT DIFFERENT BRIDGE AND STRUCTURE TYPES

#### 3.1 Beams and floors

##### Example 1: Continuous 2-span pre-stressed concrete beam

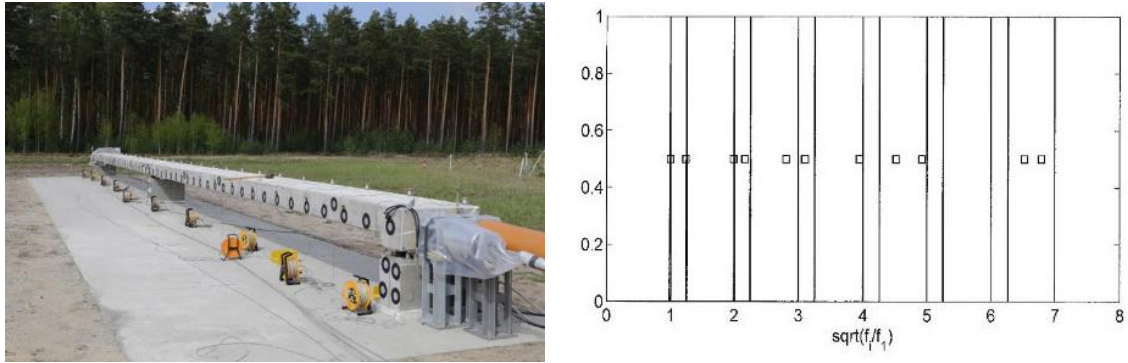


Figure 2: 2-span beam (a), regular sequence of the natural frequencies (theory) and  $\square$  measurements (b).

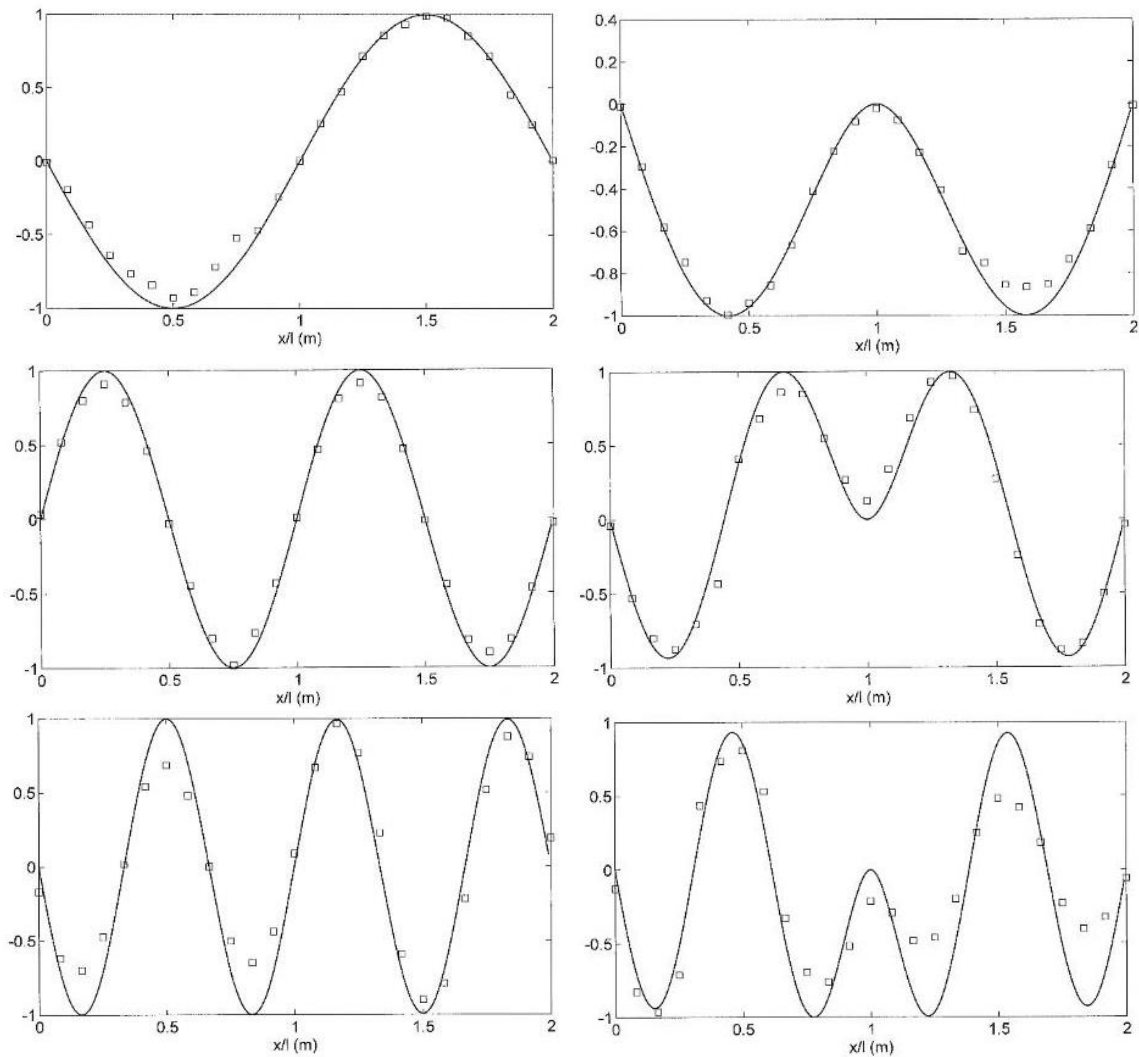


Figure 3: Calculated mode shapes of the 2-span beam of length  $2l$ , first, second and third antimetric (left) and symmetric (right) mode,  $\square$  measurement results.

A 2-span pre-stressed concrete beam with a total length of 24 m (2 x 12 m) and a width of 1 m has been built on the BAM test area (Fig. 2a). A line of 25 vertical geophones were installed at 1 m intervals along the bridge, and the modal analysis has been done by hammer tests. The natural frequencies appear in pairs, where the square roots of the frequencies keep always the same distance (Fig. 2b). The first six modes are presented in Figure 3 as theoretical modes (lines) and experimental results (square symbols). Each pair of natural frequencies belongs to the anti-symmetric mode with a lower frequency (Fig. 3 left) and the corresponding symmetric mode with a higher frequency (Fig. 3 right). The agreement between theory and experiment is very good.

### Example 2: 11 coupled wooden floor beams (“Neues Palais” in Potsdam)

The large (30 m x 10 m) wooden floor above a ball room in the “Neues Palais” in Potsdam has been dynamically tested (Fig. 4a). Eleven wooden floor beams (0.3 m x 0.4 m) span the length of ten meters and are connected by three layers of floorboards. The floor is divided in six rooms by non-bearing walls. The measurement line of 18 sensors along the middle axis of the floor has been shifted to three more positions at the quarter lines and along the outer bearing wall. Hammer, heeldrop and ambient measurements have been performed at this floor. In addition to the measurements, a model of eleven 10 m long beams has been built, which are clamped at both ends and which are coupled by springs along the middle axis, and where every second beam is stiffened and loaded by a non-bearing wall.

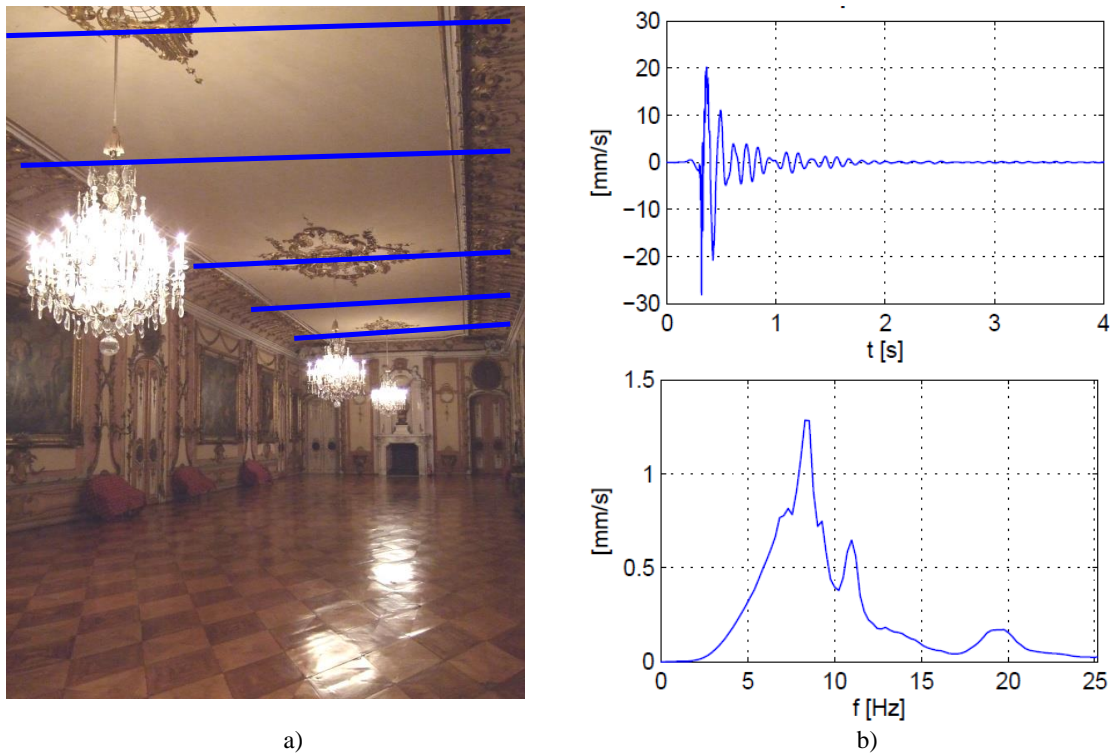


Figure 4: Floor above a large ball room with 6 rooms at the second storey (a), time history and spectrum of a heel-drop test:

All measured spectra show a maximum region between 5 and 10 Hz with some relative maxima, but without sharp peaks, see Figure 4b for an example. The wide resonance region indicates the coincidence of several natural frequencies, and a high damping can be assumed for this system.



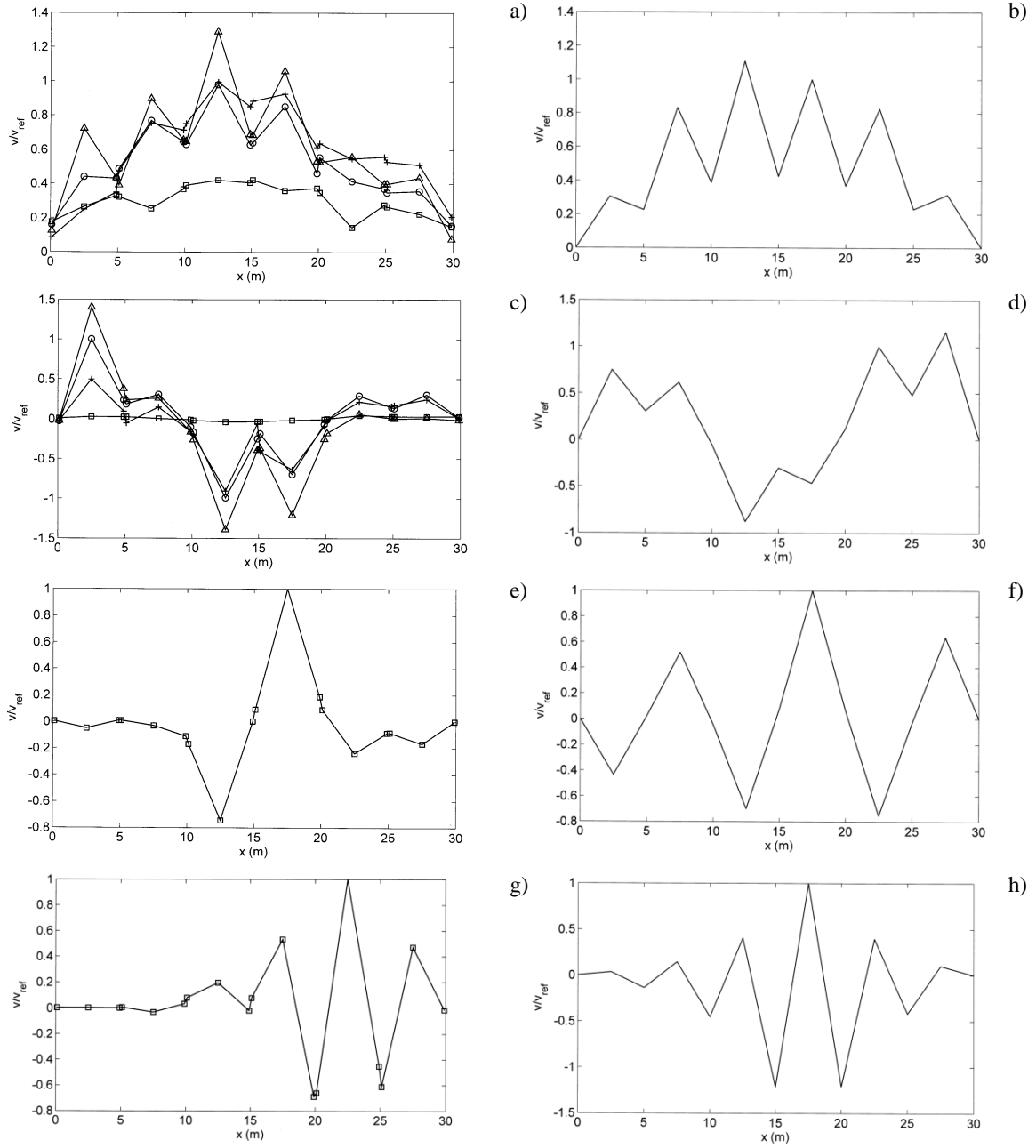


Figure 5: Measured (left) and calculated (right) vibration modes of the coupled floor and wall beams, a) 6.5 Hz (ambient), b) 7.2 Hz, c) 7.7 Hz (ambient), d) 7.7 Hz, e) 8.5 Hz (hammer) f) 8.3 Hz, g) 11.7 Hz (hammer), h) 11.7 Hz,  $\triangle$  middle,  $\circ$  outer and  $+$  inner quarter axis,  $\square$  outer wall axis in ambient measurements.

The measured and calculated vibration modes are shown in Figure 5 as amplitudes along the long axis of the floor. The first mode at about 7 Hz shows a global behaviour of the floor where the floor beams at 2.5, 7.5, ..., 27.5 m have higher amplitudes than the wall beams at 5, 10, ..., 25 m. The second mode at 7.7 Hz consists of vibrations of the floor beams where every two neighbouring rooms are in phase. The next mode at 8.5 Hz consists of vibrations of all floor beams out of phase to their neighbours while the wall beams are at rest. At a higher frequency of 11.7 Hz, the wall beams show strong amplitudes which are in anti-phase to the floor beams.

It has been found that all floor beams contribute to each natural mode even for a weak coupling of the beams.

### 3.2 Road bridges

#### Example 3: 3-span bridge with six parallel beams

The beam-type bridge has a mid span of 35 m and two side spans of 20 m (Fig. 6a). Six pre-stressed concrete beams are equally distributed across the width of 24 m. The bridge vibrations have been measured with 40 geophones on the left and right lane before and after a repair. The spectra show a maximum region between 3 and 4 Hz (Fig. 6b) where several modes are assumed. The mode shapes of the whole bridge have been calculated for a 3-dimensional finite element model (Fig. 6c). The fundamental symmetric and antimetric bending mode could also be measured by the two measurement lines. More modes exist with different combinations of upward and downward (in-phase and out-of-phase) amplitudes of the six beams. The amplitudes of the mid span are dominant for all these fundamental modes: The higher resonance frequencies in Figure 6b belong to higher bending modes of the bridge.

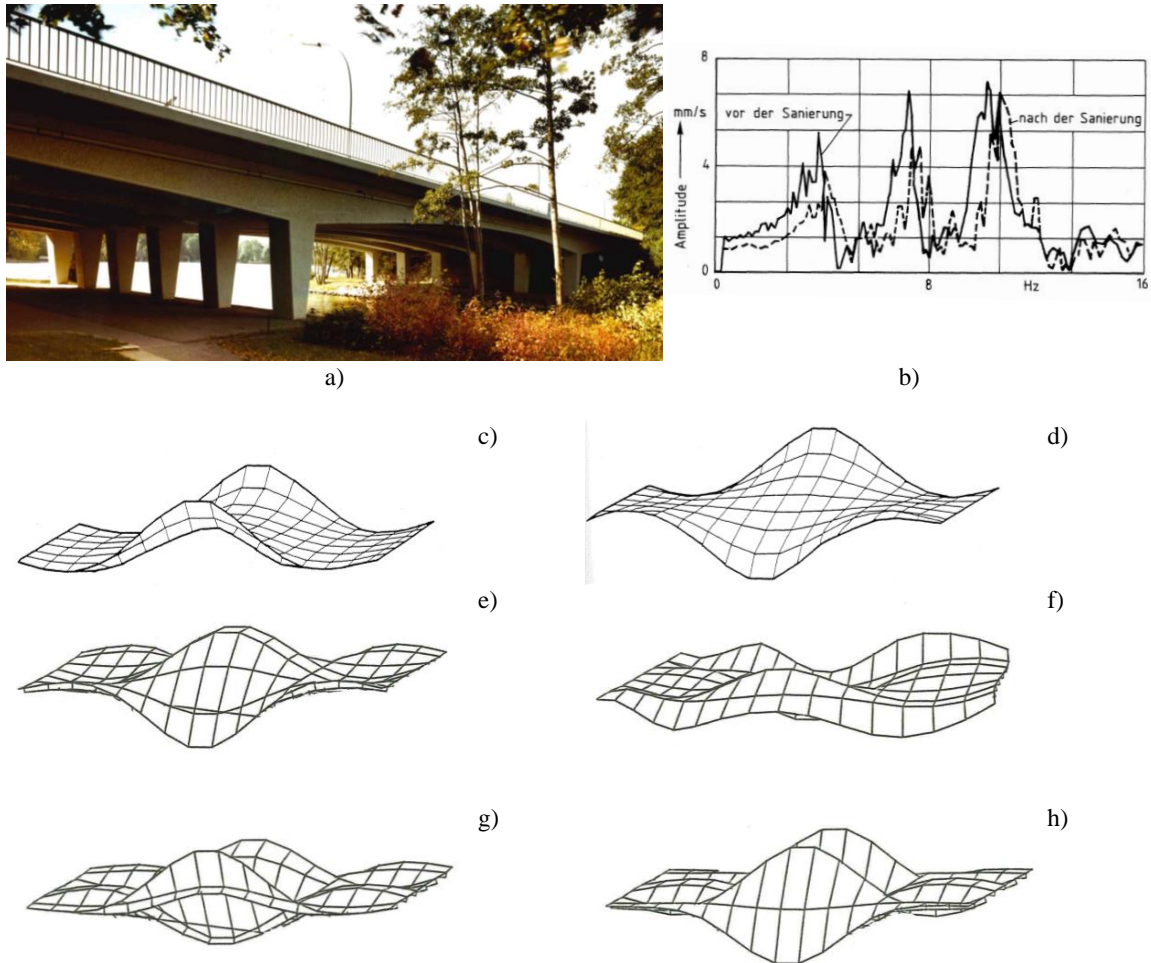


Figure 6: 3-span bridge with six parallel beams (a), mid-point spectrum before and after renovation (b), the first six mode shapes from finite-element calculation (c-h).

#### Example 4: 7-span continuous box-type highway bridge

A highway bridge of 240 m length with 7 continuous spans of approximately 35 m length (Fig. 7a) has been investigated over 35 years [2]. At the first time, the third span has been analysed under traffic excitation and by FEM calculation. The first and second bending modes and the second torsional mode could be found in the measurements in agreement with the calculated mode shapes (Fig 7c). This span has been monitored for several years, then the monitoring was extended to the first three spans. Three modal analyses measurement campaigns have

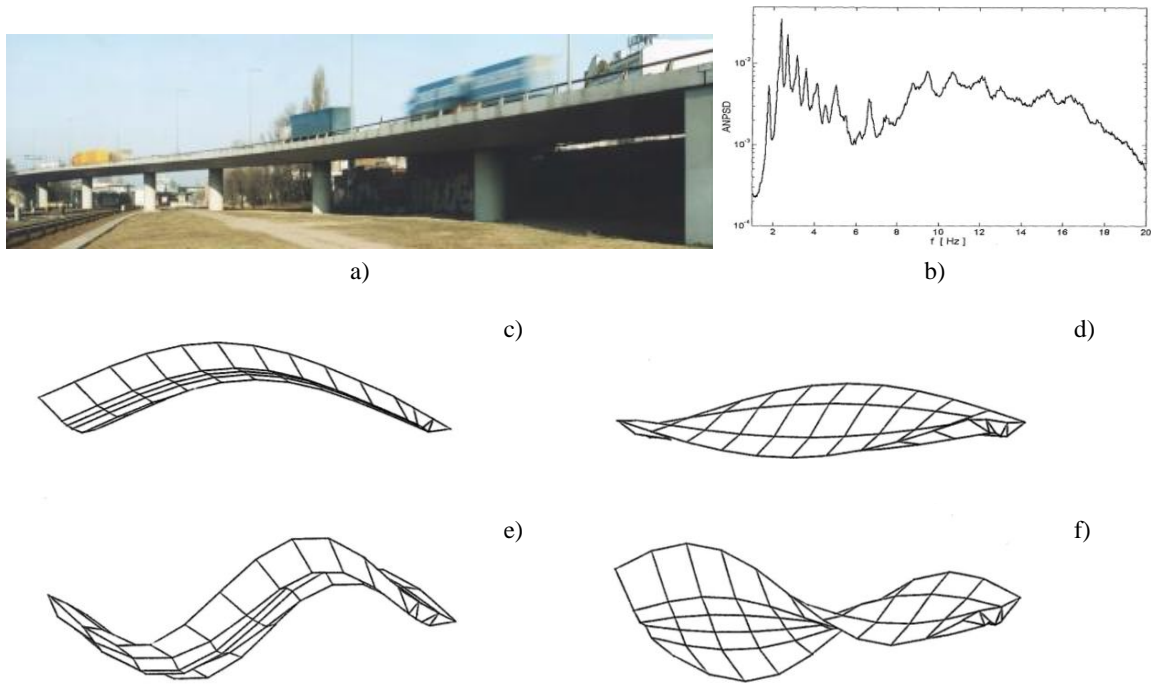


Figure 7: 7-span highway bridge (a), averaged spectrum (b), the first four mode shapes of the third span from finite-element calculation (c-f).

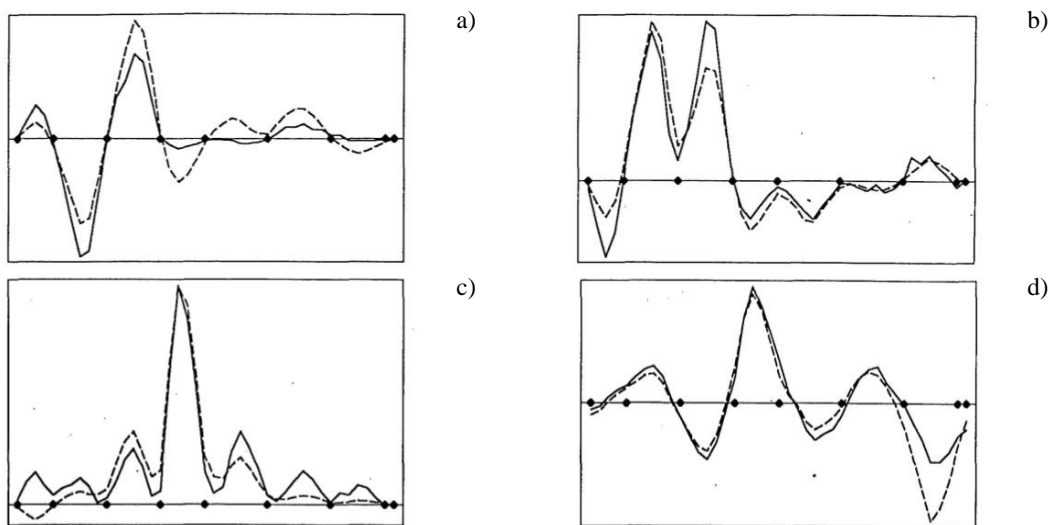


Figure 8: 1D mode shapes of the whole 7-span highway bridge from measurement (continuous line) and calculation.

been performed on the whole 7-span bridge [5]. The spectrum shows a number of clearly separated peaks (Figure 7b). The mode shapes in Figure 8 and 9 show coupled bending of the different spans where all spans have alternating minima and maxima at 2.8 Hz, pairs of neighbouring spans are in phase at 3.5 Hz, and all spans are in phase at 4.5 Hz. A torsional mode with alternating minima and maxima is found at 10.4 Hz.

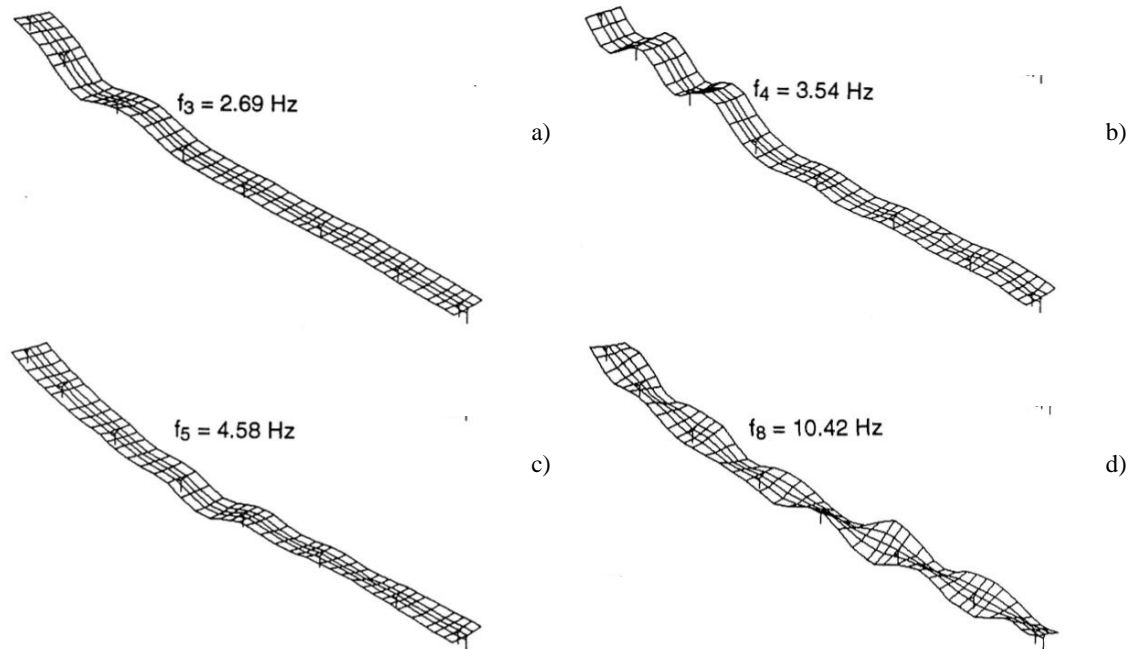


Figure 9: 3D mode shapes of the whole 7-span highway bridge from measurement.

#### Example 5: 7-span continuous steel road bridge

The bridge has a length of 264 m and a width of 18 m (Fig. 10a). The main mid span has 66 m, and at both sides are three shorter spans of half the length (33 m). There are two steel boxes along the bridge, regularly spaced cross beams, and a concrete deck. 5 measurement axes with 2 x 33 geophones have been measured to represent the mode shapes. Five examples are shown in Figure 10c. The first two modes are fundamental bending and torsional modes of the longer mid span with small contributions of the nearest side spans. The third mode consists of coupled bending vibrations of both outer spans. The mode at 4.58 Hz is the second torsional mode of the long mid span and at the same time the first torsional mode of the shorter side spans. The bending mode at 8 Hz has regular minima and maxima at equal distances. The wave length is half the side span and a quarter of the mid span so that this mode is the second bending for the shorter and the fourth bending for the long mid span. The bridge behaves like a bridge with 8 equal spans and an additional support at the mid span.

#### Example 6: 10-span simply-supported concrete bridge

The box-type bridge has an overall length of 1000 m and consists of ten simply supported spans of 100 m (Fig. 11a). Only the first span has been analysed in theory and measurement [6]. The averaged spectrum from frequency domain decomposition shows only single peaks (Fig. 11b) as if the first span is completely decoupled from the other spans. The different peaks belong to the first, second and third bending and torsional modes.

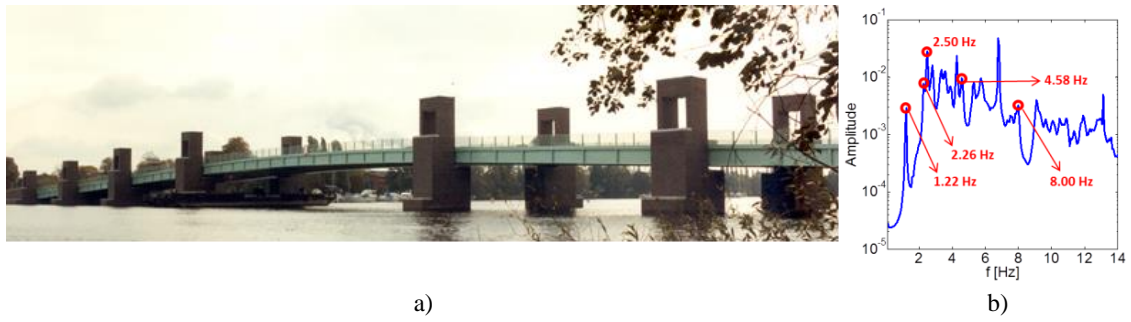


Figure 10: 7-span regular continuous bridge (a), averaged spectrum (b), 3D mode shapes from measurement (c).

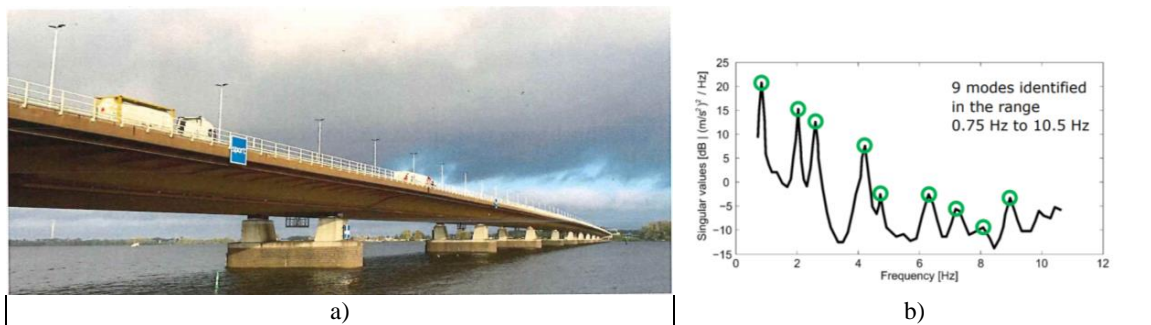


Figure 11: 10-span regular simply supported bridge (a), spectrum from frequency domain composition (b).



### 3.3 Rail bridges

#### Example 7: Long 3-span concrete rail bridge

The continuous rail bridge (Fig. 12a) has an overall length of 300 m where the support distances are 135 m for the mid span and 82 m for the side spans [7]. The concrete box has a height of 4.5 to 6 m and supports two railway lines. The monitoring of the bridge includes, besides other sensors, 2 x 13 geophones along the two railway lines which have been used to find the vibration modes during train passages and ambient excitation. The fundamental mode at 1.95 Hz is only the vibration of the longest mid span (Fig. 12b). The modes between 3 and 3.5 Hz (Fig. 12c-f) have maxima of the shorter side spans in different combinations, but also some contributions of the mid-span. At 4.85 Hz, the second bending mode of the mid span has been measured.

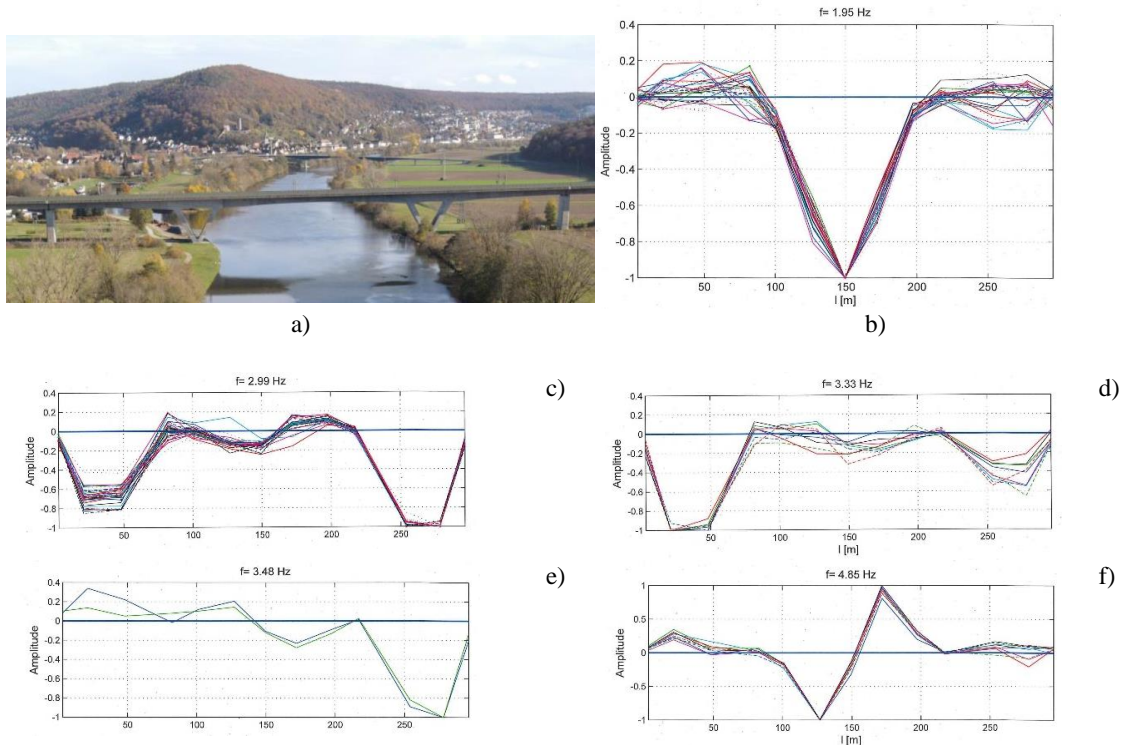


Figure 12: : 3-span railway bridge (a), first vibration mode (b), next four mode shapes from measurement (c-f).

#### Example 8: Short 2-span concrete rail bridge

The short two line rail bridge “Arroyo Bracea I” (Fig. 13a) has been analysed by the Spanish colleagues [8]. It consists of two simply supported spans of 15.25 m length and 11.6 m width. Each span consists of five concrete beams of 1 m height and a concrete deck of 0.25 m thickness. The modal analysis has been done on one of the two spans with 3 axes of 3 to 4 accelerometers. After stabilisation, three modes have been found in close neighbourhood (Fig. 13b) which are all first bending modes of the beams. All beams are in phase at 9.25 Hz, the outer beams are out of phase at 10.63 Hz (“torsion”), and the outer beams are in phase and the mid beam is out of phase at 12.75 Hz. The same mode shapes have also been calculated by two different models of this skew bridge with identical or slightly different natural frequencies, see Figure 10 and Table 4 in [8].

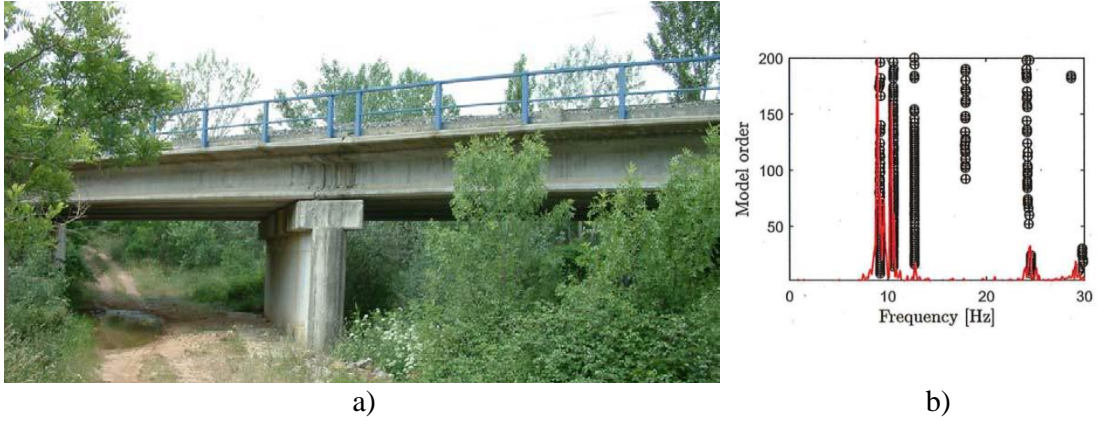


Figure 13: 2-span simply supported bridge (a), stabilization diagram from stochastic subspace identification (b).

#### 4 THEORY FOR THE BRIDGE RESONANCE FROM TRAIN PASSAGES

The problem of resonances of single-span or multi-span rail bridges is now addressed. The passage of a train excites the different modes of the rail bridge with (angular) eigenfrequencies  $\omega_j$  and mode shapes  $w_j(x)$ . The solution for the bridge vibration can be expressed in frequency domain as the superposition of the eigenmodes where each contribution is a product of three spectra

$$v(\omega) = \sum_j v_j(\omega) = F_S X(\omega) \sum_j W_j(\omega) H_j(\omega) \quad (4)$$

where  $F_S$  is one static axle load,  $X(\omega)$  is the axle-sequence spectrum,  $W_j(\omega)$  is the spectrum of the mode shape  $w_j(x)$ , and  $H_j(\omega)$  is the transfer function of the bridge. This result is derived in detail in [9]. It holds for any type of rail bridges, simply supported, elastically supported, integral, single-span, multi-span, and continuous bridges. The time domain solution is obtained via the inverse Fourier transform.

The axle-sequence spectrum of the train is

$$X(\omega) = \sum_{k=1}^n A_k \exp(-i\omega T_k) \quad (5)$$

where  $T_k$  is the delay time of the  $k$ -th axle and  $A_k$  is an amplitude factor compared to the single axle. Figure 14 shows the axle sequence and the axle-sequence spectrum for a bogie, a car with two bogies and for a train with eight cars. The single bogie shows characteristic zeros,

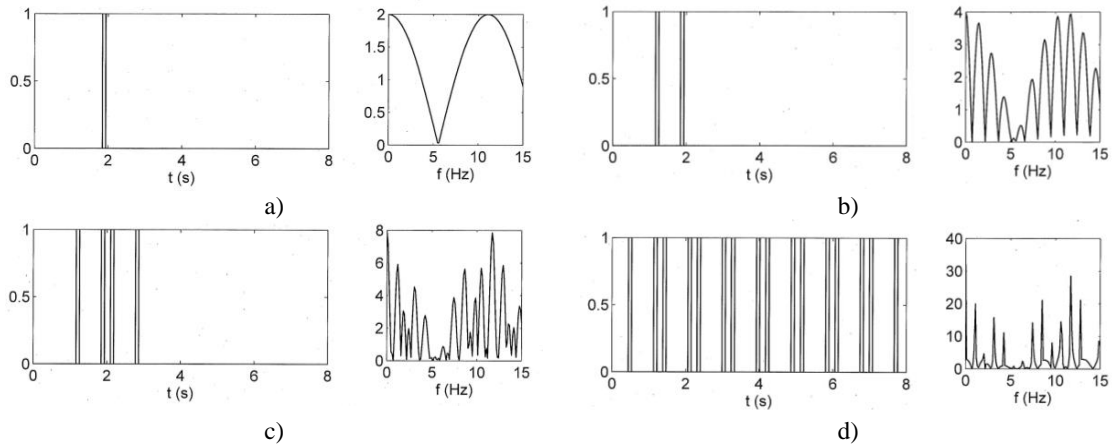


Figure 14: Axle sequence in time and frequency domain for a) a bogie, b) a car, c) two cars, and eight cars.

the whole car shows many characteristic maxima (and zeros), and these maxima turn into sharp peaks for the whole train.

The mode-shape spectrum is the frequency-dependent part of the modal force spectrum. The modal force in general is

$$F_j(\omega) = \int F'(x, \omega) w_j(x) dx \quad (6)$$

and the modal component  $F_j$  of the moving constant load  $F_S$  is

$$F_j(t) = \int F_S \delta(x - v_T t) w_j(x) dx = F_S w_j(v_T t) \quad F_j(\omega) = F_S W_j(\omega) \quad (7)$$

in time and in frequency domain where  $v_T$  is the train speed. The mode shape spectrum  $W_j(\omega)$  is the Fourier transform of  $w_j(v_T t)$ , the time history of a single unit modal force. The mode shape spectrum  $W_1(\omega)$  of a single bridge span has characteristic zeros due to the bridge length  $L$  or the passage time  $T$  respectively. The mode shape spectrum of a multi-span bridge consists of the sum of the mode shape spectra of all bridge spans

$$W(\omega) = \sum_{k=1}^n W_k(\omega) \exp(-i\omega T_k) \quad (8)$$

In case of identical bridge spans this is simply

$$W(\omega) = W_1(\omega) \sum_{k=1}^n A_k \exp(-i\omega T_k) = W_1(\omega) Y(\omega) \quad (9)$$

with a bridge-sequence spectrum  $Y(\omega)$  which is illustrated for two out-of-phase spans and for two in-phase spans in Figure 15. As for the axle-sequence spectrum, there are characteristic zeros, and the maxima can become sharper for more in-phase or out-of-phase bridge spans.

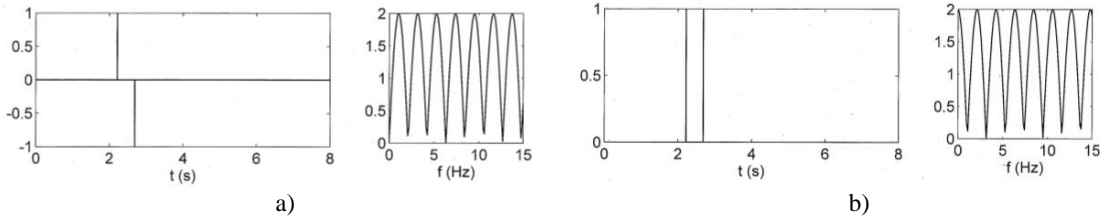


Figure 15: Bridge sequence in time and frequency domain for a) the out-of-phase mode and b) the in-phase mode.

The frequency response function  $H_j(\omega)$  for the velocity is

$$\frac{v_j(\omega)}{F_j(\omega)} = H_j(\omega) = \frac{i\omega}{m_j(\omega_j^2 + 2D_j i\omega_j^2 - \omega^2)} \quad (10)$$

and its maximum at the resonance frequency  $\omega_j$  is

$$\frac{v_j(\omega_j)}{F_j(\omega_j)} = H_j(\omega_j) = \frac{1}{m_j 2D_j \omega_j} \quad (11)$$

where  $D_j$  is the modal damping, and  $m_j$  is the modal mass

$$m_j = \int m' w_j(x)^2 dx \quad (12)$$

The resonance amplification is inversely proportional to the modal mass, the modal damping and the (angular) eigenfrequency.



## 5 APPLICATION TO THE RAIL BRIDGE EXAMPLES

### 5.1 Long bridge with slow freight train

This long rail bridge has three spans with different lengths and frequencies, and the resonance of the longest mid span is analysed as a single-span bridge. The passage of a long freight train with a low speed of 100 km/h over the long bridge lasts about 20 seconds and a time period of 65.5 s has been investigated. The corresponding modal force (Fig. 16a) shows a passage time of about 2 seconds for a single axle and a spectrum with very narrow minima or zeros. The freight train consists of 20 three-axle cars and has an axle-sequence spectrum (Fig. 16b) with very sharp peaks. If such a peak meets a zero of the modal force spectrum, the cancellation of this resonance would occur. In the present case, the second car-length frequency meets nearly a maximum of the modal force spectrum which means rather an amplification of the resonance. The frequency response function is given for the first bending mode at 1.9 Hz, with a damping of 1 % (Fig. 16c). The mass is at least proportional to the length of the bridge so that the modal mass is high. The resonance of the long-span bridge is reduced by the modal mass, increased by the low resonance frequency, and increased due to the low damping.

The response of the bridge to the passage of the freight train (Fig. 16d) follows from the three spectra in Figure 6a-c. The spectral density is very high at 240 mm/s/Hz, which is partly due to the very long train. The time history shows an increase during the train passage up to the maximum of 10 mm/s. The following vibration lasts another 20 seconds (Fig. 16e). The resonance with 10 mm/s due to a slow long freight train on a long-span bridge has also been found in the measurements (Fig. 16f).

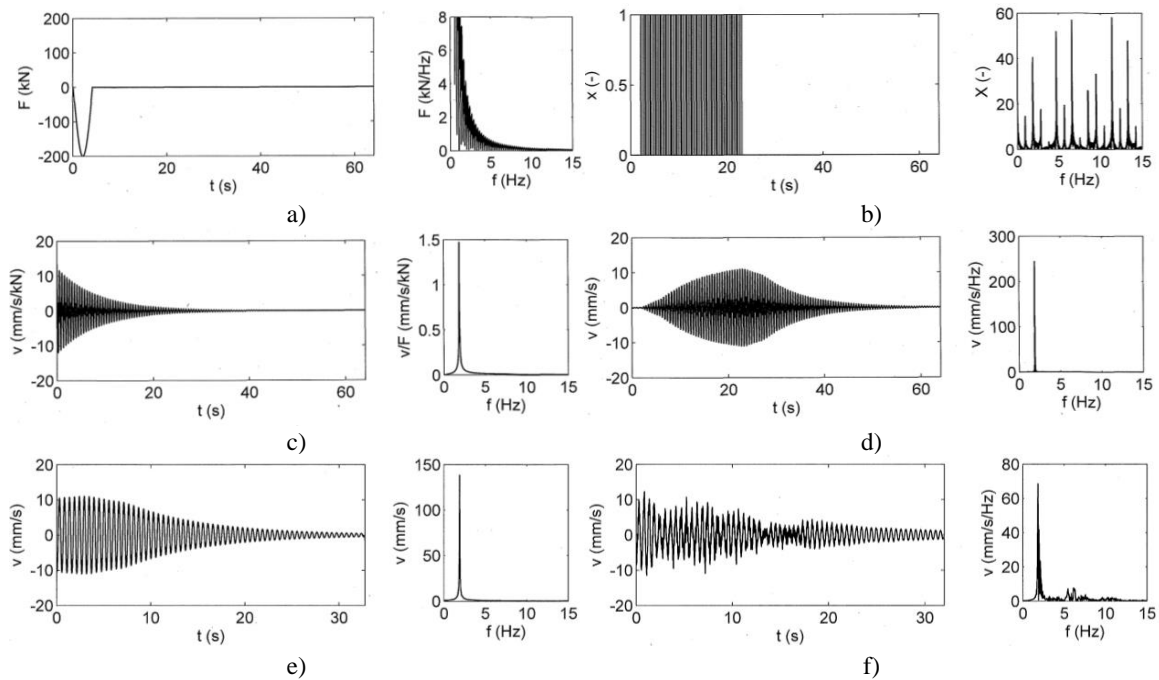


Figure 16. The passage over the long-span railway bridge with  $v_T = 100$  km/h, modal force (a), impulse and frequency response function of the bridge at 1.9 Hz,  $D = 1$  % (b), the axle sequence of the twenty 3-axle freight cars (c), response of the bridge (d), response of the bridge (partly, e), measured response (f).

### 5.2 Short bridge with highspeed train

The Arroyo-Bracea bridge is analysed for the passage by the Spanish ICE3 train, the S103 with a train speed of 280 km/h. At first it is analysed as a single simply supported bridge by the

three steps in Figure 17a-c. The very short passage time yields a high-frequency spectrum of the modal force where the first side maximum is at about 10 Hz. The axle-sequence spectrum of the ICE3 (Fig. 17b), which is a conventional train with two bogies per car, has a strong third car-length frequency which lies at 9.3 Hz for the train speed of 280 km/h. This is close to the first bending eigenfrequency of the bridge which is shown in the frequency response function in Figure 17c for the velocities and in Figure 7d for the accelerations. The resonance amplification is quite high due to the lower modal mass of the shorter bridge. If all spectra of Figures 17a-c are put together in Figure 17e, the response of the bridge shows high amplitudes of 40 mm/s in time domain and of 80 mm/s/Hz in frequency domain. This strong resonance builds up during the two seconds of the train passage. The calculated velocity and acceleration responses are compared with the experimental results of the Spanish team [8] in Figures 7g and 7h. The build-up of the resonance is not as strong as in the calculation. The calculated maximum accelerations give higher values of  $2 \text{ m/s}^2$  compared to  $1 \text{ m/s}^2$  for the measurements. The prediction, however, is very similar to the prediction in Figure 5f from time domain calculation in [8].

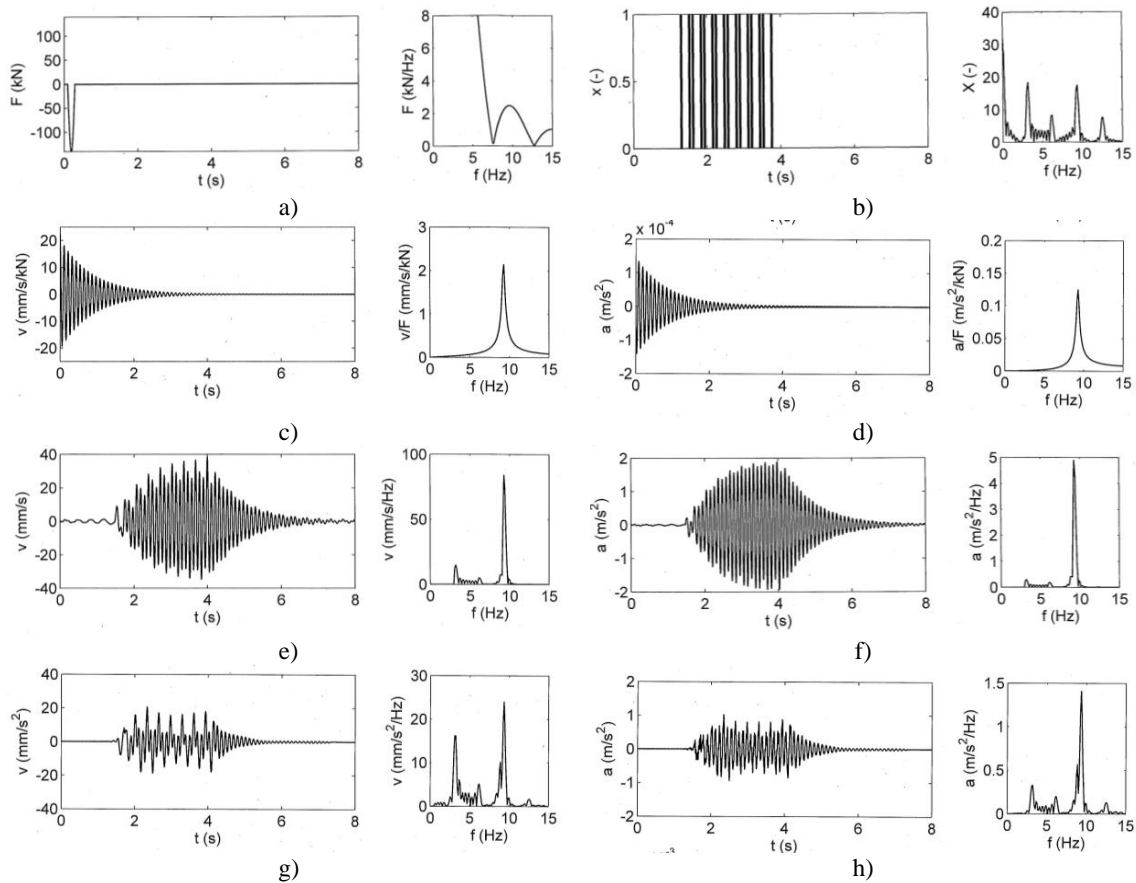


Figure 17: The passage over the short-span simply supported railway bridge with  $v_T = 280 \text{ km/h}$ , a) modal force, b) the axle sequence of the ICE3 train, c) velocity response function and d) acceleration response function of the bridge at 9.3 Hz,  $D = 2 \%$ , e) velocity response and f) acceleration response of the bridge, g) measured velocities, h) measured accelerations.

## 6 THE CONSEQUENCES OF MULTI-SPAN BRIDGES FOR RAIL TRAFFIC

Multi-span bridges of equal or different spans have coupled modes where other spans contribute more or less to the mode shape of the one dominant span. Therefore the modal mass of

this mode is always higher than the modal mass of a single-span bridge. In case of  $n$  equal spans all equally present in the mode shape

$$m_{jn} = \int m' w_{jn}(x)^2 dx = n \int m' w_{j1}(x)^2 dx = n m_{j1} \quad (13)$$

the modal mass is  $n$ -times the modal mass of the single span. Correspondingly, the maximum amplitude in the frequency response function would be only  $1/n$  of the maximum of the single bridge. The modal force, on the other hand, could be higher for the multi-span bridge. The effect on the modal force is analysed for some examples which are based on the two rail bridges.

### 6.1 Long continuous bridge with three different spans

A 3-span bridge with the dimensions of the long bridge example 7 (80 m, 120 m, 80 m) is considered. The mode shape of the lowest eigenfrequency is assumed with maxima of 0.67, 1.0, and 0.67 and compared with the single mid span in Figure 18. The corresponding modal force spectra show many maxima due to the length of the bridge and the low speed of 100 km/h. The frequency bands around each maximum are very narrow, especially for the 3-span bridge. The envelope of all maxima is similar for the single and the 3-span bridge. The only difference between the two bridges is the higher modal mass for the 3-span bridge where

$$m_{13} = \int m' w_{13}(x)^2 dx = (1 + 0.67^2) \int m' w_{11}(x)^2 dx = 1.45 m_{11} \quad (14)$$

so that a lower resonance amplitude might be expected for the 3-span bridge.

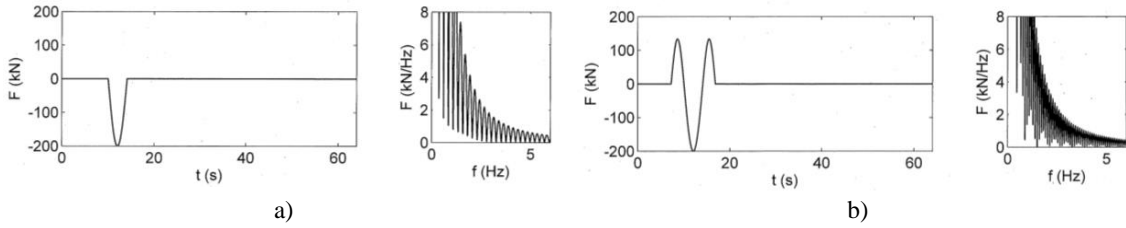


Figure 18: Modal force in time and frequency domain for a) the long single-span bridge, and b) the long 3-span bridge; 100 km/h train speed.

### 6.2 Short simply supported bridge with two or more spans

The bridge example from Spain is now idealised as two identical consecutive simply-supported beams. Two fundamental modes are considered here which have almost the same eigenfrequencies. The corresponding modal force time histories and spectra are shown in Figure 19a,b for alternating (out of phase) amplitudes and for equal (in-phase) amplitudes. The multiplication of the basic force spectrum (Fig. 17a) with the two different bridge sequence spectra (Fig. 15) yields an almost similar maximum at 10 Hz for the out-of-phase mode and an increased maximum for the in-phase mode.

If  $n$  bridge spans are considered (Figs 19c-f),  $n$  fundamental modes exist, and a rule can be found that the maximum of the out-of-phase mode stays almost constant whereas the maximum of the in-phase mode is clearly proportional to the number of spans. This is the highest maximum of all  $n$  modes. For the in-phase mode, the increase of the modal force and the increase of the modal mass compensate and the resonance amplitude is the same as for the single span bridge.

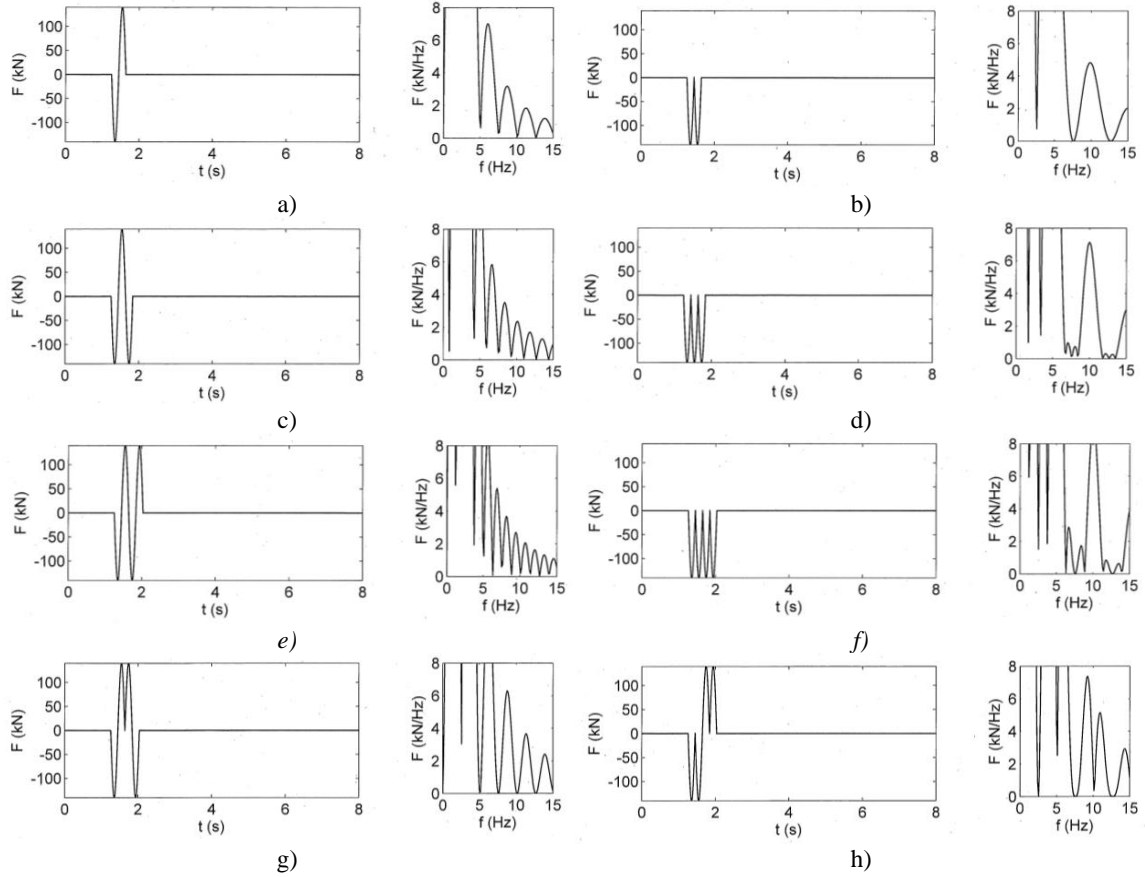


Figure 19: Modal force in time and frequency domain for a, c, e) the out-of-phase mode of a two-, three- and four-span bridge, b,d,f) the in-phase mode of a two-, three- and four-span bridge, g, h) the second and third fundamental mode long single-span bridge, and b) the long 3-span bridge; 100 km/h train speed.

So far, only mode shapes with equal amplitudes for all simply supported spans have been considered. In case of different amplitudes for different spans (as observed in the measurement examples), a closer approach to the single-span bridge can be expected. However, certain amplitude combinations can be found which result in a higher resonance amplification. If one span has the amplitude 1 and all other spans have in-phase amplitudes of

$$A_k = \frac{\sqrt{n}-1}{n-1} \quad (15)$$

the maximum resonance amplification is

$$V_n = \frac{1}{2} \frac{n-1}{\sqrt{n}-1} V_1 \quad (16)$$

which would be  $V_9 = 2.25 V_1$  for a 9-span bridge. This theoretical upper limit, however, will rarely occur, and a reduced resonance amplitude is more probable.

### 6.3 Superposition of different fundametal modes

In case of equal simply-supported spans, the superposition of the modes of closely spaced eigenfrequencies is relevant. For the first fundamental modes, the superposition will not yield a higher resonance amplification than for the single-span bridge. Only the highest fundamental mode (with in-phase amplitudes) has already the same amplitude as the single span bridge and the superposition of the other modes would give a somewhat higher amplitude. To summarize,

the multi-span simply supported bridge has a cluster of eigenfrequencies which results in a cluster of critical train speeds where the lower critical speeds have lower amplitudes and the the highest critical speed may have a higher resonance amplitude than the single span bridge.

In case of equal continuous spans, the eigenfrequencies are clearly separated, and the contributions of other eigenfrequencies to one eigenfrequency are small. All lower eigenfrequencies have a smaller resonance amplification because of the higher modal mass and the limited modal force. Moreover, the resonance amplification of the highest fundamental mode (the in-phase mode with the highest modal force) is also smaller than the resonance amplification of the single-span simply-supported bridge.

The superposition of different modes can be performed in time domain for maximum amplitudes or in frequency domain for the root mean square value which is valid for the spectrum as well as for the time history. The maximum time amplitude is quite random and a maximum of

$$\max A = \sum_{k=1}^n A_k \quad (17)$$

is possible whereas the RMS-value

$$A_{RMS} = \sqrt{\sum_{k=1}^n A_k^2} \quad (18)$$

is more stable and neighbouring eigenfrequencies have less influence. As the RMS value can be calculated in the frequency domain by the different (axle-sequence, span-sequence, modal force and bridge transfer) spectra, it is easier to find rules for the RMS value of multi-span bridges. Criteria for the RMS value would be more robust for the assessment of railway bridges than maxima of time histories.

## 7 CONCLUSIONS

Eigenfrequencies and mode shapes of multi-span structures have been analysed in theory and by eight measurement examples. Whereas a single bridge has only one fundamental mode, multi-span bridges have generally  $n$  fundamental modes where the spans contribute with different positive and negative amplitudes. In case of equal simply-supported weakly-coupled spans, a cluster of eigenfrequencies occurs. Continuous beams show modes with mixed simply and hinged support conditions and separated fundamental eigenfrequencies. As a consequence for rail bridges, the multi-span continuous bridge has lower resonance amplitudes than a single span. Simply supported multi-span bridges have usually lower resonance amplitudes for the lower fundamental eigenfrequencies, but the highest (the in-phase) fundamental mode is as critical as a single span but at a slightly higher frequency. Due to the superposition of the nearby other fundamental eigenfrequencies and modes, somewhat higher amplitudes are possible for the corresponding higher critical speed.

## ACKNOWLEDGEMENT

Thanks to all measurement teams which can be found in the reference list. Thanks also to E. Viehfuß, W. Wuttke, and F. Ziegler.

## REFERENCES

- [1] R. Rohrmann, Theoretische Ermittlung von Bauwerksschäden mit Hilfe dynamischer Methoden, *Proceedings of Symposium Zerstörungsfreie Prüfung im Bauwesen*, Berlin, 371-382, 1985.
- [2] R. Rohrmann, S. Said, W. Schmid, Automatisches Dauerüberwachungssystem am Beispiel der Westendbrücke in Berlin. *Proceedings of 6. Tagung „Dynamische Probleme - Modellierung und Wirklichkeit“*, Hannover, 1-23, 2000.
- [3] L. Auersch, Berechnung des Schwingungsverhaltens von Gebäuden bei Einwirkung von Erschütterungen, *Bauingenieur* 59, 309-317, 1984.
- [4] L. Auersch, S. Said, Methods and phenomena of single and coupled floor vibrations – measurements in apartment and office buildings, *Building Acoustics* 22, 81-108, 2015.
- [5] Y. Deger, R. Cantieni, S. Pietrzko, W. Rücker, R. Rohrmann, Modal analysis of a highway bridge: Experiment, finite element analysis and link, *Proceedings of the 13<sup>th</sup> International Modal Analysis Conference (IMAC)*, Nashville, 1995.
- [6] R. Schneider, P. Simon, F. Hille, R. Herrmann, M. Baeßler, Vibration-based system identification of a large steel box girder bridge, *Proceedings of the 12<sup>th</sup> International Conference on Structural Dynamics (EURODYN)*, Delft, 2023.
- [7] P. Simon, M. Helmrich, R. Herrmann, R. Schneider, M. Baeßler, S. Lorelli, G. Morgenthal, Maintalbrücke Gemünden: Bauwerksmonitoring und -identifikation aus einem Guss, *Bautechnik* 99, 163-172, 2022.
- [8] P. Galvín, A. Romero, E. Moliner, M. Martínez-Rodrigo, Two FE models to analyse the dynamic response of short span simply supported oblique high-speed railway bridges: Comparison and experimental validation, *Engineering Structures* 167, 48–64, 2018.
- [9] L. Auersch, Resonances of railway bridges analysed in frequency domain by the modal-force-excitation, bridge-transfer and axle-sequence spectra, *Engineering Structures* 249, 113282, 2021.

## INFLUENCE OF DEEP FOUNDATIONS IN A DECK SLAB HIGH-SPEED RAILWAY BRIDGE: A THEORETICAL STUDY

Antonio Martínez-De la Concha\*<sup>1</sup>, David Suescum-Morales<sup>2</sup> and Hector Cifuentes<sup>1</sup>

<sup>1</sup> School of Engineering, Department of Continuum Mechanics and Structural Analysis, University of Seville, Camino de los Descubrimientos, s/n, Seville 41092, Spain  
{[delaconcha.bulte](mailto:delaconcha.bulte@us.es)}@us.es

<sup>2</sup> School of Civil Engineering, Construction Engineering Area, University of Cordoba, Av. de la Universidad s/n, 14240 Belmez, Spain  
p02sumod@uco.es

**Keywords:** Dynamic analysis, high-speed trains, railway bridges, soil-structure interaction, pile foundation, infrastructure, numerical simulations

**Abstract.** *In this research it is discussed the importance of properly modeling the infrastructure of high-speed railway bridges with deep foundations when using the finite element method (FEM). To do so, it is compared an isolated deck and several complete models with different characteristics. Parameters such as the length of the piles, the stiffness of the supporting layers and the type of dynamic load (10 different trains) were explored. This study started with the analysis of various parameters that determine the behavior of deep foundations with piles in simplified models. Based on these findings, it is built a complete model. This research shows the importance of including not only the surrounding terrain but also the main substructure (i.e., piers and abutments) in the model. Recommendations on the amount of soil to include, its mechanical properties and the length of the piles needed are also provided to ensure the reliability of results when considering the soil-structure dynamic interaction. With this research, it is intend to contribute to current knowledge with a series of guidelines and tools to help structural engineers in dynamic simulations through a theoretical case study.*

## 1 INTRODUCTION

High-speed railways have requirements for bridges due to the dynamic loads associated to train traffic. Considering this, the study of the dynamic behavior of railway bridges has become a key factor in the design of such structures [1]–[5]. The stresses and strains observed in a railway bridge due to train traffic can exceed the design limits (i.e., targets), particularly if the frequency of the applied loads matches the natural frequency of the structure as a result of undesired resonance. This is why the natural frequency of the structure should be tuned away from the frequency of the loads, as explained by Shen-Haw (2003). This phenomenon can lead to the inoperability of the structure and, in extreme cases, to its collapse.

The growth of the construction of high-speed railways has increased the concern and awareness of traffic-induced vibrations among engineers and scientists [6], [7]. This has led to impose limits on maximum accelerations and deflections using different codes and to prescribe an impact factor that is used to scale up the static loads in an effort to capture the dynamic effects [8], [9]. Dynamic simulations that are often conducted with time-consuming finite element methods (FEM) have become essential for avoiding such problems. Therefore, guidelines and tools to assist structural engineers in the process are needed [10].

Hence, capturing the behavior of the structure in a realistic manner is very important. In this regard, the development of computational methods has resulted in great progress in terms of knowledge and accuracy of analysis [7], [11], [12]. Some models take into account not only the motion of the loads on the bridge, but also changes in their magnitudes due to the dynamic interaction between the structure and the train suspension [13]–[15].

The dynamic loads used in this paper follow those proposed by the European design code [9], which are based on the High-Speed Load Model (HSLM) and comprise a series of fictitious trains proposed by ERRI D214 (1999). The loads are constant in magnitude for a given axle and move along the structure following the train motion. These load recommendations can also be found in other codes such as IAPF-07 [16]. It is not possible to conduct an analysis including multibody behavior because each train is composed of the car body, bogie, wheelset, primary and secondary suspension, axle box, yaw damper, lateral damper, antirolling torsion bar, rotating arm, lateral stop and traction rod [17], [18]. This study focused on the envelope behavior of the potential traffic over the bridge, as is usual in codes.

As discussed in Martínez et al. [19], most models only include the structure and disregard the supporting terrain by applying displacement boundary conditions directly on the structure. The simple linear elastic beams or frame structure are often used to simulate the vehicle-bridge dynamic response [20]. This simplification reduces the computational cost but assumes that the soil has infinite stiffness, as pointed out by Zangeneh et al. [21].

Limited material has been published regarding the influence of the soil-structure interaction (SSI) on the behavior of high-speed railway bridges. There are even fewer studies that also cover deep foundation models (i.e., with piles). An example is the study by Takemiya [22], which explored the behavior of high-speed railway structures and the surrounding terrain in Japan through the FEM. It concluded that including the soil-structure interaction was crucial to properly capture the behavior of the structure. Mahir Ülker-Kaustell had similar findings in his simplified analysis of a portal frame railway bridge [23]. Not including the supporting soil in the model can decrease the damping of the model, increasing the magnitude of displacements during resonance [24], [25]. The boundary element method (BEM) has a great application in the study of the soil-structure interaction [26], [27], allowing for more accurate analysis. It also eliminates the need to define an external contour in the model and has been used for longer than the FEM in this field [28]. Nevertheless, we chose to use the FEM because it is widely used in the study of these structures. The BEM is less common in practical applications.



We did not find any references of previous studies that explored the SSI as well as the influence of the following parameters: (i) different soil stiffness; (ii) different soil depth (i.e., different depths of piles); (iii) a speed sweep from 20 km/h to 420 km/h; and (iv) using 10 trains with different wheelbases and loads per axle. Following the formulation used in a recent study [19], two analyses methods were used: direct integration analysis of the complete model using the Newmark method in Abaqus (Abaqus/standard, version 6.14), and modal superposition analysis using SAP2000. For the direct integration analysis of the complete model, an amplitude decay factor of  $\gamma = 0.005$  was used. We used Abaqus 6.14 and SAP2000 v14 software, which are among those most commonly used for this type of studies [29]–[31].

The main novelty from the previous research by Martínez-De la Concha et al. [19] was the study of deep foundations. Regarding this particular issue, all the parameters to build the model including the infrastructure were new. The aim of this theoretical study with the FEM was to compare the results of the dynamic impact coefficient from a model that does not include the infrastructure (e.g., surrounding soil, piers, abutment and pile foundation) to a model that includes it. We explored parameters such as the length of the piles, the stiffness of the supporting layers or the type of dynamic load (i.e., 10 different trains).

This study began with the analysis of various parameters that control the behavior of deep foundations with piles in simplified models. Based on these findings, we built a complete model. With this research, we intend to contribute to current knowledge with a series of guidelines and tools to help structural engineers in dynamic simulations through a theoretical case study.

## **2 MODEL DESCRIPTION**

### **2.1 Simplified foundation model**

The objective of these analyses was to identify and tune the parameters that control the behavior of a deep foundation model (i.e., piles and pile cap) to ensure reliable converged results. We considered parameters such as finite element size and type, pulse duration and amount of soil to be included. For this study, we developed several simplified models in which we analyzed the influence of these parameters on the response. Based on the results, we subsequently built a complete model. The first simplified model analyzed the response of a square pile cap (6.5 x 6.5 x 2.0 meters). The pile cap was supported on 4 circular piles with a length of 15 m and a diameter of 1.5 m (Figure 1).

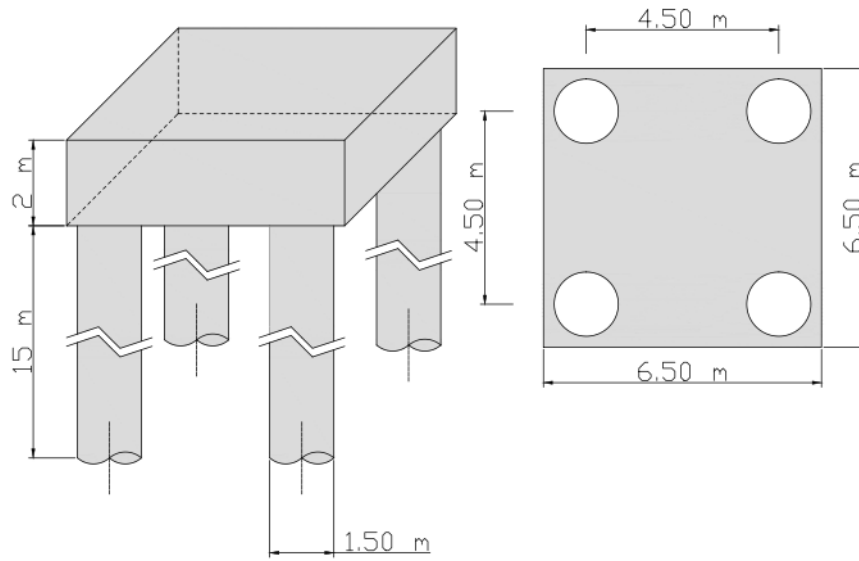


Figure 1. Model of pile cap for the simplified foundation model

The model included a portion of soil around the piles whose dimensions and characteristics were parameters to be studied. The piles and pile cap had the following mechanical characteristics: elastic modulus  $E=30$  GPa, Poisson coefficient  $\nu = 0.2$  and a specific concrete weight of  $\gamma_c = 25$  kN/m<sup>3</sup>. Two soil layers were considered: a 7 m meter deep superficial layer with softer properties ( $E = 3$  MPa,  $\nu = 0.35$  and a specific soil weight of  $\gamma_s = 20$  kN / m<sup>3</sup>); and a stiffer material layer underneath ( $E = 30$  MPa,  $\nu = 0.35$  and a specific soil weight of  $\gamma_s = 20$  kN / m<sup>3</sup>). This was still a relatively low stiffness material since we wanted to analyze the behavior of the system on a deformable elastic bed [32]. Five percent of the critical damping was used in the soil material definition [32], [33].

In the five faces defined by the soil boundary included, normal displacements were constrained. There was no relative movement in the concrete-soil interface. Instead, both meshes moved together like a continuous mesh. For this foundation model, three sensitivity studies were carried out:

1. finite element size;
2. pulse duration; and
3. volume of soil included in the model.

All model components were discretized using C3D4-type elements from the Abaqus library, that is, first-order tetrahedral elements. The models were run using direct integration in Abaqus/Explicit with the default values for numerical damping (i.e., a linear bulk viscosity of 0.06 and a quadratic bulk viscosity of 1.2). Since the same level of accuracy was not required in the entire modeled domain, local mesh refinements were applied where higher accuracy was needed. It is important to consider the effects on wave propagation when meshing the different models.

To identify the requirements for element size, the smallest model (Model 1 on Table 1) was meshed with three different element sizes – 30, 40 and 50 cm –, resulting in models with 43469; 21535; and 12772 degrees of freedom respectively. A uniform pressure load was applied on the pile cap upper face. Its magnitude was time-dependent following triangular amplitude. The response was analyzed against two different loads: a short pulse of 1 MPa maximum pressure and a duration of 10 ms; and a long pulse of 20 kPa of peak pressure and a duration of 500

ms. In both cases, the magnitude of the pulse was the same. The first one aimed to highlight the behavior during higher frequency dynamic events while the second one assessed loads that better represent the typical dynamic loads produced by train traffic. This statement follows Frýba (1996)[2].

To identify the amount of soil to include in the FEM model, it was necessary to explore it to maintain result accuracy while keeping the computation cost down. Simpler theoretical models, which can be solved analytically assuming isotropic and homogeneous linear elastic properties, consider the soil as a homogeneous half-space. Such is the case of studies conducted with the boundary element method (BEM) [35]. Hence, our models had the same conditions.

Pile cap width (6.5 m) was adopted as the characteristic length in the model. Five models with different amounts of soil were analyzed. The size of the models was the result of adding 6.5 m of soil around the pile cap and also 6.5 m of soil under the pile toe line. Subsequent models were built by adding 6.5 m of soil in each direction to the previous model. Additionally, a model with a very large portion of soil (i.e., the Limit model) was analyzed to verify that the reflection of waves in the boundary did not interfere with the simulation results meaningfully. To this end, the soil contours were moved out far enough so that the P waves had no time to reflect and return in the simulated time interval [21]. Table 1 presents the dimensions of the models described above.

Model name	Dimensions (m)			Soil under the end pile
	X	Y	Z	
Model 1	19.5	19.5	23.5	6.5
Model 2	32.5	32.5	30	13
Model 3	45.5	45.5	36.5	19.5
Model 4	58.5	58.5	43	26
Limit model	162.5	162.5	95	78

Table 1. Simplified foundation model dimensions

## 2.2 Bridge models

To analyze the bridge structure, we built two models: a model with infrastructure and a model without infrastructure. Those models were studied using a specific bridge software package: SAP2000 v14. Both models were explored using both modal superposition and direct integration. Sometimes the model includes elements such as the abutments and/or piles, but it rarely includes the soil-structure interaction [36]. Bridges are typically analyzed with models that only consider their deck [34]. The aim of our models was to assess the impact of the previous simplification. This required assessing the behavior of a simply supported isolated deck so that it could be compared with a complete one, which included the infrastructure.

### Isolated deck model

The deck of the bridge studied in this paper was identical to the one analyzed by the authors in previous research [19]. Its main characteristics are described below. In this model, we assumed displacement boundary conditions assuming infinitely stiff piers and abutments [12]. Shell elements with both membrane and plate degrees of freedoms were used. Flexural (i.e., plate) behavior considers rotational stiffness along the two axes in the element plane as well the displacement in the normal direction (i.e., Kirchoff's formulation) [29]. For the membrane

behavior, we used an isoparametric formulation that included the translational degrees of freedom in the element plane as well as the rotation within it. We considered displacements in the element plane using quadratic shape functions and out-of-plane displacements with cubic functions.

The modeled bridge had 4 spans so that the model included the interaction between spans accurately enough with an affordable computational cost. The bridge had two 30-m-long spans in the middle and one 25-m-long span at either end. The deck cross section was a 2.00-m-thick lightened slab with four 1.4-m-diameter circular lightening holes (Figure. 2). The slab was 14.00 m wide, which is standard for a double track line in Spain [8].

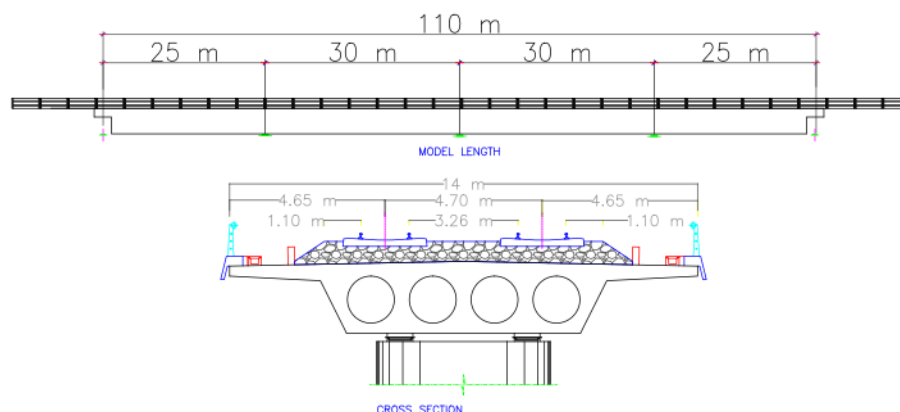


Figure. 2. Geometric description of the isolated deck model

The location of the nodes in the cross section is shown in Figure 3. The thickness of the elements was adjusted to obtain a section with the same area (i.e., same mass) as the real deck. A 1 m element size was used in the cross section and matched the element size along the bridge, resulting in approximately square elements as shown in Figure 3.

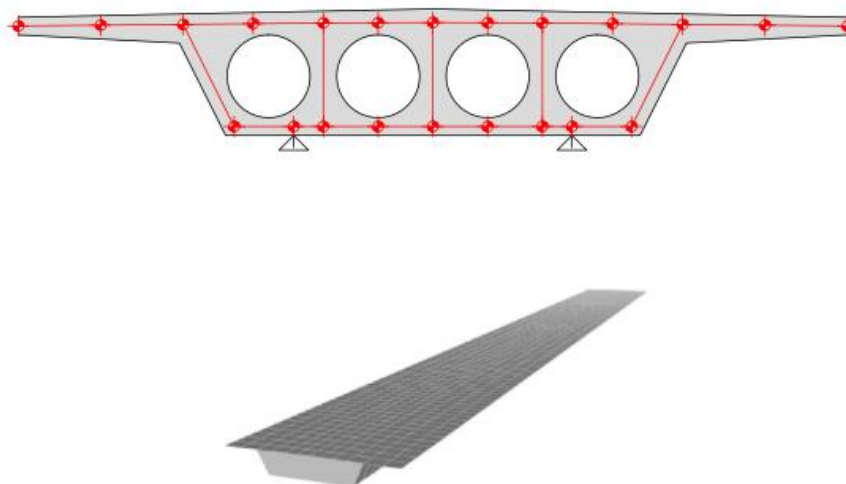


Figure. 3. Schematic view of the model cross section and mesh discretization of the isolated deck

Elements in the deck cross section were added on top of the abutments and piles to model the diaphragms. To visualize this, the elements modeling the webs and the bottom slab were concealed in Figure 4.

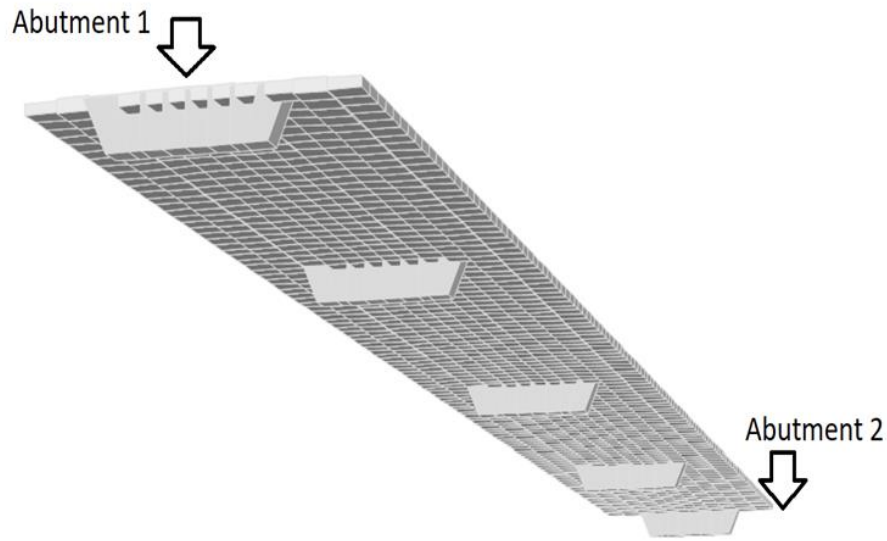


Figure. 4. Diaphragm modeling detailed view

The masses corresponding to the permanent loads were distributed over the upper slab. The permanent loads attributed to each element were as follows (kN/m): 94.84 (ballast); 6.70 (sleepers); 1.18 (rails); 5 (small wall); 3.78 (troughs); 9.59 (barrier rail) and 1.02 (railings).

The vertical displacement in all support points (Figure 3) was constrained. The lateral motion was constrained in one support location per pier/abutment. Finally, the longitudinal displacement was constrained in both support nodes only at one end of the bridge (Abutment 1). The mechanical properties of the deck were as follows: elastic modulus ( $E$ ) 30 GPa; Poisson coefficient ( $\nu$ ) 0.2; specific weight ( $\rho$ ) 25 kN/m<sup>3</sup>; and damping ( $\xi$ ) 3%.

We applied universal dynamic A train loads, also known as High-Speed Load Model (HSLM) loads. They consist of 10 trains with different wheelbases and loads per axle in various configurations [6]. These are the dynamic loads recommended by the main regulations for the design of new railway lines [9], [16]. Following the standards [16], a 350 km/h design speed was considered and, consequently, a speed sweep was analyzed from 20 km/h to 420 km/h (i.e., 1.2 times the design speed) with a 10 km/h step.

The traffic load was distributed among the nodes under the railway in the cross section. The applied force on each node was proportional to the surface of the sleeper over it (Figure 5). It was assumed that the load propagates uniformly with a 1/4 slope through the ballast and the sleeper distributes the load uniformly. This load application procedure is described in the Spanish code for this type of structures [16].

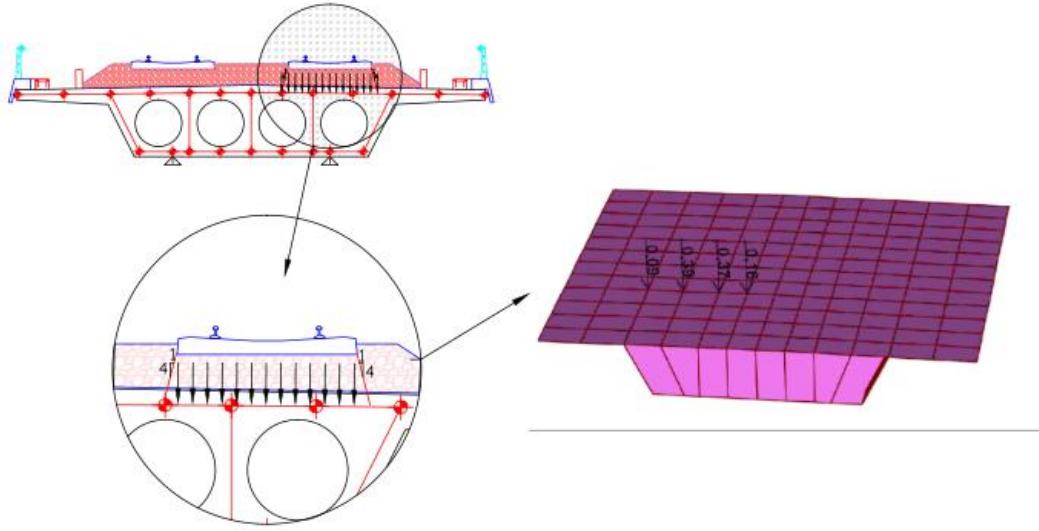


Figure 5. Load modeling in the cross section for the isolated deck model and complete model

In the longitudinal direction, the load was distributed in a linear fashion among two consecutive sections based on the distance between the load and the section at that particular time. This resulted in a series of triangular history loads as the different axles of the train traveled over a specific cross section of the bridge (Figure 6).

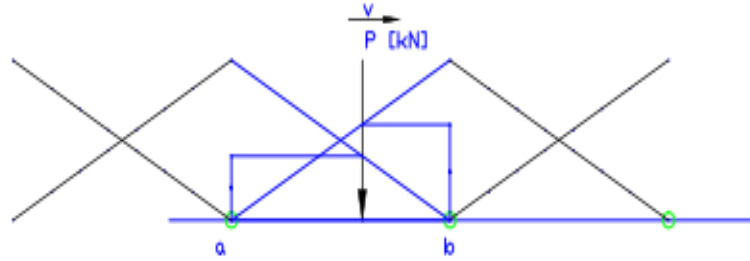


Figure 6. Longitudinal load distribution

The study focused on the central section of the bridge, specifically on the node of the upper slab that is centered with the track where the time-history loads are applied. This node captures the displacements of the track supports and ultimately of the trains that travel on top of them. We compared the maximum vertical displacement observed in this node during the entire simulation.

Dynamic amplification is captured by the impact factor ( $\Phi$ ), a commonly used parameter [6], [16] that normalizes the maximum deflection observed among all trains and across all speeds with that of the UIC-71 train [9] statically. For this paper and following the results of previous research [19], a different definition of the impact factor was used. Instead of using the UIC-71 train, each train dynamic response was normalized with its own static deflection.

### Complete model of the railway bridge

In this section, the soil-structure interaction was introduced into models with deep foundations. The model used in this section consisted of a deck that was identical to that described in Section 2.2, both geometrically and regarding loads. That deck was supported by 10-m-high abutments and 3 piers. The outboard piers were 20 m high while the pier at the center of the bridge measured 25 m. The abutments were of the closed type and consisted of a 1.00-m-thick and 10-m-high front wall with two lateral walls (i.e., wing walls) that were also 1.00 m thick. The abutment foundations were pile caps (14.00 x 6.00 x 2.00 m) with 6 piles 1.50 m in diameter. The pile caps were flush with the wing walls and protruded 2.00 m beyond the front walls. The pier foundations were 6.00 x 6.00 x 2.00 m pile caps with 4 piles 1.50 m in diameter. Figure 7 represents the structure described above.

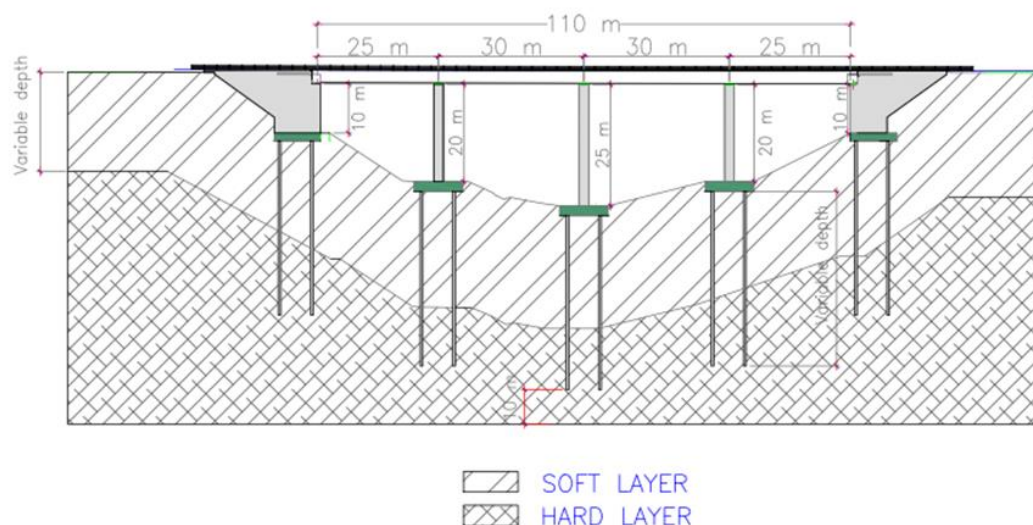


Figure. 7. Longitudinal section of the complete model

The piers were modeled with 1.00 x 1.00 m shell elements similar to those used on the deck. The pier cap was modeled with the same type of element and its mesh was adjusted so that the nodes would coincide with the deck above. The foundations of the piers were modeled with 1 m 8-node solid hexahedral elements based on the standard isoparametric formulation. For the pier-footing connection, the two bottom layers of nodes in the piers were rigidly coupled with three rows of nodes on the surface of the footing. This implied that they all moved as a rigid body, which modeled the embedding of the pier in the footing while allowing strains in the surrounding area. The abutments were also discretized in a similar way, with shell elements in the walls and solid elements in the foundations. Everything described above is shown in Figure 8.

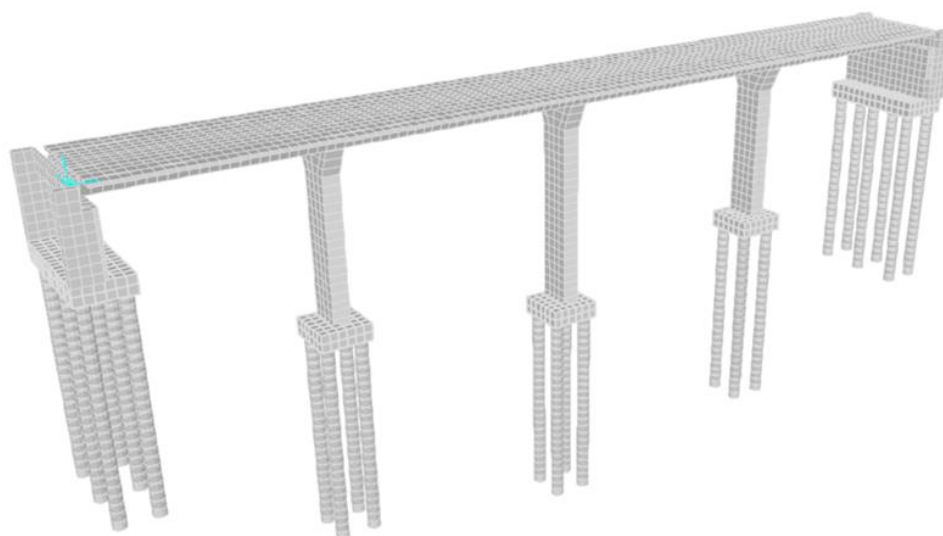


Figure 8. Complete model discretization without soil

A peculiarity of the abutments was that the soil inside them, specifically that contained between the wing walls and the back face of the front one, was included in the model as a solid element and matched the abutment element size. Thus, the overall stiffness and inertia of the system was better captured since it included the interaction with the backfill soil. The complete model also included the soil around the abutment and around the pile caps and piles. The model was extended with an additional 14 m of discretized soil around the foundation for a global model width of 34 m since the pile caps were 6 m wide ( $6 + 2 \times 14$ ). The soil depth of the soil included was 10 m greater than the deepest pile (i.e., middle pier foundation). The volume of soil included in these models was chosen in accordance with the results presented in Section 3.1.2.

Regarding soil stiffness, two different layers were considered: a soft layer, whose thickness and stiffness were variables to be explored, and a hard layer underneath, which extended 10 m below the deepest pile. The piles were always embedded 10 m within the stiffer material, whose mechanical properties were constant through the study. Normal displacements were constrained on the soil boundary faces. A summary of the models analyzed is presented in Table 2 using Figure 9 to illustrate one of them.

Soft layer depth (m)	Hard layer depth (m)	Pile foundation (m)	Modeled soil Depth (m)
4	20	12	24
6	20	14	26
8	20	16	28
10	20	18	30
12	20	20	32
14	20	22	34
16	20	24	36

Table 2. Complete model dimensions



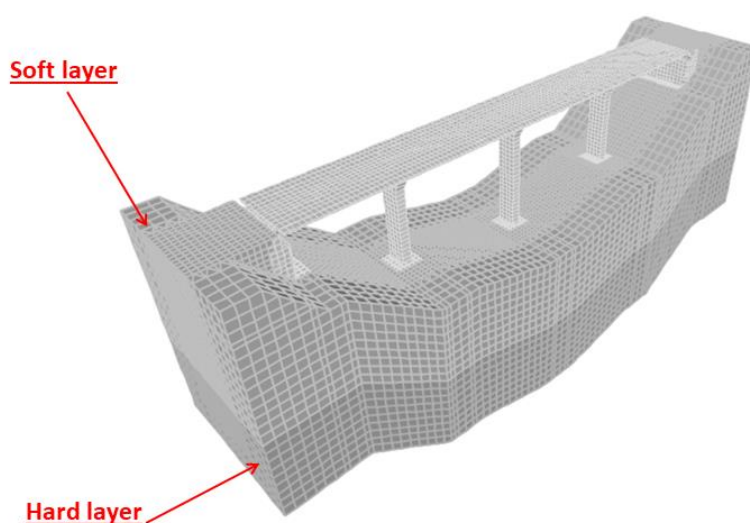


Figure. 9. Complete model discretization

Multiple analyses using different soil stiffness were performed to verify the importance of including the soil substructure while modeling deep foundation structures when considering their dynamic behavior. These stiffnesses were related to the wave propagation velocity ( $C_s$ ,  $C_p$ ,  $C_r$ ) through the equations that govern the behavior of homogeneous isotropic materials, whose derivation can be found in Yang and Hung [37]. To estimate the stiffness of the terrain, the shear wave velocity ( $C_s$ ) was used following the values and criteria proposed by seismic regulations.

For the hard layer material (i.e., the bottom one), we used a shear wave velocity of 800 m/s, which translates to a 3,500 MPa Young's modulus material and remained unchanged through the studies. This corresponds to Type I ground (compact rock) according to the NSCP-07 [38], Type A ground (rock or other rock-like geological formation) in the Eurocode 8 [39] and Type B ground (i.e., rock) in the ASCE-7 [40]. For the soft layer material, three different stiffness levels were analyzed for all the depths listed in Table 2 (4, 6, 8, 10, 12, 14 and 16 m). Table 3 shows the mechanical properties of the selected soft layer material options next to their description or classification according to the different codes.

$C_s$ (m/s)	E (MPa)	NCSP-07	EC-8	ASCE 7
100	55	IV Soft cohesive soil	D Loose to medium cohesionless soil	E Soft Clay soil
300	500	III Average compactness	C Dense sand	D Stiff soil
575	1800	II Fracture rock	B Very dense sand	C Very dense soil

Table 3. Soft layer material properties and classifications  $C_s$  (m/s)

### 3 RESULTS AND DISCUSSIONS

#### 3.1 Simplified foundation model

The influences of the various parameters that control the dynamic behavior of the simplified foundation models were analyzed. Based on these results, we subsequently built complete models.

##### Finite element size

Before considering the influence of element size, we analyzed the effect of the meshing technique (i.e., pattern) on the results. To do so, we compared the displacement response in the center of the bottom face of the pile cap when subjected to a short pulse (10 ms and 10 MPa) in the smallest foundation model variant (19.5 x 19.5 x 23.5) with two different mesh configurations. The first one – uniform mesh – had elements of similar dimensions throughout the domain (50 cm); the second one – locally refined mesh – had elements that increased in size in the soil when moving away from the foundation, from 50 cm at the interface with the foundation to 250 cm in the model outer contour. Figure 10 shows a comparison of these two meshing alternatives.

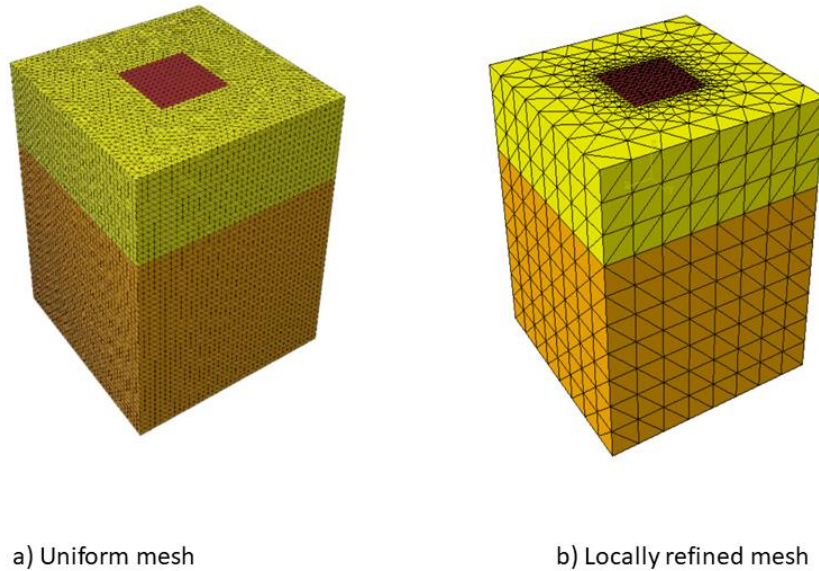


Figure 10. Meshing technique comparison: uniform mesh (a) and locally refined mesh (b)

As shown in Figure 11, both meshing techniques yielded similar results. Therefore, the foundation dynamic behavior appeared to be insensitive to the meshing technique for this particular application. The mesh sizes and seeding techniques explored did not have a meaningful impact on the response of interest. The results obtained were effectively the same both for the uniform mesh model (Figure 10 a) and the locally refined mesh (Figure 10 b). Therefore, the locally refined mesh was chosen to minimize computational cost.

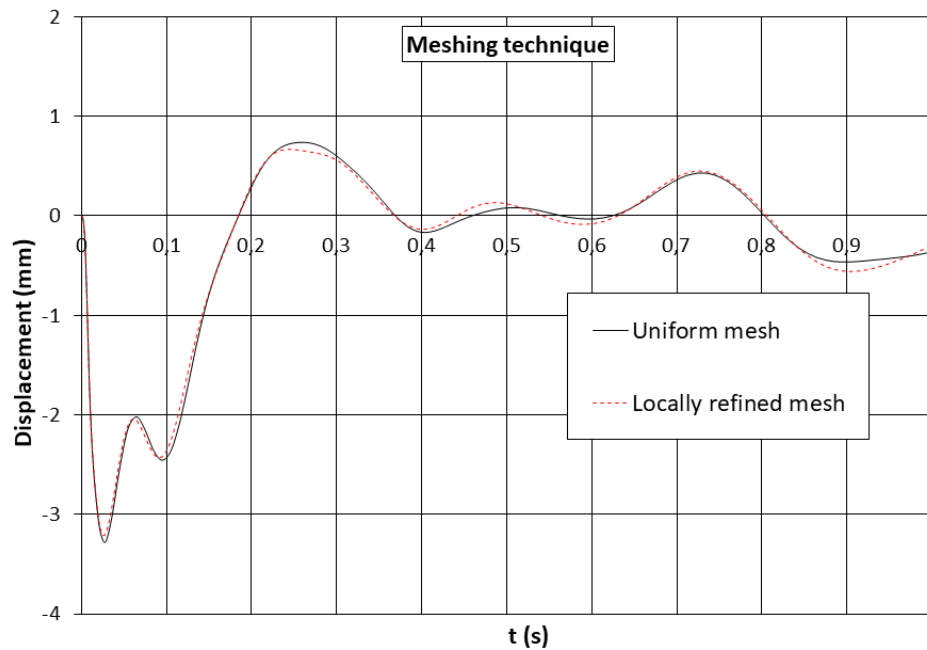


Figure. 11. Results of the comparison of different mesh techniques in the simplified foundation model

Using the locally refined mesh technique, three element sizes were tested in the foundation, pile cap and piles: 30 cm, 40 cm and 50 cm, obtaining the following maximum displacement results (Table 4). The seeding on the soil outer boundary was kept at 250 cm across all models.

Element size (cm)	Maximum displacement (mm)
30	3.226
40	3.203
50	3.180

Table 4. Maximum displacement for different element sizes

Similarly, for the locally refined models, the mesh refinement in the foundation, which ranged between 30 and 50 cm, did not affect the measured response either (Table 4). Consequently, a refined mesh of 50 cm in the interface was selected for the following studies with simplified foundations.

#### **Influence of pulse duration and the amount of soil included**

The response to a pulse of 10 ms (i.e., short pulse) was studied in the four models where the pile cap was surrounded by one, two, three or four times its dimension in soil (Table 1). In addition, a much larger model (162.5 x 162.5 x 95) was studied (Limit model). The vertical motion at the center of the bottom face of the pile cap is represented in Figure 12.

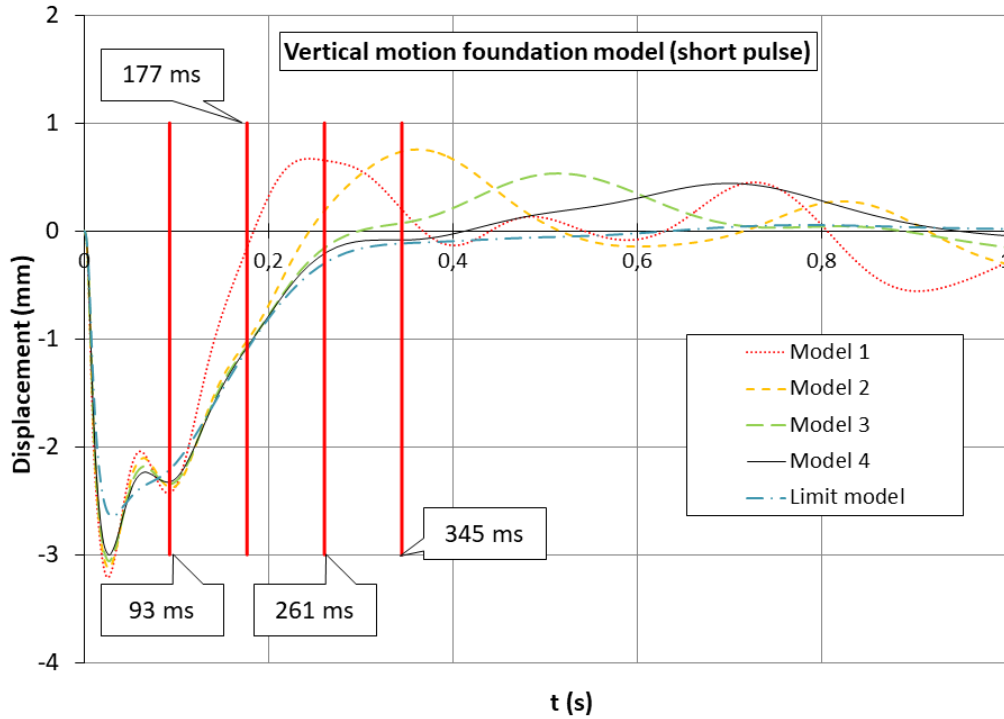


Figure 12. Terrain size response comparison under a 10 ms pulse (short pulse)

A sudden settlement in the pile cap was observed immediately after the pulse, with a peak value that was very similar across models and that occurred approximately at 30 ms. After this first settlement, there was a high frequency oscillation that could not be due to the reflection of waves in the boundary since it occurred at the same time in all models. If it were due to the boundary wave reflection, the oscillation would be delayed by the increasing distance to the boundary.

In addition, the curves in Figure 12 diverged from the Limit model solution when the wave front, which had reached the boundary and bounced back, returned to the pile cap (93 ms, 177 ms, 261 ms, 345 ms). This high frequency oscillation that occurred at around 60 ms was indeed associated with the longitudinal vibration that occurs in the piles themselves. This can be proven by increasing the mass of the piles making the phenomenon disappear (not shown in this research).

Figure 13 shows the maximum vertical displacement in the center of the footing against the ratio between the total model mass and the foundation mass. The solution converged with mass ratios over 600. This result was higher than the previous data obtained in shallow foundation models [41], where good results were obtained with a mass ratio in the order of 100. This showed a relevant difference between shallow foundations and deep foundations for a short pulse.

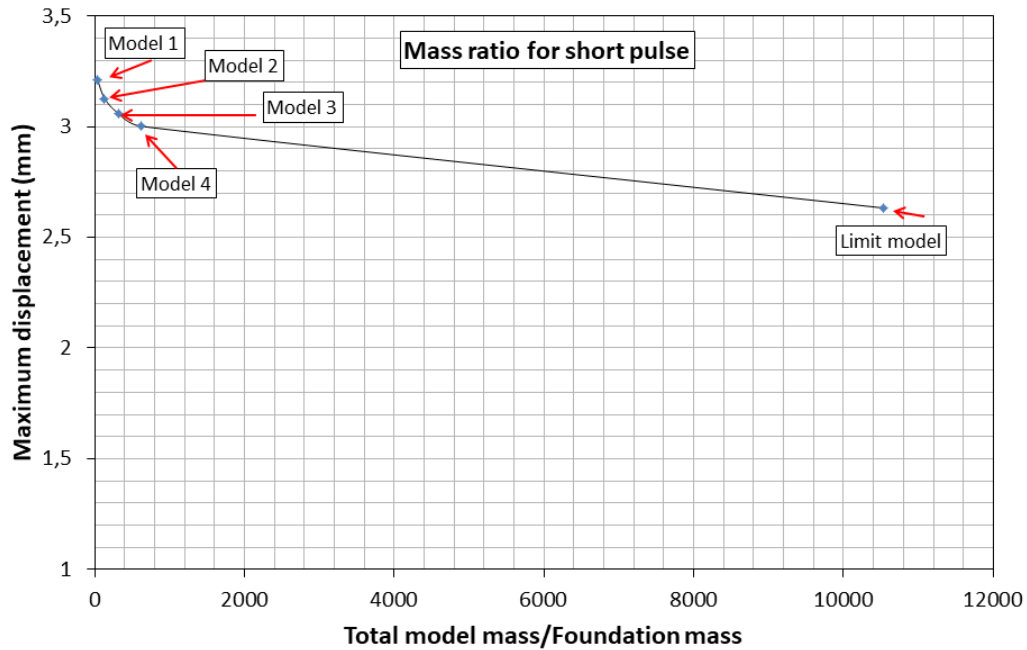


Figure 13. Maximum vertical displacements in the footing center for different total mass to footing mass ratios (short pulse)

It is important to highlight that the excitation trains actually produce on the foundations of structures has a lower frequency content than the one analyzed so far. For this reason, the previous analysis was reproduced with a longer duration pulse – 500 ms – and a lower pressure – 20 KPa. Figure 14 shows the results under this new loading condition where more coincidences were observed.

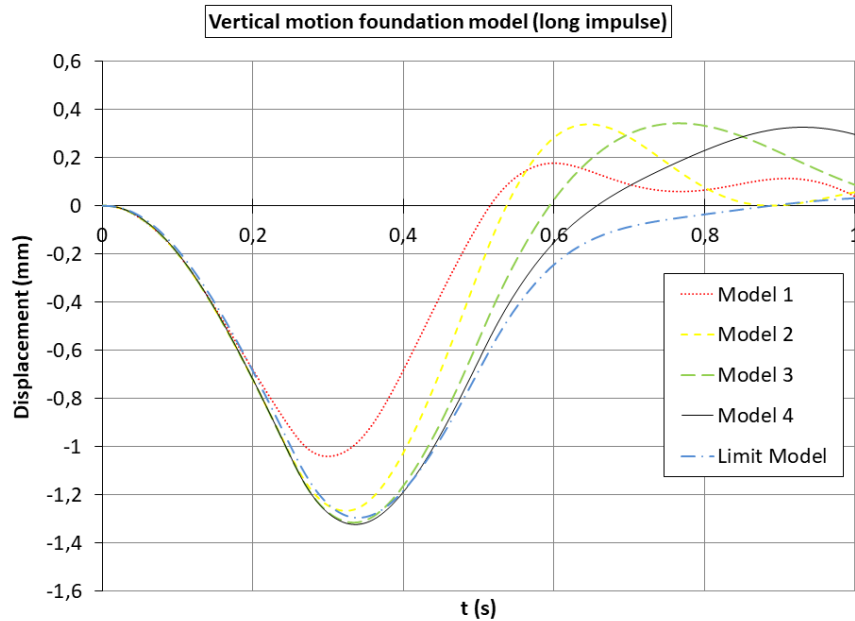


Figure 14. Terrain size response comparison under a 500 ms pulse (long pulse)

Figure 15 shows the peak response against the ratio of the masses included in the model for long pulse analysis. We observed how the mass that should be included in the model was significantly smaller than that required for short pulse analysis. In fact, the difference in results between Model 2 (32.5 x 32.5 x 30 m) and Model 4 (162.5 x 162.5 x 95 m) was only 2.17%, with the second model mass being only 130 times the mass of the foundation. Nevertheless, based on the aforementioned analysis, it was still necessary to include more soil in the deep foundation models than it was in the shallow foundation models, which only required a 20 total mass to foundation mass ratio under lower frequency excitation [19]. For longer pulses, (i.e., those that characterize the loading on high-speed railway bridge foundations), results were less sensitive to the amount of soil included, requiring as little as 100 times the mass of the foundation (Figure 15).

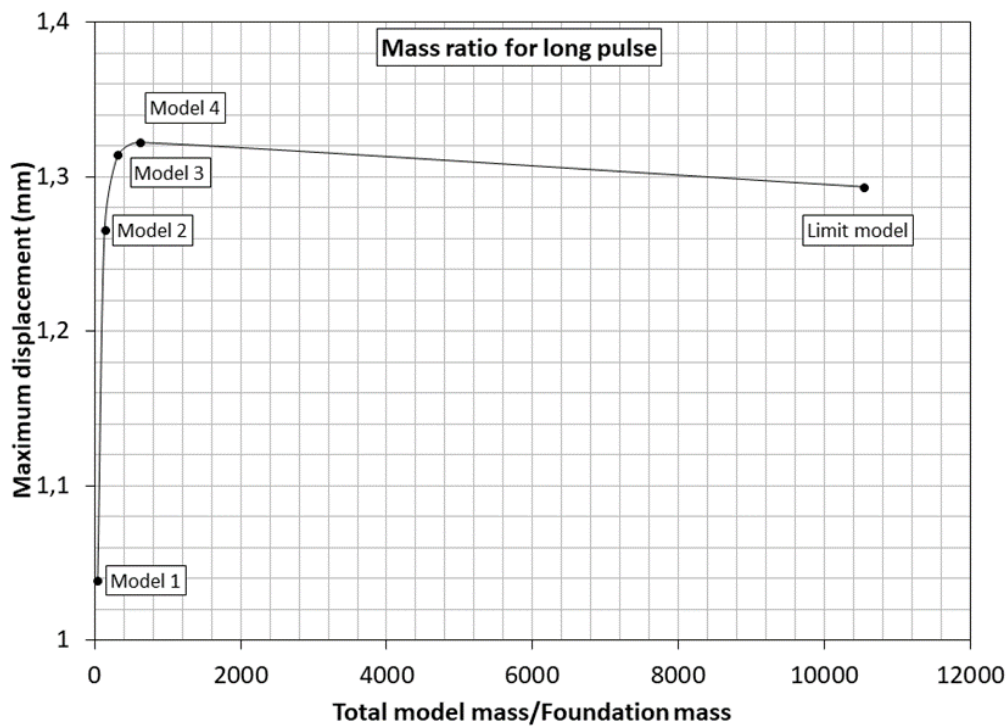


Figure 15. Maximum vertical displacements in the footing center for different total mass to footing mass ratios (long pulse)

### 3.2 Bridge model

#### Isolated deck

The objective of this analysis was to evaluate the impact factor with traditional boundary conditions. These results were used as a benchmark to be compared against results of models where the soil substructure was included in order to understand its influence on the impact factor. Importantly, the impact factor definition used in this paper does not follow that specified in some standards such as the IAPF [16]. In those standards, the normalizing static load produces higher deformations and consequently lower impact factors. Figure 16 represents the recorded maximum displacement of the depicted node in Section 2.2.1 in 10 km/h speed increments for every HSLM train history load.

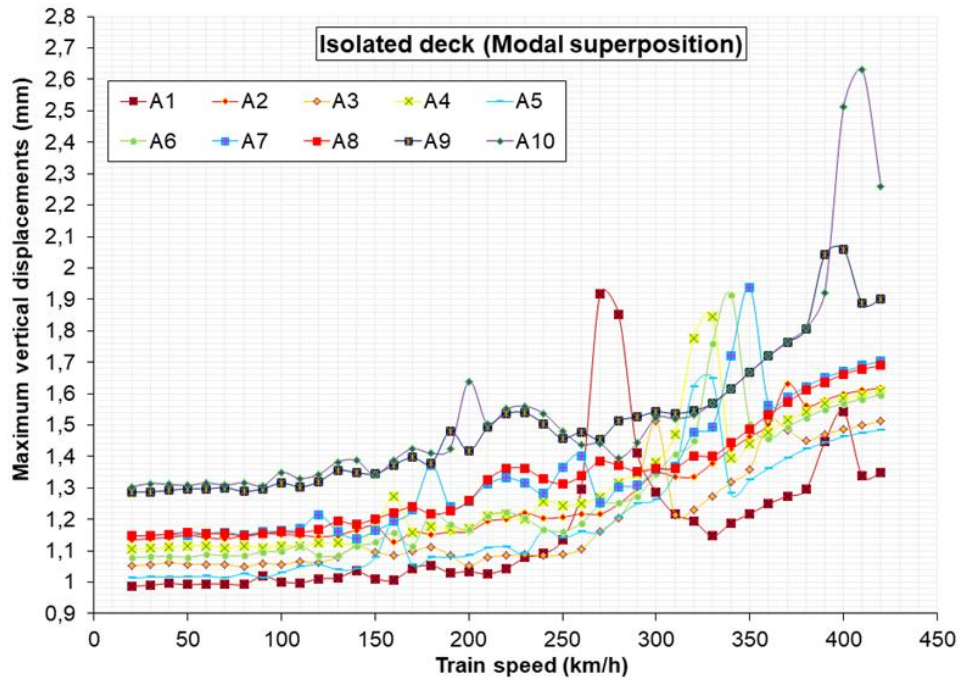


Figure. 16. Maximum vertical displacements in the isolated deck model (100 modes)

Modal superposition was used to obtain these results. The first 100 modes were used and captured 90.24% of the mass participation ratio associated to the vertical degrees of freedom. Results did not show any appreciable response amplification until 270 km/h were reached in the A1 train. This matched the bridge first resonance speed for A1 trains: 272.23 km/h. The resonance speed was obtained by multiplying the mode frequency by the distance between bogies of a particular train [42]. This same behavior also occurred with the other trains at higher speeds. In particular, the A10 train doubled its static response at 410 km/h. Proença et al. [43] explored the effect of the type of track on the dynamic behavior of a high-speed railway bridge with 4 spans, also obtaining the maximum displacement for the A10 train.

Additionally, it was also shown previously [19] that these types of structures are well represented using the first few modes with the superposition method. More specifically, only a 0.228% difference was measured when comparing the superposition solution to that of a fully integrated model with the Newmark method (Impact factor - modal superposition = 2.011 vs. Impact factor - direct integration = 2.016).

### Complete model of the railway bridge

The computational cost associated to performing an analysis in a model that includes piers, abutments, soil and deep foundations using direct integration methods is unreasonable when we consider the number of analyses that need to be performed (i.e., multiple trains at multiple speeds). Modal superposition should be used.

#### *Analysis with the number of modes included in the modal superposition*

A sensitivity analysis of the number of modes included in the modal superposition was performed considering 100, 200, 300, 400 and 500 modes. As the number of modes increased, the recorded maximum deflections also rose. Nevertheless, all the responses grew approximately proportionally across trains and speeds.



Figure 17 shows maximum displacement results obtained in models in which a 10 m soft layer of soil ( $C_s = 100$  m/s) rests over a harder terrain ( $C_s = 750$  m/s) for the A1 and A10 trains in the HSLM [9], [16]. Maximum displacements for all the trains covered in the HSLM were computed but only A1 and A10 are represented for better readability of the results. As shown in Figure 17, the worst train-speed combination (A10 at 410 km/h) appeared to be independent of the number of modes included in the superposition analysis. The A10 train always exhibited a resonance at 410 km/h with a peak value that exceeded the maximum displacement for the A1 train and any other train in the HSLM at any speed, regardless of the number of modes included.

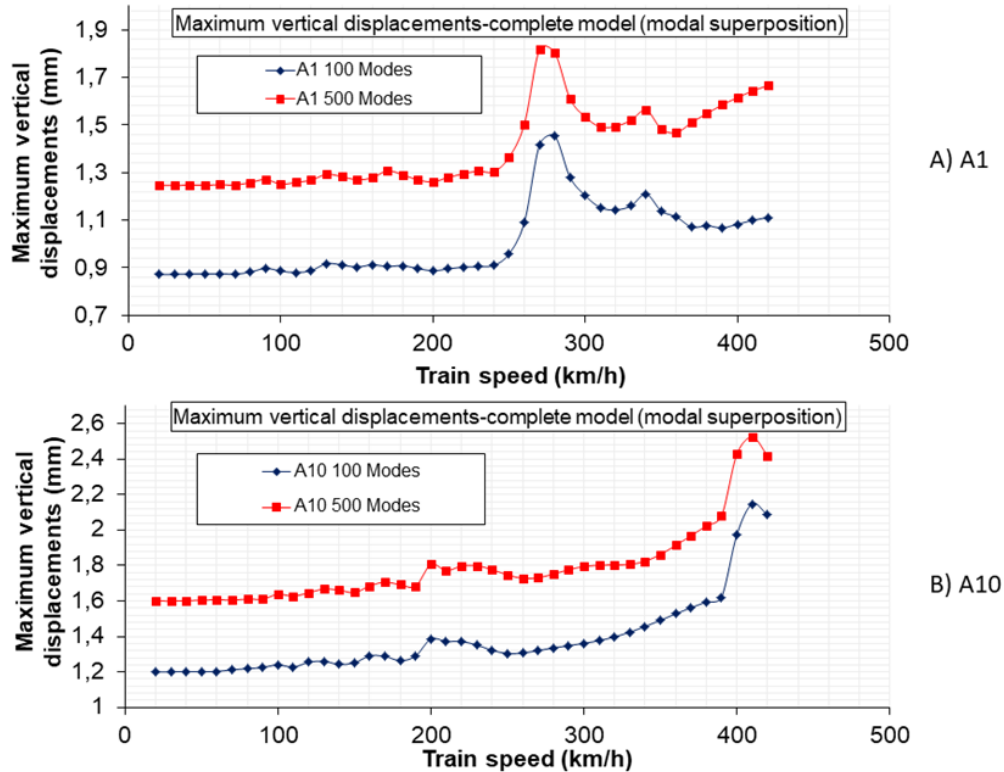


Figure 17. Maximum vertical displacements in the complete model (100-mode and 50-mode solutions for A1 and A10 trains)

The maximum displacement increased with the number of modes included in the modal superposition solution without any sign of convergence, as observed in Figure 17. Consequently, the worst train-speed combination was rerun using direct integration to obtain accurate results. Given the results presented, it was decided to run the analysis sweeps in speeds and trains using modal superposition with 500 modes followed by a direct integration analysis of the worst case model: the one with the train-speed combination that produced the highest displacements.

#### *Soil stiffness sensitivity analysis*

Figure 18 summarizes, for the train-speed combinations that produced the greatest displacements, the maximum vertical displacement for different soft layer material properties and depths. The maximum displacement for the isolated deck is also included for comparison. Please note that these are results obtained using direct integration in the worst cases identified through modal superposition.



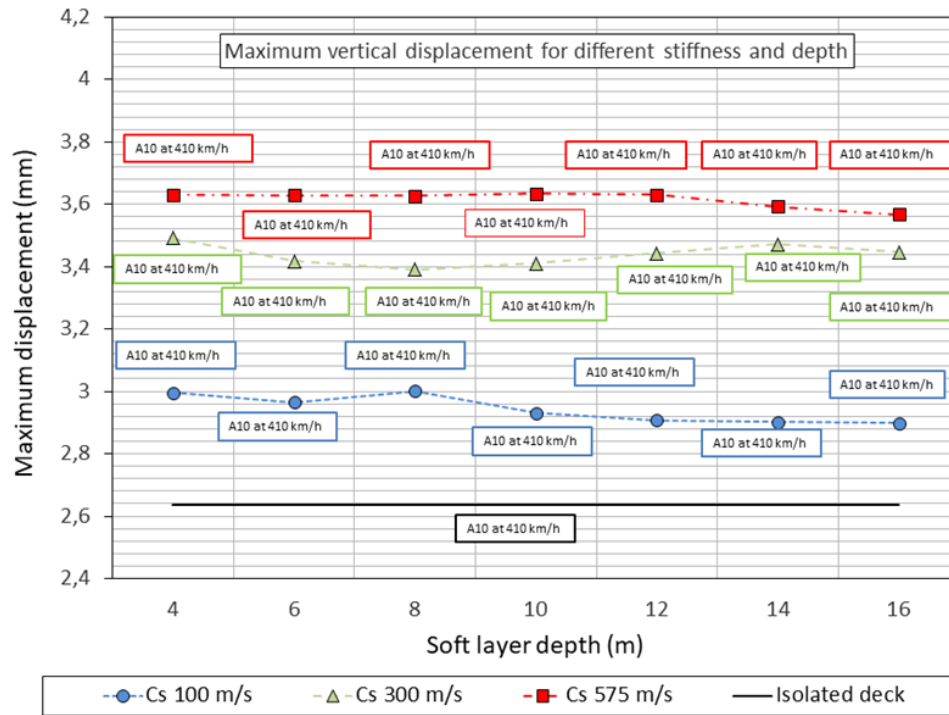


Figure 18. Maximum vertical displacements for different soft layer material stiffness and depth

When considering the effects of the soft layer material stiffness and depth (Figure 18) on the maximum displacement results, the response appeared to be insensitive to the depth of this superficial softer material layer but not to its stiffness. For the range of depths of soft material analyzed – 4 to 16 m – there was not a meaningful variation in the maximum displacement for a given layer stiffness, with all the results within 4% for each stiffness. However, the stiffness of this superficial layer played an important role in the final results, with higher maximum deflections when higher stiffness properties were used. This was the opposite of the effect on the static solution.

The train-speed combinations that produced the greatest displacements were 380, 390 and 410 km/h for A10 and A2 trains according to the HSLM classification used (Figure 18) [6]. The lack of trend in the speeds and type of train that produced the worst responses highlights the importance of exploring all types of trains used in the research and a wide range of speeds. Figure 19 shows, for the train-speed combinations that produced the greatest displacements, the maximum impact factor ( $\Phi$ ) for different soft layer material properties and depths. The impact factor for the isolated deck is also included for comparison.

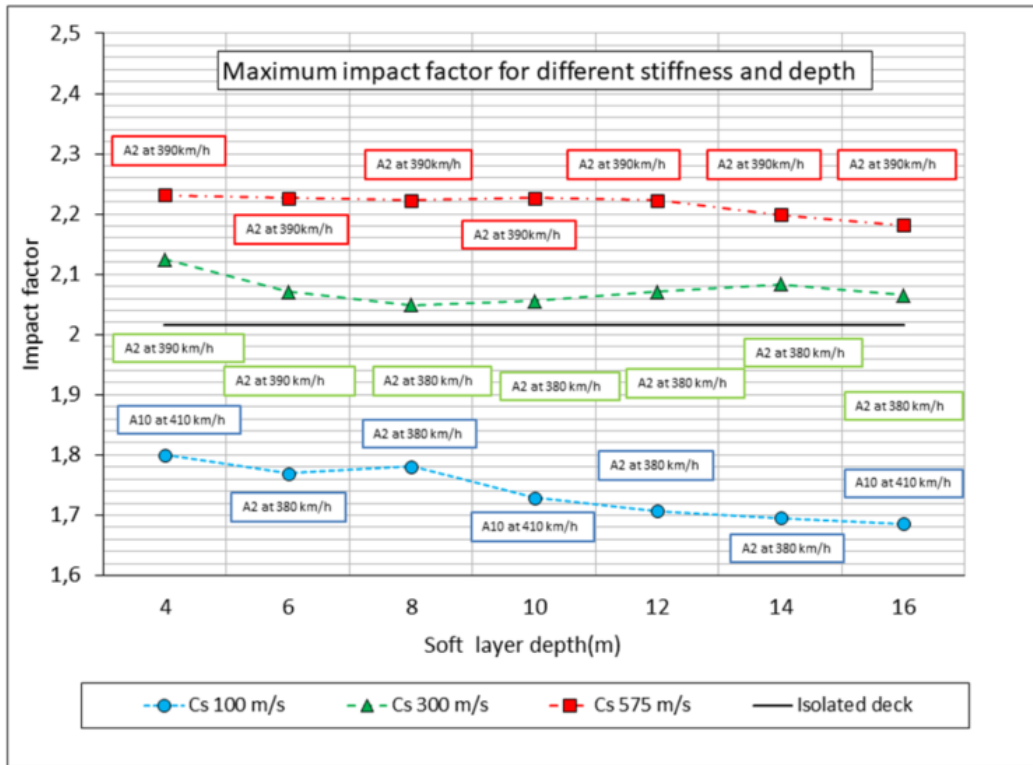


Figure 19. Maximum impact factor for different soft layer material stiffness and depth

When the results were analyzed in terms of the impact factor (Figure 19), which assesses dynamic amplification, we observed the following: response amplification depended very little on the soft layer depth but increased with its stiffness. This helps to understand why maximum displacement grows with soil stiffness. Even though a stiffer superficial layer slightly decreased the static deflection, the effect of stiffness on the impact factor coefficient was so important that it dominated the resulting dynamic maximum deflections.

When comparing these results with the benchmark – results of the isolated deck model – the maximum displacements of the isolated deck were even lower than the softer soft layer models. The impact factor coefficient lies somewhere between the different stiffness levels used for the soft layer. In other words, the isolated deck did not follow the trend defined by the stiffness of the soft layer material. To understand this, please note that, for an infinitely stiff soft layer material, the model analyzed would still include deformable piers and abutments. This conclusion could also be reached using stiffer soil models, but those models would not be realistic because they would not require deep foundations. This highlights the importance of including not only the surrounding terrain but also the main infrastructure (i.e., piers and abutments) in the model.

#### 4 CONCLUSIONS

The aim of the manuscript was to compare the results of the dynamic impact coefficient of a model without any infrastructure (i.e., isolated deck) with those of a model that included infrastructure (i.e., complete model). The research was conducted using the finite element method. First, the effect of model parameters (i.e., element size, pulse duration and volume of soil included in the model) was studied in a simplified foundation model.

Based on the results, some complete models were built with different variables: soil stiffness and depth, depth of the piles and a speed sweep from 20 km/h to 420 km/h, using 10 trains with different wheelbases and loads per axle. The following conclusions can be drawn from the simplified foundation models:

1. In this study, mesh sizes and seeding techniques did not have a meaningful impact on the response. Results showed convergence with a finite element size of 50 cm, regardless of the type of mesh used.

2. For a short pulse, associated to higher frequency events, significant differences were observed in the maximum displacements with the amount of soil included. In this case, a mass ratio of about 600 is recommended between total model mass and foundation mass.

3. For longer pulses, such as those that characterize the loading on high-speed railway bridge foundations, results were less sensitive to the amount of soil included. A total mass/foundation mass ratio of 100 was enough.

4. We found a relevant difference between shallow foundations and deep foundations.

In addition, the following conclusions can be drawn from the bridge models:

1. There were no differences (regarding the impact factor) between using modal superposition or direct integration for an isolated deck (Impact factor – modal superposition = 2.011 vs. Impact factor – direct integration = 2.016)

2. The sensitivity analysis to the number of modes included in the modal superposition for the complete model indicated that, as the number of modes increased, the recorded maximum deflections also rose.

3. To be more efficient (i.e., reduce computational cost), it is recommended to run the analysis sweeps in speeds and trains using modal superposition with 500 modes followed by a direct integration analysis of the worst case model (which produces the highest displacements).

4. The maximum displacement results were insensitive to the depth of the superficial softer material considered in the complete model.

5. The changes in the maximum displacement with the stiffness of the superficial layer played an important role in the final results. With the highest stiffness for this superficial layer ( $E=1800$  MPa), the maximum displacement was 27.28% higher than in the isolated deck.

6. The dynamic response amplification (i.e., impact factor) depended very little on the soft layer depth but increased with its stiffness.

7. The isolated deck did not follow the trend defined by the stiffness of the soft material. To understand this, please note how, with an infinitely stiff soft layer material, the analyzed model would still include deformable piers and abutments.

8. The previous conclusion highlights the importance of including not only the surrounding terrain but also the main substructure (i.e., piers and abutments) in the model.

### Acknowledgments

The authors would like to acknowledge the financial support provided for this research by the Spanish Ministry of Economy and Competitiveness within the framework of project BIA2013-48352-P. D. Suescum-Morales would also like to acknowledge the financial support from the Spanish Ministry of Education (<http://www.mecd.gob.es/educacion-mecd/>) through grant FPU 17/04329

### REFERENCES

- [1] G. DIANA and F. CHELI, “Dynamic Interaction of Railway Systems with Large Bridges,” *Veh. Syst. Dyn.*, vol. 18, no. 1–3, pp. 71–106, Jan. 1989, doi:

- 10.1080/00423118908968915.
- [2] L. Frýba, *Vibration of solids and structures under moving loads*. Springer Netherlands, 1972. Accessed: May 19, 2017. [Online]. Available: [https://books.google.es/books?hl=es&lr=&id=EjH0CAAAQBAJ&oi=fnd&pg=PR5&dq=Vibration+of+solids+and+structures+under+moving+loads&ots=vvAuIAi-9e&sig=TopNdQF8Qc4NvcxX\\_odueVPlI0Y#v=onepage&q=Vibration+of+solids+and+structures+under+moving+loads&f=false](https://books.google.es/books?hl=es&lr=&id=EjH0CAAAQBAJ&oi=fnd&pg=PR5&dq=Vibration+of+solids+and+structures+under+moving+loads&ots=vvAuIAi-9e&sig=TopNdQF8Qc4NvcxX_odueVPlI0Y#v=onepage&q=Vibration+of+solids+and+structures+under+moving+loads&f=false)
- [3] M. Klasztorny, “Vertical vibrations of a multi-span beam steel bridge induced by a superfast passenger train,” *Struct. Eng. Mech. An Int. J.*, vol. 12, no. 3, pp. 267–281, 2001, Accessed: May 30, 2024. [Online]. Available: <https://www.dbpia.co.kr/journal/articleDetail?nodeId=NODE09866329>
- [4] M. Shamsi and A. Ghanbari, “Nonlinear dynamic analysis of Qom Monorail Bridge considering Soil-Pile-Bridge-Train Interaction,” *Transp. Geotech.*, vol. 22, p. 100309, Mar. 2020, doi: 10.1016/J.TRGEO.2019.100309.
- [5] H. Xia, N. Zhang, and G. De Roeck, “Dynamic analysis of high speed railway bridge under articulated trains,” *Comput. Struct.*, vol. 81, no. 26–27, pp. 2467–2478, Oct. 2003, doi: 10.1016/S0045-7949(03)00309-2.
- [6] “ERRI Specialists’ Committee D214, ‘Rail Bridges for Speeds 2000km/h, Final Report Part A Synthesis of the Results of D214 Research,’ European Rail Research Institute, 1999. - References - Scientific Research Publishing.” <https://www.scirp.org/reference/referencespapers?referenceid=924494> (accessed May 30, 2024).
- [7] C. Johansson, N. Á. N. Nualláin, C. Pacoste, and A. Andersson, “A methodology for the preliminary assessment of existing railway bridges for high-speed traffic,” *Eng. Struct.*, vol. 58, pp. 25–35, 2014, doi: 10.1016/j.engstruct.2013.10.011.
- [8] ADIF Ministerio de Fomento Gobierno de España, “IGP-5 Instructions and recommendations on Spanish Railway Structures.” 2011.
- [9] Comité Europeo de Normalización, “Eurocódigo 1: Acciones en estructuras: Cargas de tráfico en puentes.” 2010.
- [10] C. Svedholm, “Efficient Modelling Techniques for Vibration Analyses of Railway Bridges.” <https://www.diva-portal.org/smash/record.jsf?pid=diva2%3A1073647&dswid=8187> (accessed May 30, 2024).
- [11] J. M. Goicolea, F. Gabaldón, and F. Riquelme, “Design Issues for Dynamics of High Speed Railway Bridges,” *Int. Assoc. Bridg. Maint. Safety, Porto*, no. section 2, 2006, Accessed: May 17, 2017. [Online]. Available: <http://postgrado.mecanica.upm.es/papers/goicolea-paper-iabmas06-2.pdf>
- [12] M. Majka and M. Hartnett, “Effects of speed, load and damping on the dynamic response of railway bridges and vehicles,” *Comput. Struct.*, vol. 86, pp. 556–572, 2008, doi: 10.1016/j.compstruc.2007.05.002.
- [13] E. Esmailzadeh and N. Jalili, “Vehicle–passenger–structure interaction of uniform bridges traversed by moving vehicles,” *J. Sound Vib.*, vol. 260, no. 4, pp. 611–635, Feb. 2003, doi: 10.1016/S0022-460X(02)00960-4.
- [14] K. Knothe and S. L. Grassie, “Modelling of Railway Track and Vehicle/Track Interaction at High Frequencies,” *Veh. Syst. Dyn.*, vol. 22, no. 3–4, pp. 209–262, Jan. 1993, doi: 10.1080/00423119308969027.
- [15] S. G. M. Neves, A. F. M. Azevedo, and R. Calçada, “A direct method for analyzing the vertical vehicle–structure interaction,” *Eng. Struct.*, vol. 34, pp. 414–420, Jan. 2012, doi: 10.1016/J.ENGSTRUCT.2011.10.010.

- [16] Ministerio de Fomento Gobierno de España, *Instrucción de acciones a considerar en puentes de ferrocarril (IAPF)*. Ministerio de Fomento, Centro de Publicaciones, 2010.
- [17] H. Gou, C. Liu, H. Hua, Y. Bao, and Q. Pu, "Mapping relationship between dynamic responses of high-speed trains and additional bridge deformations," *JVC/Journal Vib. Control*, vol. 27, no. 9–10, pp. 1051–1062, May 2021, doi: 10.1177/1077546320936899/ASSET/IMAGES/LARGE/10.1177\_1077546320936899-FIG15.JPEG.
- [18] M. Szafranski, "A dynamic vehicle-bridge model based on the modal identification results of an existing EN57 train and bridge spans with non-ballasted tracks," *Mech. Syst. Signal Process.*, vol. 146, p. 107039, Jan. 2021, doi: 10.1016/J.YMSSP.2020.107039.
- [19] A. Martínez-De La Concha, H. Cifuentes, and F. Medina, "A Finite Element Methodology to Study Soil-Structure Interaction in High-Speed Railway Bridges," *J. Comput. Nonlinear Dyn.*, vol. 13, no. 3, 2018, doi: 10.1115/1.4038819.
- [20] H. Li, Z. Yu, J. Mao, and L. Jiang, "Nonlinear random seismic analysis of 3D high-speed railway track-bridge system based on OpenSEES," *Structures*, vol. 24, pp. 87–98, Apr. 2020, doi: 10.1016/J.ISTRUC.2020.01.003.
- [21] A. Zangeneh, A. Andersson, and C. Pacoste, "Identification of soil-structure interaction effect in a portal frame railway bridge through full-scale dynamic testing," vol. 159, no. October 2017, pp. 299–309, 2018, doi: 10.1016/j.engstruct.2018.01.014.
- [22] H. Takemiya and X. C. Bian, "Shinkansen high-speed train induced ground vibrations in view of viaduct-ground interaction," *Soil Dyn. Earthq. Eng.*, vol. 27, no. 6, pp. 506–520, Jun. 2007, doi: 10.1016/J.SOILDYN.2006.11.003.
- [23] M. Ülker-Kaustell, R. Karoumi, and C. Pacoste, "Simplified analysis of the dynamic soil-structure interaction of a portal frame railway bridge," *Eng. Struct.*, vol. 32, pp. 3692–3698, 2010, doi: 10.1016/j.engstruct.2010.08.013.
- [24] J. Vega, A. Fraile, E. Alarcon, and L. Hermanns, "Dynamic response of underpasses for high-speed train lines," *J. Sound Vib.*, vol. 331, no. 23, pp. 5125–5140, Nov. 2012, doi: 10.1016/J.JSV.2012.07.005.
- [25] A. Zangeneh, C. Svedholm, A. Andersson, C. Pacoste, and R. Karoumi, "Dynamic Stiffness Identification of Portal Frame Bridge-Soil System using Controlled Dynamic Testing," *Procedia Eng.*, vol. 199, pp. 1062–1067, Jan. 2017, doi: 10.1016/J.PROENG.2017.09.293.
- [26] A. Doménech, L. Bonet, and P. Museros, "Interacción vehículo-estructura en puentes ferroviarios de hormigón pretensado en situaciones de resonancia. Validación del método del amortiguamiento adicional propuesto por el Eurocódigo 1," 2009, Accessed: May 17, 2017. [Online]. Available: [https://riunet.upv.es/bitstream/handle/10251/11807/Tesina\\_A.Domenech.pdf?sequence=1](https://riunet.upv.es/bitstream/handle/10251/11807/Tesina_A.Domenech.pdf?sequence=1)
- [27] A. Romero, M. Solís, J. Domínguez, and P. Galvín, "Soil-structure interaction in resonant railway bridges," *Soil Dyn. Earthq. Eng.*, vol. 47, pp. 108–116, 2013, doi: 10.1016/j.soildyn.2012.07.014.
- [28] J. Domínguez and J. Roeset, "Dynamic stiffness of rectangular foundations," *NASA STI/Recon Tech. Rep. N*, 1978.
- [29] K. J. Bathe, *Finite Element Procedures*. Prentice Hall, 1996.
- [30] S.-H. Kim and M. Shinozuka, "Development of fragility curves of bridges retrofitted by column jacketing," *Probabilistic Eng. Mech.*, vol. 19, no. 1–2, pp. 105–112, Jan. 2004, doi: 10.1016/j.probenmech.2003.11.009.
- [31] J.-W. Lin, C.-W. Chen, and S.-H. Chung, "Modeling and assessment of bridge

- structure for seismic hazard prevention,” *Nat. Hazards*, vol. 61, no. 3, pp. 1115–1126, Sep. 2011, doi: 10.1007/s11069-011-9969-3.
- [32] L. Cañizo *et al.*, *Geotecnia y cimientos*. Madrid: Escuela Técnica Superior de Ingenieros de Caminos, Canales y Puertos, Servicio de Publicaciones de Alumnos, 1970.
  - [33] Ministerio de Fomento Gobierno de España, *Norma de Construcción Sismorresistente: Puentes (NCSP-07)*. Ministerio de Fomento, Centro de Publicaciones, 2008.
  - [34] L. Frýba, “Traffic loads on railway bridges,” *Dyn. Railw. Bridg.*, pp. 183–198, 1996, doi: 10.1680/dorb.34716.0010.
  - [35] A. Romero, P. Galvín, and J. Domínguez, “Comportamiento dinámico de viaductos cortos considerando la interacción vehículo-vía-estructura-suelo,” *Rev. Int. Métodos Numéricos para Cálculo y Diseño en Ing.*, vol. 28, pp. 55–63, 2012, doi: 10.1016/j.rimni.2011.11.004.
  - [36] M. D. Martínez-Rodrigo, “Atenuación de vibraciones resonantes en puentes de ferrocarril de Alta Velocidad mediante amortiguadores fluido-viscosos,” Universidad Politécnica de Valencia, 2009.
  - [37] Y. B. Yang and H. H. Hung, *Wave Propagation for Train-Induced Vibrations*. World scientific, 2009.
  - [38] Ministerio de Fomento, *NCSP-07, norma de construccion sismorresistente: Puentes (NCSP-07)*. Madrid: Ministerio de Fomento, Centro de Publicaciones, 2008.
  - [39] C. E. de N. CEN, “Eurocódigo 8: Parte 1 : Reglas generales , acciones sísmicas y reglas para edificación,” 2018.
  - [40] ASCE/SEI, “Minimum design loads for buildings and other structures,” *ASCE Stand.*, p. 608, 2010, doi: 10.1061/9780784412916.
  - [41] A. Martínez-De la Concha, H. Cifuentes, and F. Medina, “A Finite Element Methodology to Study Soil–Structure Interaction in High-Speed Railway Bridges,” *J. Comput. Nonlinear Dyn.*, vol. 13, no. 3, p. 031010, Jan. 2018, doi: 10.1115/1.4038819.
  - [42] B. H. Kim, J. Lee, and D. H. Lee, “Extracting modal parameters of high-speed railway bridge using the TDD technique,” *Mech. Syst. Signal Process.*, vol. 24, no. 3, pp. 707–720, Apr. 2010, doi: 10.1016/J.YMSSP.2009.11.010.
  - [43] J. M. Proença, H. Casal, and M. Neves, “EFFECT OF THE TYPE OF TRACK ON THE DYNAMIC BEHAVIOUR OF HIGH SPEED RAILWAY BRIGDES”.

## A STUDY OF THE CONTRIBUTION OF BENDING, TORSION AND DISTORSION FOR THE DYNAMIC RESPONSE OF CURRENT STRUCTURAL TYPES IN HIGH-SPEED RAILWAY BRIDGES

José M. Goicolea<sup>1</sup>, Nicola Tarque<sup>1</sup>, Andrea Tapia<sup>1</sup>, Alfredo Cámara<sup>1</sup>, Khanh Nguyen<sup>2</sup>

<sup>1</sup> Universidad Politécnica de Madrid, E.T.S. de Ing. Caminos, Canales y P., 28040 Madrid  
{jose.goicolea,nicola.tarque, andreastephanie.tapia,alfredo.camara}@upm.es

<sup>2</sup> Universidad Politécnica de Madrid, E.T.S. de Ing. Aeronáutica y del Espacio, 28040 Madrid  
khanhnguyen.gia@upm.es

**Keywords:** railway bridges, modal analysis, high-speed railways, bending modes, torsional modes, Finite Elements, bridge dynamics

**Abstract.** *The bridges and viaducts in modern high-speed railway lines in the Spanish and European networks have often cross sections for twin tracks, with transversal sections of different structural types. For instance, in the Spanish network, built in the last 35 years, the typical cross sections span a width of 14m, including 1) open sections with monolithic slab on “I” or “U” type girders, 2) full slab hollowed section, 3) closed sections with single cell box girders. In this study the range of bridges considered will be mainly short to medium spans and longitudinally simply supported on piles and abutments, which are the cases which exhibit more significant dynamic responses. Considering the eccentricity of the traffic loads for twin track cross sections we aim to analyse the coupled bending and torsional dynamic effects. In this work we study the dynamic behaviour using 3D beam semi-analytical modal analysis procedures with a versatile and fast open software developed in-house [1]. This software permits efficient and fast parametric calculations for complete collections of bridges from given lines. However, the cross sections of open type do not comply well with the beam hypothesis of rigid cross sections, so in addition 3D finite element models are developed to evaluate the distortion of the cross section in the dynamic response, and to calibrate the assigned torsional stiffness for equivalent beam models. Due to the lower torsional stiffness of the open cross sections, the torsional and bending modes have eigenfrequencies of the same order, and develop significant coupling between them in the dynamic response under the traffic actions of high-speed trains. The results of this work lead to practical guidelines and conclusions regarding the cases in which torsional vibrations are relevant in the dynamic response of railway bridges.*

[1] CALDINTAV v3, software for dynamic analysis of railway bridges, K Nguyen, J Goicolea et al, <http://w3.mecanica.upm.es/caldintav/>, 2021.

## INFLUENCE OF THE SOIL-STRUCTURE COUPLING ON THE DYNAMIC BEHAVIOUR OF A PORTAL FRAME RAILWAY BRIDGE

Josep Chordà-Monsonís<sup>\*1</sup>, Juan C. Sánchez-Quesada<sup>1</sup>, Emma Moliner<sup>1</sup>, Antonio Romero<sup>2</sup>, Pedro Galvín<sup>2,3</sup>, María D. Martínez-Rodrigo<sup>1</sup>

<sup>1</sup>Universitat Jaume I  
Avgda. Vicent Sos Baynat s/n, 12071, Castelló de la Plana, Spain  
e-mail:chordaj@uji.es

<sup>2</sup> Universidad de Sevilla  
Camino de los Descubrimientos s/n, 41092, Sevilla, Spain

<sup>3</sup> ENGREEN, Laboratory of Engineering for Energy and Environmental Sustainability  
Camino de los Descubrimientos s/n, 41092, Sevilla, Spain

**Keywords:** Railway underpass, vibrations, acceleration, experimental data, track irregularities

**Abstract.** *Portal frame bridges are partially-buried structures with a dynamic response strongly influenced by the surrounding soil. As a consequence, predicting their dynamic behaviour is difficult, as simulating the soil-structure interaction in an accurate manner requires an elevated computational effort. For this reason, this interaction mechanism is rarely included in the numerical models. Nevertheless, the research on this topic highlights that this is indeed a determinant cause of discrepancy between numerical and experimental predictions. In this work, a complete study on an existing portal frame is carried out. First, the modal parameters are identified from experimental data. Then, a 3D finite-element numerical model considering the track-bridge-soil system is implemented. Perfectly matched layers are used at the model boundaries to reduce the computational cost. After evaluating the soil-structure interaction, the resulting data is used to implement a simplified version of the model on which the soil is substituted by a series of spring-damper elements. After calibration, this model is used to predict the dynamic response of the portal frame under operating conditions. Dynamic excitation mechanisms such as track irregularities are also taken into account. As results highlight, the applied methodology allowed to reproduce the modal and dynamic behaviour of the bridge with reasonable accuracy in an efficient manner.*



## 1 INTRODUCTION

Among a growing demand to enhance more sustainable alternatives in industrial and logistic processes, railway transportation networks are adapting with new lines and more demanding traffic conditions. This constitutes a challenge, as the infrastructure needs to be adapted to the terrain in a coherent way while managing the interaction with other transportation networks and ensuring safe conditions in the infrastructures. In this sense, portal frame bridges are a widely used solution on modern railway lines. These structures are used as underpasses and facilitate regular roads to pass under the railway tracks. Portal frames consist of a partially-buried reinforced concrete rigid frame flanked by integral wing walls and surrounded by an embankment. As most of its surface is in direct contact with the soil, the dynamic response of portal frames is heavily influenced by the soil-structure interaction (SSI) [1]. Nevertheless, due to the high associated computational cost, this interaction mechanism is seldom included in the numerical models dedicated to predict the dynamic response of these structures [2].

As it is known, due to the large contact area with the soil, these bridges possess a notable capacity to dissipate energy. This affects in a significant way their modal properties and dynamic behaviour under passing trains. As a consequence, neglecting the dynamic stiffness of the surrounding soil in the numerical models may be causing divergences between numerical and experimentally identified modal parameters [3]. Besides, an incorrect assessment of SSI effects could lead to misleading results when determining the resonance speed on particular trains, which depends on the soil damping [4], resulting into inefficient structural designs [5]. On the contrary, including SSI in the numerical models could bring a more realistic evaluation of the Serviceability Limit States of existing bridges when a change in the traffic conditions is required and to more cost-efficient bridge designs. Thus, this effect should be included in the dynamic analyses of portal frames to predict their dynamic response in a precise way, because, as previous research has found, the exact influence of the soil on portal frames is not yet well known. This may be explained by a lack of reliable simple models to simulate the SSI, as few are the works that conduct experimental-numerical validations [1].

In view of this, in the present contribution, a complete study on an existing portal frame is carried out with the following objectives: (i) to identify the modal parameters of the bridge from experimental data and (ii) to predict its dynamic response under passing trains in an accurate and efficient manner. To this aim, a 3D finite-element (FE) numerical model of the structure is implemented including the track-bridge-soil system. The soil domain is padded with perfectly matched layers (PML) to absorb the radiating soil waves and avoid spurious wave reflections. This complete model is used to obtain frequency-dependent impedance functions that will simulate the effect of the soil-structure contact in a subsequent simplified model. Then, the track and bridge parameters are calibrated and an experimental-numerical comparison of the bridge modal parameters is conducted to evaluate the adequacy of the model. Finally, the dynamic response of the bridge under train passages is investigated. Randomly-generated track irregularities are included in the numerical model to assess the rail condition in a more realistic way.

This paper is organised as follows. In Section 2, the bridge under study is described. Section 3 addresses the identification of the bridge modal parameters. In Section 4, the main characteristics of the complete and simplified models are detailed. The process of implementing the SSI with spring-damper elements is also addressed and validated. The complete formulation of the dynamic problem and the excitation mechanisms taken into account are outlined in Section 5. Subsequently, the dynamic response of the bridge under train passages is evaluated in Section

6. Finally, the main conclusions of the work are summarised in Section 7.

## 2 BRIDGE UNDER STUDY

The focus of the investigation is a portal frame railway bridge. It is located in the high-speed (HS) line Madrid-Sevilla, in the Ciudad Real – Brazatortas section at the kilometric point 31+200. The bridge deck is a broad structure of 22.1 m width and 8 m span length. The section of the underpass consists of a rectangular integral box of 5.7 m height built with reinforced concrete. The bridge holds three tracks: two for HS services and one for conventional traffic. This condition leads to the most characteristic feature of the portal frame, as it is divided along its width in two sections by means of a longitudinal joint, resulting in two coupled structures: one below the conventional traffic track and another under the HS tracks. Figure 1 shows two images of the portal frame. The bridge dimensions can be seen on Figure 2.



Figure 1: Different views of the portal frame under study.

## 3 MODAL IDENTIFICATION

Bridge experimental data was acquired in September 2022 in a in-field campaign carried out by the authors with the aim to characterise the modal parameters of the portal frame. A total of 27 piezoelectric accelerometers were used to record the dynamic response of the structure with a nominal sensitivity of 10 V/g. The sensors were located on the inner face of the slab, just as indicated in Figure 3: 18 on the top slab (shown in red); 6 on the inner side of the vertical walls at a height of 2.6 m (shown in yellow); and 3 on the floor (shown in blue).

In this way, the dynamic response of the bridge was recorded under 27 train passages and also under ambient vibration conditions. The data was obtained at a sampling frequency of 4096 Hz and then decimated to 256 Hz. A Chebyshev filter of 1 Hz was applied. Then, an operational modal analysis (OMA) was carried out. The Enhanced Frequency Domain Decomposition method (EFDD) was used to identify the bridge vibration modes. The analysis allowed to assess that due to the slab decoupling on two separate structures, the underpass has an asymmetric modal behaviour, on which the bridge sections (HS and conventional) participate in different proportion. Consequently, coupled or mixed modes appear, on which the deformation is perceivable on both sections. However, in some cases, uncoupled modes are also detected.

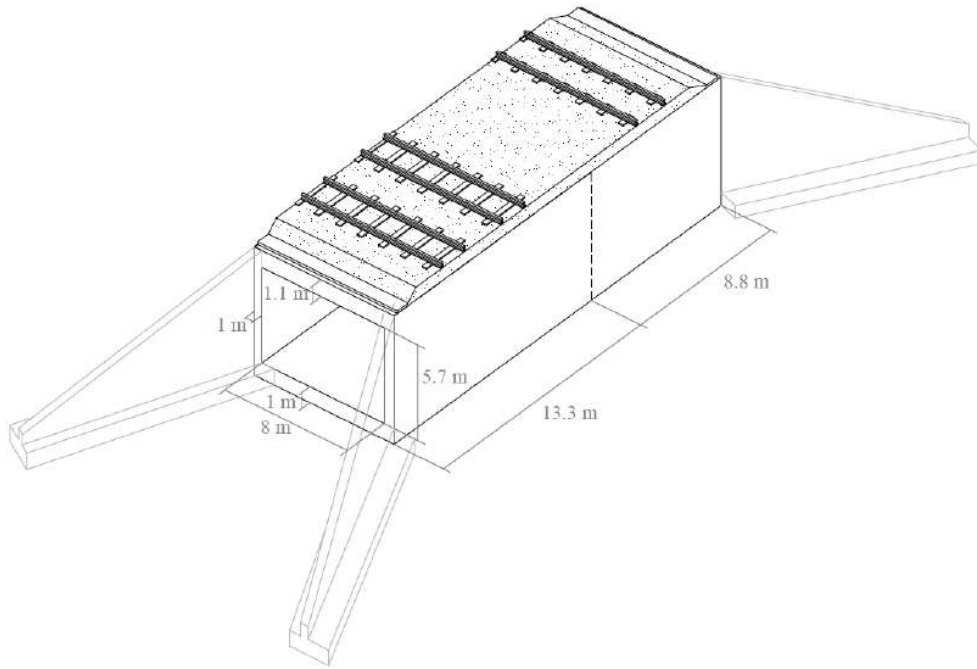


Figure 2: Dimensions of the whole structure.

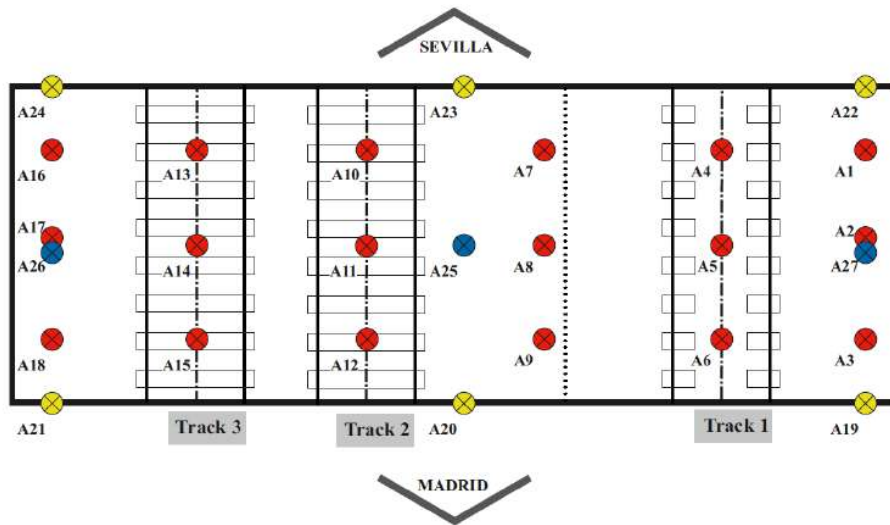


Figure 3: Scheme representing the accelerometer layout. The colours red yellow and blue stand for sensors located on the top slab, vertical walls and bottom slab, respectively.

Figure 4 shows the identified modal parameters of the bridge, where the dashed line in the mode shapes represents the longitudinal joint that divides the structure. In general, as the bridge width is larger than its length, the transverse bending is predominant in the majority of modes, with the exception of the first three frequencies. Mode 1 represents the decoupled longitudinal bending mode of the HS section. Modes 2 and 3 are very close in frequency. The second mode

could be considered as a transition step to the proper fundamental longitudinal bending mode of the conventional section in  $f_3$ . Modes 4, 6, 7 and 8 stand for particular transverse bending modes of the conventional section, practically decoupled from the rest of the bridge. Finally, modes 5 and 9 a predominant transverse deformation of the HS section. It is worth mentioning that the accelerometer layout allows for a fairly good resolution of the mode shapes representation on the top slab. Still, some additional spatial resolution would be required in order to perfectly capture the mode shape of higher frequency modes such as the one in  $f_9$ , which results to be quite similar to  $f_5$ . High damping ratios have been detected, especially in the first four modes, which evinces the strong influence of the soil in this structure.

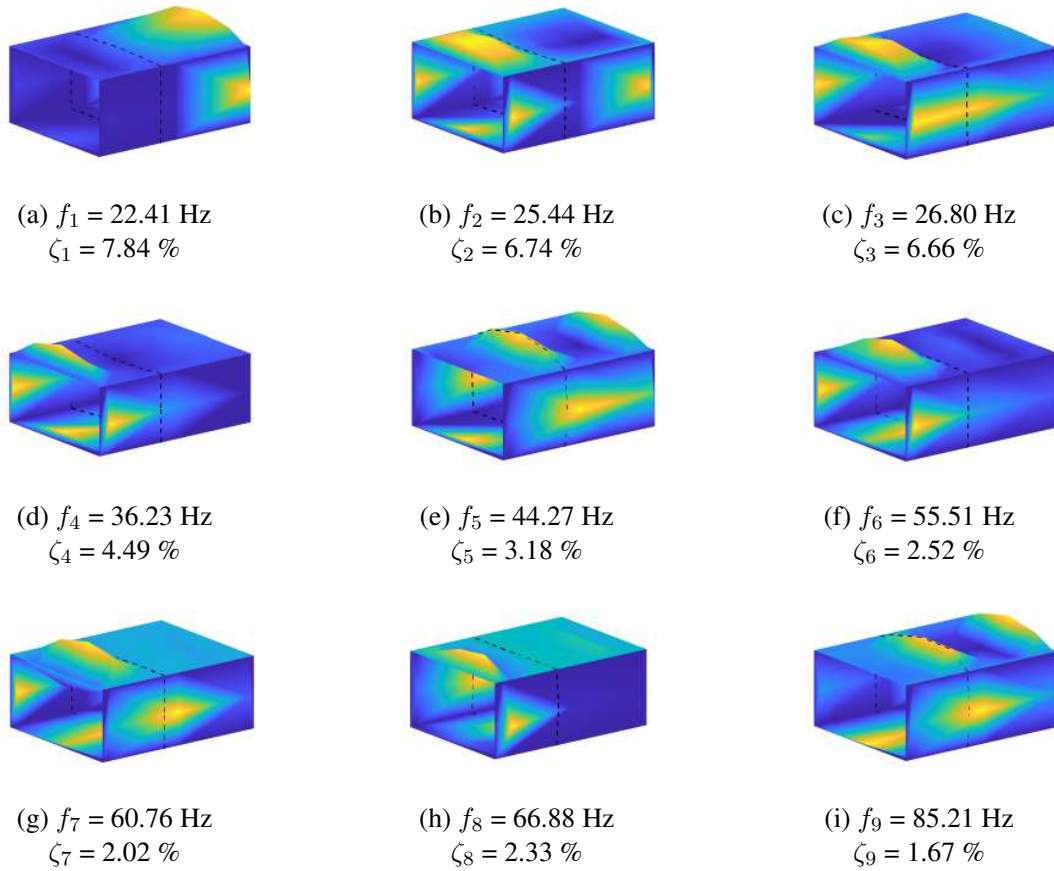


Figure 4: Measured modal parameters of the portal frame.

#### 4 NUMERICAL APPROACH

This section addresses the numerical procedure followed with the aim to reproduce the dynamic response of the portal frame with an admissible computational cost. To this purpose, a complete 3D FE numerical model is implemented considering the track, the bridge and the surrounding soil. This model is used as a first step to evaluate the effect of the SSI on the bridge. The results are then used to configure a new simplified version of the previous model to perform a complex modal dynamic time-history analysis.

#### 4.1 The soil-bridge-track model

First, a detailed 3D FE numerical model of the portal frame is implemented in ANSYS(R) v.22.1. In this model, the tracks, the bridge structure and the surrounding soil are represented. Both track and backfill are prolonged 7.5 m at the bridge sides. To avoid spurious wave reflections, the soil boundaries are padded with solid PML elements to absorb propagating waves. This allows for the reduction of the soil domain and thus for a lower computation time. Proper soil and PML lengths are set to  $L_{soil} = 6.0$  m and  $L_{PML} = 0.5$  m, respectively, to ensure the adequacy and stability of the results, as indicated in Figure 5(a). With regards to the PML, three layers of elements are introduced. The mesh in the PML region is discretised to satisfy the condition stated in Reference [6] by which between 5 and 20 elements should fit in a single wave length  $\lambda = 2\pi c_s/\omega$ , being  $c_s$  the shear wave propagation speed of the soil and  $\omega$  the highest identified frequency of the bridge. The different parts of the model are meshed as follows. Solid elements with isotropic elastic behaviour are used to mesh the soil domain (SOLID185). The bridge is meshed with shell elements (SHELL181). The track, ballast and sleepers are also meshed with solid (SOLID185) finite elements. Rail pads are represented by means of spring-dampers (COMBIN14), and rails are simulated with Timoshenko beams (BEAM188). Non-structural elements such as handrails are also included in the numerical model as lumped masses (MASS21). The soil domain under the bridge is considered homogeneous with  $c_s = 350$  m/s. This value is selected on the basis of a preliminary calibration step conducted on the complete model. The soil domain forms a prism of dimensions  $24 \text{ m} \times 49.1 \text{ m} \times 7.5 \text{ m}$ . In total, the model has 1,340,132 degrees of freedom (DOF). A picture of the complete model is shown in Figure 5(b). The mechanical properties of the track, bridge and soil are listed in Table 1:

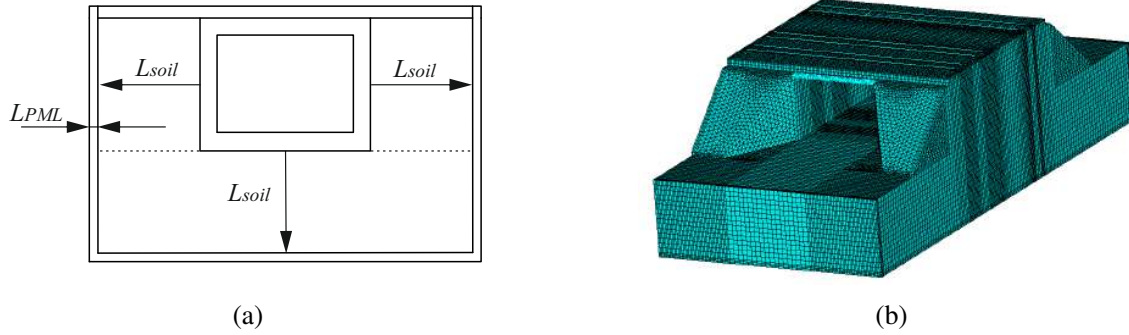


Figure 5: Soil-bridge-track numerical model. (a): Dimensions of the soil and PML domains, and (b): 3D view of the model.

#### 4.2 The soil-track-bridge simplified model

A simplified version of the previous model is implemented with the aim of implementing the inertial decoupling of the bridge-track system from the surrounding soil. Thus, the soil domain is now substituted by a series of discrete linear frequency dependent spring-dampers that simulate the dynamic interaction of the soil with the portal frame. These elements are arranged along 65 uniformly distributed points over the area of the bridge-soil interface at the bridge walls and the bottom face of the box slab. Three spring-dampers are located in each point, two tangential and one perpendicular to the surface, following the three space directions

Entity	Part	Property	Symbol	Value	Unit
Track	Rail	Elastic modulus	$E_r$	$2.10 \cdot 10^{11}$	Pa
		Moment of inertia	$I_r$	$3038 \cdot 10^{-8}$	m <sup>4</sup>
		Linear mass	$m_r$	60.34	kg/m
	Rail pad	Stiffness	$K_d$	$1.00 \cdot 10^8$	N/m
		Damping	$C_d$	$7.50 \cdot 10^4$	N/m
	Sleepers	Elastic modulus	$E_p$	$3.60 \cdot 10^{10}$	Pa
		Poisson's ratio	$\nu_p$	0.2	–
		Mass	$m_p$	320	kg
	Ballast	Elastic modulus	$E_b$	$1.10 \cdot 10^8$	Pa
		Poisson's ratio	$\nu_b$	0.2	–
		Density	$\rho_b$	1950	kg/m <sup>3</sup>
		Height	$h_b$	0.728	m
Bridge	Slab	Elastic modulus	$E_l$	$35.71 \cdot 10^9$	Pa
		Poisson's ratio	$\nu_l$	0.2	–
		Density	$\rho_l$	1950	kg/m <sup>3</sup>
	Joint	Elastic modulus	$E_j$	9522.50	Pa
		Poisson's ratio	$\nu_j$	0.2	–
		Density	$\rho_j$	2500	kg/m <sup>3</sup>
Soil	Whole domain	Shear wave speed	$c_s$	350	m/s
		Poisson's ratio	$\nu_s$	0.2	–
		Density	$\rho_s$	1950	kg/m <sup>3</sup>

Table 1: Mechanical properties of the model.

(X, Y, Z), as indicated in Figure 6(a). The DOFs of this model are reduced to 175,904. The simplified model is shown in Figure 6(b). As for the remaining boundary conditions, the nodes of the bottom ballast area under the tracks that were previously in contact with the soil are considered clamped in this approach.

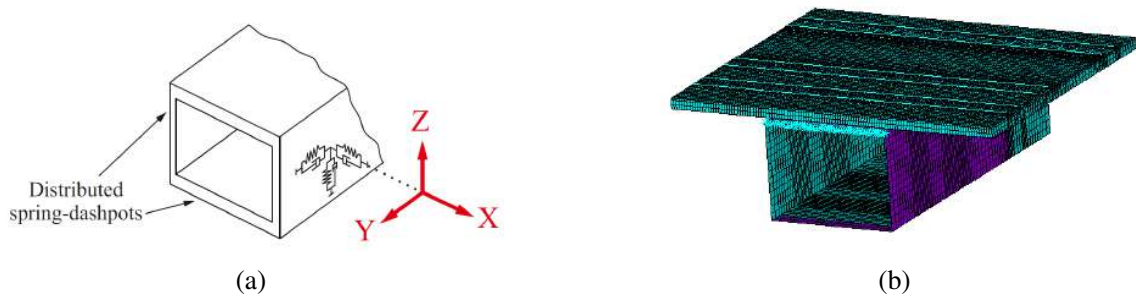


Figure 6: Simplified model. (a): Distribution and orientation of the frequency dependent spring-dashpots, and (b): 3D view of the model.

### 4.3 SSI implementation and validation

In order to calibrate the spring-dampers implemented in the simplified model, the SSI is first evaluated on the soil-track-bridge model. To this aim, a harmonic analysis is carried out. A distributed vertical force  $F_s(\omega)$  applied on both rails of track 2 on the bridge span length acts as the dynamic loading. At each spring-damper location, the dynamic stiffness can then be calculated as the quotient between the force input and the displacement at that point in the corresponding direction:  $K_{v,d}(\omega) = F_s(\omega)/U_s(\omega)$ . This yields the following properties of stiffness  $K_v(\omega) = \text{Re}[K_{v,d}(\omega)]$  and damping  $C_v(\omega) = \text{Im}[K_{v,d}(\omega)]/\omega$  for each spring-damper element [2]. Despite these results being dependent on the frequency, the differences among the stiffness and damping values in the bridge frequency range of interest [22.4–85.2] Hz are not significant. Hence, all spring-dampers within the simplified model are tuned to a constant magnitude at the fundamental frequency of the bridge  $f_1$ .

To complete the process, a subsequent calibration step is conducted on the bridge mechanical properties, namely on the ballast density and on the elastic modulus of the bridge slab. As the portal frame presents an asymmetric modal behaviour, the authors have found that the mechanical properties of the HS and conventional sections need to be differentiated in order to obtain a good approximation to the experimental modal parameters. The updated parameters are listed on Table 2. After this calibration, the properties of the spring-dampers were recalculated accordingly. The variation with respect to the previous values was minimal, leading to stable results.

Parameter	Bridge section	Nominal	Updated	Variation	Unit
Ballast density	Conventional	1950	1560	-20%	kg/m <sup>3</sup>
	High Speed		2340	+20%	
Slab elastic modulus	Conventional	35.71	30.35	-15%	GPa
	High Speed		26.07	-27%	

Table 2: Mechanical properties of the bridge sections before and after calibration.

Following, Figure 7 shows a comparison of the bridge modes. Numerical mode shapes, represented in black, are computed with the simplified model according to the procedure explained in this section. The experimental ones are depicted in grey colour.



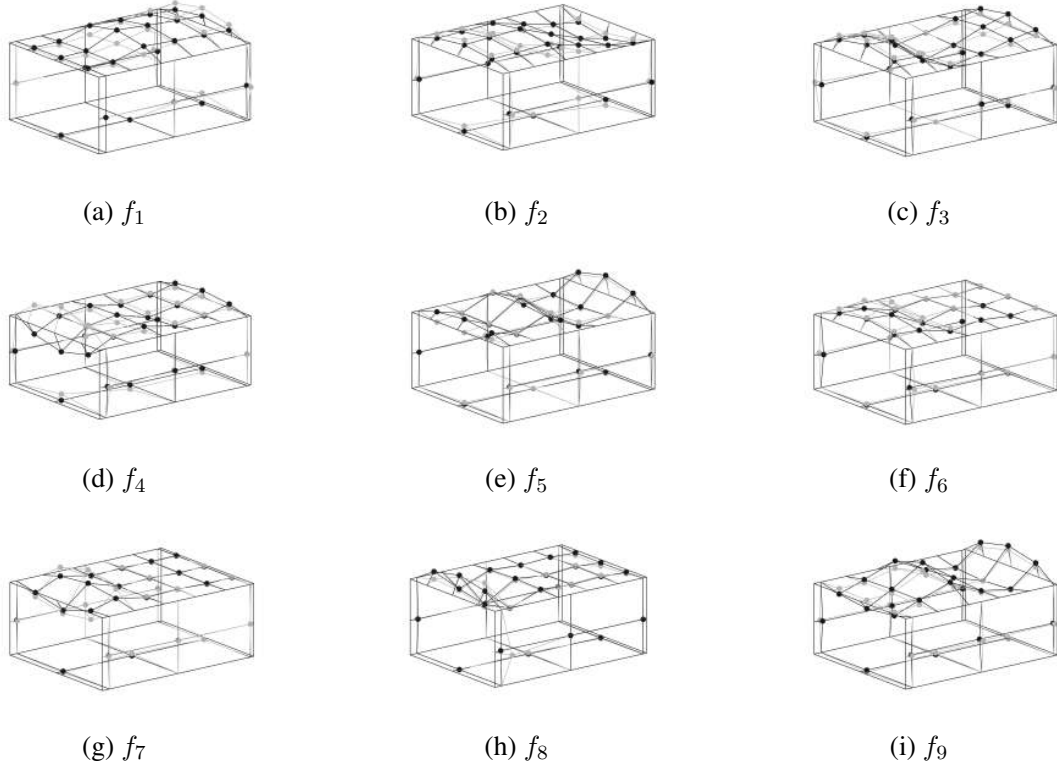


Figure 7: Experimental-numerical comparison of the bridge mode shapes.

Below, in Table 3 the details of this comparison are listed. The second and third columns show the experimental and numerical frequencies of each mode, respectively. The fourth column indicates the difference between these two values in percentage. Finally, in the fifth column, the modal assurance criterion (MAC) is calculated considering the accelerometers underneath the top slab (A1 to A18), and is used to assess the similarity between experimental and numerical pairs. As can be seen, there is a reasonably good agreement in terms of frequencies in the majority of the modes. The highest divergence in absolute value is given in  $f_5$  with a value of 15.6%. Nonetheless, a difference lower than 3% is attained in 5 modes:  $f_1$ ,  $f_2$ ,  $f_3$ ,  $f_7$  and  $f_8$ , being less than 1% in the first four cases. The MACs indicate also a satisfactory degree of correlation, especially among the highest modes.



Mode	$f_{exp}$ [Hz]	$f_{num}$ [Hz]	$d_{e-f}$ [%]	MAC [-]
$f_1$	22.41	22.23	-0.8	0.611
$f_2$	25.44	25.59	0.6	0.483
$f_3$	26.80	26.93	0.5	0.740
$f_4$	36.22	34.05	-6.0	0.694
$f_5$	44.27	37.38	-15.6	0.769
$f_6$	55.51	63.57	14.5	0.811
$f_7$	60.76	60.94	0.3	0.878
$f_8$	66.88	65.25	-2.4	0.881
$f_9$	85.21	72.50	-14.9	0.832

Table 3: Numerical frequencies compared to their experimental values and MACs.

## 5 SOLUTION TO THE SSI DYNAMIC PROBLEM

After calibration is completed, the dynamic behaviour of the portal frame is evaluated with the simplified model. The first part of this section addresses the formulation of the dynamic problem with SSI, which by means of complex modal superposition (CMS) to calculate the bridge response under passing trains [7]. The second part of the section explains an additional normalisation step required to operate with the modal shapes between ANSYS and MATLAB. Lately, in the third part of this section, excitation mechanisms involved in the dynamic problem such as track irregularities and their simulation are explained.

### 5.1 The SSI interaction problem

The equilibrium equation of the system, applied to the bridge model containing  $N$  DOFs with initial conditions of displacement  $\mathbf{u}(0) = \mathbf{u}_0$  and velocity  $\dot{\mathbf{u}}(0) = \dot{\mathbf{u}}_0$ , is:

$$\mathbf{M}\ddot{\mathbf{u}}(t) + \mathbf{C}\dot{\mathbf{u}}(t) + \mathbf{K}\mathbf{u}(t) = \mathbf{F}(t) \quad (1)$$

Mass, stiffness and damping matrices are represented as  $\mathbf{M}$ ,  $\mathbf{K}$  and  $\mathbf{C}$ . Because of the SSI effect introduced by the spring-damper elements, the damping in the interaction problem is non-proportional i.e.,  $(\mathbf{M}^{-1}\mathbf{C})(\mathbf{M}^{-1}\mathbf{K}) \neq (\mathbf{M}^{-1}\mathbf{K})(\mathbf{M}^{-1}\mathbf{C})$ . As a result, the mode shapes are complex and the position of each DOF is defined by amplitude and phase. Thus, a set of  $2N$  equations is needed to evaluate the solution of the  $N$  DOF of the structure, that can be written from Eq. 1 as a first order differential matrix equation:

$$\mathbf{A}\dot{\mathbf{y}}(t) + \mathbf{B}\mathbf{y}(t) = \mathbf{P}(t) \quad (2)$$

where:

$$\mathbf{A} = \begin{bmatrix} \mathbf{C} & \mathbf{M} \\ \mathbf{M} & \mathbf{0} \end{bmatrix} \quad \mathbf{B} = \begin{bmatrix} \mathbf{K} & \mathbf{0} \\ \mathbf{0} & -\mathbf{M} \end{bmatrix} \quad \mathbf{P} = \begin{bmatrix} \mathbf{F}(t) \\ \mathbf{0} \end{bmatrix} \quad \mathbf{y}(t) = \begin{bmatrix} \mathbf{u}(t) \\ \dot{\mathbf{u}}(t) \end{bmatrix} \quad (3)$$

being  $\mathbf{y}$  the state vector and  $\mathbf{A}$  and  $\mathbf{B}$  two real and symmetric matrices of dimensions  $2N \times 2N$ . If the free vibration case is considered, Eq. 2 yields:

$$\mathbf{A}\dot{\mathbf{y}}(t) + \mathbf{B}\mathbf{y}(t) = \mathbf{0} \quad (4)$$

The trial solution can be obtained as  $\mathbf{y}(t) = \Psi_j e^{s_j t}$ , where  $s_j$  is the  $j$ -th element of a total set of  $2N$  eigenvalues and  $\Psi_j$  are the corresponding eigenvectors:

$$\Psi_j = \begin{bmatrix} \phi_j \\ s_j \phi_j \end{bmatrix} \quad (5)$$

Then, natural frequencies, damped natural frequencies and modal dampings are determined from the eigenvalues as  $\omega_j = |s_j|$ ,  $\omega_{dj} = |\text{Im}[s_j]|$  and  $\zeta_j = -\text{Re}[s_j]/|s_j|$ , respectively. The solution to Eq. 2 can be expressed as:

$$\mathbf{y}(t) = \sum_{j=1}^{2N} \Phi_j z_j(t) \quad (6)$$

Taking into account the orthogonality conditions  $\Psi_j^T \mathbf{A} \Psi_k = 0$  and  $\Psi_j^T \mathbf{B} \Psi_k = 0$  for any pair of modes  $j \neq k$  (where the superscript  $T$  indicates matrix transpose) and normalising the eigenvectors to the matrix  $\mathbf{A}$  (i.e.,  $\Psi_j^T \mathbf{A} \Psi_j = 1$ ), Eq. 2 results into a set of  $2N$  uncoupled equations [7], where  $p_j(t) = \Psi_j^T \mathbf{P}(t)$ :

$$\dot{z}_j(t) + \alpha_j z_j(t) = p_j(t) \quad (7)$$

This is a non-stiff differential equation that can be addressed numerically. In this work, this equation is solved by means of a Runge Kutta (4,5) explicit algorithm [8].

## 5.2 Complex modal superposition: normalising the mode shapes

In order to solve the dynamic problem under moving loads, the bridge modal shapes are calculated with ANSYS(R) v.22.1 via complex modal analysis. In this case, the results obtained are normalised to the mass matrix  $\mathbf{M}$ . As the CMS method is carried out in MATLAB(R) v.24, it is required to normalise the mode shapes computed with ANSYS to the matrix  $\mathbf{A}$ , in accordance to the formulation seen in the previous section. To do so, it is possible to obtain the following scaling parameter  $\delta_j$  by developing  $\Psi_j^{T,M} \mathbf{A} \Psi_j^M = 1$ , where the superscript  $M$  indicates normalisation to the  $\mathbf{M}$  matrix (i.e., ANSYS mode shapes). In this process, a simplification is assumed when addressing  $\Psi_j^{T,M} \mathbf{A} \Psi_k^M = 0$ , as  $s_j$  does not correspond to its conjugate  $s_j \neq \bar{s}_k$  but to the same eigenvalue  $s_j = s_k$ . This allows to solve the dynamic problem by means of exporting the ANSYS modal information, which leads to a good approximation to the experimental results.

$$\delta_j = 2m_j \omega_j \zeta_j + 2m_j s_j = 2(\omega_j \zeta_j + s_j) \quad (8)$$

Thus, parameter  $\delta_j$  allows the mode shapes normalisation obtained with ANSYS to the  $\mathbf{A}$  matrix (indicated by the  $A$  superscript):

$$\Psi_j^A = \Psi_j^M / \sqrt{\delta_j} \quad (9)$$

Subsequently, by developing  $\Psi_j^{T,M} \mathbf{B} \Psi_j^M = \alpha_j$ , and scaling as indicated in Eq. 9, it can be derived that  $\alpha_j = (\omega_j^2 - s_j^2)/\delta_j$ , which is necessary to solve Eq. 7. Eventually, the bridge displacements are calculated by means of CMS from the equation below, that takes into account that, because of the non-proportional damping, eigenvalues and eigenvectors are pairs of complex conjugates. In this way, to compute the portal frame response, all the bridge identified

modes with its conjugates (i.e., in a range from 22.23 to 72.50 Hz, see Table 3) are normalised to the  $\mathbf{A}$  matrix and used to calculate the solution.

$$\mathbf{u}(t) = \sum_{j=1}^N 2\text{Re}[\phi_j z_j(t)] \quad (10)$$

### 5.3 Effect of rail irregularities

Apart from the parametric excitation, caused by the effect of moving loads on rails fixed with discrete supports, in the present contribution, the bridge response is determined by the combined influence of the quasi-static and dynamic contributions [9]. The quasi-static train excitation is modelled as constant moving forces, neglecting the inertial effects of the vehicle. The dynamic excitation considered is due to random rail unevenness. In this manner, the bridge displacement  $u_b$  at the wheel-rail contact point equals the sum of the rail displacement  $u_r$  due to the quasi-static contribution and the rail irregularity  $u_{w/r}$  [10]:

$$u_b = u_r + u_{w/r} \quad (11)$$

The random track unevenness is modelled based on a power spectral density function (PSD), as per ISO-8608 [11, 12]. The irregularity profile  $r(x)$  is obtained based on a zero-mean stationary ergodic random process defined by its PSD function  $S(\kappa)$ :

$$S(\kappa_n) = S(\kappa_0) \left( \frac{\kappa_n}{\kappa_0} \right)^{-w} \quad (12)$$

where  $S(\kappa_0)$  is the one-sided PSD function that characterises the process,  $\kappa_0$  is the initial wave-number,  $\kappa_n$  is the wave-number sampling and  $w$  is the PSD exponent. The irregularity profile  $r(x)$  is then calculated as the sum of harmonic series:

$$r(x) = \sum_{n=1}^{N_p} \sqrt{2 S(\kappa_n) \Delta\kappa} \cos(\kappa_n x - \varphi_n) \quad (13)$$

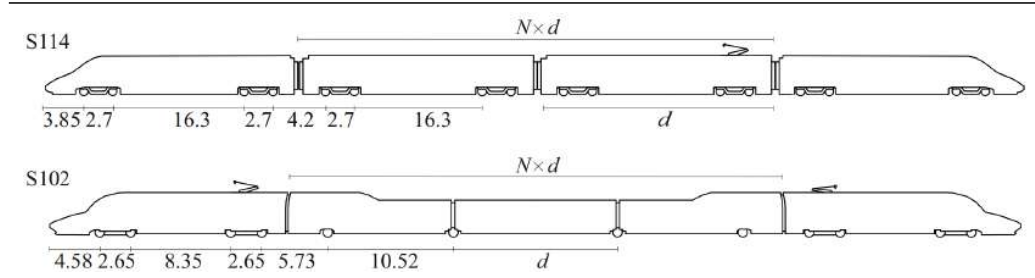
being  $N_p$  the number of points considered,  $\Delta\kappa$  the wave-number step and  $\phi_n$  the random phase angle following a uniform distribution in  $[0, 2\pi]$ . An artificial irregularity profile is generated considering a good track condition  $S(\kappa_0) = 1 \times 10^{-9} \text{ m}^3/\text{rad}$  [13]. The initial wave-number is set to  $\kappa_0 = 1 \text{ rad/m}$ , and the PSD exponent is assumed as  $w = 3.5$ , as usually considered for modern HS railway lines. The sampling wave-number  $\Delta\kappa$  is determined based on the train speed and frequency bridge to be studied. The irregularity profile is used to approximate the vehicle-track interaction force  $F_{v/t}$  in a first approach as a result of the track unevenness, as shown in Eq. 14:

$$F_{v/t}(x, \omega) = m_w \cdot \frac{d^2 r(x)}{dt^2} + K_{d,t}(\omega) \cdot r(x) \quad (14)$$

where  $m_w$  is the vehicle unsprung mass, whose value is assumed as 2000 kg in the present work. The track dynamic stiffness  $K_{d,t}(\omega)$  is determined by means of a harmonic analysis considering two identical vertical punctual forces applied on each rail at midspan  $F_{r1}(\omega) = F_{r2}(\omega)$ . The rail displacement at those points is obtained as  $U_{r1}(\omega)$  and  $U_{r2}(\omega)$ . Then, the track dynamic stiffness is computed as  $K_{d,t}(\omega) = ((F_{r1}(\omega) + F_{r2}(\omega))/((U_{r1}(\omega) + U_{r2}(\omega))/2))$ . This parameter is calculated separately for each track. In this contribution, it is considered that the track dynamic stiffness at mid span is representative of the whole track length.

## 6 RESULTS

In this section, the dynamic response of the portal frame is predicted. To this purpose, the transit of RENFE S114 and S102 articulated trains on their duplex configuration is simulated. Table 4 lists the following information about the train passages: the circulating track, the travelling direction (M: Madrid, S: Sevilla), the scheme of axles and coaches configuration (L: locomotive and C: carriage), the circulating speed  $V$ , the number of coaches per train, the characteristic distance  $d$  and the average axle load  $P$ .



Train	Track	Ride	Scheme	$V$ [km/h]	$N$	$d$ [m]	$P$ [kN]
S114	3	S-M	L-2C-L//L-2C-L	236.5	2	25.9	153
S102	2	M-S	L-12C-L//L-12C-L	242.1	12	13.14	165

Table 4: Data about the passages of RENFE S102 and S114 trains.

An experimental-numerical comparison of the bridge vertical acceleration response during these passages is carried out. In the case of the S114 train, as it was circulating on track 3, this comparison is conducted considering the experimental data acquired at accelerometer A15 (see Figure 3). With respect to the S102 train, data from the accelerometer A11 is used, which was located below track 2 at midspan.

Figure 8 shows the corresponding results for both trains S114 (a-b) and S102 (c-d) in time and frequency domains. The black line stands for the experimental data, whereas the red one indicates numerical response. Both signals are filtered applying two Chebyshev filters with high-pass and low-pass frequencies of 1 Hz (order 3) and 30 Hz (order 10), respectively. As can be seen, the numerical response keeps a good adjustment with the experimental data. Regarding the frequency content of the acceleration, the signals present several peaks at low frequencies that are related to the characteristic distance of the trains  $d$  between shared axles (i.e.,  $f = V/d$ ) and subsequent harmonics. The peaks nearing 20-25 Hz correspond to bridge modes. In those cases, it can be observed that the numerical signal partially overestimates the bridge response. This may be understandable, as additional energy dissipation mechanisms such as the vehicle suspensions are not considered in the present model, leading to a higher numerical response.

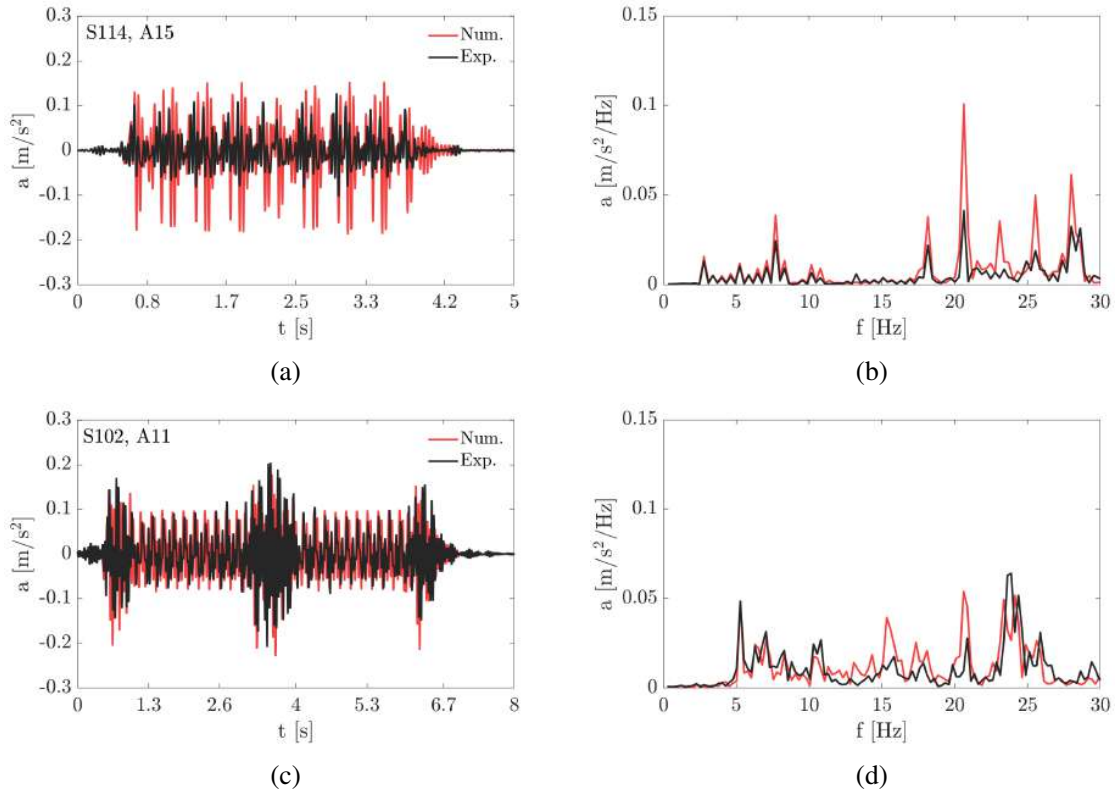


Figure 8: Experimental-numerical comparison of the passages of the trains S114 duplex (a-b) in the accelerometer A15 and S102 duplex (c-d) train in the A11.

## 7 CONCLUSIONS

In this study, the dynamic behaviour of an existing portal frame is investigated. With this aim, the experimental data obtained during an in-field campaign is processed to obtain the modal parameters of the bridge. Then, a complete 3D FE numerical model of the structure considering the track-bridge-soil system is implemented. PML elements are used in this initial version of the model to reduce the computational cost. Following, the SSI is evaluated to configure a simplified version of the model, in which the effect of the soil is simulated with distributed linear spring-dampers at the soil-bridge interfaces. After a calibration process, the modal behaviour of the portal frame is assessed, obtaining a good approximation to the experimental modal parameters. In the last part of the work, the dynamic response of the bridge is simulated with the simplified model considering two train passages. In summary, the following can be concluded:

- The identification process was a key part of the bridge study, as it allowed to detect the unusual modal bridge behaviour due to the partial decoupling in two sections by the longitudinal joint. This turned out to be determinant in the calibration steps carried out afterwards.
- The use of PML elements allowed to increment the efficiency of the model with a smaller soil domain when assessing the SSI with the track-bridge-soil model, reducing in consequence the computation time.

- The implementation of the simplified model led to a fast method to analyse the modal and dynamic bridge behaviour. This permitted to compute the numerical mode shapes and frequencies with a reasonable accuracy with respect to the experimental counterparts.
- Regarding the assessment of the bridge dynamic response, a good estimation is achieved both in the time and in the frequency domains. In this last case, it is observed that the numerical response slightly overestimates the experimental signal in several frequency peaks corresponding to bridge structural modes. This circumstance may be probably explained by the fact that the vehicle is not considered in the numerical model. Otherwise, its suspension systems would absorb a part of the bridge vibration, altering the resultant response. In any case, the prediction is still accurate to show the validity of the followed approach.

The results obtained in this work could help to better understand the influence of SSI on portal frames, as well as to improve current methodologies to predict their dynamic response under operating conditions in an accurate and efficient manner. Further advancements could be made in this regard, enhancing our capacity to assess the integrity and safety of existing structures and to design new bridges in more sustainable and efficient ways.

## 8 ACKNOWLEDGEMENTS

The authors acknowledge the following institutions for their financial support: Universitat Jaume I (PREDOC/2022/26); Spanish Ministry of Science and Innovation, Agencia Española de la Investigación (AEI), FEDER EU Funds (PID2022-138674OB-C2); Regional Government of Economic Transformation, Industry, Knowledge and Universities of Andalusia (PROYEXCEL 00659), and the Andalusian Scientific Computing Centre (CICA).

This project has received funding from the Europe's Rail Joint Undertaking under Horizon Europe research and innovation programme under grant agreement No. 101121765 (HORIZON-ER-JU-2022-ExplR-02). Views and opinions expressed are however those of the author(s) only and do not necessarily reflect those of the European Union or Europe's Rail Joint Undertaking. Neither the European Union nor the granting authority can be held responsible for them.

## REFERENCES

- [1] A. Zangeneh, C. Svedholm, A. Andersson, C. Pacoste, Identification of soilstructure interaction effect in a portal frame railway bridge through full-scale dynamic testing, *Engineering Structures*, **159**, 299-309, 2018.
- [2] P. Galvín, A. Romero, E. Moliner, Connolly, E., Martínez-Rodrigo, M.D., Fast simulation of railway bridge dynamics accounting for soil-structure interaction, *Bulletin of Earthquake Engineering*, **23**, 3195-3213, 2022.
- [3] A. Zangeneh, S. François, G. Lombaert, C. Pacoste, Modal analysis of coupled soil-structure systems, *Soil Dynamics and Earthquake Engineering*, **144**, 106645, 2021.
- [4] M.D. Martínez-Rodrigo, P. Galvín, A. Doménech, A. Romero, Effect of soil properties on the dynamic response of simply-supported bridges under railway traffic through coupled boundary element-finite element analyses, *Engineering Structures*, **170**, 78-90, 2018.

- [5] P. Salcher, Effect of soil-structure interaction on the dynamics of portal frame railway bridges. *Bautechnik* **97**(7), 490-498, 2020.
- [6] C. Coronado, N. Gidwani, Calculation of dynamic impedance foundations using finite element procedures. *San Francisco: Bechtel Power Corporation Nuclear security & Environmental*, 2016.
- [7] W.C. Hurty, M.F. Rubinstein, Dynamics of structures. *Hoboken: Prentice-Hall Inc.*, 1965.
- [8] L.F. Shampine, M.W. Reichelt, The Matlab ode suite. *SIAM Journal of Scientific Computing*, **18**, 1-22, 1997.
- [9] G. Lombaert, G. Degrande, Ground-borne vibration due to static and dynamic axle loads of InterCity and high-speed trains *Journal of Sound and Vibration*, **319**, 1036-1066, 2016.
- [10] A. Romero, M. Solís, J. Domínguez, P. Galvín, Soil-structure interaction in resonant railway bridges *Soil Dynamics and Earthquake Engineering*, **47**, 108-116, 2013.
- [11] International Organization for Standardization (ISO), mechanical vibration - road surface profiles - reporting of measured data *ISO-8608:2016 Techreport, Geneva, Switzerland*, 2016.
- [12] J. Chordà-Monsonís, E. Moliner, P. Glavín, M.D. Martínez-Rodrigo, E. Zacchei, A. Tadeu, I. Ferraz, A. Romero, Dynamic load allowance o long-span modular steel bridges. *Engineering Structures*, **282**, 115835, 2023.
- [13] M. Germonpré, G. Degrande, G. Lombaert, A track model for railway-induced ground vibration resulting from a transition zone. *Journal of Rail and Rapid Transit*, **232**(6), 1703-1717, 2018.

## INVESTIGATION OF DIFFERENT METHODOLOGIES FOR SIMULATING THE GROUND-BORNE VIBRATION RESPONSE OF BUILDINGS DUE TO UNDERGROUND RAILWAY TRAFFIC

Robert Arcos<sup>1,2,\*</sup>, Yazdan Shafieyoon<sup>2</sup>, Arnau Clot<sup>1,2</sup>, Kenny F. Conto<sup>2</sup> and Jordi Romeu<sup>2</sup>

<sup>1</sup>Serra Húnter Fellow  
Universitat Politècnica de Catalunya  
e-mail: {robert.arcos,arnau.clot}@upc.edu

<sup>2</sup> Acoustical and Mechanical Engineering Laboratory (LEAM)  
Universitat Politècnica de Catalunya (UPC)  
Carrer Colom 11, 08222 Terrassa (Barcelona), Spain  
e-mail: {yazdan.shafieyoon,kenny.fernando.conto,jordi.romeu}@upc.edu

**Keywords:** Railway-induced vibration, Ground-borne vibration, Numerical modelling, Building vibration response, Building-tunnel coupling.

**Abstract.** *Simulating the vibration response of buildings due to underground railway traffic is a highly demanding computational task because of the heterogeneity of domain types involved in the system. While the track-tunnel-soil system is typically handled using two-and-a-half-dimensional approaches, exploiting the invariance of that part of the system in the longitudinal direction, the building structure is usually modelled employing three-dimensional methods. Thus, to strongly couple these two subsystems along with considering the moving nature of the train excitation result in the mentioned computational complications. In this paper, various methods for the assessment of the building floor vibration due to a train pass-by are compared in terms of accuracy and computational effort. In this context, the errors committed when not accounting for the dynamic interaction between the tunnel and the building or when considering the moving roughness approach, where the train loads are not moving, are compared with the uncertainty induced by the roughness spectra. An iterative method will be included in the discussion of the computational effort.*



## APPLICATION OF THE MOVING MODES METHOD TO THE DYNAMICS OF INFINITELY LONG FLEXIBLE TRACKS WITH DISCRETE SUPPORTS

José L. Escalona<sup>1</sup>, Rosario Chamorro<sup>1</sup>, Álvaro Brazales<sup>2</sup>, Javier F. Aceituno<sup>2</sup>

<sup>1</sup> Dept. of Mechanical and Manufacturing Eng., University of Seville  
Camino de los Descubrimientos s/n, 41092, Sevilla, Spain  
e-mail: {escalona, rchamorro}@email.address

<sup>2</sup> Dept. of Mechanical and Mining Eng., University of Jaén  
Campus Científico-Tecnológico s/n, 23700, Linares, Spain  
{brazales, jaceitun}@ujaen.es

**Keywords:** moving modes method, vehicle-track dynamics, track flexibility, model order reduction, moving loads

**Abstract.** *This work extends the Moving Modes Method (MMM) [1-2], that was developed by the authors for the dynamic analysis of the vehicle track-system in railway applications, to the analysis of the deformation of discretely supported tracks.*

*The MMM is a method that was developed in the context of Flexible Multibody Systems (FMBS) for the analysis of the coupled vehicle-track dynamics. The main difficulty of this type of analysis is that the flexible track can be considered as an infinitely long body that deforms only in a narrow area whose position varies in time. The Finite Element Model (FEM) of the track based on nodal coordinates is highly inefficient for this type of analysis. The MMM can be considered as a Model Order Reduction (MOR) technique for this specific, by technologically very important, application. The main properties of the MMM are:*

- 1. The FEM mesh is defined in a non-material volume that moves with the vehicle with the same forward velocity. Therefore, the MMM is an Arbitrary Eulerian-Lagrangian (ALE) approach [3].*
- 2. Track deformation is described using as base vectors -the moving modes- the frequency response modes of the track subjected to a load with harmonically varying amplitude.*
- 3. A small set of moving modes is defined under each wheel-rail contact pair to describe the track deformation.*

*The increase in computational efficiency and accuracy of the MMM when compared with other FEM-based simulations, or co-simulations, is more significant than the increase in the complexity of the resulting equations of motion due to the more involved kinematics.*

The main drawback of the MMM was the inability to account for the effect of discrete supports (sleepers) in the system dynamics. This work presents an extension of the MMM that accounts for the effect of the discrete supports.

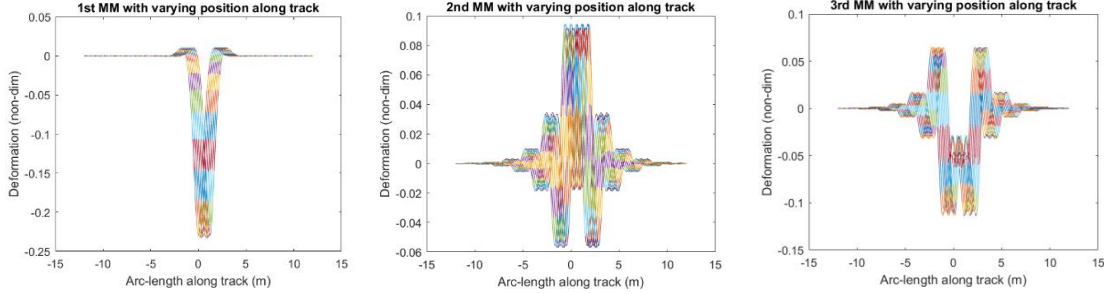


Figure 1. First 3 moving modes obtained at different locations along the sleeper-to-sleeper distance

Figure 2 shows the first three moving modes calculated with a 2D FEM of a rail track using realistic track parameters that can be found in [4]. The modes are obtained with a load that varies its position along the sleeper-to-sleeper distance. It can be observed that the modes vary very slightly. However, this slight difference can result in dynamic effects that can be important in railway dynamics.

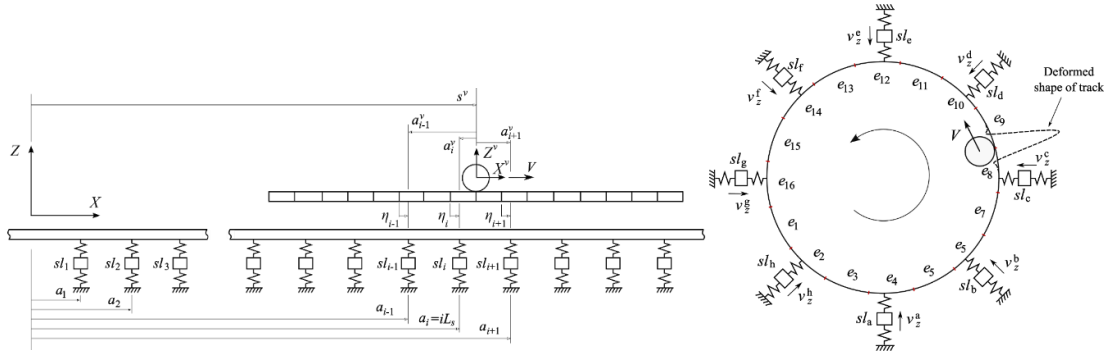


Figure 2. Moving mesh (left) and circular track (right) concepts

The MMM that accounts for the discrete supports is based on the ALE moving mesh concept, that is shown in the left of Fig. 2, and on the circular track concept, that is described in the right of Fig. 3.

## References

1. Chamorro, R., Escalona, J.L., González, M.J., "An approach for modelling long flexible bodies with application to railroad dynamics", *Multibody System Dynamics*, 26, 135–152, 2011.
2. Recuero, A.M., Escalona, J.L., "Dynamics of the coupled railway vehicle-flexible track system with irregularities using a multibody approach with moving modes", *Vehicle System Dynamics*, 52(1), pp. 45-67, 2013.
3. Donea, J, Huerta, A, Ponhot, J.Ph, Rodríguez-Ferran, A , "Arbitrary Lagangian-Eulerian methods", in: E. Stein, R. Borst, T.J.R. Hughes (Eds.), *Encyclopedia of Computational Mechanics*, John Wiley and Sons, 2004.
4. Shen, C., Deng, X., Wei, Z., Dollevoet, R., Zoeteman, A., & Li, Z., "Comparisons between beam and continuum models for modelling wheel-rail impact at a singular rail surface defect". *International Journal of Mechanical Sciences*, 198, 1-16, 2021.

## EFFECTIVENESS OF ACOUSTIC BARRIERS FOR MITIGATING TRAIN TRAFFIC NOISE

**R. Velázquez-Mata<sup>1</sup>, A. Romero<sup>1</sup>, A. Tadeu<sup>2</sup>, M.D. Martínez-Rodrigo<sup>3</sup>, E. Moliner<sup>3</sup> and  
P. Galvín<sup>1</sup>**

<sup>1</sup>Escuela Técnica Superior de Ingeniería, Universidad de Sevilla,  
Camino de los Descubrimientos, ES-41092, Spain  
e-mail: {rvmata, aro, pedro galvin}@us.es

<sup>2</sup>Itecons, Institute of Research and Technological Development in Construction, Energy, Environment  
and Sustainability,  
Rua Pedro Hispano, 3030-289 Coimbra, Portugal  
e-mail: tadeu@itecons.uc.pt

<sup>3</sup>Universitat Jaume I, Department of Mechanical Engineering and Construction,  
Avda. Sos Baynat s/n, ES-12071 Castellón, Spain  
e-mail: mrodrigo@uji.es, molinere@emc.uji.es

**Keywords:** Boundary integral equation, Acoustic, Barrier, Traffic noise.

**Abstract.** *One of the factors that most severely affects the health of citizens is environmental noise. Noise pollution has serious health effects and is therefore controlled by regulations and guidelines using engineering tools and urban planning [1]. In the case of railway traffic, if possible, infrastructure managers design the lines as underground when they cross the cities. If not, several mitigation measures can be used to reduce noise pollution. Up to now, the most common attenuation tools are the acoustic barriers that reflect and absorb sound waves. Their effectiveness depends on the location, height and length, the source of noise, and the surface of the soil. Several methodologies to obtain the properties of the acoustic barriers have been standardized [2, 3, 4, 5, 6, 7, 8].*

*The design of the barrier has been studied for many years and is critical in determining its effectiveness in reducing noise [9].*

*This paper presents a new boundary element formulation using an exclusively numerical procedure [10] to assess the performance of acoustic barriers using the insertion loss index. Numerical analysis is not constrained by the shape of the barrier due to the versatility of the formulation.*

## REFERENCES

- [1] Directive E. Directive 2002/49/EC of the European parliament and the Council of 25 June 2002 relating to the assessment and management of environmental noise. Official Journal of the European Communities. 2002.
- [2] for Standardization EC. EN 1793-4:2015. Road traffic noise reducing devices - Test method for determining the acoustic performance - Part 4: Intrinsic characteristics. In situ values of sound diffraction. Brussels, Belgium; 2015.
- [3] for Standardization EC. EN 1793-5:2016. Road traffic noise reducing devices - Test method for determining the acoustic performance - Part 5: Intrinsic characteristics. In situ values of sound reflection under direct sound field conditions. Brussels, Belgium; 2016.
- [4] for Standardization EC. EN 1793-6:2018+A1:2021. Road traffic noise reducing devices: Test method for determining the acoustic performance - Part 6: Intrinsic characteristics - In situ values of airborne sound insulation under direct sound field conditions. Brussels, Belgium; 2021.
- [5] for Standardization IO. ISO 10847:1997. Acoustics: In situ determination of insertion loss of outdoor noise barriers of all types. Geneva, Switzerland; 1997.
- [6] of America ANSIS. ANSI/ASA S12.8-1998 (R2013). Methods for determination of insertion loss of outdoor noise barriers. Melville, New York; 2013.
- [7] of Transportation FHWA. Highway Noise Barrier Design Handbook. Washington, DC; 2000.
- [8] of Transportation FHWA. Noise Measurement Handbook. Final Report. Washington, DC; 2018.
- [9] Martinez-Orozco JM, Barba A. Determination of Insertion Loss of noise barriers in Spanish roads. *Applied Acoustics*. 2022;186:108435. Available from: <https://www.sciencedirect.com/science/article/pii/S0003682X21005296>.
- [10] Velázquez-Mata R, Romero A, Domínguez J, Tadeu A, Galvín P. A novel high-performance quadrature rule for BEM formulations. *Engineering Analysis with Boundary Elements*. 2022;140:607-17. Available from: <https://www.sciencedirect.com/science/article/pii/S095579972200145X>.

## OPTICAL DATA COLLECTION DEVICE FOR PREDICTING WEAR ON RIGID CATENARY WITH RESULTS ON MALAGA METRO INFRASTRUCTURES

Rafael J. Luque<sup>1\*</sup>, Pedro Reyes<sup>2</sup>, Montserrat Simarro<sup>3</sup>, Sergio Postigo<sup>4</sup>, Vid Bačić<sup>2</sup>, Juan J. Castillo<sup>5</sup>

<sup>1</sup>Dept of Mechanical Engineering. University of Malaga  
29071 Malaga, Spain  
e-mail: rafaeljesuslqa@uma.es

<sup>2</sup>Dept of Mechanical Engineering. University of Malaga  
29071 Malaga, Spain  
pedrozuniga1798@gmail.com, msimarro@uma.es, spostigo@uma.es, vidbacic@uma.es,  
juancas@uma.es

**Keywords:** Catenary wear, Measurement device, Rail test, Optical measurement, Wear model

**Abstract.** *The reliability and safety of the transport of people and goods by rail depends, among other factors, on the correct maintenance of the installations. A fundamental part of this mode of transport is the system responsible for supplying power to the trains. The catenary, whether in flexible or rigid configuration, is an element subjected to intense use, the wear of the contact wire being one of the main factors to be considered during its maintenance. Knowledge of its condition as well as of the installation parameters that may affect its deterioration would help reduce its wear and minimize the risk of damage.*

*To this end, an innovative optical data acquisition device has been developed by the Mechanical Engineering Department of the University of Malaga. The main goal of this device is to provide reliable data on railway facilities for the prediction of rigid catenary wear, with specific applications in a subway infrastructure. This device, designed to move along the train tracks, represents an important advance in the monitoring and maintenance of railway infrastructures. Equipped with a precision camera and laser technology, the device can accurately quantify the wear experienced by the contact wire, allowing a detailed assessment of its condition over time.. In particular, the device not only measures contact wire wear but also generates a three-dimensional map of the infrastructure. This paper describes the design of the device, the functionalities and sensors that incorporates, as well as a sample of measurements taken under real operating conditions. The results achieved show that the device can perform the measurements for which it was designed satisfactorily. These measurements can be performed manually, semi-automatically, and fully autonomously. All these functionalities provide valuable information for maintenance management and planning, enabling more informed and efficient decisions to ensure the integrity and optimal operation of railway infrastructures.*

## 1 INTRODUCTION

The transport of people and goods by rail has proven to be a more efficient and economical alternative to other means of transport thanks to its high load capacity, flexibility, and environmental friendliness. Appropriate maintenance of the installations contributes to guaranteeing safety and reliability during use.

The Mechanical Engineering group of the University of Malaga has been investigating the dynamic behavior of the pantograph-catenary interaction in recent years [1]. Among these studies, the group has evaluated the influence of operating parameters, such as train speed and pantograph preload, and installation characteristics, such as span length and support position, on the forces appearing in the pantograph-contact wire, particularly in the case of rigid catenary [2][3]. These forces are closely related to the wear produced in the contact wire [4].

Based on the knowledge of the limitations of track maintenance and the current measures that exist to directly monitor the contact wire, a device has been developed to remotely measure wire wear and other parameters related to the facility. (Figure 1). This measurement is carried out without the need for an element in direct contact with the wire. Furthermore, given that the chances of being able to introduce a measuring device in a real test inside railway infrastructures are conditioned by the availability of the installation's operations center, it was decided to incorporate several extra sensors to obtain the maximum possible information from the infrastructure in each of the tests performed.

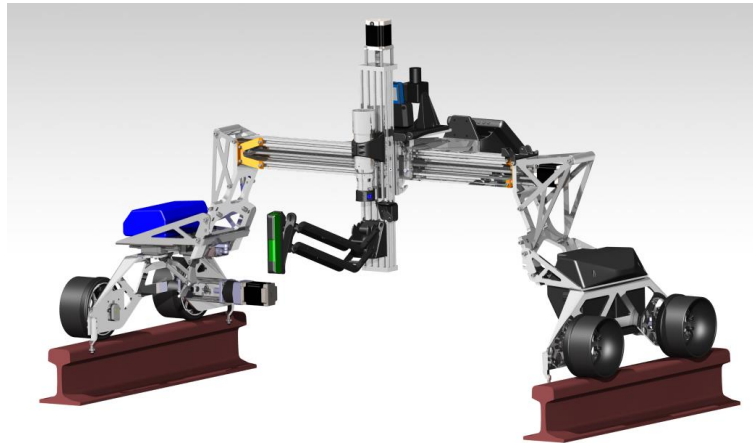


Figure 1. 3D model of the device.

It should be noted that the condition and positioning of the components of the rail infrastructure have a direct influence on the wear models and consequently on the expected results. This is because the distribution of the various supports of the catenary profile along the track affects the form of wear generated over time. Therefore, it is not only sufficient to distribute the supports evenly but other factors must also be considered to achieve a good wear performance of the installation. These factors are related to the height variation in the supports, overlap sections, and the eccentricity of the catenary itself along the infrastructure. It is, therefore, necessary to collect all these data to be able to incorporate them into the models. This way, it will be possible to predict wire wear evolution and provide adequate indications to increase the service life of the installation.

Thus, the design and equipment planned make the device a multi-objective instrument, capable of accurately obtaining essential data on the current conditions of the installation, which can be beneficial for preventive maintenance of the installation.

Once the device was developed and manufactured, it was successfully tested in the Malaga Metro facilities in the sections between the "Universidad" and "Atarazanas" stations of line 1, in a 5.6 km route under the tunnel (Figure 2). Figure 3 shows the device on one of the test days.



Figure 2. Malaga Metro lines.

The sensors incorporated in the device make it possible to obtain the exact position of each of the rigid catenary supports and the wear that exists in the desired areas or points along the route. In addition, a 3D representation of the position of the catenary in that area was obtained, making it possible to quantify the offset that exists in that section of the installation.

The points selected to measure the wire wear were not chosen randomly; a sensorized box was previously developed and installed onto one of Metro Malaga's mobile units. Based on the measurements obtained, the zones where the effects of electric arc wear were most frequently found were located. All these measurements have been possible thanks to the research project in which the Mechanical Engineering Department of the University of Malaga is involved.



Figure 3. Measuring device positioned on the rails of the Malaga Metro track.



## 2 METHODOLOGY OF MEASUREMENT

The device developed consists of two clearly differentiated systems. The first one is responsible for longitudinal movement along the track. To this end, automatically controlled electric motors are used. In addition, the non-driving wheels incorporate angular position encoders, which allow the distance, and therefore the position, advanced by the device during the measuring process to be known at all times. The device also incorporates prismatic guides that allow the transversal and vertical displacement of the cameras and optical lasers.

Secondly, the device is equipped with all appropriate sensors to carry out the necessary measurements to assess the state of the installation and with an on-board computer data processing system. In addition, it incorporates a camera system with which, in the first instance, the system locates the position of the contact wire by means of an image recognition algorithm that detects the contact wire. This information is used to center the device in the appropriate position. An inclined optical laser is then directed toward the area of the wire to be measured. This laser makes it possible to create a line that is modified according to the wear present on the contact wire. If the wire is new, the profile of the wire can be distinguished, as shown in Figure 4(a). However, as the wear increases, the line becomes progressively flatter, as shown in Figure 4(b).

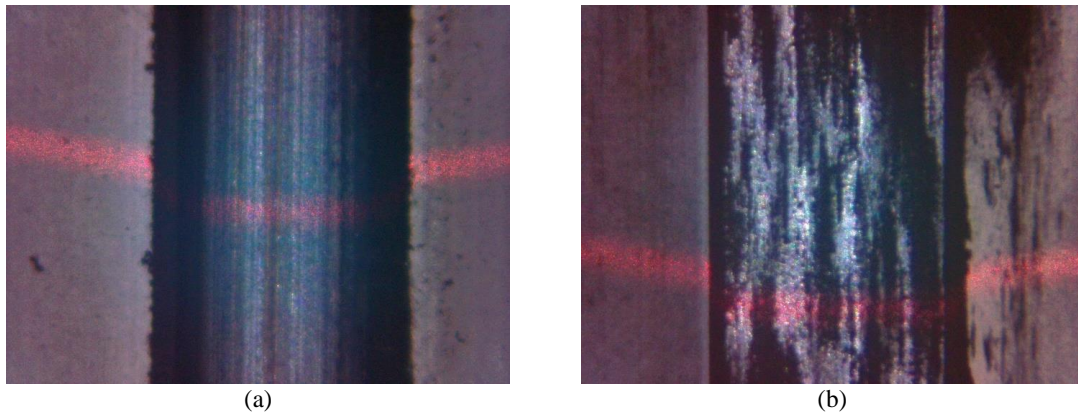


Figure 4. Comparison between different wire conditions. (a) Contact wire with low wear. (b) Contact wire with wear.

Thanks to a laser meter, the height of the zone to be observed is determined, allowing the main camera to focus on the correct range of values, thus obtaining a clear image from which valuable information can be inherited.

Once the device is located and centered around the contact wire zoned, and with the laser beam in the area, the main camera is used to take detailed photographs of the contact area. The main camera is an optical sensor adapted for telescopic lenses, as shown in Figure 5. This provides a detailed image of enough quality to measure wear values directly on it. This is possible because the height values of the point being measured, the focal length, and the size of each pixel in the image are known, allowing real distances to be measured from the photograph.



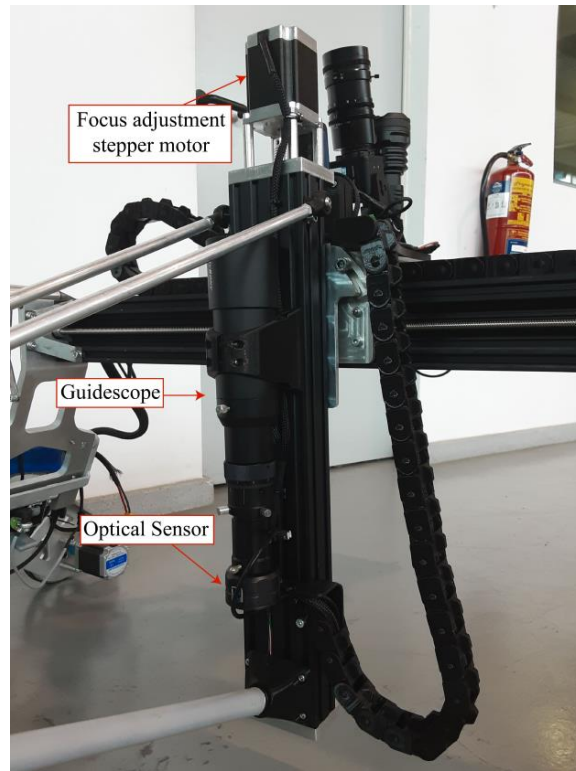


Figure 5. Detail of the main camera with the optical sensor and the guidescope.

### 3 MEASURING SENSORS

Table 1 shows the various sensors incorporated in the developed device together with the specific purpose for which they are intended, and the value of the measurement accuracy provided by the manufacturer of each of them.

Sensor	Measurement objective	Accuracy
Linear potentiometer	Rail gauge	$\pm 0,01$ mm
Angle encoder	Distance traveled and kilometre point	$\pm 0,1$ mm
IMU	Slopes and irregularities along the track	$\pm 0,1$ %
Laser meter	Height of rigid catenary	$\pm 5$ mm
LiDAR	Catenary offset along the infrastructure	$\pm 20$ mm
HD camera	Positioning of the main camera	12 Mpx
Optical Sensor	High-definition image capture	8 Mpx
Telescopic Scope	Zoom into the study area	X5 increase

Table 1: Inspection and measurement sensors

Figure 6 shows the distribution of most of the sensors on the device. Both cameras and the laser meter are placed on the moving platform of one of the axles, allowing them to be aligned with the catenary.

However, the LiDAR is in a fixed position in the center of the device, which allows the reference point to be kept constant for correct post-processing.

The linear potentiometer intended to measure the rail gauge makes use of a damper and an opening mechanism that allows the device to move one of its supports. This possibility of movement is blocked by the rail gauge, thus allowing this value to be obtained. Figure 7 shows the track gauge measurement system described above.

Encoders are placed on the non-driving wheels in such a way that the measurement made is a direct measurement on the rail that does not pass through the control of the device, avoiding failures in the reading due to loss of steps or power.

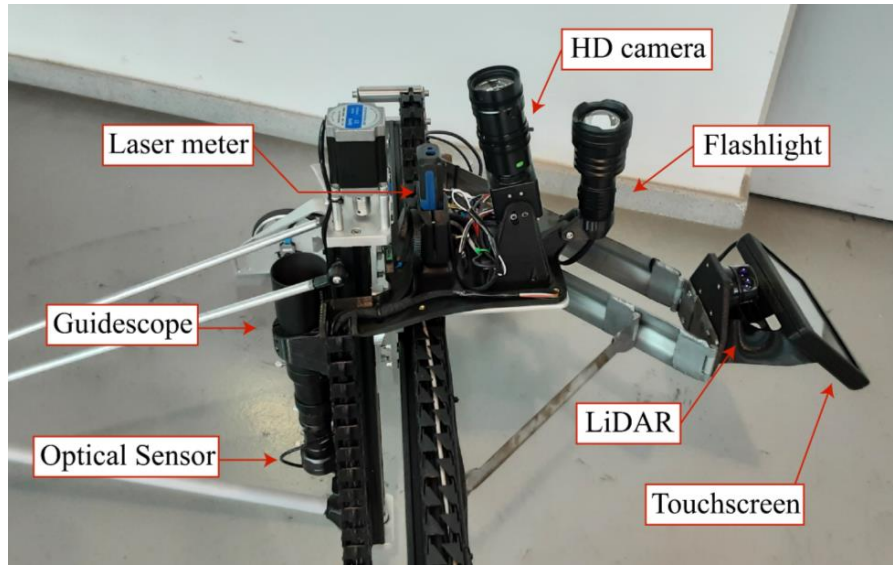


Figure 6. Detail of the measuring components of the device.

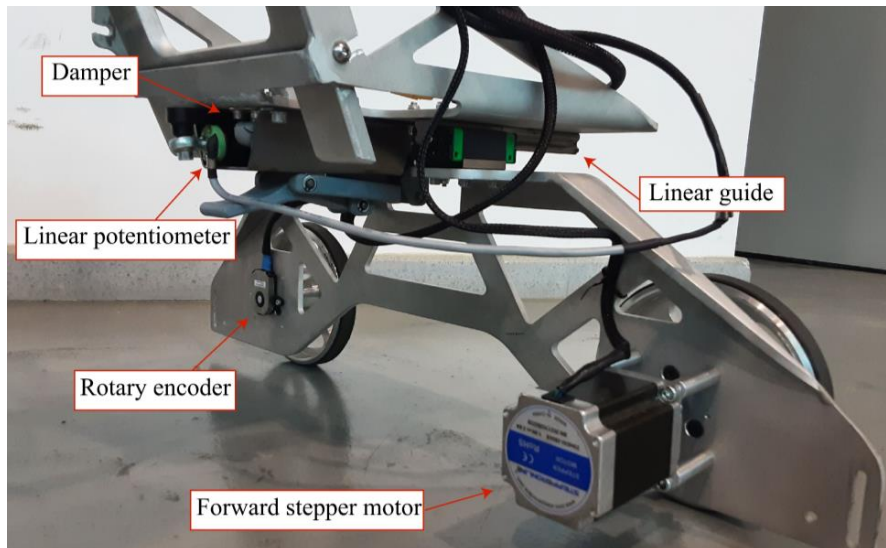


Figure 7. Detail of mobile support of the rail gauge measuring device.

#### 4 CHARACTERISTICS OF THE DEVICE

As previously indicated, the device has 3 axes of movement. The first one is dedicated to focusing the main camera. Next, the second one allows moving the different cameras transversally to the direction of the rails. Finally, the third axis allows the device to move along the rails. The whole structure is supported on 4 wheels, two of which are driven wheels. The other two wheels do not traction the device, being connected to angular encoders.

All movements of the axes are controlled by stepper motors controlled by a processor, which also collects and manages the data and performs all the calculation procedures for the autofocus. The device can be controlled via a built-in touch screen or by remote control over a local network using any device that can be connected to the network.

The device has a built-in 691.1 Wh battery that allows tests to be carried out for up to 8 hours continuously with all sensors in operation. This makes it possible for tests to be executed during complete maintenance periods without interruption.

As shown in Figure 8, the device can be folded. This is to facilitate its transport without the need to use any special vehicle, as it is designed so that the device with all its elements can fit into a standard-size car once folded.

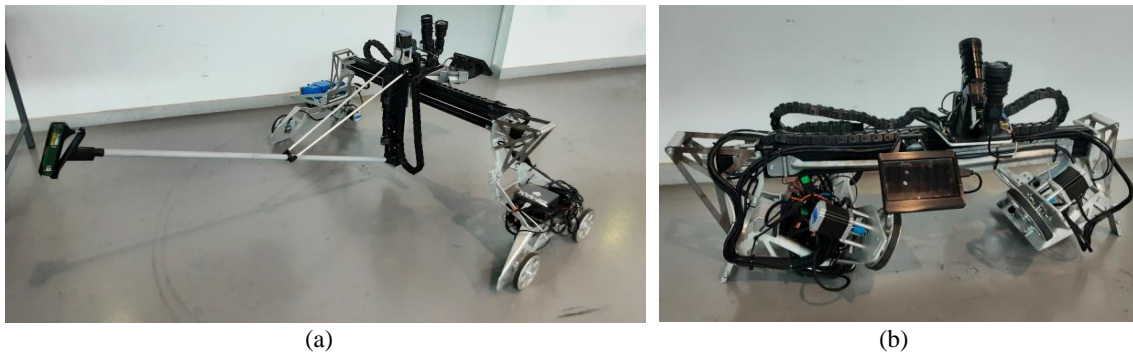
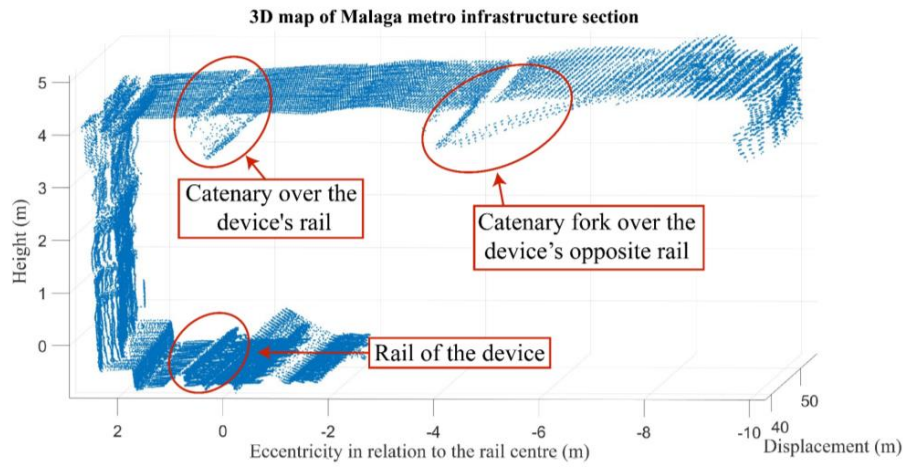


Figure 8. Measuring device in its two positions. (a) Unfolded for use on the rail. (b) Folded for transportation.

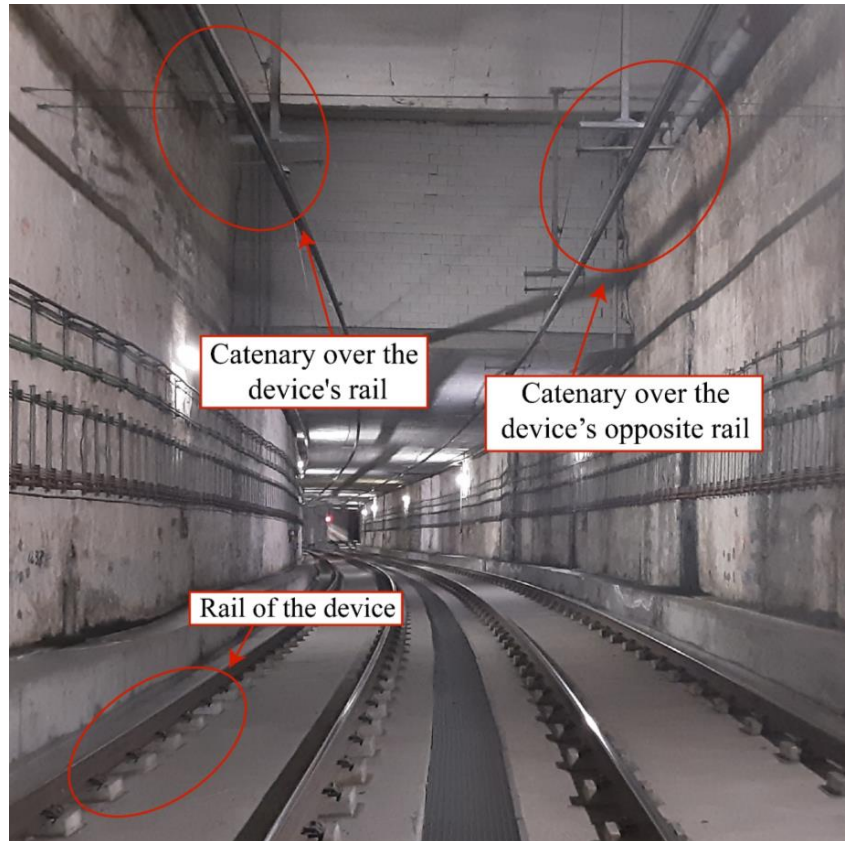
#### 5 RESULTS OBTAINED

Results obtained in the tests performed so far are mainly related to the catenary offset and the obtaining of a 3D point map that allows to provide measurement values of the catenary position and its offset.

The 2D LiDAR used for the device has been configured to obtain different reference points of both the rail and the catenary. The LiDAR locates the position of one of the rails, one of the walls, and the entire upper vault of the tunnel including the catenary in both directions in the same sweep. Figure 9 shows an example of the measurements obtained in one of the selected sections. It shows the rail at the bottom and the catenary sections at the top. In addition, it can be seen that the device can recognize catenary bifurcations in the opposite direction of the rail.



(a)



(b)

Figure 9. Data collected by LiDAR. (a) Point cloud generated for a section of Malaga metro infrastructures. (b) Example view of one of the sections of the Malaga metro infrastructure.

Another parameter that has been studied thanks to the data collected by LiDAR has been the height of the catenary. Figure 10 shows the catenary height measured on a section of the installation's route. In this section, the average catenary height was 4.44 m, with maximum and minimum values of 4.47 and 4.42 m respectively.

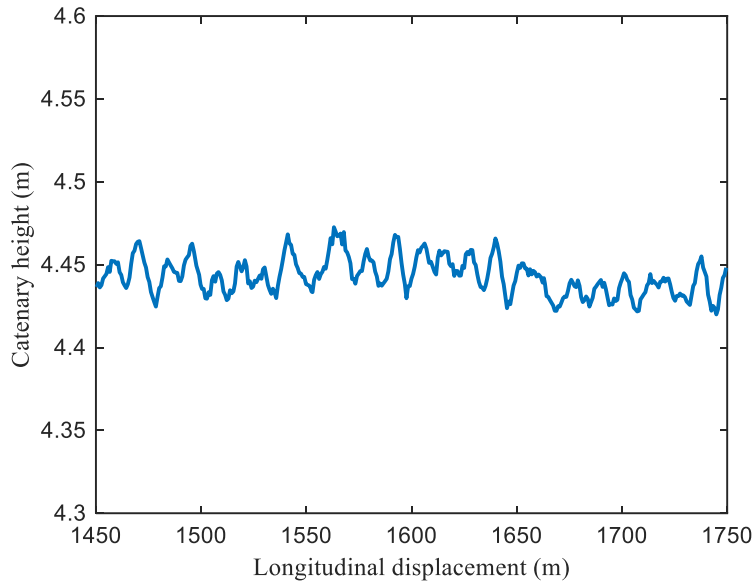


Figure 10. Catenary height.

Figure 11 shows the zigzag movement of the catenary on a section between stations of the Metro Malaga infrastructure. It shows a lateral displacement of the catenary in the range of -175 to +192 mm, with an average value of 20 mm.

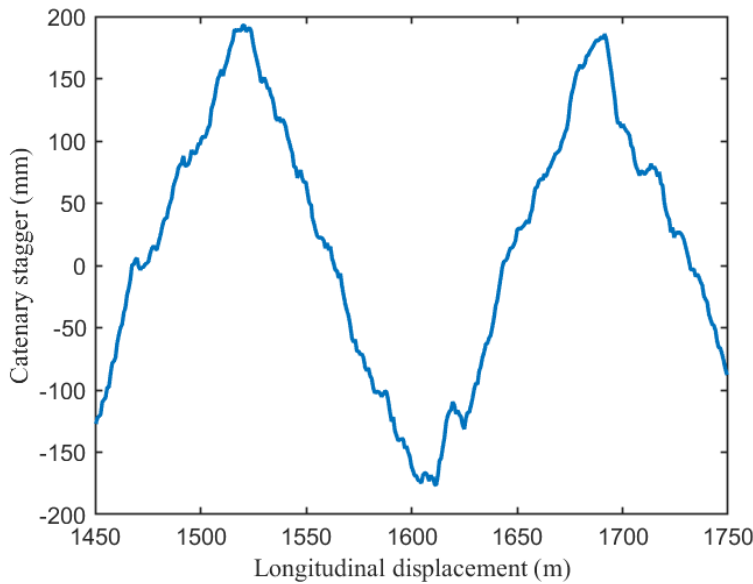


Figure 11. Catenary stagger.

## 6 CONCLUSIONS

This work presents a device capable of conducting measurements related to the characteristics of the installation and the state of wear of the catenary contact wire. The device moves along the rail, being able to carry out the inspection and measurement tasks automatically. These measurements, in addition to testing the condition of the wire, will be used as input for wear models, thus allowing the remaining service life to be determined more precisely. The device has been successfully tested in the installations of Metro de Málaga, obtaining satisfactorily all the measurements for which it was designed.

The main features of the device are:

- Ability to move autonomously along the rail.
- Manual, semi-automatic, and automatic measurement.
- Equipped with sensors to measure rail gauge, distance traveled, rail irregularities, catenary height and offset, and contact wire status.
- Foldable, small size, and low cost.

## ACKNOWLEDGEMENTS

The authors would like to thank METRO DE MALAGA S.A. for allowing the testing of the developed device and the conducting of measurements in their installations. In particular, we would like to thank all the staff of the company who have been involved in this activity.

## FUNDING

This work was partly supported by the Economy Transformation, Industry, Knowledge and Universities Council of the Andalusian Regional Government under grant PROYEXCEL\_00379, and partly by the University of Malaga.

## REFERENCES

- [1] M. Simarro, S. Postigo, J.A. Cabrera, J.J. Castillo, A procedure for validating rigid catenary models using evolutionary techniques. *Comput Struct.* 202;228,2019
- [2] Bommar PT, inventor, Bommar PT, assignee, Overhead rigid power conductor, U.S., Patent, No. US3985211A, 1976-10-12.
- [3] A. Oya, M. Shimizu, T. Mandai, K. Nishi, M. Tago, Application of overhead rigid conductor line to mountain tunnel of conventional lines, *Proceedings of the IEEE international conference on industrial technology*, 2005.
- [4] M. Simarro, S. Postigo, M. Prado, A. Pérez, J.J. Castillo, Analysis of contact forces between the pantograph and the overhead conductor rail using a validated finite element model, *Eng. Struct.*, 225, 2020.



## MODELLING RAILWAY-INDUCED VIBRATIONS USING A 2.5D HYBRID SBM-MFS METHODOLOGY

Hassan Liravi<sup>1</sup>, Arnau Clot<sup>1</sup>, Robert Arcos<sup>1</sup> and Jordi Romeu<sup>1</sup>

<sup>1</sup> Acoustical and Mechanical Engineering Laboratory (LEAM), Universitat Politècnica de Catalunya  
(UPC)

C/ Colom, 11, 08222 Terrassa (Barcelona), Spain.

e-mail: {hassan.liravi, arnau.clot, robert.arcos, jordi.romeu}@upc.edu

**Keywords:** Wave propagation, Singular boundary method, Method of fundamental solutions, Railway-induced vibrations.

**Abstract.** *Rail transport is a sustainable and reliable system for transporting passengers and freight. In urban environments, however, noise and vibrations caused by railway traffic can affect people working or living close to railway lines. Modelling the vibration impact caused by railway traffic in such situations is extremely useful for assessing the efficiency of potential abatement solutions. However, due to the complexity of the problem, accurate results require the use of sophisticated numerical models, that often require significant modelling efforts and high computational costs. The aim of this paper is to present the application of a novel numerical 2.5D meshless methodology to ground-borne railway-induced vibration problems. The approach, which combines the use of the singular boundary method (SBM) and the method of fundamental solutions (MFS), is used for modelling the track-soil interaction as well as the propagation of elastic waves through the soil. The accuracy and computational efficiency of the approach is compared with those of alternative numerical strategies for numerical examples considering at-grade and underground railways.*

## ASSESSING THE DYNAMIC RESPONSE OF SKEWED RAILWAY BRIDGES THROUGH DETAILED MODELLING

Juan C. Sánchez-Quesada<sup>1,\*</sup>, Emmanuela Moliner<sup>1</sup>, Antonio Romero<sup>2</sup>, Pedro Galvín<sup>2</sup>,  
María D. Martínez-Rodrigo<sup>1</sup>

<sup>1</sup>Universitat Jaume I  
Av. Vicent Sos Baynat, s/n, 12071, Castelló de la Plana, Spain  
\*e-mail: jquesada@uji.es

<sup>2</sup> Universidad de Sevilla  
Camino de los descubrimientos s/n, 41092, Seville, Spain

**Keywords:** Railway bridges, Vehicle-track-bridge-interaction, Track unevenness, Numerical-experimental comparison.

**Abstract.** *In Europe the sustainable and smart mobility strategy, aims to double high speed railway traffic by 2030 and tripling it by 2050. This ambitious objective requires to overcome the interoperability challenges between the different railway systems of the European countries. Regarding the railway infrastructures, the European Union Agency for Railways recently published a technical note with the investigations needed for closing the technical specifications for interoperability on railway bridge dynamics. The train-track-bridge interaction problem is currently a matter of concern and its investigation is far to be fully closed. Furthermore, it is essential to predict the structural dynamic response realistically with reasonable computational cost, both in the design phase and over the service life. In this context, the work presented herein is devoted to the analysis of railway-induced vibrations of high speed railway bridges composed by pre-stressed concrete girder decks and multiple simply-supported spans of short to medium lengths. This investigation focuses on the adequacy of using highly detailed three-dimensional finite element models of the bridge for the prediction of the structural dynamic response under operational conditions. A particular bridge configuration is evaluated: pre-stressed concrete simply-supported girder bridges with high levels of obliquity. The presented bridge numerical models include: (i) a detailed discretisation of the track platform; (ii) transverse diaphragms at the span ends; and (iii) successive oblique simply-supported spans weakly coupled through the ballast track layer. For this purpose, the digital twins of two similar real bridges with spans lengths of 15 and 25 meters are developed and updated with experimental measurements. Finally, different approaches for the railway vehicle modelling are considered to quantify the agreement between experimental and numerical predictions: (i) the simple moving load model; (ii) a multibody three-dimensional train model accounting for the interaction effect and track irregularities. Conclusions regarding the dynamic performance of the aforementioned structures and the influence of vehicle-bridge interaction phenomena are finally presented.*



## 1 INTRODUCTION

In Europe, the decarbonisation of transport and the impulse of sustainable mobility are at present top priorities towards the so-called Green Deal. In this context, the Sustainable and smart mobility strategy, foresees that high-speed rail traffic will double by 2030, and freight traffic by 2050. Regarding railway infrastructures and, more specifically, bridges and viaducts, the European Union Agency for Railways recently published a technical note on the investigations needed to close the Technical Specifications for Interoperability open points on railway bridge dynamics [1]. Therefore, the train-track-bridge interaction problem is a matter of concern and investigation are far to be concluded.

Railway bridges composed by simply supported (SS) spans of short to medium length are critical in terms of train induced vibrations, and thus, an accurate prediction of the vertical acceleration levels under traffic actions is essential. Many current standard methods rely on the premise that the response of SS railway bridges is dominated by the first longitudinal bending mode, and therefore, simplified beam models are accepted in preliminary steps of the design process. However, this may not be the case for double-track bridges with highly skewed decks. Preliminary studies about the influence of end diaphragms on the dynamic performance of oblique girder bridges have been performed [2], but most of the work found disregard the weak coupling exerted between successive spans through the ballast bed. In this study, two detailed 3D finite element (FE) models of real skewed double-track girder bridges with multiple SS spans are developed, including an accurate representation of the ballasted track.

In order to quantify the numerical improvement reached when the vehicle-bridge-interaction effect is included, an experimental-numerical comparison of the vertical acceleration response at the deck level under operating conditions is performed, considering different modelling techniques for the vehicle and accounting for the track irregularities.

## 2 REAL BRIDGES UNDER STUDY

Two existing railway bridges, constitute the starting point for this investigation: the bridges over Arroyo Bracea and Jabalón watercourses, from now on Arroyo Bracea I and Jabalón bridges. Arroyo Bracea I bridge is composed by two identical 15.25 m SS spans and crosses the river with high skewed decks. Jabalón bridge is also a SS oblique bridge with similar skewness formed by three equal spans of 24.9 m. The deck of both structures is composed by a cast-in-place concrete slab which rest over five high pre-stressed concrete I girders. Both bridges are of the same typology regardless the differences on the slab thickness ( $s_{tk}$ ), girder high ( $g_h$ ) and equispaced distance between girders ( $g_d$ ). Beyond the presented discrepancies, the ballast track layout and components are identical in both cases (Figure 1).

In 2016 and 2019 two experimental programs were carried out by the authors in order to identify Arroyo Bracea I and Jabaón bridges [3, 4]. In these experimental campaigns, the first five natural frequencies, mode shapes and damping ratios (under ambient and free vibration) were identified. The aforementioned modes correspond to the first longitudinal bending, first torsion, first transverse bending, second torsion and second transverse bending modes of the instrumented deck, which are listed in Table 1 in ascending order.

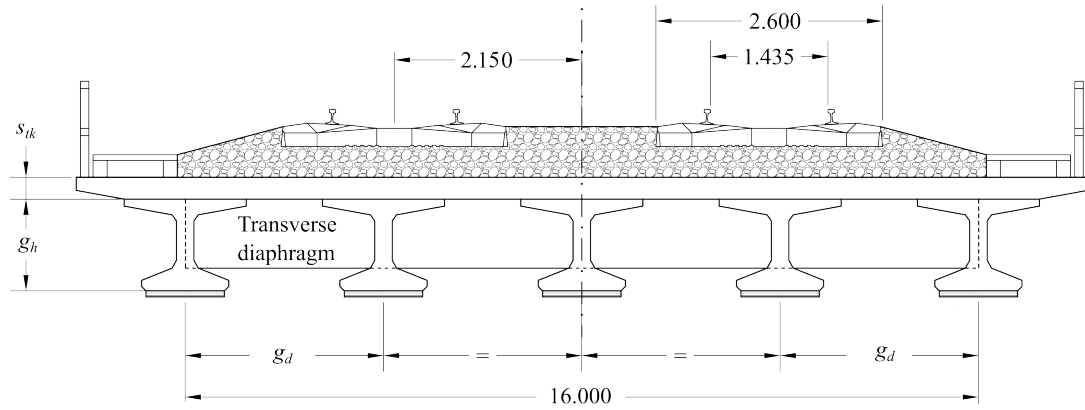


Figure 1: Arroyo Bracea I and Jabalón bridges cross-section.

### 3 METHODOLOGY AND RESULTS

The FE models of Arroyo Bracea I and Jabalón bridges include a continuous representation of the ballasted track and also the transverse diaphragms at each span end. The numerical models of these bridges contain the real number of spans along with 15 m of track extension on both sides. For the sake of clarity, the Figure 2 only shows some detailed views of the Jabalón FE model, developed in ANSYS(R)17, and not displaying the entire model.

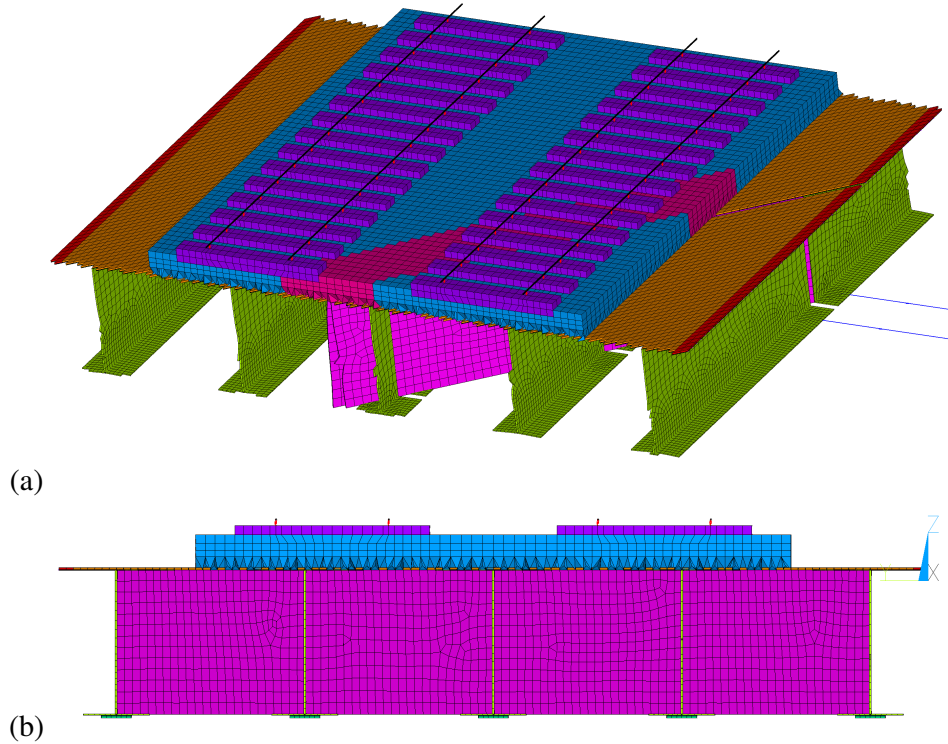


Figure 2: (a) Clipped view of the Jabaón FE model; and (b) detailed view of Jabalón FE model cross sections.

These bridges are calibrated with a genetic algorithm, in order to reproduce the modal parameters experimentally identified of the bridges, in terms of natural frequencies and mode

shapes. The correspondence between the experimentally identified modal parameters and those predicted by the calibrated numerical models is provided in Table 1, in terms of frequency differences and MAC numbers. The first two modes, whose contribution to the transverse response of the bridges under passing trains is expected to be significant, are especially well adjusted according to the modal pairing results.

Bridge	Arroyo Bracea I Bridge					Jabalón Bridge				
Mode (i)	1	2	3	4	5	1	2	3	4	5
$f_i^{exp}$ (Hz)	9.25	10.63	12.75	17.92	24.57	6.30	7.20	9.30	24.00	24.50
$f_j^{num}$ (Hz)	9.22	11.04	12.67	17.86	27.72	6.09	7.41	9.88	19.07	22.89
$e_{i,j}$ [%] (-)	+0.28	-3.87	+0.61	+0.34	-12.84	+3.40	-2.86	-6.29	+20.52	+6.58
MAC (-)	0.96	0.94	0.95	0.98	0.58	0.93	0.95	0.95	0.68	0.75

Table 1: Experimental and numerical frequencies for modes under 30 Hz.  $f_i^{exp}$  and  $f_j^{num}$  denotes experimental and numerical frequencies. Frequency differences ( $e_{i,j}$ ) and MAC numbers for the paired modes after calibration is presented.

Considering these updated FE models, experimental-numerical comparison of the deck vertical acceleration under train passages are performed to evaluate the model accuracy. The numerical predictions are computed by mode superposition and consider different vehicle approaches for the railway excitation. These assumptions sweep from the simplest moving loads model to a developed multibody three-dimensional train model accounting for the track irregularities. The proposed track vertical unevenness of each rail in the multibody train model, is computed according to the stochastic process presented in H. Claus and W. Schiehlen [5]. Considering a high level of track irregularities, several track profiles are generated in accordance with the intervention criteria defined in EN-13848-5 standard when wavelengths in the range [3, 25] m are considered. The one which results in a better numerical-experimental adjustment is selected. According to EN-13848-6 the resultant irregularities profiles are categorised as D and E classes in Arroyo Bracea I and Jabalón bridges, respectively. The modal damping ratios identified during the experimental campaign under free vibration are assigned to the paired modes, while the recommended EN-1991-2:2003 damping ratios are used for the non-paired numerical modes.

The vertical acceleration underneath girders in Arroyo Bracea I and Jabalón bridges were recorded for several trains passages. The Figure 3 presents two columns associated to the bridge under study and a particular train passage: the first one shows resonance on Arroyo Bracea I bridge structure when it is crossed by the conventional train S103 at  $279 \text{ km}\cdot\text{h}^{-1}$ , and the second shows the non-resonance condition in the structure of Jabalón bridge when it is traversed by the conventional train S104 at  $249 \text{ km}\cdot\text{h}^{-1}$ . Two points are selected for each train passage in Figure 3, depending on whether they belong to the vertical-supports or not. As a result, Figure 3 is composed by four subfigures (a-d), where the fast Fourier transform of the vertical acceleration, the location of the measurement point and the time domain response under the train passage are engaged. The experimental response is represented in red trace, while three alternative numerical approaches used for the vehicle are superimposed in different colours: moving load model (TLM) in black trace, grey solid line for the multibody approach neglecting irregularities (VBI), and the black dotted line for the results which include the rail irregularities (VBI  $\eta$ ). The numerical and experimental responses have been filtered applying two third order Chebyshev filters with high-pass and low-pass frequencies of 1 Hz and 30 Hz, respectively.

In the first column of Figure 3, the resonance case, the measured speed approaches the theoretical velocity of the third order resonance of Arroyo Bracea I bridge fundamental mode. In Figure 3 (a) the results for the point located at the centre of the span are presented. In this location, the frequency associated to the resonant mode stands out more prominently compared to other frequency components and the acceleration response in the time domain gradually amplifies as the train axes pass through. The acceleration level in the point located in the bridge support is lower and the contributions above 15 Hz are clearly visible, Figure 3 (b). It is also noticeable that the three different numerical approaches adopted for the railway excitation yield very similar predictions in the low frequency range [1,11] Hz, which suggests that the VBI effects do not play a significant role on the dynamic response of this bridge. As it is well known, the interaction between the bridge and the vehicle becomes relevant specially at resonance and under two current conditions: (i) when the frequency of the vehicle's suspended masses aligns closely with the natural frequencies of the bridge, and (ii) when the train mass is relevant when compared to the mass of the bridge. None of these situations happened in this recorded train passage.

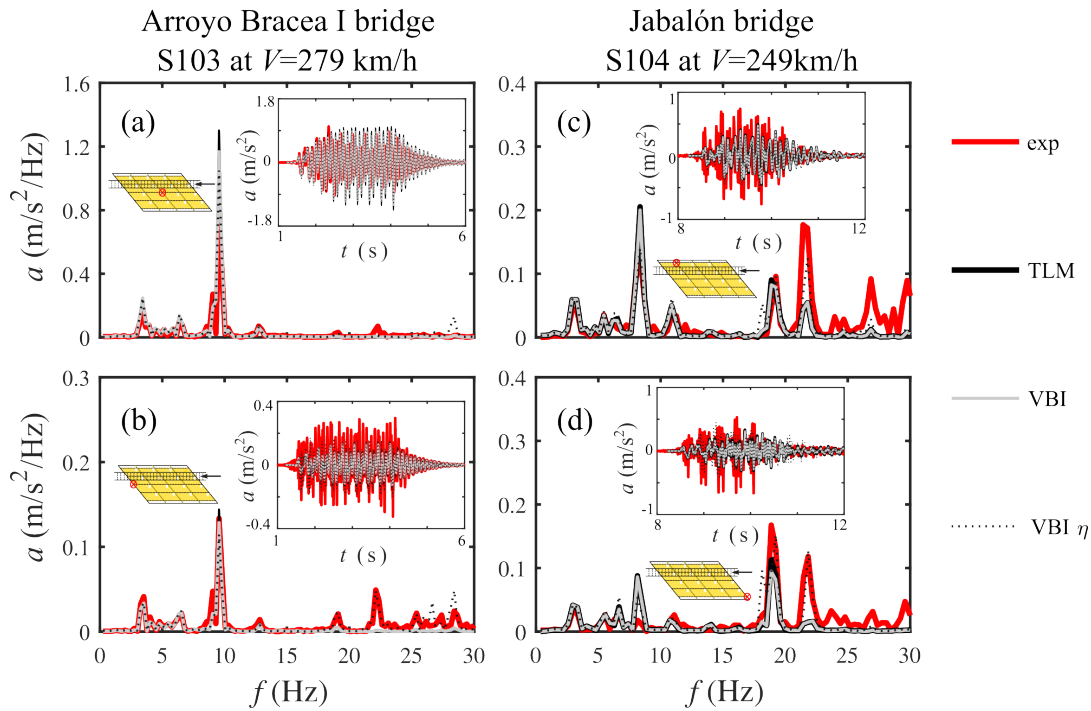


Figure 3: Numerical-experimental comparison of vertical acceleration under S103 conventional train in Arroyo Bracea I bridge (a-b); and S104 conventional train in Jabalón bridge (c-d).

In the second column of Figure 3, the vertical acceleration levels in the Jabalón bridge under non-resonance condition is presented. Figure 3 (c) display the results at the point located at quarter span in the external girder closest to the loaded track, while Figure 3 (d) shows the response at the second support associated with the girder farthest from the loaded track. The frequency domain representations exhibit a clear contribution of the bogie passing frequency and to lower natural frequencies of the bridge. They are well predicted by the three numerical

approaches, with negligible differences between them. As can be observed, the VBI has a minor influence in the response, which can be explained by the higher span length of Jabalón bridge, and lower train-to-bridge mass ratio, and to the non-resonant passage of the train.

The numerical predictions depicted in Figure 3 are reasonable accurate and the frequency peak associated to the excitation and also the corresponding to the first two structural modes are well predicted. In the analysed cases, the differences between the three vehicle models become more relevant for frequencies higher than 15 Hz due to the effect of track irregularities, which introduce higher frequency contributions in the dynamic response. It is also noticeable that the consideration of track irregularities in the numerical model improves the correlation with the experimental measurements, especially at higher frequencies.

#### 4 CONCLUSIONS

The numerical-experimental comparison of the vertical acceleration levels performed on two existing girder bridges under operating conditions highlights the complex dynamic behaviour of oblique medium-span bridges, with a vibratory response that differs from the classic beam-type structure that has been extensively studied in the literature from analytical and numerical perspectives. Under non-resonant conditions, the frequency content of the forced structural response exhibits the participation of several frequency contributions, with the bogie/axle passing frequency and the first two natural frequencies (first longitudinal bending and first torsion) of the bridges being the most relevant. These frequencies are well predicted by the numerical models and are clearly visible in the frequency range [1,11] Hz of the deck acceleration response, which is attributed to the successful updating of the FE models with experimental data. The fitting between measured and predicted levels of accelerations is worse at higher frequencies, since the FE model reproduces with less accuracy frequency contents above 11 Hz. For this reason, the correlation with the experimental measurements improves under resonant train passages and for the sensors located far from the abutments, which acceleration response is less affected by these high frequency contributions.

The results show that the inclusion of the track irregularities introduce higher frequency contributions in the dynamic response (above 15 Hz) allowing a better fitting between experimental measurements and numerical predictions. In this study the vertical track unevenness is unknown. However, the effects of irregularities can be accurately quantified carrying out a statistical analysis.

#### 5 ACKNOWLEDGEMENTS

The authors would like to acknowledge the financial support provided by the Spanish Ministry of Science (research project PID2022-138674OB-C2); Andalusian Ministry of University, Research, and Innovation (PROYEXCEL 00659); Andalusian Scientific Computing Centre; and Generalitat Valenciana (AICO/2021/200).

#### REFERENCES

- [1] ERA, ERA technical note on work needed for closing TSI open points on bridge dynamics, *Technical Note, Bridge dynamics*, ERA1193-TD-01-2022.

- [2] E. Moliner, A. Romero, P. Galvín, M.D. Martínez-Rodrigo, Effect of the end cross beams on the railway induced vibrations of short girder bridges, *Engineering Structures*, **201**, 109728, 2019.
- [3] P. Galvín, A. Romero, E. Moliner, M.D. Martínez-Rodrigo, Two FE models to analyse the dynamic response of short span simply-supported oblique high-speed railway bridges: Comparison and experimental validation, *Engineering Structures*, **167**, 48-64, 2018.
- [4] P. Galvín, A. Romero, E. Moliner, G. De Roeck, M.D. Martínez-Rodrigo, On the dynamic characterisation of railway bridges through experimental testing, *Engineering Structures*, **226**, 111261, 2021.
- [5] H. Claus, W. Schiehlen, Modelling and simulation of railway bogie structural vibration, *Vehicle system dynamics: International Journal of Vehicle Mechanics and Mobility*, **29**, s1, 538-552, 1998.

## INBRIDGE4EU PROJECT FOR BRIDGE DYNAMICS: TOWARDS INTEROPERABILITY IN THE EUROPEAN RAILWAY NETWORK

Pedro Galvín<sup>1</sup>, José M. Goicolea<sup>2</sup>, Antonio Martínez de la Concha<sup>1</sup>, María D. Martínez-Rodrigo<sup>3\*</sup>, Emma Moliner<sup>3</sup>, Javier Naranjo<sup>1,2</sup>, Carlos Rodrigo<sup>3</sup>, Antonio Romero<sup>1</sup>, Nicola Tarque<sup>2</sup>

<sup>1</sup> Universidad de Sevilla, Escuela Técnica Superior de Ingeniería, 41092 Sevilla  
e-mail: {pedrogalvin, delaconcha, aro}@us.es

<sup>2</sup> Universidad Politécnica de Madrid, E.T.S. de Ing. Caminos, Canales y P., 28040 Madrid  
{jose.goicolea, nicola.tarque}@upm.es

<sup>3</sup> Universitat Jaume I, Departamento de Ingeniería Mecánica y Construcción, 12071 Castellón  
{mrodrigo, molinere, crodrigo}@uji.es

**Keywords:** railway bridges, interoperability, European railway network, bridge dynamics.

**Abstract.** *In this contribution the objectives and initial activities from the InBridge4EU project are presented. InBridge4EU was awarded to a consortium of 11 members, including two infrastructure managers, DB Netz AG and ADIF, and four Spanish universities: Universidad Politécnica de Madrid, Universidad Politécnica de Valencia, Universidad de Sevilla and Universitat Jaume I de Castellón. The project's proposal is aligned with the European's Rail Joint Undertaking overall targets in the following domains: (i) contribute towards the achievement of the Single European Railway Area by defining Europe-wide harmonized standards and interoperability criteria; (ii) improving bridges' structural analysis to optimise the railway capacity meeting user demand; (iii) establishing criteria for bridges' structural performance, increasing the quality and consistency of the service; and (iv) contributing to reduce the design and maintenance cost of bridges stock, improving the competitiveness of the European rail system overall. Detailed analysis is being carried out for 9 railway lines belonging to 5 different countries in the European Union covering a wide range of structural types and maximum speeds. The overall objective of InBridge4EU project is to develop a dynamic interface between railway bridges and rolling stock, proposing new methods compatible with existing regulations, and approaching the analysis of existing infrastructures, which role is critical for the sustainability of the European rail system. The project is organized in seven work packages that aim to address the 11 different Work Streams stipulated in the call topic and in the ERA Technical Note [1].*

## 1 INBRIDGE4EU PROJECT: MAIN OBJECTIVES AND PARTICIPANTS

InBridge4EU project started on September 1<sup>st</sup> 2023. The project is funded by Europe's Rail Joint Undertaking under Horizon Europe research and innovation program. The overall objective of InBridge4EU is to develop a dynamic interface between railway bridges and rolling stock, proposing new methods compatible with existing regulations, namely INF TSI [2], LOC&PAS TSI [3], EN 15528 [4], EN 1990-Annex A2 [5] and EN 1991-2 [6], and approaching the analysis of existing infrastructures, which role is critical for the sustainability of the European rail system. 11 entities including two Infrastructure Managers and four Spanish universities (see Fig. 1 left) participate in the consortium, led by Universidade do Porto. The project is articulated in seven work packages with the following objectives:

- WP1: Definition of Dynamic Line Categories for ensuring compatibility of the interface between trains and bridges. Objective: to improve the practical methods available for determining the train-bridge interface for dynamic loading effects, based on the use of spectral methods and transient dynamic analysis.
- WP2: Identification of critical bridge parameters for the assessment of the economic impact of the new DTCs. Objective: to estimate the time and cost of physical works required for implementing each proposed DTC in average on a line.
- WP3: Revision of the dynamic factors  $\phi'$  and  $\phi''$ . Objective: to propose revised formulae for the dynamic factors  $\phi'$  and  $\phi''$  stipulated in the Annex C of EN 1991-2 [6].
- WP4: Revision of damping in railway bridges. Objective: estimating damping in different bridge types based on experimental data and identifying the main parameters that most influence the damping values of existing railway bridges and the main reasons for the wide range of damping values observed in similar structures.
- WP5: Revision of bridge deck acceleration limit. Objective: to provide additional background to a revised limit criteria for vertical bridge deck acceleration.
- WP6: Recommendations for dynamic compatibility checks. Objective: proposing recommendations to the regulatory bodies, namely the European Union Agency for Railways (ERA) and the European Committee for Standardization (CEN), for reviewing or implementing updates in the current Eurocodes and Technical Specifications for Interoperability (TSI) based on the research carried out in WP1 to WP5.
- WP7: Project coordination, scientific quality assurance and dissemination, exploitation and communication.

## 2 WP2: IMPLEMENTATION OF BRIDGE DATA BASE

The coauthors of this contribution participate actively in WP2 tasks. In WP2, during the first year of the project, an extensive and representative set of European railway bridges needs to be selected, and relevant data needed to evaluate their dynamic performance retrieved and stored in a database. Starting from the beginning of the second year, time-step calculation (TSC) transient dynamic analyses will be performed over the complete database under real train models / MU classes and under the new DTCs proposed in WP1. From the analysis of the database realistic worst-case combinations of critical parameters for use in parametric studies will be identified. From the detection and evaluation of the bridges that do not meet the economic technical acceptance criteria an estimation of the resources required for implementing each DTC on a



particular line will be presented. Relevant output will also be provided in relation to the appropriateness of different model updates and of the use of the classical beam line model for the analysis of certain bridge configurations.

So far, 10 railway lines from 5 EU countries have been selected covering different maximum design speeds (see Figure 1 right). Relevant information from about 50 bridges per line has been retrieved with the intensive participation of the corresponding Infrastructure Managers, including technical drawings and experimental data (Figure 2 left). In parallel, a cloud database has been designed and made accessible to all the partners in the consortium (Figure 2 right). The data base will accommodate the bridges data and the results of posterior analyses.

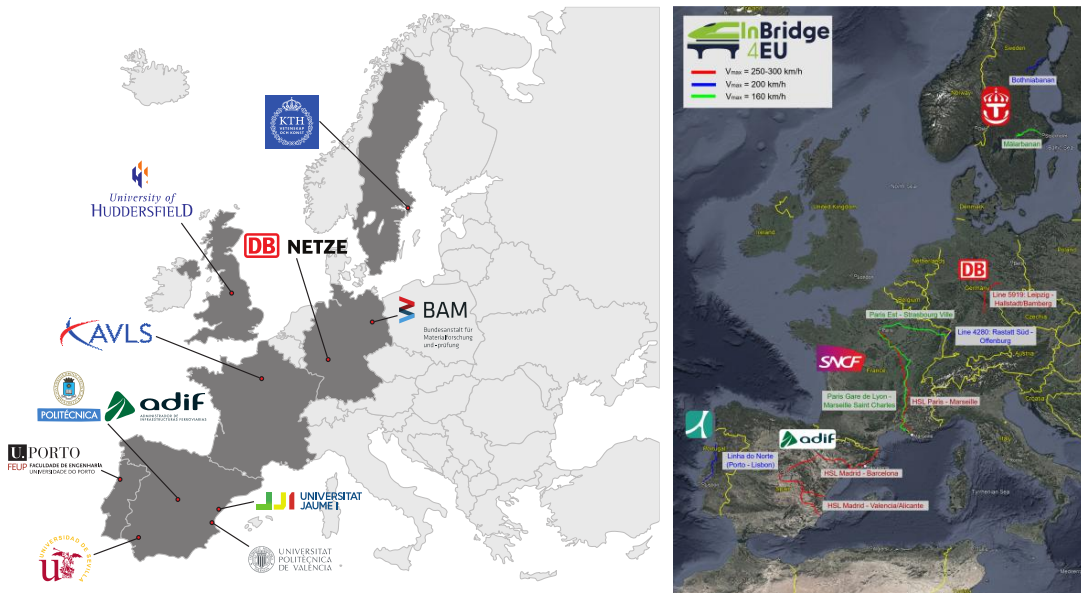


Figure 1: InBridge4EU consortium (left) and selected railway lines (right).

### 3 WP2: FUTURE TASKS

In the upcoming months, time step calculations will be performed with different complexity models for the bridges, depending on the configuration. Interaction phenomena will be disregarded (i.e., vehicle-bridge, soil-bridge) and modal superposition will be admitted, limiting the computation costs. Detailed 3D numerical models will be used for the bridges requiring further investigation to confirm if they meet the technical bridge acceptance criteria. For those failing this last check, the nature of the likely physical works most appropriate in each situation (e.g. strengthening, stiffening, deck substitution, complete substitution) will be identified and economically appraised. From the statistical analysis of the database, realistic bridge parameter combinations, the distribution of most critical parameters and most critical parameter combinations considering parameter interrelations will be identified. Existing bridge configurations that cannot be adequately represented by simple line beam models in dynamic analyses will be identified and the limitations of the beam-type analysis will be evaluated and compared to alternative models.

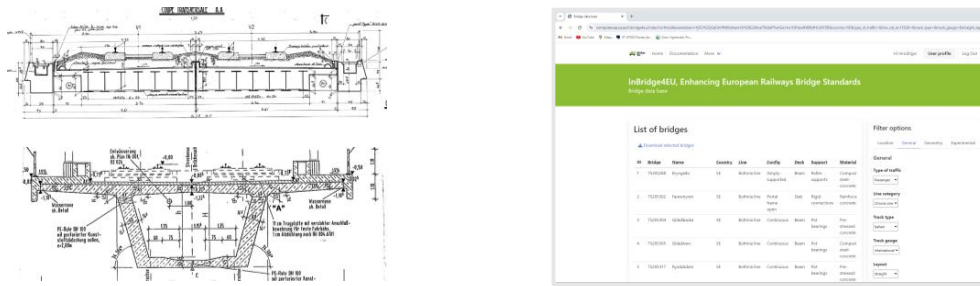


Figure 2: Example of bridge deck typologies (left) and cloud data base interface (right).

## 4 CONCLUSIONS

The outcomes of the project will have a clear impact on the current European normative documents related with bridge dynamics and on the harmonisation of working methods across European countries. The outcomes will consequently influence the design of new railway bridges and the evaluation/monitoring of existing ones. In addition, InBridge4EU results will influence over time several critical aspects related to railway bridges and respective interaction with rolling stock.

## 5 ACKNOWLEDGEMENTS

This project has received funding from the Europe's Rail Joint Undertaking under Horizon Europe research and innovation programme under grant agreement No. 101121765 (HORIZON-ER-JU-2022-ExplR-02). Views and opinions expressed are however those of the author(s) only and do not necessarily reflect those of the European Union or Europe's Rail Joint Undertaking. Neither the European Union nor the granting authority can be held responsible for them.

## REFERENCES

- [1] ERA Technical Note (2022). ERA1193-TD-01-2022 - ERA technical note on work needed for closing TSI open points on bridge dynamics, European Union Agency for Railways (ERA). Valenciennes.
- [2] INF TSI (2019). Technical specifications for interoperability relating to the 'infrastructure' subsystem of the rail system in the European Union, Official Journal of the European Union. Brussels.
- [3] LOC&PAS TSI (2019). Technical specification for interoperability relating to the 'rolling stock - locomotives and passenger rolling stock' subsystem of the rail system in the European Union, Official Journal of the European Union. Brussels.
- [4] EN 15528 (2021). Railway applications - Line categories for managing the interface between load limits of vehicles and infrastructure, European Committee for Standardization (CEN). Brussels.
- [5] EN 1990-Annex A2 (2001). Eurocode 0: Basis of structural design - Annex 2: Application for bridges (normative), European Committee for Standardization (CEN). Brussels.
- [6] EN 1991-2 (2003). Eurocode 1: Actions on structures - Part 2: Traffic loads on bridges, European Committee for Standardization (CEN). Brussels.

**3rd Conference on Structural Dynamics (DinEst 2024)**  
**Seville, September 2024**  
**Analytical and computational dynamics session**

## VIBRATORY ANALYTICAL-COMPUTATIONAL MODEL OF A NEONATAL INCUBATOR

Alejandro Rincón Casado<sup>1</sup>, \*Mauricio Larrodé Díaz<sup>2</sup>

<sup>1</sup> Cádiz University  
Department of Mechanics and Industrial Design, College of Engineering  
e-mail: alejandro.rincon@gm.uca.es

<sup>2</sup> Cádiz University  
Department of Mechanics and Industrial Design, College of Engineering  
e-mail: mauricio.larrodediaz@alum.uca.es

**Keywords:** FEM modeling; neonatal incubator; parametric optimization; accelerometers

**Abstract.** *This study consists of the vibratory analytical computational model of a neonatal incubator. Neonatal incubators produce vibrations when in operation and this can cause discomfort in the newborn. The objective of this research is to reduce the modal frequencies of the system and improving the comfort of the newborn. The vibrations in a parallelepiped have been analyzed simulating a neonatal incubator and the frequencies produced by hitting it with a hammer in an anechoic chamber have been studied experimentally.*

*In addition, a computer simulation has been carried out using Ansys, generating a geometry of a box and the modal frequencies have been studied. These obtained frequencies have been compared with experimental studies. Using a genetic algorithm, the best frequency of the geometry has been sought in order to find an ideal geometry that reduces the frequencies and thus has fewer vibrations in the incubator.*

### 1. RESUMEN

A transparent methacrylate parallelepiped has been manufactured and open at the lower base simulating a real neonatal incubator to perform experimental measurements in an anechoic chamber. This camera is isolated from external noises, obtaining more efficient results without external interference. Accelerometers have been placed on the lateral and upper faces of the parallelepiped as we see in the Figure 1. By hitting it with a hammer, some values have been obtained that, through the Fourier Transform, frequency graphs have been obtained.

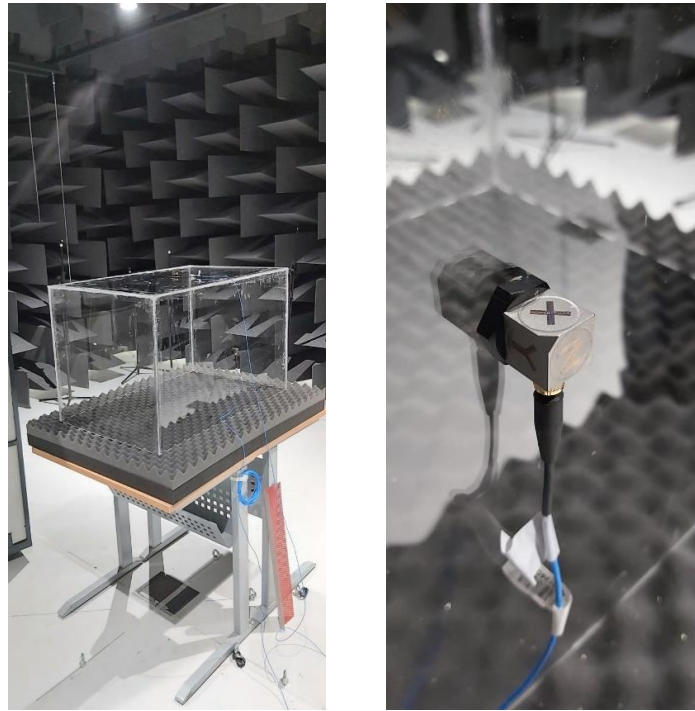


Figure 1. Accelerometer placed in parallelepiped

Once this is done, a geometry model just like the real parallelepiped has been generated in the Ansys software to calculate the modal frequencies. In this program, the input values have been parameterized using an algorithm for both dimensions and thickness and obtaining the output value, which would be the frequency. The results of both models (experimental and computational) are compared and it is observed that the frequencies approach 14 Hz. The comparison between the computational model and the experiment allows the FEM model to be calibrated and guarantee reliable results for the second phase of geometric optimization.

Subsequently, many cases of different dimensions can be obtained in Ansys and obtaining a modal frequency that allows us to obtain a more optimal geometry and with the least harmful frequencies for the neonate. Currently, we are working on a genetic algorithm in Matlab that generates different geometry models using input data and that, by applying artificial intelligence, we obtain a system that, by introducing the dimensions and thicknesses, calculates the modal frequency for that model and thus be able to have the control of vibrations when manufacturing a neonatal incubator.

With this work, we seek to obtain an optimal design that minimizes the harmful effects of vibrations on the neonate. Reducing noise and vibrations in neonatal incubators is of vital importance, as it can negatively affect their development and health. In this sense, this study can be very useful for improving the design of incubators and, therefore, improving the comfort of neonates from a vibration point of view.

## Referencias

- [1] Rincón Casado, A.; Larrodé-Díaz, M.; Fernandez Zacarias, F.; Hernández Molina, R. Experimental and Computational Model for a Neonatal Incubator with Thermoelectric Conditioning System. *Energies* 2021, *14*, 5278.

## VALIDATION OF CFD SIMULATION WITH FLUID-STRUCTURE INTERACTION BY MEANS OF AEROELASTIC TESTS IN PHYSICAL WIND TUNNEL

\*Ángel Vidal<sup>1</sup>, María Macías<sup>1</sup>, Manuel Castillo<sup>1</sup> and Álvaro Serrano<sup>2</sup>

<sup>1</sup> MC2 Estudio de Ingeniería, Grupo TYPESA  
c/ Condesa de Venadito 5<sup>a</sup>, 28027 Madrid  
e-mail: mc2@mc2.es

<sup>2</sup> Director técnico de MC2 Estudio de Ingeniería, Grupo TYPESA  
c/ Condesa de Venadito 5<sup>a</sup>, 28027 Madrid  
e-mail: alvaro.serrano@mc2.es

**Keywords:** Wind-structure interaction, PV tracker, Computational Fluid Dynamics, Wind tunnel test

### Abstract.

*This paper presents the results obtained in the validation of a 2D CFD (Computational Fluid Dynamics) numerical simulation of wind-structure interaction by means of physical testing in a wind tunnel laboratory.*

*The structure studied is a horizontal axis solar tracker.*

*First, the structure is described, which consists of a series of large-span, low-mass solar panels arranged on a horizontal axis formed by a steel tube. The numerical simulation reproduces the wind tunnel boundary conditions around the tracker and by means of finite volume technique allows to analyze the fluid dynamics at each time step, in this case the wind generated in the tunnel under low turbulence conditions.*

*The structure is also solved stepwise by direct integration in time, so that the fluid simulation can update the contour geometry. With this two-way interaction it is possible to couple the response of the two domains, the structural and the fluid.*

*To validate the results obtained, a mobile physical model of the tracker with the same mechanical and kinematic properties as those simulated computationally has been made. The monitoring of the response of the model during the physical wind tunnel tests is the standard used to compare with the results of the numerical simulation.*

*The procedures used in this work to characterize the tracker response are the history of the tracker embedding torque moment and the capture of the motion with video camera and subsequent post-processing.*



*Finally, a hybrid methodology is proposed for the control of lightweight structures against wind action when aeroelastic instabilities are activated or at least the deformations under wind action are sufficiently important to cause a non-linear wind behavior around the structure.*

## ADVANCED NUMERICAL MODELLING FOR NONLINEAR DYNAMIC SOIL-STRUCTURE INTERACTION

J.M. Torres<sup>1,2</sup>, S. Andrés<sup>1</sup>, and R. Jiménez<sup>1</sup>

<sup>1</sup>ETS Ingenieros de Caminos, Canales y Puertos  
Universidad Politécnica de Madrid  
address: C/ Profesor Aranguren 3, Madrid, Spain  
e-mail: josemanuel.torres.serrano@alumnos.upm.es

<sup>2</sup> Ove Arup and Partners, SAU  
address: Alfonso XI 12, Madrid, Spain  
e-mail: josemanuel.torres@arup.com

**Keywords:** Numerical modelling, finite element analysis, nonlinear dynamic soil-structure interaction.

**Abstract.** *This article details a modeling strategy for studying dynamic soil-structure interaction (DSSI), specifically the seismic response of a reinforced concrete structure founded on piles. A 3D nonlinear finite element global model is introduced, allowing a comprehensive analysis of the entire soil-foundation-structure system in a single step. While finite element analysis remains the primary approach for contemporary DSSI problems, challenges arise in its practical application. One such challenge is reconciling the distinct natures of structural elements - bounded domain - and soil – unbounded domain-. Another challenge involves modelling interfaces between foundation elements and the surrounding soil, crucial for DSSI due to their significant contributions to energy dissipation and deformation. These sophisticated models, capable of incorporating multiple phenomena simultaneously, require meticulous validation. In this case, the numerical model is validated against analytical and empirical solutions for determining axial pile resistances in compression and alternative software for vertical seismic wave propagation. The findings affirm the model's effectiveness in enhancing understanding of structures' behavior under seismic loads, considering their interaction with the soil. This positions the model as a potential starting point for further studies, such as fragility assessments, contributing to the field's knowledge advancement. Furthermore, it underscores the advocacy for utilizing sophisticated methods over simpler alternatives when assessing the seismic response of pile-supported structures.*



## A SIMPLIFIED PROCEDURE TO TRACK THE TENSION FORCE: NUMERICAL VALIDATION

**Belén Vecino<sup>1\*</sup>, Luis Chillitupa-Palomino<sup>1</sup>, Javier Naranjo-Pérez<sup>2</sup>, Carlos M.C. Renedo<sup>1</sup>, Iván M. Díaz<sup>1</sup>, and Jaime H. García-Palacios<sup>1</sup>**

<sup>1</sup>Department of Continuum Mechanics and Theory of Structures, ETSI Caminos, Canales y Puertos,  
Universidad Politécnica de Madrid  
Calle Profesor Aranguren 3, Madrid, 28040  
e-mail: b.vecino@alumnos.upm.es, luis.cpalomino@upm.es, carlos.martindelaconcha@upm.es,  
ivan.munoz@upm.es, jaime.garcia.palacios@upm.es

<sup>2</sup>Department of Continuum Mechanics and Structural Analysis, ETSI, Universidad de Sevilla  
Camino de los descubrimientos, Seville, Spain  
e-mail: jnaranjo3@us.es

**Keywords:** Cable dynamics, External tendons, Tension force estimation, Model updating.

**Abstract.** *Recently, bridge collapses due to brittle fracture of grouted post-tensioning external tendons have been reported, highlighting the importance of structural health monitoring to prevent and predict these situations that strongly compromise safety. Non-destructive testing techniques based on the vibration response have proven their reliability in this aspect, as they allow continuous monitoring of the tendon modal parameters and the estimation of tension force. The tension force can be indirectly estimated from the modal properties of the tendon. A simplified method to track the tension force is proposed, which consists of calibrating the tendon model by obtaining the equivalent modal lengths for each natural frequency in such a way that general boundary conditions are considered for each mode. This study proposes a first numerical validation of this method through a detailed finite element model of a tendon. The finite element tendon model is subjected to a given stressing force; the bending stiffness and all other relevant parameters of the tendon are also known, subsequently, a modal analysis is performed to obtain the natural frequencies. The first twenty natural frequencies numerically calculated are then used to estimate the tension force based on the simplified method presented previously, the modal length calibration and optimization for each natural frequency is carried out for this example, and the estimated tension force and bending stiffness can be obtained. These results are compared with the finite element model of the tendon and then, the proposed tension force estimation procedure can be validated.*

## 1 INTRODUCTION

External post-tensioning systems are commonly used in the construction and rehabilitation of highway and railway bridges due to two main advantages: i) the ease of tendon replacement and ii) the possibility of the re-tensioning of tendons. In addition, this technology stands out for being economical and for its ease of installation, monitoring, inspection, and maintenance. However, bridge collapses have been reported due to corrosion under mechanical stress of the grouted external tendons. In this type of tendons, when a strand breaks, the bond between the strands and the grout leads to the re-anchoring of the strand in the grout and a stress redistribution to the adjacent strands [1]. Thus, it is difficult to detect corrosion damage from the modal properties and the estimated tension force, since the degradation of the effective tension force of the bonded tendons is not proportional to the increase of damage.

Thus, reliable methods to continuously estimate the effective tension force considering general boundary conditions are needed since direct measurements in existing tendons are difficult to carry out. This paper proposes a simplified methodology to estimate the effective tension force from the modal properties of the tendon, taking advantage of the relationship between the natural frequencies and the tension force [2]. Thus, from the general semirigid solutions, equivalent modal lengths for each considered mode are derived and then, the effective tension force is estimated using all the considered modes. The main objective of this paper is to numerically validate the method for estimating the tension force through a detailed FE model of a tendon where all the relevant properties are known: i) the tension force  $T$ , ii) the bending stiffness  $EI$ , iii) the mass per unit length  $\rho$ , iv) the total length  $L$ , and v) the natural frequencies  $f_i$ . Hence, assuming that only the natural frequencies are known (which are actually measured) and  $\rho$  and  $L$  are also known,  $T$  and  $EI$  are estimated.

The outline of this paper is as follows. In Section 2, the FE model of the tendon used for the validation is described, as well as the analysis followed. Section 3 presents the methodology for the estimation of tension force and compares the results obtained with those of the FE model. Section 4 addresses some conclusions.

## 2 FE MODEL

### 2.1 FE model description

The model reproduces a 31-strand grouted external tendon with a total length of 12.7 m that has been stressed with a tension force of 4500 kN. This type of tendon consists of prestressing steel strands surrounded by a HDPE duct that is filled with a grout injection, which adherently covers all the strands and provides some degree of corrosion protection. The grout has a density of 2250 kg/m<sup>3</sup> and an elastic modulus of 25 GPa.

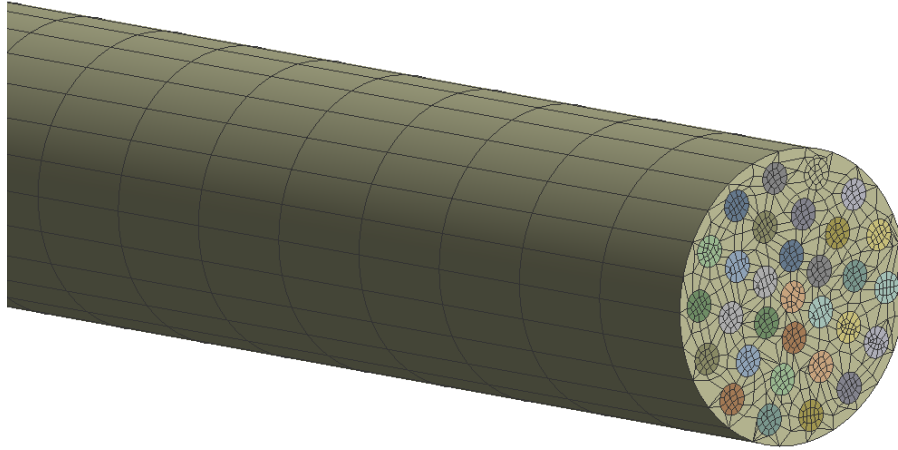


Figure 1: FE tendon used for the analysis.

The steel strands consist of six external wires that helically surround a central wire, but a circle with equivalent mechanical and material properties is assumed. Considering that the effective area of a strand  $A_{strand}$  is  $139 \text{ mm}^2$  provided by the manufacturer, the equivalent diameter,  $\phi_{eq}$ , is:

$$A_{strand} = \frac{\pi \phi_{eq}^2}{4} \rightarrow \phi_{eq} = 13.3 \text{ mm}. \quad (1)$$

The density of the steel strands is  $7850 \text{ kg/m}^3$  and the elastic modulus  $E_s$  is  $195.5 \text{ GPa}$ . The internal diameter of the duct is  $14 \text{ cm}$ , its thickness is  $6 \text{ mm}$ , and its density is  $950 \text{ kg/m}^3$ . However, the duct is not included in the model geometry for simplicity and its mechanical behaviour has been replaced by modelling a perfectly elastic grout with an equivalent density  $\rho_{g,eq}$  of  $2547.7 \text{ kg/m}^3$ , obtained as shown in equation 2:

$$\rho_{g,eq} = \frac{A_g \rho_g + A_d \rho_d}{A_g}, \quad (2)$$

where  $A_g$  is the cross-sectional area of the grout,  $\rho_g$  is the density of the grout,  $A_d$  is the cross-sectional area of the duct, and  $\rho_d$  is the density of the duct. Then, the total mass per unit length  $\rho$  can be derived.

Tendon equivalent bending stiffness  $EI$  is calculated as follows:

$$EI = E_s I_s + E_g I_g, \quad (3)$$

where  $E_s$  is the elastic modulus of the steel strands,  $I_s$  is the moment of inertia of the steel cross-section,  $E_g$  is the elastic modulus of the grout, and  $I_g$  is the moment of inertia of the grout cross-section.

Thus, the relevant parameters of the FE model needed for the tension estimation are listed in Table 1.

Table 1: Relevant parameters for the validation of the tension force estimation procedure.

$L \text{ [m]}$	$T \text{ [kN]}$	$EI \text{ [kNm}^2\text{]}$	$\rho \text{ [kg/m]}$
12.7	4500	902.422	52.848

A bilinear isotropic hardening material model has been used for steel strands, as shown in Figure 2. Mechanical properties are listed in Table 2. The von Mises plasticity criterion with associative flow rule is assumed for the plasticity of the strands.

Table 2: Mechanical properties of steel strands.

$E_s$ [GPa]	$f_{py}$ [MPa]	$\varepsilon_{py}$ [%]	$f_{pu}$ [MPa]	$\varepsilon_{pu}$ [%]	$\rho_s$ [kg/m <sup>3</sup> ]
195.5	1760	0.9	1900	6	7850

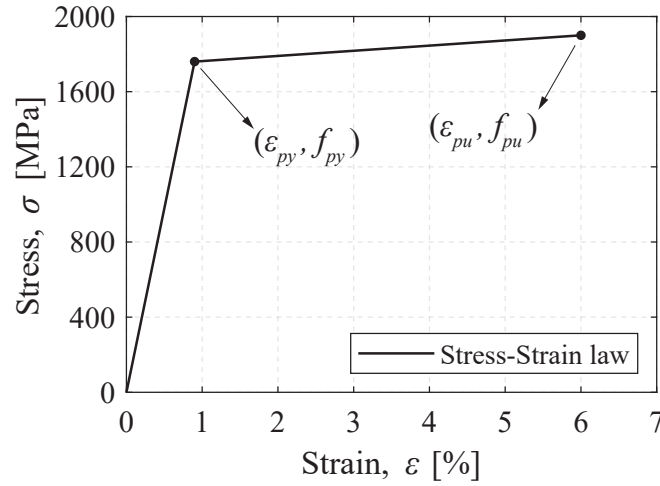


Figure 2: Steel strand stress-strain law.

The boundary conditions on the FE model are fixed supports at both ends of the strands, so displacements and rotations in all directions are constrained. The interface of steel and grout is modelled using a bonded contact, the nodes of the grout element are shared with those of the strand elements.

## 2.2 Analysis description

A non-linear static analysis divided into different load steps has been performed. During the analysis, the tensioning of the strands and the grouting of the tendon are modelled in different steps. Different factors cause the non-linearity: i) the non-linear constitutive law of steel, ii) the consideration of large deformations, and iii) the activation of grout elements to reproduce grout injection. A sparse direct solver and the Newton-Raphson algorithm with convergence in forces and displacement have been used. The steps of the analysis are the following:

1. Stressing of the strands by applying a thermal load: The stressing force of the tendon  $F_{pu}$  is 4500 kN, which corresponds to the 55% of the strands ultimate limit strength  $f_{pu}$ . This stress state has been achieved in the model by applying a thermal load to the steel strands (before the grout elements have been activated) with a temperature decrease  $\Delta T$  equal to:

$$\Delta T = \frac{F_{pu}}{E_s A_s \alpha}, \quad (4)$$

where  $A_s$  is the steel area of the tendon and  $\alpha$  is the thermal expansion coefficient, taken as  $1.2 \cdot 10^{-5} \text{ }^\circ\text{C}^{-1}$ .

## 2. Grout activation to simulate the injection.

Then a modal analysis is performed to obtain the frequencies used for the estimation procedure of the tension force assessed in Section 3.

The results obtained from the FE analysis are the first 20 natural frequencies (which are expected to be measured experimentally), which are shown in Table 3. These results are the input for the tension estimation procedure, whose methodology and results obtained are presented in Section 3.

Table 3: Frequencies obtained from the FE analysis.

Modal order	Frequency $f_i$ [Hz]	Modal order	Frequency $f_i$ [Hz]
1	12.815	11	208.25
2	26.04	12	237.84
3	40.054	13	269.43
4	55.186	14	302.97
5	71.704	15	338.45
6	89.815	16	375.83
7	109.67	17	415.06
8	131.39	18	456.11
9	155.03	19	498.92
10	180.64	20	543.45

## 3 TENSION FORCE ESTIMATION

### 3.1 Methodology

The methodology for estimating the tension force consists of calibrating the general analytical model of the tendon considering several natural frequencies. That is, assuming a tendon with rotational stiffness at both ends as shown in Figure 3. The equation that governs the transverse displacement of a taut tendon with bending stiffness is as follows:

$$EI \frac{\partial^4 v(x, t)}{\partial x^4} - T \frac{\partial^2 v(x, t)}{\partial x^2} + \rho \frac{\partial^2 v(x, t)}{\partial t^2} = 0, \quad (5)$$

with the following general boundary conditions:

$$v(0) = 0, \quad (6)$$

$$v(L) = 0, \quad (7)$$

$$EI v''(0) = k_{r1} v'(0), \quad (8)$$

$$EI v''(L) = k_{r1} v'(L), \quad (9)$$

where  $v(x, t)$  [m] is the transversal displacement. Numerical methods are required to solve this equation since it has no analytical solution. Therefore, the solution of this equation cannot

be used directly to estimate in-line and continuously (of a monitoring system) the effective tension force. An optimisation algorithm has to be executed to carry out the estimation of the effective tension force, which becomes inoperative. Thus, the proposed methodology calibrates an equivalent modal length for each mode and the analytical solution for the simply supported taut cable applies.

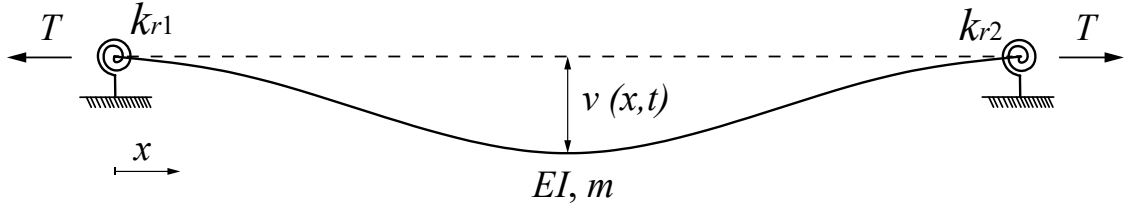


Figure 3: Tendon with bending stiffness and rotational springs at both ends.

The proposed tension estimation procedure is as follows:

1. The frequencies obtained from the FE analysis  $f_i$ , and shown in Table 3, are used as an input to the estimation procedure based on the calibration of the continuous model (Equations 5-9). The results obtained from this calibration are: i) the tension force  $T_c$ , ii) the bending stiffness  $EI_c$ , iii) the stiffness of the one-end rotational spring  $k_{r1,c}$ , and iv) the stiffness of the rotational spring at the other end  $k_{r2,c}$ . A genetic algorithm programmed in Matlab is used to carry out the calibration, where the objective function is the difference between the frequencies obtained from the estimated tension and the frequencies obtained from the FE model (Table 3). The calibration is performed a certain number of times, in this case, 8 times, to obtain weighted averages of these values as a function of the inverse of the minimised objective function, so that more importance is given to the result that leads to a lower value of the objective function.
2. Taking into account that the tension force can be written as [3]:

$$T = 4\rho L_i^2 \left( \frac{f_i}{i} \right)^2 - \frac{EI}{L_i^2} i^2 \pi^2, \quad (10)$$

for each mode  $i$ . Minimizing the error between  $T$  and  $T_c$ , obtained from calibrating the general tendon (equation 10),  $L_i$  for each considered mode is extracted. Thus, in what follows to the stimated tension force  $\hat{T}$  will be derived from equation 10.

3. Applying equation 10, 20 values of  $T$  will be derived so that the estimated value will be the mean value.
4. Applying equation 10, to two frequencies, an estimated value of  $\hat{EI}$  can be derived [3]:

$$EI = \frac{\rho L^4}{\pi^4} \left[ \left( \frac{2\pi f_r}{r\gamma_r} \right)^2 - \left( \frac{2\pi f_s}{s\gamma_s} \right)^2 \right] \frac{1}{r^2\gamma_r^2 - s^2\gamma_s^2}, \quad (11)$$

$\widehat{EI}$  is the average value.

5. Finally, using equation 10, the first 20 natural frequencies  $\widehat{f}_i$  are estimated using  $\widehat{T}$  and  $\widehat{EI}$ . The root mean square error between the calculated natural frequencies and the frequencies obtained from the FE model is calculated as:

$$RME = \sqrt{\frac{1}{20} \sum \left( \frac{f_i - \widehat{f}_i}{f_i} \right)^2}. \quad (12)$$

The RME should be small enough. It does mean that  $L_i$  calculated are correct.

### 3.2 Results

The first step for the tension force estimation is the calibration of the mathematical model using a genetic algorithm. The input parameters are the frequencies  $f_i$  obtained from the FE analysis and presented in Table 3, the length of the tendon  $L$  and the mass per unit length  $\rho$ , which are listed in Table 2, are considered to be known. The results obtained are the tension force  $T_c$  calibrated, the bending stiffness  $EI_c$  calibrated, and the stiffness of the rotational springs at both ends  $k_{r1,c}$  and  $k_{r2,c}$ , and are shown in Table 4.

Table 4: Results of the mathematical model calibration.

$T_c$ [kN]	$EI_c$ [kNm <sup>2</sup> ]	$k_{r1,c}$ [N/m <sup>2</sup> /m]	$k_{r2,c}$ [N/m <sup>2</sup> /m]
4870	809	$3.5066 \cdot 10^{14}$	$5.5234 \cdot 10^{14}$

Then, the values of  $L_i$  are obtained using  $T_c$  and  $EI_c$ , so the tension force  $\widehat{T}$  and bending stiffness  $\widehat{EI}$  can be estimated using the equations 10 and 11. These results are shown in Table 5. As can be seen, the estimated results coincide with the results of the mathematical model calibration.

Table 5: Results of  $\widehat{T}$  and  $\widehat{EI}$  estimation.

$\widehat{T}$ [kN]	$\widehat{EI}$ [kNm <sup>2</sup> ]
4870	809

Then, equation 5 is solved using numerical methods (as it does not have an analytical solution) to obtain the frequencies  $f_{i,num}$  from the estimated tension force  $T$  and estimated bending stiffness  $EI$ . These results are shown in Table 6. These numerical frequencies ( $f_{i,num}$ ) are compared with those obtained from the FE analysis ( $f_i$ ) to evaluate the error and determine whether it is acceptable. Hence, the root mean square error is obtained from equation 12 is  $7.37 \cdot 10^{-5}$ , a sufficiently low value to consider that the estimation performed is correct.

Table 6: Frequencies obtained numerically from the estimated  $T$  and  $EI$ .

Modal order	Frequency $f_{i,num}$ [Hz]	Modal order	Frequency $f_{i,num}$ [Hz]
1	12.836	11	207.90
2	26.06	12	237.94
3	40.036	13	270.22
4	55.085	14	304.77
5	71.481	15	341.62
6	89.448	16	380.78
7	109.13	17	422.28
8	130.77	18	466.12
9	154.38	19	512.32
10	180.06	20	560.88

However, as mentioned before, this procedure presents an important drawback related to resolution time. In this case, the genetic algorithm has taken 1h 27min to complete the calibration of the mathematical model.

#### 4 CONCLUSIONS

A simplified procedure to estimate the effective tension force in external post-tensioning tendons has been proposed. A FE model of a tendon has been created as a specimen. Thus, the natural frequencies of this model are the inputs to the simplified procedure, which makes use of a preliminary calibration of equivalent model lengths considering general boundary conditions. The application of this method avoids to solve the general partial differential equation of the tendon with bending stiffness, which cannot be solved in line since it has not analytical solution. The next step is to validate the proposed procedure in real tendons in a bridge.

#### 5 ACKNOWLEDGEMENTS

Research project PID2021-127627OB-I00 funded by MCIN AEI/10.13039/501100011033/FEDER, EU. Belén Vecino acknowledges the Fundación Agustín de Betancourt for the financial support provided for the development of her doctoral thesis.

#### REFERENCES

- [1] Sharon L. Wood S. L., Christopher A. McKinstry, Jun Ki Lee. (2013) Residual Tensile Capacity of Grouted Post-Tensioned Tendons. *ACI Structural Journal*, **110**, 2561-2572. doi: 10.14359/51686164
- [2] Naranjo-Pérez, J., Vecino, B., Díaz, I.M., Renedo, C.M.C., García-Palacios, J.H. (2023). Tension Force Estimation of Post-tensioning External Tendons Through Vibration-Based Monitoring: Experimental Validation. *Experimental Vibration Analysis for Civil Engineering Structures. EVACES 2023*. Lecture Notes in Civil Engineering, vol 432. Springer, Cham. doi: 10.1007/978-3-031-39109-5\_10
- [3] Yong-Hui, H., Ji-Yang, F., Rong-Hui, W., Quan, G., Rui, R., Ai-Rong, L. (2014). Practical formula to calculate tension of vertical cable with hinged-fixed conditions based on vibration method. *Journal of Vibroengineering*, 16(2).



## A SIMPLE AND EFFICIENT 3D FINITE ELEMENT FOR DYNAMIC ANALYSIS OF SHELL STRUCTURES

José M. Martínez Valle<sup>1</sup>

<sup>1</sup> Department of Mechanics. Division of Continuum Mechanics and Theory of Structures. University of Córdoba (Spain). Building Leonardo Da Vinci. Campus of Rabanales. Córdoba (Spain)  
e-mail: jmvalle@uco.es

**Keywords:** Finite elements, shells, dynamic analysis, locking.

**Abstract.** *The dynamic study of shell structures remains a focus of interest for researchers and engineers. Phenomena such as wind, earthquakes, impacts etc., may induce oscillatory motions in structures, which must be calculated taking into account this aspect. In this conference, we present a simple three-dimensional finite element that allows modelling thin and moderately thick shells subjected to dynamic actions (including bending stresses-deformations) with satisfactory precision, arranging a few elements (and even a single one, for flat shells) through the thickness of the shell. Due to its simplicity, the element chosen for this purpose is a modified version of the classic trilinear hexahedron, with displacements as the only nodal degrees of freedom. As it is well known, low-order finite elements like this, suffer from shear locking for bending dominated problems. Encouraged once again by its simplicity, this defect is remedied by resorting to the technique of the mixed interpolation of the tensorial components of the strain tensor, known as MITC, originally developed for degenerated shell finite elements. As far as the author is concerned, this technique has not been proposed for 3D shell elements and in view of the results obtained for different tests, the performance of the proposed element for general shells has been outstanding.*

## DYNAMIC MODE DECOMPOSITION METHOD FOR MODEL ORDER REDUCTION OF A NON-LINEAR ELASTIC BEAM

Mikel Merino-Olagüe<sup>\*1,3</sup>, Aitor Plaza<sup>2</sup>, and Xabier Iriarte<sup>1,2</sup>

<sup>1</sup>Engineering Department. Public University of Navarre  
31006, Pamplona (Spain)

<sup>2</sup> Institute of Smart Cities (ISC). Public University of Navarre  
31006, Pamplona (Spain)

<sup>3</sup> NAIR Center  
31006, Pamplona (Spain)

e-mail: mikel.merino@unavarra.es, aitor.plaza@unavarra.es, xabier.iriarte@unavarra.es

**Keywords:** Dynamic Mode Decomposition, Model Order Reduction, Data-Driven.

**Abstract.** *In recent years, data-driven techniques have become increasingly important in the field of engineering. Among these techniques, Dynamic Mode Decomposition (DMD) algorithm has different applications in the field of mechanical engineering (i.e. fluid dynamics, robotics or temperature fields). This method uses time series data of a particular system and performs a spatio-temporal decomposition from which the so-called dynamical modes that characterise the dynamics of that system are extracted. In this particular work, this algorithm and some improved versions of it have been used to obtain different reduced order models of a non-linear elastic cantilever beam. To this end, the beam has been modelled using the Finite Element Method and dynamic simulations have been carried out under different variable loading conditions. Data on displacements, velocities and accelerations have been obtained and used for the application of the different DMD algorithms. Once this discrete linear model is obtained, it is used to repeat the same dynamic simulations previously carried out using FEM. It has been verified that the model obtained using the DMD algorithm obtains results comparable to those of the FEM model with a considerable saving in terms of computational cost. Finally, simulations have been carried out for load cases other than the original ones and the results have been compared again with FEM models, again obtaining very similar results with a computational cost several orders of magnitude lower.*

## 1 INTRODUCTION

In recent years, data-driven techniques have become increasingly important in the field of mechanical engineering. These techniques have a multitude of applications, including modelling and control of mechanical systems, system identification, and predictive maintenance. In terms of modelling, they enable the creation of reduced-order mathematical models for complex, high-dimensional mechanical systems. These models allow for dynamic simulations to be performed at a computational cost significantly lower than that of the original systems, and they can even facilitate simulations of systems whose dynamic equations are unknown.

The Dynamic Mode Decomposition (DMD) algorithm is a data-driven technique that utilizes time series data from a given system to perform spatio-temporal decomposition[1]. Through this decomposition, the dynamic modes that characterize the system's behaviour are extracted, allowing for the creation of a reduced model of the system.

This algorithm has been widely used in Computational Fluid Dynamics (CFD), where the high dimensionality of the data obtained makes its interpretation challenging. The DMD algorithm enables the creation of reduced-order linear models characterized by their modes, facilitating control and simulation. Using DMD modes, Schmid et al. [2] analysed the vortices generated in the expansion of a helium jet, while [3] applied the same approach to a laminar water jet. Bagheri [4] employed the DMD algorithm to analyse the wake generated by fluid flow around a cylindrical solid. Additional applications in fluid mechanics can be found in references [5, 6, 7].

Applications of DMD in other fields can be also found in the literature. For example, Grosek and Kutz [8] used the algorithm for video processing to separate the background from the foreground, successfully identifying cars on a highway and people in a train station. Proctor and Eckhoff [9] used DMD modes to identify patterns in the spread of different infectious diseases, such as influenza, measles, and poliovirus type 1. Brunton et al. [10] applied the DMD algorithm in neuroscience, analysing high-dimensional data sets to identify patterns of brain activity during different motor tasks and sleep. An alternative version of the DMD algorithm, known as Higher Order Dynamic Mode Decomposition (HODMD), is discussed in reference [11] and was used to analyse wind flows in wind turbine blades. For further information and additional applications, readers are referred to the following sources: [12, 13].

Its use in solid mechanics has been quite limited to date. Saito and Kuno [14] used the DMD algorithm for experimental modal analysis. They simulated a discrete 6-degree-of-freedom mass-spring-damper system and obtained its time series data. From the eigenvalues and DMD modes, they extracted the modal parameters of the original system, finding satisfactory results in cases where the noise in the data had a low standard deviation. Additionally, they applied the DMD algorithm to real data from the motion of a cantilever beam. While they successfully obtained the frequencies and modes, the damping parameters were not as accurately determined. On the other hand, Das et al. [15] used the DMD algorithm to derive the dynamic model of a highly non-linear robotic actuator. They obtained position and velocity data from a dynamic simulation of the robotic arm, which was modelled using the Finite Element Method (FEM). From this data, they developed a reduced-order linear dynamic model. This reduced model was able to reproduce the behaviour of the large FEM model with a small relative error, thereby allowing the use of highly extended linear control techniques. Snyder and Song [16] utilized the extended version of the DMD algorithm, known as Extended Dynamic Mode Decomposition (EDMD), to develop a linear model of an inverted pendulum on a wheeled cart. By employing this extended version, they increased the size of the data vector using terms derived

from applying non-linear functions to the original data vector. This approach allowed them to obtain a more accurate reduced-order linear model, which facilitated the application of linear control techniques. Finally, Hari and Biglarbegian [17] demonstrated additional applications of the DMD algorithm in solid mechanics. One notable application involved deriving the reduced model of a non-linear elastic structure modelled using the Finite Element Method. They applied a displacement to the free end of the beam and conducted a static simulation. By analysing the position data at various time points during the simulation, they obtained reduced linear models that were three orders of magnitude smaller than the original model. This application is particularly relevant to the present paper, which focuses on developing reduced dynamic models for a non-linear beam similar to that in [17]. However, unlike Hari and Biglarbegian's work, our paper derives reduced models from dynamic simulations. It is demonstrated that linear dynamic models can be obtained from data derived from dynamic FEM simulations. These models are capable of replicating the same dynamic simulations with a significantly lower computational cost.

The remainder of this work is organized as follows. First, in Section 2, we describe the theoretical foundations of the different DMD methods. Section 3 briefly outlines the methodology used to extract the data that feeds the DMD methods. Finally, Section 4 presents some of the obtained results and compares them. In the end, Section 5 provides the conclusions of the work.

## 2 THEORETICAL FOUNDATIONS OF THE DMD METHODS

The DMD is a data-driven technique used to analyse the dynamics of complex systems. It is particularly useful for extracting spatio-temporal patterns from time series data. DMD method searches for the value of  $\mathbf{A}$  that best advances the system to the next state  $\mathbf{x}_{k+1}$  from the current state  $\mathbf{x}_k$ . This operator  $\mathbf{A}$  captures the dynamics of the system, projecting the current state to the next state. If one assumes uniform sampling in time, this becomes:

$$\mathbf{x}_{k+1} \approx \mathbf{A}\mathbf{x}_k \quad (1)$$

The DMD algorithm starts with obtaining temporal data regarding the state of a dynamic system. The data is organized into two different matrices,  $\mathbf{X}$  and  $\mathbf{X}'$ , where each column represents the system's state at different time instances. These matrices are also known as *snapshots*. The matrix  $\mathbf{X}$  contains the system states at consecutive time instances, whereas  $\mathbf{X}'$  represents the system states at the subsequent time steps, that is, it is shifted by a certain time interval relative to matrix  $\mathbf{X}$ , yielding:

$$\mathbf{X} = \begin{bmatrix} | & | & & | \\ \mathbf{x}_1 & \mathbf{x}_2 & \dots & \mathbf{x}_{m-1} \\ | & | & & | \end{bmatrix} \quad \text{and} \quad \mathbf{X}' = \begin{bmatrix} | & | & & | \\ \mathbf{x}_2 & \mathbf{x}_3 & \dots & \mathbf{x}_m \\ | & | & & | \end{bmatrix}, \quad (2)$$

where  $m$  is the number of time instances for which the system data is available, and  $n$  is the size of the system state, such that  $\mathbf{X}, \mathbf{X}' \in \mathbb{R}^{n \times m-1}$ . The DMD algorithm utilizes the matrices  $\mathbf{X}$  and  $\mathbf{X}'$  to search for the linear operator  $\mathbf{A}$  that best fits in the equation

$$\mathbf{X}' \approx \mathbf{A}\mathbf{X}. \quad (3)$$

The value of the operator is obtained by solving the equation

$$\mathbf{A} \approx \mathbf{X}'\mathbf{X}^\dagger \quad (4)$$

where  $\mathbf{X}^\dagger$  is the so-called Moore-Penrose pseudo-inverse.

## 2.1 Model reduction algorithm

It is well known that Singular Value Decomposition (SVD) is a highly efficient method for obtaining the value  $\mathbf{X}^\dagger$ . This decomposition is given by:

$$\mathbf{X} = \mathbf{U}\mathbf{\Sigma}\mathbf{V}^* = [\tilde{\mathbf{U}} \quad \tilde{\mathbf{U}}_{rem}] \begin{bmatrix} \tilde{\mathbf{\Sigma}} & 0 \\ 0 & \tilde{\mathbf{\Sigma}}_{rem} \end{bmatrix} \begin{bmatrix} \tilde{\mathbf{V}}^* \\ \tilde{\mathbf{V}}_{rem}^* \end{bmatrix} \approx \tilde{\mathbf{U}}\tilde{\mathbf{\Sigma}}\tilde{\mathbf{V}}^* \quad (5)$$

where  $\mathbf{U} \in \mathbb{R}^{n \times n}$ ,  $\mathbf{\Sigma} \in \mathbb{R}^{n \times (m-1)}$ ,  $\mathbf{V} \in \mathbb{R}^{(m-1) \times (m-1)}$ ,  $\tilde{\mathbf{U}}$  is a unitary matrix  $\in \mathbb{R}^{r \times r}$ , and  $\tilde{\mathbf{V}}$  is a unitary matrix  $\in \mathbb{R}^{r \times (m-1)}$ . Note that  $*$  denotes the complex conjugate transpose of a matrix. The subscript *rem* denotes the remaining  $m - 1 - r$  singular values that have been truncated. The truncation value  $r$  must be appropriately chosen to ensure that  $\tilde{\mathbf{\Sigma}}$  is a square matrix and that  $\mathbf{X}^\dagger$  can be obtained. Thus, an approximation of the matrix  $\mathbf{A}$  is obtained as

$$\mathbf{A} \approx \bar{\mathbf{A}} = \mathbf{X}'\tilde{\mathbf{V}}\tilde{\mathbf{\Sigma}}^{-1}\tilde{\mathbf{U}}^* \quad (6)$$

where  $\mathbf{A} \in \mathbb{R}^{n \times n}$ . By projecting the matrix  $\bar{\mathbf{A}}$  using  $\tilde{\mathbf{U}}$  yields a representation of the reduced dynamic model that is given by the equation

$$\tilde{\mathbf{x}}_{k+1} = \tilde{\mathbf{U}}^* \bar{\mathbf{A}} \tilde{\mathbf{U}} \tilde{\mathbf{x}}_k = \mathbf{X}'\tilde{\mathbf{V}}\tilde{\mathbf{\Sigma}}^{-1}\tilde{\mathbf{U}}^* \tilde{\mathbf{x}}_k = \tilde{\mathbf{A}} \tilde{\mathbf{x}}_k \quad (7)$$

where  $\tilde{\mathbf{x}} \in \mathbb{R}^r$  and  $\tilde{\mathbf{A}} \in \mathbb{R}^{r \times r}$ . Note that the first  $r$  eigenvalues of  $\mathbf{A}$  coincide with those of  $\tilde{\mathbf{A}}$ .

The eigenvalues of the reduced linear operator provide information about the system's temporal dynamics, such as growth rates and oscillatory behaviour. The eigenvectors, or DMD modes, provide the spatial structures associated with these dynamics.

## 2.2 Dynamic Mode Decomposition with control (DMDc)

Dynamic Mode Decomposition with Control (DMDc) is an extension of the standard Dynamic Mode Decomposition (DMD) proposed in [18] to utilize both measurements of the system and applied external inputs in extracting the underlying dynamics. It incorporates the effect of control inputs  $\mathbf{u}_k$  into the system's dynamics along with the state variables  $\mathbf{x}_k$ . This allows for the analysis and modelling of systems where external inputs or controls influence the state evolution.

DMDc seeks to identify a linear system that includes both the state and control dynamics:

$$\mathbf{x}_{k+1} \approx \mathbf{A}\mathbf{x}_k + \mathbf{B}\mathbf{u}_k \quad (8)$$

Here,  $\mathbf{A}$  represents the system dynamics matrix and  $\mathbf{B}$  represents the control input matrix.

Similar to DMD, DMDc uses matrices  $\mathbf{X}$  and  $\mathbf{X}'$  of state data at different time instances, but it also includes matrices of control inputs:

$$\Upsilon = \begin{bmatrix} | & | & & | \\ \mathbf{u}_1 & \mathbf{u}_2 & \dots & \mathbf{u}_{m-1} \\ | & | & & | \end{bmatrix} \quad (9)$$

Equation 3 now becomes:

$$\mathbf{X}' = \mathbf{A}\mathbf{X} + \mathbf{B}\Upsilon \quad (10)$$

and can be rearranged as:

$$\mathbf{X}' = [\mathbf{A} \quad \mathbf{B}] \begin{bmatrix} \mathbf{X} \\ \Upsilon \end{bmatrix} = \mathbf{G}\Omega \quad (11)$$

Matrix  $\mathbf{G}$  can be solved and reduced by applying the same algorithm presented in Section 2.1. The original system described in Equation 8 can be reduced, resulting in:

$$\tilde{\mathbf{x}}_{k+1} \approx \tilde{\mathbf{A}}\tilde{\mathbf{x}}_1 + \tilde{\mathbf{B}}\mathbf{u}_k \quad (12)$$

where  $\tilde{\mathbf{x}} \in \mathbb{R}^r$  and  $\mathbf{u} \in \mathbb{R}^l$ ,  $\tilde{\mathbf{A}} \in \mathbb{R}^{r \times r}$ , and  $\tilde{\mathbf{B}} \in \mathbb{R}^{r \times l}$ . Note that the first  $r$  eigenvalues of  $\mathbf{A}$  coincide with those of  $\tilde{\mathbf{A}}$ .

### 2.3 Extended Dynamic Mode Decomposition without (EDMD) and with control (EDMDc)

Extended Dynamic Mode Decomposition (EDMD) is an enhancement of the standard DMD method. It was presented in [20] as a data-driven method for approximating the leading eigenvalues, eigenfunctions, and modes of the Koopman operator. Unlike standard DMD, which operates directly on the state variables, EDMD transforms the state variables into a higher-dimensional space using a set of non-linear functions (observables) to capture more complex dynamics. This new state can be referred as *lifted state space*. This set of observable functions  $\{g_1, g_2, \dots, g_k\}$  is chosen to map the state space to a higher-dimensional feature space and they can be polynomials, trigonometric functions, or other non-linear transformations. The new state of the system  $\mathbf{y}$  is represented in this higher-dimensional space, where the dynamics may appear more linear, and it is defined as:

$$\mathbf{y} = \begin{bmatrix} g_1(\mathbf{x}) \\ g_2(\mathbf{x}) \\ \vdots \\ g_k(\mathbf{x}) \end{bmatrix}$$

where  $\mathbf{x}$  is the original state vector.

Similar to DMD, EDMD seeks a linear operator  $\mathbf{A}_Y$  such that:

$$\mathbf{y}_{k+1} \approx \mathbf{A}_Y \mathbf{y}_k \quad (13)$$

The eigenvalues and eigenvectors of the operator  $\mathbf{A}_Y$  provide insights into the dynamics in the lifted space. This operator can be easily found following the same procedure presented above. That is, creating two matrixes  $\mathbf{Y}$  and  $\mathbf{Y}'$  that contain the system states at consecutive time instances and the shifted one and solve and reduce the equation system

$$\mathbf{Y}' \approx \mathbf{A}_Y \mathbf{Y} \quad (14)$$

applying the algorithm described in Section 2.1. Once the system is reduced, Eq. 13 can be approximated as:

$$\tilde{\mathbf{y}}_{k+1} = \tilde{\mathbf{A}}_{\mathbf{Y}} \tilde{\mathbf{y}}_k. \quad (15)$$

This version of the methods presents a series of advantages. By using non-linear observables, EDMD can model more complex, non-linear behaviours that standard DMD cannot. It is more flexible, as EDMD can be tailored to different systems by choosing appropriate sets of observables. Finally it generalizes the DMD framework to a broader class of dynamical systems, providing a more powerful tool for data-driven modelling. Finally, it should be noted that this method can be extended to include the control input, in the same way as the DMDc algorithm.

## 2.4 Higher Order Dynamic Mode Decomposition without (HODMD) and with control (HODMDc)

Higher Order Dynamic Mode Decomposition (HODMD) was proposed in [19] and it is an extension of the standard DMD that aims to improve the accuracy and robustness of the decomposition, especially in the presence of noise and complex dynamics. HODMD achieves this by incorporating higher-order information into the analysis, which helps in capturing more detailed temporal structures and dynamics of the system. Instead of using single snapshots of the system state, HODMD uses higher-order snapshots, which are vectors composed of multiple consecutive states. This creates a more detailed representation of the system's dynamics over time.

In this case, the algorithm DMD is modified so that the next instant is predicted from  $d$  previous states, so that equation 3 becomes

$$\mathbf{x}_{k+d} \simeq \mathbf{A}_1 \mathbf{x}_k + \mathbf{A}_2 \mathbf{x}_{k+1} + \dots + \mathbf{A}_d \mathbf{x}_{k+d-1} \quad (16)$$

which can be written in matrix form as

$$\mathbf{v}_{k+1} \simeq \mathbf{T} \mathbf{v}_k \quad (17)$$

where

$$\mathbf{v}_k = \begin{bmatrix} \mathbf{x}_k \\ \mathbf{x}_{k+1} \\ \dots \\ \mathbf{x}_{k+d-2} \\ \mathbf{x}_{k+d-1} \end{bmatrix} \quad \text{and} \quad \mathbf{T} \equiv \begin{bmatrix} 0 & 1 & 0 & \dots & 0 & 0 \\ 0 & 0 & 1 & \dots & 0 & 0 \\ \dots & \dots & \dots & \dots & \dots & \dots \\ 0 & 0 & 0 & \dots & 1 & 0 \\ \mathbf{A}_1 & \mathbf{A}_2 & \mathbf{A}_3 & \dots & \mathbf{A}_{d-1} & \mathbf{A}_d \end{bmatrix} \quad (18)$$

As in the previous cases, the data is organized in matrix form in the following two shifted snapshot matrices  $\mathbf{V}$  and  $\mathbf{V}'$ . The reduced operator  $\mathbf{T}$  can be obtained applying the aforementioned SVD based algorithm to the following system:

$$\mathbf{V}' \approx \mathbf{T} \mathbf{V} \quad (19)$$

yielding the following system:

$$\tilde{\mathbf{v}}_{k+1} = \tilde{\mathbf{T}} \tilde{\mathbf{v}}_k. \quad (20)$$

HODMD enhances accuracy and robustness by incorporating higher-order information, which allows it to capture more complex dynamics and filter out noise effectively. This results in more reliable models and detailed representations of temporal evolution, making HODMD ideal for analysing complex, high-dimensional data. Finally, it should be noted that this method can be extended to incorporate control inputs, similar to the DMDc algorithm.

### 3 METHODOLOGY

This section explains the methodology used to obtain different reduced models by means of the algorithms presented. For this purpose, three steps have to be carried out.

Firstly, a cantilever beam was modelled using the FEM software Ansys Mechanical APDL 2020 R2. The beam has a length of 1000 mm and a square cross-section of  $30 \times 30 \text{ mm}^2$ . A material with an elastic modulus of 500 MPa was used to achieve large deformations with small loads, along with a Poisson's ratio of 0.33, a density of  $2700 \text{ kg/m}^3$ , and damping proportional to the mass matrix of 0.3. The FEM model consists of 1000 beam elements, each with 2 nodes and 6 degrees of freedom. To represent the clamping, all degrees of freedom of one of the end nodes were restricted. This node is located at the origin of the reference system, as shown in Figure 1a.

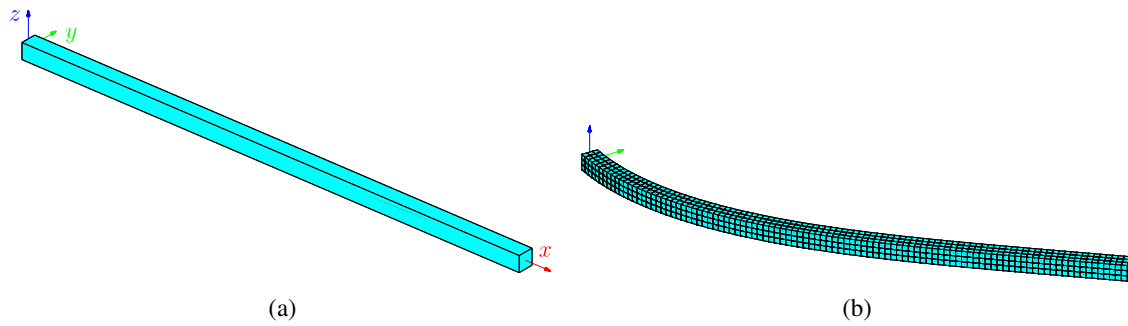


Figure 1: (a) Original undeformed beam and used reference system. (b) FEM results of the deformed beam showing the large deformations.

Next, various dynamic simulations (with and without control) were carried out using the FEM software. In all cases, the default implicit integrator was used with a time step of 0.01 seconds, and the simulation was run for 5 seconds. Figure 1b shows the final result of one of these simulations, illustrating the non-linear deformation of the element under study. The FEM software provides all the time series of displacements, velocities, accelerations, and applied forces for each of the nodes.

Third and finally, with the displacement and velocity data obtained from the FEM simulations, the snapshot matrices  $\mathbf{X}$  and  $\mathbf{X}'$  were constructed. Additionally, for the cases with control, the external forces applied to the nodes were used to construct  $\mathbf{Y}$ . These matrices were utilized to apply the proposed algorithms in this work.

Depending on the method employed, the obtained different reduced systems were used to simulate the dynamic models again. As in the FEM simulations, a time step of 0.01 seconds was used, and the total simulation time was 5 seconds. Finally, the matrix  $\mathbf{U}$  was used to project the results obtained in the reduced basis back to the original basis. This allowed for the comparison of the results obtained from FEM simulations and the DMD methods.

### 4 RESULTS

The results obtained will be divided into two sections, which refer to the two load cases applied to the beam.



#### 4.1 Non-external load case

The first simulations have been carried out without the application of external loads and with arbitrary initial conditions across the whole beam. In this case, using the  $x$  and  $y$  displacement and velocity data from the non-linear simulation, different models have been generated and simulated using DMD. The relative errors for  $r = 6, 10, 16$  are 0.1208, 0.1201 and 0.0276. Figure 2a shows the comparison of displacements of the free-end node of the beam for the different DMD models w.r.t. the FEM model. It is clear that a linear model obtained by DMD with  $r = 16$  is able to reproduce the displacements almost perfectly. As it can be seen, the models with  $r = 6$  and  $r = 10$  are still somewhat distant from the FEM simulation. On the other hand, it has been seen that from  $r = 16$  onwards the results do not improve and unstable eigenvalues appear in the DMD models. Obviously, this type of models are not valid for simulation since their displacements tend to infinity diverging from the real displacements.

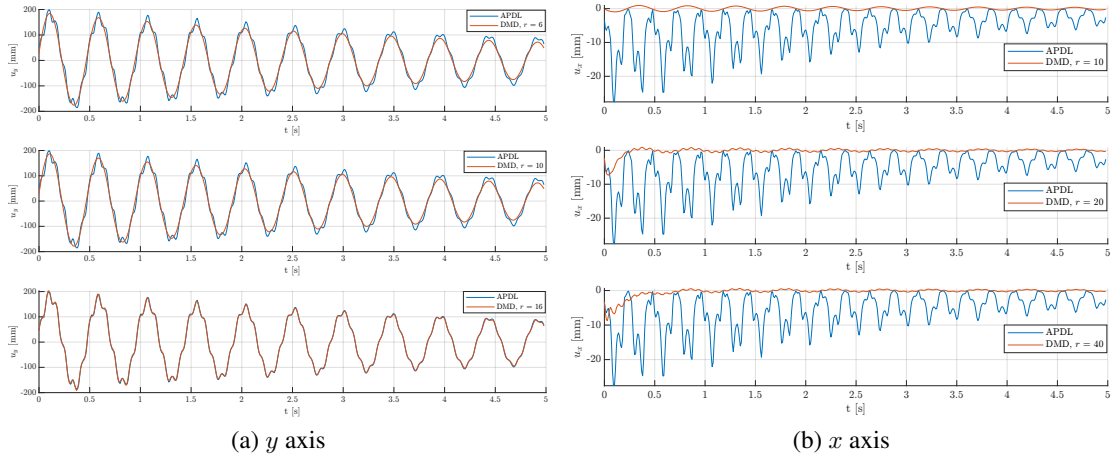


Figure 2: Free-end node displacement time series comparison for different model reductions.

Regarding the computational cost, the simulations carried out in Ansys Mechanical APDL has taken a total of 48.11 seconds on a computer with a 3.00 GHz Intel Core i5-9500 CPU, 32 GB RAM and an Intel UHD Graphics 630 (CFL GT2). The simulations of the reduced linear models carried out using MatLab took 0.08 seconds. Within this time, the obtention of the model from the SVD and its subsequent simulation are included. Therefore, the simulation time of the reduced models is practically 3 orders of magnitude less despite being carried out using interpreted code as opposed to the compiled and more efficient code of the FEM program.

If the displacement of the beam along the  $x$  axis is analysed the results are less promising. Figure 2b shows that despite increasing  $r$ , the reduced model is not able to reproduce the displacements of the free-end node. One possible reason may be the more accentuated non-linearity along  $x$ . Applying the HODMD algorithm can be a potential solution to the problem as it can be seen in Figure 3. With a reasonable value of  $d = 8$  the FEM simulation is correctly reproduced.

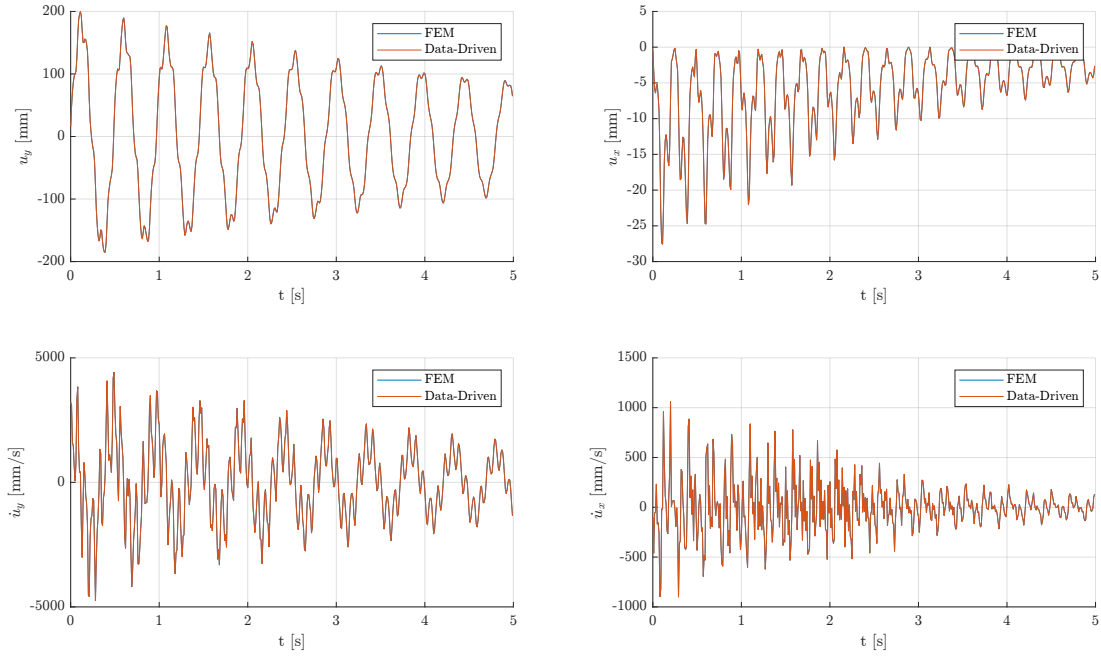


Figure 3:  $x$  axis free-end node displacement comparison for different HODMD models.

## 4.2 Variable external load case

In the previous section, it has been shown that the DMD algorithm is able to partially model the non-linear behaviour of a beam under arbitrary initial conditions by means of a small order linear model. In this section, it will be tested whether the DMD algorithm and its variants are able to model the non-linear beam under time-varying loads. For this purpose, the non-linear FEM beam model has been simulated under a sinusoidal load in the  $y$  direction applied to all nodes with amplitude 0.1 N and frequency 0.5 Hz. As in the previous section, the displacements and velocities of the nodes in the  $x$  and  $y$  directions have been used as input data to the data-driven algorithms. Figure 4a shows that higher values of  $r$  are required in order to achieve a good performance of the ROM. The model with  $r = 8$  is completely invalid, with  $r = 50$  and  $r = 200$ , there is a slight improvement in the first instants of time, but after about 0.25 seconds, the results differ completely. Finally, if all the singular values of the SVD of the matrix  $\mathbf{X}$  are taken, i.e.  $r = 499$  is used, the DMD model manages to capture the non-linearities of the beam and results are almost the same as those of the FEM model.

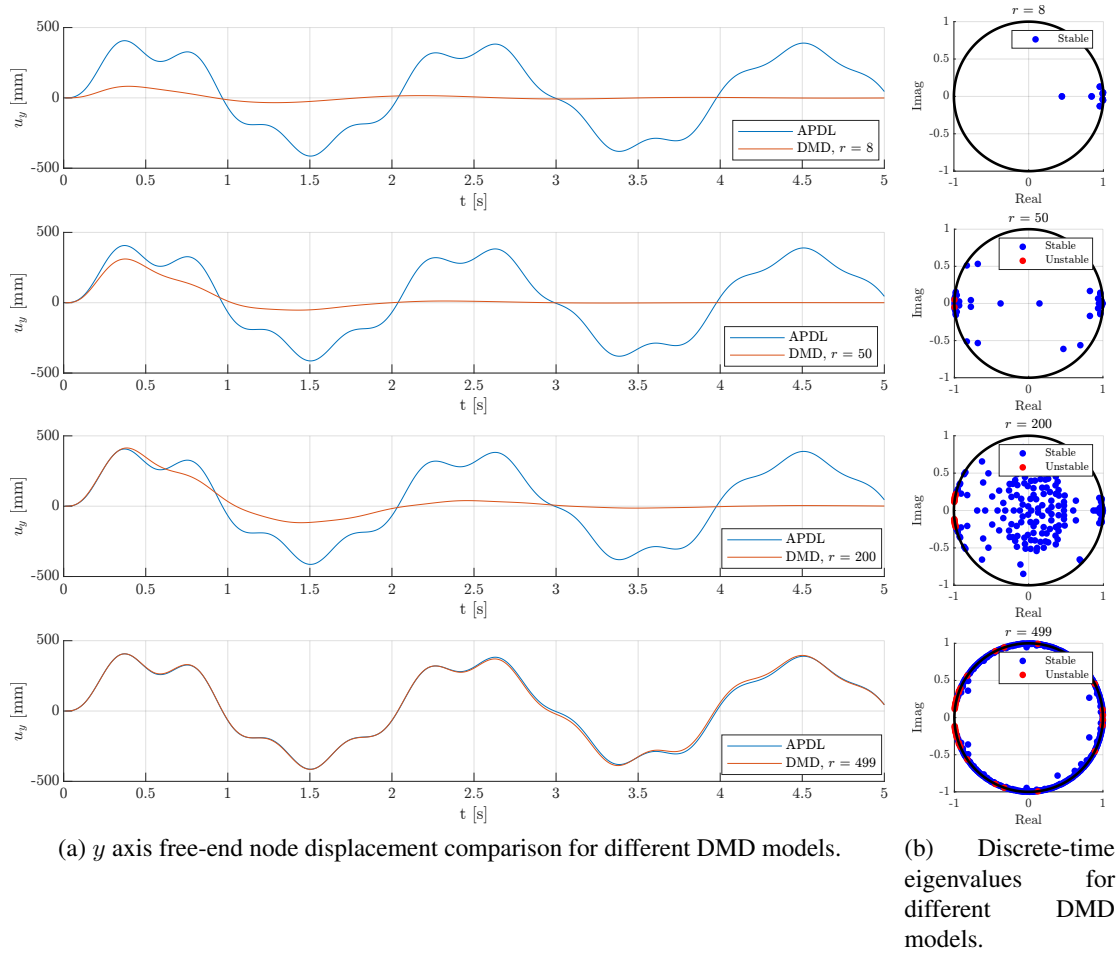


Figure 4: Free-end node displacement time series comparison for different model reductions.

Figure 4b shows the eigenvalues of  $\tilde{\mathbf{A}}$  for different ROMs. As it can be seen some of them appear outside the unit circle (marked in red), i.e. they are unstable. Therefore, if a simulation is carried out with these models, the results will tend to infinity, moving away from the original data. Not only do unstable eigenvalues appear in the model with  $r = 499$ , but also in models with  $r = 50$  and  $r = 200$ . In fact, from  $r = 10$  onwards all the models have one or more unstable eigenvalues. It is clear that it is necessary to use different data-driven methods to obtain accurate and stable models. As in section 4.2, the HODMD method has been applied first. Different values of the parameter  $d$  have been tested and 12 has been found as the optimal value with relative errors of less than  $10^{-2}$ . Figure 5 shows the comparison between the APDL and the HODMD model results. It can be clearly seen that the ROM is highly accurate, but it can not be used for different load cases as the external load is not an input of the model.

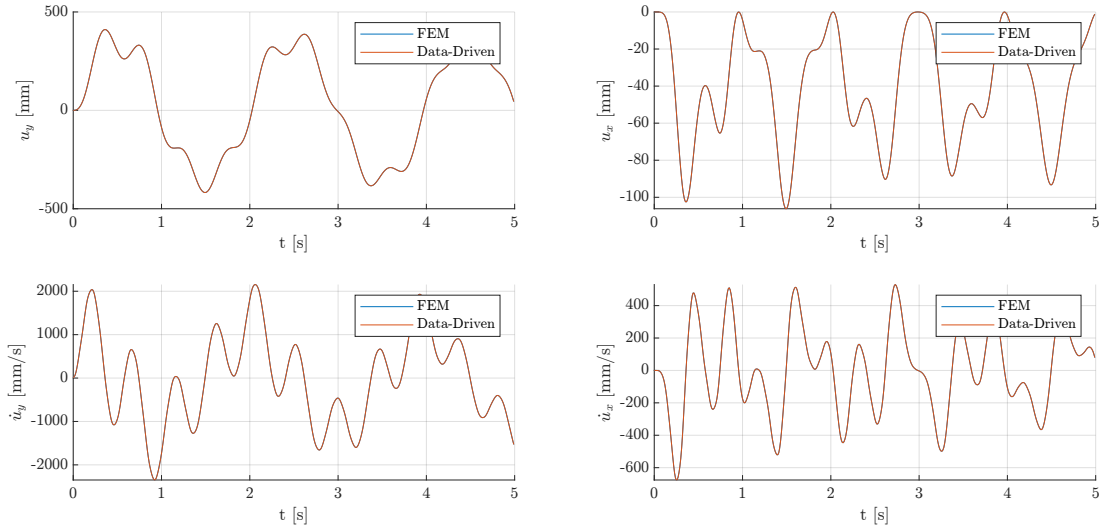


Figure 5: Free-end node displacement time series comparison between HODMD model simulation and FEM simulation.

It is desired to have a ROM with the external load as an input, in order to simulate the beam under different external loads. The DMDC algorithm is the obvious decision to achieve this purpose. Figure 6 shows the results obtained for a DMDC model. The model has great accuracy predicting the  $y$  displacements of the free-end node as shown in Figure 6a, but fails at  $x$  displacements as it can be seen in Figure 6b. The more accentuated non-linearities in this direction could be the main reason for this behaviour as stated in section 4.1.

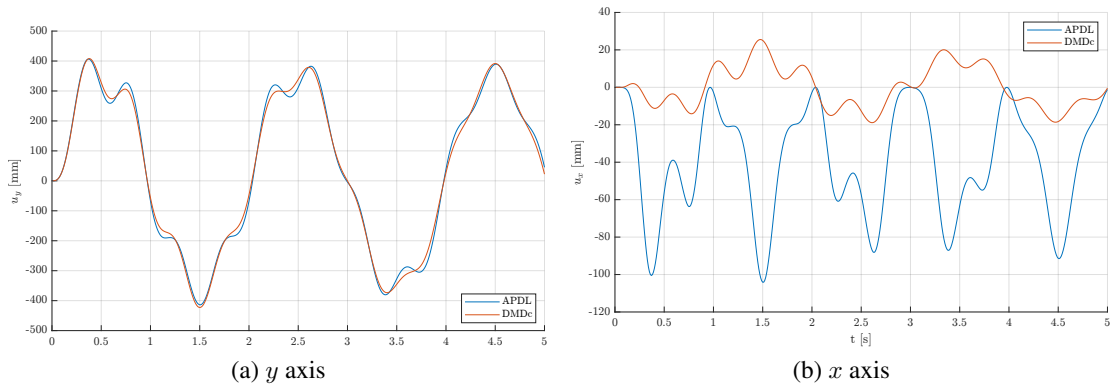


Figure 6: Free-end node displacement time series comparison between DMDC model simulation and FEM simulation.

Extending the dictionary of observables with non-linear functions i.e. applying the EDMDC method does not provide better results as shown in Figure 7. Different functions have been applied to form the data matrices but non of them has been succesfull. Figure 7a shows the  $y$  displacement comparison and 7b shows the  $x$  displacement comparison for a set of observables created by adding the  $\dot{x}^2$  term to the state of the system.

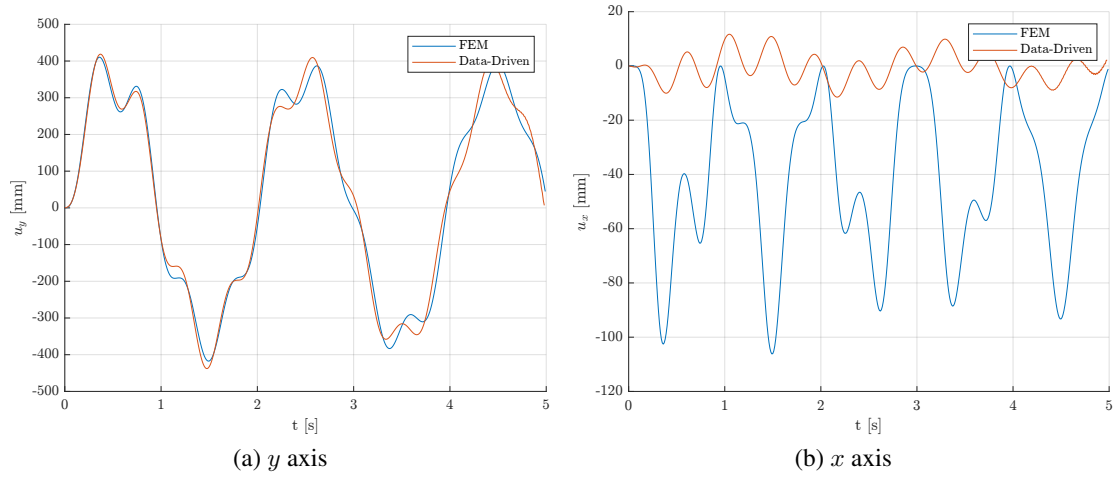
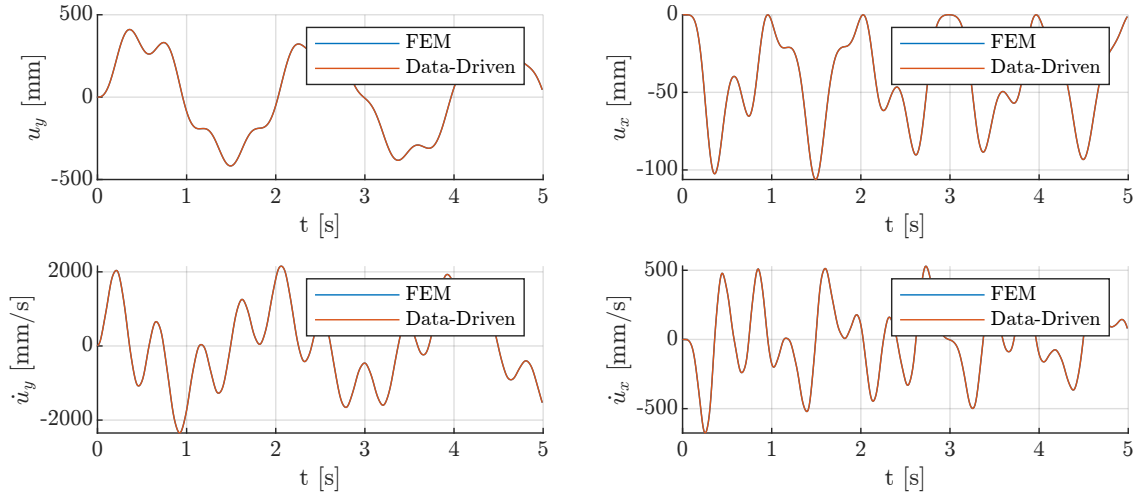
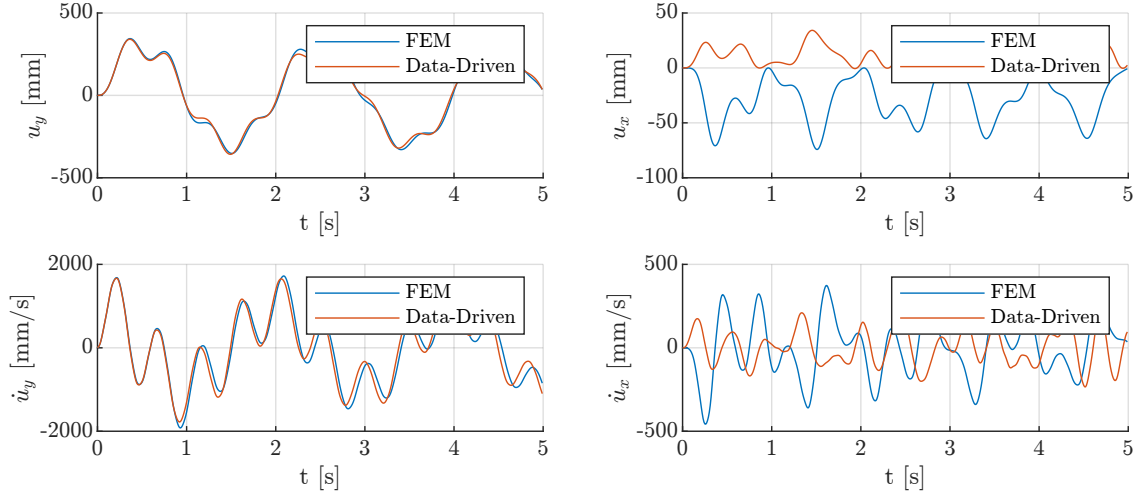


Figure 7: Free-end node displacement time series comparison between EDMDc model simulation and FEM simulation.

In section 4.1 the HODMD model has been successful at characterizing the  $x$  axis nonlinearities. Applying the HODMDc method is the logical step in order to get an accurate model with the possibility to run under different external loads. Figure 8 shows the training and validation results regarding the HODMDc method. The ROM performs really well with the training data, reproducing perfectly the FEM simulation as shown in Figure 8a. The validation data has been obtained from a FEM simulation with the same type of load as the training data but with a different amplitude. When applying this load to the reduced model, the results differ significantly from those of the FEM model, especially on the  $x$ -axis, as shown in figure 8b. It is evident that the reduced model is not able to generalise and therefore does not allow the beam to be simulated under other loads.



(a) Comparison of ROM w.r.t. training data



(b) Comparison of ROM w.r.t. validation data

Figure 8: Free-end node displacement time series comparison between HODMDc model simulation and FEM simulation.

The lack of generalisation is a great drawback of the different data-driven models, but their computational efficiency (3 orders of magnitude in average w.r.t FEM models) might be used to accelerate simulations. In the example shown in figure 9 a DMDc model is fitted using 5 seconds of the FEM model simulation and is used to simulate the remaining 15 seconds. When compared with a full 20 second FEM simulation, it shows similar results with a significantly faster computation time.

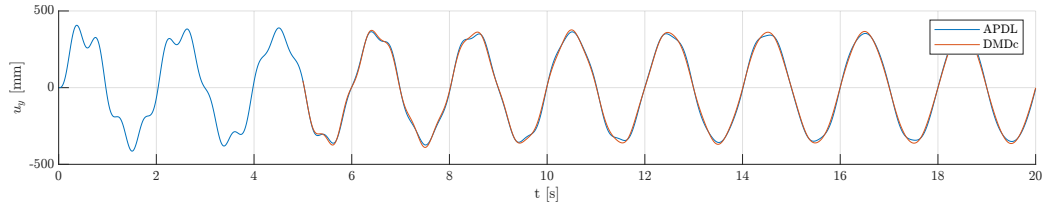


Figure 9: Free-end node displacement time series comparison between combined simulation and FEM simulation.

## 5 CONCLUSIONS

This work presents the data-driven DMD technique and its improved versions, which allow the derivation of reduced linear models capable of partially representing the dynamic richness of a non-linear beam. Using data obtained from the FEM software Ansys Mechanical APDL 2020 R2, various models were fitted and the same simulations were reproduced with varying degrees of satisfaction, achieving a computational cost several orders of magnitude lower.

In the case of a beam oscillating freely (without load), the DMD method fails when the initial conditions are random. It is unable to reproduce the longitudinal displacement, but it does so for the vertical displacement, which exhibits more linear behaviour. Conversely, the HODMD method is capable of reproducing both displacements and also their velocities.

When an external harmonic load is added, the DMDc method partially reproduces (only in the vertical axis) the behaviour of the beam but fails to generalize to other loads. Additionally, it exhibits unstable poles, leading to eventual divergence of the solution if one wants to use it for time simulation. The same behaviour is observed with the EDMDC method. In contrast, the HODMDc method is capable of predicting the system's behaviour, but it cannot generalize the reduced model to other external loads.

One potential application of the obtained models is to accelerate simulations. This application is particularly valuable in long-duration simulations that require extensive computational time.

In conclusion, some of the data-driven techniques introduced in this article enable the derivation of reduced linear models for highly non-linear dynamic systems, facilitating their subsequent analysis, simulation, and control.

## REFERENCES

- [1] Kutz, J. Nathan, et al. Dynamic mode decomposition: data-driven modeling of complex systems. Society for Industrial and Applied Mathematics, 2016.
- [2] Schmid, Peter J., et al. Applications of the dynamic mode decomposition. Theoretical and computational fluid dynamics 25 (2011): 249-259.
- [3] Schmid, Peter J. Application of the dynamic mode decomposition to experimental data. Experiments in fluids 50 (2011): 1123-1130.
- [4] Bagheri, Shervin. Koopman-mode decomposition of the cylinder wake. Journal of Fluid Mechanics 726 (2013): 596-623.
- [5] Holmes, Philip. Turbulence, coherent structures, dynamical systems and symmetry. Cambridge university press, 2012.

- [6] Ilak, Miloš, and Clarence W. Rowley. Modeling of transitional channel flow using balanced proper orthogonal decomposition. *Physics of Fluids* 20.3 (2008).
- [7] Rowley, Clarence W., et al. Spectral analysis of nonlinear flows. *Journal of fluid mechanics* 641 (2009): 115-127.
- [8] Grosek, Jacob, and J. Nathan Kutz. Dynamic mode decomposition for real-time background/foreground separation in video. *arXiv preprint arXiv:1404.7592* (2014).
- [9] Proctor, Joshua L., and Philip A. Eckhoff. "Discovering dynamic patterns from infectious disease data using dynamic mode decomposition." *International health* 7.2 (2015): 139-145.
- [10] Brunton, Bingni W., et al. "Extracting spatial-temporal coherent patterns in large-scale neural recordings using dynamic mode decomposition." *Journal of neuroscience methods* 258 (2016): 1-15.
- [11] Vega, Jose Manuel, and Soledad Le Clainche. Higher order dynamic mode decomposition and its applications. Academic Press, 2020.
- [12] Tu, Jonathan H. Dynamic mode decomposition: Theory and applications. Diss. Princeton University, 2013.
- [13] Brunton, Steven L., and J. Nathan Kutz. Data-driven science and engineering: Machine learning, dynamical systems, and control. Cambridge University Press, 2022.
- [14] Saito, Akira, and Tomohiro Kuno. Data-driven experimental modal analysis by dynamic mode decomposition. *Journal of Sound and Vibration* 481 (2020): 115434.
- [15] Das, Apurba, M. Nabi, and Francisco Chinesta. Modeling soft robotic actuators using data-driven model reduction. 2020 28th Mediterranean Conference on Control and Automation (MED). IEEE, 2020.
- [16] Snyder, Gregory, and Zhuoyuan Song. Koopman operator theory for nonlinear dynamic modeling using dynamic mode decomposition. *arXiv preprint arXiv:2110.08442* (2021).
- [17] Simha, C. Hari Manoj, and Mohammad Biglarbegian. A note on the use of Dynamic Mode Decomposition in mechanics. *Mechanics Research Communications* 120 (2022): 103848.
- [18] Proctor, Joshua L., Steven L. Brunton, and J. Nathan Kutz. "Dynamic mode decomposition with control." *SIAM Journal on Applied Dynamical Systems* 15.1 (2016): 142-161.
- [19] Le Clainche, Soledad, and José M. Vega. "Higher order dynamic mode decomposition." *SIAM Journal on Applied Dynamical Systems* 16.2 (2017): 882-925.
- [20] Williams, Matthew O., Ioannis G. Kevrekidis, and Clarence W. Rowley. "A data-driven approximation of the koopman operator: Extending dynamic mode decomposition." *Journal of Nonlinear Science* 25 (2015): 1307-1346.



## ANALYTICAL AND NUMERICAL MODELLING OF NON-LINEAR DYNAMIC BEHAVIOUR OF A FLEXIBLE CABLE SUBJECT TO MOTION

S. S. Gomez\*, Shagun Agarwal, O. Colomés

Faculty of Civil Engineering and Geosciences, Delft University of Technology, The Netherlands  
email: s.sanchezgomez-1@tudelft.nl

**Keywords:** Mooring model, finite-strain theory, Galerkin decomposition, PDEs on manifolds.

### Abstract.

*In view of the European Green Deal, offshore renewable energies are crucial and, particularly, floating technologies are a must, including: Floating Offshore Wind Turbines (FOWT) and Offshore Floating Photovoltaics (OFPV). In this work we will present semi-analytical and numerical models that characterize the dynamic and nonlinear behaviour of flexible mooring lines subject to large motions for OFPV. This work is part of The Merganser project, an academia-industry partnership led by SolarDuck, which aims at building a pilot 500kWp platform in the North Sea. Our specific goal is to assess the feasibility of highly flexible synthetic polyester cables to moor floating platforms in the challenging shallow water conditions of the North Sea.*

*Within the framework of this project, the authors of this paper are working in the design and execution of an experimental testing to define material properties and dynamic behaviour of polyester ropes, together with the development of a numerical model. The behaviour of flexible ropes is an important subject of study due to its wide range of applications: cable-supported bridges, guyed towers, mooring of offshore structures, etc. For this reason, different models tailored to the specific application have been developed. Even though, most models assume only tensile forces, its behaviour in reality is rather complex and may require experimental investigation for completeness in the engineering practice.*

*Given this complexity, it seems reasonable, that most models found literature are developed by means of numerical tools. This, however, entails certain drawbacks: the lack of flexibility to implement material models, the interpretation of results, and expensive computational efforts and time. To overcome these issues, these authors are developing a semi-analytical fast computing model.*

*In this paper, we present the recent developments and initial results of a semi-analytical model that includes geometrical non-linearities due to the large displacements taking into account the static gravitational weight. These results are compared to a novel numerical finite element model that includes the geometrical non-linearity and non-linear elasticity of the material. A clear approximation of the results to the experimental values will make the semi-analytical model a complementation of the numerical tool for initial design and optimization.*

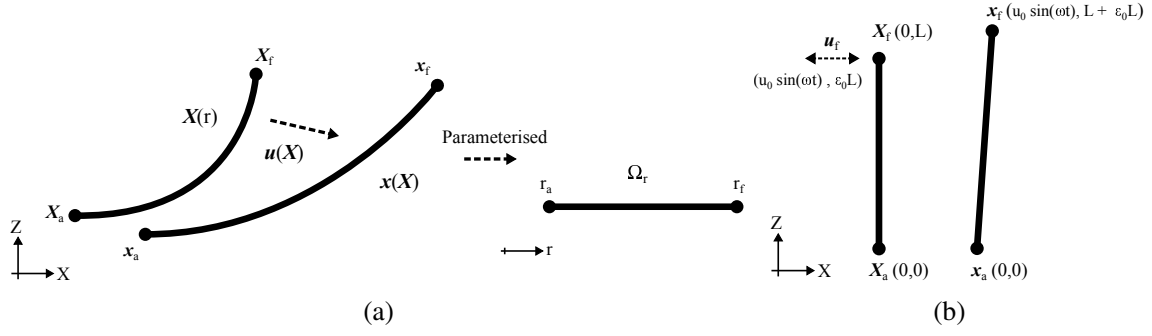


Figure 1: (a) Schematic of numerical formulation, highlighting the un-deformed  $\Gamma_X$  and deformed  $\Gamma_x$  configurations, the displacement field  $u(X)$  and the reference domain  $\Omega_r$ . (b) Schematic of the specific problem studied using the analytical and numerical approach.

## 1 Problem setting

In this manuscript, we limit our analysis to a two-dimensional problem within the vertical XZ plane. The problem is characterized by a mooring line positioned between an anchor point, denoted as  $x_a$ , and a fairlead, denoted as  $x_f$ , as shown in Fig. 1a. We examine the dynamic response of the line to periodic excitation through both numerical and analytical approaches. For this study, we exclude the effects of the surrounding fluid on the mooring. Additionally, the line is assumed to have a constant Young's modulus  $E$ , cross-sectional area  $A$ , and density  $\rho_s$ . The analysis concentrates on the geometric nonlinearity of the problem and its impact on the dynamic response of the line.

## 2 Formulation: Analytical

Let us consider the problem at hand, a mooring line with length  $L$ , where the displacement field  $\mathbf{u}(\mathbf{X}, t) = [u_x(\mathbf{X}, t), u_z(\mathbf{X}, t)]$  in the reference coordinate system  $\mathbf{X} = [X, Z]$  is described as follows:

$$u_X(\mathbf{X}, t) = u(X, t) + u_0(X); \quad u_Z(\mathbf{X}, t) = v(X, t) + v_0(X) \quad (1)$$

where  $u(X, t)$  is the displacement in the midplane in the X-direction and  $v(X, t)$  in the Z-direction. Likewise,  $u_0(X)$  and  $v_0(X)$  are the initial displacement in the X- and Z-direction, respectively. Using the defined displacement field and assuming that the cable deforms along the X-coordinate, the strain field can be defined solely by the diagonal component of the Green's strain tensor as follows:

$$\epsilon_{XX}(\mathbf{X}, t) = \frac{\partial}{\partial X} u_X(\mathbf{X}, t) + \frac{1}{2} \left[ \left( \frac{\partial}{\partial X} u_X(\mathbf{X}, t) \right)^2 + \left( \frac{\partial}{\partial X} u_Z(\mathbf{X}, t) \right)^2 \right] \quad (2)$$

The stress is computed by the diagonal component of the Kirchhoff stress tensor, ignoring the Poisson effects as  $\sigma_{XX} = E\epsilon_{XX}$ , where  $E$  is the Elasticity Modulus. By using the Lagrangian formalism ( $\lambda = \int_A (k_{\text{kinetic}} - u_{\text{strain}}) dA$ ) for 1-dimensional continuous systems described by Eq. 3,

$$\frac{\partial}{\partial t} \frac{\partial \lambda}{\partial \dot{u}_i} + \frac{\partial}{\partial x_j} \frac{\partial \lambda}{\partial u_{i,j}} = q_i \quad (3)$$

where where  $u_i$  are the components of the displacement field  $\mathbf{u}(\mathbf{X}, t)$ , the following equations of motion for the displacements in the longitudinal  $u(X, t)$  and transverse  $v(X, t)$  directions are formulated with the following boundary conditions:

$$u(0, t) = v(0, t) = 0 \quad u(L, t) = U_0 \sin(\omega t) \quad v(L, 0) = 0 \quad (4)$$

Eq. 3 is solved by means of the Galerkin decomposition. The solution of is assumed in the following form:

$$u(X, t) = \sum_{n=1}^N U_n(X) \psi_n(t) + \frac{X}{L} U_0 \sin(\omega t) + u_0(X) \quad (5)$$

$$v(X, t) = \sum_{m=1}^M V_m(X) \phi_m(t) + v_0(X) \quad (6)$$

where  $U_n(X)$  and  $V_m(X)$  are admissible functions that satisfy the boundary conditions (Eq. 4) and  $\psi_n(t)$  and  $\phi_m$  are time-dependent generalised coordinates.

### 3 Formulation: Numerical

The numerical formulation is developed for a flexible rope with large displacements. For these structures, it is essential to distinguish between the un-deformed and deformed configurations. In such cases, physical equilibrium is satisfied in the deformed configuration. Such analysis is often referred to as geometrically nonlinear analysis, or finite-strain analysis.

We denote the un-deformed and deformed configurations as  $\Gamma_{\mathbf{X}}$  and  $\Gamma_{\mathbf{x}}$ , respectively. These are 1-dimensional manifolds, immersed in 2-dimensional space,  $\mathbb{R}^2$ . The difference between the two configurations is the displacement field  $\mathbf{u}(\mathbf{X})$ , i.e

$$\mathbf{x} = \mathbf{X} + \mathbf{u}(\mathbf{X}) \quad \text{where } \mathbf{X} \in \Gamma_{\mathbf{X}} \subset \mathbb{R}^2 \text{ and } \mathbf{x} \in \Gamma_{\mathbf{x}} \subset \mathbb{R}^2 \quad (7)$$

For cables and ropes, the  $\Gamma_{\mathbf{X}}$  and  $\Gamma_{\mathbf{x}}$  manifolds can be parameterised using a 1-dimensional reference domain,  $\Omega_r \subset \mathbb{R}$ . Hence, there exists a map  $\mathbf{X}(r) : \mathbb{R}^1 \rightarrow \mathbb{R}^2$  from 1-dimensional reference domain to 2 dimensional space, as indicated in Fig. 1b.

The physical equilibrium satisfied in the deformed configuration is given by

$$\rho_s \mathbf{x}_{tt} - \text{div}_{\Gamma} \boldsymbol{\sigma}(\mathbf{x}) = \mathbf{f}(\mathbf{x}) \quad \forall \mathbf{x} \in \Gamma_{\mathbf{x}} \quad (8)$$

Here  $\boldsymbol{\sigma}(\mathbf{x})$  is the Cauchy stress on  $\Gamma_{\mathbf{x}}$ ,  $\mathbf{f}(\mathbf{x})$  is the body force, and  $\text{div}_{\Gamma}$  is the divergence calculated along the manifold  $\Gamma_{\mathbf{x}}$ . The corresponding equilibrium in the un-deformed configuration is given by

$$\rho_s \mathbf{u}_{tt}(\mathbf{X}) - \text{Div}_{\Gamma} \mathbf{K}(\mathbf{X}) = \mathbf{F}(\mathbf{X}) \quad \forall \mathbf{X} \in \Gamma_{\mathbf{X}} \quad (9)$$

where  $\mathbf{K}$  is the first Piola–Kirchhoff stress tensor and  $\mathbf{F}(\mathbf{X})$  is the body force on  $\Gamma_{\mathbf{X}}$ . We consider Saint Venant–Kirchhoff model for the hyper-elastic material. For cables, this gives

$$\mathbf{K} = \mathbf{F}_{\Gamma} \cdot \mathbf{S} = 2\mu \mathbf{F}_{\Gamma} \cdot \mathbf{E}_{\text{tang}} \quad (10)$$

where  $\mathbf{F}_{\Gamma}$  is the surface deformation gradient,  $\mu = \frac{E}{2(1+\nu)}$  and  $\mathbf{E}_{\text{tang}}$  is the Cauchy–Green strain tensor. The transformation of derivatives and divergence operators from the un-deformed to

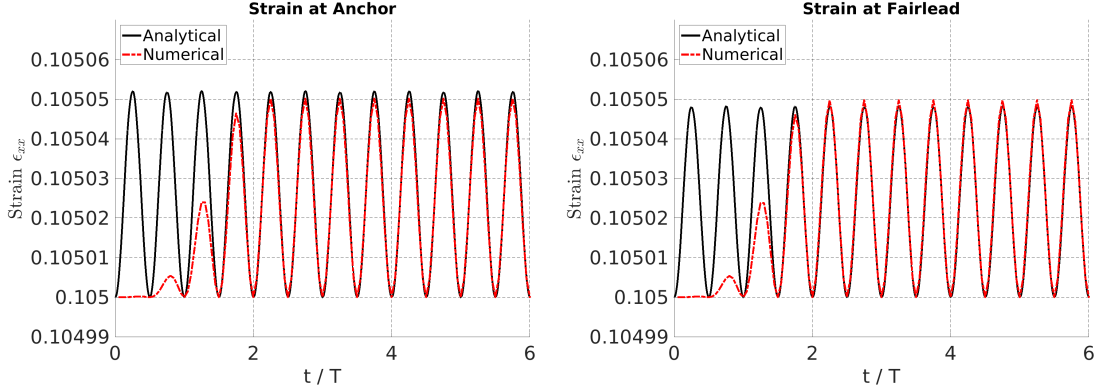


Figure 2: Strain at Anchor and Fairlead for  $u_0 = 0.1\text{m}$  and  $f = 0.5\text{Hz}$ , with pre-tension  $\epsilon_0 = 0.1$

deformed configuration is done using geometric quantities and operators based on *Tangential Differential Calculus* [1]. The weak-form is evaluated for Eq. 9

$$\begin{aligned} A \int_{\Gamma_X} \rho_s \mathbf{w} \cdot \mathbf{u}_{tt} d\Gamma + A \int_{\Gamma_X} \nabla_X^{\Gamma, dir} \mathbf{w} : \mathbf{K}(\mathbf{u}) d\Gamma \\ - A \int_{\Gamma_X} \mathbf{w} \cdot \mathbf{F} d\Gamma - \int_{\partial\Gamma_X} \mathbf{w} \cdot \hat{\mathbf{H}} d\partial\Gamma = 0 \end{aligned} \quad (11)$$

The governing equations are solved using finite-element method. We use the standard Galerkin approach, with linear polynomial shape function. The time-stepping was done using the generalised  $\alpha$  scheme. The system was modelled using state-of-the-art *Julia* based FEM library *Gridap* [2].

#### 4 Results

In this abstract, we focus on a conceptual problem of a tensioned mooring line. We consider a line with length  $L = 10\text{m}$ , with  $A = 0.01\text{m}^2$ ,  $\rho_s = 100\text{kg m}^{-3}$ ,  $E = 10\text{MPa}$  and Lamé constant  $\mu = \frac{1}{2}E$ . The line is pre-tensioned with 10% strain, i.e.  $\epsilon_0 = 0.1$ . The displacement of the fairlead is controlled as a periodic excitation with amplitude  $u_0$  and frequency  $f$ .

The first test is conducted for periodic excitation of the fairlead, with  $u_0 = 0.1\text{m}$  and  $f = 0.5\text{Hz}$ . Fig. 2 presents the time-series of the strain at both the anchor and the fairlead, obtained from the analytical and numerical models. In the numerical model, the periodic excitation of the fairlead is gradually ramped up over two wave cycles to prevent the excitation of spurious waves. The analytical model shows a slightly higher strain at the anchor compared to the fairlead. Overall, there is a good agreement between the analytical and numerical results.

Fig. 3 shows the hardening resonances computed by means of the analytical model. The results correspond to an increase of the oscillation amplitude with the increase of the excitation amplitude  $u_0 \in [0.01, 0.8]$ . The black dots in the plot describe the maximum amplitude after steady-state is reached during the frequency sweep ranging from  $f \in (0, 12]\text{Hz}$ .

#### REFERENCES

- [1] T.P. Fries and D. Schöllhammer. A unified finite strain theory for membranes and ropes. *Computer Methods in Applied Mechanics and Engineering*, 365:113031, 2020.

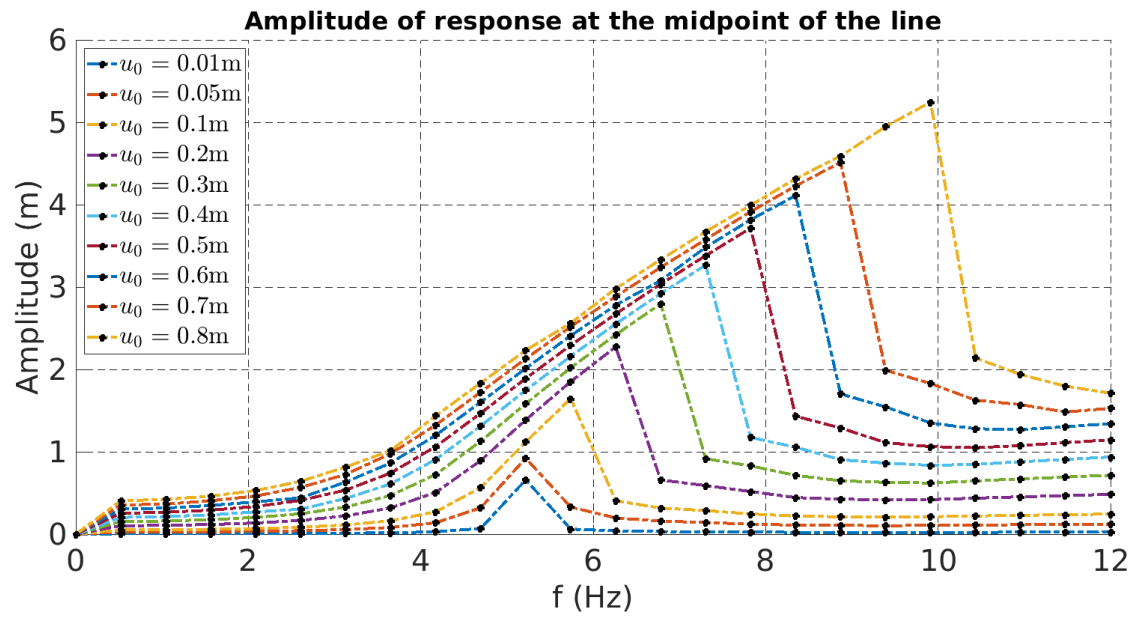


Figure 3: Plot showing the hardening behaviour of the mooring line, obtained from the analytical model.

- [2] Santiago Badia and Francesc Verdugo. Gridap: An extensible Finite Element toolbox in Julia. *Journal of Open Source Software*, 5(52):2520, August 2020.

## PREDICTING COLLAPSE MECHANISMS IN MASONRY BUILDINGS THROUGH THE USE OF RIGID BODY DYNAMICS

Nicola Tarque<sup>1,2\*</sup>, José M. Goicolea<sup>1</sup>, Leonel Lipa<sup>2,3</sup>, Luca Pelà<sup>3</sup>

<sup>1</sup> Universidad Politécnica de Madrid, E.T.S. de Ing. Caminos, Canales y P., 28040 Madrid  
{nicola.tarque, jose.goicolea}@upm.es

<sup>2</sup> Gerdis Research Group, Civil Eng. Division, Pontificia Universidad Católica del Perú, Lima  
leonel.lipa@puclp.edu.pe

<sup>3</sup> Universitat Politècnica de Catalunya, Dpto. de Ing. Civil y Ambiental, 08034 Barcelona  
luca.pela@upc.edu

**Keywords:** rigid body dynamics, finite element, collapse mechanism, masonry

**Abstract.** *Studying masonry buildings' structural stability, dynamic behaviour and seismic safety is not straightforward. It involves the knowledge of how the masonry components behave, the mechanical properties and the interaction among all the parts, and the difficulty increases when dealing with historical constructions. One way to analyse the entire behaviour of masonry structures is through highly nonlinear numerical models, considering micro or macro modelling. This work shows a simplified -but rigorous- methodology for analysing the possible collapse mechanisms of two case studies: a dry-stone wall and an unreinforced earthen building. In both cases, the dynamics of rigid bodies are used within the finite element method in Abaqus software. Each stone is modelled as a rigid body for the stone walls, and the interaction among them is calibrated based on the normal and tangential properties at the contact zones. For the adobe building, the literature indicates that some macro parts are previously formed before they collapse under dynamic actions. Then, the model of the entire adobe building is formed by macro earthen parts placed together with contact zones. In both models, the external action is represented by an acceleration record at the base. The advantage of using the dynamics of rigid bodies is reducing the degrees of freedom in the entire building. As a result, the different failure mechanisms of the stone and adobe buildings are discussed, showing the advantages of the dynamics of rigid bodies for a rapid seismic vulnerability analysis of masonry constructions.*

## 1 INTRODUCTION

Archaeological evidence suggests that the use of masonry in construction dates to the beginnings of human civilisation. Some earliest examples are structures near Lake Hullen, Israel (9000-8000 B.C.). These structures were built with circular and semi-subterranean dry-joint masonry, possibly using stone and brick [3]. On the other hand, in the Middle East, in Göbekli Tepe (9500 - 8000 B.C.), oval-shaped masonry temples of rounded stone joined with mud mortar were found [4]. Also, in South America, the inhabitants of Caral (2500 - 1800 B.C.), Peru, built temples and dwellings with irregular stone masonry joined with mud mortar and earthen constructions [5].

Numerical modelling techniques can be employed for the structural evaluation of masonry construction, whether dry-joint or mortared. These techniques include the Finite Element Method (FEM) [7], the Discrete Element Method (DEM) [8] or even a combination of both [9]. FEM evaluates the stress state within the structural elements as a continuum but with the added capability of incorporating discontinuities like joints. This versatility makes FEM a popular choice for such analyses.

FEM analysis of masonry with mortar joints offers three approaches: micro-modeling (most detailed), simplified micro-modeling (moderately detailed), and macro-modeling (least detailed). Micro-modelling treats each brick and the mortar joint as separate elements for the most accurate geometry. Simplified micro-modelling incorporates part of the mortar in each masonry unit, so the mortar thickness disappears, and the geometry of each unit is increased in height and length. Macro modelling, the fastest but least detailed approach, considers the entire structure as a single uniform material.

Unlike mortared masonry, dry-joint structures require different FEM modelling approaches. Macro modelling treats the entire wall as one material, offering a quick but less detailed analysis. Discontinuous modelling, on the other hand, represents each unit geometry and relies on specific contact laws to simulate their interactions, providing a more accurate but computationally expensive solution [10].

While micro-modelling and discontinuous modelling offer a deeper understanding of a structure's behaviour by capturing local failures, they come at the cost of increased computational time. To address this, masonry units can sometimes be simplified as rigid bodies, reducing the complexity and making the analysis faster.

Generally, rigid bodies are used with stone or other very rigid material units in masonry. But, it could also be used for the case of earthen constructions since these have been shown to disarticulate into macro-blocks under the action of earthquakes [11], and it can be hypothesised that each of these macro-blocks is a rigid body that also interacts in their contact zones. Thus, the rigid body dynamics methodology can be used both for the case of dry-joint stone masonry and for the global behaviour of earthen buildings. Therefore, this work shows the use of rigid body dynamics within the FEM, in combination with contact laws, applied to the analysis of the possible collapse mechanisms of stone and earthen constructions. The results demonstrate the reliability of the methodology in reproducing the collapse mechanisms and, thus, proposing mitigation alternatives.

## 2 NUMERICAL MODELING

This research proposes a Finite Element Method (FEM) based methodology implemented within Abaqus software to analyse the out-of-plane and in-plane behaviour of masonry walls. Two distinct wall types are investigated: stone walls (block-to-block interaction) and adobe walls (macro-block interaction). Each unit is modelled with rigid bodies for the stone wall case, and the joints are modelled using normal and tangential contact properties. Each macro-block

(composed of previously identified adobe units and mortar joints) is modelled as a rigid body for the adobe walls.

## 2.1 Mechanical behaviour of rigid bodies

Rigid bodies are non-deformable elements comprised of multiple nodes and surfaces. Each solid's motion is governed by a single reference node with six degrees of freedom (three translations and three rotations) [12]. The single node is typically placed at the mass centre. Interactions between bodies occur through defined contact zones at their joints, characterised by normal and tangential stiffness properties. The primary advantages of rigid bodies include significantly reducing computational time and accurately representing potential failure modes within the masonry walls.

## 2.2 Contact Properties

Within mechanical contact analysis, the contact zone is assumed to be rigid and devoid of overlap or deformation. Normal and tangential stiffness are contact behaviour's primary parameters [13]. The normal force is expressed by Equation (1):

$$F_n = K_n \Delta U_n A_c \quad (1)$$

where  $\Delta U_n$  is the relative displacement between two bodies in contact,  $K_n$  is the contact normal stiffness, and  $A_c$  is the contact area.

In the case of tangential behaviour, the shear force is obtained with Equation (2):

$$F_t = K_t \Delta U_t A_c \quad (2)$$

where  $K_t$  is the tangential stiffness and  $\Delta U_t$  the relative movement of the bodies due to shear deformation.

The maximum shear force at the contact is obtained by equation (3):

$$F_t = F_n \tan \varphi \quad (3)$$

where  $\varphi$  is the contact friction angle, and  $\tan \varphi$  is the coefficient of friction. When this force is reached, the blocks slide [14].

## 3 CASE STUDIES

Subsequent sections present the results of the nonlinear dynamic analysis of a stone and adobe masonry construction.

### 3.1 Model 1: Wall of the twelve-angled stone

This wall is in Cusco, Peru, near the main square (Figure 1), and is part of the Archbishop's Palace. The lower section is constructed with dry-laid, tightly fitted stone, while the upper section is made of adobe. No data on the wall's overall thickness is available, leaving it unclear whether it's a single, double, or composite wall. The model considers the wall a single-layer structure to simplify the analysis and validate the methodology used.





Figure 1: Wall of the twelve-angled stone (a) View of the street (b) Wall with the twelve-angled stone.

Lipa et al. [15] modelled a section of the wall measuring 5.50 m long, 5 m high, and 0.80 m thick (Figure 2). Each stone was precisely drawn using graphic design software and subsequently exported to Abaqus for finite element analysis. The methodology adopted rigid bodies to represent each stone unit. For this first case, the wall's upper part (made of adobe) was modelled using linearly elastic material. Material properties for both the blocks and joints are presented in Table 1. These properties were obtained from a combination of sources, including data from previous studies by [16] and [17].

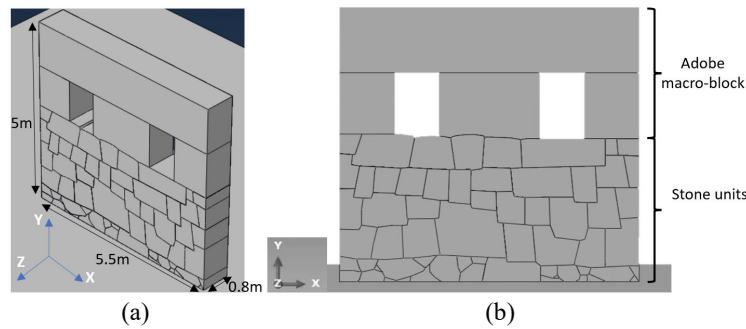


Figure 2: Abaqus model of case 01 (a) 3D view (b) Front view.

	Property	Symbol	Value
Stone units (rigid)	Density	$\rho_r$	2300 kg/m <sup>3</sup>
	Density	$\rho_a$	1631 kg/m <sup>3</sup>
Upper part (adobe, elastic)	Modulus of Elasticity	$E$	200 MPa
	Poisson's ratio	$\nu$	0.3
Dry joint	Normal stiffness	$K_n$	$2 \times 10^8$ N/m <sup>3</sup>
	Coefficient of Friction	$\tan \varphi$	0.4

Table 1: Physical and mechanical properties of materials and joints for case 01.

The wall's dynamic behaviour was evaluated by subjecting it to a series of earthquake excitations applied perpendicularly to its surface. The selected seismic input was the Paruro earthquake of 2014 [18], considered one of the strongest recorded in the region, with a peak ground acceleration (PGA) of 0.1g. Subsequently, the same earthquake record was scaled to higher PGA values of 0.3g, 0.5g, and 0.6g to investigate the response under intensified seismic conditions, which may be produced due to soil conditions or significant earthquakes. The boundary conditions were respected for the analysis to be representative. The duration of the applied seismic signal was 30 s.

Numerical post-earthquake analysis revealed minimal damage to the wall following the 0.1g seismic event (Figure 3a). However, evaluation under the scaled earthquake with a PGA of 0.3g (Figure 3b) indicated residual displacements within the adobe masonry section. When subjected to the earthquake scaled to even higher PGA values of 0.5g and 0.6g (Figures 3c and 3d), the wall exhibited collapse behaviour. This involved the disintegration of the upper adobe section and the breakdown of the stone units. An explicit dynamic analysis framework was employed for this investigation, utilising a time step of  $2.5 \times 10^{-5}$  s.

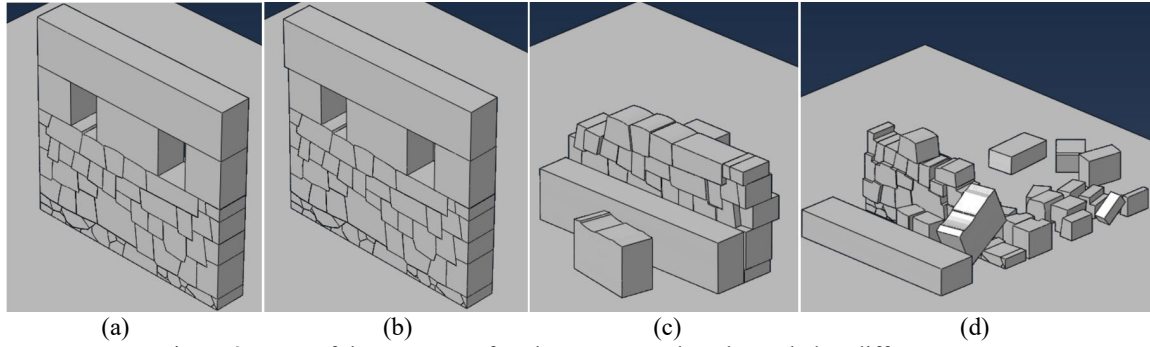


Figure 3: State of the structure after the Paruro earthquake scaled to different PGA. (a) 0.1g (b) 0.3g (c) 0.5g (d) 0.6g.

### 3.2 Model 2: Adobe construction

A numerical model of an adobe building, experimentally tested on a shaking table at the Pontificia Universidad Católica del Perú [11], is presented here. The physical structure comprised two stories at a  $\frac{1}{2}$  scale, but only the first level was modelled to demonstrate the proposed methodology. The structure has a rectangular base with dimensions of 2.06 m x 1.82 m and a total height of 1.33 m. It was built on an elastic reinforced concrete beam measuring 2.06 m x 1.82 m x 0.30 m. The adobe walls have a uniform thickness of 0.22 m. Two windows are in the side walls (aligned with the direction of shaking), and a door is on the front facade. Experimental observations during the shaking table test revealed a tendency for the adobe structure to crack and form larger macroblocks. In this case, the macroblocks are idealised as bodies interacting in known interface zones, as illustrated in Figure 4. The material properties employed for this second case study are detailed in Table 2.

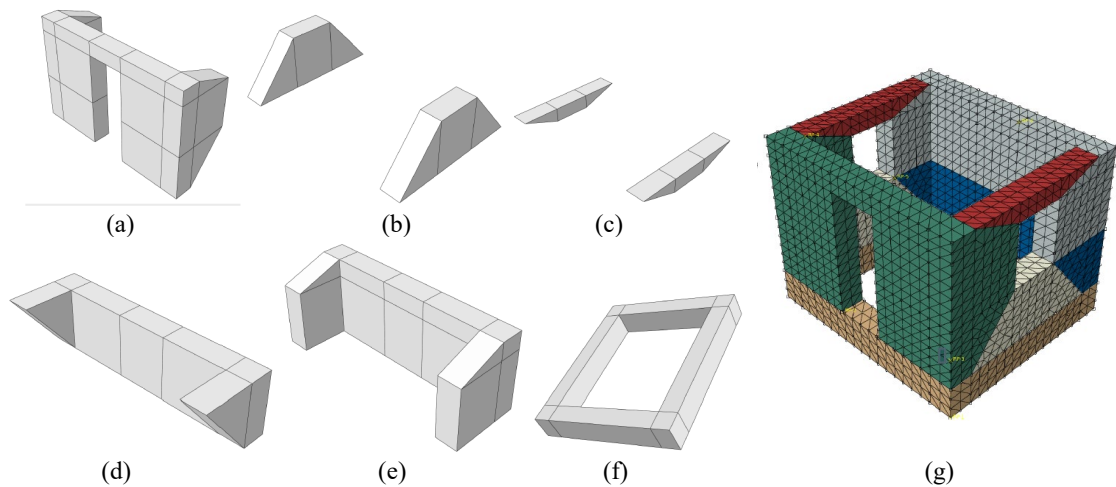


Figure 4: Numerical model of the adobe building. (a) Part-1, (b) Part-2, (c) Part-3, (d) Part-4, (e) Part-5, (f) Part-6, (g) Complete structure. The different colours indicate the macroblocks formed during the experimental test.

	Property	Symbol	Value
Concrete block	Density	$\rho_r$	2200 kg/m <sup>3</sup>
	Modulus of Elasticity	$E$	28000 MPa
Adobe macroblocks	Density	$\rho_a$	1800 kg/m <sup>3</sup>
	Modulus of Elasticity	$E$	200 MPa
	Poisson's ratio	$\nu$	0.2
Dry joint	Normal stiffness	$K_n$	10 x 10 <sup>9</sup> N/m <sup>3</sup>
	Coefficient of Friction	$\tan \varphi$	0.35

Table 2: Physical and mechanical properties of materials and joints for case 02.

A unidirectional earthquake record obtained in Lima during the 1970 Huaraz earthquake was applied to the model's base to simulate seismic excitation. This signal was oriented parallel to the structure's windows. The chosen displacement time history was scaled to achieve a maximum value of 60 mm. The seismic excitation had a total duration of 15 s. An implicit dynamic analysis framework was employed here, utilising an initial time step of 0.1 s for the gravity load and 0.01 s for the dynamic load.

The numerical simulation corroborates the experimental observations. Under this earthquake intensity, the adobe macro-blocks, modelled as rigid bodies in this analysis, exhibit relative movements and displacements concerning each other (Figure 5a). Furthermore, the contact pressures between the macro-blocks can be determined at any given time (Figure 5b).

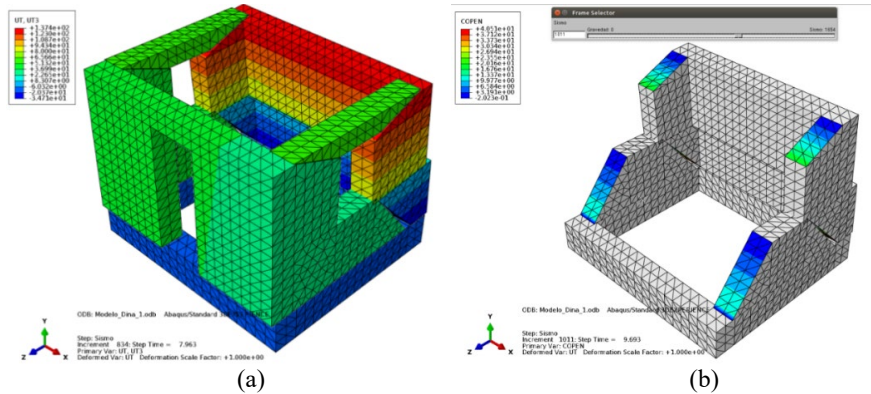


Figure 5: Visualisation of results (a) displacement U3 in mm (direction of the earthquake) at 8 s of the movement (b) pressure between blocks (N/mm).

#### 4 CONCLUSIONS

This study demonstrates the versatility of employing rigid body dynamics within the Finite Element Method (FEM) framework. Also, the computational time needed for structural analysis is significantly reduced by utilising rigid bodies, which require only 3 degrees of freedom (DOF) for translation and 3 DOF for rotation per element. Furthermore, when applied to masonry structures, this approach effectively captures damage and collapse mechanisms, as evidenced by the two case studies. This capability allows for evaluating seismic behaviour under various earthquake intensities and facilitates informed decisions regarding the need for additional structural elements to ensure stability and prevent damage. Complete collapse might not be the primary concern for structures with historical significance. Even earthquakes causing relative and permanent movement between stones can threaten the heritage value. Therefore, the

proposed methodology offers a valuable tool for assessing the seismic vulnerability of masonry structures. Future research includes incorporating seismic demand analysis considering regional seismic amplification, developing experimental programs to characterise joint behaviour, and utilising Python programming to streamline the digital construction of structures with repetitive patterns.

## REFERENCES

1. P.B. Lourenço, J. G. Rots, J. Blaauwendraad, "Two approaches for the analysis of masonry structures: micro and macro-modeling. Heron", 1995.
2. L. Cavaleri, M. Zizzo, P. G. Asteris, "Residual out-of-plane capacity of infills damaged by in-plane cyclic loads". *Engineering Structures*, 209, 109957, 2020.
3. P. B. Lourenço, "Masonry structures, overview". *Encyclopedia of Earthquake Engineering*, pp. 1-9, 2014.
4. L. Clare, "Göbekli Tepe, Turkey". A summary of research at a new World Heritage Site (2015–2019), 2020.
5. J. Canziani, "Ciudad y territorio en los Andes: contribuciones a la historia del urbanismo prehispánico". Second Edition, Fondo Editorial PUCP, 2017.
6. S. Santa-Cruz, D. Daudon, N. Tarque, C. Zanelli, J. Alcántara, "Out-of-plane analysis of dry-stone walls using a pseudo-static experimental and numerical approach in scaled-down specimens". *Engineering Structures*, 245, 112875, 2021.
7. P. B. Lourenço, "A user/programmer guide for the micro-modeling of masonry structures". Report 03.21.1.31.35. University of Minho, 1996.
8. P. A. Cundall, O. D. Strack, "A discrete numerical model for granular assemblies". *Geotechnique*, vol. 29(1), pp. 47-65, 1979.
9. A. Munjiza, J. P. Latham, "Comparison of experimental and FEM/DEM results for gravitational deposition of identical cubes". *Engineering Computations*, 21(2/3/4), pp. 249-264, 2004.
10. L. Lipa, N. Tarque, L. Pelà, J. M. Goicolea, "Seismic numerical analysis of an Inca stone wall in Sacsayhuaman using rigid body dynamics within a finite element framework". *Engineering Failure Analysis*, 108254, 2024.
11. N. Tarque, M. Blondet, J. Vargas, R. Yallico, "Rope mesh as a seismic reinforcement for two-storey adobe buildings". *Bulletin of Earthquake Engineering*, 20, pp. 3863–3888, 2022.
12. J. M. Goicolea, J. C. G. Orden, "Dynamic analysis of rigid and deformable multibody systems with penalty methods and energy-momentum schemes". *Computer methods in applied mechanics and engineering*, 188(4), pp. 789-804, 2000.
13. P. R. Refachinho de Campos, A. Gay Neto, "Rigid body formulation in a finite element context with contact interaction". *Computational Mechanics*, 62, pp. 1369-1398, 2018.
14. J.C. Quezada, E. Vincens, R. Mouterde, J.C. Morel, "3D failure of a scale-down dry-stone retaining wall: A DEM modelling". *Engineering Structures*, 117, pp. 506-517, 2016.
15. L. Lipa, N. Tarque, L. Pelà, J.M. Goicolea, "Estudio numérico de la capacidad al volteo de muros de piedra Inca. Caso de estudio: muro con la piedra de los 12 ángulos en Cusco, Perú". En el I Congreso Internacional de Patrimonio de la Obra Pública y de la Ingeniería Civil. Toledo, Spain, 2023.
16. L. Lipa, N. Tarque, L. Pelà, J. M. Goicolea, "Evaluation of the Seismic Behaviour of an Inca Stone Wall Using Rigid Body Dynamic Methods". In *International Conference on Structural Analysis of Historical Constructions*, pp. 1102-1113, 2023.

17. N. Tarque, G. Camata, A. Benedetti, E. Spacone, "Alternative approach for reproducing the in-plane behaviour of rubble stone walls". *Earthquakes and Structures*, 13(1), pp. 29-38, 2017.
18. J. Alva, C. Ortiz C, "Registros acelerométricos del sismo de Paruro – Cusco del 27 de setiembre de 2014". National University of Engineering, Engineering Civil Faculty, Postgraduate, 2014.

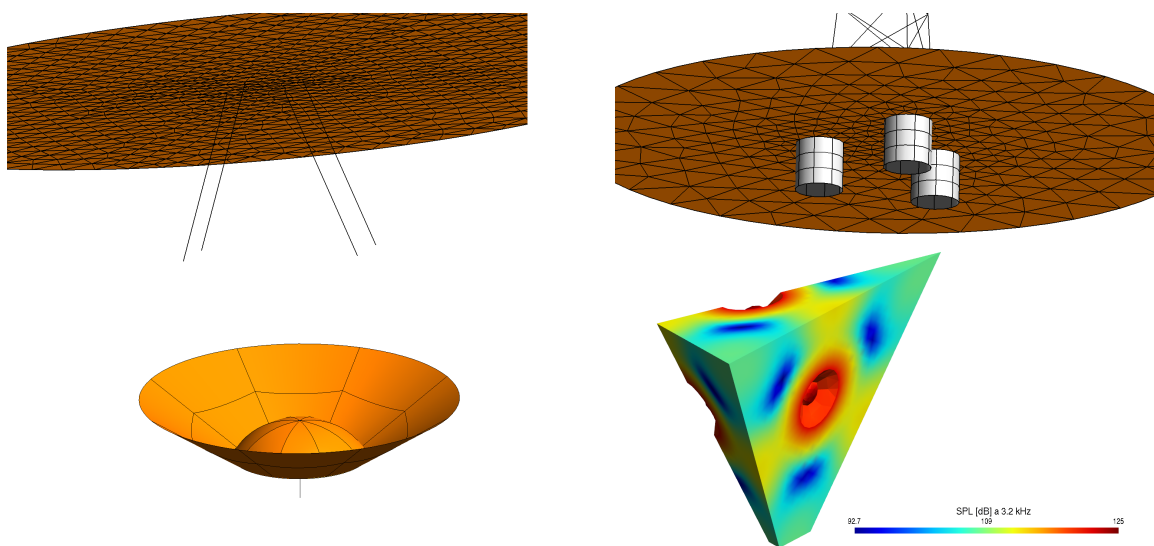
## MULTIFEBE: OPEN-SOURCE PACKAGE FOR MIXED-DIMENSIONAL BOUNDARY ELEMENT – FINITE ELEMENT MODELS FOR COUPLED LINEAR MECHANICS

Jacob D.R. Bordón\*, Guillermo M. Álamo, Luis A. Padrón,  
Juan J. Aznárez and Orlando Maeso

Instituto Universitario de Sistemas Inteligentes y Aplicaciones Numéricas en Ingeniería  
Universidad de Las Palmas de Gran Canaria, Las Palmas de G.C., 35017, Spain  
e-mail:{jacobdavid.rodriguezboron, guillermo.alamo, luis.padron,  
juanjose.aznarez, orlando.maeso}@ulpgc.es

**Keywords:** Boundary elements, Finite elements, Open source, Soil-Structure Interaction, Fluid-Structure Interaction

**Abstract.** *MultiFEBE is an open source package able to perform linear static and dynamic analysis of problems involving the interaction between structural elements and their surrounding media through advantageous mixed-dimensional couplings [1]. Among others, it includes structural beam and shell finite elements, and ordinary and crack boundary elements for fluid, elastic and poroelastic (Biot's theory) media. This code gathers and enriches several coupling approaches previously developed in our group which, together with a convenient linkage to external pre- and post-processing utilities, lead to a quite broad analysis tool for studying Soil-Structure Interaction, Fluid-Structure Interaction and Acoustics problems.*



*Top left: inclined pile foundation. Top right: suction caisson tripod offshore wind turbine.  
Bottom left: speaker cone. Bottom right: tetrahedron loudspeaker.*

*In particular, it comprises the beam finite element to boundary element elastic soil coupling developed by Padrón et al. [2], shell finite element to boundary element inviscid fluid and/or elastic or poroelastic soil coupling developed by Bordón et al. [3], and multi-domain boundary element coupling between inviscid fluid, elastic and/or poroelastic soil of Aznárez et al. [4].*

*The code is mainly written in modern Fortran in a conventional procedural paradigm, but using types (classes) to encapsulate high-level data and procedures. Low-level computational routines are organized within a library of interrelated modules, which facilitates reusability and extension for other problem-specific solvers. OpenMP is used where possible to fully benefit from multi-core processors. The solver is able to read and write files for Gmsh and GiD pre- and post-processors. It has been released at GitHub (<https://github.com/mmc-siani-es/MultiFEBE>) under a GPL 2.0 license, which encourages the community to use, modify and take part in its development.*

*The aim of this contribution is the diffusion of the package including recent updates, and the presentation of results from a selected range of problems showing its capabilities.*

## ACKNOWLEDGMENTS

This work was funded by the Ministerio de Ciencia, Innovación y Universidades and the Agencia Estatal de Investigación of Spain (MCIN/AEI/10.13039/501100011033) through research project PID2020-120102RB-I00.

## REFERENCES

- [1] J.D.R. Bordón, G.M. Álamo, L.A. Padrón, J.J. Aznárez and O. Maeso, MultiFEBE: A multi-domain finite element–boundary element solver for linear mixed-dimensional mechanical problems, *SoftwareX* 20, 101265, 2022.
- [2] L.A. Padrón, J.J. Aznárez and O. Maeso, BEM-FEM coupling model for the dynamic analysis of piles and pile groups, *Engineering Analysis with Boundary Elements* 31, 473–484, 2007.
- [3] J.D.R. Bordón, J.J. Aznárez and O. Maeso, Dynamic model of open shell structures buried in poroelastic soils, *Computational Mechanics* 60, 269–288, 2017.
- [4] J.J. Aznárez, O. Maeso and J. Domínguez, BE analysis of bottom sediments in dynamic fluid-structure interaction problems. *Engineering Analysis with Boundary Elements* 30, 124–136, 2006.



## STEADY-STATE OSCILLATION ANALYSIS: NONLINEAR SOLUTIONS FOR A ROTATING CANTILEVER BEAM

González-Carbajal, J.<sup>1</sup>, Rincón-Casado, A.<sup>2</sup>, García-Vallejo, D.<sup>1</sup> and Domínguez, J.<sup>1</sup>

<sup>1</sup>Department of Mechanical Engineering and Manufacturing  
Universidad de Sevilla, 41092 Seville, Spain  
e-mail: {jgcarbajal,dgvallejo,jaime}@us.es

<sup>2</sup> Department of Mechanical Engineering and Industrial Design  
University of Cadiz, 11519 Puerto Real, Spain  
e-mail: alejandro.rincon@uca.es

**Keywords:** rotating beam, multiple time scales, absolute nodal coordinate formulation, nonlinear oscillation, Frobenius method.

**Abstract.** *The rotating beam problem serves as a widely-used benchmark for evaluating nonlinear finite element methods. Its distinctive feature is the interplay between axial and transverse deformations caused by centrifugal forces. This dynamic behavior results in a centrifugal stiffening effect, which can only be accurately modeled by either incorporating a kinematic coupling of axial and transverse deformations or employing a nonlinear description of elastic forces. This study introduces simplified rotating beam models that capture the centrifugal stiffening effect by incorporating an axial-to-transverse kinematic coupling of the beam centerline. These models facilitate a discussion on their accuracy and enable a meaningful analysis of nonlinear oscillations during steady-state rotation. The performance of these simplified models is evaluated against finite element solutions obtained using the absolute nodal coordinate formulation.*

*This study employs a finite element model using the Absolute Nodal Coordinate Formulation (ANCF) to generate numerical results for comparison with the developed simplified analytical model. The ANCF model's index-3 differential algebraic equations of motion were numerically integrated using a second-order implicit integrator (trapezoidal rule) with a  $1.0 \times 10^{-3}$  s time step. Baumgarte's method was applied to stabilize the rheonomic constraints from the rotating clamped end during integration.*

*After mesh convergence analysis, a model with 16 quadratic beam elements was selected. This model comprises 132 nodal coordinates, resulting in 130 degrees of freedom when accounting for the two nonlinear constraints. Simulations ran for 15 seconds, ensuring at least five complete cycles of steady oscillations for amplitude and frequency averaging in all cases. The numerical study aims to generate points on the backbone curve for various spinning angular velocities. To produce nonlinear oscillations of different amplitudes, the acceleration time (T) in the simulations was varied, using values of 3.375 s, 3.25 s, 3 s, 2.75 s, 2.5 s, and 2 s. Shorter acceleration times lead to increased amplitude of steady nonlinear oscillations.*



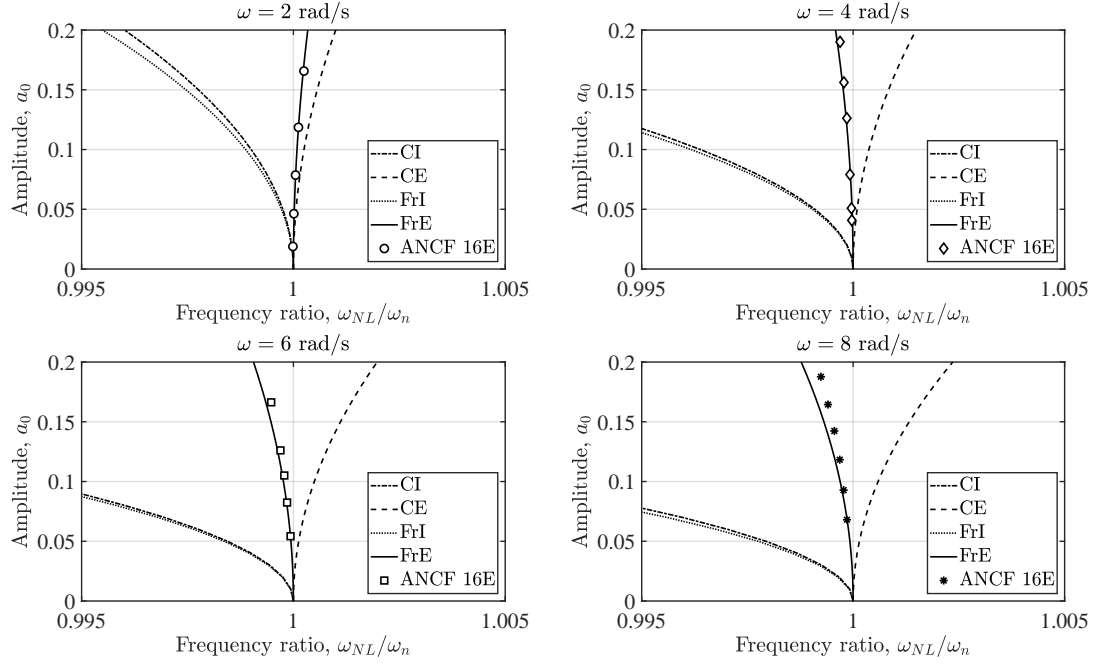


Figure 1: Comparison of the different solutions obtained for different  $\omega = 2, 4, 6, 8$  rad/s. The acronyms CI, CE, FrI and FrE stand for the type of shape function and the use or not of the assumption of inextensibility (C = cantilever mode shape function, Fr = Frobenius approximation shape function, I = inextensible, E = extensible). The finite element results correspond to the acronym ANCF 16E.

Figure 1 compares various solutions derived in this study with the previously described finite element results. The solutions differ based on whether they assume inextensibility and whether they describe deformation using the cantilever beam mode or the Frobenius approximation for the rotating beam mode. Comparisons are shown for four spinning angular velocities ( $\omega = 2, 4, 6, 8$  rad/s). The analytical solutions significantly deviate from the actual backbone curve obtained by the ANCF finite element model, except when both elongation effects and the Frobenius mode are incorporated. The solution combining the Frobenius approximation with elongation consideration aligns well with the ANCF solution for moderately large amplitudes (deformations under 20 % of beam length) and moderately high spinning angular velocities. For context, an 8 rad/s angular velocity approximately doubles the linear natural frequency of the rotating beam at that velocity ( $\omega_n = 4.1242$  rad/s). It's important to note that at higher angular velocities, higher modes are expected to contribute significantly, rendering the one-degree-of-freedom models presented here invalid.

According to Fig. 1, not considering the beam's extensibility results in overestimating the softening behaviour of the inertial terms. In addition, approximating the beam transverse deflection by the first transverse vibration mode of a cantilever beam instead of using the vibration mode of the rotating beam, here obtained using Frobenius approximation, results in overestimating the hardening.

**3rd Conference on Structural Dynamics (DinEst 2024)**  
**Seville, September 2024**  
**Bridge dynamics and vibration control session**

## DYNAMIC EVALUATION OF A SCALED-DOWN BRIDGE SUBJECTED TO MEMBER REMOVALS

Juan C. Reyes-Suárez<sup>\*1</sup>, Manuel Buitrago<sup>1</sup>, Brais Barros<sup>1</sup>, Jose M. Adam<sup>1</sup>

<sup>1</sup> ICITECH, Universitat Politècnica de València. Camino de Vera s/n, 46022 Valencia, Spain  
address  
{jcreysu1,mabuimo1,bbargon,joadmar}@upv.es

**Keywords:** Bridges, Truss, Steel, Robustness, Progressive Collapse, Computational modeling, OMA, Dynamics

**Abstract.** *Aging bridges are among the most important and vulnerable points in a country's road and railway networks. The growing number of aging bridge collapses led to considerable losses in economic and social fields. The correct understanding of the phenomena through computational models combined with a real-time monitoring strategy plays a fundamental role in risk identification and mitigation and in avoiding extensive replacement or structural retrofitting costs. Bridge collapse usually starts as a local failure that propagates to other parts of the structural system, leading to general failure through a phenomenon known as progressive collapse. This study analyzes the dynamic response of a 1/3.5 scaled-down version of a real steel truss bridge (Quisi bridge) subjected to member losses. The scaled-down bridge was designed following the similitude theory and considering the scaling and size effects. Preliminary studies were driven to define the failure scenarios. The bridge was later built and tested to validate its dynamic response through Operational Modal Analyses (OMAs).*

## 1 INTRODUCTION

Bridges play a fundamental role in every country's transportation network, as they are a sustainable and effective way to transport goods and people. Among the different bridge typologies, steel truss bridges were one of the engineers' favorite types because of their lightweight, considerable strength, and ability to cross long spans. Nonetheless, bridges designed and built a hundred years ago must withstand new loads, extreme events due to climate change, and degradation actions such as fatigue and corrosion [1], [2]. Thus, the new structural requirements push the aging structures to their limits and, in some cases, induce local failures that can propagate and result in a phenomenon called “Progressive Collapse” [3], [4]. Several studies have been conducted to identify the so-called “local failures” and their influence on the bridge's structural behavior [5], [6]. Numerical modeling [7], [8] and experimental campaigns [1] have also proven worthwhile for building an integrated framework for identifying local failures and anticipating disproportionate collapse, an essential strategy for effective risk mitigation.

Developing this strategy requires the identification of the state variables involved, and studying its relative sensitivity during a local failure event is of primary interest. One of the possible alternatives is related to the structural dynamic response and its associated parameters. A structure can be characterized by its vibration modes, eigenfrequencies, and eigenvalues. Additionally, these parameters can be measured in situ and the laboratory using ambient vibration testing or Operational Modal Analysis (OMA). The structural dynamic response has been applied to characterize and understand the behavior of aging steel truss bridges with remarkable results [9]. Therefore, this type of technology could be of interest while developing a novel holistic and cost-effective approach to anticipate the failure propagation of aging bridges.

This study is part of the Pont3 project. It aims to analyze the structural dynamic response of an aging bridge structure subjected to failure scenarios using the Operational Modal Analysis in a scaled version of the real bridge at the ICITECH laboratories of the *Universitat Politècnica de València*.

## 2 METHODOLOGY

### 2.1 The Quisi Bridge

The structure under study corresponds to the Quisi Bridge, a steel truss bridge part of the Valencian railroad network. The bridge was built in the early 1900s and consists of 6 symmetrically distributed spans of 21.5, 21.1, and 42 m, respectively. The bridge structural typology corresponds to two Pratt trusses with riveted joints as the main connection between the structural elements. The truss system consists of top chords for tensile forces, bottom chords for compressive forces, vertical and diagonal members to transfer the shear forces between the chords, and horizontal and vertical bracings to provide lateral and vertical stiffness to the structure. Trusses are linked by floor beams and crossed longitudinally by stringers.

The test specimen tested in the lab corresponds to a scaled version of the real bridge. Dimensions and cross-sections were designed and later manufactured following the similitude theory, considering the scaling and size effects (Figure 1). So, the test specimen consists of a 6 m long and 1 m tall replica of one of the isostatic spans of the Quisi Bridge. The scaled version of the bridge uses t-shaped sections as chords and stringers, W-shaped beams as floor beams, and

angles for verticals, diagonals, and bracings, as the original cross sections involve built-up sections with unusual and noncommercial shapes; members were linked through welding as riveted connections pose several building issues in a scaled model.

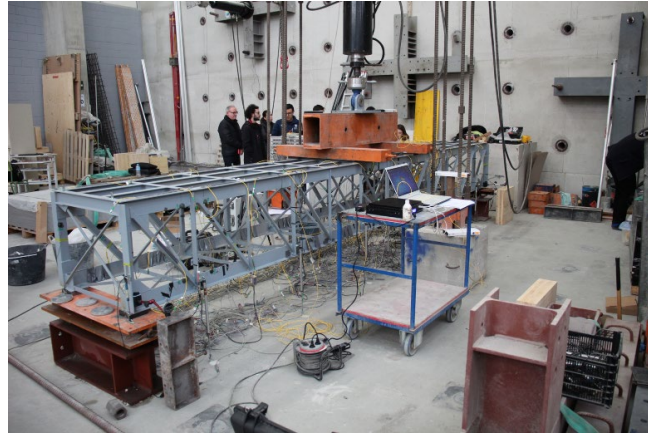


Figure 1 Scaled bridge during the ambient vibration test.

## 2.2 General Set-Up

The experimental campaign was conducted at the ICITECH laboratories in the Universitat Politècnica de Valencia. The scaled bridge was disposed longitudinally over the strong floor and placed over hinge supports on both sides and a ball bearing box on the right side to allow rotation and horizontal movements (Figure 2), thereby simulating the real support conditions of the Quisi bridge. The load was applied vertically through a hydraulic jack equipped with a load cell with a 250 kN capacity. To apply the load, a system of steel profiles was assembled on the top of the bridge so that the desired load was correctly transferred from the jack to the selected node or element.



Figure 2 Hinged and Roller Supports

The central part of the study was centered around the effect of local damage and its influence on the bridge dynamic response. Therefore, the test was split into nine subtests where local damage was reproduced by removing specific elements from the bridge, i.e., cutting the elements employing an angle grinder. Each local damage case was cataloged as a “Damage Scenario” as shown in Table 1. Damage scenarios were established by a review of the state of the art [7], [10], [11], and by using numerical models to identify the more vulnerable elements.

DS	Element Removed
DS1	Horizontal Bracing (P*)
DS2	Horizontal Bracing (C**)
DS3	Vertical Bracing (P*)
DS4	Vertical Bracing (C**)
DS5	Column
DS6	Lower chord
DS7	Floor Beam (P*)
DS8	Floor Beam (C**)
DS9	Diagonal

Table 1 Damage Scenarios

\*(P) stands for partial

\*\* (C) stands for complete

As part of the Pont3 project, the subtests required measurements beyond the dynamic response, that is, in terms of stresses, strains, displacements, and the general structural response. Consequently, the bridge in its non-damaged state was initially loaded, and the state variables were measured. After unloading the structure, the vibration measurements were carried out to proceed with the element removal (Figure 4) and repeat the process to the damaged structure. Once the subtest was finished, the bridge was repaired. To remain in the elastic range, the maximum applied load was limited to 80 kN as numerical models showed that a greater load would initiate the yielding and buckling phenomenon. The repair was performed with small steel pieces with identical cross-sections to avoid major stiffness changes.

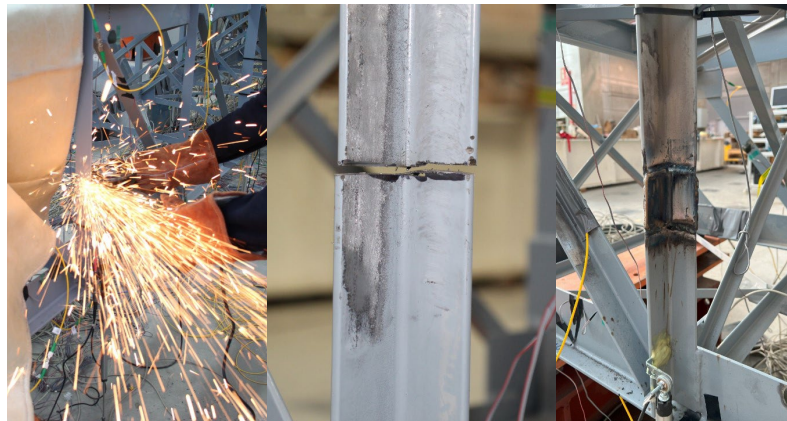


Figure 3 Element Removal and Repairing

Regarding the load application point, two setups were picked. On the one hand, the load was applied to the four external upper nodes next to the center span (Figure 6) to activate, more significantly, the flexural behavior of the truss chords. On the other hand, the upper internal nodes of the center span were chosen to study the load distribution system (stringers and floor beams) response. The load setup plays a fundamental role in the dynamic response of the bridge,

as its mass (423.5 kg) is smaller than the auxiliary components used for the loading system (526 kg).

### 2.3 OMA, Vibrations and Dynamic Response

The dynamic response of the bridge was captured with 3 Micron Optics uniaxial optical accelerometers (Figure 1) in combination with a Hyperion instrument platform as the data acquisition module. Accelerometers have an input range of  $\pm 0.1g$  and  $1g$  when frequencies fall below 10 Hz; the frequency range is between 0 and 100 Hz; an output noise lesser than  $1 \mu g/Hz^{1/2}$ ; and a 2500 nm/g sensitivity. The three devices were fixed to the structure using steel screws which, at the same time, were glued to the structure with a Multi-Component Epoxy Adhesive.



Figure 4 Micron Optics Uniaxial Accelerometer

The vibration measurements were carried out in two steps. Initially, and for the non-damaged structure, an exhaustive ambient vibration test with a multi-setup configuration was carried out to characterize the different modal parameters. Accelerometers were placed longitudinally in 6 different alternating positions: At the upper chords over the joints corresponding to  $\frac{1}{4}$ ,  $\frac{1}{2}$ , and  $\frac{3}{4}$  of the bridge's total length for the two truss systems (Figure 1). Sensor location is justified by the upper chord's relative stiffness in contrast to the other elements, avoiding noise from any local vibrations. For every measurement position, sensors were oriented in longitudinal and perpendicular directions, i.e., along the global x and y-axis. The multi-setup configuration is justified as the measurement locations exceed the available sensors. To correlate the measurements while avoiding the non-stationarity conditions, two sensors located at the first third of the bridge span (in vertical and perpendicular directions) were set as the reference, leaving just one as the moving sensor and, thus, avoiding the zero displacement zones for the different vibration modes. The moving sensor switched location and orientation ten times for wider data acquisition in the ambient vibration measurement.

Vibration modes, frequencies, and periods were determined through the ambient vibration test. Due to time limitations and the project's scope, a mono-setup configuration was picked as the methodology to carry on with the OMA for the damage scenarios. Accelerometers were disposed at  $\frac{1}{4}$ ,  $\frac{1}{2}$ , and  $\frac{3}{4}$  of the bridge's total length with one particularity; the one at the center span was on the other plane. Two measurements were carried out for the mono-setup configuration, orienting the accelerometers in the same direction (perpendicular or vertically) and then



switching orientations. The procedure was executed for every damage scenario in its non-damaged and damaged state. Mono-setup configuration can bring difficulties while identifying torsional modes; however, the issue can be overcome by comparing it with the multi-setup analysis.

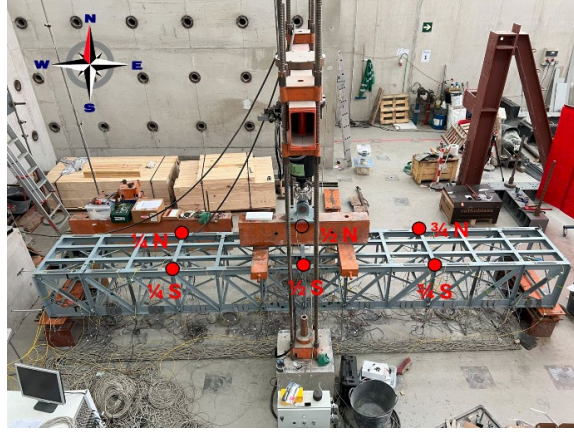


Figure 5 Sensor Locations

### 3 RESULTS

#### 3.1 General Dynamic Response

Vibrations were analyzed with the software ARTeMIS Modal, and modal parameters were determined by the Frequency Domain Decomposition (FDD) technique. The multiset-up analysis allowed the principal vibration modes and their characteristic periods and frequencies to be found. The first two modes are set at 5.8 and 7.9 Hz frequencies, and their behavior is directly related to lateral modes, an expected result as the ball bearing support leaves a little gap allowing horizontal translations. The third mode, with a frequency of 17.77 Hz, corresponds to a clear flexural bending mode and exhibits a single-wave deformation behavior at the center of the span. Mode 4, with a frequency of 20.41, reveals a two-wave lateral bending mode, while mode 5 (23.93 Hz) corresponds to a combination of torsional and lateral modes. A pure torsional mode can be distinguished at a frequency of 30.86 Hz. The 6<sup>th</sup> mode seems to be the limit for recognizable behaviors. Results are arranged and shown in Table 2 and Figure 1.

Mode	Frequency [Hz]	Period [s]	Type
1	5.86	0.171	Lateral
2	7.91	0.126	Lateral
3	17.77	0.056	Vertical Bending
4	20.41	0.049	Two Wave Lateral Bending
5	23.93	0.042	Torsional
6	30.86	0.032	Torsional
7	37.21	0.027	Combination
8	40.33	0.025	Combination
9	44.04	0.023	Combination
10	49.81	0.020	Combination



Table 2 Multi-Setup Vibration Modes and Frequencies

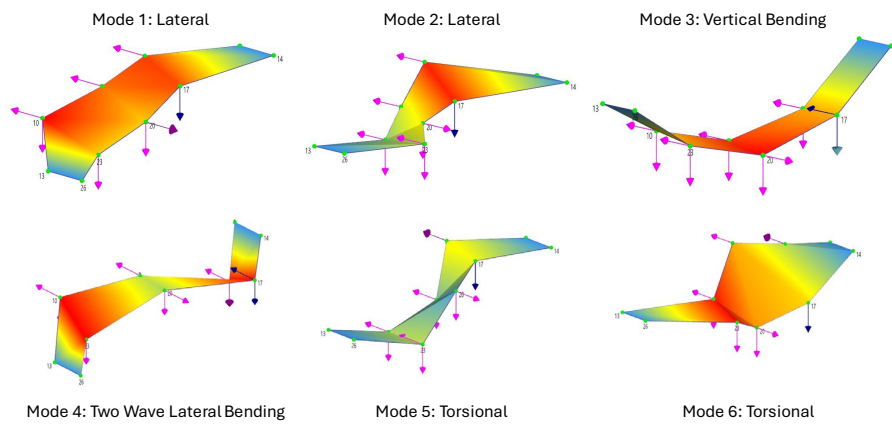


Figure 6 Vibration Modes

### 3.2 Preliminary Results of Damage Scenarios Dynamic Response

As preliminary results of the damage scenarios ambient vibration test analysis, the relative variation of the frequencies are presented in Figure 7 and Figure 8. For both analyses, the structure showed a detectable stiffness degradation. The loss of the bottom chord induced a loss in the vertical bending mode frequency, hence a loss in the bridge's vertical stiffness. On the other hand, the loss of the transversal beam induced drops in the lateral mode characteristic frequency, thus a reduction in its lateral stiffness. More delicate analyses are to be done for other modes and damage scenarios.

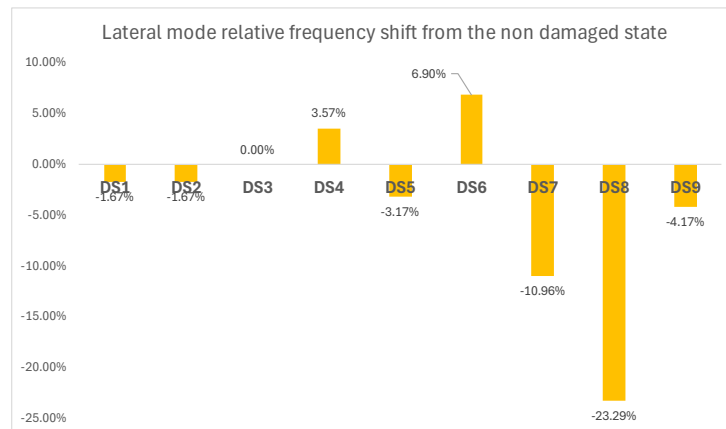


Figure 7 Lateral mode frequency variation for different failure scenarios.

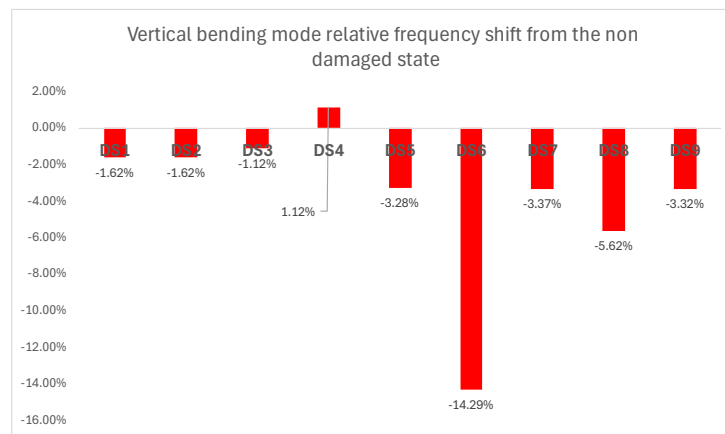


Figure 8 Vertical Bending mode frequency variation for different failure scenarios.

## 4 CONCLUSIONS AND FUTURE WORKS

The OMA analysis with prior multiset up testing configuration proved to be useful for determining the structural dynamic response. The ten measurements helped to categorize the different vibration modes and their characteristic eigenfrequencies and periods. As expected, the bridge with roller support exhibited a dominant lateral mode in the horizontal direction and a dominant vertical bending mode in the vertical direction, while higher frequency modes corresponded to torsional and two wave lateral bending modes combination. The damage scenario's dynamic response preliminary results showed interesting results in sensitivity. Analysis of the dominant horizontal lateral mode and the dominant vertical bending mode showed variations in their respective frequencies, a signal of stiffness loss depending on the damage scenario.

In future works, a deeper analysis of the results obtained for the different scenarios seems to be necessary. Looking for patterns and behaviors over the different vibration modes would be of benefit for anticipating the disproportionate collapse. Additionally, results are to be compared with a well-calibrated numerical model and run multiple failure scenarios.

## 5 ACKNOWLEDGMENTS

The authors wish to acknowledge the funding received for the Pont3 project (ref: PID2021-124236OB-C31) funded by MCIN/AEI/10.13039/501100011033 and "ERDF A Way of Making Europe."

## REFERENCES

- [1] M. Buitrago, E. Bertolesi, P. A. Calderón, and J. M. Adam, "Robustness of steel truss bridges: Laboratory testing of a full-scale 21-metre bridge span," *Structures*, vol. 29, pp. 691–700, Feb. 2021, doi: 10.1016/j.istruc.2020.12.005.
- [2] K. Wardhana and F. C. Hadipriono, "Analysis of Recent Bridge Failures in the United States," *Journal of Performance of Constructed Facilities*, vol. 17, no. 3, pp. 144–150, Aug. 2003, doi: 10.1061/(ASCE)0887-3828(2003)17:3(144).

- [3] J. M. Adam, F. Parisi, J. Sagaseta, and X. Lu, “Research and practice on progressive collapse and robustness of building structures in the 21st century,” *Eng Struct*, vol. 173, pp. 122–149, Oct. 2018, doi: 10.1016/j.engstruct.2018.06.082.
- [4] S. A. Derseh and T. A. Mohammed, “Bridge structures under progressive collapse: A comprehensive state-of-the-art review,” *Results in Engineering*, vol. 18, p. 101090, Jun. 2023, doi: 10.1016/j.rineng.2023.101090.
- [5] S. López, N. Makoond, A. Sánchez-Rodríguez, J. M. Adam, and B. Riveiro, “Learning from failure propagation in steel truss bridges,” *Eng Fail Anal*, vol. 152, p. 107488, Oct. 2023, doi: 10.1016/j.engfailanal.2023.107488.
- [6] G. Anitori, J. R. Casas, and M. Ghosn, “Redundancy and Robustness in the Design and Evaluation of Bridges: European and North American Perspectives,” *Journal of Bridge Engineering*, vol. 18, no. 12, pp. 1241–1251, Dec. 2013, doi: 10.1061/(ASCE)BE.1943-5592.0000545.
- [7] G. Caredda, M. C. Porcu, M. Buitrago, E. Bertolesi, and J. M. Adam, “Analysing local failure scenarios to assess the robustness of steel truss-type bridges,” *Eng Struct*, vol. 262, p. 114341, Jul. 2022, doi: 10.1016/j.engstruct.2022.114341.
- [8] S. Liu, F. M. Bartlett, and W. Zhou, “Alternative Load Paths in Steel through-Truss Bridges: Case Study,” *Journal of Bridge Engineering*, vol. 18, no. 9, pp. 920–928, Sep. 2013, doi: 10.1061/(ASCE)BE.1943-5592.0000436.
- [9] B. Barros, B. Conde, M. Cabaleiro, and B. Riveiro, “Deterministic and probabilistic-based model updating of aging steel bridges,” *Structures*, vol. 54, pp. 89–105, Aug. 2023, doi: 10.1016/j.istruc.2023.05.020.
- [10] X. Chen, H. Li, A. K. Agrawal, M. Ettouney, and H. Wang, “Alternate Load Paths Redundancy Analysis of Steel Truss Bridges,” *Journal of Bridge Engineering*, vol. 27, no. 11, Nov. 2022, doi: 10.1061/(ASCE)BE.1943-5592.0001943.
- [11] G. Brunell and Y. J. Kim, “Effect of local damage on the behavior of a laboratory-scale steel truss bridge,” *Eng Struct*, vol. 48, pp. 281–291, Mar. 2013, doi: 10.1016/j.engstruct.2012.09.017.

## DYNAMIC CHARACTERIZATION AND VIBRATION SERVICEABILITY ASSESSMENT OF AN ULTRA-HIGH STRENGTH CONCRETE FOOTBRIDGE USING NUMERICAL AND EXPERIMENTAL TECHNIQUES

Carlos Rodrigo Villar<sup>1</sup>, María D. Martínez Rodrigo<sup>1</sup>, David Hernández Figueirido<sup>1</sup>,  
Víctor Roda Casanova<sup>1</sup> and Joaquín L. Sancho Bru<sup>1</sup>

<sup>1</sup> Universitat Jaume I  
Av. Vicent Sos Baynat, s/n, 12071, Castello de la Plana, Spain  
e-mail: {crodrigo,mrodrigo,hernandd,vroda,sancho}@uji.es

**Keywords:** Pedestrian bridges, ultra-high strength concrete, finite element modelling, experimental testing, modal analysis and vibration serviceability.

**Abstract.** *Pedestrian bridges, known for their slender and lightweight designs, are susceptible to significant vibrations during operational conditions. This study focuses on the dynamic characterization and numerical simulation of a recently inaugurated pedestrian bridge constructed using ultra-high strength concrete in Puçol, Spain. The slender design of the footbridge coupled with the relatively recent introduction of this material raises concerns about its long-term performance and susceptibility to vibrations. With the aim of characterizing the structure dynamic properties and assessing the level of vibrations induced by crossing pedestrians, different in-situ experimental tests are conducted. Operational modal analysis (OMA) tests, using both a hammer and ambient excitation, are conducted to study the structure dynamic behavior. Furthermore, the vibration serviceability of the structure, based on current codes, is assessed through different tests in which the footbridge is subjected to typical usage conditions, such as pedestrians walking or running across the bridge. Finally, a detailed finite element model of the footbridge is implemented and updated from the dynamic identified properties. From the numerical-experimental comparison, preliminary conclusions are drawn regarding the general state of the footbridge.*

## 1 INTRODUCTION

The present work characterizes the vibrational behavior of lightweight and slender pedestrian bridges using experimental and numerical models. Specifically, studies focus on a footbridge made of Ultra High Performance Concrete in Puçol, Valencian Community

## 2 EXPERIMENTAL PROGRAM

The dynamic properties of the footbridge are characterized applying Operational Modal Analysis (OMA) techniques with 20 piezoelectric seismic mass transducers of the Brüel & Kjaer 8340 model positioned along the structure. The data is acquired with the software BK Connect through two bus modules LAN-XI 25.6 kHz Type 3058, and afterwards is processed using ARTEMIS Modal Pro software. Four modes of interest are identified under 10 Hz: lateral bending ( $f_1=2,45$  Hz ;  $\xi_1=1,17\%$ ), vertical bending ( $f_2=3,09$  Hz ;  $\xi_2=1,03\%$ ), torsion ( $f_3=5,19$  Hz ;  $\xi_3=1,31\%$ ) and the second vertical bending mode ( $f_4=9,86$  Hz ;  $\xi_4=0,67\%$ ).

## 3 SERVICEABILITY ASSESSMENT

The most widely applied guidelines in Europe (HiVoSS and Sétra) are used as a reference to compare the resonance risk of the frequencies obtained. According to both guidelines, the lowest natural frequencies ( $f_1=2,45$ ;  $f_2=3,09$  Hz) fall within the ranges associated with low resonance risk (Figure 1).

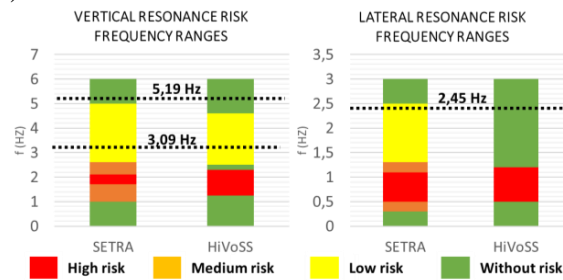


Figure 1: Serviceability assessment.

## 4 NUMERICAL MODEL

The experimental results have been compared to the values provided by a numerical model of the footbridge implemented in SAP2000 (Figure 2). For the development of the footbridge model, a bar-type modelling approach with 3D beam finite elements is chosen, taking advantage of the similarity between the main span structure and a Howe-type truss. The 3,5 cm thick deck is modelled as a thin shell with 24 degrees of freedom. Lastly, a linear and elastic behaviour of the concrete is assumed. The initial values of these properties are shown in Table 1.

The footbridge is simply supported on piers, through neoprene pads, at two points on each end. This type of boundary condition allows displacements along the longitudinal (X) and transverse (Y) axes of the beam. Therefore, these supports are modelled in a first approach as restraints in the vertical axis (Z) at the four corners of the footbridge base.

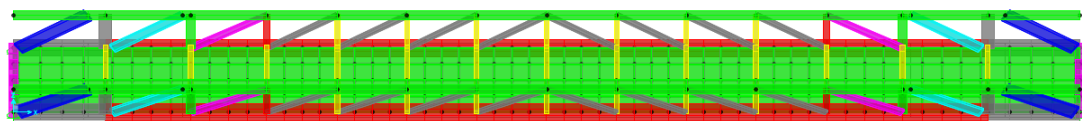


Figure 2: Numerical model of the span with the identification of each element.

## 5 OPTIMIZATION

Finally, the optimization of the numerical model is carried out by defining an objective function (Equation 1) to maximize, which unifies the criteria of relative error in frequency and MAC. The combination of parameters that best fits the numerical model is the one that maximizes this equation, which takes values between [0,1].

$$F_{obj} = \sum_{i=1}^n w_i \cdot (1 - e_i^{freq}) \cdot MAC_i \quad (1)$$

Variations of the nominal properties of the model ( $E_{HPF}$  and  $\rho_{HPF}$ ) of up to  $\pm 10\%$  are considered. The objective function (Equation 1) was calculated with the weights  $w_2 = 0,5$  for the vertical bending mode,  $w_3 = 0,35$  for torsion, and  $w_4 = 0,15$  for the second vertical bending mode. After this process, the final parameters of the model are as follows.

Parameter	Initial Value	Variation	Optimized value
$E_{HPF}$ (GPa)	45	+10%	49,5
$\rho_{HPF}$ (kg/m <sup>3</sup> )	2500	-5%	2375
$E_{HMAR}$ (GPa)	33,6	0%	33,6
$\rho_{HMAR}$ (kg/m <sup>3</sup> )	2300,79	0%	2.300,79
$J_{torsion}$ upper chord (cm <sup>4</sup> )	$3,00 \cdot 10^4$	$\times 3$	$9,00 \cdot 10^4$
$J_{torsion}$ lower chord 1 (cm <sup>4</sup> )	$1,98 \cdot 10^5$	$\times 3$	$5,93 \cdot 10^5$
$J_{torsion}$ lower chord 2 (cm <sup>4</sup> )	$3,73 \cdot 10^5$	$\times 3$	$1,12 \cdot 10^6$

Table 1: Initial and calibrated parameters of the numerical model.

Table 2 represents a comparison between the frequencies of those modes that have been identified in the experimental campaign and the numerical model (Figure 3). The first vibration mode has not been identified numerically.

Mode	Modal shape	Experimental		Initial model	Optimized model
		f (Hz)	$\xi$ (%)	f (Hz)	f (Hz)
1	Lateral bending	2,446	1,170	----	----
2	Vertical bending	3,093	1,026	2,798	2,991
3	Torsion	5,193	1,312	3,869	5,404
4	Vertical bending (2 <sup>nd</sup> )	9,854	0,671	8,925	9,760

Table 2: Comparison of the numerical and experimental model results.

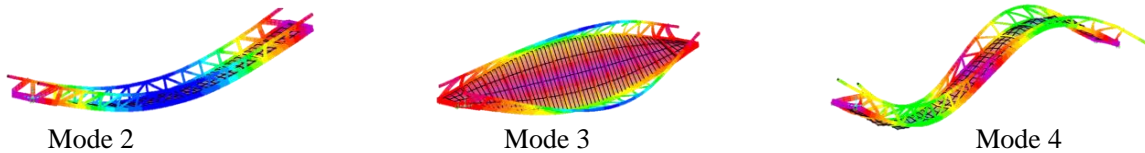


Figure 3: Modal shapes identified with the numerical model.

## 6 CONCLUSION

The modes of the numerical model exhibit values close to the frequencies determined using OMA techniques, with deviations below 5%. However, the first lateral bending mode is not obtained numerically. This aspect is studied in further analysis by introducing the piers into the model and increasing the lateral stiffness of the supports.

## A COMBINED CFD-FEM APPROACH TO STUDY WIND-INDUCED VIBRATIONS IN A REAL CABLE STAYED BRIDGE

María Infantes<sup>1\*</sup>, Ángel Vidal<sup>1</sup>, Manuel Castillo<sup>1</sup> and Álvaro Serrano<sup>2</sup>

<sup>1</sup> MC2 Estudio de Ingeniería, Grupo TYPSA  
C/ Condesa de Venadito 5ª, 28027 Madrid  
e-mail: mc2@mc2.es

<sup>2</sup> Director técnico de MC2 Estudio de Ingeniería, Grupo TYPSA  
C/ Condesa de Venadito 5ª, 28027 Madrid  
e-mail: alvaro.serrano@mc2.es

**Keywords:** Computational fluid dynamics, Wind-induced vibrations, Aerodynamics, Cable stayed bridge.

**Abstract.** *Wind-induced vibrations are currently a major concern in the performance of cable-stayed bridges. The aerodynamic instability study has become a fundamental requirement for the increasingly challenging design of this type of bridge. In the present work, a particular analysis of the wind-induced instability and buffeting responses of a real cable stayed bridge is addressed. The bridge has a span arrangement of 150+400+150 m and its deck is located more than 25.0 m over the SHWL. Pylons are diamond shaped concrete structures 128.50 m high and the deck is a continuous prestressed concrete twin box girder 24.5 m wide and 3.0 m deep. In the analysis, a computational hybrid approach is adopted. A CFD scheme is used to numerically characterize the flutter derivatives of different cross sections of the bridge. For this purpose, several transient calculations with fluid-structure interaction and different boundary conditions are performed. Afterwards, the motion induced load is calculated on the basis of these flutter derivatives. An explicit dynamic analysis is then performed in a 3D FEM model of the complete bridge. The results of this study have made it possible to more confidently define the final design of the bridge, improving its robustness to aeroelastic phenomena.*

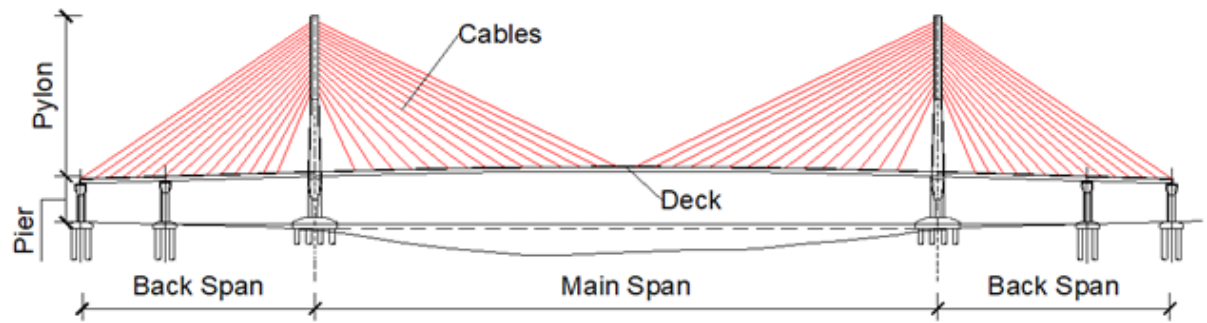


Figure 1: Cable stayed bridge. Elements

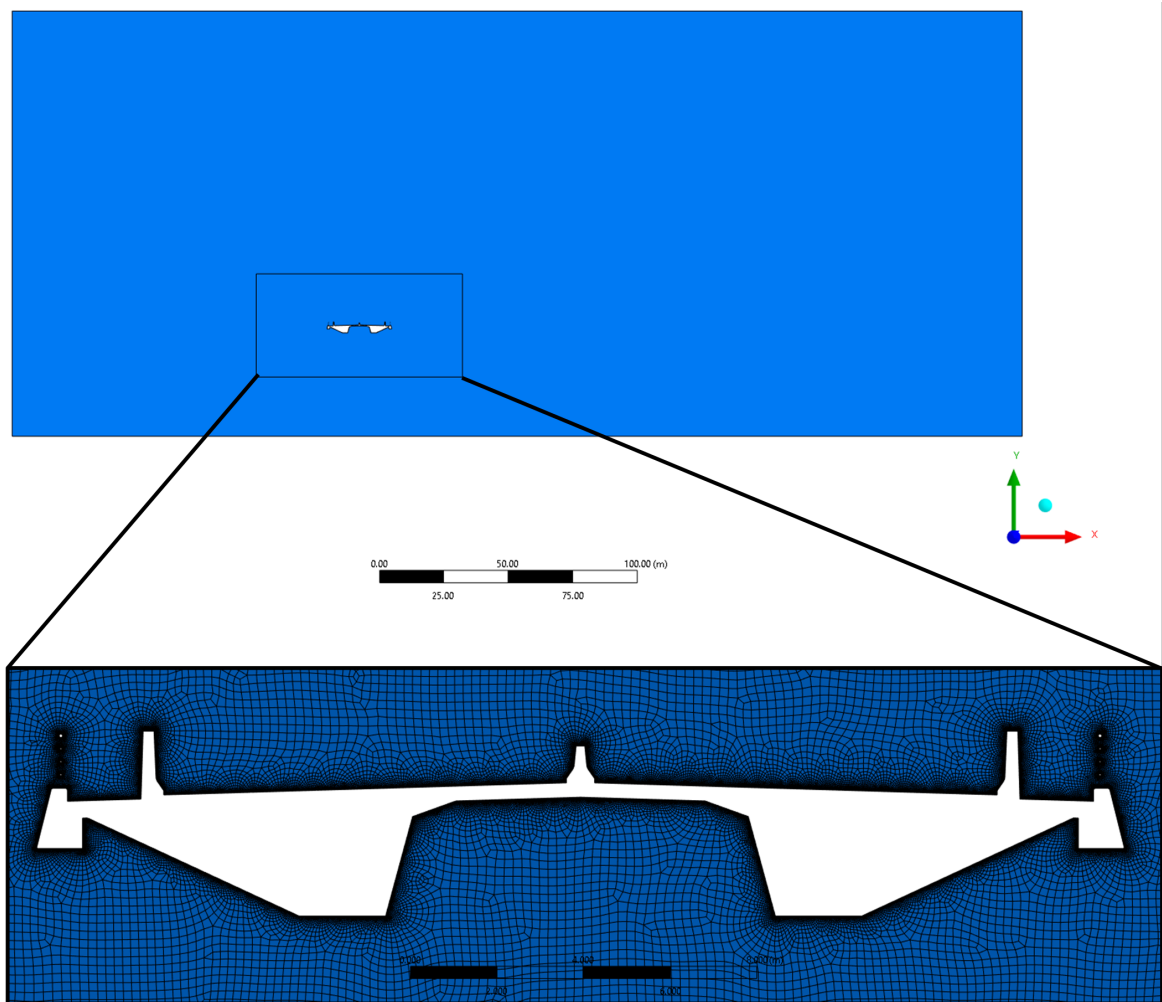


Figure 2: Spatial domain under study. Detail of the mesh in the vicinity of the cross section



**3rd Conference on Structural Dynamics (DinEst 2024)**  
**Seville, September 2024**  
**Seismic engineering and soil-structure dynamic interaction session**

## A MULTI-TASK LEARNING APPROACH FOR DYNAMIC STIFFNESS OF FOUNDATIONS IN POROELASTIC LAYERED MEDIA

Alejandro E. Martínez-Castro (\*)<sup>1</sup>, A. Sánchez López-Cuervo<sup>2</sup>, and R. Gallego<sup>3</sup>

Departamento de Mecánica de Estructuras e Ingeniería Hidráulica. Universidad de Granada

<sup>1</sup>e-mail: [amcastro@ugr.es](mailto:amcastro@ugr.es)

<sup>2</sup>e-mail: [antonioluis@ugr.es](mailto:antonioluis@ugr.es)

<sup>3</sup>e-mail: [gallego@ugr.es](mailto:gallego@ugr.es)

**Keywords:** Dynamic Soil-Structure Interaction, Dynamic Stiffness, Foundations, Boundary Elements

**Abstract.** Efficiently computing the dynamic stiffness of foundations in layered media is a critical undertaking for assessing the dynamic response of vital structures. This is particularly pertinent in the design of offshore wind turbines, where the foundation system's stiffness and damping characteristics play a pivotal role. These attributes are indispensable for predicting fatigue life and determining ultimate limit states. This communication introduces a rapid assessment method employing a meta-model grounded in Deep Learning techniques.

Our proposed model aims to identify an enhanced physical domain through Transfer Learning, transitioning from low-resolution physical domains to more intricate schemes such as complex layered systems and poroelasticity. This approach facilitates a swift evaluation of dynamic stiffness.

To construct the requisite database of dynamic stiffness values, we developed a three-dimensional Green function for multilayered elastic and poroelastic half space in the frequency domain. This function is tailored for source and receiver locations at the top free surface. The fundamental solution incorporates potential displacements, angular Fourier transform, and radial Hankel transform. Implementing the Julia programming language, we optimized the computation of the Inverse Hankel Transform, and a Boundary Element Method code was formulated with a traction singular shape function for rectangular foundations.

To assess the Deep Learning metamodel's adaptability to complex physical domains involving multiple layers and poroelasticity, we expanded the number of features. The initial deep neural network was designed and trained for two-layer elastic half-space configurations. The optimization of network hyperparameters was based on rigorous error analysis. Additionally, a Transfer Learning approach was explored to construct deep neural networks accommodating more advanced physics, including diverse layers and poroelastic properties. The use of a Multi-Task learning approach is explored, and compared to previous works developed by authors.

Numerical tests unequivocally affirm the efficacy of our proposed methodology in rapidly computing the dynamic stiffness of foundations. The low computing times achieved are in line with industry requirements, reinforcing the practicality and efficiency of our approach for real-world applications.

## POST-SEISMIC DYNAMIC PROPERTIES STUDY AND DAMAGE VALIDATION OF A STEEL ARCH BRIDGE WITH AN INTERMEDIATE DECK

José L. Ordoñez<sup>1</sup>, Luis E. Romera<sup>2</sup>, and Arturo N. Fontán<sup>2</sup>

<sup>1</sup> Escuela de Ingeniería Civil

Universidad Técnica de Machala, Av. Panamericana, Vía Pasaje- Machala, Ecuador.

e-mail: [jlordonez@utmachala.edu.ec](mailto:jlordonez@utmachala.edu.ec), web page: <http://www.utmachala.edu.ec>

<sup>2</sup> Mecánica de Estructuras, Centro de Innovación Tecnológica en Edific. e Ing. Civil (CITEEC)

ETSI Caminos, Universidade da Coruña, Campus de Elviña s/n, 15071 Coruña, España.

e-mail: [arturo.fontan@udc.es](mailto:arturo.fontan@udc.es), [l.romera@udc.es](mailto:l.romera@udc.es), web: <http://gme.udc.es/>, <https://www.udc.es/citeec/>

**Keywords:** Seismic design, bridge vibrations, operational modal analysis, damage evaluation

**Abstract.** *On 18 March 2023, an earthquake of magnitude 6.64 Mw occurred in the Gulf of Guayaquil, causing significant damage to various structures in the city of Machala (Ecuador), despite the earthquake having a moderate magnitude. One of the structures affected was the arch bridge presented in this work, located at an epicentral distance of 53 km.*

*The arch bridge is an overpass with a U-shaped geometry, constructed using HSS tubular sections in the arch, deck and hangers (Figure 1). It is used for pedestrian and light vehicle traffic. Following a visual inspection, the main damage observed in the structure was the breakage of some connections of the cross bracing under the deck and cracks in the areas of connection of the foundations with the steel structure of the arch and the hangers (Figure 2).*



Figure 1: Structural system of the arch bridge



Figure 2: Location of damage from the March 2023 earthquake

In order to ascertain the level of safety of the structure following the earthquake and to determine whether the observed damage is limited to that identified in the visual inspection, a three-dimensional numerical model of the structure has been created (Figure 3). The post-seismic dynamic properties of the structure have been experimentally measured using environmental vibration and the installation of accelerometers (Figure 4). The damage observed has been introduced into the numerical model, which shows that the first transverse mode of vibration (X direction) with a period of 0.62 s is the most affected by the damage caused by the earthquake. This period coincides with that obtained in the in-situ measurements, thereby validating the developed numerical model.

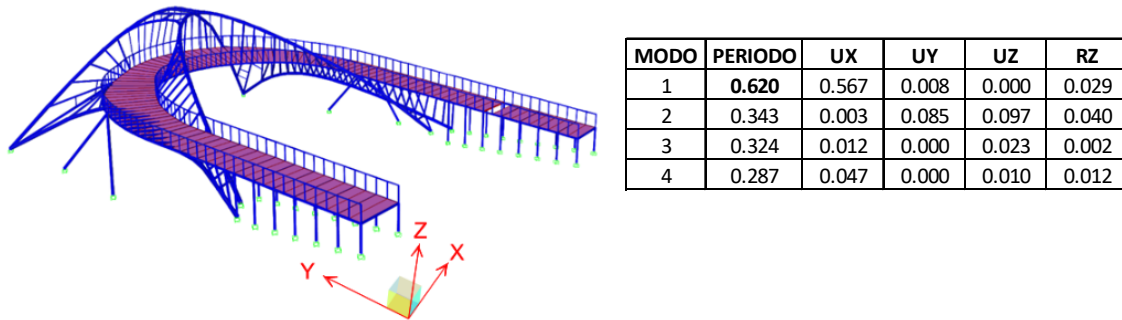


Figure 3: Bridge model: vibration modes and effective masses in each direction

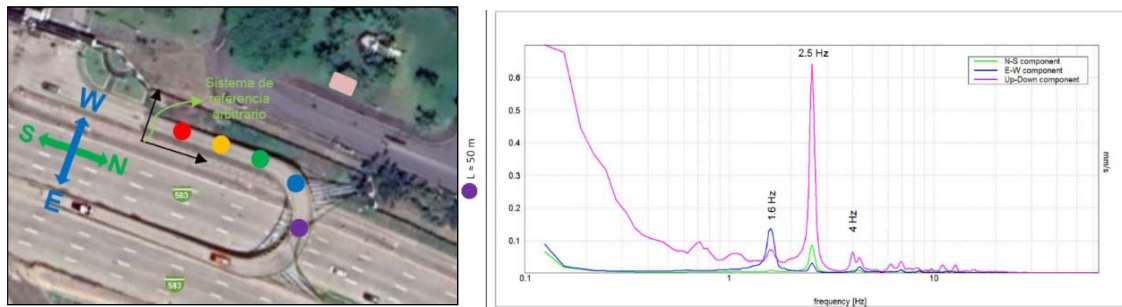


Figure 4: Location of acceleration measurements with ambient vibration and frequency spectra obtained

Furthermore, data from the ACH1 earthquake monitoring station of the Geophysical Institute of the National Polytechnic School of Ecuador, situated at the Technical University of Machala in close proximity to the bridge under study, was utilised to obtain elastic response spectra for the three spatial components of the earthquake (Figure 5).

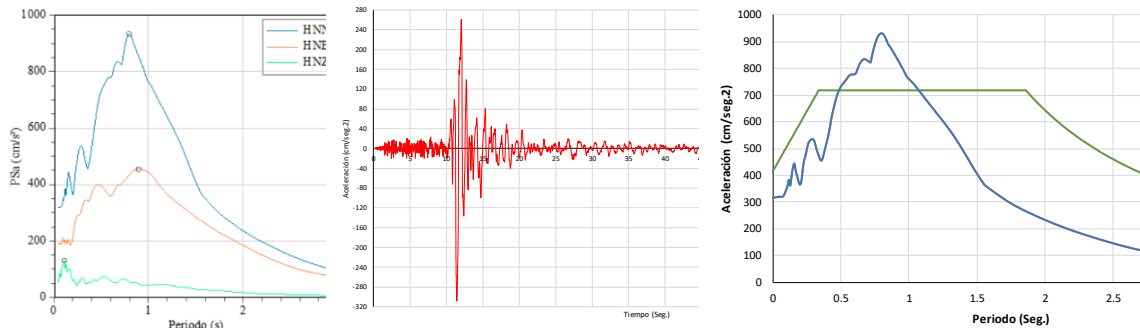


Figure 5: March 2023 earthquake: response spectra of station ACH1 (<https://www.igepn.edu.ec/>), recorded accelerometer and comparison of the measured transverse spectrum with the elastic design spectrum for soft soil E

*The numerical model has been employed to calculate the spectral and temporal response to the earthquake considering both the original state of the bridge and its damaged state, verifying the need for repairs. The refurbishment entailed reinforcing areas of the foundations, installing new bracing and adding SCH40 tubular profiles to the lower part of the deck and the upper central hangers (Figure 6).*



Figure 6: Reinforcement of arches and bridge foundation

*Reinforcements have been introduced into the model to evaluate their effect and the changes in stiffness they introduce. It was found that most of the repairs modify only the vertical stiffness. In the event of a new earthquake, the diagonal bracings are the elements that receive the greatest seismic load, as they already showed rupture in the March 23 earthquake, and will again be the first elements where the bridge will dissipate energy in the transverse direction if a new earthquake occurs. Consequently, it can be argued that these elements should have been reinforced and optimised.*

## DYNAMIC STRUCTURAL RESPONSE OF FOUR-LEGGED JACKET-SUPPORTED OFFSHORE WIND TURBINE CONSIDERING THE EFFECT OF WIND AND SEISMIC GROUND MOTION DIRECTIONALITY

Carlos Romero-Sánchez\* and Luis A. Padrón

Instituto Universitario de Sistemas Inteligentes y Aplicaciones Numéricas en Ingeniería  
Universidad de Las Palmas de Gran Canaria, Las Palmas de Gran Canaria 35017, Spain  
e-mail: {carlos.romero, luis.padron}@ulpgc.es

**Keywords:** Offshore wind turbines, Jacket, Soil-structure interaction, Ground motion directionality, OpenFAST.

**Abstract.** *The expansion of offshore wind energy in recent years has increased the use of jacket substructures and the seismic analysis of offshore wind turbines has become a relevant factor to consider. Jackets are the second preferred choice of developers and are expected to account for 13.4% of the share in the near future [1]. The depth and seismic risk increase the relevance of soil-structure interaction on the design and on the response of the support structures of these turbines.*

*This study aims at investigating the influence of the direction of wind and seismic ground motion on the structural response of four-legged jacket support substructures for Offshore Wind Turbines located in areas with seismic risk. The response of the system is simulated using an OpenFAST [2] model that takes into account multi-support seismic input, soil–structure interaction and kinematic interaction [3]. The NREL 5 MW wind turbine supported on the jacket designed for the phase I of the OC4 project is considered [4]. The parametric analysis is performed considering different angles of wind and seismic shaking direction according to the quarter symmetry of the structure. Specifically, seven wind directions and thirteen seismic ground motion directions were used. In order to study the seismic response, four different accelerograms have been considered, including accelerograms recorded at onshore and offshore stations. The selected recorded accelerograms are normalized to a common Peak Ground Acceleration (PGA).*

*The study discusses the specific ranges of the angle of misalignment between wind and seismic shaking directions within which the maximum internal forces are expected to be found. This usually occurs when the ground motion is aligned with one of the diagonals of the base of the jacket and not aligned with the wind direction. Combinations with aligned wind and ground motion directions are never the worst case. The shaking direction tends to have a large influence on the peak internal forces.*

Furthermore, the results show the significance of the aeroelastic damping, with the highest accelerations at the tower top being observed when seismic shaking acts along the side-to-side direction. This phenomenon can also be observed in the trajectories of the nacelle subjected to the different load directions.

This work was funded by the Ministerio de Ciencia, Innovación y Universidades and the Agencia Estatal de Investigación of Spain (MCIN/AEI/10.13039/501100011033) and FEDER through research project PID2020-120102RB-I00 and the research fellowships TESIS2022010011 (C. Romero Sánchez) from the Program of predoctoral fellowship from the Consejería de Economía, Conocimiento y Empleo (Agencia Canaria de la Investigación, Innovación y Sociedad de la Información), Spain of the Gobierno de Canarias and Fondo Social Europeo.

## References.

- [1] Musial W, Spitsen P, Duffy P, Beiter P, Marquis M, Hammond R, et al. Offshore wind market Report: 2022 edition. Technical report, National Renewable Energy Laboratory (NREL), Golden, CO (Unites States); 2022.
- [2] National Renewable Energy Laboratory. OpenFAST documentation. Release v3.5.2. 2024, <https://openfast.readthedocs.io/en/main/>. Code published at <https://github.com/OpenFAST/openfast>.
- [3] Romero-Sánchez C, Padrón LA. An implementation of multi-support input motion into OpenFAST for the earthquake analysis of offshore wind turbines. *Eccomas Proceedia COMPDYN 2023*;172–185.
- [4] Vorpahl F, Popko W, Kaufer D. Description of a basic model of the “UpWind reference jacket” for code comparison in the OC4 project under IEA Wind Annex XXX. Technical report, Fraunhofer Institute for Wind Energy System Technology (IWES), Germany 450;2011.



## SEISMIC VULNERABILITY OF A '60S REPRESENTATIVE SOCIAL HOUSING TYPE IN MALAGA SPAIN

Beatriz Zapico-Blanco<sup>1\*</sup>, Enrique Vazquez<sup>1</sup>, Antonia Sillero-Ruz<sup>1</sup> and Hermes Ponce Parra<sup>2</sup>

<sup>1</sup> Department of Building Structures and Geotechnical Engineering, Universidad de Sevilla  
Reina Mercedes, 2. 41012 Sevilla, Spain  
{bzapico, ev}@us.es, [antsilruz@alum.us.es](mailto:antsilruz@alum.us.es)

<sup>2</sup> Department of Mechanical Engineering, Universidad Politécnica de Madrid  
Moncloa - Aravaca, 28040 Madrid, Spain  
[hermes.ponce@upm.es](mailto:hermes.ponce@upm.es)

**Keywords:** Seismic Vulnerability Assessment, RFEM6, Social Housing, Numerical Modelling, Reinforce concrete existing Buildings

**Abstract.** *Forecasting future earthquake losses in hazardous zones is a multifaceted challenge, necessitating an evaluation of site-specific seismic hazards and an analysis of building vulnerability in exposed areas. Assessing the seismic vulnerability of each individual structure within a city would demand impractical resources. Consequently, contemporary methodologies rely on the assumption that the attributes and performance of any given building can be approximated by response of a standard structure representing a specific building type.*

*In the context of the social housing complexes constructed in southern Spain during the mid-20th century, this approach is particularly pertinent. Many social housing units were built using similar structures, lacking seismic provisions, not only within the same cluster but also across different regions. These buildings can be divided in few typologies with very little variation. An study on the vulnerability of any of those typologies would be easily extrapolated to extensive exposed areas.*

*This study focuses on medium-rise reinforced concrete apartment buildings, which is found to be one of the prevalent social housing typologies in the region. Computational parametrical modelling is used, first to create a basic model representing the general typology employing Rhino + GrassHopper. Then, this model is adapted to a specific building, located in the city of Málaga. This buildings' original drawings are retrieved from the Municipal Archive and analysed in depth. The main seismic deficiencies of it are highlighted and its geometry, loads and materials are identified and used for the implementation of the specific numerical model. A preliminary seismic analysis is performed on this model using the FEA software RFEM 6. Both the desk study and the numerical analysis point out the vulnerability of the building, and more in-depth analysis are prescribed.*

## 1 INTRODUCTION

Residential neighbourhoods built in Andalusia between the 1950s and 1970s represent an important part of the region's architectural heritage. However, many of these buildings were erected before the implementation of rigorous seismic regulations[2], making them susceptible to structural damage in the event of a significant seismic event. The seismic vulnerability of these old neighbourhoods poses considerable risks to the safety of residents and the integrity of the structures [3]. Earthquakes can cause damage and partial or total collapses of buildings, endangering human lives and causing substantial economic losses.

In addition to the physical hazards, seismic vulnerability also has social and cultural implications. These neighbourhoods often house communities with historical ties and deep-rooted traditions, making their preservation crucial for maintaining the identity and social fabric of cities. Therefore, mitigating the seismic vulnerability in these old residential neighbourhoods is of vital importance, not only to ensure the safety of residents but also to safeguard the architectural and cultural heritage of the region.

The city of Malaga is in one of the areas with the highest seismic risk in Spain, due to its proximity to the subduction zone between the Eurasian and African tectonic plates. Its proximity to the Alboran Fault and other relevant geological structures, combined with its geology, which includes areas of soft alluvial soils that can significantly amplify seismic waves, exposes it to seismic hazard that cannot be ignored. In 1680, for example, an earthquake with an intensity of VIII-IX (EMS-98) shook southeastern Spain, affecting much of the Iberian Peninsula and causing serious damage in the city of Malaga.

Recognized as one of the most important and emblematic cities in the Autonomous Community of Andalusia, Malaga boasts an extensive and varied architectural and urban development. Social housing represents a good portion of this development, especially in the decade of the '60s. In this work, the neighbourhood *25 Años de Paz* has been selected as an exponent of this type of constructions, being highly representative of such buildings.



Figure 1: Málaga, Spain (Google Earth)

The objective of the present work is to carry out a seismic evaluation of a representative social housing neighbourhood from Malaga, to understand the vulnerability of social housing buildings typical from the '60s. The conclusions will serve to propose strategies and recommendations to mitigate seismic vulnerability, preserving architectural heritage and ensuring the safety of the resident communities.

## 2 METHOD

The present work is framed in a larger project (EMC21\_00255) focused on the mitigation of the seismic vulnerability of Andalusian social housing. As such, it builds up on several steps already taken within the project.

First, original drawings of many social housing neighbourhoods have been retrieved from several Andalusian's Archives. These drawings have been thoroughly studied and used to classify the social housing buildings [3]. Out of this, several main typologies have been identified and their structural variables have been determined, classified and parameterized. These variables include the number of floors, the floor height, the number of load bearing frames, their spans, etc..

3D parametric computational models were created for the main typologies, using the software Rhino and Grasshopper. Rhino, formally known as Rhinoceros, is a powerful 3D modelling software widely used in architecture and design. Grasshopper, a visual programming language plugin for Rhino, extends its functionality by enabling parametric modelling and algorithmic design. With Grasshopper, the design can be changed by manipulating geometric shapes and parameters through a node-based interface, allowing for greater flexibility and exploration in the design process. In the project at hand, the duo allows for the creation of basic models that can easily be converted into specific buildings by changing the value of some parameters.

In particular, one building typology outstands for its repetitiveness and potential vulnerability, and this is the H shaped moment resistant reinforced concrete moment frame block from the decade of 1960 [3][6], that can be found in many Spanish cities with virtually the same scheme (Figure 2 and Figure 3). This selection of representative typologies and parametric modelling process is, however, out of the scope of the present work and is only presented here to provide context.



Figure 2: Similar blocks in Sevilla (left), and Jerez (right), Spain. Aereal view (Google Earth).

Going back to the present study, a GIS database of the social housing in the city of Málaga was created, based on open data, like the cadastre. This database was completed with the information retrieved from several archives which were visited (Municipal, Provincial Historical and Urban Planning Department archives), obtaining the original drawings of social housing units. The GIS was used to determine preliminary neighborhoods pertaining to each of the main typologies identified within the project. Out of them, the ones with the most complete original data (mainly drawings) and higher representativeness were identified. Finally, the neighborhood of *25 Años de Paz* was selected, for being the one with the best qualities.

The drawings of the selected project were used to determine the main seismic deficiencies of the constructions. Then, they were also used to adapt the general 3D model of the typology, obtaining a computational model with the geometry and structural composition of the buildings.



Finally, the seismic behaviour of the structural model was analysed, via modal and modal-spectral analysis, to assess the building vulnerability.

### 3 A REPRESENTATIVE NEIGHBOURHOOD: 25 AÑOS DE PAZ, MÁLAGA

The neighbourhood *25 Años de Paz* has been selected as representative of social housing units from the '60s. It was built in 1965 in Huelin, a working-class area of the city. The triangular shape of the plot (Figure 3) allows the neighbourhood to fit seamlessly with the surrounding streets and existing buildings. It comprises, in a nod to its name, 25 housing blocks. All the blocks have an almost north-south orientation. The west of the plot is structured in the form of semi-detached houses that form rows of 3 or 4 buildings, sharing only a portion of one of their facades. On the east side of the plot, however, there are both semi-detached houses and standalone blocks. This variety creates pathways and green areas in the form of plazas and parks, utilizing the spaces that naturally form between the buildings to create public areas.



Figure 3: *25 Años de Paz*, Málaga, Spain (Google Earth)

#### 3.1 The typical unit configuration

The typical units in *25 Años de Paz*, which has five storeys (ground floor plus four), consists of two symmetrical blocks joined by the staircase core, forming an H shape. Each floor houses four apartments, each with a total constructed area of 54.31 m<sup>2</sup>. The use of the H-shaped floor plan appears multiple times in the construction of social neighbourhoods from this period. This responds to a series of architectural, functional, and urban planning factors that make it a very valid option for this type of development. Firstly, the H shape allows all the apartments, even those with a very small floor plan, to have access to natural light and ventilation from two sides. This configuration allows for a better distribution of space, both inside the buildings and in the shared exterior spaces. The courtyards and open areas created between the wings of the building can be used for gardens, playgrounds, or common areas, thereby improving the community environment and fostering social interaction among residents.

The structural system of the blocks in the neighbourhood consists of reinforced concrete moment resistant frames. In total, each unit has five load-bearing frames, three of which are complete, with six bays including the stairway section, and two fragmented ones with four bays, resulting in the characteristic courtyards of the H-shaped blocks (Figure 4).

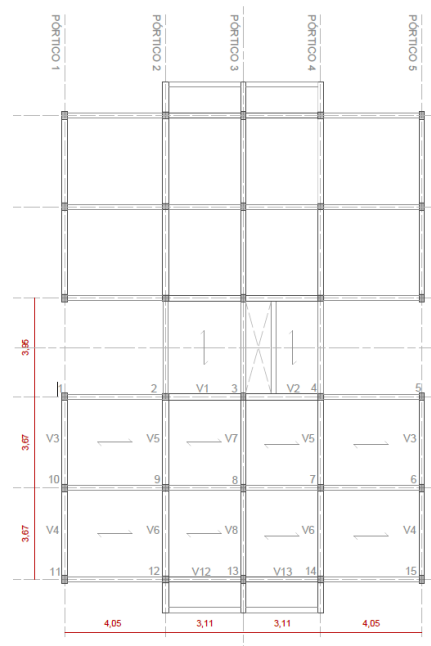


Figure 4: Typical unit structural configuration

The span of the openings is 4.05 m at the ends and 3.11 m at the centre. The span between the floors among the three central frames is 3.67 m, while the outer floors have a span of 3.95 m. These floors are unidirectional, with poured-in-place ribs and ceramic vaults.

The ground floor has a height of 2.5 m, not including the rise of the staircase at ground level, which adds about 0.87 m, making the total 3.37 m. The typical floor has a slightly lesser height of 2.5 m (not including the thickness of the slab), and the roof floor has a height of 2.44 m. The ground floor slab is solved with a slab on crawl space of the same nature as the rest of the floors.

The foundation of the structure is shallow, executed with isolated footings connected by reinforced concrete tie beams (Figure 5).

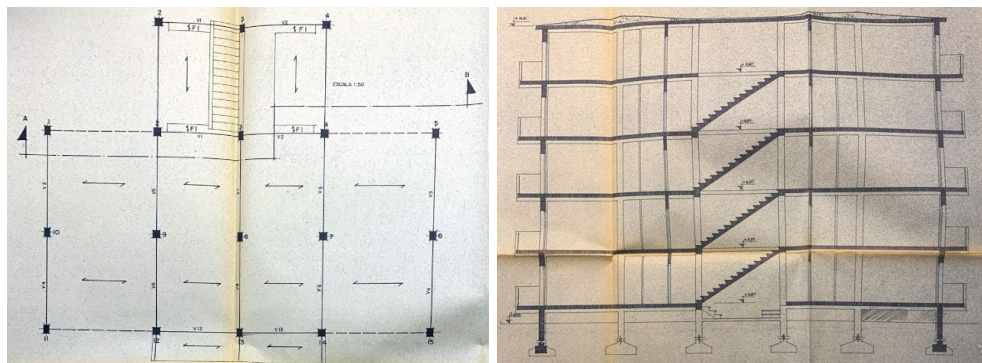


Figure 5: Typical unit plan view and lateral cross section, original drawings, Municipal Archive of Málaga

### 3.2 Main seismic deficiencies detected during the desk study

The units in *25 Años de Paz* display a different lateral load resistance system for each direction. In the direction of the load-bearing frames (strong direction), the system relies on moment resistant beam-column connections. The dynamic behaviour of these connections will strongly influence the building's response and will, in turn, depend on the definition and execution of

the reinforcements. On the perpendicular or weak direction, the system relies on the stiffness of the slabs and their connection to the beams. These slabs, composed of reinforced concrete joists and a layer of composite concrete (of unknown thickness) on top, have a stiffness that is difficult to determine and potentially limited. This asymmetric and potentially low capacity to transfer lateral forces increases the building's vulnerability.

Furthermore, the presence of a slab on crawl space leads to the existence of short columns (Figure 5). During an earthquake, a short column and a regular column with the same cross-section would undergo the same lateral deformation. However, the short column is much stiffer than a regular column, so it will attract a larger portion of the seismic load. If a short column is not designed for this demand, it may suffer significant damage that could lead to failure, usually due to shear.

While the layout of these blocks may appear symmetrical, the presence of the courtyards disrupts the structural system and weakens its response to dynamic loads. Additionally, for adjacent buildings, the inadequacy of their structural connections fails to prevent collisions between buildings in the event of a seismic event.

The updated seismic hazard map [1] assigns Málaga a base ground acceleration of 0.16g, corresponding to a moderate to high hazard level. However, a large part of Málaga sits on soft alluvial soils, such as Huelin and the neighbourhood under discussion [4]. These soils amplify ground shaking during an earthquake, increasing the effects on buildings. According to the study by Irizarry [4], the seismic amplification produced by the soil in the location of the neighbourhood is significant, with an increase of up to one point in macroseismic intensity, reaching a scenario of intensity VIII-IX.

Although the socio-economic situation of a neighbourhood does not directly impact its seismic vulnerability, they are related. Low-income communities have fewer resources to invest in preparedness and building maintenance measures and often have less access to information and education about seismic risks. After an earthquake, these communities face greater challenges in recovery and rebuilding, prolonging the disruption. According to Instituto Nacional de Estadística ([INE](#)), the average household income varies significantly, and the buildings studied show incomes of around 10.000 euros, indicating a low to medium socio-economic level, aligned with vulnerable areas according to Egea [5].

For all these reasons, a more in-depth study of the seismic performance of these structures is prescribed.

## 4 COMPUTATIONAL MODELLING

The computational analysis of structures plays a crucial role in the structural design and analysis of buildings. Through the use of specialized software, it is possible to create detailed virtual models of structures. These models allow for analyzing the behavior of materials, evaluating applied loads and forces, and predicting how the structure will respond to different scenarios, such as earthquakes or wind loads.

In this work, the program [RFEM 6](#) has been employed. RFEM 6 is a cutting-edge structural Finite Element analysis and design software developed by Dlubal Software. It can be integrated with Rhino, being able to import geometries and loads generated by this program.

### 4.1 Building geometry materials and cross section definition

Based on the data obtained from the project original documentation and site visits, a geometric model has been developed. One of the general 3D models created within the project for H shaped buildings (see section 2) was used and adapted to the case at hand (Figure 6), using Rhino and GrassHopper.

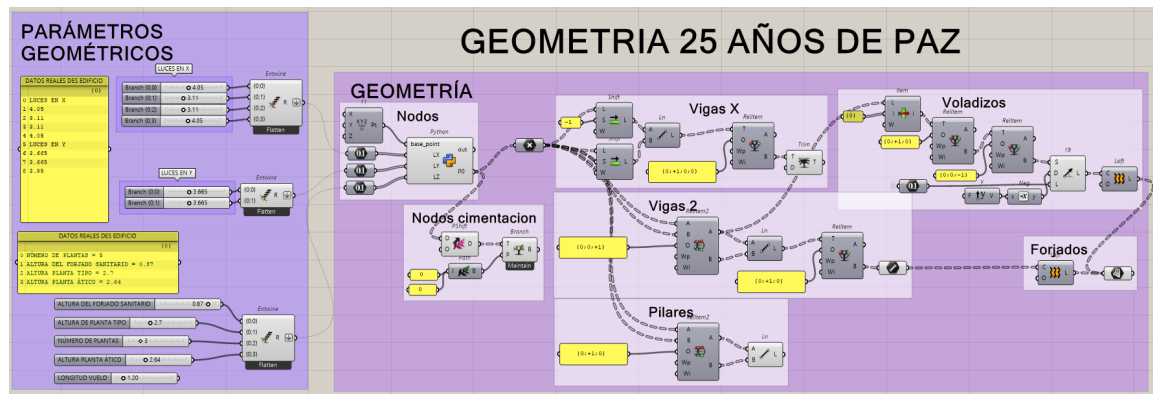


Figure 6: Grasshopper definition for developing the geometry of the structure

The resulting 3D model is then exported to RFEM 6. Here, the materials (concrete and steel) data have been defined for linear elastic analysis, and the sections have been assigned according to the information in the original drawings (Figure 5).

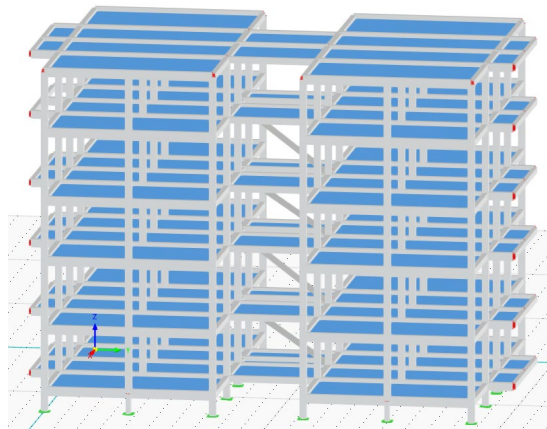


Figure 7: Structural model in RFEM

The resulting model includes bar elements to simulate beams and columns, and surface elements to simulate floor slabs. The latter, being one-way spanning slabs, have only been considered to account for self-weight and to distribute other loads. They have not been assigned stiffness to contribute to the structural analysis.

A rigid diaphragm constraint has been assumed at the nodes of each floor level. The brick masonry elements have not been considered as structural members; only their weight has been taken into account. The structure is considered fixed at the foundation level, without soil-structure interaction.

The materials used in the model are C16/20 concrete and B420S reinforcing steel. The rigidity modifications specified by EC8-4.3.1(7) have not been taken into account.

#### 4.2 Load Definition

Actions from EN 1991-1, with the Spanish National Annexes CEN 2015-09, and the Spanish code NCSE-02 for seismic action have been considered, and EN 1992-1 with the National Annex CEN 2014-11 has been considered for concrete design.

In particular, the permanent gravitational action, two variable gravitational load cases for the typical floor and roof, one snow load case, two wind load cases, and the seismic action have been accounted for.

For the seismic calculation, a basal seismic acceleration of 0.16g has been selected, in accordance with the code. Two calculations have been performed, considering both non-ductile and low-ductility behaviour.

Two design situations have been defined:

- ULS (STR/GEO) - Permanent and transient, according to EN 1990 UNE 2019-04 Eq. 6.10
- ULS (EQU) - Seismic according to EN 1990 UNE 2019-04

The program automatically generates the load combination cases for each considered design situation in accordance with the selected code.

### 4.3 Analysis

In this preliminary study, the model has been analysed for the two design situations described above, obtaining diagrams of internal forces and nodal displacements. The forces have been verified for the permanent and transient load combinations (STR/GEO) and for the seismic load combinations. In addition to this, a modal response spectrum analysis has been implemented.

In a second step, a concrete member checks have been performed, in order to verify whether the existing reinforcement is sufficient for the applied loads.

## 5 RESULTS AND DISCUSSION

After performing the analysis, it was verified that the sections of the members are adequate to withstand the forces due to both permanent and variable loads.

In line with the consideration made in 3.2, the modal analysis shows that the first mode has an excessively high period (1.30 s), probably due to the fact that the tie beams do not provide sufficient stiffness to stabilize the model. This is also observed in the displacement results plot for the seismic combination in the x-direction (tie frames), where displacements of 7 cm appear at the building top, equivalent to a drift ratio of  $H/212$  (Figure 8).



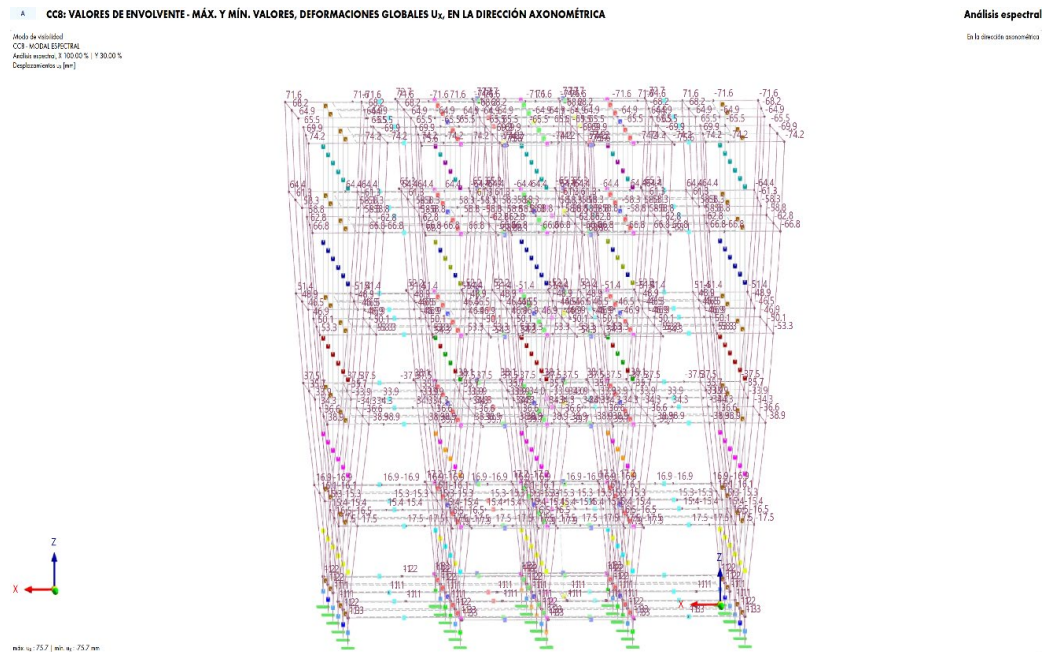


Figure 8: Displacement results plot for the seismic combination in the x-direction

In the direction of the gravity frames, the fundamental period is 0.63 s, suitable for a 6-story building, and the maximum displacement at the top for the seismic combination in the Y-direction is 4.1 cm (H/362).

Analysing the results of the seismic loading combinations, moment reversals are observed in the beams (Figure 9), which are not designed for such an effect. If the beam reinforcement detailing is reviewed, it is found that the anchorage length of the bottom bars is not adequate for developing tension at the bar ends.

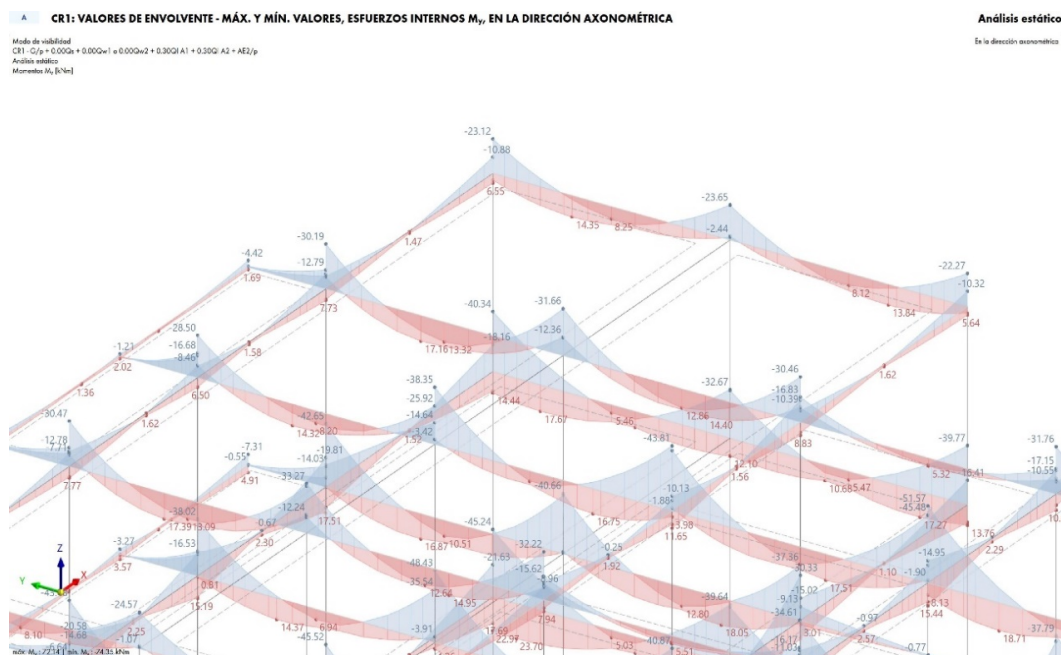


Figure 9: Bending moment reversal in beams

Additionally, the column checks performed by the program indicate that there is a large number of members with insufficient reinforcement (Figure 10).

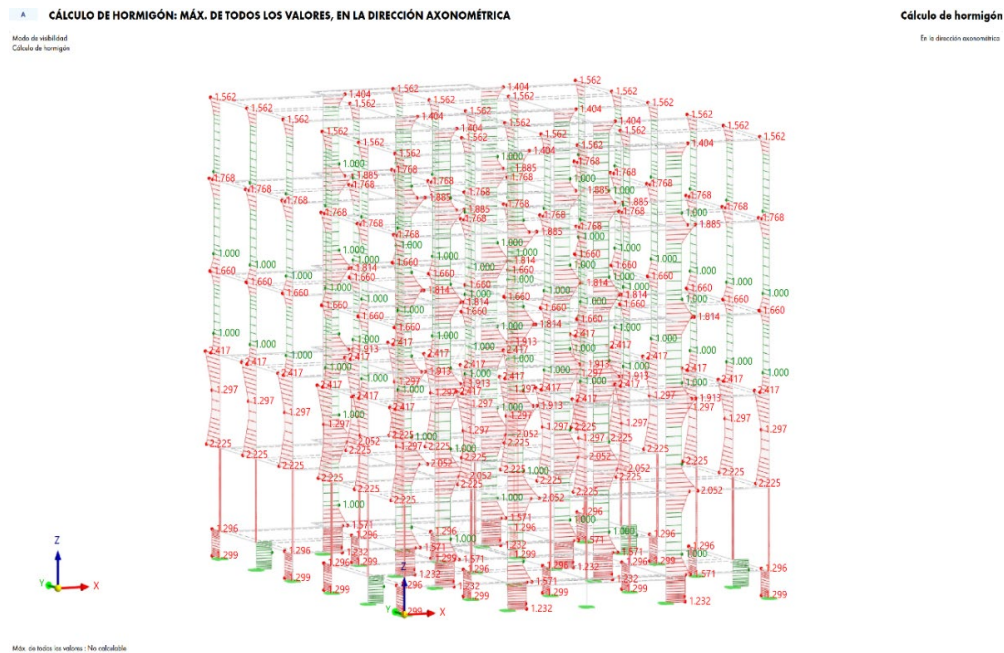


Figure 10: Concrete bars utilization factor. Bars in red show insufficient reinforcement.

The existing reinforcement does not meet the code requirements for zones with a design seismic acceleration equal to or greater than 0.12g, for example the maximum tie spacing criterion.

In general, some of the basic premises of seismic design are not met, such as avoiding short columns, or dimensioning the structural joints with a spacing greater than twice the maximum seismic displacement.

Structural retrofitting is often necessary for existing buildings that do not meet current seismic design codes. Some potential reinforcement measures include:

- Adding new structural elements like concrete shear walls or steel bracing to increase lateral stiffness and strength.
- Jacketing of columns with steel casings or concrete encasement to enhance shear and confinement capacity.
- Strengthening of inadequate beam-column joints with steel haunch elements or fiber-reinforced polymer wrapping.

The selection of techniques depends on the specific deficiencies identified, construction materials, architectural constraints, and cost considerations. In particular, seismic retrofitting of aged urban residential areas presents unique challenges, such as:

- Extensive building inventories requiring evaluation and potential reinforcement.
- Complexity of implementing comprehensive interventions across multiple privately-owned properties.
- Constrained urban layouts that limit accessibility for construction activities.
- Necessity to minimize disruptions and the temporary relocation of residents.

- Variability in existing construction materials, methods, and states of preservation.
- Limited financial resources of homeowners or communities.

Key considerations include the development of cost-effective, standardized retrofit solutions, the creation of incentive programs, the establishment of legislative frameworks for mandatory actions, and the implementation of community outreach and participatory processes. An area-wide approach, rather than focusing on individual buildings, may prove more effective.

## 6 CONCLUSIONS

In the present study, the seismic vulnerability of a typical Spanish social housing unit from the '60s has been assessed. For that end, a numerical model of a representative neighbourhood in the city of Malaga has been used, performing a modal response spectrum analysis.

The analysis results for the case study building highlight key seismic vulnerabilities that require mitigation. While the forces from gravity loads are acceptable, the structural system exhibits excessive lateral flexibility, with the first mode period being excessively high due to inadequate tie beam stiffness. Seismic displacements are significant in the tie beam frames direction. Moreover, the beams are not suitably detailed for moment reversal effects, with inadequate bar anchorage lengths. Numerous columns have insufficient reinforcement, not meeting code requirements for the design seismic acceleration. These deficiencies underscore the need for comprehensive seismic retrofitting.

The seismic assessment and retrofitting of existing buildings present multifaceted challenges that require carefully considered solutions. While structural interventions are often necessary to enhance life safety and mitigate seismic vulnerabilities, they must be balanced with preserving architectural heritage values.

For individual buildings, a range of retrofit techniques are available depending on the specific deficiencies and construction typologies. These include adding new lateral load-resisting elements, enhancing deformation capacities of existing members and, improving load transfer mechanisms. Judicious selection and design of retrofit measures should aim to minimize impacts on the aesthetic, authentic fabric of the structure.

When addressing seismic risk in old urban residential neighbourhoods, the complexities are further amplified. Large building inventories, private ownership patterns, restrictive site constraints, and socioeconomic factors necessitate a coordinated, area-based approach. Affordable standardized retrofitting schemes, legislative mandates, financial incentives, and inclusive community outreach processes may facilitate more effective mitigation.

## 7 ACKNOWLEDGEMENTS

This work is part of the project EMC21\_00255 *Mitigation of seismic vulnerability of residential buildings in large, old neighborhoods in Andalusia*, funded by the Junta de Andalucía, Consejería de Universidad, Investigación e Innovación, through its EMERGIA program for research talent attraction.

The research team would like to express gratitude to the Municipal Archive of Málaga, The Provincial Historical Archive of Málaga and the Municipal Management of Urban Planning, Works, and Infrastructure of Málaga City Council, particularly Enrique Doncel González. Their collaboration made this work possible.

## REFERENCES

- [1] IGME (Instituto Geológico y Minero de España). ZESIS (Zonificación Sísmica de España). [Online]. Available: [info.igme.es/zesis](http://info.igme.es/zesis) [Accessed: May 29, 2024].
- [2] Ministerio de Planificación del Desarrollo “Norma Sismorresistente P.D.S-1”, Gobierno de España, 1974. (Decreto 3209/1974, de 30 de agosto, BOE núm 279).
- [3] Zapico-Blanco B. et al, Seismic vulnerability preliminary assessment of southern Spain social housing from 1965 to 1975”, *Proceedings of the 18th World Conference on Earthquake Engineering*, Milan, Italy, 2024.
- [4] Irizarry, J., et al. “Escenarios de riesgo sísmico para la ciudad de Málaga”. 3er congreso nacional de ingeniería sísmica. Asociación Española de Ingeniería sísmica Girona, 8-11 mayo 2007.
- [5] Egea, C., Nieto, J.A., Domínguez, J. and González, R., (2008). Vulnerabilidad del tejido social de los barrios desfavorecidos de Andalucía. Centro de Estudios Andaluces, Consejería de la Presidencia, Junta de Andalucía. ISBN: 978-84-691-4406-0
- [6] Zapico-Blanco B., Quezada, M. Vázquez, E., Morales-Ramirez, A., Pineda, P. & Escolano D. (2024). Seismic vulnerability a 1950-1960s representative Social Housing type in southern Spain, *Proceedings of the 18th World Conference on Earthquake Engineering*, Milan, Italy.

## SEISMIC VULNERABILITY ASSESSMENT OF SOCIAL HOUSING UNITS IN AYAMONTE (SW IBERIAN PENINSULA)

Beatriz Zapico-Blanco<sup>1\*</sup>, Carlos Baena-Arrabal<sup>1</sup> and Francisco M. Alonso-Chaves<sup>2</sup>

<sup>1</sup> Department of Building Structures and Geotechnical Engineering, Universidad de Sevilla  
Reina Mercedes, 2. 41012 Sevilla, Spain  
bzapico@us.es

<sup>2</sup> Department of Earth Sciences, Universidad de Huelva  
Bulevar de las Artes y las Ciencias, s/n., 21007 Huelva, Spain  
alonso@uhu.es

**Keywords:** Seismic Vulnerability Assessment, Vulnerability Index, Macroseismic Method, Social Housing, Ayamonte, GIS.

**Abstract.** Ayamonte is a city in the south-western of Iberian peninsula, close to the border with Portugal. It is located in a seismically active region, influenced by the Azores-Gibraltar Transform Fault. Some historical events associated with this fault are the 1755 Lisbon earthquake, one of the most devastating shakings in recorded history, which seriously affected Ayamonte: the bell tower of the Parish Church of El Salvador that was destroyed, as well as the temple of San Francisco and the convent of Santa Clara. In addition to this, the city is mainly located on marshland, a soft kind of soil that increases the intensity of the shaking experimented by the buildings through the amplification of the seismic ways as they travel through it. The lack of risk awareness among the population and insufficient preventive measures from institutions further exacerbated the challenge.

*In some of its neighborhoods, the city's vulnerability to seismic hazards is heightened by the elevated amount of social housing units, characterized by limited budgets, lack of seismic considerations, and minimal architectural diversity. Typically housing socially vulnerable residents and facing high population density, these communities are more susceptible to seismic risks, but these factors also contribute to an exponential impact of its seismic vulnerability study and risk mitigation.*

*In the present work, the seismic vulnerability assessment of Ayamonte's social housing buildings is undertaken. The foundation of the study involves extensive data collection, utilizing a Geographic Information System (GIS) database created with open sources like the cadastre and Google Maps. The GIS incorporates the characteristics of identified neighborhoods to determine building typology. A thorough examination of original drawings, technical specifications, and visual inspections is carried out to extract crucial parameters for understanding the seismic response of each building type. Subsequently, a vulnerability assessment is conducted using the vulnerability index method defined in the European Macro-Seismic approach, modified by the authors to adapt to Spanish post-war construction. The average expected damage state is Moderate to Heavy, which involve important reparations and evacuation of the inhabitants which could be avoided by preventive and sustainable interventions.*



## 1 INTRODUCTION

Ayamonte is a city in the southwest of the Iberian Peninsula, located on the eastern bank of the Guadiana River estuary, on the border between Spain and Portugal. It is situated in a seismically active region, integrated into seismic zone number 13 of Iberia [1]. Seismicity in the region is related to the Azores – Gibraltar fracture zone. This zone crosses the Gulf of Cadiz from west to east, generating diffuse seismicity that has been explained in a tectonic scenario known in geological literature as the San Vicente Transpressive Zone [2]. Among other historical seismic events in this region is the 1755 Lisbon earthquake, which was one of the most devastating tremors recorded in recent history along with the subsequent tsunami, or the 1969 Horseshoe earthquake, with a magnitude of 7.9, with a maximum intensity of VIII-IX, felt with intensity VI in Ayamonte. Additionally, the city is partially located on marshland, a type of soft soil that increases the intensity of the tremor experienced by buildings by amplifying seismic waves as they pass through.



Figure 1: Ayamonte, Huelva, Spain (Google Earth)

During the decades of the 1950s, 60s, and 70s, due to the country's reindustrialization and the population flow from rural to urban areas, Spain experienced a great need for housing in cities. The response to this need was the construction of thousands of units of social housing, creating new residential areas in the peripheral zones of many cities. Spain did not have modern seismic codes until 1974, when the Seismic Resistant Construction Standard (NCSR) was published [3]. Therefore, these units of social housing were built without seismic considerations. These buildings, having already exceeded their useful life, are often located in socially vulnerable areas of the city and, consequently, are usually poorly maintained. These facts, combined with the typically low construction quality of these neighbourhoods, suggest that their seismic vulnerability may be high, as seen in the deficiencies identified in this type of building by the authors [4]. As a result, a seismic event in the area could cause serious damage, generating the need for repair and renovation works, and even, depending on the level of damage, demolition and reconstruction. Buildings and their technologies significantly impact the environment: they

account for 40% of energy consumption, a third of greenhouse gas emissions, 30% of raw material use, and 25% of solid waste [5]. Repairs generate CO<sub>2</sub> and may require relocations, increasing unsustainability after earthquakes. In most cases, these neighbourhoods have been designed following very similar typologies. Therefore, the assessment of the seismic vulnerability of these buildings has a potentially considerable impact, and the results could be extrapolated not only to other cities in Spain but also to international contexts.

The objective of the present work is to carry out a macroseismic evaluation of the city of Ayamonte, to understand the vulnerability of its social housing buildings. The work constitutes an essential first step for the mitigation of this vulnerability.

## 2 METHOD

For the assessment of the seismic vulnerability of social housing buildings in Ayamonte, the Vulnerability Index Method has been employed, specifically the LM1 or macroseismic method defined in the Risk-UE project [6]. This method is suitable for European residential buildings and for working on a macro-scale, that is, on entire populations rather than specific buildings. Vulnerability index values are assigned to each building based on a series of parameters, obtained from the observation of post-earthquake damage in various European locations. Consequently, it follows a Performance-Based Design (PBD) philosophy. A given vulnerability index will result in an expected level of damage for a certain seismic action. This action is expressed in terms of intensity. The method has been modified and adapted by the authors to the particularities of Spanish post-war constructions.

A typological vulnerability index is first determined, based on the structural system of the buildings. In the case at hand, two structural systems have been identified: unreinforced masonry load-bearing walls (URM) and moment resistant reinforced concrete frames (RC). The typological vulnerability indexes for these two systems are 0.74 and 0.64, respectively.

Next, a series of vulnerability index modifiers are determined for each building, based on geometrical and mechanical parameters, which allow for a more detailed evaluation. In this case, the following modifiers were selected: soil type, seismic design level of the current code, vertical irregularity, presence of soft story and short columns, plan irregularity, slope of the ground, relative position in height and plan within the block, and misalignment of floors.

Three complementary sources were used to determine the parameters. Firstly, a GIS was created from open data sources such as the cadastre, INE, IGN, etc. From these sources, data on the footprint, perimeter, and shape of the buildings, year of construction, ground slope, etc., were extracted. Secondly, the digitization of original project documents of the buildings, found in the Municipal Archive of Ayamonte, was carried out. The in-depth analysis of these documents (plans, reports, measurements, etc.) allows for an understanding of the structural system of the buildings, their construction details, the existence of short columns or misaligned floors, etc. Finally, to complete the information, an exterior visual inspection of the buildings was conducted, partly in situ and partly through Google Maps, Google Street View, and Google Earth.

Once the total vulnerability index for each building is obtained, its expected damage is calculated using the following correlation (1) by Bernardini [7]:

$$\mu = 2,5 + \tanh \left( \frac{I + 6,25 \cdot V - 13,1}{2,3} \right) \quad (1)$$

where  $\mu$  is the estimated mean damage,  $V$  is the total vulnerability index, and  $I$  is the seismic intensity of the considered scenario. This value is used to determine the expected damage state [8], which can range from *None* to *Destruction*.

### 3 GEOLOGICAL FRAMEWORK

The recent tectonic uplift of the southwest of the Iberian Peninsula has exposed rocks in Ayamonte that were deposited on the continental margin of the peninsula during its Mesozoic geodynamic evolution, as well as its variscan basement (Figure 2). Over both types of tectonic units (with basement-cover type geometric relationships) lie Neogene sediments from the Guadalquivir Basin and Quaternary (unconsolidated) materials. The variscan basement is composed of an alternation of Carboniferous slates and greywackes, and discordantly over them, red sandstones attributed to the beginning of sedimentation during the Triassic outcrop. These materials are arranged NNE-SSW and dip towards the SE. The assemblage is located on the northern margin of the Hoya Cabrera gully. To the south of this gully, the rest of the Mesozoic sedimentary cover outcrops, consisting of various types of carbonate, volcanic, and volcano-sedimentary rocks. These rocks follow a NNE-WSW trend and dip gently, also towards the SE. The historic centre of Ayamonte is situated on these materials, and the soil there can be considered as hard (Figure 2).

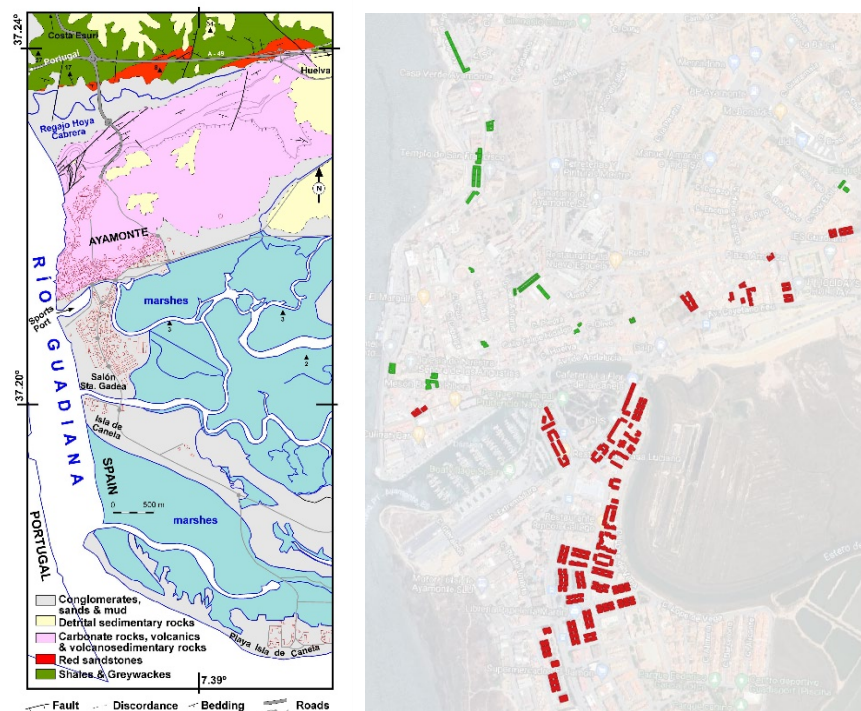


Figure 2: Geological map of Ayamonte (left) and type of soil considered for each building unit (right), developed by the authors.

The Neogene sediments of Miocene-Pliocene age are conglomerate and sand strata (with varying grain sizes), discordant over the previous units. These detrital sediments outcrop in the topographically highest parts coinciding with the reliefs to the north and northeast of Ayamonte. The Quaternary materials (conglomerates, sands and muds) extend widely over the topographically lowest areas surrounding the city of Ayamonte. These deposits represent sedimentation associated with estuarine environments, as well as various surface forms associated with the current coastal dynamics. These materials typically outcrop at altitudes below 10 meters and have low cohesion (in some cases, none). The marina area and the urban development in the southernmost part of the city, such as the Salón de Santa Gadea, are situated on these materials, where the ground can be considered as "soft" for the purposes of this study (Figure 2).



#### 4 SEISMIC SCENARIOS CONSIDERED

The LM1 macroseismic method defines seismic action deterministically using intensity. In this study, the 1755 Lisbon earthquake has been chosen for this scenario. To enable a comparison, a second probabilistic scenario based on Eurocode 8 [9] is also considered.

Known as the Great Lisbon Earthquake, the earthquake on November 1, 1755, is regarded as one of the most significant events to have occurred in Western Europe. Located southwest of Cape St. Vincent, it is assigned an approximate magnitude of 8.5 [10]. The earthquake and subsequent tsunami caused extensive destruction and countless deaths in Portugal and Spain. Figure 6 shows the intensities assigned by [10] in southwest Spain, where Ayamonte experienced an intensity of VII (Figure 3).

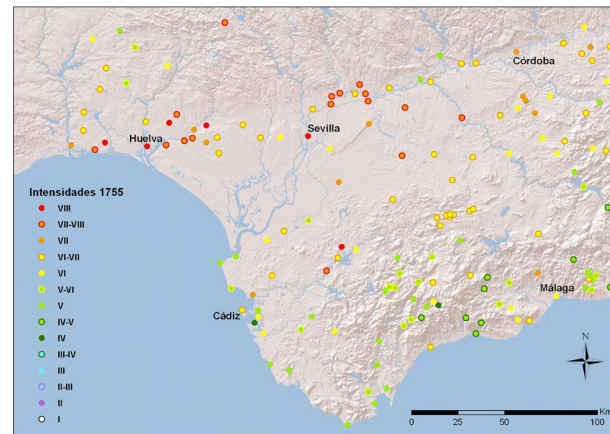


Figure 3: Intensities assigned for the 1755 Lisbon earthquake [11].

Regarding the probabilistic scenario, Eurocode 8 and the new Spanish standard still under review, NCSR-23, define seismic action through peak ground acceleration on type A soil ( $a_{gR}$ ). For Ayamonte, this value is 0.12g for a return period of 475 years according to the Spanish Hazard map [12]. According to the correlation between  $a_{gR}$  and seismic intensity proposed by the IGN [12], the resulting intensity is VI-VII.

Consequently, an intensity of VII, covering both the deterministic scenario of the Lisbon earthquake and the probabilistic scenario based on the codes, will be considered.

#### 5 DAMAGE STATES

For the definition of damage states, this study is based on the work of Lantada [13], which in turn is based on [8], where the following categorisation is established (Table 1):

Mean damage (m)	Expected Damage State	Description
0.0 – 0.5	None	-
0.5 – 1.5	Slight	Appearance of initial cracks
1.5 – 2.5	Moderated	Appearance of many cracks in structural elements. Repair is necessary.
2.5 – 3.5	Heavy	Cracks in all structural elements, some severe. The building cannot be occupied.
3.5 – 4.5	Very Heavy	Collapse of structural elements. Demolition is necessary.
4.5 – 5.0	Destruction	Collapse or very close or collapse

Table 1: Damage states description

## 6 BUILDING ANALYSIS - CORRELATIONS

Based on data from the cadastre, the city of Ayamonte has a total of 2,984 buildings, of which 2,563 are residential. Over 700 of these residential units were constructed in the post-war period, as shown in Table 2. Of these, 243 units are designated as social housing.

Decade	Number of residential buildings constructed	Number of social housing units constructed
'50s	273	6
'60s	219	133
'70s	226	104

Table 2: Residential units built per decade in Ayamonte.

The original project documents for 141 of these units were digitised and analysed, while the information for the remaining units was completed through external visual inspection, expert opinion and inference rules.

When analysing exclusively the units for which original project data is available, a correlation can be found between the design year and the building typology. URM buildings are the earliest to appear chronologically, being the only typology present in projects from the 1950s and part of the 1960s. In 1968, this structural type disappears, giving way to RC structures (Figure 4).

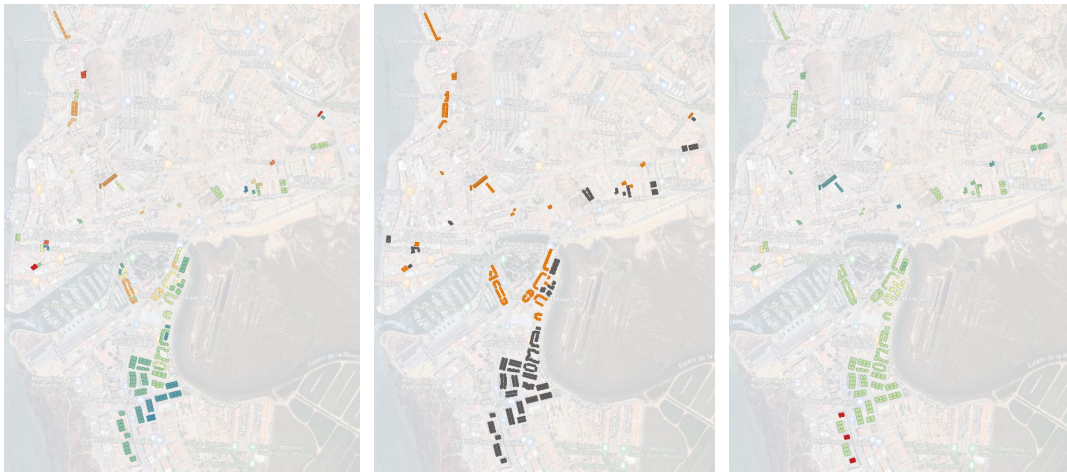


Figure 4: Representation of the buildings under study in the implemented QGIS. Left: Project year, from 1950 (red) to 1975 (blue). Centre: Structural typology: RC (grey) and URM (orange). Right: Number of storeys, from 2 (blue) to 8 (red).

On the other hand, the design date is not present in the cadastre, but the construction date is. This date is, on average, three years later than the design date, so it can be estimated that a building constructed in 1954 was designed around 1951.

These two correlations were used as inference rules to determine, along with expert opinion, the typologies of buildings for which original documentation was not available.

The main observed volumetric types are the linear block and the H-shaped block (henceforth referred to as linear and H). Relating the architectural typology to the structural system, it can

be stated that 95% of the URM buildings have a linear type, compared to 35% of the RC frame buildings. In this latter group, 55% of the buildings have an H-shaped footprint (Figure 5).



Figure 5: Main volumetric types: H (in green) and lineal (in orange).

Regarding adjacency, three different setups have been found: isolated blocks, attached blocks, and adjacent blocks. The latter have some party wall segments but do not form a continuous linear aggregate (Figure 6).



Figure 6: Examples of isolated unit (left), attached units (centre) and adjacent units (left).

Most buildings are of medium height, ranging from four to seven storeys for RC frame buildings and from three to five storeys for URM buildings (see Table 3 and Figure 4). No high-rise buildings have been observed in URM, only in RC frame structures.

Height class	Number of storeys		% of buildings
	RC	URM	
Low	1 – 3	1 – 2	2%
Mid	4 – 7	3 – 5	77%
High	8 or more	6 or more	21%

Table 3: Building's height class per structural system.

## 7 RESULTS AND DISCUSSION

After evaluating the vulnerability of social housing buildings constructed between the years 1950 and 1975 in Ayamonte, the results obtained for a seismic event of intensity VII can be observed in Figure 7. According to the predictions, during such an event, all studied buildings would sustain damage (there are no buildings with a mean damage smaller than 0.5). Partial or total collapses of buildings (states *Very Heavy* and *Destruction*) are not expected. However, most buildings would sustain *Moderate* and *Heavy* damage states, which imply significant repairs after the earthquake and, in the case of *Heavy* damage state, also the evacuation of the buildings.



Figure 7: Expected damage state for a seismic event of intensity VII. *Slight* (green), *Moderated* (orange) and *Heavy* (red).

If a mean damage value is calculated for the whole city, taking into account the number of floors and the area of each building to perform a weighted average, a mean damage value of 2 is obtained, equivalent to a *Moderate* damage state. Indeed, 60% of the buildings would fall into this damage state, while 25% would have *Slight* damage and 15% *Heavy* damage (Figure 8).

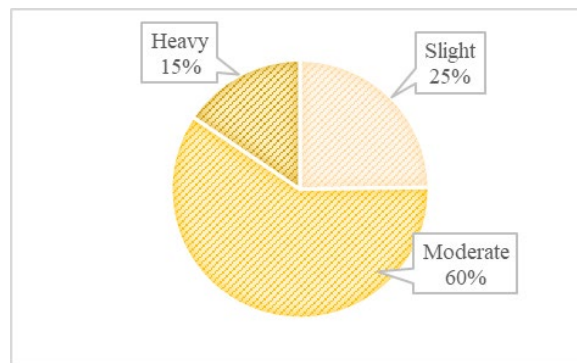


Figure 8: Percentage of buildings per Damage State

When analysing the data by structural typology, both typologies contribute equally to the *Heavy* damage state, while the *Moderate* state is more populated by RC frame buildings and the *Slight* state by URM buildings. These results can be seen in Figure 9.

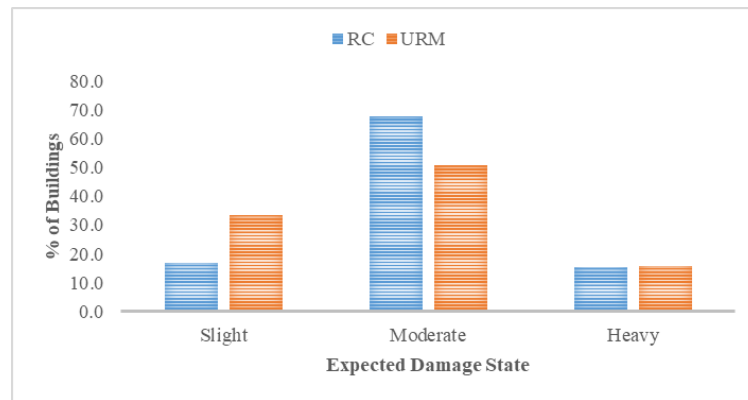


Figure 9: Percentage of buildings of each structural typology per Damage State

When analysing damage based on soil type (Figure 10), it can be observed that the majority of *Moderate* and *Heavy* damage occurs on soft soil, while *Slight* damage is concentrated on the hardest soil.

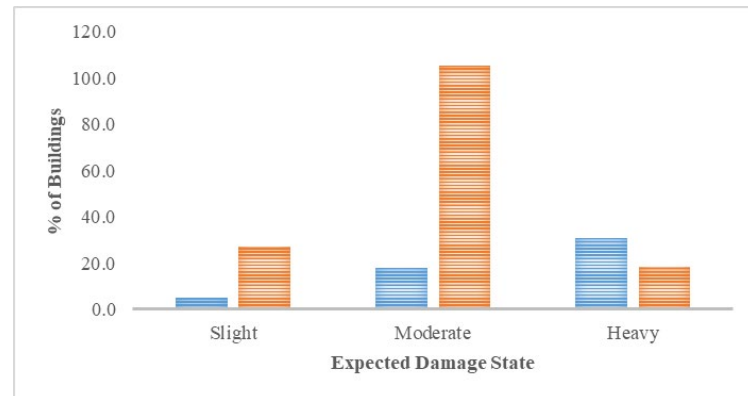


Figure 10: Percentage of buildings on each soil type (hard in blue and soft in orange) per Damage State

Lastly, considering the number of floors, in Figure 11 it can be observed that *Heavy* damage is concentrated in buildings with 4 and 5 floors. All buildings with more than 6 floors suffer *Moderate* damage, while the lowest ones suffer *Slight* damage.

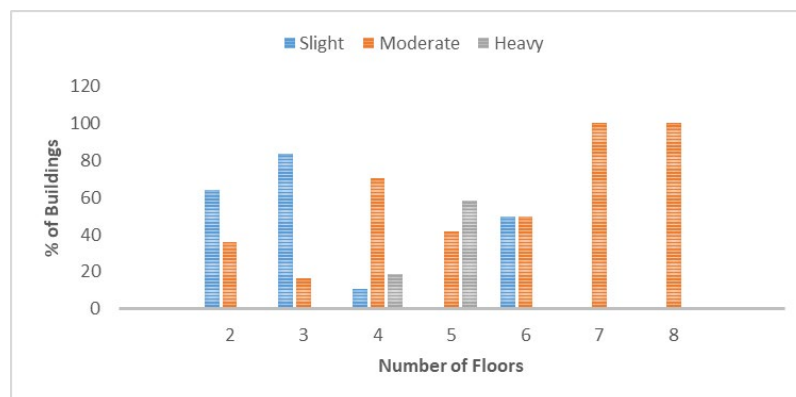


Figure 11: Percentage of buildings for each number of floors per Damage State



## 8 CONCLUSIONS

The present study aims to understand the seismic vulnerability of social housing buildings constructed in Ayamonte between the years 1950 and 1975. These neighbourhoods, characterized by high occupational density and strong identities, represent an important part of the Spanish urban heritage. Their cultural and historical value is associated with the collective memory they embody. These buildings are not only significant from a functional perspective but also as witnesses to the historical, social, and architectural evolution of the 20th century.

For this purpose, the vulnerability index method is employed, following a version of the LM1 macroseismic method modified by the authors to adapt it to Spanish post-war constructions. The evaluation is conducted through a GIS map using QGIS software. Data of the buildings are obtained from open sources, visual inspections, and original plans present in the Municipal Archive of Ayamonte.

The seismic scenario is chosen after considering a historical deterministic option (the Lisbon earthquake of 1755) and a probabilistic one based on the seismic hazard map updated in 2015. The result is an intensity level VII. For the local soil effect, a study based on the geology of Ayamonte has been conducted by the authors, concluding that there are mainly two types of soil in the city: soft soil (marsh), in the south, and hard soil in the north.

After calculating the total vulnerability index of each building considering its structural system and a series of modifiers, the expected mean damage for the selected intensity is calculated, and an expected damage state is assigned. The expected damage state for the majority of the buildings under study (60%) is *Moderate*, 25% of them would show a *Slight* damage state, and for the remaining 25%, a *Heavy* damage state is expected.

Considering that a *Moderate* damage state presupposes the need for extensive repairs after a seismic event, and that buildings with a *Heavy* damage state cannot be occupied before evaluation and rehabilitation, the detriment that lack of preparation would entail to the population residing in these buildings, as well as to society, is evident. In addition to this, the evacuation of families, repairs, and potential demolitions and reconstructions constitute a highly unsustainable process, as well as the loss of part of our urban and cultural heritage from the 20th century.

Based on this, it is concluded that the seismic vulnerability of social housing buildings constructed in Ayamonte between 1950 and 1975 is significant, and a detailed study of them is recommended to design preventive, sustainable, and respectful interventions for the neighbourhoods and their inhabitants.

## 9 ACKNOWLEDGEMENTS

This work is part of the project EMC21\_00255 *Mitigation of seismic vulnerability of residential buildings in large, old neighborhoods in Andalusia*, funded by the Junta de Andalucía, Consejería de Universidad, Investigación e Innovación, through its EMERGIA program for research talent attraction.

The research team would like to express gratitude to the Municipal Archive of Ayamonte and especially to its archivist, María Antonia Moreno Flores, for their collaboration in the realization of this work, without which it would have been impossible.

## REFERENCES

- [1] IGME (Instituto Geológico y Minero de España). ZESIS (Zonificación Sísmica de España). [Online]. Available: [info.igme.es/zesis](http://info.igme.es/zesis) [Accessed: May 29, 2024].

- [2] Alonso Chaves FM, García Navarro E, Camacho Cerro MA, Fernández Rodríguez C (2011) Propuesta sismotectónica para la terminación oriental de la Zona de Fractura de Azores - Gibraltar entre el Banco de Gorringe y el Banco del Guadalquivir. *Geogaceta* 50:11–14
- [3] Ministerio de Planificación del Desarrollo “Norma Sismorresistente P.D.S-1”, Gobierno de España, 1974. (Decreto 3209/1974, de 30 de agosto, BOE núm 279).
- [4] Zapico-Blanco B. et al, Seismic vulnerability preliminary assessment of southern Spain social housing from 1965 to 1975”, *Proceedings of the 18th World Conference on Earthquake Engineering*, Milan, Italy, 2024.
- [5] Sinha, R., Lennartsson, M., & Frostell, B. (2016). Environmental footprint assessment of building structures: A comparative study. *Building and Environment*, 104, 162-171.
- [6] Lagomarsino, S. & Giovinazzi, S., Macroseismic and mechanical models for the vulnerability and damage assessment of current buildings. *Bulletin of Earthquake Engineering*, 4(4), pp. 415–443, 2006. <https://doi.org/10.1007/s10518-006-9024-z>
- [7] Bernardini, A. et al., 2007. Vulnerabilità e previsione di danno a scala territoriale secondo una metodologia macrosismica coerente con la scala EMS-98. In *In Proceedings of the 12th Conference of the Italian National Association of Earthquake Engineering - ANIDIS*. 10-14 June, Pisa, Italy
- [8] Grünthal, G., 1998. European Macroseismic Scale 1998 (EMS-98), European Seismological Commission, Subcommission on Engineering Seismology, Working Group Macroseismic Scales R. Musson, J. Schwarz, & M. Stucchi, eds., Luxembourg: Cahiers du Centre Européen de Géodynamique et de Séismologie
- [9] CEN, "Eurocode 8: Design of structures for earthquake resistance - Part 3: Assessment and retrofitting of buildings," EN 1998-3, European Committee for Standardization, Brussels, 2005.
- [10] Martínez Solares, J.M. y Mezcua, J. (2002), “Catálogo sísmico de la Península Ibérica (880 a.C.-1900)”, Monografía nº18, Instituto Geográfico Nacional, Madrid, 253 pp.
- [11] Irizarry, J., Murphy P., y Goula, X. “Vulnerabilidad y riesgo sísmico a escala municipal para la Bahía de Cádiz”. 4º Congreso Nacional de Ingeniería Sísmica. Granada, 18-20 de mayo de 2011.
- [12] IGN, Actualización de mapas de peligrosidad sísmica de España 2012, Centro Nacional de Información Geográfica (CNIG), 2017, DOI: 10.7419/162.05.
- [13] Lantada N et al. Seismic hazard and risk scenarios for Barcelona, Spain, using the Risk-UE vulnerability index method. *Bull Earthquake Eng.* Apr. 2010;8(2):201-229. <https://doi.org/10.1007/s10518-009-9148-z>
- [14] Martínez Solares, J.M. y Mezcua, J. (2002), “Catálogo sísmico de la Península Ibérica (880 a.C.-1900)”, Monografía nº18, Instituto Geográfico Nacional, Madrid, 253 pp.
- [15] Irizarry, J., Murphy P., y Goula, X. “Vulnerabilidad y riesgo sísmico a escala municipal para la Bahía de Cádiz”. 4º Congreso Nacional de Ingeniería Sísmica. Granada, 18-20 de mayo de 2011.

## SELECT.FC: METHODOLOGY, CALIBRATION, APP AND DATABASE TO ASSESS AND SELECT FRAGILITY CURVES FOR SEISMIC RISK STUDIES

<sup>1</sup> Navas-Sánchez L.<sup>1\*</sup>, Jiménez-Martínez M.<sup>2</sup>, Hernández-Morales L.P.<sup>3</sup>, González-Rodrigo B.<sup>4</sup>, Hernández-Rubio O.<sup>5</sup>

<sup>1</sup> Higher Technical School of Architecture, Universidad Politécnica de Madrid (UPM), Madrid 28013, Spain  
laura.navas.sanchez@upm.es

<sup>2</sup> School of Surveying, Geodesy and Cartography Engineering, Universidad Politécnica de Madrid (UPM), Madrid 28031, Spain; maribel.jimenez@upm.es

<sup>3</sup> Universidad Politécnica de Madrid (UPM), Madrid, Spain  
lisandra.hernandez@alumnos.upm.es

<sup>4</sup> School of Forest Engineering and Natural Resources, Universidad Politécnica de Madrid (UPM), Madrid 28040, Spain; beatriz.gonzalez.rodriago@upm.es

<sup>5</sup> Geolyder SL, Madrid 28020, Spain; orlando.hernandez@geolyder.com

**Keywords:** fragility curves, seismic vulnerability, seismic risk, Central America,

### Abstract.

*Fragility curves (FCs) are crucial for evaluating structural performance against seismic risks, depicting the probability of damage at varying hazard levels. Using appropriate FCs is essential to ensure accurate damage and loss calculations for specific construction types. This study introduces "Select.FC", a methodology featuring a multidimensional index to assess and select the most suitable FCs from existing literature. The index evaluates various variables, assigning scores to each, and ranks FCs from A to F based on their suitability, simplifying result interpretation and enhancing reliability.*

*The evaluation dimensions include technical suitability, local system compatibility, and similarity between candidate and target building types, encompassing 15 variables. Technical suitability is inherent to the FC and the most time-consuming, assessing variables inherent to FCs, while the other two dimensions depend on specific construction features. The methodology's scores were calibrated using the Fuzzy Analytic Hierarchy Process applied to expert survey results, involving 30 international professionals.*

*Additionally, herein is made public a free online application, "Select.FC", with a database of over 50 evaluated FCs which implements the said methodology. The App permits the evaluation of all the FCs included in the database for the specific typology of the area under study and obtaining of the class of adequacy. A QR code for accessing to the App is provided. Future work will expand the FC database with more pre-assessed technical suitability dimensions and allows users to input and classify their own FCs.*



## INTRODUCTION

Seismic risk, determined by the combination of hazard, exposure and vulnerability, is the measurement of the damage expected in a given interval of time, based on factor as the seismicity and the resistance of constructions, among others. Seismic risk studies allow for a probabilistic evaluation of the consequences that these ground movements could have on the structure or set of structures considered. Therefore, when conducting seismic risk studies, experts have to deal with with a multitude of uncertainties, especially in the methods used to assess the factor involved. For instance, one critical aspect is the choice of fragility curves that represent the vulnerability of each typology of buildings exposed.

Fragility curves (FCs) are the graphical representation of the probability of reaching or exceeding a limit damage state given a level of ground shaking and constitute the most extended decision-making tool to establish the relationship between hazard and damages. The employment of adequate FCs is key to evaluate the performance of constructions against seismic risks accurately since selecting an inappropriate FC for a given construction typology can significantly affect the accuracy of damage and loss calculations. Moreover, the selection of an accurate FC can aid to understand the risks associated with the specific types of structures.

Nonetheless, despite this fact, many of the FCs commonly used in seismic risk studies for highly vulnerable areas were designed for regions with higher GDP and more research investment, hence different construction techniques and materials quality compared to the areas being studied [1]. For said reason, having a methodological approach for evaluating and selecting FC for seismic risk studies and a practical manner to employ it like a web application is crucial.

In this line, this contribution presents the *Select.FC* integral approach that renders as easy as possible to researchers the selection of the most appropriate FC for a region. This work integrates and unites:

- a proposal for giving ranges and rankings to assess the suitability of a particular curve for a given area by means of a multidimensional index [1] named *Select.FC*;
- the calibration and validation the scores assigned to the variables involved in the methodology through an expert survey analyzed employing the fuzzy set method;
- a web application (App) also called *Select.FC*, which includes a comprehensive database of FCs with the technical variables already assed.

## 1 SELECT.FC METHODOLOGY

### 1.1 Select.FC: a methodology to assess and select fragility curves

The methodology for assessing and selecting seismic FCs involves the following steps [1]. Initially, it is crucial to identify and characterize the types of buildings under study. Following this, a comprehensive search of available scientific literature is undertaken, including research projects, journal articles, theses, conference papers, and other relevant sources. This search is focused on sources related to the characterization of buildings pertinent to the specific area being analyzed.

Next, a rating index is developed from a set of proposed variables aimed at evaluating key aspects of the identified FCs for the building types being studied. Figure 1 outlines the conceptual framework, dimensions, and variables of this index, indicating the maximum scores for each aspect in brackets. Using this index, a classification is created to determine the suitability of the FCs for each identified building type.

The Final Index, which has a maximum score of 100 points, is calculated based on a multi-dimensional index known as the Global Index. This Global Index is adjusted by a reduction coefficient that reflects how well the curve fits a particular building type within the studied region, referred to as the Building Class Similarity dimension. The similarity between the building types of the candidate functions and that of the region under study is determined by considering the quantity and nature of their attributes.

Essential characteristics considered in this assessment include the lateral load-resisting system, number of stories, ductility, year of construction, and compliance with seismic regulations, as these are significant in terms of the seismic vulnerability of the building typology being analyzed. The fragility curve must correspond to a building type made of the same material as the one under investigation.

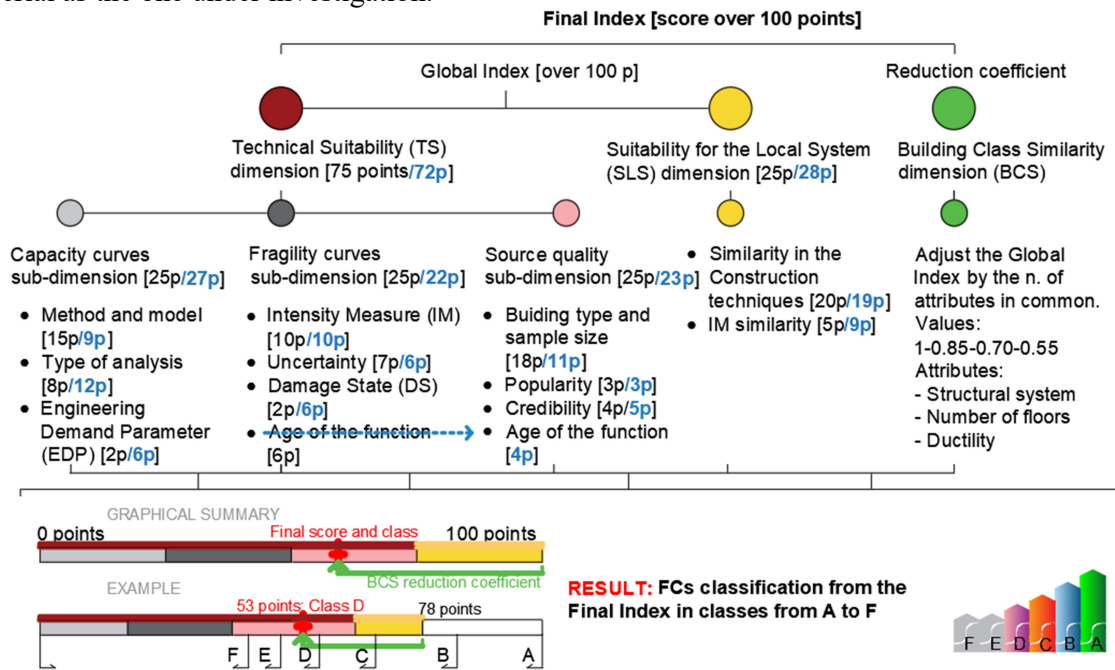


Figure 1: dimensions and variables of the index proposed to evaluate FCs. Source: adapted from [1]. Scores given in the original proposal included in [1] in black. Scores resulting from the calibration herein after described in blue.

The Global Index consists of two main dimensions: the *Technical Suitability* of the Fragility Curve (FC) and the *Suitability for the Local System*. The *Technical Suitability* dimension is further divided into three sub-dimensions: *Capacity*, *Fragility*, and *Quality*. Each of these dimensions and sub-dimensions includes various variables that allow for a comprehensive evaluation of the FCs. These variables were selected based on previous studies in the field [2], [3] and [4].

The *Capacity* sub-dimension includes variables related to the *Method and Model* used, the *Type of Analysis* performed, and the *Engineering Demand Parameter* (EDP) considered in constructing the curve. The *Fragility* sub-dimension pertains to characteristics directly related to the FCs being evaluated, such as the *Intensity Measure* (IM) used, the source of *Uncertainty* associated with FCs that are treated, and the *Damage State thresholds* considered. The *Quality* sub-dimension assesses whether the capacity and fragility curves are derived from existing structures or building prototypes and considers the *Sample Size* of buildings used; and variables related to the *Authenticity* and *Credibility* of the study, taking into account the type of publication in which the FC is proposed (e.g., scientific article, doctoral thesis, confer-

ence paper). Additionally, it includes the *Popularity* of the FCs, measured by the number of citations in Google Scholar of the study proposing the curve and the *Publication Year* of the study that proposes the curve.

The *Suitability for the Local System* dimension evaluates the degree to which the FCs are appropriate for the local context based on variables such as the *Similarity in Construction Techniques* and the *Similarity of Intensity Measures* (IMs). This dimension assesses the adequacy of the FCs for the building typologies of the specific zone under study.

## 1.2 Calibration of the methodology

The multidimensional index proposed by [1] is constructed using scores assigned to each variable, sub-dimension, and dimension according to the criteria set by the research group's experts. However, determining the weights for the different variables in a multidimensional index is a complex and crucial process for developing a composite index, as it requires combining various variables and dimensions into a single indicator. Consequently, in the second phase of the research, validating the assigned weights was considered essential. Hence, once the methodology was established, the scores given to the variables and dimensions were calibrated employing an international survey so as to base the new pounding in a wider expert criterion.

The online survey summarized in Figure 2, available in both Spanish and English, was conducted specifically to gather expert opinions on the weights or relative importance of each variable, sub-dimension, and dimension included in the previously described multidimensional index for rating FCs.

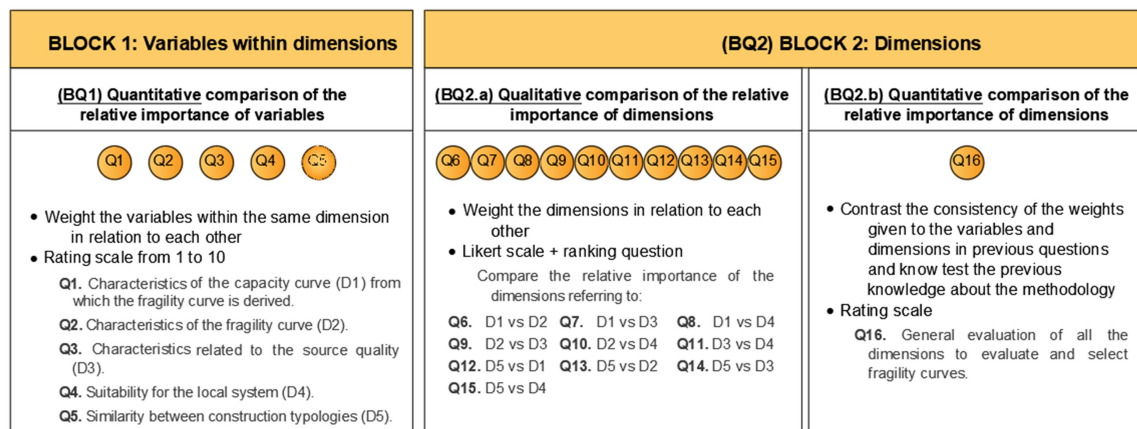


Figure 2: Schema of the survey

The survey has a total of 16 questions (from Q1 to Q16) divided into two blocks (BQ1 and BQ2). The first block (BQ1, from Q1 to Q5) relates the scores of variables pertaining to the same dimension. The objectives, in this case, are to compare the relative importance of the variables included in the same dimension for the selection of a FC and to introduce the variables pertaining to each dimension for the BQ2. The BQ2 presents two sets of questions: the first of these (BQ2a, from Q6 to Q15) qualitatively compares the relative importance of dimensions, thus allowing us to establish the scores given to each dimension, knowing the variables that pertain to each of them. In the second one (BQ2b, Q16), different dimensions are quantitatively compared. In other words, the BQ1 asks the expert to assign a score on a scale of 1 to 10 to each of the twelve variables included in the global index. In the BQ2a, the experts are required to compare successive pairs of different dimensions of the index to collect

the relative importance they assign to each one in comparison with the rest; whereas in the BQ2b the experts must assign a score from 0 to 100 to each of the five dimensions. All questions are compulsory.

A total of 30 experts with high level of expertise in the subject matter answered the survey. These experts generally have significant specialization reflected in their research activities and high-quality scientific publications or professional work. They were contacted via email and provided with a cover letter explaining the purpose of the survey and its relation to the study. The responses come from various countries, including Europe, North, Central and South America. Nonetheless, expert responses are inherently subjective, uncertain, and potentially inconsistent [5]. To address these limitations, the fuzzy analytical hierarchy process (FAHP) method was implemented to refine the weighting system derived from the expert survey.

### Fuzzy hierarchical analysis

The analytical hierarchy process (AHP) is a method developed to work with complicated systems, including choosing among numerous options [6]. The AHP is based on a hierarchical split of the problem into its parts; the analysis then assists the decision-makers who, through pairwise comparisons, can understand the influence of the considered elements in the hierarchical structure. In this research, the AHP is employed to calibrate the weights of variables, dimensions and sub-dimensions based on expert criteria.

In particular, the Fuzzy AHP method highlights the most prominent variables used in constructing the indices and assigns them the highest weight. By integrating expert responses and the FAHP method, it is possible to improve the objectivity of the weights and reduce the uncertainty when combining expert opinion on a particular variable and turning it into a single value. Said uncertainty may be due several factors, such as, lack of understanding of the task, expert bias, experts' disinterest in the survey, or plain human error. Furthermore, FAHP is the most appropriate one in situations where there is a likelihood of ambiguity and fuzzy results when gathering opinions from experts to create composite indexes [5].

Figure 3 schematizes how the survey responses are treated to enhance expert weights by subjecting them to the FAHP method to calculate fuzzy weights and interval weights. In summary, the responses to BQ1 from the expert survey are used to derive the relative weights of the different variables of each dimension and sub-dimension. Whereas the responses to BQ2a and BQ2b allow us to compute the weights of the dimensions of the multidimensional index. Once the weight of each dimension is established, these dimension and sub-dimensions' weights are used to ensure that the total weight of the variables within each dimension equals the dimension's weight derived from BQ2a and BQ2b.

The scores resulting from the analyses described are summarized in blue in Figure 1.

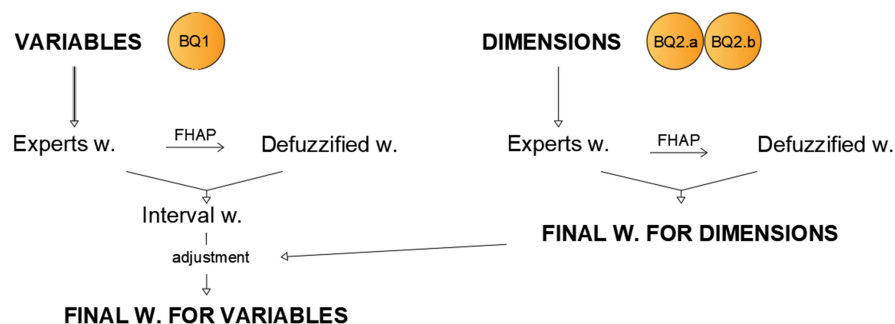


Figure 3: Schema of the analyses implemented to the survey for enhancing the weighting system. W: weight

## 2 WEB APPLICATION AND DATABASE

The interest in creating a web application implementing the *Select.FC* methodology arises from the difficulties linked to dealing with data bases and scoring a great number of variables inherent to the FCs assessment and selection. The application addresses the aforementioned problems by automating the evaluation process, centralizing and structuring the data, providing a dedicated technological tool, and offering a detailed glossary to facilitate the understanding and application of the methodology. A very relevant advantage that the *Select.FC* methodology offers for its use as a basis for a web application lies in the practicality when evaluating the curves: the most expensive dimension in terms of time spent only has to be evaluated once and its score is valid for all areas and structural systems (see Figure 4 for an example). In other words:

- The technical dimension is independent of the study area, or the type of building analyzed; that is, it depends solely on the method used to prepare the fragility curves. Therefore, once determined for a specific fragility curve, said value is valid for any seismic risk study. Furthermore, this dimension is the one that includes the majority of variables and the most time-consuming.
- The dimension of the local system depends solely on the characteristics of the area under study. Therefore, the value determined for this dimension is valid for any type of building within that area.
- The building class similarity reduction coefficient is the only dimension that must be adjusted for each building type according to its attributes (material, structural system, number of floors and ductility).

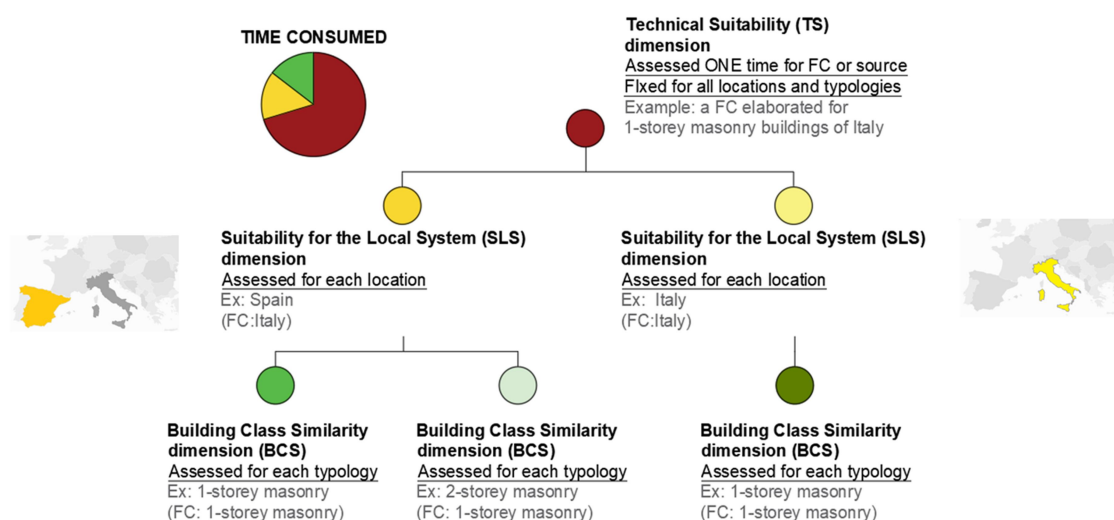


Figure 4: Schema of the practicality of the methodology for implementing it in an App. Source: PhD defense [7]

The created App is able to classify curves automatically according to the results of the evaluations, following the methodology established by *Select.FC* to guarantee accuracy and eliminate human errors in categorization. Furthermore, it allows the download of an Excel file with detailed technical information and specific scores for each variable, facilitating subsequent analysis and presentation of results in a structured manner. Up until June 2024, the App includes a database created with a Structured Query Language, QLS 2019, which comprises more than 50 FCs with the technical dimension assessed.

Figure 5 illustrates the Graphical Interface of the App, developed in [8], which contains filters to search for fragility curves in the database. These filters include two that are compulsory, *Materials* and *Height Range*, and four that are optional, *Structural System*, *Ductility*, *Country of origin* and *Intensity Measurement*. Once the filtering has been carried out, all the FCs that correspond to the indicated conditions and their characteristics corresponding to the technical dimension will be displayed. The said features have already been evaluated. Next, to facilitate starting the evaluation process of the two remaining dimensions, *Suitability to the local system* and *Building Class Similarity*, three additional fields appear.: (i) *Similarity between Construction Techniques*, (ii) *Similarity between Intensity Measurements* and (iii) *Building Class Similarity*. Once the options that best fit the study have been selected, the App provides an Excel file with all the curve data and the scores and classes obtained from the evaluation (see figure 6). A QR code for accessing to the *Select.FC* web App is included in Figure 7.

Figure 5: Graphical interface of the App. Source: [8]

ID	Tipología evaluada	Autor	Descripción según taxonomía GEM	Building class similarity	Similarity in Construction techniques	IM similarity	Method and model	[...]	CAPACITY	FRAGILITY	QUALITY	TECHNICAL	LOCAL SYSTEM	GLOBAL INDEX	FINAL INDEX	CLASS
CF1	Mampostería integral 1 piso (ductil)	E. Calderón (2018) based on Hidalgo (2017)	MCR+CBH/LWAL+DUC/HEX:1/IRRE/FN	1.00	20	5	12	[...]	22	24	22	68	25	93.0	93.0	A
CF2	Mampostería integral 1 piso (ductil)	Calderón and Silva (2019)	MR/LWAL+DUC/H EX:1 and MCF/LWAL+DUC/HEX:1	0.85	20	5	6	[...]	16	17	23	56	25	81.0	68.9	B
CF3	Mampostería integral 1 piso (ductil)	Calderón and Silva (2019)	MR/LWAL+DUC/H EX:2 and MCF/LWAL+DUC/HEX:2	0.70	20	5	6	[...]	16	17	23	56	25	81.0	56.7	C
CF4	Mampostería integral 1 piso (ductil)	Calderón and Silva (2019)	MR/LWAL+DNO/HEX:1 and MCF/LWAL+DNO/HEX:1	0.70	20	5	6	[...]	16	17	23	56	25	81.0	56.7	C
CF5	Mampostería integral 1 piso (ductil)	Villar Vega (2017)	MCF/LWAL+DUC/HEX:1	0.85	10	5	3	[...]	13	20	21	54	15	69.0	58.7	C
CF6	Mampostería integral 1 piso (ductil)	Villar Vega (2017)	MCF/LWAL+DNO/HEX:1	0.70	10	5	3	[...]	13	20	21	54	15	69.0	48.3	D
DATA				VARIABLES				RESULTS						CLASS		

Figure 6: Example of the data proportionated by the Excel file. Source: [8]



## PENDIENTE

Figure 7: QR code for accessing to the *Select.FC* web App

### 3 CONCLUSIONS AND FUTURE LINES OF RESEARCH

This work has presented a recent methodology for assessing and selecting fragility curves. The *Select.FC* method proportionates a multidimensional index that allows the scoring and ranking in classes from A to F of the FC depending on its level of adequacy to represent the behavior of the typology of the region under study in the face of an earthquake.

Moreover, we have introduced how the scores given to the dimensions, sub-dimensions and variables involved in this methodology have been calibrated: by carrying out a survey to international experts and analyzing the results employing the Fuzzy Analytical Hierarchy Process to reduce the uncertainty inherent to the process of combining expert opinion on a particular variable or set of them and turning it into a single value.

Finally, an easy to use web application that implements the methodology has been made public. The *Select.FC* App provides to the seismic risk experts a database of more than 50 FCs from all over the world with the technical dimension already assessed and a graphical interface that enormously facilitates the evaluation of the rest of the less time-consuming dimensions. Furthermore, the App permits the user to download the results to analyze and custom variables and scores in case it is needed. A QR code for accessing to the App is provided in Figure 7.

To conclude, future lines of research should implement the evaluation of custom fragility curves by functionality that allows users to evaluate their own fragility curves within the application and add it to the data base.

### REFERENCES

- [1] Navas-Sánchez L, Jiménez-Martínez M, González-Rodrigo B, Hernández-Rubio O, Dávila-Migoya LD, Orta-Rial B, Hidalgo-Leiva D (2023) A methodology to assess and select seismic fragility curves: Application to the case of Costa Rica. *Earthquake Spectra* 39:1380–1409. doi: 10.1177/87552930231171177
- [2] Stone H, Gunasekera R, Ishizawa O (2017) On the use of existing seismic fragility and vulnerability. In: Proceedings of the 16th World Conference on Earthquake Engineering-WCEE. Santiago de Chile, pp 9–13
- [3] Maio R, Tsionis G (2015) Seismic fragility curves for the European building stock: Review and evaluation of analytical fragility curves. Ispra, Italy
- [4] Rossetto T, D'Ayala D, Meslem A (2014) Evaluation of existing fragility curves. In: Pitilakis K, Crowley H, Kaynia A (eds) SYNER-G: Typology Definition and Fragility functions for Physical Elements at Seismic Risk. Springer, Dordrecht, pp 47–93
- [5] Al Fozaie MT, Wahid H (2022) A Guide to Integrating Expert Opinion and Fuzzy AHP When Generating Weights for Composite Indices. *Advances in Fuzzy Systems*. doi: 10.1155/2022/3396862

- [6] Saaty RW (1987) The analytic hierarchy process—what it is and how it is used. *Mathematical modelling* 9:161–176. doi: [https://doi.org/10.1016/0270-0255\(87\)90473-8](https://doi.org/10.1016/0270-0255(87)90473-8)
- [7] Navas-Sánchez L. (2023) *Vulnerability of buildings and non-structural elements: insights from the 2011 Lorca earthquake*. PhD: Universidad Politécnica de Madrid and Alma Mater Studiorum-University of Bologna.
- [8] Hernández-Morales L. P. *Desarrollo de una aplicación web que integra la metodología Select.FC para la evaluación y clasificación de curvas de fragilidad sísmica* MFT: Universidad Politécnica de Madrid



## SEISMIC ASSESSMENT OF A UNESCO WORLD HERITAGE SITE THE GREAT MOSQUE IN CÓRDOBA

J. M. Torres<sup>\*1</sup>, P. Negrette<sup>1</sup>, P. García<sup>1</sup>, C. Merino<sup>1</sup> and B. Zapico-Blanco<sup>2</sup>

<sup>1</sup> Ove Arup and Partners, SAU  
Alfonso XI 12, Madrid, Spain  
josemanuel.torres@arup.com

<sup>2</sup> Department of Building Structures and Geotechnical Engineering, Universidad de Sevilla  
Reina Mercedes, 2. 41012 Sevilla, Spain  
bzapico@us.es

**Keywords:** heritage building, seismic assessment, nonlinear response history analysis.

**Abstract.** *The present work illustrates the seismic assessment of a line of arches in the oldest section of the Great Mosque in Córdoba, using advanced finite-element analysis. Historical structures, often subject to various modifications and insufficient maintenance, pose challenges in predicting their seismic response. Due to the historical and cultural importance of the Great Mosque and the complexity of its seismic behavior, a nonlinear response history analysis (NLRHA) is considered the most suitable method for assessment. This paper outlines the steps involved in constructing the numerical model and executing the NLRHA. In particular, the development of tri-directional hazard-specific ground motions adheres to state-of-the-art techniques, and the masonry structure's advanced material model captures relevant failure modes in its seismic response. The results show that the numerical model aligns well with expected failure modes, instilling confidence in the chosen modeling strategy. Furthermore, this study can be seen as a basis for subsequent work to include a more representative portion of the monument and continue gaining insight into its global dynamic response. This is particularly noteworthy considering the consistent structural framework in some parts of the Great Mosque, and the observed advantages of employing sophisticated methods over simpler ones for assessing historical buildings.*

## 1 INTRODUCTION

Modern earthquake engineering is a young discipline of engineering, recognized as starting in the 1920s. After 100 years, it is beginning to be a mature field, with multiple specialties trying to improve our understanding of earthquakes and their consequences for human beings. However, we have been building for many more years, so historical constructions have not been able to benefit from this recent knowledge and they were *designed* only considering gravity loads. This fact leads to significant challenges to structural engineers and architects when dealing with seismic risk mitigation of historical constructions. Furthermore, the lack of maintenance and alterations over time may also worsen the building's *natural* seismic resistance.

Existing heritage should be preserved for future generations as it is, accordingly, interventions must be minimized when structural strengthening is deemed necessary. With this objective, it is considered necessary to *sharpen the pencil* as much as possible in the analysis phase. To this end, it is essential to carry out advanced analysis and modelling to characterize the seismic behaviour of these constructions and to try to benefit from state-of-the-art knowledge in earthquake engineering.

Córdoba is deemed to be a moderate seismic area in a worldwide context, but it is located in one of the Spanish regions with the highest seismic activity. Therefore, it is of special national interest to study and evaluate the seismic response of building in the city and particularly of those with a singular value as is the case of the Great Mosque.

This paper presents a response history analysis of a 3D finite element model representing a portion of the Great Mosque. The analysis is carried out with the LS-DYNA® [1] and *ad-hoc* Grasshopper scripts have been developed to generate the finite element mesh from a CAD-based geometry model of the line of arches under study.

## 2 STRUCTURE DESCRIPTION

The Great Mosque of Córdoba was inscribed on the UNESCO World Heritage List in 1984 and the property was extended in 1994 to include part of the Historic Centre, the Alcázar (the fortress), and extending south to the banks of the River Guadalquivir, the Roman Bridge and the Calahorra Tower. The total area encompasses 80.28 ha.

The Great Mosque, with its juxtaposition of cultures and architectural styles, has retained its material integrity. It was built in the 8<sup>th</sup> century, over the remains of the Visigoth Basilica of San Vicente. There were consecutive extensions carried out over three centuries, and in 1236 the Christian Cathedral was installed. The greatest reconstruction was carried out in the Renaissance period, between 1523 and 1599, which resulted in its present structure of space. Its continued religious use has ensured in large part its preservation.

The total area of the monument is more than 22,000 square meters, with a length of 174 meters long and 128.4 meters wide.



Figure 1: Aerial view of the monument. Source: Flickr

We focus on the study of a single line of arches corresponding to the original Mosque (Abderraman I) and the first extension (Abderraman II).

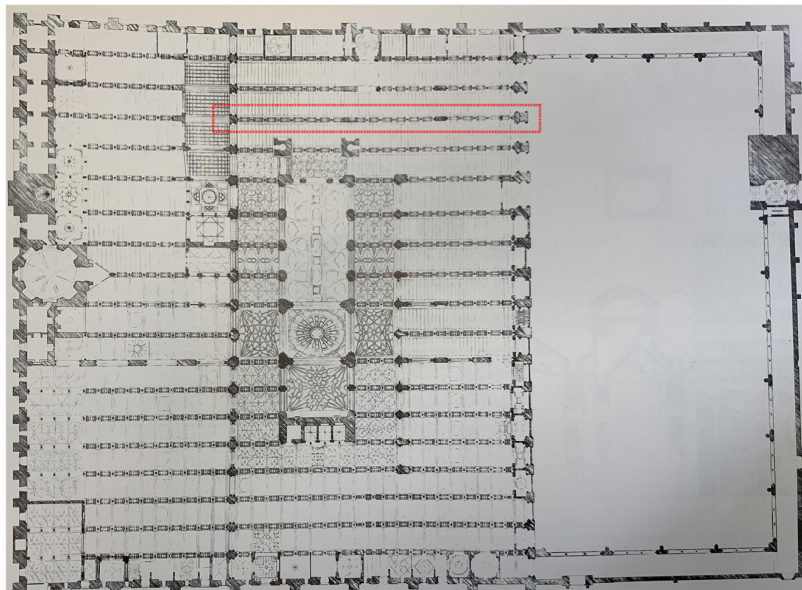


Figure 2: Location of the line of arches studied in this work. Source: [2]

It has been decided to study a limited and reduced part of the building, which is still considered sufficiently representative of the difficulties that may arise in modeling the entire building as a whole:

- It contains a representative portion of most of the materials used in the rest of the monument.
- The structural system is the predominant one in the building.

Moreover, the numerical model is kept small and manageable to understand the observed behavior and to add complexity step by step. So successfully modeled this part, it is considered that lessons learned would greatly ease the modelling and analysis of larger portions of the building.

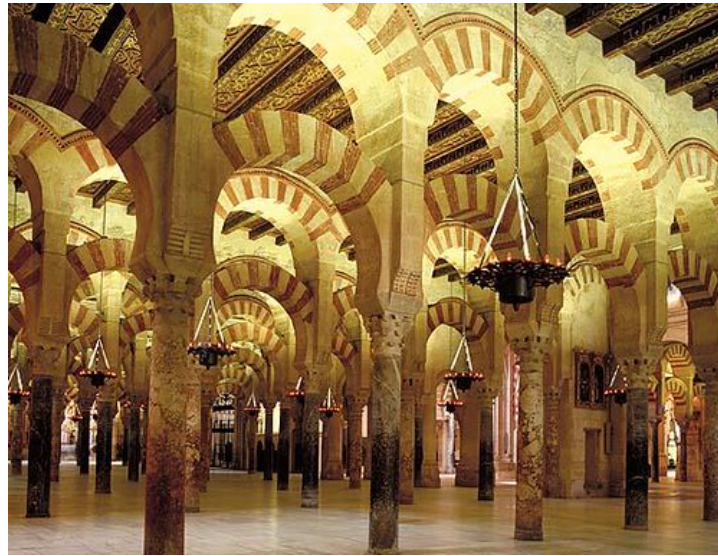


Figure 3: Part of the line of the studied line of arches.

### 3 SEISMIC ANALYSIS

#### 3.1 Approach

The most appropriate analysis method to employ on a project depends on the nature of the building structural system and its regularity, the specific seismic performance objectives and ductility targets adopted, the requirements of governing codes of practice and the level of design seismic hazard [3]. The main traditional analytical techniques used for buildings include equivalent linear static analysis, response spectrum analysis, pushover analysis and response history analysis.

Due to the historical and cultural relevance of the Great Mosque, in addition to the numerous building alterations over time affecting the building's seismic resistance, a non-linear response history (NLRH) analysis is considered the most suitable method to assess its seismic performance.

A NLRH analysis of a detailed finite-element model requires solving the equation of motion for the structure when excited by a ground-motion time series. It explicitly accounts for structural non-linearity, multiple modes of vibration and how the distribution of forces within the building evolves during the shaking. It also presents many advantages for modelling heritage structures [4].

#### 3.2 Ground motion selection

A key ingredient in performing a NLRH analysis is the selection of a hazard-consistent set of ground motions. In this work, the hazard at the specific site of interest is obtained thanks to the Spanish NCSR-22 code [5], which is still in drafting phase. This national standard is based on EC8 and guides the construction of elastic acceleration response spectra (horizontal and vertical) considering many factors influencing the hazard, such as soil conditions.

The return period associated with the spectra is 975 years for the near collapse (NC) requirement. Therefore, this is the return period associated with the seismic hazard in the analysis.

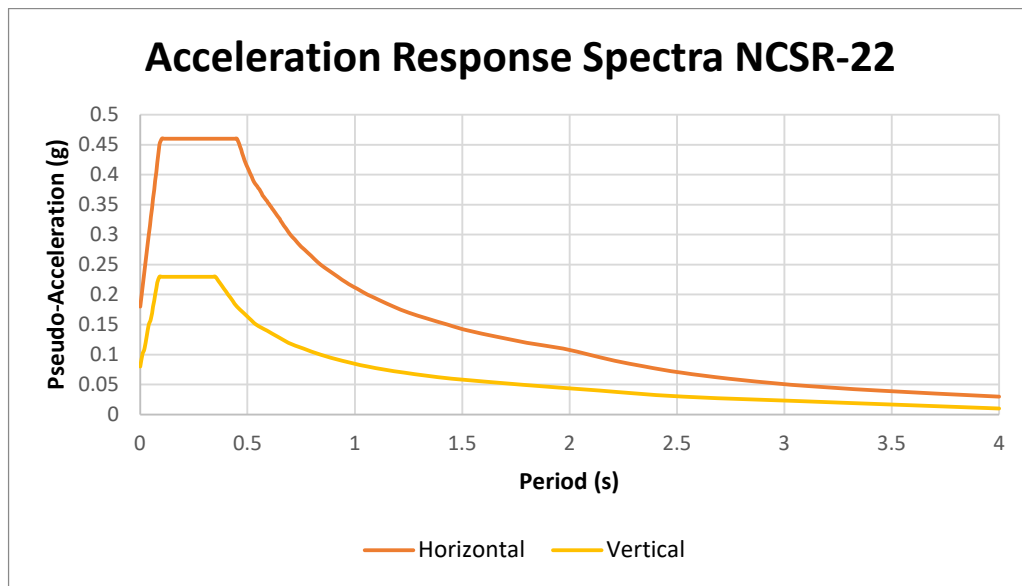


Figure 4: Horizontal and vertical target response spectra.

These spectra provide a mean to uncouple the seismic hazard and response analysis. Once the seismic hazard is defined, ground-motion (GM) time series must be obtained from recorded ground motion databases, or through simulations.

Natural GMs show superiority against artificial signals [6], so it has been decided to use real accelerograms from the PEER Strong Motion Database [7] and to modify them to be compatible with the target spectra. The seed selection was primarily based on  $V_{s30}$  values compatible with available geotechnical information [8] (between 300 and 500 m/s). Only the horizontal components of ground motion were considered for the seed record selection. A preliminary selection of 44 records was performed based on the criterion above.

The horizontal components of these records were matched individually to the corresponding target spectra (Figure 4) through wavelet modification using the software RSPMatch2005b [9] [10]. This spectral matching process was applied to spectral periods ranging from 0.1 to 4s, easing the matching procedure. Horizontal seed records were also initially linearly scaled to achieve a better match with the target spectra.

Among the pre-selected records, the final selection was based on the comparison between the original time histories and the matched ones, being careful that the spectral matching procedure did not substantially alter the original characteristics of the records in terms of acceleration, velocity and displacement time histories, significant duration and Fourier spectra.

The seed records finally selected are presented in Table 1 along with the original Record Sequence Number (RSN) from the PEER database.

#	RSN	EQ name	Year	Station name	Magnitude	Mechanism	$R_{jb}$ (km)	$V_{s,30}$ (m/s)
1	316	Westmorland	1981	Parachute Test Site	5.9	Strike slip	16.54	349
2	730	Spitak, Armenia	1988	Gukasian	6.77	Reverse Oblique	23.99	344
3	881	Landers	1992	Morongo Valley Fire Station	7.28	Strike slip	17.36	396



4	958	Northridge-01	1994	Camarillo	6.69	Reverse	34.78	351
5	1149	Kocaeli, Turkey	1999	Atakoy	7.51	Strike slip	56.49	310
6	1762	Hector Mine	1999	Amboy	7.13	Strike slip	41.81	383
7	2111	Denali, Alaska	2002	R109 (temp)	7.9	Strike slip	42.99	342
8	3747	Cape Mendocino	1992	College of the Redwoods	7.01	Reverse	29.22	493
9	3856	Chi-Chi, Taiwan -04	1999	CHY014	6.2	Strike slip	37.89	348
10	4840	Chuetsu-oki, Japan	2007	Joetsu Kita	6.8	Reverse	28.97	334
11	8166	Duzce, Turkey	1999	IRIGM 498	7.14	Strike slip	3.58	425

Table 1: Seed records.

Horizontal time history records were then spectrally matched. Vertical signals were, instead, scaled in a such a way that the mean of all vertical response spectra would not fall below the -10% of the vertical target. This is obtained by scaling vertical records so that they matched the vertical target at a period of  $T=0.01s$ .

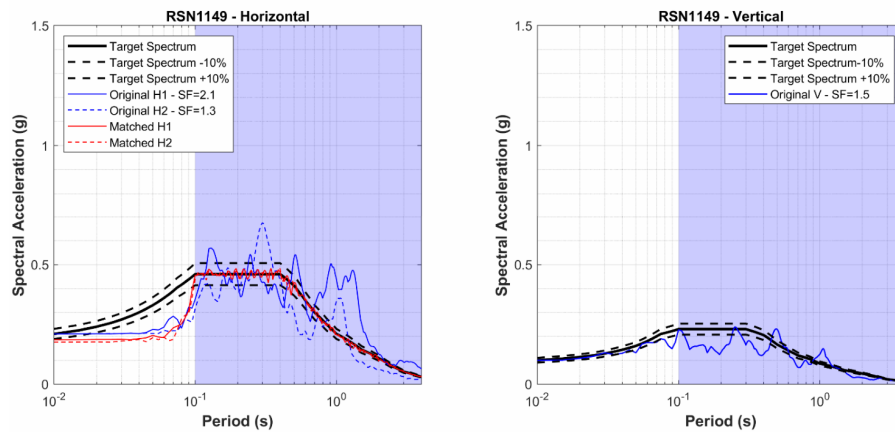


Figure 5: Results for seed record 5 in terms of response spectra for the horizontal spectrally matched components (left) and scaled vertical component at PGA (right).

This input ground acceleration histories will be applied at the base of the building.

#### 4 NUMERICAL MODELING

This section presents the details of the numerical modeling of the line of arches studied in this work. Arup has experience in advanced seismic analysis of ancient [4] and modern [11] masonry buildings with LS-DYNA®. It is a commercial finite-element analysis program suitable for applications involving dynamic loads and contact problems due to its strong capabilities for running response history analyses.

#### 4.1 Model generation

The definition of the finite element model was done using the Oasys Primer [12] pre-processor for LS-DYNA. Primer is a very useful tool for preparing and modifying LS-DYNA models quickly. However, typically efficient workflows include defining the model geometry within CAD software and then creating the primer file.

In the present work, the Rhinoceros 3D plug-in named Grasshopper was used to define the geometry and then Grasshopper plug-ins developed by Arup were employed to convert the CAD-based geometry into a finite element model in Oasys Primer. Once the finite element model is in the pre-processor, materials, boundary conditions, connections and other analysis parameters are set up to prepare the model for the NLRH analyses.

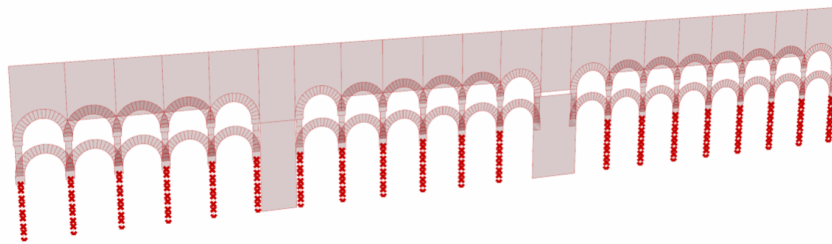


Figure 6: Perspective of the initial geometry in Rhinoceros created in Grasshopper.

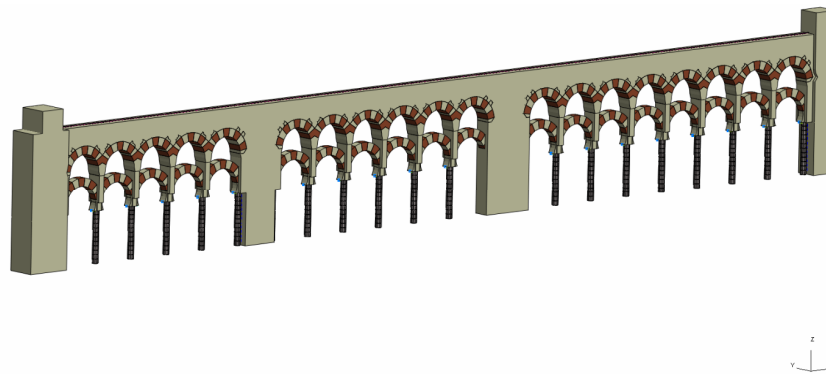


Figure 7: 3D finite element model in Primer. Isometric view

#### 4.2 Material models

##### 4.2.1. Masonry

The definition of the nonlinear material model for masonry is of paramount importance. Knowing this importance, Arup has made an effort to develop a proprietary material model in LS-DYNA for URM walls [13]. The material model is used with 2D shell elements, representing the composite behavior of the bricks and the mortar together. It considers the orientation of bed (horizontal) and head (vertical) mortar joints, the influence of the interlocking of units and several possible failure modes relevant to the seismic response of URM.

Although this material model is considered sufficient for representing the typical failures appearing in the Great Mosque, further studies to better characterize the material properties are still necessary to calibrate all material model parameters.

#### 4.2.2. Columns

Circular columns are made out of marble and granite. An elastic material has been adopted assuming that the failure of the system will be initiated due to the failure of the interface/joint of the masonry walls/arches and not the failure of the columns. Marble columns have  $E=60$  GPa and granite columns  $E=20$  GPa. These values were obtained from [14][15].

#### 4.3 Connections and interfaces

Connections between building components are typical details that represent both potential deficiencies and possible sources of energy dissipation under seismic excitation. In this model, the connection between the columns and the arches was considered as critical. To simulate the friction, five discrete elements with frictional properties were defined between columns and masonry piers and lower arches, representing the friction support of these ones on top of the columns. This modelling approach tries to capture the possible in-plane rocking of the masonry on top of the columns.

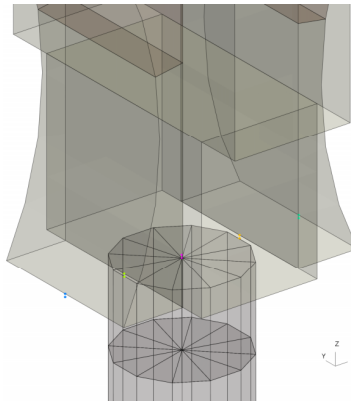


Figure 8: Modeling detail with the 5 discrete elements capturing friction.

#### 4.4 Boundary conditions

As described in Section 2, a line of arches corresponding to the original Mosque (Abderaman I) and the first extension (Abderaman II) was modelled. A fixed-base condition is followed; thus, soil structure interaction effects are neglected, and lateral boundaries are non-deformable solid rigids representing the inertia from the walls running perpendicular to the line of arches.

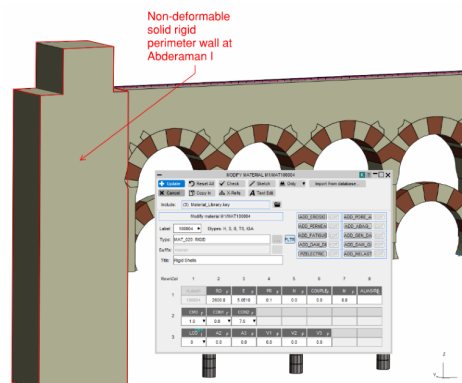


Figure 9: Lateral boundary conditions.



The roof is not modelled explicitly. Its out-of-plane stiffness is not considered. However, a lineal imposed load is included to account for the roof weight.

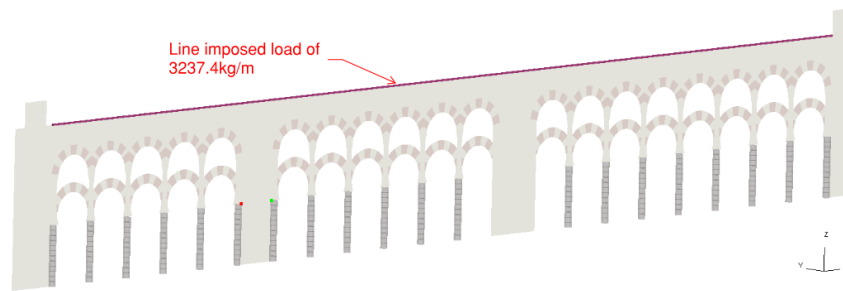


Figure 10: Dead load representing roof weight.

#### 4.5 Other modeling considerations

- Ground motions were applied using a boundary prescribed motion at the base of the columns and after the model is stabilized under gravity. This happens one second after starting the analysis.
- During the gravity phase, global damping is applied to prevent elements from vibrating when their own weight is ramped up.
- A 2% frequency-independent viscous damping ratio is applied to all the elements of the structure.
- A 5% stiffness-proportional damping ratio is applied to all masonry elements to reduce noise from their outputs.

### 5 RESULTS

With the 11 seed records spectrally matched, 11 NLTH analyses were carried out. The main objective was to check whether the numerical model was robust enough to reproduce the dynamic behavior of the individual line of arches. To illustrate this behavior, some plots are discussed hereinafter.

#### 5.1 Base shears

Base shear in Y direction (weak direction) is smaller than that in the X direction, due to the low stiffness of the line of arches in the out-of-plane direction of the model. In-plane stiffness is much higher, attracting more loads. This behavior is consistent with cracking pattern in the walls and with displacements

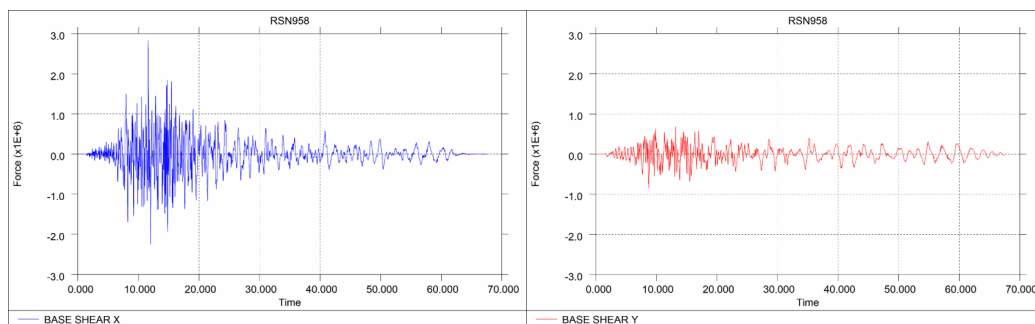


Figure 11: Base shear in global X and Y directions. Seed record: RSN 958.

## 5.2 Cracking pattern

Differences in stiffness lead to stress concentration in specific zones. Three main points of damage accumulation are identified: the base of the intermediate walls, the area above the upper arches close to the rigid perimeter walls and the lower arches close to stiff elements (i.e. walls). In addition, a diagonal cracking at the top of the intermediate walls is observed.

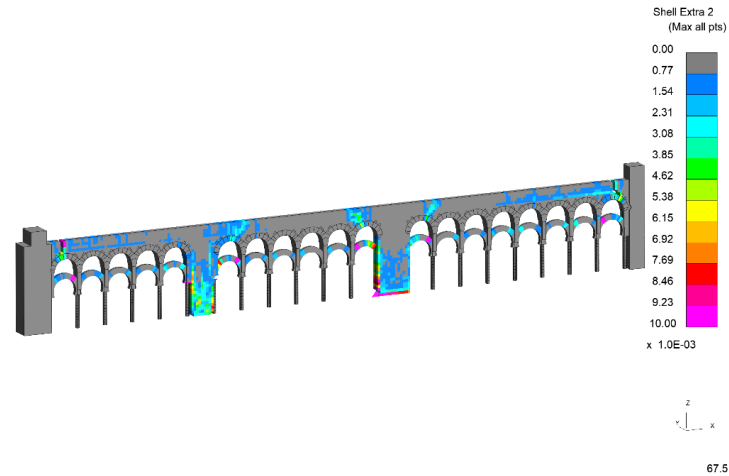


Figure 12: Cracking pattern capped up to 10mm. Seed record: RSN 958.

## 5.3 Out-of-plane (OOP) behavior

In the monument, out-of-plane restraint is provided by a timber diaphragm between parallel arches. This out-of-plane stiffness was not introduced in the model, but the tributary weight of the timber roofing was. Consequently, important displacements in Y direction are observed, compatible with the boundaries of the model.

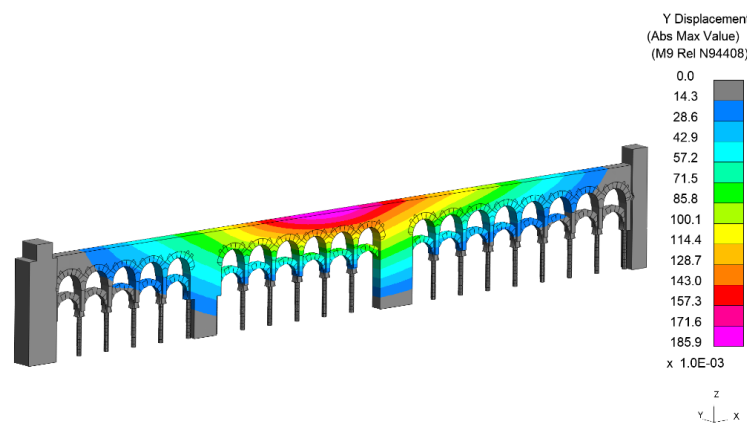


Figure 13: Maximum out-of-plane displacement. Seed record: RSN 1149.

## 6 CONCLUSIONS AND FUTURE WORK

This paper presents a practical application of an advanced finite-element analysis method for the seismic assessment of the Great Mosque in Córdoba. This work is intended to be an extension of the methodology applied in other projects by Arup and aims to

initiate a journey of state-of-the-art seismic assessments for Iberian historical heritage, particularly in the south of Spain.

11 NLTH analyses were performed to validate and analyse the behaviour of one line of arches of the Great Mosque. The main objective of this work was to demonstrate and prove that the numerical model reflects the expected failure modes given the material properties, the boundary conditions and the seismic action applied. These sophisticated models and analyses constitute a valuable tool to understand the seismic behavior of structures and in particular, of heritage buildings with a long life behind.

Future studies will aim to (1) calibrate the material properties with in-situ tests, (2) include dynamic soil-structure interaction effects as well as local soil conditions (i.e. site response) and (3) extend the model to study the complete building. This last line of progress might be facilitated by the regularity in the resisting system in some parts of the monument.

## 7 ACKNOWLEDGEMENTS

The authors would like to acknowledge Arup for providing a license of the commercial software LS-DYNA for the development of this work. Moreover, the authors gratefully acknowledge the collaboration and assistance of the Most Reverend Dean and Chapter of Córdoba Cathedral and would also like to especially express their sincere gratitude to Professor Gabriel Rebollo Puig, the monument's Conservation Architect, for his unwavering generosity with his time and expertise, which has been invaluable to this project.

## REFERENCES

- [1] ANSYS, Keyword User's Manual, LS-DYNA R.14, 2023.
- [2] A. Capitel, La Catedral de Córdoba, p. 38. 1985.
- [3] D. N. Grant and E. Booth, Earthquake Design Practice for Buildings, 4th edn. ICE Publishing London, UK. 2020.
- [4] D. N. Grant, D. Dozio, P. Fici and R. Sturt, Case studies on seismic assessment of historical buildings using advanced analysis, *Proceedings of the Institution of Civil Engineers – Engineering History and Heritage* 175(3): 95–106, 2022.
- [5] NCSR-22, Norma de construcción sismorresistente parte general y edificación, 2022.
- [6] J. Baker, B. Bradley, and P. Stafford, Seismic hazard and risk analysis, Cambridge University Press, Cambridge, United Kingdom, 2021.
- [7] B. Chiou, R. Darragh, N. Gregor and W. Silva, NGA project strong-motion database, *Earthquake Spectra*, 24(1):23-44, 2008.
- [8] Cabildo Catedral de Córdoba. *Plan Director Mezquita-Catedral de Córdoba* 2020. 2021. <https://mezquita-catedraldecordoba.es/en/comunicacion/plan-director/>
- [9] N.A. Abrahamson, Non-stationary spectral matching, *Seismological research letters* 63(1), 30, 1992.
- [10] J. Hancock, J. Watson-Lamprey, N.A. Abrahamson, J.J. Bommer, A. Markatis, E. McCoy and R. Mendis, An improved method of matching response spectra of recorded earthquake ground motion using wavelets. *Journal of Earthquake Engineering*, 2006.

- [11] M. Easton, D. N. Grant and L. Hulme, *La Sagrada Familia: approaches to seismic analysis*, *11<sup>th</sup> International Conference on Structural Analysis of Historical Constructions*, Springer, Cham, Switzerland, 2019.
- [12] Primer, Keyword User's Manual, LS-DYNA R.14, 2023.
- [13] R. Sturt, C. Avanes, B. Muriithi, M. Bernardi and Y. Huang, *A masonry material model for seismic analysis in LS-DYNA: Implementation and Validation*, *16<sup>th</sup> European Conference on Earthquake Engineering*, Thessaloniki, Greece, 2018.
- [14] Zapico Blanco B, Rodriguez Mariscal JD, Zapata Rodriguez E, Romero Arroyo JA, Fernandez Ancio F, Solís Muñiz M. *Preserving the Great Mosque of Cordoba (Spain): A Preliminary Mechanical Characterization of Its Original Natural Stone*. *Engineering Proceedings*. 2023; 53(1):7. <https://doi.org/10.3390/IOCB2023-15180>
- [15] Rodríguez-Mariscal JD, Zapico Blanco B, Valverde Garrido N, García-Calabrés Ibáñez FJ, González Pozo M, Solís Muñiz M. *Preserving the Great Mosque of Córdoba (Spain): Characterization of Natural Stone Based on Rebound Hammer and Ultrasonic Tests*. *Engineering Proceedings*. 2023; 53(1):13. <https://doi.org/10.3390/IOCB2023-15185>

## DYNAMIC ANALYSIS OF A 7<sup>TH</sup> FLOOR CONCRETE PREFABRICATED BUILDING

Berna Istegün<sup>1\*</sup>, Pelayo Fernández<sup>2</sup>, Natalia García-Fernández<sup>2</sup>  
and Manuel Aenlle-López<sup>2</sup>

<sup>1</sup> Department of Civil Engineering, Sakarya University, Turkey  
e-mail: [bernaistegun@sakarya.edu.tr](mailto:bernaistegun@sakarya.edu.tr)

<sup>2</sup> Department of Construction and Building Engineering, University of Oviedo, Spain  
{fernandezpelayo, garciafnatalia, aenlle}@uniovi.es

**Keywords:** Dynamic Analysis, OMA, Numerical Models, Model-Updating.

**Abstract.** *In recent years, the application of SHM techniques has seen significant growth, driven by the need to ensure the safety, longevity, and performance of engineering structures. To address these needs, SHM methodologies have evolved and can be broadly categorized into two types: Modal-Based SHM, which relies solely on experimental data, and Model-Based SHM, which integrates experimental modal parameters with a numerical model of the structure. It is considered best practice to use a complementary approach that combines both techniques to improve the understanding of the dynamic behavior of a structure during the SHM process. This approach typically involves the use of Operational Modal Analysis (OMA) in conjunction with the development of a Finite Element Model (FEM) of the structure as an initial phase of the SHM process. By combining these methods, it is possible to achieve a more comprehensive assessment of structural integrity and better predict potential problems, thus improving the overall effectiveness of SHM strategies.*

*In this work, the dynamic behaviour of a 7<sup>th</sup> floor concrete prefabricated building is analyzed using Operational Modal Analysis.*

### 1. STRUCTURE AND TEST SET UP

The construction of the building (see Fig. 1) was completed in 2010. The majority of the structure was constructed using prefabricated structural concrete components. The main dimensions of the building are 50 x 36 m and a height of 34 m which is located in Mieres (Asturias). Its construction is non-uniform, with some interior gardens supported by lateral structural walls or a large glass facade on one side, connected by steel trusses. The structure comprises seven

storeys, with the final three floors dedicated to laboratories and offices. The building is situated in close proximity to a coal mine. The hot water from the mine galleries is pumped into the building to provide heat, thereby utilizing geothermal energy. The operation of the pumps results in the generation of certain vibrations within the building. Therefore, it was decided to analyze the dynamic behaviour of the building for further investigations in the future.

To measure the accelerations two Guralp Adquisition systems were used. Each one was equipped with GPS in order to synchronize the signals. Eleven measurement points were used in the experiments (see Figure 1) using two Data-Sets. One triaxial sensor, located in the top floor of the building, was used as reference sensor for both Data-Sets. Another 2 triaxial sensors, as well as 2 uniaxial sensors, were used to complete the measurement points. The sampling frequency was 50 Hz. Both equipments were connected by Ethernet being the data received in a remote PC.

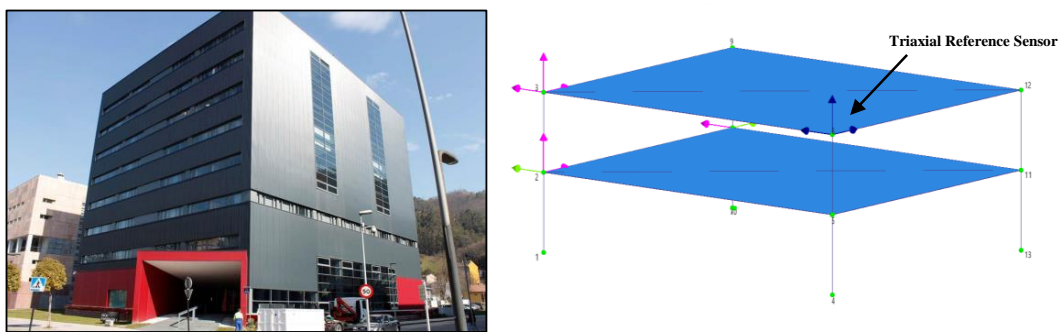


Figure 1. Research Building at EPM Campus (Mieres) and Test Set-Up used in the experiments.

## 2. OMA IDENTIFICATION

The data collected during several days was processed in ARTEMIS MODAL software being the modal parameters identified using the Enhanced Frequency Domain Decomposition (EFDD) technique [2]. The singular value decomposition (SVD) is presented in Figure 2.

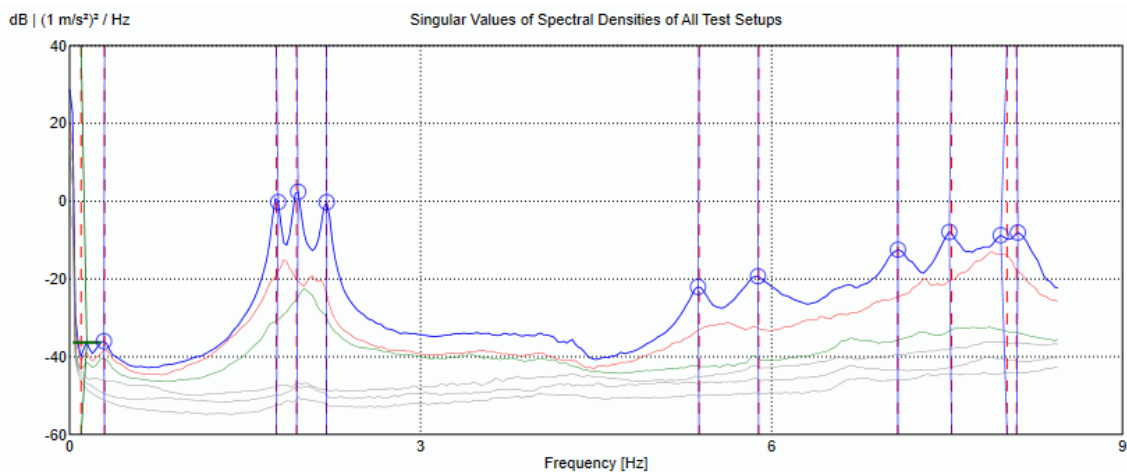


Figure 2. SVD for the EFDD Modal Identification Technique.

The natural frequencies and damping ratios identified for the building are presented in Table 1. In addition, mode shapes of the 1st and 2nd bending and torsion modes are shown in Fig.3.

Although the modes are not repeated, some of them can be considered closely-spaced modes. The modal parameters presented in Table 1 were identified as global modes (bending and torsion), but rigid body modes could also be identified at low frequencies. These modes involve vertical movements and exhibit high complexity, suggesting that the vibration level of the ground is negligible and it must be analyzed in more detail in the future, attaching sensors to both the ground and the building.

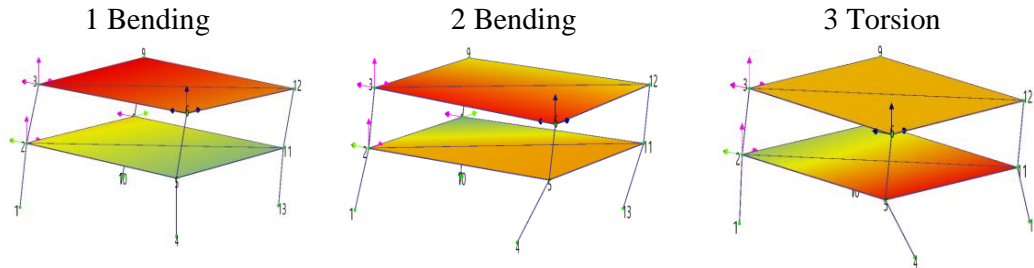


Figure 3. First 3 mode shapes of the building.

Mode	Shape	Frequency [Hz]	Damping [%]
1	1 <sup>st</sup> Bending (x)	1.76	1.138
2	1 <sup>st</sup> Bending (y)	1.94	1.084
3	Torsion	2.19	1.041
4	2 <sup>nd</sup> Bending (x)	5.38	1.328
5	2 <sup>nd</sup> Bending (y)	5.89	2.171

Table 1. Natural frequencies and damping ratios of the building.

### 3. CONCLUSIONS

- The modal parameters of a 7-story building, constructed with prefabricated concrete elements, have been estimated with operational modal analysis.
- Five vibration modes have been identified in the measured frequency range: 4 bending modes and 1 torsional mode.
- From the modal analysis, some vertical modes of the floors at very low frequencies have been identified, which could correspond to ground movements. These rocking-modes should be studied in future works.

### ACKNOWLEDGEMENTS

The authors would like to thank the Ministry of Science and Innovation of Spain for the financial support received in the project “Real-time fatigue monitoring and calculation of civil and industrial structures” (MCI-20-PID2019-105593GB-I00/AEI/10.13039/501100011033).

## REFERENCES

- [1] Muñiz-Calvente, Álvarez-Vázquez, Pelayo, Aenlle, García-Fernández, Lamela-Rey. A comparative review of time- and frequency-domain methods for fatigue damage assessment. *International Journal of Fatigue*. 2022;163.
- [2] R. Brincker, C. Ventura. *Introduction to Operational Modal Analysis*. John Wiley & Sons. 2015.



## EXPERIMENTAL AND NUMERICAL SEISMIC EVALUATION OF CONNECTION SYSTEMS BETWEEN REDUCED-SECTION BEAMS AND STEEL-CONCRETE COMPOSITE COLUMNS

Hugo Pillajo<sup>1</sup>, Luis Romera<sup>2</sup> and Ruth Gutiérrez<sup>3</sup>

<sup>1</sup> Carrera de Ingeniería Mecánica, Universidad Técnica “Luis Vargas Torres” de Esmeraldas  
Esmeraldas, Ecuador  
e-mail: hugo.pillajo@utelvt.edu.ec

<sup>2</sup> Mecánica de Estructuras, Centro de Innovación Tecnológica en Edific. e Ing. Civil (CITEEC)  
ETSI Caminos, Universidade da Coruña, Campus de Elviña s/n, 15071 Coruña, España.  
e-mail: [l.romera@udc.es](mailto:l.romera@udc.es), web page: <http://gme.udc.es/>, <https://www.udc.es/citeec/>

<sup>3</sup> Laboratorio de Análisis Estructural, Centro de Invest. en Tecnol. Navales e Industriales (CITENI)  
Escuela Politécnica de Ingeniería, Universidade da Coruña, C/Mendizábal, s/n, 15403, Ferrol  
e-mail: [ruth.gutierrez@udc.es](mailto:ruth.gutierrez@udc.es), web page: <https://citeni.udc.es/laboratorios/analisis-estructural/>

**Keywords:** Beam-column connections, reduced beam section, seismic analysis, continuity plates

**Abstract.** *The AISC 358-22 code stipulates the utilisation of pre-qualified beam-column connections with reduced section beams (RBS) in order to guarantee the formation of plastic hinges in earthquake-resistant frames. In Ecuador, the beam-column connections employed are typically formed by welded steel I-beams rigidly connected to the column by flanges and web welds. The column is constructed from two longitudinally welded steel U-sections filled with concrete. Welded continuity steel plates are not typically incorporated inside the column, to connect the beam flanges and the metal section plates of the column (Figure 1), due to the complexity of the construction process.*



Figure 1. A representative example of beam-column connection without the inclusion of continuity steel plates.

*The objective of this study is to analyse the behaviour of RBS beam-column connections in a steel building, determining if they comply with the requirements of resistance and floor drift angle. It is important to note that Ecuador is located in a high seismic zone. The behaviour of these connections without continuity plates is characterised by reduced ductility and brittle fracture of the connection at the weld between the beam flange and the column plate.*

In order to enhance the ductility of the connection, two alternative continuity plates for the RBS beam-column composite connection are subjected to experimental and numerical analysis in this study (Figure 2).

The beams and columns are manufactured to full scale and the welding of the connections is conducted in accordance with the actual positions and environments on site (Figure 3). Experimental tests until failure are conducted and compared with the results of numerical models developed with Abaqus software.

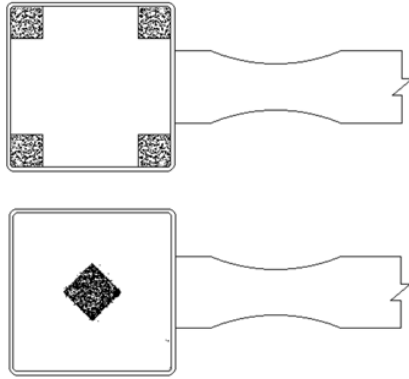


Figure 2. Internal continuity plate configurations



Figure 3. Welding of the connection.

The proposed designs were subjected to numerical calculations against cyclic seismic loads and experimental testing at the Centro de Investigación de la Vivienda de la Escuela Politécnica Nacional de Quito (Ecuador). The specifications of the American codes AISC 341-22, AISC 358-22, FEMA 350-00 and AWS D1.1-20 were followed in the fabrication and testing of the connections (Figure 4).

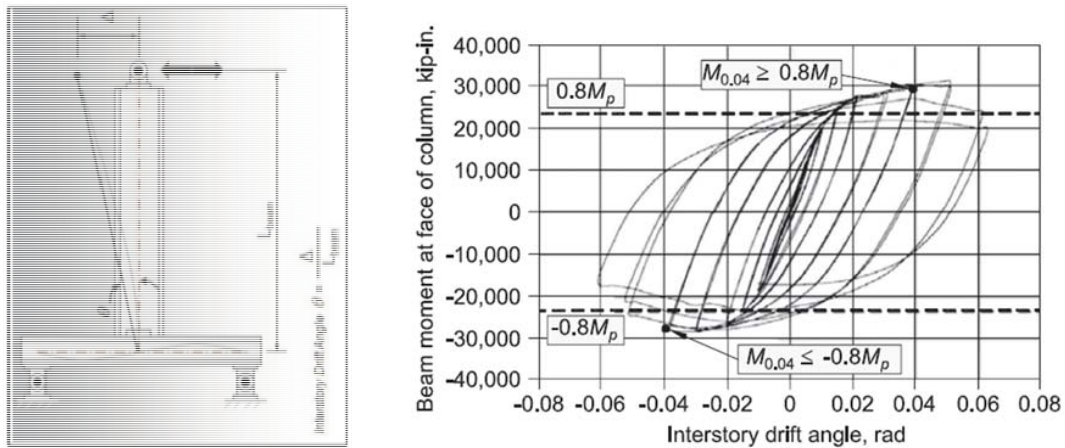


Figure 4. Cyclic test requirements for the connection (AISC 341-22) and hysteresis cycles obtained in an experimental test.

The results obtained at the experimental level demonstrate that the connections meet the qualification requirements of AISC 341-22 (Figure 4), thereby improving the ductility of the connection. Furthermore, the experimental results have allowed the validation of the numerical models that are subsequently applied to inner connections with four RBS beams and one column.

## INFLUENCE OF SOIL TO STRUCTURE INTERACTION IN DYNAMIC LOADING OF TYPICAL SPANISH RC RESIDENTIAL BUILDING FROM THE ‘60S

Beatriz Zapico-Blanco<sup>1\*</sup>, Manuel Vázquez-Boza<sup>1</sup>, Jesús Fabra Forján<sup>1</sup>, Diego Francisco  
Fernández<sup>2</sup> and Celia Montesinos Gañán<sup>1</sup>

<sup>1</sup> Department of Building Structures and Geotechnical Engineering, Universidad de Sevilla  
Reina Mercedes, 2. 41012 Sevilla, Spain  
{bzapico, mboza}@us.es  
{jesusfabra322, celiamont3}@gmail.com

<sup>2</sup> Escuela Politécnica de Mieres, Universidad de Oviedo  
Gonzalo Gutierrez Quiros, 33600 Mieres, Asturias  
[uo276332@uniovi.es](mailto:uo276332@uniovi.es)

**Keywords:** Seismic Vulnerability Assessment, Social Housing, SSI, Existing Buildings, Soil Model

**Abstract.** *Andalusia experiences moderate seismic activity due to the convergence of the Eurasian and African tectonic plates. While significant earthquakes are rare, frequent low-magnitude tremors necessitate incorporating earthquake engineering into building design to ensure stability and safety. Social housing from the 1960s in Andalusia is particularly vulnerable to seismic activity due to aging structures, outdated construction techniques, and the absence of modern seismic codes. Preserving these buildings offers social, cultural, and economic benefits, including affordable housing, historical significance, and sustainability. Assessing their seismic vulnerability requires considering Soil-Structure Interaction (SSI), especially for buildings on soft soils, which amplify ground motion.*

*This study explores the relevance of incorporating SSI in the evaluation of Andalusian social housing, constituting a first step for accurate vulnerability assessment and effective retrofitting strategies to enhance seismic performance. With this aim, a model including structure and soil is created for a representative building of the ‘60s, located in Jerez de la Frontera, Cádiz.*

## 1 INTRODUCTION

Andalusia presents a moderate seismic activity compared to other regions worldwide [1]. This is attributed to its position at the boundary where the Eurasian and African tectonic plates converge. While major earthquakes are uncommon, the region experiences frequent tremors of lower magnitude [2]. Historical records reveal exceptions, with the 1954 earthquake near Almería reaching a magnitude of 7.0, the strongest recorded in the region [3]. Despite the relatively low risk of catastrophic earthquakes, Andalusia's susceptibility to seismic activity necessitates incorporating earthquake engineering principles into building design and construction to guarantee their stability and safety during potential tremors [4].

Social housing projects from the 1960s in Andalusia may be particularly susceptible to seismic activity due to several factors. Their age often means they were built before modern seismic codes were implemented, potentially lacking features designed to withstand earthquake forces. Natural deterioration over time can further weaken these structures, making them even more vulnerable. Construction materials and techniques used in the 1960s might not have prioritized earthquake resistance, potentially utilizing lower quality materials or lacking proper reinforcement detailing. Design considerations like the use of brittle, unreinforced elements or vertical irregularities in the building profile can increase vulnerability too.

Despite these vulnerabilities, preserving social housing from the 1960s offers significant social, cultural, and economic benefits. These buildings hold historical significance, representing a specific period in Andalusia's efforts to address housing shortages and improve living conditions [5]. They can foster strong community ties among residents, contributing to the social fabric and cultural identity of neighbourhoods. In a region facing increasing property values and potential gentrification, preserving social housing provides affordable housing options and helps maintain the social and cultural diversity of these areas. Refurbishing existing structures can be significantly cheaper than building entirely new ones [6]. Furthermore, it promotes sustainability by reducing the need for new construction materials and minimizing environmental impact associated with demolition and construction waste [7]. Social housing projects from the 1960s may be well-integrated into existing urban plans, with established infrastructure and access to amenities. Preserving them can avoid disrupting existing infrastructure and neighbourhood dynamics. In some cases, the basic structure could be adapted to meet modern standards of living comfort and energy efficiency through careful combined renovation [8].

In order to achieve a sustainable preventive refurbishment, the first step is to thoroughly assess the buildings vulnerabilities, considering the building's structural elements, materials, and construction techniques. For basic assessments of low-rise buildings on stiff soil sites, the effects of Soil to Structure Interaction (SSI) might be neglected. Simplified approaches focusing on the building structure itself are often used in these cases. However, when high-rise and/or irregular buildings are studied, or when the soil could be amplifying the seismic action, neglecting SSI could seriously affect the results of the assessment.

When assessing the vulnerability of social housing from the 1960s the consideration of SSI is of relevance, given that many of these buildings are located on soft soils, which tend to amplify ground motion, subjecting the building to stronger shaking forces [9]. Ignoring soil effects could underestimate the actual seismic loads the structure needs to withstand. In addition to this, the foundation transfers the building's weight and seismic forces to the underlying soil. Different soil types have varying stiffness and load-bearing capacities. A proper assessment needs to consider how the foundation interacts with the soil under seismic loading. Neglecting SSI could lead to underestimating the potential for foundation failure during an earthquake, especially for these older buildings, which are not designed for dynamic loading. Furthermore, during an earthquake, the building doesn't just respond to ground motion; it can also influence the soil

behaviour. The building's vibrations can interact with the soil, potentially causing additional stresses and deformations. Ignoring this dynamic interaction could lead to inaccurate predictions of the building's overall response [10].

In the present study, the SSI is incorporated in the assessment of typical Andalusian social housing units, in order to obtain a more realistic picture of the seismic forces acting on the building and its foundation. This leads to a more accurate assessment of the building's vulnerability and potential damage during an earthquake and will also influence the development of targeted retrofitting strategies. These strategies can address weaknesses in the foundation-soil interaction and improve the building's overall seismic performance.

## 2 SAN BENITO NEIGHBOURHOOD

The San Benito neighbourhood, situated northwest of the city of Jerez de la Frontera in Cádiz, Spain, exemplifies the rapid urban development and evolving construction standards that characterized the Francoist era. Built during the 1960s to address the growing housing demand in the region, the estate stands as a testament to the challenges and adaptations faced by engineers and architects during a period of significant changes.



Figure 1: Aerial view of the Polígono de San Benito, Google Maps. Type C buildings are highlighted.

Conceived in 1967, the original project envisioned 922 subsidized housing units, encompassing three distinct building typologies (Figure 1):

Type A: Four-story cruciform-shaped blocks

Type B: Ten-story H-shaped blocks

Type C: Ten-story linear blocks

The initial design employed a metallic structure and direct foundation system, based on geotechnical investigations conducted by the Cádiz Public Works Department. These investigations deemed the terrain suitable for a working load of  $2 \text{ kg/cm}^2$ .

Construction commenced in March 1967 with the Type A buildings, proceeding without major issues. However, during the excavation of foundations for the taller buildings (Type B and Type C), a challenging ground condition emerged. Below a depth of 4 meters, the soil encountered was found to be saturated and unstable, rendering it unsuitable for direct foundation support.

This unforeseen ground condition necessitated a project redesign, incorporating a comprehensive geotechnical study of these materials in 1969. The revised structural solution involved



employing driven piles extending 12 meters to the underlying stable stratum for the affected buildings: four out of eight Type B buildings and two out of three Type C buildings.

Concurrently, the introduction of the earthquake-resistant building code PGS-1 in 1968 prompted a shift from the initial metallic structure to reinforced concrete. This material substitution proved more economical, as it reduced horizontal forces transmitted to the foundations.

The San Benito neighbourhood's adaptation to stricter seismic design requirements, coupled with the discovery of challenging ground conditions during construction, and the project's execution within a period of rapid urban development and evolving construction standards, makes it a compelling case study for examining soil-structure interaction under dynamic loading.

This study concentrates on the type C buildings (see Figure 1). This typology has been selected as pilot study because of its representativeness and relative simplicity, which will allow to establish a clear path for the study of the rest of the buildings.

### 3 BUILDING CONFIGURATION

The structure under study is a ground floor plus nine-story reinforced concrete building. Its main façade is 20.2 m long, the secondary one is 13.51 m long and the total height of the building is 30.05 m. Although it is a quite regular building, it shows a footprint irregularity, in the shape of setback at the ground floor, and an irregularity in height, being the ground floor higher than the rest of the storeys (Figure 2).



Figure 2: Elevation view of the studied building, photo taken by the research team (left) and image from the original drawings retrieved at the Historical Provincial Archive of Cádiz (right)

The original project documents of the building were retrieved at the Historical Provincial Archive of Cádiz. The documents were thoroughly analysed to obtain a clear picture of the building's structure.

A complete in-situ campaign was performed on the building. It was inspected in order to double check its geometry and the relative position of the structural elements. Thermal pictures were taken to confirm the type of floor employed and the locations of beams, columns and installations. The quality of the materials was tested by means of rebound hammer tests and

ultrasound tests. Finally, the natural frequency of the building was measured by means on ambient vibrations and an accelerometer. As will be seen in section 4.4, a geophysical campaign was also performed to obtain information about the soil.

The main structure is formed by reinforce concrete columns and beams, completed with cast in situ joists and ceramic vaults for the floors. A deep foundation system consisting of 35 cm x 35 cm reinforced concrete piles driven to refusal with a length of 12 meters is employed. The piles are arranged in both triangular and square groups on a continuous pile cap of 0.5 meters thickness.

## **4 GEOTECHNICAL PROPERTIES**

### **4.1 Geological setting**

Jerez de la Frontera, nestled in the southwestern extremity of the Guadalquivir Basin, is a testament to the geological forces that have shaped the region over millions of years. This Cenozoic foreland basin, formed in the aftermath of the Alpine orogeny, bears witness to the deposition of post-orogenic sediments that lie discordantly upon the pre-orogenic materials of the Subbetic domain. Understanding the geological context of Jerez de la Frontera is crucial for assessing the geotechnical properties of the terrain and the behaviour of structures constructed upon it.

According to Gutiérrez Mas et al. [13] and the Estudio Previo de Terrenos del Ministerio de Fomento [16], the stratigraphic succession in Jerez de la Frontera comprises the following units, from base to top:

- Upper Miocene Marls (25 m): These marls transition into highly plastic sandy clays in the upper levels, exhibiting high bearing capacity but susceptible to alteration upon hydration.
- Lower Pliocene Sands (17 m): These fine-grained white to yellow sands, occasionally interbedded with sandstone layers and scattered fossils, possess moderate bearing capacity.
- Lacustrine Marly Limestones (5 m): These white marly limestones of Pliocene age contain fossils and flint nodules.

To determine the geotechnical properties of the subsurface formations, two prior geotechnical studies were consulted: one from 1969, conducted as part of the redesign of the Polígono housing estate project; and a second one from 2004, carried out for the construction of an Administrative and Social Services Center nearby.

Additionally, a geophysical study was undertaken within the framework of the Junta de Andalucía research project EMC21\_00255 to determine the shear wave velocities of the geotechnical materials.

### **4.2 1969 Geotechnical Study**

The 1969 geotechnical study, conducted as part of the redesign of the Polígono housing estate project in Jerez de la Frontera, Spain, provides a crucial window into the subsurface conditions of the area. By meticulously analysing the field and laboratory tests performed, we can gain a deeper understanding of the geological profile and geotechnical properties of the terrain.

The cornerstone of the 1969 geotechnical study lies in the comprehensive fieldwork undertaken during the month of August 1969. This involved the execution of four boreholes with

core extraction, enabling the retrieval of fourteen undisturbed soil samples for subsequent laboratory testing. Additionally, eighteen static cone penetration tests (CPTs) were conducted to complement the borehole data.

The interpretation of the core samples recovered from the boreholes yielded a detailed stratigraphic profile of the subsurface, as depicted in Figure 3. This profile serves as a valuable tool for understanding the geological makeup of the terrain and its implications, revealing the presence of three distinct geological strata:

- Clayey sand (0-4.5 m): This unit comprises a moderately compact sandy clay, characterized by its ability to retain some moisture and exhibit moderate bearing capacity.
- Clay (4.5-12 m): This deep-seated unit is composed of a stiff clay, distinguished by its low permeability and high bearing capacity.
- Marl: Located below the clay strata, very compact and hard.

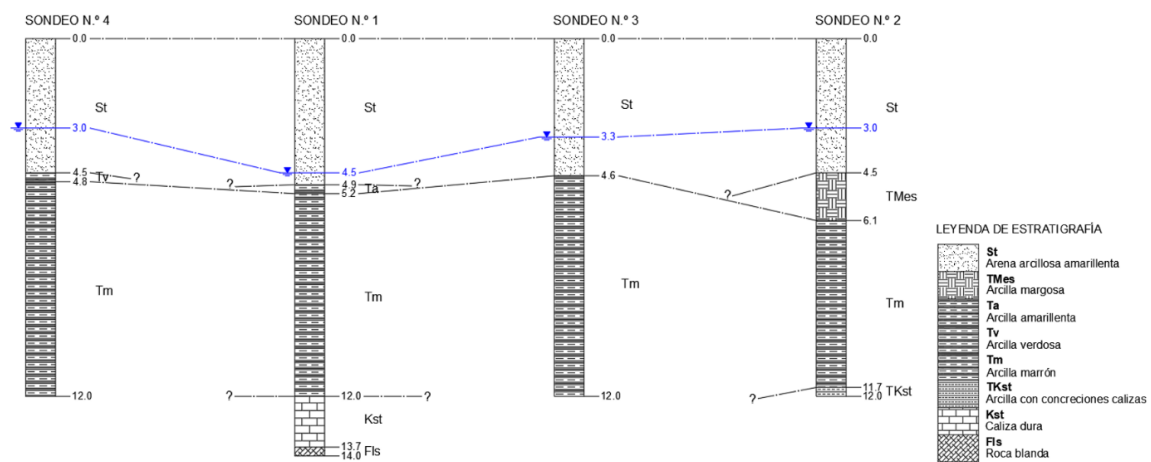


Figure 3: Stratigraphic profile from 1969 geotechnical report

The 1969 geotechnical study included also combination of field and laboratory tests. Among these tests, static cone penetration tests (CPTs) and laboratory analyses of undisturbed soil samples played a pivotal role in characterizing the geotechnical properties of the terrain.

Static cone penetration tests (CPTs) provide a direct measure of the soil's resistance to penetration, offering valuable insights into its strength and deformation characteristics. These tests involve driving a cone-tipped probe into the ground at a constant rate while measuring the force required to maintain that rate. Two critical parameters obtained from CPTs are the cone resistance, which measures the resistance of the cone tip to penetration, reflecting the soil's overall strength; and the friction ratio, calculated by dividing the skin friction by the cone resistance, which provides an indication of the soil's dilative behaviour and sensitivity to shear deformation. The total resistance is measured in-situ as the sum of the cone resistance and the skin friction. The dashed line in Figure 4 represents this total resistance, while the continuous line shows the variations in cone resistance with depth. These variations can be interpreted to identify different soil layers and their corresponding geotechnical properties.



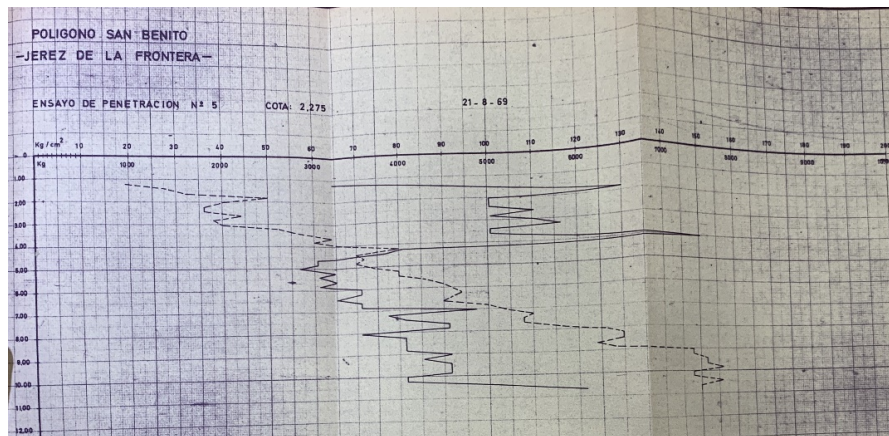


Figure 4: Static cone penetration tests record. cone resistance (continuous line, in  $\text{kg}/\text{cm}^2$ ) and total resistance (dotted line, in kg).

Despite their usefulness, CPTs have certain limitations. In the 1969 study, the 10-ton capacity of the testing equipment occasionally resulted in "rejection" in shallow, hard layers, potentially masking the behaviour of underlying softer soils.

To complement the field data from CPTs, the 1969 study subjected undisturbed soil samples to a battery of laboratory tests. These tests shed light on the soil's composition, moisture content, deformation characteristics, and strength:

- Particle Size Distribution (PSD): This test determines the proportions of different particle sizes (sand, silt, clay) in the soil, influencing its permeability, water retention, and strength.
- Atterberg Limits: These limits (liquid limit, plastic limit) provide an indication of the soil's plasticity and potential for volume change due to moisture variations.
- Dry Unit Weight ( $\gamma_d$ ): This parameter represents the weight of soil per unit volume when dry, reflecting its density and compaction characteristics.
- Unconfined Compressive Strength ( $q_u$ ): This test measures the soil's ability to resist compressive forces, providing an indication of its shear strength.

#### 4.3 2004 Geotechnical Study

The 2004 geotechnical study, conducted for the construction of an Administrative and Social Services Center in Jerez de la Frontera, Spain, complements the 1969 study by providing additional insights into the subsurface conditions of the area. This study employed a combination of field and laboratory tests to characterize the soil profile, assess its compatibility and expansivity potential, and evaluate the likelihood of soft compressible or collapsible soils, including a comprehensive field investigation program:

- Borehole with core extraction: A single borehole was drilled to retrieve undisturbed soil samples for laboratory testing.
- Standard Penetration Tests (SPT): Four SPTs were conducted within the borehole to assess soil density or consistency.
- Continuous Dynamic Penetration Tests (DPSH): Two DPSH tests were performed to supplement the SPT data and provide a continuous record of soil resistance.

In addition to the field investigations, the 2004 geotechnical study also subjected undisturbed soil samples to a battery of laboratory tests to further characterize their properties:

- Particle Size Distribution (PSD)
- Moisture Content: This parameter measures the amount of water present in the soil, which can affect its compaction characteristics, shear strength, and susceptibility to volume changes.
- Atterberg Limits
- Dry Unit Weight ( $\gamma_d$ )
- Unconfined Compressive Strength ( $q_u$ )

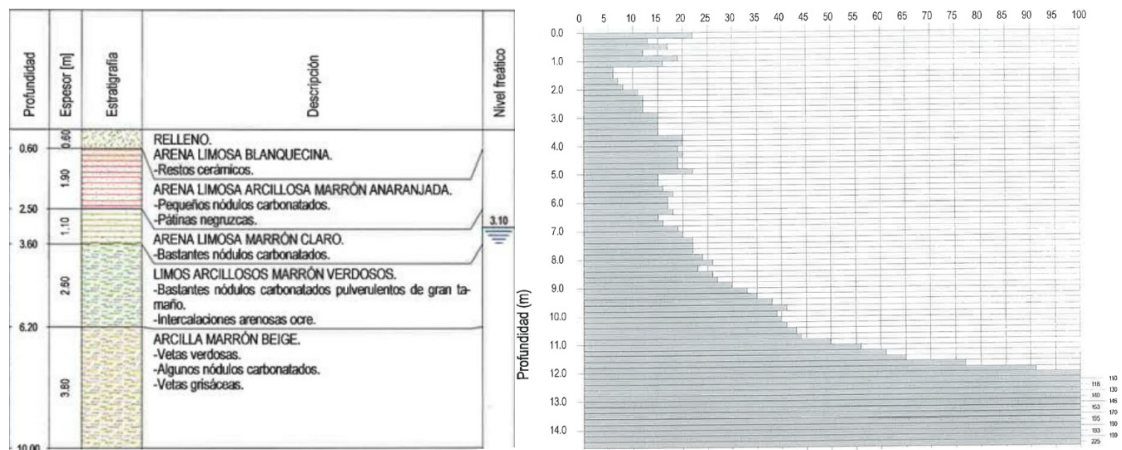


Figure 5: Stratigraphy (left) and DPSH penetration test record (right) of the 2004 Borehole

Figure 5 presents two crucial elements from the 2004 study. First, the stratigraphy of the 2004 Borehole, depicting the soil profile encountered in the borehole, with the presence of three distinct layers:

- Fill (0-1 m): A loose, poorly compacted fill layer.
- Sandy Clay (1-4 m): A moderately compact sandy clay layer.
- Clay (4-10 m): A stiff clay layer with high plasticity.

Secondly, the DPSH penetration test record. This graph illustrates the variations in penetration resistance with depth during a DPSH test. The shape of the curve and the overall resistance values can be used to infer soil type and consistency.

#### 4.4 2024 Geophysical Testing

In March 2024, a geophysical study was conducted to investigate the materials and their seismic velocities along Maestro Álvarez Beigbeder Street in Jerez de la Frontera. This street forms the southeastern boundary of the San Benito Industrial Estate and runs parallel to the profile depicted in Figure 3.

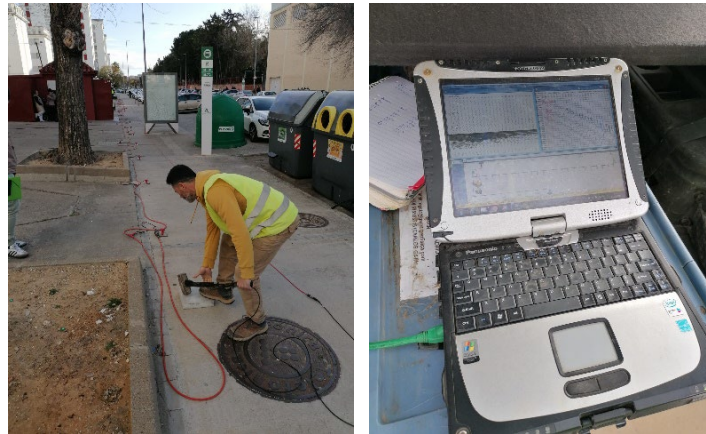


Figure 6: Works during the geophysical campaign

The geophysical campaign employed two-dimensional (2D) MASW seismic surveys along two sections of the street, each with lengths of 170 and 235 meters, respectively. Figure 6 provides a glimpse into the fieldwork. The MASW method involves calculating the shear wave ( $V_s$ ) seismic velocities by analysing the spectral content of surface waves (Rayleigh and Love). Approximately two-thirds of the measurable seismic energy at the surface is associated with these surface waves. To conduct the MASW surveys, 24 low-frequency triaxial geophones were deployed simultaneously, spaced 2.5 meters apart. To cover the length of each profile, the geophones were moved in segments. After triggering the first 12 positions, the corresponding geophones were relocated. The recorded seismic velocities ranged from approximately 190 m/s to 360 m/s. According to the International Code Council [14], lower velocities correspond to less compact, almost loose materials, while higher velocities indicate moderately to very compact materials.

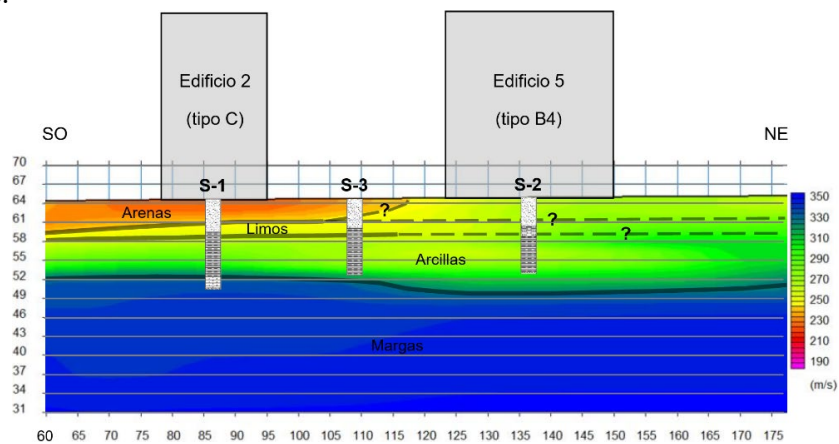


Figure 7: One of the geophysical profiles obtained during the campaign.

Figure 7 presents a section of the second profile that lies beneath the buildings under study. By analysing the profile's velocities and incorporating information from the 1969 and 2004 borehole and penetrometer data, the approximate positions of the contacts between the four strata identified in both geotechnical studies were determined.

#### 4.5 Conclusions

The geotechnical studies of 1969 and 2004, along with the geophysical study of 2024, exhibit consistency in their findings, indicating a similar stratigraphy, albeit with minor variations in the definition of the layers and their properties. Table 1 summarizes the representative values of the descriptive properties of the strata under the type C building under study, obtained by comparing all available data.

Layer	Stretch	Thickness [m]	w [%]	I <sub>p</sub> [°]	ρ <sub>d</sub> [g/cm <sup>3</sup> ]	ρ <sub>t</sub> [g/cm <sup>3</sup> ]	Fines [%]	Classif. USCS
Muddy	Drained	3	11	5	1.7	1.9	39	SM-
clayey sand	Undrained	1.5	22			2.1		SC
Clay	Undrained	7	32	41	1.58	1.9	87	CH
Marl	Undrained	>19	-	-	-	-	-	-

Table 1: Physical properties of the layers

Direct information on the strength (cohesion and friction angle) and deformation (elastic moduli and Poisson's ratio) properties of the strata in the vicinity of the San Benito Industrial Estate was not available from any geotechnical study. Therefore, these parameters were estimated using experimental correlations. The following methods were employed:

- ROM 0.5-0.5 Standard: Table 2.4.3 of this standard allows for correlating the properties with the compactness and consistency of the strata obtained from the standard penetration and Borros tests in the 2004 study.
- Código Técnico de la Edificación (CTE) Foundation Document: Figure D.1 of this document enables correlation between the SPT N-value and the friction angle.
- Robertson and Campanella [17] Formula: This formula estimates the friction angle of granular soils, while Schmertmann's [18] formulas provide estimates for the oedometric modulus and undrained cohesion, all based on the cone tip resistance from CPT tests.
- Theoretical Formula from Elasticity (Eq. 1): This formula relates shear wave velocity to elastic modulus:

$$E = 2\rho V_s^2 (1 + \nu) \quad (1)$$

where E is the elastic modulus,  $V_s$  is shear wave velocity,  $\rho$  is the soil density and  $\nu$  is the Poisson's ratio, which can be approximated as 0.3.

- The following empirical formulas were used for correlating shear wave velocity with undrained cohesion: Agaiby and Mayne [11], L'Heureux and Long [15], Duan et al. [12]

Based on the results of these methods, representative values were estimated and summarized in Table 2. Considering that the data will be used for dynamic calculations, the deformation moduli were determined from the shear wave velocities, resulting in values for small strains, which are especially pertinent to the analysis (L'Heureux & Long, [15]).

Layer	Vs [m/s]	N <sub>B</sub>	N <sub>SPT</sub>	Consistency	q <sub>u</sub> [kPa]	s <sub>u</sub> [kPa]	c [kPa]	φ [°]	E [MPa]
Muddy clayey sand	210	6-12	22	Loose-medium	70-285	–	7	33	230
Clay	275	20-50	24-26	Hard	350-430	100	50	28	375
Marl	350	100-200	–	Hard	1130	200	50	28	605

Table 2: Mechanical properties of the layers

## 5 MODELLING

The software Plaxis 2D was employed for the modelling of both the soil and the building. It is a powerful finite element software specifically designed for geotechnical engineering applications. It allows engineers to model and analyse the behaviour of soil and rock structures under various loading conditions. It can simulate a wide spectrum of soil and rock behaviours. These models incorporate characteristics like elasticity, plasticity, creep, and advanced strength criteria (e.g., Mohr-Coulomb, Hardening-Soil).

To optimize our analysis process and enhance productivity, we have implemented an automated workflow that effectively integrates Excel, Spyder (Python), and Plaxis 2D. Our system utilizes a Python script to establish a seamless interaction between a comprehensive Excel-stored database and the Plaxis 2D software. This setup is particularly crucial as Plaxis 2D, despite its powerful capabilities in modelling complex geotechnical problems, involves time-consuming and repetitive tasks that can hinder efficiency. By automating these processes, our workflow significantly reduces the manual effort required in data entry and model setup, which are prone to human error.

The enhanced automation allows for a single-click modelling of an entire building, translating a 3D structure into a 2D plane in Plaxis 2D. Each plate element within the building model possesses unique characteristics, tailored to replicate the real-world complexities of structural behaviour. In addition to structural modelling, the automated system meticulously models the soil stratigraphy, incorporating various soil strata and their specific properties directly into the simulation. This comprehensive approach ensures that all critical aspects of geotechnical and structural interactions are accurately represented.

Furthermore, the automated setup streamlines the process of applying different analysis conditions necessary for static, modal, and dynamic analysis. With this automation, we can rapidly configure and execute these analyses, making it possible to efficiently assess the structural response under various loading conditions.

Overall, this method not only saves time but also enhances the accuracy and reliability of our engineering analyses, allowing us to focus on more complex challenges and innovative solutions in our engineering practices.

A modal analysis of the building is conducted using the snap-back method, aimed at calibrating the model based on in-situ measurements of the building's fundamental period. For the calculation of free vibration, viscous boundaries are implemented both laterally within the model and at the lower extremity in the y-axis direction. In opting for viscous boundaries, dampers are utilised instead of applying fixed constraints in a specific direction. This approach allows for the simulation of energy dissipation similar to that occurring in the natural soil environment (Figure 8).



A sensitivity analysis on the soil parameters was performed: dynamic versus static (plastic), with the aim of assessing the impact of different soil conditions on the building's fundamental period and determining which set of parameters is the most accurate.

Three situations were compared: with the soil modelled as completely rigid, using dynamic parameters, and using static parameters.

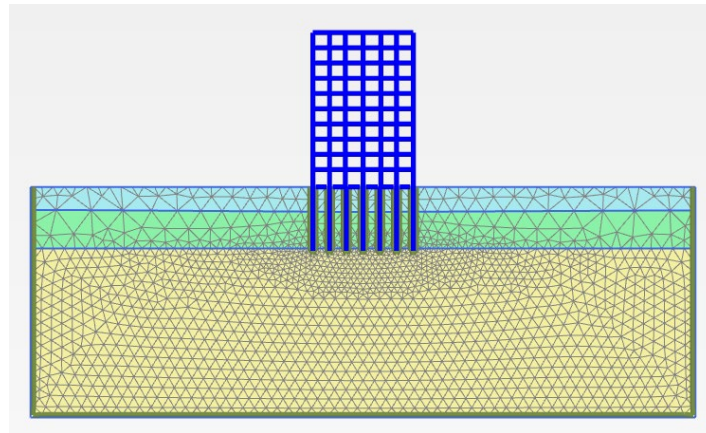


Figure 8: 2D Meshed model of the linear Polígono San Benito building in Plaxis 2D software

## 6 RESULTS AND DISCUSSION

Modal analysis is conducted using the snap-back method, initiated from an in-situ test that captured the fundamental frequency of the first vibration mode. The building calibration is performed under three hypotheses: employing dynamic soil parameters adjusted according to velocities from geophysical testing, using plastic parameters where the modulus of elasticity is derived from correlations with various standards, and considering the soil as infinitely rigid, thus isolating the building's structural response.

Spectral acceleration response (PSA) graphs are obtained at the highest point of the building for each of the hypotheses, the peak of these graphs corresponding to the building's fundamental period (Figure 9).

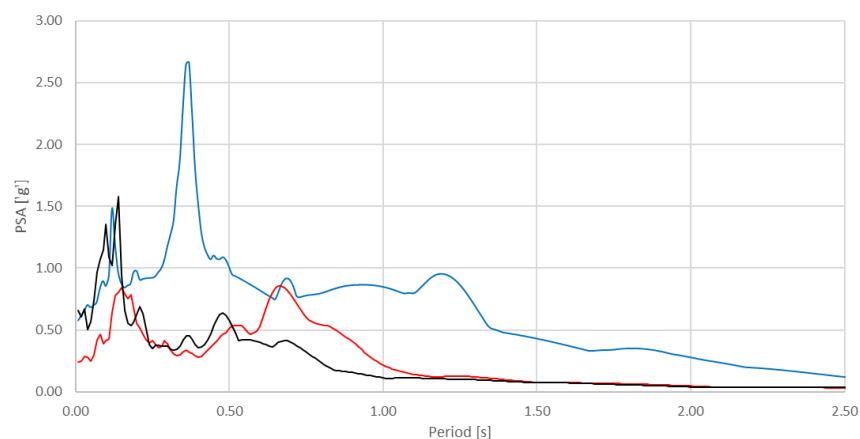


Figure 9: Spectral acceleration response for each soil parameter hypothesis. Rigid (blue), plastic (red) and dynamic (black) soil parameters.

The following results were obtained, displaying the modulus of elasticity used for each stratum (Table 3):

Layer	E [kN/m <sup>2</sup> ]			Measured <i>In-situ</i>
	Dynamic	Plastic	Rigid	
Muddy clayey sand	22.9E4	18.1E3	10E6	-
Clay	37.4E4	22.2E3	10E6	-
Marl	60.3E4	11.0E4	10E6	-
Period [s]	0.14	0.66	0.37	0.53

Table 3: Modulus of soil elasticity and fundamental periods for each hypothesis model

The fundamental period of the building measured during the in-situ campaign was 0.53 s. The numerical model includes only the structural elements of the building, neglecting the stiffness added to the system by elements like external walls and internal partitions. Based on this, it is expected that the fundamental period of the model will be slightly higher than the measured one, indicating a more flexible building.

It can be observed that the using the plastic parameters of the soil provides the best results. The use of dynamic parameters, being more rigid, results in a sharp decrease in the building's period, thereby distorting the natural frequency alignment. Employing rigid soil parameters, which is equivalent to ignoring the SSI, the natural frequency appears lower than that measured in-situ.

## 7 CONCLUSIONS AND FUTURE WORKS

Preserving social housing from the 1960s in Andalusia offers social, cultural, and economic benefits. These buildings hold historical significance and foster community identity. They can be refurbished more cost-effectively than entirely new structures, promote sustainability by re-using existing materials, and avoid disrupting established neighbourhoods. However, their age, pre-modern seismic codes, and potential deterioration over time can make them vulnerable to earthquakes. Construction materials and techniques used in the 1960s might not have prioritized earthquake resistance, and design elements like unreinforced masonry or vertical irregularities can concentrate seismic forces. While Andalusia experiences lower seismic activity, even moderate earthquakes pose a threat if structures are not adequately prepared. A thorough seismic assessment is crucial to determine the actual seismic risk of each building, and, within it, the effect of SSI cannot be neglected.

In the present work, a pilot model of a typical '60s social housing unit has been modelled and analysed, including the soil and the SSI, using the software PLAXIS.

It can be established that this method allows for the direct consideration of SSI effects by integrating both the soil and the structure within the same model, thereby yielding results that are closely approximate and highly representative of reality.

Automation can be effectively implemented to study different building typologies, conduct extensive sensitivity analyses, and explore various soil types

Based on the results observed, the soil significantly influences the fundamental period of the building. If the soil is not considered, the structure exhibits a fundamental period of 0.37 seconds, which positions the analysis too far on the side of safety, potentially underestimating seismic response. However, with the soil accounted for, this extends to 0.66 seconds, contrasting with the in-situ test result, which indicates a fundamental period of 0.53 seconds.

## 8 ACKNOWLEDGEMENTS

This work is part of the project EMC21\_00255 *Mitigation of seismic vulnerability of residential buildings in large, old neighborhoods in Andalusia*, funded by the Junta de Andalucía, Consejería de Universidad, Investigación e Innovación, through its EMERGIA program for research talent attraction.

The research team would like to express gratitude to the Historical Provincial Archive for their collaboration in the retrieval of the original project documents of the buildings; and also to the neighbours of San Benito, for welcoming us into their houses and being of so much help.

## REFERENCES

- [1] Benito, B.; Navarro, M.; Gaspar-Escribano, J. M.; Vidal, F.; Góngora, A.; García Rodríguez, M. J.; Martínez Solares, J.M. (2008). Seismic Hazard in Andalusia Region (Southern Spain). Proc. Of the 14th World Conference on Earthquake Engineering, 9 pp., October 12-17, 2008, Beijing, China
- [2] Gaspar-Escribano, Jorge M., Vidal Sánchez, Francisco, Navarro Bernal, Manuel, Góngora, Ana, García Rodríguez, María José and Martínez Solares, José Manuel (2008). [\*Seismic hazard in Andalusia region \(Southern Spain\)\*](#). In: "14th World Conference Earthquake Engineering", 12/10/2008-17/10/2008, Pekín (China).
- [3] Gayen, S., Villalta, I.V. ad Haque, Sk.M, Earthquake hazard scenario and seismic micro-zonation assessment in Málaga province of Spain, European Journal of Geography, Vol10, number 1:117-133 (2019)
- [4] [Think Hazard - Andalusia - Earthquake](#) - ThinkHazard (2023)
- [5] Giannino, M.A.; Orabona, F. Social housing in urban regeneration. Regeneration heritage existing building: Methods and Strategies. TeMA-J. Land Use Mobil. Environ. 2014, 15
- [6] Crawford, K., Johnson, C. E., Davies, F., Joo, S., & Bell, S. (2014). Demolition or refurbishment of social housing? A review of the evidence. UCL Urban Lab and Engineering Exchange
- [7] Sinha, R., Lennartsson, M., & Frostell, B. (2016). Environmental footprint assessment of building structures: A comparative study. Building and Environment, 104, 162-171
- [8] Royal Institute of British Architects (2019). Conservation, modernisation & adaptation of existing buildings. Design matters. <https://www.architecture.com/knowledge-and-resources/resources-landing-page/conservation-modernisation-and-adaptation-of-existing-buildings>
- [9] Kramer, S. L. (1996). Geotechnical Earthquake Engineering. International series in civil engineering and engineering mechanics. Prentice Hall, New Jersey ISBN 0-13-374943-6
- [10] Sharma N, Dasgupta K, Dey A (2018) A state-of-the-art review on seismic SSI studies on building structures. Innov Infrastruct Solut 3(22):1–16
- [11] Agaiby, S. S., & Mayne, P. W. (2015). Relationship between Undrained Shear Strength and Shear Wave Velocity for Clays. Proceedings of the 6th Symposium on Deformation Characteristics of Geomaterials, 358-365.



- [12] Duan, W., Cai, G., Lio, S., & Puppala, A. J. (2019). Correlations between Shear Wave Velocity and Geotechnical Parameters for Jiangsu Clays of China. *Pure and Applied Geophysics*, 176(2), 669-684. <https://doi.org/10.1007/s00024-018-2011-x>
- [13] Gutiérrez Mas, J. M., Martín Algarra, A., Domínguez Bella, S., & Moral Cardona J. P. (1991). *Introducción a la Geología de la Provincia de Cádiz*. Servicio de Publicaciones. Universidad de Cádiz.
- [14] International Code Council (2006). *International Building Code: Structural and fire- and life-safety provisions (seismic, wind, accessibility, egress, occupancy and roof codes)*.
- [15] L'Heureux, J. S., & Long, M. (2016). Correlations between Shear Wave Velocity and Geotechnical Parameters in Norwegian Clays. *Proceedings of the 17th Nordic Geotechnical Meeting: Challenges in Nordic Geotechnics*.
- [16] Ministerio de Fomento (1997). *Estudio Previo de Terrenos – Itinerario Jerez de la Frontera-Los Barrios – Tramo: Jerez de la Frontera-Los Barrios*.
- [17] Robertson, P. K., & Campanella, R. G. (1983). Interpretation of Cone Penetration Test. *En Canadian Geotechnical Journal* (Vol. 20).
- [18] Schmertmann, J. H. (1978). *Guidelines for Cone Penetration Test: Performance and Design* (Tech. Rep. No. FHWA-TS-78-209). United States Federal Highway Administration, Office of Research and Development <https://rosap.nhl.bts.gov/view/dot/958>

# SEISMIC VULNERABILITY ASSESSMENT OF THE ARCH-STRUCTURE IN THE HISTORICAL CITY OF MEDINA AZAHARA

Wouter Kroon<sup>1</sup>, Rita. Esposito<sup>1</sup>, Satya Sharma<sup>1</sup> and Beatriz Zapico-Blanco<sup>2\*</sup>

<sup>1</sup> Faculty of Civil Engineering and Geoscience, Delt University of Technology  
Stevinweg 1, 2628 CN Delft, The Netherlands  
[w.b.kroon@student.tudelft.nl](mailto:w.b.kroon@student.tudelft.nl)  
{r.esposito, s.sharma-9}@tudelft.nl

<sup>2</sup> Department of Building Structures and Geotechnical Engineering, Universidad de Sevilla  
Reina Mercedes, 2, 41012, Sevilla, Spain  
\*bzapico@us.es

**Keywords:** Seismic analysis, Heritage, Medina Azahara, Natural Stone Masonry, Modal push-over analysis, Arched structure

## EXTENDED ABSTRACT

### 1. INTRODUCTION

The historical city of Medina Azahara in Córdoba stands as one of the best-preserved remnants of the Umayyad Caliphate of Córdoba. This heritage site holds immense significance for the region and has earned recognition on the UNESCO World Heritage List. More than a tourist attraction, the city serves as a testament to medieval Spanish culture and symbolises the identity of Andalusia. Despite its importance, the structural integrity of the site, particularly concerning seismic loading, has seen limited research. Earthquakes are not uncommon in the region and pose a risk of causing irreparable damage.

The focus of this study is a free-standing natural stone and brick-masonry arch-structure comprising four connected arches—the sole remaining component of what was once a larger porticoed gallery with fourteen passable arches. The primary aim is to assess the structural response of this arch-structure to seismic loading, employing finite element models and using a modal pushover analysis. All models are created in the DIANA FEA environment. Several sensitivity analyses are undertaken, such as element type (i.e. solid or shell elements), to optimize the numerical model. Material properties input for these models is based on material properties used for research on similar structures, such as the Mosque-Cathedral of Córdoba, and data from an ongoing material characterisation testing campaign, and the numerical models are calibrated based on in situ measurements of the structure fundamental period with ambient vibrations.



Figure 1: Arch-structure in Medina Azahara, Córdoba

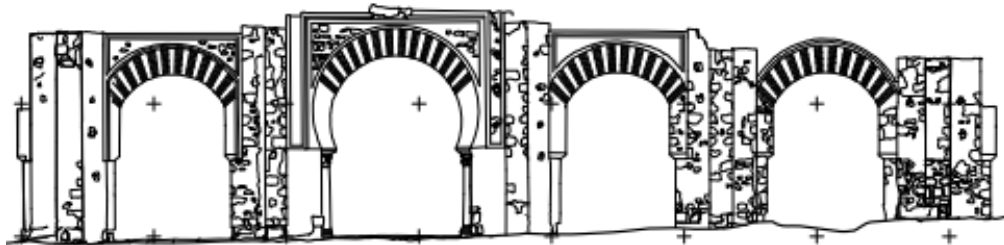


Figure 2: Drawing of the arch-structure in Medina Azahara, Córdoba (Almagro, 2011)

## 2. MEDINA AZAHARA AND THE GREAT PORTICO

Standing as a UNESCO World Heritage Site, Medina Azahara, or "the Shining City," embodies the zenith of Islamic Spain's caliphal power. Built by Caliph Abd ar-Rahman III, it served as a symbol of his authority and rivalled the grandeur of rival caliphates. Medina Azahara's significance lies in its exquisite blend of Islamic, Byzantine, and Roman architectural styles, reflecting the vibrant cultural exchange of the era. The intricate details, from water features to poetry inscriptions, offer a window into the artistic mastery of the time. Furthermore, the city's well-defined zones, showcasing the royal palace, administrative buildings, and residential areas, provide valuable insights into Islamic urban planning principles.

The Great Portico constitutes the most emblematic, symbolic, and ceremonial entrance to the heart of the Alcázar enclosure. It served as a monumental entrance to the heart of the palace complex. This grand, arcaded gallery was initially designed with fourteen arches, a blend of rounded segmental and the distinctive horseshoe style. It wasn't just functional - the white plasterwork and alternating red brick and limestone voussoirs (wedge-shaped stones) showcased a decorative flair. This ceremonial gateway witnessed the Caliph reviewing his troops from a rooftop viewpoint overlooking a vast open space known as the Plaza de Armas or al-Muzara, which served as the army's training ground.

However, the passage of time led to alterations. Four of the northern arches were eventually closed off to create additional rooms, including a latrine. Thankfully, archaeological efforts tell another part of the story. Excavations led by Don Félix Hernández between 1970 and 1975 unearthed the remains of this extensive arcade. Building on this legacy, Don Rafael Manzano

Martos, who served as director-conservator from 1975 to 1985, undertook restoration efforts. His work included raising four of the fourteen arches back to their original height, offering a glimpse of the portico's former grandeur. The Great Portico stands as a testament to both the architectural and ceremonial significance within Medina Azahara, and understanding it allows us to appreciate the architectural marvels and cultural richness of Islamic Spain during its caliphal peak.

In the context of Medina Azahara (10<sup>th</sup> century AD), arched structures were a well-established and essential construction technique, a prevalent construction method throughout the Spanish Islamic world. They were widely used in palaces, mosques, public buildings, and even bridges. Brick and stone were common materials for constructing arches, often utilizing voussoirs for stability. Skilled masons developed techniques for creating different arch shapes like segmental, horseshoe, and pointed arches. Studying the behavior of arches in Medina Azahara can offer valuable information applicable to other heritage buildings with similar structures.

### **3. SEISMIC HAZARD**

Although the Iberian Peninsula experiences moderate seismic activity, Medina Azahara's situation directly on the Guadalquivir Depression raises concerns. Historical evidence even suggests strong earthquakes may have contributed to the city's abandonment.

Intriguingly, recent research on the city's abandonment points towards the possibility that earthquakes may have played a role. Studies suggest strong tremors, potentially reaching MSK/EMS VIII intensity, might have occurred around the 11th century, potentially contributing to the city's demise. While the precise intensity of past earthquakes in Medina Azahara's immediate location may require further investigation, this evidence underscores the importance of understanding the Arch-Structure's vulnerability to seismic events. By assessing its potential weaknesses, we can take proactive measures to safeguard this cultural treasure from future earthquakes.

### **4. PROPERTIES OF THE FINITE ELEMENT MODELS**

Figures 1 and 2 show an image of the remaining structure as well as a drawing of the arch-structure (taken from *PLANIMETRÍA DE MADĪNAT AL-ZAHRĀ'* by Almagro (2011)). The dimensions of the structure are by lack of in-situ measurements on the geometry of the structure (at the time of constructing the model) estimated from this drawing and other drawings from the same report. The model-geometry is shown in figure 3. A 3-dimensional model is chosen over a 2-dimensional, because the accuracy of a more complex model is deemed more important than a lower computing time. The model only uses regular solid finite elements with linear interpolation. Later versions will include interface elements at specific mortar joints. Some other simplifications were adapted in the model. Most notably, the inclination in the terrain on which the structure stands, is neglected and in initial versions of the model the top part of the fourth arch from the left is included, which in reality does not exist anymore. Lastly, the structure is fixed at its base in all directions and rotations.

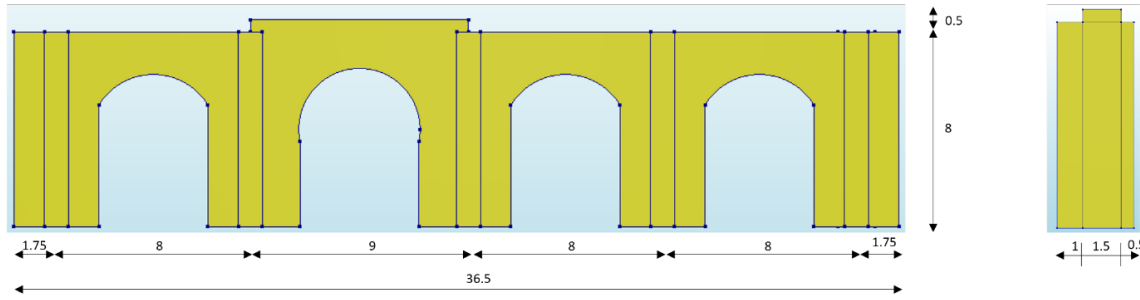


Figure 3: Estimated dimensions of the arch-structure (in meters)

## 5. MATERIAL PROPERTIES

The initial model defines only a single material: stone masonry for the entire structure. This is a simplification as the arches also consist of a combination of brick-masonry and solid natural stone blocks, which will be included in later versions of the model. The columns are made out of stone masonry. The defined properties of the stone-masonry material are based on the properties for limestone-masonry used in the research by Requena-Garcia-Cruz et al. (2023) on the Mosque-Cathedral of Córdoba. The data from the ongoing material characterisation testing campaign was used to verify the validity of the use of these values for the model of the arch-structure in Medina Azahara.

## 6. MODAL PUSHOVER ANALYSIS

The behaviour of the arch-structure to seismic loading is analysed using a modal pushover analysis. Firstly, an eigenmode analysis was performed. From this analysis there could be concluded that two modes were significant for the behaviour of the structure. One mode for the in-plane dynamic behaviour and one mode for the out-of-plane behaviour. (From the eigenmode analysis one more mode could be considered for the out-of-plane behaviour in combination with the first out-of-plane mode but is not done for the current pushover analysis). Subsequently, a modal pushover analysis was performed in both the in-plane and out-of-plane direction separately. The out-of-plane pushover gave a significantly lower resistance compared to the in-plane pushover.

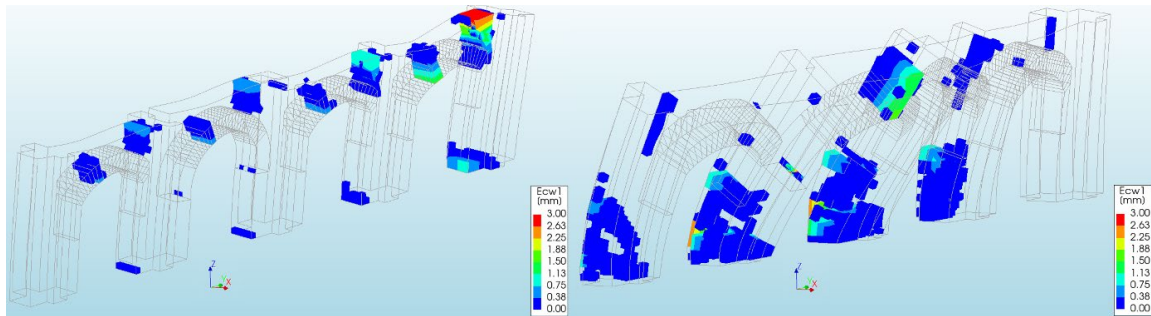


Figure 4: Crack pattern and deformation plot (deformation scaling factor: x500) of in-plane (left) and out-of-plane (right) pushover analysis

## 7. STRUCTURAL RESPONSE

In figure 4, the crack pattern and the scaled deformation of the in-plane and out-of-plane pushover analysis, respectively, is shown. The crack patterns show the high tensile stress areas in the structure induced by the pushover loads, respectively. A sway mode dictates the in-plane behaviour and causes cracking in the arches beside the column. For the out-of-plane behaviour

mainly the second arch from the left seems to topple over, causing cracking in its columns and in the top-middle of the arch.

## **8. DISCUSSION**

Due to estimations and assumptions on, for example, the material properties, the results of the current analysis could give a good prediction of the behaviour of the arch-structure, but only a general indication of its capacity. Future versions of the finite element model will include a combination of different materials (solid natural stone and clay brick-masonry), as well as masonry joints, and some simplifications will be eliminated, such as the missing top of the right-most arch.

### **Conclusion and future works**

The preliminary results of this research have showed the structural response of the free-standing arch-structure, specifically subjected to two different modal pushover loads. Concluded from the first analysis, the out-of-plane pushover is the critical load compared to the in-plane pushover load. The deformation plots with the crack patterns gave an indication of places in the structure where high stresses and cracking could occur due to seismic loading. Future analyses would include models with three materials: stone-masonry, brick-masonry and solid natural stone blocks, mortar joints modelled using interface finite elements and modal pushover analyses combining pushover loads (e.g. two out-of-plane modal pushover loads), if deemed relevant to the study. Emphasis will be laid on the structural response to out-of-plane modal pushover loading.

## KINEMATIC INTERACTION FACTORS FOR BUCKET FOUNDATIONS IN HOMOGENEOUS SOILS USING MULTIFEBE

**Cristina Medina, Jacob D.R. Bordón, Luis A. Padrón\*, Juan C. Galván, Juan J. Aznárez,  
and Orlando Maeso**

Instituto Universitario de Sistemas Inteligentes y Aplicaciones Numéricas en Ingeniería  
Universidad de Las Palmas de Gran Canaria, Las Palmas de G.C., 35017, Spain  
e-mail: {cristina.medina, jacobdavid.rodriguezboron, luis.padron,  
juancarlos.galvan, juanjose.aznarez, orlando.maeso}@ulpgc.es

**Keywords:** Bucket, Foundation, Kinematic response, Soil-Structure Interaction

**Abstract.** *The knowledge of the way in which foundations respond to incoming seismic waves is essential when analyzing the dynamic behaviour of structures subjected to earthquake loads. Among the different methodologies available to tackle this problem, a substructuring approach is useful in many cases. Under such approach, the dynamic properties of a foundation are synthesized into impedance functions and kinematic interaction factors, which are later employed to represent the foundation under a certain structure when studying the seismic response of the system.*

*The available technical literature contains impedance functions and kinematic interaction factors for the most common types of foundations and soils, especially for embedded footings and pile foundations [1–7]. The available information for the specific case of the dynamic response of bucket foundations is, on the contrary, not so abundant. Liingaard et al. [8] or He and Kaynia [9] provided impedance functions for flexible buckets in viscoelastic soils, and for rigid buckets in Biot’s poroelastic soils, respectively. However, to the authors’ knowledge, kinematic interaction factors for this type of problem are not readily available in the literature in a format that allows their direct incorporation into a substructuring analytical or numerical model of a structure.*

*For this reason, kinematic interaction factors for bucket foundations subjected to vertically–incident shear waves are presented in this work. To do so, a numerical methodology implemented in the software MultiFEBE [10] and based on a boundary element – finite element model of a flexible bucket foundation is employed. The flexible skirt is modelled using shell finite elements while the subsoil is modelled as a zoned-homogeneous viscoelastic soil using the boundary element method. Viscoelastic homogeneous soils are initially considered.*

*Results are provided in terms of real and imaginary parts of the translational and rotational kinematic interaction factors as a function of dimensionless frequency. A variety of representative foundation geometries is studied, giving rise to a series of dimensionless plots that cover a wide range of possible cases.*



### **Acknowledgements**

*This work was funded by the Ministerio de Ciencia, Innovación y Universidades and the Agencia Estatal de Investigación of Spain (MCIN/AEI/10.13039/501100011033) through research project PID2020-120102RB-I00.*

### **References**

- [1] Gazetas G. (1991) *Formulas and charts for impedances of surface and embedded foundations. Journal of Geotechnical Engineering* 117(9), 1363–1381.
- [2] Gazetas G., Fan K., Kaynia A. and Kausel E. (1991) *Dynamic interaction factors for floating pile groups. Journal of Geotechnical Engineering* 117(10), 1531–1548.
- [3] Fan K., Gazetas G., Kaynia A. and Kausel E. (1991) *Kinematic seismic response of single piles and pile groups. Journal of Geotechnical Engineering* 117 (12), 1860–1879.
- [4] Mylonakis G. and Gazetas G. (2002) *Kinematic pile response to vertical P-wave seismic excitation. Journal of Geotechnical and Geoenvironmental Engineering* 128(10), 860–867.
- [5] Mylonakis G., Nikolaou S. and Gazetas G. (2006) *Footings under seismic loading: Analysis and design issues with emphasis on bridge foundations. Soil Dynamics and Earthquake Engineering* 26(9), 824–853.
- [6] Zheng C., Mylonakis G., Kouretzis G. and Luan L. (2022) *Kinematic seismic response of end-bearing piles to S-waves. Soil Dynamics and Earthquake Engineering* 163, art. no. 107547.
- [7] Medina C., Padrón L.A., Aznárez J.J., Santana A. and Maeso O. (2014) *Kinematic interaction factors of deep foundations with inclined piles. Earthquake Engineering and Structural Dynamics* 43(13), 2035–2050.
- [8] Liingaard M., Andersen L. and Ibsen L.B. (2007) *Impedance of flexible suction caissons. Earthq Eng Struct Dyn* 36, 2249–2271.
- [9] He R. and Kaynia A.M. (2021) *Dynamic impedances and load carrying mechanism for skirted foundations. Marine Structures* 79, art. no. 103023.
- [10] Bordón J.D.R., Álamo G.M., Padrón L.A., Aznárez J.J. and Maeso O (2022) *Multi-FEBE: A multi-domain finite element–boundary element solver for linear mixed-dimensional mechanical problems. SoftwareX* 20, art. no. 101265.

## EXPERIMENTAL INVESTIGATION OF PILE INSTALLATION SETTINGS UNDER COUPLED AXIAL-TORSIONAL EXCITATION

S.Sanchez Gomez<sup>1</sup>, A. Tsetas<sup>1</sup>, and A. Metrikine<sup>1</sup>

<sup>1</sup>Delft University of Technology  
address

e-mail: {s.sanchezgomez-1; a.tsetas; a.metrikine}@tudelft.nl

**Keywords:** GDP shaker, pile dynamics, Lab scale experiments, axial-torsion vibrations.

**Abstract.** *Offshore wind is a primary source of renewable energy. The international sustainability targets require a significant increase of offshore wind capacity. This leads to ever increasing size of offshore wind turbines (OWTs), water depth of installation and distance to shore. At present, OWTs are primarily supported by bottom-fixed foundations such as monopiles. Monopile installation is mostly performed by means of impact hammering. However, this method raises major environmental concerns related to underwater noise emissions, which can be only partially mitigated by employing costly sound-proofing measures. As a result, alternative installation techniques that are environmentally friendly and high-performing are vital for the offshore wind industry.*

*Vibratory pile driving is an efficient alternative to impact piling. To further boost the potential of vibratory technologies, the Gentle Driving of Piles (GDP) was developed and successfully tested throughout an extensive experimental campaign that was executed during 2019 in the Port of Rotterdam. This technology is based on the combination of high-frequency torsional and low-frequency vertical vibrations, aiming to improve the pile installation process. The preceding field campaign showcased the installation performance of the GDP method and pointed towards potential technical improvements.*

*This work, focuses on the introduction of new and unique features in the context of vibratory and GDP methods. Specifically, a lab-scale shaker that accomplishes frequency-amplitude decoupling of the input excitation has been designed, engineered and manufactured. Frequency-amplitude coupling is a common constraint in standard vibratory devices, operating based on the counter-rotation of eccentric masses. The present shaker consists of a main optimized aluminium block that is connected with three linear hydraulic actuators, two positioned horizontally and one positioned vertically, in order to generate torsional and vertical vibrations. The actuators are position-controlled during installation, and their amplitude and frequency are variable and independent to each other. Furthermore, an experimental campaign was designed and executed, in which the new lab-scale GDP shaker was employed to install piles into the soil; the respective results are discussed herein. Particular emphasis is placed on the effect of the different shaker settings on the installation performance, which is studied by means of direct shaker (input) and pile measurements.*

## SEISMIC ANALYSIS OF THE ACCESS VIADUCTS IN THE FOURTH BRIDGE OVER THE PANAMÁ CANAL PROJECT

A. José Hernández-Carrillo Venegas<sup>1</sup>

<sup>1</sup> Ayesa Ingeniería y Arquitectura  
Avenida Marie Curie s/n. Polígono Tecnológico La Cartuja. Sevilla, España.  
e-mail: ajhernandez@ayesa.com

**Keywords:** Seismic design, Seismic Isolation, Friction Pendulum Bearing (FPB), Time Histories Analysis, Rayleigh and Modal damping

**Abstract.** *The Consortium Panama Fourth Bridge has contracted Ayesa for the independent checking (CAT III) of the Fourth Bridge project over the Panama Canal. This project entails the construction, in Panama City, of a cable-stayed bridge with a main span of 485 meters and a clearance of 75 meters over the Panama Canal, accompanied by approximately 2500 meters of access viaducts linking it to the new East and West interchanges positioned on either side of this unique bridge.*

*Panama experiences significant seismic activity due to its location in a tectonically active area. This condition, coupled with the project's critical role crossing one of the world's most important waterways, has necessitated a highly stringent seismic design.*

*This paper elucidates the seismic strategy being implemented in the design for one of the access viaducts of this project and expounds on the methodology employed in the structural modelling conducted by Ayesa as the independent supervisor of the project, with a particular focus on aspects related to modelling.*



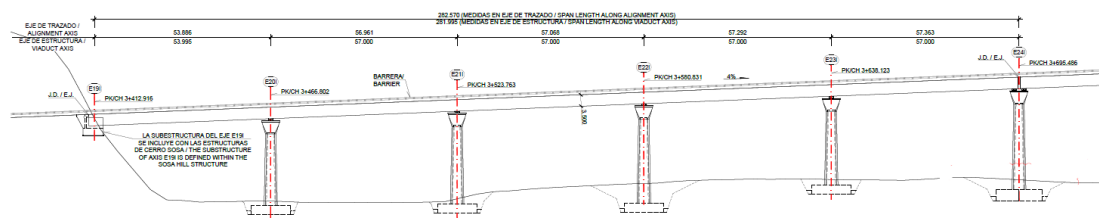


Figure 2: Longitudinal Section of selected Access Viaducts for this paper

## 2.2 Seismic hazard

The study area is situated on the Panama microplate, surrounded by numerous subduction zones with adjacent plates such as the Caribbean to the North, the Andean and South American to the East, the Cocos to the West, and the Nazca to the South, with movements of several tens of millimeters per year. Consequently, it is a tectonically very active region with high deformation rates, where a large number of highly active faults such as Pedro Miguel, Limón, Azota, Miraflores, and Río Gatún are located, causing significant earthquakes. This is evidenced by historical seismic records in the study area, with earthquake magnitudes exceeding 7.00 in an area with a radius of less than 250 kilometers.

This high seismicity with very close active faults, combined with the significant project requirements and the importance of the structures (critical or essential), has required the development of specific Seismic Studies, in particular, a Probabilistic Seismic Hazard Analysis (PSHA) and a Site-Specific Ground Motion Response Analysis (SRA). These studies have defined the seismic action that requests the structures being designed.

## 2.3 Seismic design requirements

The design requirements for the bridges covered in this paper, in addition to the corresponding regulations, are defined in the Project Specifications [1] to which they belong. Regarding the seismic design criteria for the Access Viaducts, the following aspects are highlighted:

- For durability reasons, steel structures is not acceptable except for the main bridge.
- Two levels of seismic risk are considered: Functional Evaluation Earthquake (FEE) with a return period of 475 years and Safety Evaluation Earthquake (SEE) with a return period of 2475 years.
- The admissible damage levels for each of these earthquakes are summarized in the following table. As can be seen, the damage levels are very low considering the magnitude of the earthquakes, as it is intended that the structures remain usable after a seismic event with minimal repairs, maintaining traffic continuity.

Component	Damage level	
	FEE	SEE
Main members of superstructure	Without damage	Minimum damage
Secondary members of superstructure	Without damage	Minimum damage
Columns	Minimum damage	Repairable damage
Bearings	Without damage	Repairable damage
Expansion Joints	Minimum damage	Repairable damage

Table 1: Admissible damage level.

- A calculation is mandatory through nonlinear time-history analysis for both FEE and SEE using the acceleration time histories derived from the Site Response Analysis (SRA) conducted.

## 2.4 Seismic design strategy

In general, and according to reference [2], three types of seismic strategies can be defined in bridge design:

- Type 1. Ductile Substructure with Essentially Elastic Superstructure. This category includes conventional plastic hinging in columns, walls, abutments and even foundations.
- Type 2. Essentially Elastic Substructure with a Ductile Superstructure: This category applies only to steel superstructures,
- Type 3. Elastic Superstructure and Substructure with a Fusing Mechanism between the Two. This category includes seismically isolated structures and structures in which supplemental energy-dissipation devices.

Considering the project's constraints (concrete structures, high seismicity, and low damage level), only the Type 3 strategy is feasible. Therefore, a seismic isolation system has been considered between the deck and the piers, which reduces damage to both the piers and the foundation during the seismic event by concentrating dissipation, damping, and isolation at the supports. With this strategy, inelastic behavior of the substructure does not make sense since it is intended that the isolators work and plastic hinges do not form in the substructure as explained in reference [3].

Given the above, and despite allowing repairable damage in the piers (yielding is allowed without requiring their replacement) after the SEE, the design is considered an essentially elastic behavior of the piers.

Among the different types of isolators that exist, those selected for this project for the Access Viaducts have been friction ones, specifically the Double Concave Friction Pendulum (DFP) which comprises two sliding concave surfaces with an articulated slider.

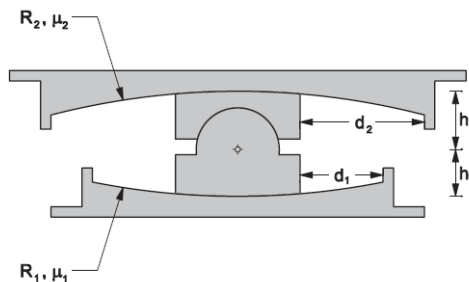


Figure 3: Scheme of a DFP with sliding surfaces of different displacement capacities

The reasons for this choice are argued as follows:

- The high vertical load they must support due to the type of deck and spans considered.
- The 50-year service life required by the Project Specifications [1], which is difficult to achieve with other types of supports that are not pendulum-based.
- The choice of the DFP over the single-concave friction pendulum (SFP) is because, although the behavior is quite similar for the SEE, it shows better performance for smaller but more frequent earthquakes like the FEE, transmitting lower forces to the substructure.

The DFP acts as an adaptive isolation system since stiffness and damping vary in proportion to the level of input ground motion. Additionally, the dimensions of the DFP bearings are smaller than those of the SPF, as the total deformation is divided into two surfaces [4]. This allows for a reduction in the pier capitals' size.

### 3 STRUCTURAL MODEL

#### 3.1 General Description

The bridge has been calculated by using the MIDAS Civil Software. A three – dimensional models by means of frame elements with six degrees of freedom nodes has been considered taking into account the geometry of the structure.

The influence of the adjacent section to the one considered here is accounted for by including an additional span in the model beyond the pier where the expansion joint is located.

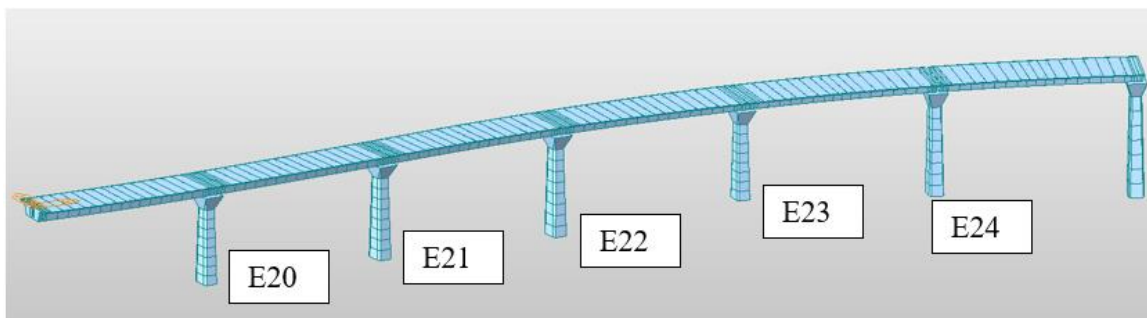


Figure 4: Structural model of the analyzed bridge and column denomination

The deck rests on the piers through two supports modeled using general links. The eccentricity of the deck concerning the supports is considered by including the corresponding offsets.

Regarding boundary conditions, the piers have a perfect embedment in the ground. Although regulations like reference [3] allow considering a strategy based on transient foundation uplift or foundation rocking involving separation of the foundation from the subsoil, which reduces demands due to greater flexibility of the pier and energy loss caused by this effect, this phenomenon is not considered in this case. It should be noted that the footings are anchored to the ground to ensure their stability against overturning during the earthquake, so under these conditions, rocking cannot be considered.

Another interesting aspect due to its influence on the results is the stiffness of the columns in the models. An earthquake will cause a loss of stiffness in the columns due to cracking. Therefore, regulations allow considering a reduction in stiffness in the calculation models, which will result in a decrease in design forces at the expense of increasing displacements. This reduction in inertia for the models carried out in this project is evaluated at around 50% compared to the gross inertia.

Considering the above, all aspects related to soil-structure interaction are greatly simplified compared to a foundation with piles where nonlinear Winkler springs or impedance functions are used in the models. The nonlinearities of the presented model are exclusively focused on the support devices, which will better delimit their influence on the obtained results.

Regarding the analysis method, direct integration has been employed according to Newmark's method (constant acceleration).

### 3.2 Acceleration Time Histories

The acceleration time histories have been obtained from the PSHA and SRA specifically developed for this project. As a starting point, horizontal and vertical acceleration response spectrums (ARS) at the foundation level are obtained. The next image shows these design spectrums for a return period of 2475 years (SEE) and a 5% damping system. For simplicity and greater interest, this will be the only earthquake analyzed in this paper.

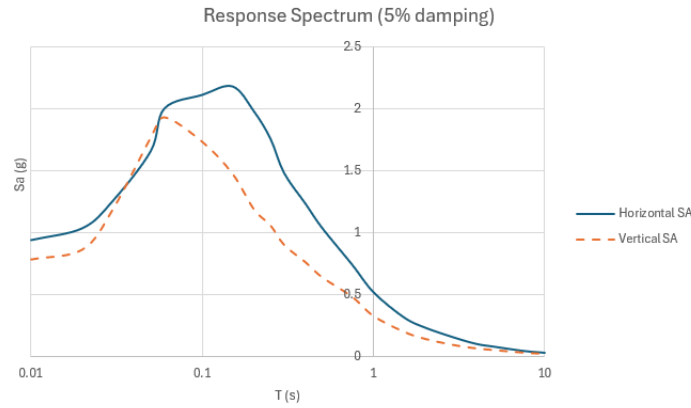


Figure 5: Horizontal and Vertical Design Spectrum for a return period of 2475 years ( $\varepsilon=5\%$ )

Considering these spectrums, it has been defined the acceleration time histories. First, it is selected some seed time histories, determined by the magnitude and other relevant seismic source characteristics appropriate to the design earthquake and bridge site. These seed time histories are scaled so that the resultant mean spectrum developed from the scaled response spectra closely matches the target response spectrum. With this methodology it is required a minimum of three sets of time histories (X,Y,Z), using the maximum of these three responses. It is also possible to consider a suite of seven time histories, then using the average of the seven responses [2, 3]. In our case, the SRA defines three sets of time histories, so the maximum value of the results is considered for the designs.

In the horizontal plane, the accelerograms are oriented with respect to the Pedro Miguel fault, one of the most active in the area, arranged in a parallel and perpendicular direction to it.

### 3.3 Friction pendulum bearing definition

As a starting point, it is worth reviewing the basic operation of a simple pendulum support (SFP), given by the pendulum action of the vertical load  $W$  that generates the restoring stiffness  $K_p$  and the friction force  $F_0$ .

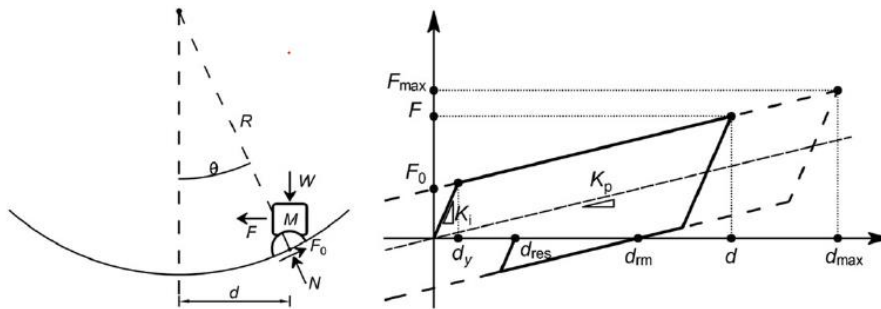


Figure 6: Principles of the Friction Pendulum System and Idealized bilinear hysteretic behavior [5]



$$F = F_0 + K_p \cdot d; K_p = \frac{W}{R} = \frac{M \cdot g}{R}; F_0 = \mu \cdot N \approx \mu \cdot W; T = 2 \cdot \pi \cdot \sqrt{\frac{M}{K_p}} = 2 \cdot \pi \cdot \sqrt{\frac{R}{g}} \quad (1)$$

These equations (1) indicate several interesting aspects highlighted below:

- Once the friction is overcome, the stiffness of the pendulum and therefore the horizontal force transmitted depends on the surface radius and the weight acting on it. The heavier the weight and the smaller the radius, the stiffer the isolator's behavior.
- The natural period of the isolation only depends on the radius of the sliding surface R.

The seismic isolators are defined in the calculation models using nonlinear general link. Regardless of the number of surfaces depending on the type of support (simple, double, or triple), the parameters that commercial calculation programs (such as MIDAS or SAP) require to define the properties of each of these surfaces in horizontal displacement are explained below

- Stiffness ( $K_i$  in figure 5). For current bearings, the pre-sliding stage of motion has a quasi-rigid behavior with this initial stiffness.
- Radius of Sliding Surface (R in figure 5)
- Slow and fast frictional coefficient ( $\mu_s$  and  $\mu_f$ ) and rate parameter ( $r$ ). The friction coefficient  $\mu$  of sliding is a variable value depending on the state of lubrication, sliding velocity, contact pressure and temperature. Commercial software as MIDAS or SAP considers the following relation (2) proposed by Constantinou [6], with  $v$  the sliding velocity.

$$\mu = \mu_f - (\mu_s - \mu_f) \cdot \exp(-r \cdot |v|) \quad (2)$$

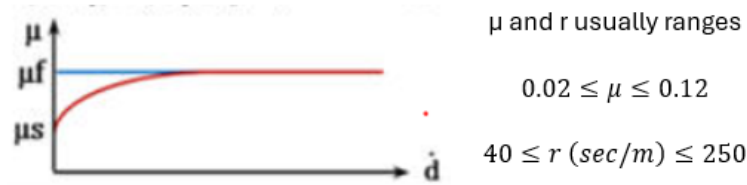


Figure 7: Coefficient of sliding as function of sliding velocity [5]

The determination of these parameters is not easy or unique as it depends on many factors. For this reason, suppliers of these supports must perform tests to quantify them and their range of variation. This circumstance makes that at the design level, regulations [3] require a double calculation with values above and below those defined as nominal.

- Displacement limits before impact occurs on each of the surfaces.

In the vertical direction, these isolators are assumed to be infinitely rigid when compressed and free when uplifted.

Using nonlinear pendulum supports in calculation programs has a relatively high computational cost, significantly increasing with the number of surfaces. For this reason, in the models made by Ayesa for the SEE earthquake, where large displacements occur, the double pendulum supports (DFP) defined in the project have been replaced by equivalent single pendulum supports (SFP) making the area enclosed by their respective hysteresis diagrams for the maximum displacement equal, which equals the energy dissipated by the system. The following table defines the DFPs defined in the project and the equivalent SFP considered in the calculation model.

Parameter	DFP	Equivalent SFP
Stiffness $K_i$ (Top surface)	10000 KN/m	10000 KN/m
Stiffness $K_i$ (Bottom surface)	10000 KN/m	
Radius (Top surface)	3.50 m	5.53 m
Radius (Bottom surface)	2.80 m	
$\mu_s$ and $\mu_f$ (Top surface)	0.075	0.055
$\mu_s$ and $\mu_f$ (Bottom surface)	0.055	
Stop distance (Top surface)	0.50 m	1.05 m
Stop distance (Bottom surface)	0.55 m	

Table 2: Considered parameters of isolations.

### 3.4 Damping

The damping values to be considered in the project are defined in the Project Specifications [1] based on the material and the expected damage level. A damping ratio  $\varepsilon$  of 5% has been employed.

Among the many different ways of expressing damping phenomena in the structural models, proportional damping (or classical damping) is most frequently used in numerical analyses of structures. Two main procedures are usually employed for constructing a classical damping matrix: Rayleigh method and Caughey method.

Rayleigh damping assumes that the damping matrix is proportional to the mass and stiffness matrix. In this case the damping matrix is formulated by means of the damping ratios and natural frequencies of two modes.

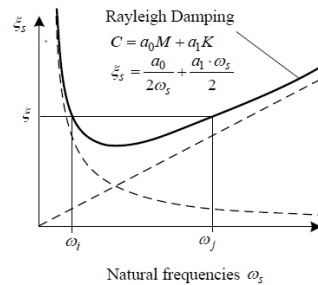


Figure 8: Variation of modal damping ratios with natural frequency according to Rayleigh method

With this formulation, a symmetric damping matrix with a significant number of zero-value terms is obtained. Using a direct integration method, this fact is significant as it greatly simplifies the computational effort.

However, it presents the problem of choosing the two modes, especially in cases where there are numerous important modes with different frequencies that may be representative of the system's response. It should be noted that for modes located between the two selected, the damping ratio  $\varepsilon$  will be underestimated, while for values outside this interval, the damping will be overestimated.

To solve this problem, specifying values for damping ratios in more than two modes, we need to consider the general form for a classical damping matrix, known as Caughey damping (Modal damping if all modes are considered). However this methodology has an important problem: damping matrix is a full matrix and the computational effort for analyzing large system increases significantly with respect to Rayleigh method. This fact makes Caughey damping not widely used in practical analyses [7].

In the case of the structure studied, the vibration modes (obtained with effective stiffness of the isolators) present very variable frequencies, as shown in the following figures obtained in MIDAS. This circumstance can pose a problem in considering the Rayleigh method.

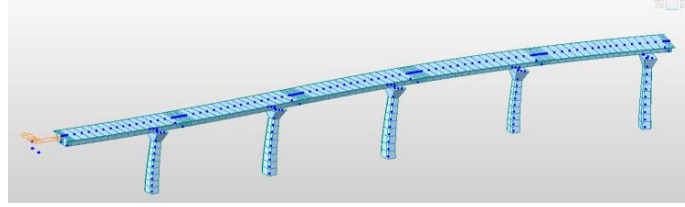


Figure 9: Vibration mode shape due to the slab (horizontal,  $T=3.14$  sec).

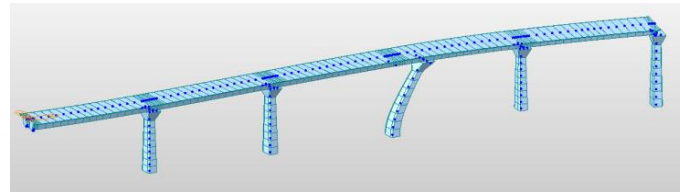


Figure 10: Vibration mode shape due to the central column ( $T=0.55$  sec).

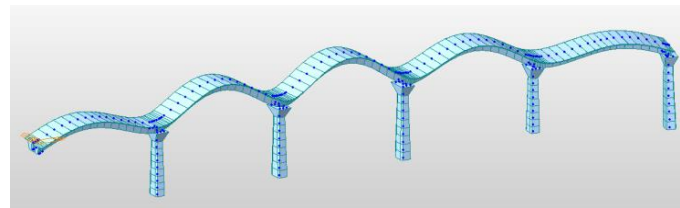


Figure 11: Vibration mode shape due to the slab (vertical,  $T=0.25$  sec).

However, it has been verified that using the Modal method with direct integration demands an excessive calculation time, making it often unfeasible, especially when there are many non-linearities such as those due to deep foundations present in other access viaducts of the project. This reason has ultimately led us to consider the Rayleigh method, considering as representative modes, in this case the horizontal ( $T=3$  sec) and vertical ( $T=0.25$  sec) vibration of the slab, verifying the hypothesis's validity through sensitivity analysis.

### 3.5 Main results

As a summary of the results obtained in the calculations, some of the most significant are shown below.

The extreme moments at the base of the columns are shown in the following graph. These forces are such that a reinforcement of the column of about 0.01 of its gross area is sufficient.

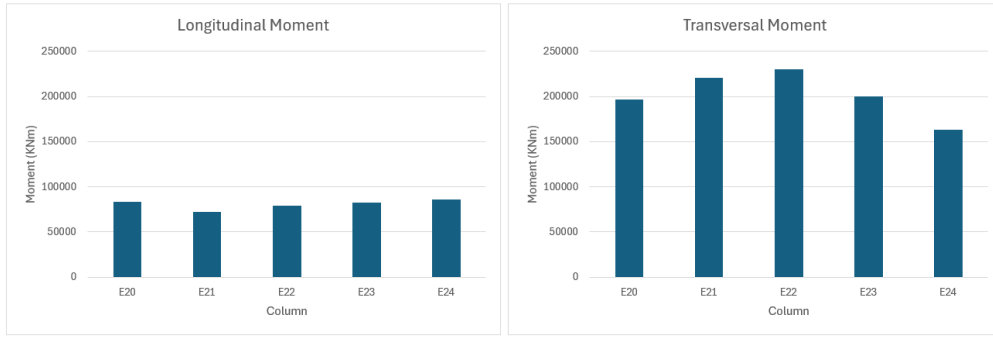


Figure 12: Maximum ABS values of moments in the base of the columns

The extreme displacements and shear forces in the support devices of each column are shown below.

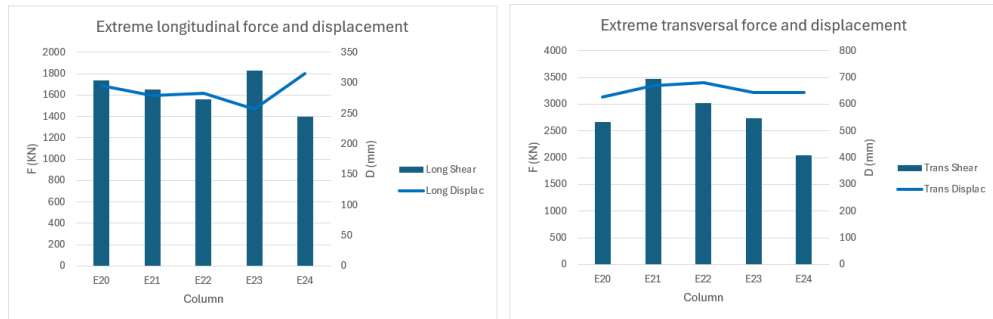


Figure 13: Maximum ABS displacements and shear forces in isolator bearings

As observed, the longitudinal displacements and forces are smaller than the transverse ones, possibly due to the greater stiffness of the piers in the transverse direction.

The next figure illustrates the total force-displacement hysteresis loops in a representative isolator (column E21) for one of the three sets of considered acceleration time histories. Since the bridge is subjected to a vertical motion, the axial force variation is high, which causes a constant modification of the isolator's stiffness (as is known, dependent on the weight-radius ratio of the support), causing this irregular shape compared to the smooth force-displacement loops typically found in the literature for the case where the vertical force does not vary.

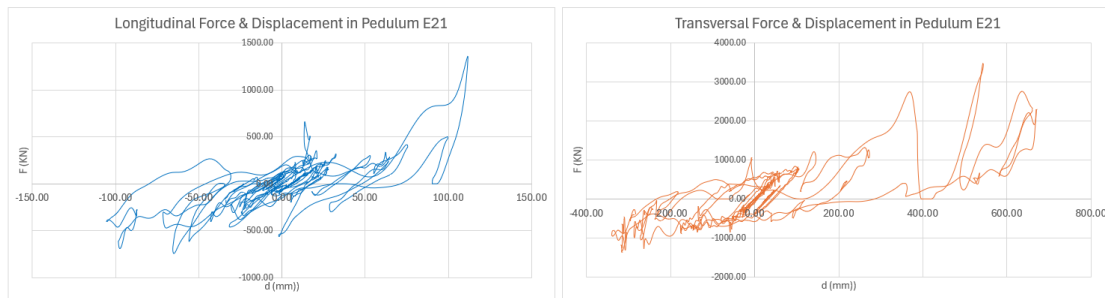


Figure 14: Longitudinal and transversal hysteresis loops in seismic isolators of column E21

## 4 SENSITIVITY ANALYSIS OF THE STRUCTURAL CALCULATION

### 4.1 Objective

This section presents the results for the sensitivity analysis regarding the influence of some parameters on the design results of the bridge.

### 4.2 Influence of the damping method

As explained in the previous sections, the models have been executed considering Rayleigh damping with values of 5% for periods of 0.25 sec and 3.0 sec.

These same models have been executed considering modal damping, setting a value of 5% for all modes. The resolution of this calculation has had a high computational cost, taking about 60 times longer than the Rayleigh method. It should be noted that in this model, the number of nonlinearities is not very high and is due only to the support devices, but in more complex models, this is crucial, even making it impossible to calculate with this type of damping.

The following graph shows the comparison of maximum moments at the base of the columns. As observed, the results are quite similar, with little difference in each case.

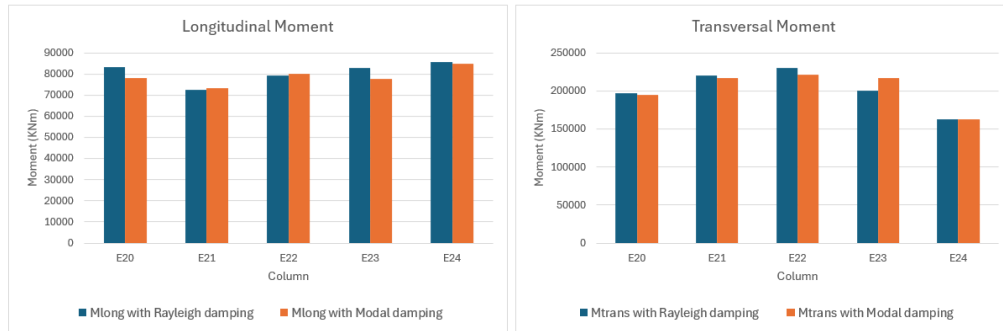


Figure 15: Comparative of design moments in base of columns

The following figure shows the comparison between maximum displacements and shear forces obtained in the friction pendulums in both calculation cases. Again, the results are quite similar.

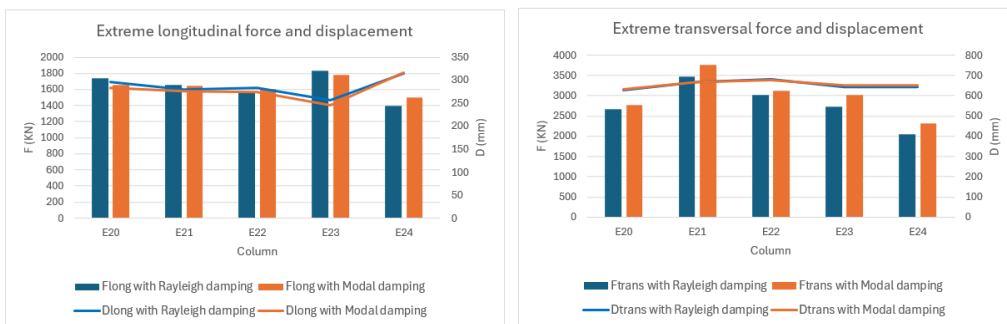


Figure 16: Comparative of maximum ABS shear force and displacement at friction pendulums

Therefore, it can be concluded that with an appropriate choice of the two main frequencies in Rayleigh damping, the results obtained are quite similar in both cases. Not using the Modal method significantly reduces the computational effort of the models, which can be very relevant when they are particularly complex.

### 4.3 Influence of the vertical ground motion

The effects of the vertical shaking in the design of the isolated structures with sliding bearings have been analyzed for different authors, for example, reference [8].

To study this influence, the models have been executed without considering vertical earthquake action, i.e., only considering the earthquake's action in the horizontal plane (parallel and perpendicular to the Pedro Miguel fault).

The following graphs show the comparison of design moments at the base of columns. It can be observed that the presence of vertical shaking has an influence on the results, increasing the design moments of the columns, especially in the transverse direction.

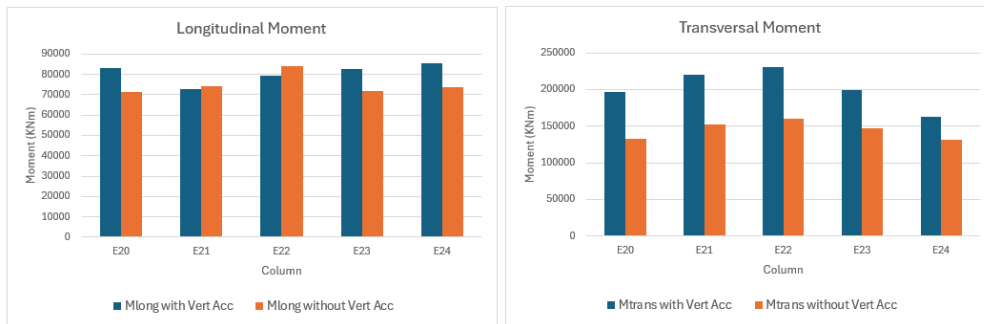


Figure 17: Comparative of design moments at base of columns

To understand this effect, it is interesting to analyze what happens in the support devices. As a starting point, the following figure shows the comparison between the minimum and maximum axial forces (considering negative compression) acting on the support devices.

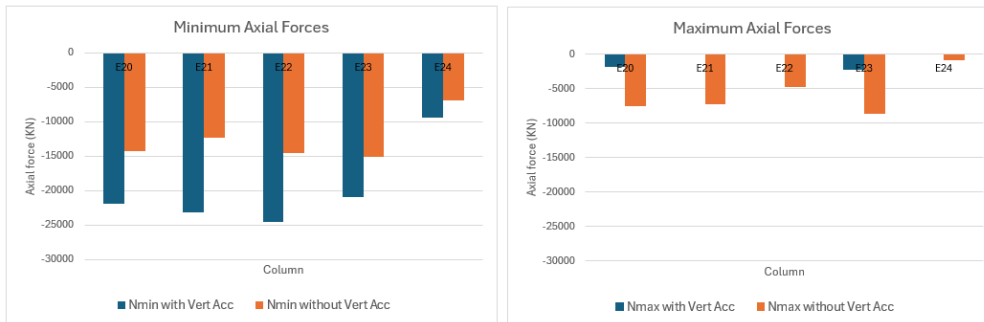


Figure 18: Comparative of axial force in the friction pendulums

Two aspects of the previous figure are highlighted:

- Since friction pendulum isolators do not have tension capacity, the isolator will experience uplift when they reach zero axial force. This situation occurs in three columns.
- For the situation without vertical shaking, contrary to what might seem, the axial force acting on the supports is variable, although in a much smaller range than with vertical shaking, and never causing uplift. This circumstance is due to the transverse earthquake component due to the lever effect generated by the different height between the center of gravity of the deck and the two supports, leaving one more compressed than the other, and this situation is variable due to the modification of the aforementioned transverse component.

The following images show the comparison between the maximum displacements and shear forces obtained in the friction pendulums in both calculation cases.

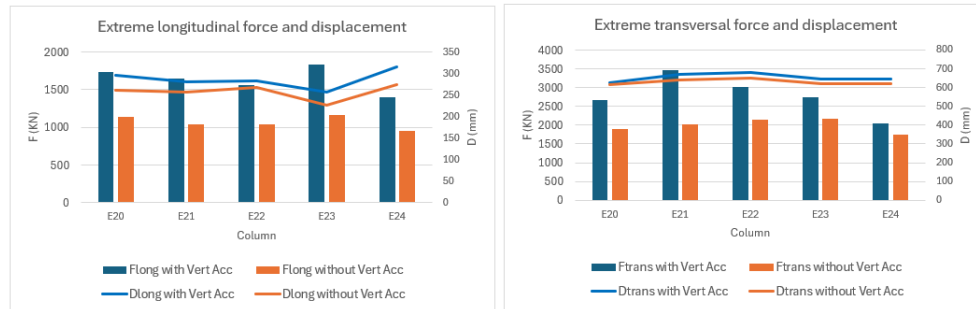


Figure 19: Comparative of maximum ABS shear force and displacement in the friction pendulums

From the previous figure, it can be deduced that, although there is little difference in displacements in each case, the influence of vertical shaking is especially relevant in the case of shear force, which increases with vertical shaking.

This effect is shown in more detail below. For one of the supports (column E21) and one of the three sets of calculation accelerograms, the displacements and shear force obtained with and without vertical shaking have been represented. For simplicity, the longitudinal direction is considered, and the results are extensible to the transverse case, taking the time interval between 15 sec and 40 sec as the most significant.

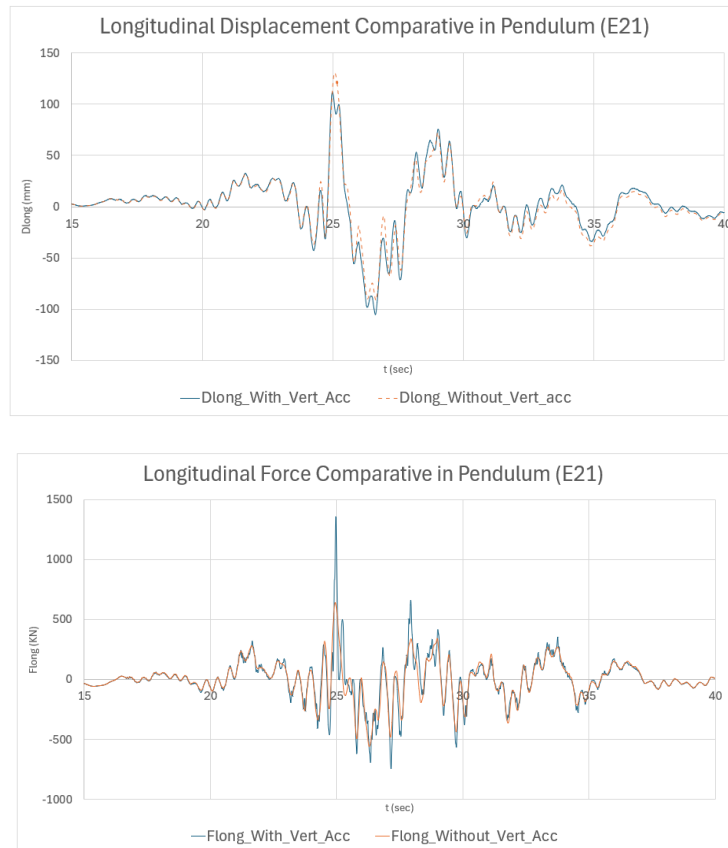


Figure 20: Longitudinal displacement and shear force history in the friction pendulum E21

These figures confirm what was previously indicated. Vertical shaking has a minimal effect on isolator displacement. On the contrary, in the horizontal shear force, there is a significant influence, and this is due to the variations occurring in the axial force. The following figure shows this effect in a time interval around the maximum longitudinal shear ( $t=24.97$  sec), also showing how the vertical force varies.

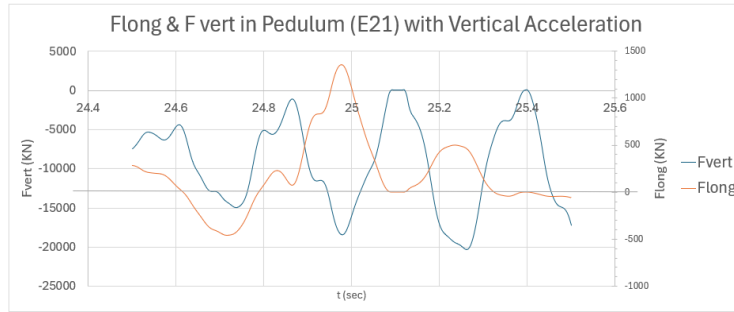


Figure 21: Longitudinal shear force & axial force history in the friction pendulum E21

The peaks in the horizontal force value coincide with the peaks of maximum compression of the supports. The sudden increase in the shear force is correlated to the uplift and spiked vertical acceleration.

The vertical component of ground motion significantly increases the base shear. Thus omitting the vertical component may lead to underestimation of force demands.

#### 4.4 Influence of the frictional coefficient of isolators

In the results shown so far, a friction coefficient of 0.055 has been considered for both low and high speed. As indicated, the friction coefficient is a variable value influenced by various factors such as age, pressure, cleanliness, or temperature, in addition to the sliding velocity itself.

To study this influence, the models have been executed considering a friction coefficient of 0.02 for both high and low speed, corresponding to a lubricated support with very low friction.

In this case, we focus on the results obtained for the pendulum supports. The following graphs show the comparison between the maximum displacements and shear forces obtained in the friction pendulums for each of the considered friction coefficients.

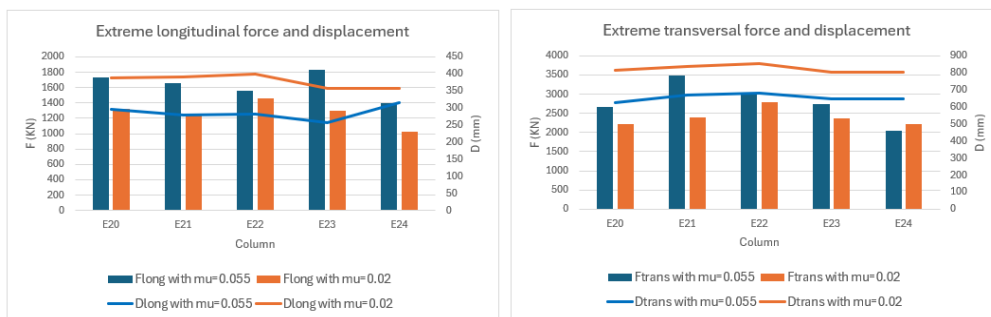


Figure 22: Comparative of maximum ABS shear force and displacement in the friction pendulums

The results obtained reveal that when friction is higher, the shear force is greater, and the displacement is smaller. That is, the support behaves in a stiffer manner. This effect can be inferred by considering the hysteresis diagrams of one and the other support with less force-



displacement area (and therefore dissipated energy) for the lower friction support, considering the different limiting friction force when sliding begins. The following figure shows this effect in the transverse displacement diagrams of one of the supports (E21) subjected to one of the three sets of calculation accelerograms.

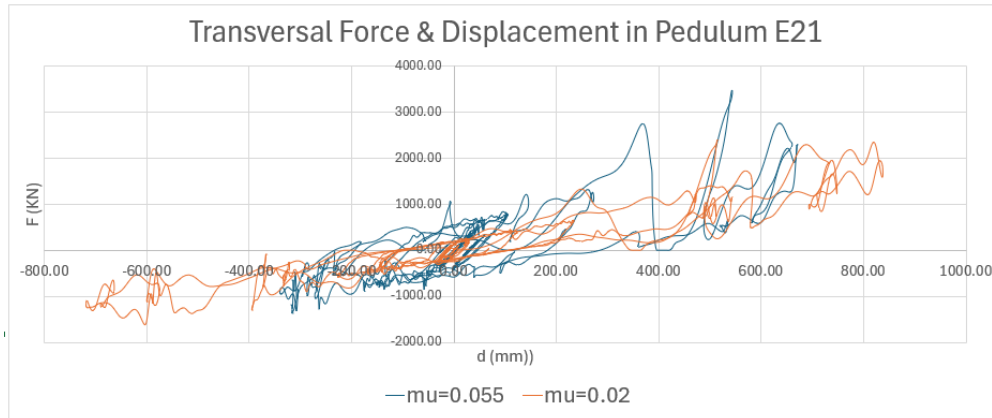


Figure 23: Comparative of hysteresis loop in the friction pendulum E21 with different frictional coefficients

This variability in the obtained results justifies that regulations propose a double calculation with values of these parameters above and below the nominal ones, and that suppliers define the range of variation to be considered through tests.

## 5 CONCLUSIONS

This article describes the structural modelling carried out for the seismic calculation of a viaduct with pendulum-type isolators. The structure is part of one of the access viaducts of the Fourth Bridge project over the Panama Canal, currently under drafting.

The considerations made in defining the model inputs are described in detail, with special emphasis on acceleration time histories, the definition of pendulum supports, and the methodology considered for defining the damping matrix.

Finally, comparative analyses are presented to study the sensitivity of the obtained results when modifying certain parameters, particularly the use of Rayleigh or Modal damping, the influence of considering or not vertical shaking, and the influence of modifying the friction coefficient of pendulum supports.

## REFERENCES

- [1] Ministerio de Obras Públicas de Panamá. Pliego de Cargos del Proyecto “*Diseño y Construcción del Cuarto Puente sobre el Canal de Panamá*”, No. 2016-0-09-0-99-LV-004736, 2016.
- [2] American Association of State Highway and Transportation Officials, Guide Specifications for LRFD Seismic Bridge Design, 2<sup>nd</sup> edition, 2011.
- [3] American Association of State Highway and Transportation Officials, Guide Specifications for Seismic Isolation Design, 4<sup>th</sup> edition, 2014.

- [4] M. Malekzadeh<sup>1</sup>, T. Taghikhany, Adaptive Behavior of Double Concave Friction Pendulum Bearing and its Advantages over Friction Pendulum Systems, Sharif University of Technology, 2010.
- [5] Felice Carlo Ponzo, Antonio Di Cesare, Gianmarco Leccese, Domenico Nigro, Shake table testing on restoring capability of double concave friction pendulum seismic isolation systems, Earthquake Engineering and Structural Dynamics, DOI: 10.1002/eqe.2907, 2017.
- [6] M.C. Constantinou, P. Tsopelas, Y-S Kim, S. Okamoto, NCEER-Taisei Corp. Research Program on Sliding Seismic Isolation Systems for Bridges: Exp and Analytical Study of Friction Pendulum System (FPS), Technical Report NCEER-93-0020, 1993.
- [7] Anil K. Chopra, Dynamics of structures. Theory and Applications to Earthquake Engineering, ISBN-10: 1-29-224918-8, ISBN-13: 978-1-29-224918-6, eBook ISBN-13: 978-1-29-224920-9, 2020.
- [8] Rushil Mojidra, Keri L. Ryan, Influence of Vertical Ground Motion on Bridges Isolated with Spherical Sliding Bearings, PEER Report No. 2019/08, 2019.

## SEISMIC ASPECTS IN THE PROJECT OF LINES 2 AND 4 OF THE LIMA METRO (DINEST 2024)

Julio RODRÍGUEZ-SÁNCHEZ<sup>1</sup>, Antonio Jesús DÍAZ-MORENO<sup>2</sup>, Jose MARTIN  
ROMERO<sup>2</sup> and Ignacio HINOJOSA SÁNCHEZ-BARBUDO<sup>3</sup>

<sup>1</sup> MSc. Civil Engineer,  
AYESA Ingeniería y Arquitectura  
e-mail: [jrsanchez@ayesa.com](mailto:jrsanchez@ayesa.com)

<sup>2</sup> MSc. Mechanical Engineer,  
AYESA Ingeniería y Arquitectura  
e-mail: [adiazmoreno@ayesa.com](mailto:adiazmoreno@ayesa.com)  
[jmartin@ayesa.com](mailto:jmartin@ayesa.com)

<sup>3</sup> Ph.D. Civil Engineering, Associate Professor at University of Seville,  
AYESA Ingeniería y Arquitectura  
e-mail: [ihinojosa@ayesa.com](mailto:ihinojosa@ayesa.com)

**Keywords:** Earthquakes, Numerical Modeling, Seismic Design, Soil-Structure Interaction

**Abstract.** *Underground structures are the main part of crucial infrastructures in cities and should withstand severe earthquakes without any loss of capacity. L2&L4 of Metro Lima is the most ambitious underground transportation facility that is planned in South America, and is located in the Pacific Ring of Fire, one of the world's most active seismic areas. Station designs incorporated the last innovations in the Earthquake Engineering field, as the most recent developments in seismicity, dynamic behavior of materials and soil-structure interaction. An optimal, reliable, robust and safe design was achieved, which arouse satisfaction in all the different entities involved in the project..*

## 1 INTRODUCTION

L2&L4 Metro Lima is the largest underground train project under construction in Latin America. Construction is in charge of CJV (FCC-Dragados-Impreglio-COSAPI), and AYESA Engineering and Architecture plays the designer role for the stations.

City of Lima is situated in one of the world's most hostile tectonic environment, the Pacific Ring of Fire, where large earthquakes occur on a regular basis. Seismic conditions are then of capital importance for the project during both design and construction process.

Underground structures provide the necessary infrastructure for many services and facilities in modern cities. In the majority of cases, they are expensive and difficult to build. Additionally, their failure might often compromise other aboveground structures in their vicinities. For these reasons they should be designed to resist severe seismic events if they are located in cities like Lima. Stochastic processes that govern seismic events and dynamic behavior of buried structures make their design process a very complex, challenging task that is still unsolved nowadays.

Several simplified approaches are used in practical engineering for design of underground structures. Those might be divided into two main groups: force-based and deformation-based methods.

Force-based methods simplify the seismic action as a static pressure on the wall that results in the same maximum forces than those achieved during the earthquake event. Examples of this method are shown in [1]. This method assumes dynamic thrust to be an inertial force applied to the structure. This condition mainly applies for cantilever walls, so it might not be properly applied for design of underground structures.

Displacement-based methods simplify the seismic action as the maximum drift of the buried structure which will take place during the earthquake. Examples of this methods can be found in [2]. This method assumes the seismic action to have a horizontal swing effect only (racking), and thus displacement-based design is useful for box-like shaped structures, like cut-and-cover tunnels. Nevertheless, author states that underground structures may behave in a more complicated way that cannot be approximated by this method.

The structural system of the typical station is composed by column-piles, which sustain the gravity loading of the roof and the slabs, and by retaining walls, which resist lateral forces coming from earth pressures and earthquake excitation. Then, they do not comply hypothesis of displacement-based methods.

Both force and displacement-based methods were shown to poorly predict behavior of simple-shaped buried structures, as in [3]. The authors show that a more reliable approach is needed for seismic design of underground structures. They also recommend full-time history dynamic analysis as the most accurate method for seismic design, according to laboratory tests data.

This approach was adopted for the seismic design of L2 & L4 Metro Lima. Current state-of-the-art and latest innovations were applied to the project, as stated in [4] and [5], and also in cooperation with the University of California Berkeley. This approach was successfully used to develop an optimal, reliable, robust and safe design, with great satisfaction of both contractor and administration..

## 2 METHODS

First, seismic design scenarios were determined through a probabilistic seismic hazard analysis (PSHA). Then, geotechnical model of the site was elaborated based on available tests and bibliographical data. Shear wave velocity ( $V_s$ ) profile was used to compute the input seismic signal for the numerical model. Both geotechnical and structural models were implemented in finite element software PLAXIS2D. Mesh and boundary conditions were especially treated in order to develop an accurate dynamic numerical model. Finally, dynamic calculations were performed, and obtained results were utilized to feed the structural design process.

### 2.1 Determination of design seismic scenarios

PSHA is the most proper method to determine the different scenarios for seismic design [6]. PSHA allows the designer to quantify all uncertainties that are inherent to the process of seismic design scenario determination through the definition of the different involved stochastic variables.

The main variables that have been used to determine the level of seismic excitation are moment magnitude  $M_w$ , distance to fault rupture  $R$ , failure mechanism  $F$  and shear wave velocity of the upper 30m of soil  $V_3$ .

Two different scenarios were chosen, which were called Operational Basis Earthquake (OBE) and Maximum Conceivable Earthquake (MCE). The structure should be fully operational after the first scenario takes places, while repairable damage is allowed for the second. It was arranged with the client that OBE corresponds to a return period of 1000 years, and MCE to 2500 years.

Historical site seismicity of Lima was studied in order to determine a Gutenberg-Richter law [6].  $M_w$  for OBE and MCE scenarios were computed, given 8.9 and 9, respectively.  $R_D$  was assumed to be equal to the distance to the nearest active fault for all cases due to the lack of information. This distance was measured as about 40km. Fault rupture type was chosen as subduction intraplate because of the local tectonic environment.  $V_s$  was determined from the in-situ shear wave velocity tests carried out in the station area. A value of 550 m/s was obtained.

Target response spectra for each scenario were obtained through usual ground motion prediction equations (GMPE), as in [4], with unit weight factors for the applicable GMPEs. Mean plus half standard deviation was used for calculation of target response spectra, for the sake of safety. Those response spectra are the expected maximum seismic demand at surface, in terms of accelerations, that the earthquake associated to each scenario will induce to the soil-structure system.

### 2.2 Elaboration of the geotechnical model

For a typical station of the project, a large number of in situ and laboratory tests were carried out (area of Mercado Santa Anita station). The aim of the tests was the geotechnical characterization of the site, and especially the development of its  $V_s$  velocity profile.

Lima is founded on a very thick gravel deposit which was formed by the Rimac river floods. Depth to rock was unknown for Mercado Santa Anita site, since bedrock was not found in any of the soundings nor the shear wave velocity tests. Water table was not found either in the area for a depth above 60m. This soil is very stiff and strong and can sustain slopes up to  $82^\circ$ . Soil was classified as poorly-graded gravel GP. Mean uniformity coefficient ( $U$ ) was computed as 166, with average grain size of 30m. Large boulders were found in samples. Low fine content with low plasticity was observed. Unit weight ranged between  $20\text{kN/m}^3$  and  $22\text{kN/m}^3$ . An

anthropic fill R with low resistance and stiffness was found over the gravel deposit. Several layers of silty sand SM were reached with boreholes. Those layers are weaker than the gravel deposits.

It was decided to divide the gravel deposit into three different layers. They correspond to the different degree of compactness, which affects the  $V_s$ . Then, GP-Ss, GP-Sm and GP-Sf were differentiated for gravels with  $V_s < 400$  m/s,  $V_s < 600$  m/s and  $V_s > 600$  m/s respectively.

Shear strength parameters for cohesion  $c$  and friction angle  $\phi$  of the different soils were obtained from laboratory tests and from in-situ large-scale direct shear tests. Different shear strength parameters were given to R, GP-Ss, GP-Sm, GP-Sf and SM. Tensile strength was taken as  $\sigma_t = c / \tan \phi$ . Dilatancy cut-off was accounted for by choosing a parameter  $\delta = 0.09$  for soils with positive dilatancy angle, as recommended by [7].

Hardening Soil with Small-strain Stiffness model (HSsmall) was selected as the constitutive model to simulate soil behavior. This was done since HSsmall can accurately predict both the static and dynamic behavior of soils, and also the hysteretic damping that strain cycles trigger.

HSsmall relates shear stiffness to minor confining pressure  $\sigma_3$  and plastic parameters  $c$  and  $\Phi$  as:

$$G_c = G_o^r \left( \frac{\sigma_3 \cdot s_1 \cdot \Phi + c \cdot \cos \Phi}{100 k \cdot s_1 \cdot \Phi + c \cdot \cos \Phi} \right)^m \quad (1)$$

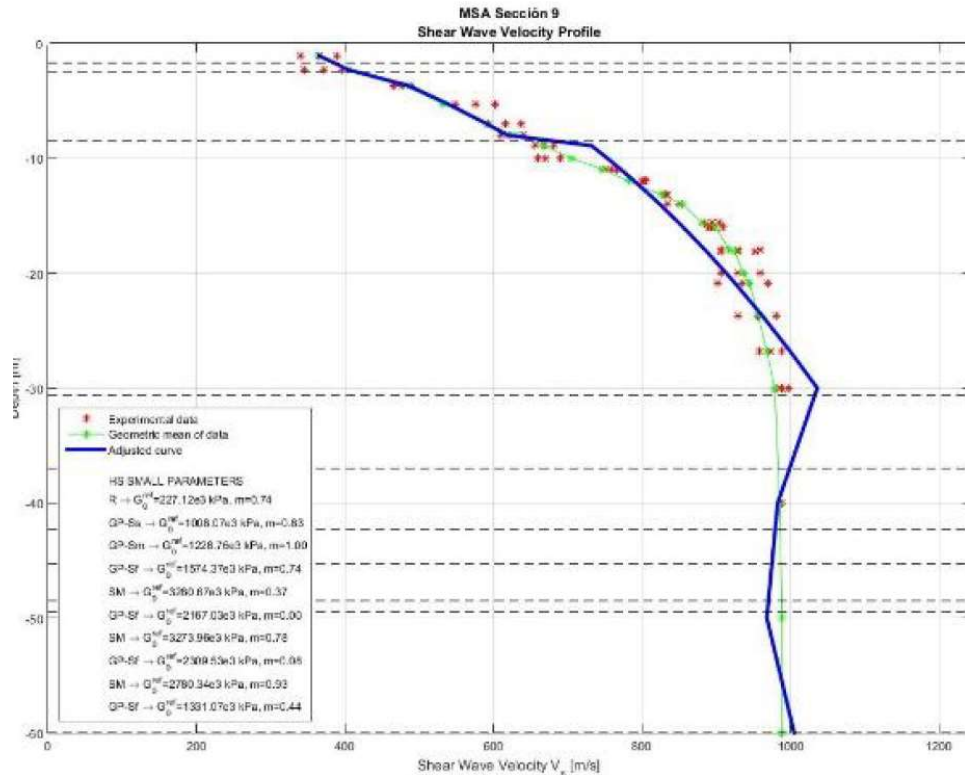


Figure 1. Shear wave velocity profile fitting.

Stiffness parameters were based on the results of the shear wave velocity tests and on bibliographical data. Small-strain shear modulus was directly computed from the  $V_s$ . An optimization procedure was coded to determine the parameters  $G_0^r$  and  $m$  for each layer that provided the best fit to the mean of the  $V_s$  measured in the field for each depth.

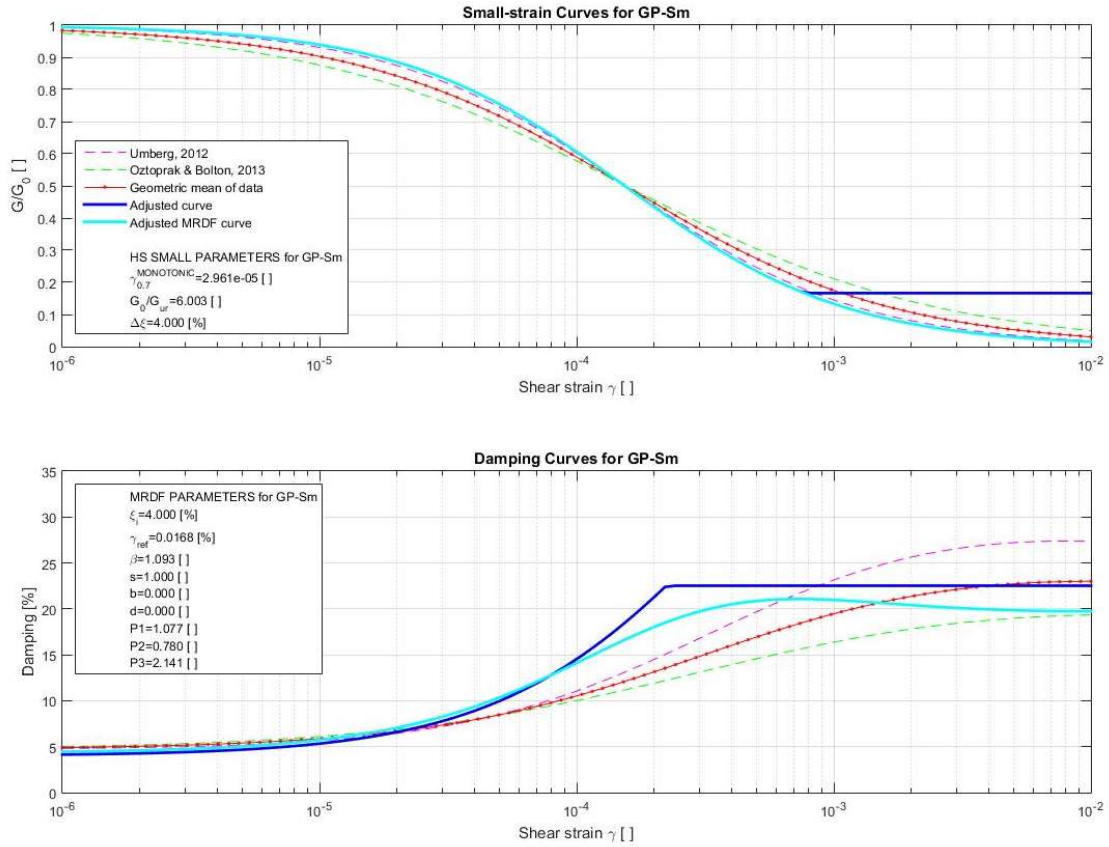


Figure 2. SM1 stiffness reduction curve fitting (right)

PLAXIS implements the stiffness degradation curves following the formulation in [7]. Stiffness degradation curves for the different layers were computed to best-fit the mean from [8] and [9] utilizing formulation implemented in PLAXIS. An optimization procedure was coded in order to obtain the parameter  $\gamma_{0.7}$ , and also the value of damping at small strains for the soil for each different layer differentiated in the soil profile. Uniformity coefficient ( $U_c$ ) was limited to  $U_c = 100$ , since authors of the used formulations do not recommend to use higher values due to database limitations.

Damping at small strains was introduced as Rayleigh damping. Value of damping came from the fitting process, and period range was chosen as  $0.2T - 2.0T$ , where  $T$  is the natural period of the soil deposit, in accordance with [5]. For Mercado Santa Anita, it was found that  $T = 0.40s$ .

Layer	Top [m]	Bot. [m]	$\gamma$ [kN/m <sup>3</sup> ]	e [ ]	e <sub>min</sub> [ ]	e <sub>max</sub> [ ]	$\alpha$ [ ]	$\beta$ [ ]	c [kPa]	$\Phi$ [°]	$\Psi$ [°]
R	0	1.7	16.7	0.56	0.25	0.75	0.4571	3.92E-04	1	28	0
GP-Ss	1.7	2.5	20	0.19	0.15	0.25	1.1468	9.83E-04	15	34	2
GP-Sm	2.5	8.5	21	0.19	0.15	0.25	1.1468	9.83E-04	27.5	36.5	4.5
GP-Sf1	8.5	30.6	22	0.19	0.15	0.25	1.1075	9.49E-04	40	39	7
SM1	30.6	37	16.95	0.56	0.25	0.75	0.2041	1.75E-04	5	30	0
GP-Sf2	37	42.3	22	0.19	0.15	0.25	0.9745	8.35E-04	40	39	7
SM2	42.3	45.3	16.95	0.56	0.25	0.75	0.1946	1.67E-04	5	30	0
GP-Sf3	45.3	48.5	22	0.19	0.15	0.25	0.9446	8.10E-04	40	39	7
SM3	48.5	49.5	16.95	0.56	0.25	0.75	0.1906	1.63E-04	5	30	0
GP-Sf4	49.5	60	22	0.19	0.15	0.25	0.9168	7.86E-04	40	39	7

Table 1: State, strenght and small-strain damping parameters of soils used for analysis in PLAXIS.

Layer	Top [m]	Bot. [m]	E <sub>ref</sub> [kPa]	E <sub>ref</sub> [kPa]	E <sub>ref</sub> [kPa]	m [ ]	$\gamma$ [ ]	G <sub>ref</sub> [kPa]
R	0	1.7	30283	30283	90848	0.74	2.59E-05	227120
GP-Ss	1.7	2.5	134413	134413	403240	0.83	2.45E-05	1008100
GP-Sm	2.5	8.5	163840	163840	491520	1.00	2.96E-05	1228800
GP-Sf1	8.5	30.6	209920	209920	629760	0.74	4.00E-05	1574400
SM1	30.6	37	437427	437427	1312280	0.37	1.73E-04	3280700
GP-Sf2	37	42.3	288933	288933	866800	0.00	4.87E-05	2167000
SM2	42.3	45.3	436533	436533	1309600	0.78	2.00E-04	3274000
GP-Sf3	45.3	48.5	307933	307933	923800	0.08	5.19E-05	2309500
SM3	48.5	49.5	370707	370707	1112120	0.93	2.13E-04	2780300
GP-Sf4	49.5	60	177480	177480	532440	0.44	5.50E-05	1331100

Table 2: Stiffness parameters of soils used for analysis in PLAXIS.

### 2.3 Determination of design acceleration time series

In order to perform a full-time history analysis with a numerical model, an acceleration time series is required. This accelerogram is normally applied to the base of the numerical model as an input.

Acceleration time series for both seismic scenarios should be such that they result in a peak spectral acceleration (PSA) at surface that is equal to target spectrum. Seismic records do not provide the target response spectra as PSA at surface on a regular basis, so they should be modified, through a process called spectral matching [10], in order to fulfill that condition.

Then, a certain seismic record, called seed ground motion, is spectrally matched to make its PSA to be equal to the target spectrum. This modified record is the expected earthquake excitation at surface for a certain seismic scenario.

Spectral matching process was undertaken according to [5]. First, Maule Earthquake (Chile, 2011) record at Puente Alto was used as the seed ground motion. This was done because it



corresponds to an earthquake with similar characteristics to that expected in Lima for the OBE seismic scenario: a subduction intraplate earthquake, with  $M_w = 8.4$ ,  $R_D \sim 80$  km and  $V_s \sim 450$  m/s. Additionally, PSA of Maule Puente Alto record is similar in shape to the target spectrum, which makes the matching process easier. Also, it is an earthquake that took place in the same tectonic area as Lima, so local seismicity was implicitly implemented with the selection of the seed ground motion.

Then, a spectrally-matched ground motion was obtained for each seismic scenario, which correspond to excitation at surface. For numerical modeling purposes, an input ground motion is needed at the base of the model. This should result, after site amplification, in the spectrally-matched ground motion for each scenario.

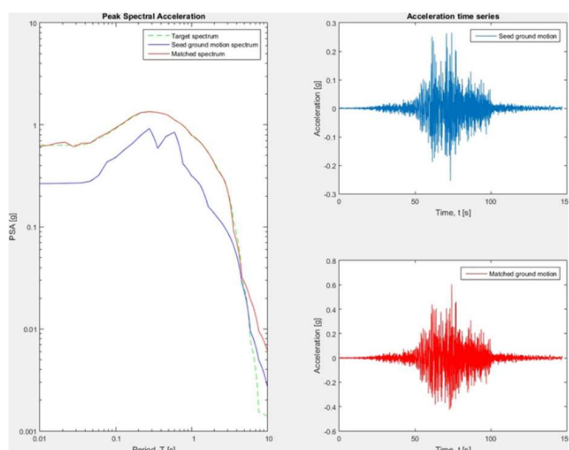


Figure 3. Spectrally-matched ground motion for MCE

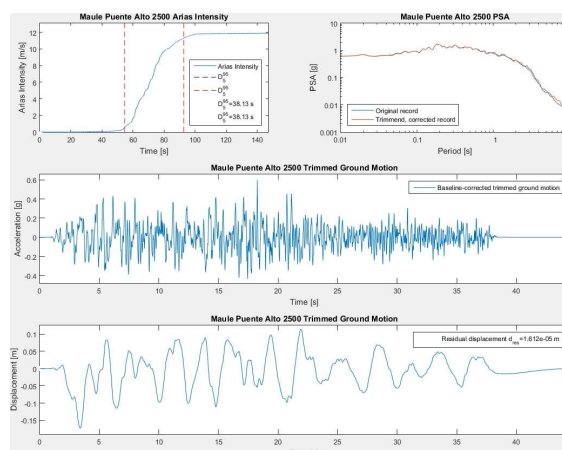


Figure 4. Trimmed ground motion for MCE scenario.

The input ground motions were obtained by means of the deconvolution process. A linear equivalent analysis was performed through wave propagation software DEEPSOIL [11], given a site profile and a surface ground motion, to obtain the seismic excitation at the base of the model, called deconvolved ground motions. Fitted MRDF parameters were used in the software. A within motion was assumed for deconvolution. Thus, deconvolved ground motions are those that will propagate from the bottom of the model to the top resulting in the spectrally-matched ground motion for each seismic scenario.

Deconvolution process assumes equivalent linear behavior of the soil. This means that no plastic deformations will occur during the seismic excitation. While this is true, upward propagation of the deconvolved ground motion will provide the associated spectrally-matched motion. If plastic deformation takes place, as in large earthquakes or weak soil, propagated ground motion will differ from the spectrally-matched motion. Nevertheless, the differences will be significant only in period ranges that are much shorter and much larger than that of

the soil-structure system. Then, seismic demand on the system will be accurately computed regardless of the existence of plastic behavior, and design of structural members could be adequately performed

In order to reduce computational effort, a trimming and filtering procedure was specifically developed for this project. Motion was trimmed to its significant duration, which is the time

comprised between the one at which 5% and 95% of Arias intensity are achieved. Then, a recursive high-pass Butterworth filter with corner frequency of  $0.1H$  was applied to baseline-correct the trimmed motion.

## 2.4 Elaboration of structural model

For a typical station of the project as Mercado Santa Anita Station was thought to be a  $150\text{m} \times 30\text{m}$  retaining wall-supported pit. 12 rows of two 10m-to-15m spaced pile-columns will support the slabs. Three slabs were designed, which correspond the ceiling, the hall floor and the station bottom, which provide restraint for the horizontal forces on retaining walls, mainly coming from earth pressures and seismic actions. The pile-columns withstand the major part of the vertical loads. Also, lateral deflections due to earthquake will pose some additional forces on them that should be taken into account for design.

Section which design is presented was called S09 and is shown in Figure 5.

For the piles, embedded beam row elements in PLAXIS were used. They simulate the behavior of a row of structural elements with skin friction and end bearing resistance located at a certain spacing. For the walls, plate elements in PLAXIS were used. They model the behavior of continuous structural elements with an interface that simulates the reduction of soil stiffness and strength in close contact with it.

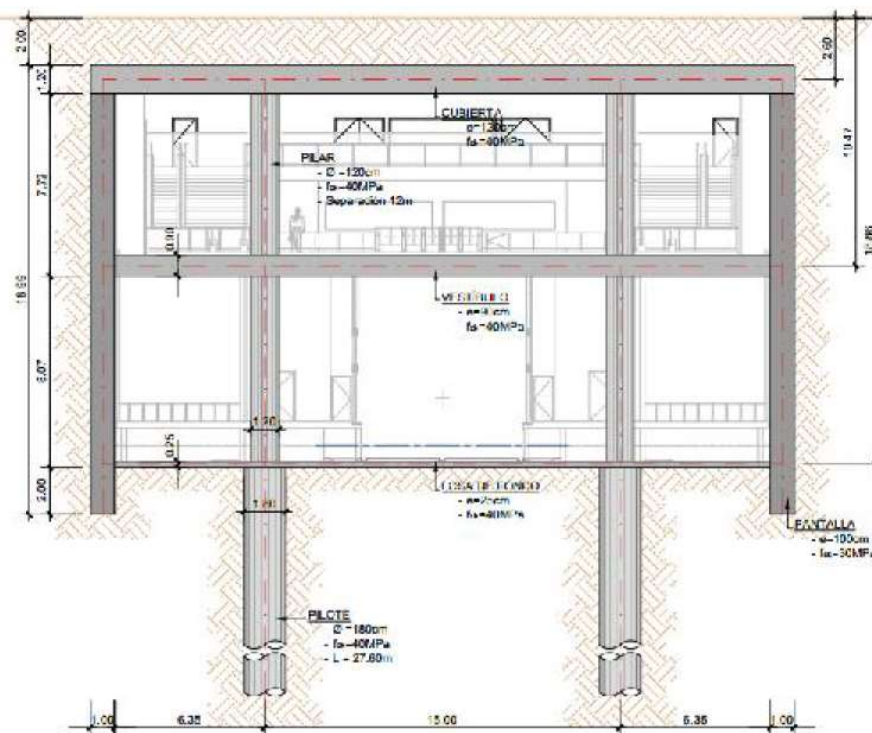


Figure 5. S09 section. [ $f_{ck}=40\text{MPa}$  for all elements except for the 100cm-thick retaining walls -  $f_{ck}=30\text{MPa}$ ,  $f_{yk}=420\text{MPa}$ . Thickness of slabs are 120cm for ceiling, 90cm for the hall and 25 cm for the bottom slab. Columns and piles are 120cm and 180cm respectively].

Structural properties of these elements were computed depending on the geometry of its members for OBE scenario. Reinforcing steel for walls was designed with structural forces computed for that case, and moment-curvature ( $M-k$ ) diagrams were calculated for each different reinforcing section of each wall. Those  $M-k$  diagrams were implemented in PLAXIS for MCE scenario. An example is shown in Figure 9.

Retaining walls reinforcement was designed to behave elastically for OBE conditions. For MCE the structural capacity of the walls was checked utilizing a nonlinear elastoplastic behavior through moment-curvature diagrams. Sufficient shear strength was provided during design.

Since about 90% of the gravity loads are taken by the columns-pile system, they were designed to remain elastic for both OBE and MCE scenarios.

Skin friction and end bearing resistance of piles were obtained by averaging recommendations in [12] and [13]. Interface property  $R_i = 0.8$  was assumed, since wall is not allowed to deflect significantly because slabs are cast-in-place before deeper excavation is started.

All connections between elements were simulated as joints which allowed connecting members to rotate independently. “Consider gap closure” option was activated for all plate elements, so that soil does not immediately contact the plate when stress reversals happen if a gap develops.

## 2.5 Mesh and boundary conditions

Mesh conditions are important for dynamic analysis, since elements size should fulfill different criteria in order to accurately simulate the propagation of seismic waves into the model.

First, aliasing had to be avoided, according to [7]. Aliasing is a phenomenon that consists in the loss of information produced by the insufficient sampling rate with respect to the wave frequency. A number of nodes per element of 15 was chosen in order to increase maximum element size, for the sake of velocity in calculations. The maximum frequency of interest for the analysis was set to  $10H$ , since higher frequencies do not contribute to seismic response of soil-structure system in a significant manner.

Second, calculation time step had to be properly determined. Conditions in [7] should be fulfilled in order to guarantee the stability of the dynamic analysis. For every soil element, with a certain  $V_s$  and  $\nu$ , which refer to the Poisson’s ratio in its cyclic behavior, there is a maximum allowable time step [7]. Since  $V_s$  will vary during seismic excitation,  $\Delta t = 0.002s$  was taken, which corresponds to the mean of both of  $\Delta t$  computed for small-strain and large-strain conditions.

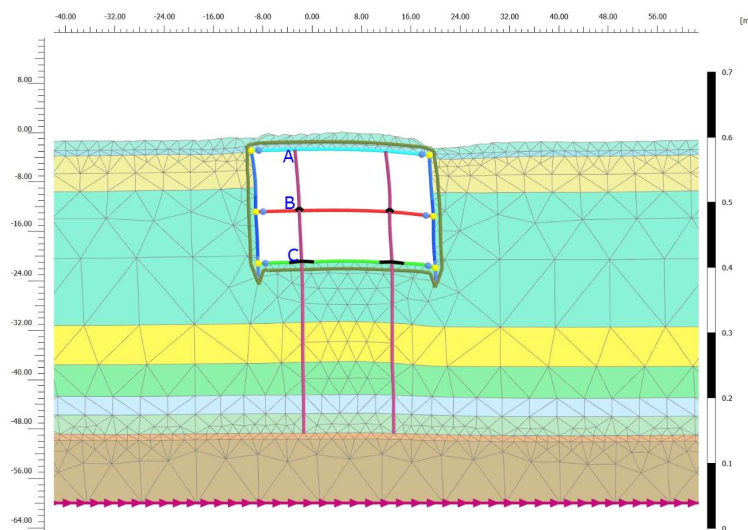


Figure 6. Deformed shape of the model.

Boundary conditions are also crucial for dynamic analysis. First, the station is located at the center of the model, which depth is about three times the maximum depth of the walls (i.e. 60m). The width of the model was taken as 2.5 times its depth, according to [14]. “None” condition in PLAXIS, also called “rigid base”, was selected for the base of the model, since “within motion” condition was taken for deconvolution. “Tied degrees of freedom” was chosen for the lateral boundaries, since it allows to compute free-field motion without boundary reflection effects. Mesh was forced to be symmetric at the lateral boundaries in order to be able to apply this condition.

Deconvolved motion for each seismic scenario was applied at the bottom of the model. A line displacement was created at that location, and an acceleration multiplier, with acceleration values at all times, was applied. “Drift correction” option was allowed in order to force PLAXIS to avoid residual velocities and displacements in the model.

### 3 RESULTS AND DISCUSSION

#### 3.1 Validation of dynamic numerical model

Deconvolved motion should propagate to surface to achieve target response spectrum at that location. Then, validation of the numerical model can be performed by comparison of target response spectrum and spectrum at surface obtained by means of PLAXIS.

Natural period of soil deposit was computed to be 0.40s. It can be checked in Figure 7 that, for periods ranging between  $= 0.2s - 2s$ , which envelope the natural period of soil profile, PLAXIS spectrum accurately matches target spectrum. This proves that the numerical model was properly developed and leads to the conclusion that it propagates shear waves in an accurate way.

Then, forces on structural members that were computed represent those that will develop when seismic excitation reaches the two scenarios that were studied.

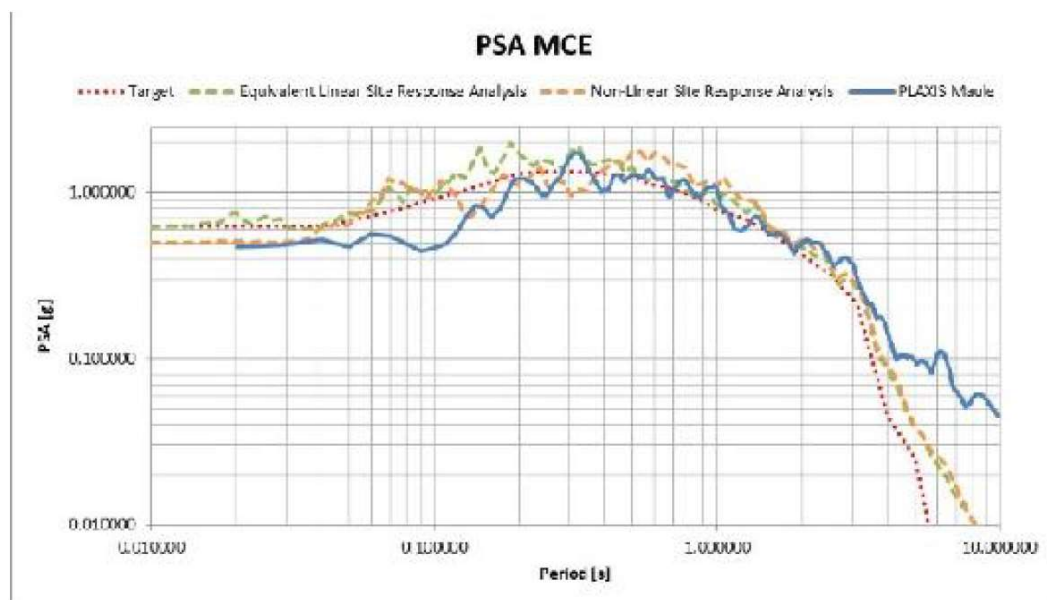


Figure 7. PSA comparison for and MCE scenario



### 3.2 Results for OBE and MCE scenarios

Forces envelope and capacity for the retaining walls of S09 in OBE and MCE conditions are shown in Figure 8.

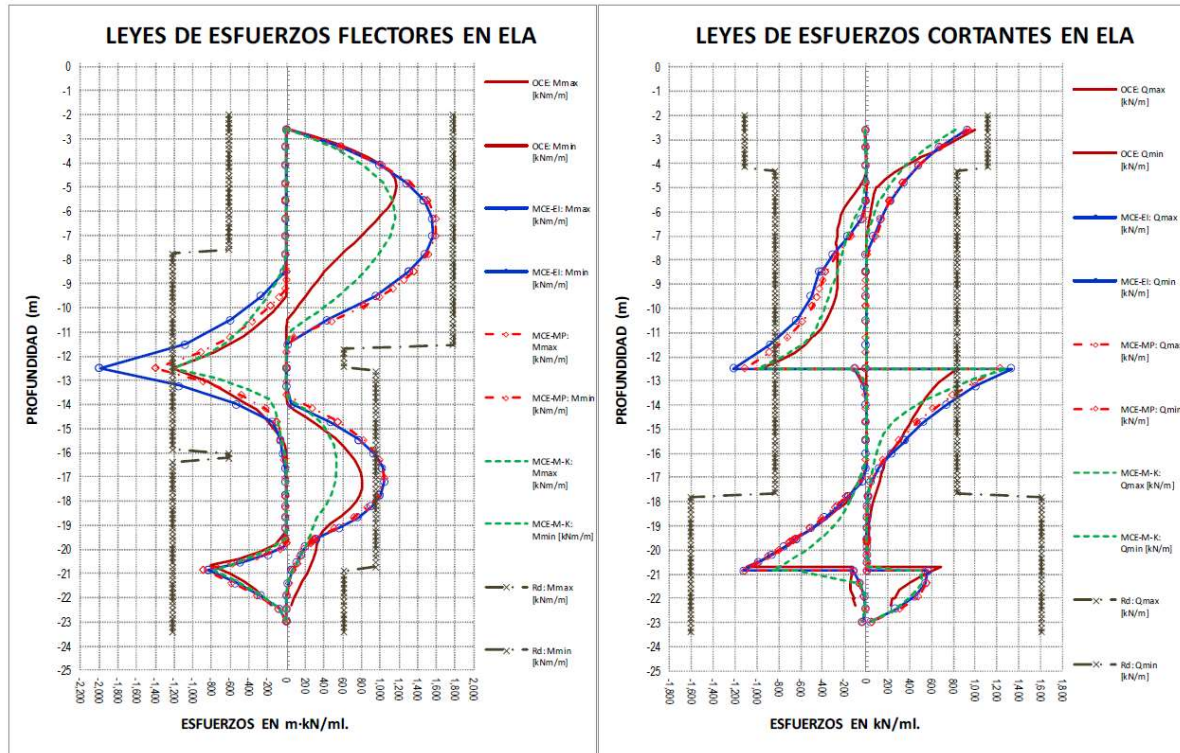


Figure 8. Forces envelopes for OBE and MCE versus capacity.

Several models of the station with different material behavior of the retaining walls were analyzed in order to perform MCE scenario checks. Considered behaviors were elastic (E-I) and elastic-perfectly plastic (M-p), which were used to predict the location of plastic hinges, and nonlinear elastoplastic (M-k), which was employed to check reinforcement capacity. Results for each model are shown in Figure 8. It can be seen that, for S-c, moment and shear capacity was exceeded, and a plastic hinged could develop. Shear strength had to be increased in order to avoid brittle failures.

Performance of the potential plastic hinge at S-c was checked with MCE forces for M-k model. When earthquake ceases, forces will return to those of the static conditions. Maximum bending moment at S-c for static and MCE were found as  $M_{M\_ELA} = 1218 \text{ KNm}$  and  $M_{M\_SERV} = 300 \text{ KNm}$ .

It was checked that reinforcement reaches plastic behavior with elongation lower than 0.2%, so performance point lays in Security Level III, according to [15]. Maximum forces for column-piles obtained for the different design scenarios in Table 3 show that ULS results are close to those of the MCE scenario, because of the partial factors that are disregarded in seismic calculations. [13].

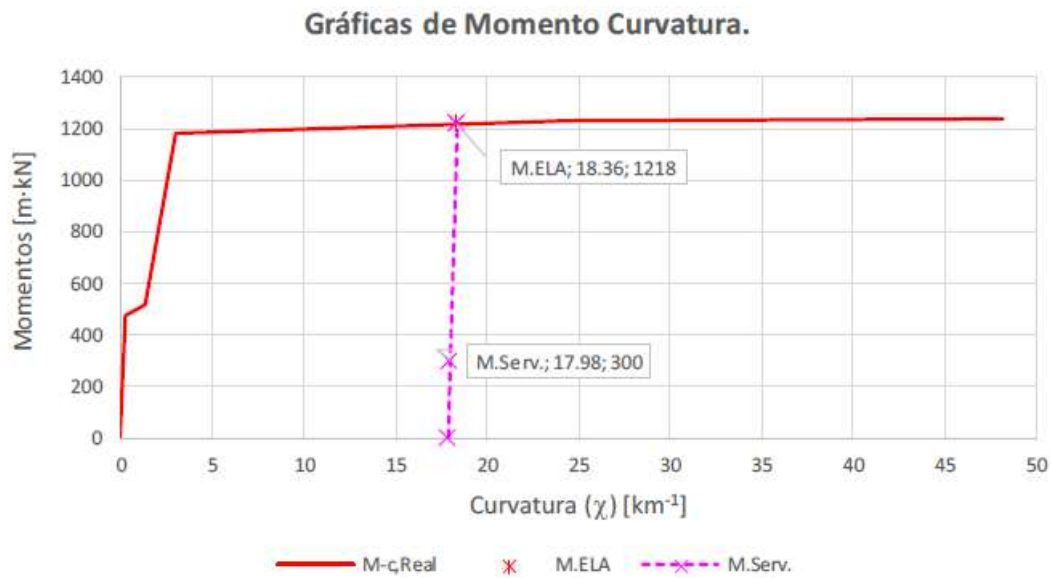


Figure 9. Performance point of S-c in MCE

		(N,M)	Efficiency
		[kN,m·kN]	[%]
<b>ULS</b>	Column	(29090,3279)	99
	Pile	(69959,3534)	52
<b>OBE</b>	Column	(22316,4100)	74
	Pile	(6350,4132)	25
<b>MCE</b>	Column	(23212,5720)	99
	Pile	(7050,6120)	52

Table 3: Forces on column-piles.

## 4 CONCLUSIONS

The methodology described in this article was successfully applied to perform an optimal, reliable, robust and safe design of the structural elements in the stations, in L2&L4 Metro Lima. This arouse satisfaction in all the different entities involved in the project.

In the authors' opinion, the methodology developed for the project will become the state-of-practice for seismic design of underground structure for the coming years.

## REFERENCES

- [1] Geraili Mikola, R., & Sitar, N. (2012). Seismic earth pressures on retaining structures in cohesionless soils. Report UCB GT 13-01. PEER
- [2] Wang, J.-N. (1993). Seismic Design of Tunnels, 1991 Parsons Brinckerhoff Monograph 7, (1993).

- [3] Tsinidis, G., Pitilakis, K., Madabhushi, G., & Heron, C. (2015). Dynamic response of flexible square tunnels : centrifuge testing and validation of existing design methodologies. *Géotechnique*, (5), 401–417.
- [4] Carlton, B. D., Pestana, J. M., & Bray, J. D. (2015). Selection of target ground motion parameters for nonlinear site response analysis, GeoEngineering Report UCB/GE/2015-01, PEER
- [5] Carlton, B. D., Pestana, J. M., & Bray, J. D. (2015). Selection of ground motion time histories for nonlinear site response analysis, GeoEngineering Report UCB/GE/2015-02, PEER
- [6] Baker, J.W., *An Introduction to Probabilistic Seismic Hazard Analysis (PSHA)*, Stanford University Press, October 2008
- [7] Brinkgreve, R. et al. (2016) PLAXIS2D, PLAXIS bv, TU Delft.
- [8] Oztoprak, S., & Bolton, M. D. (2013). Stiffness of sands through a laboratory test database. *Géotechnique*.
- [9] Umberg, D. (2012). Dynamic properties of soils with non-plastic fines. University of Texas at Austin.
- [10] Alatik, L., & Abrahamson, N. (2010). An improved method for nonstationary spectral matching. *Earthquake Spectra*, 26(3), 601–617. <http://doi.org/10.1193/1.3459159>
- [11] Hashash, Y. et al. (2002-2016) DEEPSOIL, 1-D wave propagation analysis program for geotechnical site response analysis of deep soil deposits, Board of Trustees of University of Illinois at Urbana-Champaign
- [12] AASHTO LRFD Bridge Design (2012)
- [13] EN 1997-1 (2004)
- [14] Amorosi, A., Boldini, D., & Elia, G. (2010). Parametric study on seismic ground response by finite element modelling. *Computers and Geotechnics*, 37(4), 515–528.
- [15] FEMA 365





## EXPERIMENTAL METHODOLOGY FOR MONITORING PHYSICAL MAGNITUDES OF SLENDER STRUCTURES USING WEARABLE DEVICES

Guillermo Fernández<sup>1\*</sup>, Ismael García<sup>1</sup>, Alfonso Gómez<sup>2</sup>, Pedro Gil<sup>3</sup>  
and Tomislav Jarak<sup>1</sup>

<sup>1</sup> ITAP, University of Valladolid (Spain)

e-mail: [guillermo.fernandez.ordonez@uva.es](mailto:guillermo.fernandez.ordonez@uva.es) (Corresponding author), [garciaismael@uva.es](mailto:garciaismael@uva.es),  
[tomislav.jarak@uva.es](mailto:tomislav.jarak@uva.es)

<sup>2</sup> Escuela de Ingenierías Industriales, University of Valladolid (Spain)

e-mail: [alfonso.gomez.bravo@uva.es](mailto:alfonso.gomez.bravo@uva.es)

<sup>3</sup> Department of Signal Processing and Communications, University of Alcalá (Spain)

e-mail: [pedro.gil@uah.es](mailto:pedro.gil@uah.es)

**Keywords:** Wearable Sensors, Synchronization, IMUs, SHM, Human Motion, GRFs

**Abstract.** Experimental techniques for monitoring physical magnitudes in dynamic applications have always been the subject of a large number of contributions resulting in novel methodologies. One of the main drawbacks underlying the use of classic analog instruments is their cost and manipulation. In order to minimize those factors, wearable Bluetooth devices emerge.

In recent years, special effort in developing wearable devices and sensors technology has been conducted [1]. These devices are intended to be easy to manipulate and, when compared to large classic DAQ systems for dynamic motion assessment, also come at a reduced cost. This work aims at providing a method that introduces different type of wearable sensors in a single physical magnitudes measure procedure, suitable for not just human motion tracking (e.g. GRFs, human gait and injury diagnosis), but also for structural dynamics applications, like slender structures. The method is also properly tested with validation procedures.

A simple methodology for monitoring dynamic physical magnitudes is depicted. In order to record as many magnitudes as possible, a combination of two different types of wearable devices is used. First, Novel Loadsols® capacitive force sensors, initially conceived for human gait addressing by GRF mapping, provide a way to track and get a force signal at a fixed sample rate  $f_L$  and in a maximum of 6 spots. Then, up to 11 Movella® Xsens DOT Inertial Measurement Units can be used to obtain triaxial acceleration, angular velocity, orientation, and magnetic field. Those IMUs also sample at a fixed  $f_S$  rate. One of the main advantages is that a smartphone can be used as a DAQ system via Bluetooth, making a fully wireless connection.

Once connected, first synchronized, and placed, measurements (Fig. 1) in different scenarios (not just the ones the devices are meant to be used, so slender structures applications arise) can

start by applying a trigger seen in sensitive signals (e.g.  $F$  in Loadsols and accel. in IMUs). Then, files containing raw recordings are generated, providing the input to a MATLAB® algorithm (Fig. 2) which makes a full data curation and synchronization consisting of: identifying time windows to average signals when needed, internal calibration (compensation of deviations) and synchronization (same trigger sample for every device type), filtering, resampling at a common  $f$  (Hz) rate and final synchronization which leads to cut time and data intervals due to different recording start times. Finally, a single set of synchronized data is obtained.

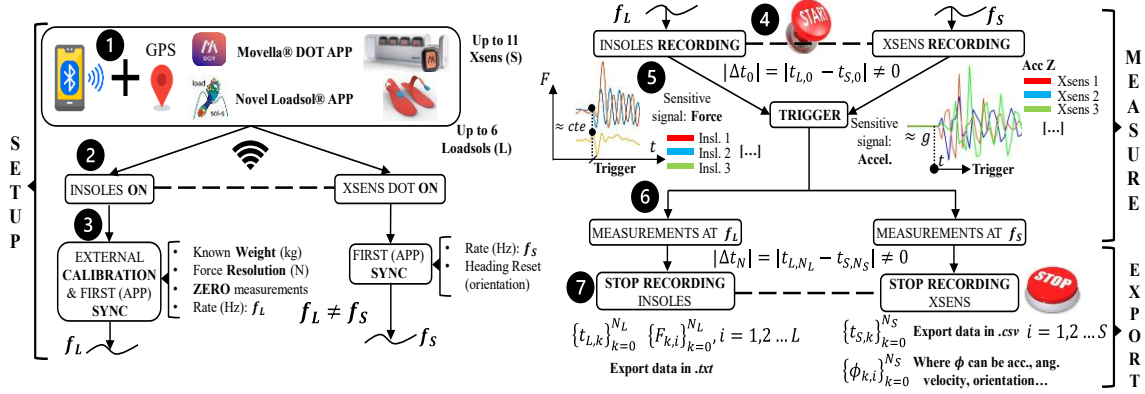


Figure 1: Measurement process with Novel Loadsol® insoles, Movella® Xsens DOT and smartphone as DAQ.

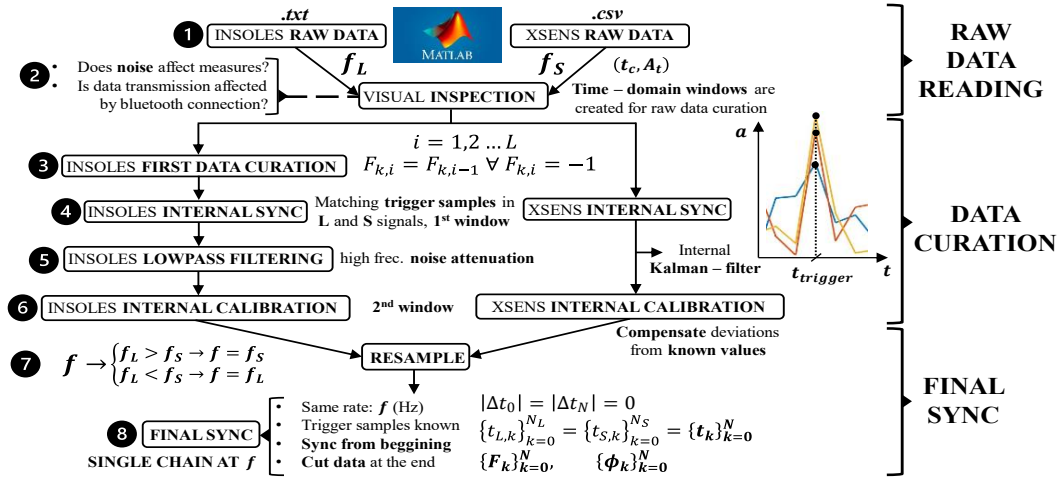


Figure 2: Data curation and final synchronization algorithm principles implemented in MATLAB®.

After the method is exposed, validation proposals arise, like the one which implies comparing performance with DAQ systems such as Dewesoft® Sirius and classic analog sensors in slender structures, as well as human gait assessment with GRFs mapping in mind.

**Acknowledgments:** The authors wish to acknowledge to the AEI, Spanish Government (10.13039/501100011033), and to “ERDF A way of making Europe”, for the partial support through the grant PID2022-140117NB-I00. The corresponding author also wishes to acknowledge to the “Investigo Program CP23/174 – Financed by the EU, NextGenerationEU”.

## References:

- [1] T. He, J. Chen, B.-G. He, W. Wang, Z.-L. Zhu, and Z. Lv, “Toward Wearable Sensors: Advances, Trends, and Challenges”, *ACM Computing Surveys*, 55, 4, pp. 1–35, 2023.

## DETECTING STRUCTURAL DAMAGE IN SLENDER CONSTRUCTIONS USING A HYBRID SYSTEM OF SUPERVISED LEARNING ALGORITHMS AND MODEL UPDATING FOR ANALYZING RAW DYNAMIC DATA

César Peláez-Rodríguez<sup>\*1</sup>, Álvaro Magdaleno<sup>2</sup>, Álvaro Iglesias-Pordomingo<sup>2</sup>, Jorge Pérez-Aracil<sup>1</sup>, Sancho Salcedo-Sanz<sup>1</sup> and Antolín Lorenzana<sup>2</sup>

<sup>1</sup> Department of Signal Processing and Communications. Universidad de Alcalá  
Ctra. Madrid-Barcelona, km 33.600, 28805 Alcalá de Henares  
e-mail: cesar.pelaez@uah.es

<sup>2</sup> ITAP. Universidad de Valladolid  
Paseo del Cauce 59, 47011 Valladolid, Spain

**Keywords:** Structure health monitoring, Structural damage detection, Artificial Neural Network, Model Updating, Supervised learning algorithms

**Abstract.** Structural modification can result from various factors, including design and construction issues, operational conditions, severe natural events, and natural aging. Often, alterations in structures are associated with damage, leading to changes in the material and geometric properties of structural components. These changes, in turn, impact the stiffness and stability of the structure. Traditional damage assessment methods, relying on periodic visual inspections, prove inefficient, especially for complex structures, necessitating highly-trained labor and easy access to monitored structural elements. Consequently, extensive research has focused on developing automated local and global Structural Health Monitoring (SHM) techniques [1]. SHM enables the early detection of damage, reducing maintenance costs, and enhancing user comfort and safety.

Vibration-based damage detection methods assess the overall performance of monitored structures by translating vibration responses, measured through accelerometers, into meaningful indices reflecting the structure's actual condition [2]. These methods encompass both parametric (model-based) approaches, identifying structural models and comparing them with undamaged structures to detect and locate modifications, and non-parametric (data-based) approaches, utilizing statistical means to directly identify damage from measured signals.

Computational learning methods, particularly Artificial Neural Networks (ANN), have proven valuable for solving structural damage assessment problems [4]. However, data-driven techniques face challenges in acquiring available data from both damaged and undamaged structures, often impractical in real-world scenarios. To overcome this, our approach implements a hybrid system for structural damage identification. This system aims to locate and identify the type and severity of damage by using the structure model to generate data from both undamaged

and damaged cases. This data is then fed into a machine learning algorithm capable of classifying the structure's status based on temporal acceleration signals.

Experimental validation of this system was conducted on a laboratory-scale model of a 4-story shear building. The implemented algorithm, outlined in Figure 1, utilizes the structure model obtained through modal identification to generate data for both undamaged and variably damaged structures. Two artificial neural networks are employed: the first to locate damage based on temporal acceleration signals and the second, once the affected floors are defined, to identify the type (change in stiffness, mass, or both) and severity of the damage suffered.

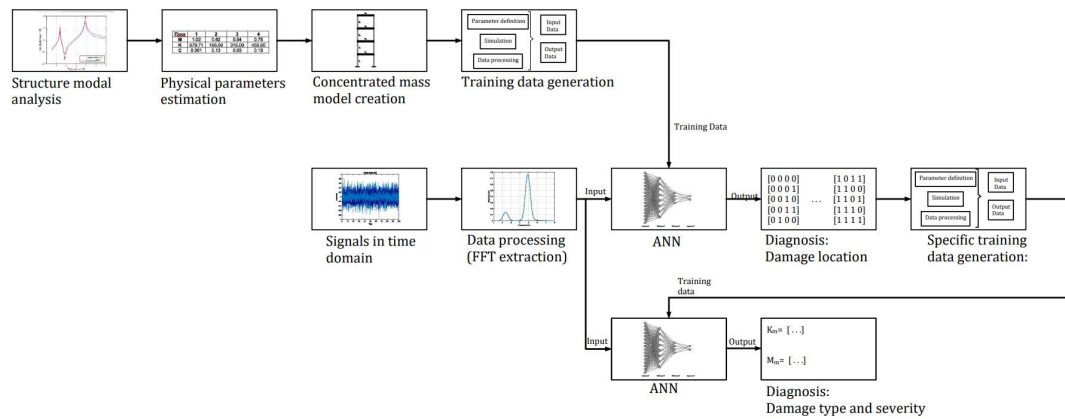


Figure 1: Scheme of the proposed methodology

## Acknowledgments

This research has been partially supported by the project PID2020-115454GB-C21 of the Spanish Ministry of Science and Innovation (MICINN). The authors also wish to acknowledge to the AEI, Spanish Government (10.13039/501100011033), and to “ERDF A way of making Europe”, for the partial support through the grant PID2022- 140117NB-I00.

## References

- [1] Anton S.R., Inman D.J., Park G., (2009) Reference-free damage detection using instantaneous baseline measurements. *AIAA J.* 47 (2009) 1952-1964.
- [2] Abdeljaber O. et al., (2016) Real-time vibration-based structural damage detection using one-dimensional convolutional neural networks. *Journal of Sound and Vibration* (2016).
- [4] Finotti R.P., et al., (2018). An SHM approach using machine learning and statistical indicators extracted from raw dynamic measurements. *Latin American Journal of Solid and Structures*, 2019, 16(2), e165.
- [5] Doebling S.W, Farrar C.R., Prime M.B., Shevirz D., (1998) A review of damage identification methods that examines changes in dynamic properties. *Shock and Vibration Digest*, 30(2), 91-105.

## APPLICATION OF T-MASS AND T-STIFFNESS CORRELATION TECHNIQUES ON A BRIDGE MODEL

N. García-Fernández<sup>1</sup>, F. Pelayo<sup>2</sup>, C. Gentile<sup>3</sup>, and M. Aenlle<sup>4</sup>

<sup>1</sup> University of Oviedo  
Department of Construction and Manufacturing Engineering, Gijón, Spain  
e-mail: garciafnatalia@uniovi.es

<sup>2</sup> University of Oviedo  
Department of Construction and Manufacturing Engineering, Gijón, Spain  
e-mail: fernandezpelayo@uniovi.es

<sup>3</sup> Politecnico di Milano  
Department of Architecture, Built Environment and Construction Engineering (DABC), Milan, Italy  
e-mail: carmelo.gentile@polimi.it

<sup>4</sup> University of Oviedo  
Department of Construction and Manufacturing Engineering, Gijón, Spain  
e-mail: aenlle@uniovi.es

**Keywords:** T-Mass, T-Stiffness, Composite bridge, Correlation techniques

**Abstract.** *In structural engineering, it is standard practice to develop a finite element (FE) model of a structure in order to predict its static and dynamic response. However, the accuracy of the results obtained from the FE model depends on its level of correlation with the real structure: Many correlation techniques exist in the current literature, however, the normalized relative frequency difference (NRFD) and the modal assurance criterion (MAC) are most used. In this paper, T-Mass and T-Stiffness indicators are employed as correlation indicators to determine the source of the discrepancies. A FE model of a real composite bridge is used as a case study. Different FE models are created introducing modifications of mass and/or stiffness. The correlation between these models is studied through the T-Mass and T-Stiffness.*

### INTRODUCTION AND THEORY

Model correlation techniques [1], [2] are methods used to compare two different models, being the normalized relative frequency difference (NRFD) and the modal assurance criterion (MAC) the most commonly used correlation techniques due to their extensive adoption in real applications and ease of implementation, although numerous correlation methods can be found in the current literature. The significance of correlation techniques is highlighted by their diverse applications in various fields.

According to the structural dynamic modification theory [3], an experimental model can be considered a dynamic modification of the numerical one. Thus, the experimental modal matrix  $\mathbf{A}$  can be expressed as a linear combination of the mass normalized numerical modal matrix  $\mathbf{B}$  by means of the expression:

$$\mathbf{A} = \mathbf{B} \mathbf{T} \quad (1)$$

where  $\mathbf{T}$  is a transformation matrix.

If there are no discrepancies in terms of mass between the numerical and the experimental mode shapes, the inner product  $\mathbf{T}^T \mathbf{T}$  must be an identity matrix (in the case of mass normalized mode shapes). Moreover, the column vectors of matrix  $\mathbf{T}$  are always orthogonal to each other, and this does not depend on the normalization used in the modal matrix  $\mathbf{A}$ . In order to have an indicator of mass discrepancies between both models, the angles between the vectors of matrix  $\mathbf{T}$  are proposed, denoted hereafter as **T-Mass**. Angles equal to 90° indicate perfect orthogonality, i.e., no discrepancies in mass.

$$\mathbf{I} = \mathbf{T}^T \mathbf{T} \quad (2)$$

If there are no discrepancies in terms of stiffness between the numerical and the experimental models, the inner product  $\mathbf{T}^T \omega_B^2 \mathbf{T}$  must be a diagonal matrix containing the natural frequencies  $\omega_A^2$  in the diagonal (in the case of mass normalized mode shapes). In order to have an indicator of stiffness discrepancies between two models, the angles between the vectors of matrix  $\mathbf{T}$  and matrix  $\omega_B^2 \mathbf{T}$  are proposed, denoted hereafter as **T-Stiffness**. Angles equal to 90° indicate perfect orthogonality, i.e., no discrepancies in stiffness.

$$\omega_A^2 \mathbf{A} = \mathbf{T}^T \omega_B^2 \mathbf{T} + \mathbf{A}^T \Delta \mathbf{K} \mathbf{A} \quad (3)$$

In this paper a finite element model of a bridge is used to study the application of T-Mass and T-Stiffness concepts.

## CASE STUDY

The Olona West Bridge is located in the Lombardy region, Italy. It consists of a steel-concrete composite deck, which is supported by two abutments and three concrete piers. The bridge has 4 spans: two central spans of 66 m long and lateral spans of 55 m.

The finite element (FE) model was developed in the ABAQUS software using beam and shell elements (Fig. 1). The steel part of the deck is modelled with two-node linear beam elements (B31) for the two main beams and the middle beam and two-node truss elements (T3D2) for the remaining parts. steel was modelled as an isotropic linear elastic material, with the following specifications: Poisson's ratio equal to 0.3, Young's modulus equal to 210 GPa, and a mass density of 7850 kg/m<sup>3</sup>. The concrete part of the deck is modelled using four-node shell elements (S4R) following the geometry specified in the documentation. The connections between the main beams and the deck are made using 'beam connectors', with a maximum distance (along the length of the beam) between each connector of 1.53 m. In this case, a simplification of the boundary conditions is assumed, and the piers are not modeled. The bridge is considered as simply supported, thus, pinned supports are modeled in one abutment whereas roller supports are considered in the other abutment and in the piers. The parapets and other auxiliary elements of the bridge are incorporated into the FE model as point masses since it is considered that they do not influence the overall stiffness of the bridge.

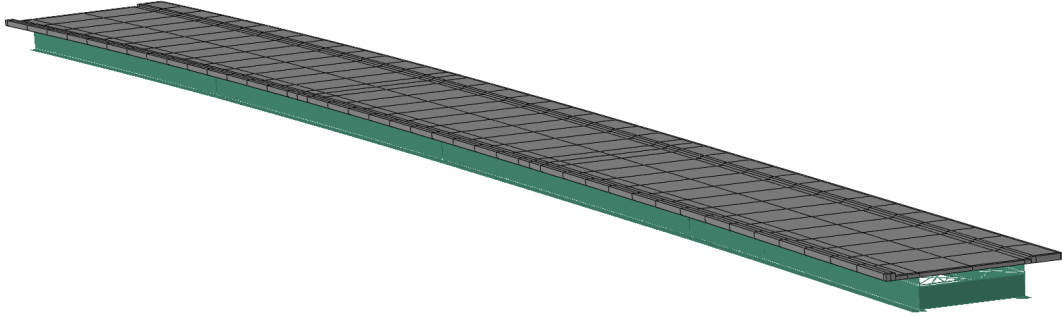


Figure 1: Finite element model of Olona bridge.

The numerical natural frequencies and mode shapes obtained with the FE model, using the Lanczos solver, are shown in Fig. 2.

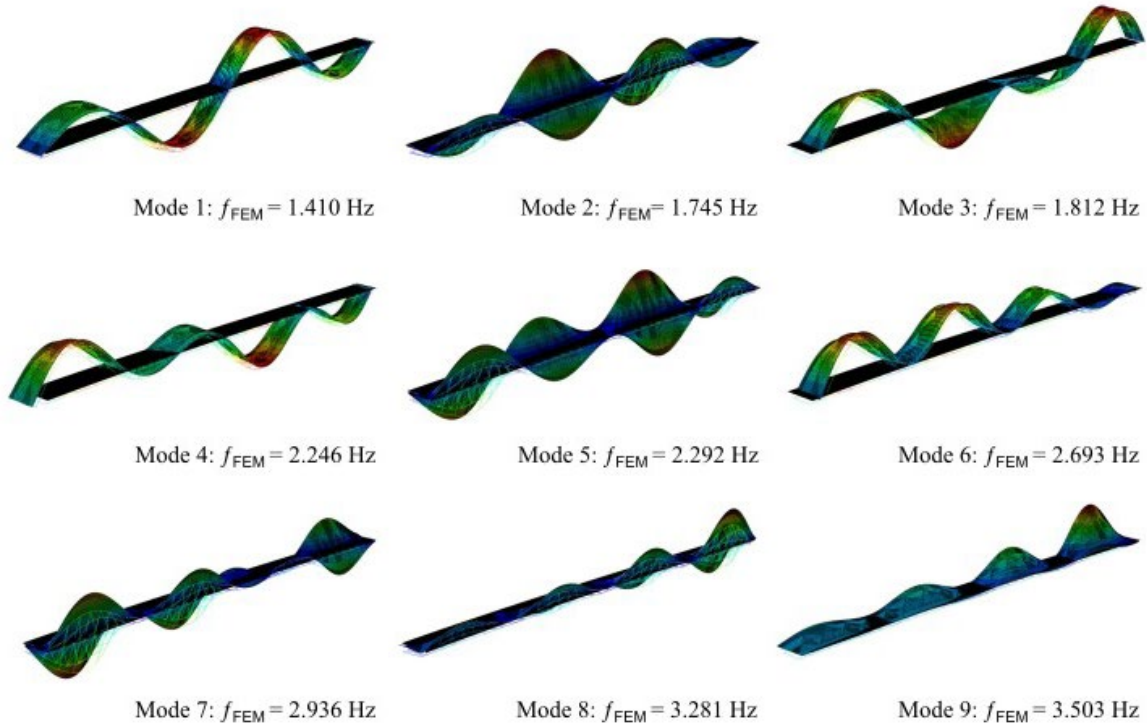


Figure 2: Finite element mode shapes and natural frequencies.

Different FE models are created by introducing mass and stiffness modifications, such as changes in mass-density and Young's modulus. The correlation between the unperturbed and the perturbed numerical models is studied, and the source of the discrepancies (mass changes or stiffness changes) is detected using the T-Mass and T-Stiffness indicators.

## CONCLUSIONS

The following conclusions can be drawn:

- The concepts of T-Mass and T-Stiffness have been used to study the correlation between different numerical models of a composite bridge.
- T-Mass and T-Stiffness can be used to know if the discrepancies between two models can be ascribed to changes in mass, stiffness or both.
- The sensitivity to mass and stiffness changes can be studied by applying T-Mass and T-Stiffness with two numerical models.

## ACKNOWLEDGEMENTS

This work was supported by the Spanish Ministry of Science and Innovation [MCI-20-PID2019-105593 GB-I00/AEI/10.13039/501100011033 and MCI-21-PRE2020-094923].

## REFERENCES

- [1] M. I. Friswell and J. E. Mottershead, Finite Element Model Updating in Structural Dynamics, vol. 38. Dordrecht: Springer Netherlands, 1995.
- [2] L. Rigner, “Modal assurance criteria value for two orthogonal modal vectors,” 1998
- [3] Avitabile P, Twenty years of structural dynamic modification - A review., *Sound and Vibration*. (2003).



## MODELLING AND DESIGN OPTIMISATION OF A MAGNETOELASTIC VIBRATION ENERGY HARVESTER FOR RAILWAY BRIDGES

J.C. Cámara-Molina<sup>1</sup>, A. Romero<sup>1</sup>, P. Galvín<sup>1</sup>, E. Moliner<sup>2</sup>, M.D. Martínez-Rodrigo<sup>2</sup> and  
P. Marín<sup>3,4</sup>

<sup>1</sup>Escuela Técnica Superior de Ingeniería Universidad de Sevilla  
Camino de los Descubrimientos s/n, ES-41092 Sevilla, Spain  
e-mail: {jcamara, aro, pedro galvin}@us.es

<sup>2</sup> Department of Mechanical Engineering and Construction Universitat Jaume I  
Avda. Sos Baynat s/n, ES-12071 Castellón, Spain  
e-mail: {mrodrigo, molinere}@uji.es

<sup>3</sup> Instituto de Magnetismo Aplicado UCM-ADIF  
28230 Las Rozas, Spain

<sup>4</sup> Departamento de Física de Materiales Universidad Complutense de Madrid (UCM)  
28040 Madrid, Spain  
e-mail: mpmarin@fis.ucm.es

**Keywords:** Magnetoelasticity, energy harvesting, railway bridges, high-speed train, tuning frequency, optimal design, additive manufacturing, genetic algorithm

**Abstract.** *This research investigates the modelling and optimisation of magnetoelastic vibration energy harvesters (MVEH) for its use in railway bridges. The electromechanical behaviour of the device is represented by an analytical model. The governing equations of the MVEH are derived from a variational formulation and allow the estimation of the energy harvested from train-induced bridge vibrations. The model is verified by the optimal design of a device that maximises the power generated. 3D printing for the substructure is considered to improve the design flexibility. The design optimisation problem is solved using a genetic algorithm constrained to geometry and structural integrity. Finally, the energy harvester performance is evaluated from in situ experimental data measured by the authors.*

## A MODEL UPDATING METHOD BASED ON T-MASS AND T-STIFFNESS CORRELATION TECHNIQUES

N. García-Fernández<sup>1</sup>, F. Pelayo<sup>2</sup> and M. Aenlle<sup>3</sup>

<sup>1</sup> University of Oviedo  
Department of Construction and Manufacturing Engineering, Gijón, Spain  
e-mail: garciafnatalia@uniovi.es

<sup>1</sup> University of Oviedo  
Department of Construction and Manufacturing Engineering, Gijón, Spain  
e-mail: fernandezpelayo@uniovi.es

<sup>1</sup> University of Oviedo  
Department of Construction and Manufacturing Engineering, Gijón, Spain  
e-mail: aenlle@uniovi.es

**Keywords:** T-Mass, T-Stiffness, Model Updating, Correlation.

**Abstract.** *Model updating methods aim to calibrate finite element (FE) models to achieve better correlation with experimental models, therefore relying on correlation techniques. Two new correlation techniques, denoted T-Mass and T-Stiffness, enable the identification of the source of discrepancies between models, allowing for an assessment of the level of discrepancies in terms of mass and stiffness. T-Mass and T-Stiffness indicators are derived from a transformation matrix  $\mathbf{T}$ . This transformation matrix  $\mathbf{T}$  allows the experimental modal matrix to be expressed as a linear combination of the numerical mode shapes, given that the experimental model can be considered a dynamic modification of the numerical model. In this paper, the model updating of a steel cantilever beam is conducted. The automated updating of FE model, created in ABAQUS, is implemented through Python scripting. Various objective functions are explored, some of which consider T-Mass and T-Stiffness indicators. The results obtained are thoroughly compared and discussed.*

## 1 INTRODUCTION

Model correlation techniques are methods used in structural dynamics to compare two different models. Two experimental models can be compared for damage detection or Structural Health Monitoring (SHM) purposes. Two numerical models can be compared for mesh convergence investigations among others. Finally, an experimental model and a numerical model are usually compared for updating a numerical model, usually a finite element model (FEM).

Model correlation techniques can be classified in four categories: eigenvalue-based criteria, eigenvector-based criteria, frequency response-based criteria and orthogonality methods. Being the normalized relative frequency difference (NRFD) (eigenvalue-based criteria) and the modal assurance criterion (MAC) (eigenvector-based criteria) the most used techniques due to their extensive adoption in real applications and ease of implementation.

As previously mentioned, one of the main applications of correlation techniques is model updating. Model updating methods are used to improve the correlation between numerical and experimental models by updating a finite element model, and they can be classified into direct methods and iterative methods. Direct methods update the elements of the stiffness and mass matrices in a one-step procedure; however, the updated mass and stiffness matrices have little physical meaning and cannot be directly related to physical changes in the finite element models. On the other hand, iterative methods (also known as parameter updating methods) modify iteratively some parameters. Iterative methods can be subdivided into sensitivity methods and optimization methods. Another possible classification is to divide iterative methods into deterministic and stochastic methods. The iterative deterministic maximum likelihood method transforms the model updating problem into an optimization problem and the objective function is defined in terms of residuals between different types of numerically and experimentally obtained data sets, most often natural frequencies and mode shapes are used. As iterative methods allow a wide choice of the parameters to be updated, usually a sensitivity analysis is required to assess the impact of modifications in the model parameters [1,2,3].

According to the structural dynamic modification theory, when an experimental model is considered a dynamic modification of a numerical model, the experimental modal matrix can be expressed as a linear combination of the numerical mode shapes, through a transformation matrix, denoted in this paper as matrix  $\mathbf{T}$  [4].

In this paper, it is proposed to use the transformation matrix  $\mathbf{T}$  as a model correlation technique, allowing to determine whether there are discrepancies between models are due to mass (T-Mass) or stiffness (T-Stiffness) discrepancies. These indicators are then used to update a finite element model of a cantilever beam through the experimental modal parameters. The FE model was created in ABAQUS and then an automated updating process was implemented through Python scripting.

## 2 THEORY

According to the structural dynamic modification theory [4], an experimental model can be considered a dynamic modification of the numerical one. Thus, the experimental modal matrix  $\mathbf{A}$  can be expressed as a linear combination of the mass normalized numerical modal matrix  $\mathbf{B}$  by means of the expression:

$$\mathbf{A} = \mathbf{B} \mathbf{T} \quad (1)$$

where  $\mathbf{T}$  is a transformation matrix.

Since the response of the structure is only measured in a few DOF's and only the modal parameters in a certain frequency range are identified, an estimation of matrix  $\mathbf{T}$  can be obtained as:

$$\hat{\mathbf{T}} = \mathbf{B}^+ \mathbf{A} \quad (2)$$

The experimental mass matrix  $\mathbf{M}_A$  can be expressed as:

$$\mathbf{M}_A = \mathbf{M}_B + \Delta \mathbf{M} \quad (3)$$

where  $\Delta \mathbf{M}$  is the mass change matrix which defines the difference in mass between both models.

Similarly, the stiffness matrix of the experimental model  $\mathbf{K}_A$  can be expressed as:

$$\mathbf{K}_A = \mathbf{K}_B + \Delta \mathbf{K} \quad (4)$$

where  $\Delta \mathbf{K}$  is the stiffness change matrix.

Premultiplication of eq. (3) by  $\mathbf{A}^T$ , and post-multiplication by  $\mathbf{A}$ , i.e.:

$$\mathbf{A}^T \mathbf{M}_A \mathbf{A} = \mathbf{A}^T \mathbf{M}_B \mathbf{A} + \mathbf{A}^T \Delta \mathbf{M} \mathbf{A} \quad (5)$$

gives:

$$\mathbf{I} = \mathbf{T}^T \mathbf{T} + \mathbf{A}^T \Delta \mathbf{M} \mathbf{A} \quad (6)$$

From eq. (6) it is derived that if there are no discrepancies in terms of mass between the numerical and the experimental mode shapes:

$$\mathbf{I} = \mathbf{T}^T \mathbf{T} \quad (7)$$

From eq. (7) is inferred that the inner product  $\mathbf{T}^T \mathbf{T}$  must be an identity matrix (in the case of mass normalized mode shapes). Moreover, the column vectors of matrix  $\mathbf{T}$  are always orthogonal to each other, and this does not depend on the normalization used in the modal matrix  $\mathbf{A}$ .

In order to have an indicator of mass discrepancies between both models, the angles between the vectors of matrix  $\mathbf{T}$  are proposed, denoted hereafter as T-Mass. Angles equal to 90° indicate perfect orthogonality, i.e., no discrepancies in mass.

Similarly, pre-multiplication of eq. (3) by  $\mathbf{A}^T$ , and post-multiplication by  $\mathbf{A}$ , i.e.:

$$\mathbf{A}^T \mathbf{K}_A \mathbf{A} = \mathbf{A}^T \mathbf{K}_B \mathbf{A} + \mathbf{A}^T \Delta \mathbf{K} \mathbf{A} \quad (8)$$

Gives:

$$\omega_A^2 \mathbf{A} = \mathbf{T}^T \omega_B^2 \mathbf{T} + \mathbf{A}^T \Delta \mathbf{K} \mathbf{A} \quad (9)$$

Here,  $\omega_A^2$  and  $\omega_B^2$  are diagonal matrices containing the natural frequencies of the experimental and numerical models, respectively.

If there are no discrepancies in terms of stiffness between the numerical and the experimental models, from eq. (9) it is inferred that:

$$\boldsymbol{\omega}_A^2 = \mathbf{T}^T \boldsymbol{\omega}_B^2 \mathbf{T} \quad (10)$$

Which means that the inner product  $\mathbf{T}^T \boldsymbol{\omega}_B^2 \mathbf{T}$  must be a diagonal matrix containing the natural frequencies  $\boldsymbol{\omega}_A^2$  in the diagonal (in the case of mass normalized mode shapes).

In order to have an indicator of stiffness discrepancies between two models, the angles between the vectors of matrix  $\mathbf{T}$  and matrix  $\boldsymbol{\omega}_B^2 \mathbf{T}$  are proposed, denoted hereafter as T-Stiffness. Angles equal to  $90^\circ$  indicate perfect orthogonality, i.e., no discrepancies in stiffness.

### 3 CASE STUDY

In order to show and validate the equations proposed in the previous section, a steel cantilever beam was assembled in ABAQUS and tested experimentally by operational modal analysis. The numerical model was automatically updated.

#### 3.1 Experimental Cantilever Beam

In this study, a lab steel cantilever beam, with a length of 1.775m and a rectangular hollow section 100x40 mm, was tested by operational modal analysis. The responses of the structure were recorded in 7 DOF's using accelerometers with a sensitivity of 100 mV/g. As shown in Fig 1, these sensors were equally spaced along the longitudinal direction of the cantilever beam.

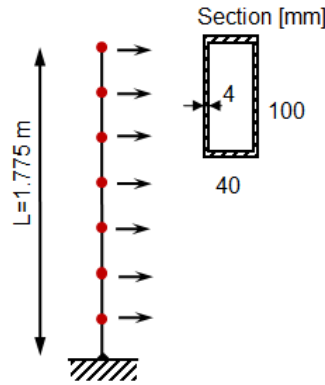


Figure 1: Experimental steel cantilever beam with equally spaced accelerometers in red.

The modal parameters were estimated with the Enhanced Frequency Domain Decomposition (EFDD) technique. The experimental mode shapes, together with their corresponding natural frequencies, are shown in Fig 2.

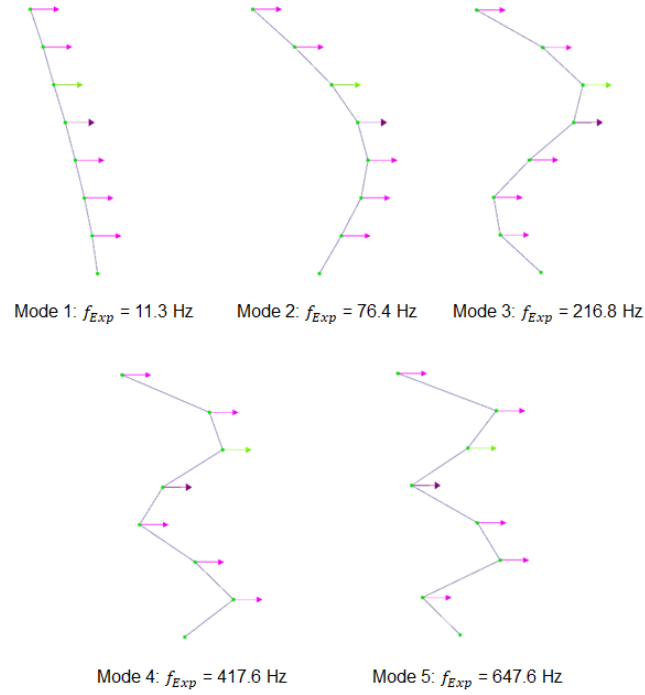


Figure 2: Experimental mode shapes and natural frequencies.

### 3.2 Finite Element Model

A shell FE model of the structure was created in ABAQUS through a Python script. Regarding the material properties, a Poisson ratio of 0.3 was considered, whereas the mass-density ( $\rho$ ) and the Young's modulus ( $E$ ) were parameterized to be considered in the updating process. The model was meshed with 8-node shell elements with reduced integration (S8R elements). As it is well known, boundary conditions are usually a source of uncertainty, thus, a perfect fixed support was not modelled and vertical springs of unknown stiffness ( $K$ ) were modelled in the base of the beam, whereas fixed boundary conditions were considered in the other directions.

The modal parameters corresponding to bending modes, in the direction of the measure DOF's, were automatically extracted with a frequency analysis.

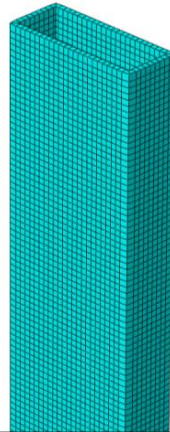


Figure 3: Finite element model (render style) showing mesh detail.

## 4 UPDATING METHODOLOGY

In the proposed updating procedure two main phases can be distinguished. An initial sensitivity analysis is required in order to evaluate the parameters to be updated, assessing the impact of these parameters' modifications in the modal properties. The second phase consists in the automated updating process of the finite element model.

### 4.1 Sensitivity Analysis

The sensitivity analysis was performed using the SAFE Toolbox [5] and, in turns, three main steps can be distinguished (see Fig. 4).

First, the input parameters to be considered in the sensitivity analysis must be defined, i.e., variables to be updated, range of these variables, sampling size, and sampling strategy. In this case, 3 variables were considered ( $E, \rho, K$ ) in the following ranges:  $[190 \leq E \leq 232 \text{ GPa}]$ ,  $[7020 \leq \rho \leq 8580 \text{ Kg/m}^3]$ ,  $[1e5 \leq K \leq 1e9 \text{ N/m}]$ . A sample size of 25 was chosen, which is considered sufficient in the literature to discriminate between influential and non-influential factors. Moreover, the Latin-Hypercube is selected as sampling strategy.

The second step consists of evaluating the FE model for the sampled input combinations. In this case, as 3 model parameters and a sampling size of 25 were considered, this results in 100 model evaluations. From each evaluation, one output parameter was obtained defined by the chosen objective function (also known as error function). Four different objective functions were considered and compared in the sensitivity analysis. The first one, denoted as  $\mathbf{O}_A$ , only considers natural frequencies:

$$\mathbf{O}_A = \sum_{i=1}^5 \frac{|f_{EXP_i} - f_{FEM_i}|}{f_{EXP_i}} \times 100 \quad (11)$$

The second one, denoted as  $\mathbf{O}_B$  only considers MAC:

$$\mathbf{O}_B = \sum_{i=1}^5 1 - \text{MAC}_{i,i} \quad (12)$$

The objective function denoted  $\mathbf{O}_C$ , only considers *TStiffness*:

$$\mathbf{O}_C = \sum_{j=1}^5 \sum_{i=1}^5 90 - T\_Stiffness_{i,j} \quad \text{subject to } i \neq j \quad (13)$$

Finally,  $\mathbf{O}_D$  considers natural frequencies and MAC [6].

$$\mathbf{O}_D = \ln \left( \sum_{i=1}^5 \frac{|f_{EXP_i} - f_{FEM_i}|}{f_{EXP_i}} + (1 - \text{MAC}_{i,i}) + 1 \right) \quad (14)$$

In the last step, taking into account the input and output samples, the sensitivity indices are calculated with the Elementary Effects Test (EET).

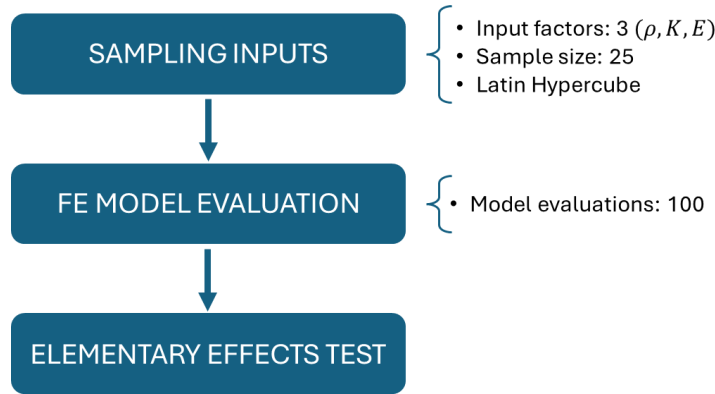


Figure 4: Sensitivity analysis workflow.

#### 4.2 Automated model updating

The updating process was automatically performed by the minimization of the selected objective function; thus, two functions were defined (see Fig. 5). The fully automated process was implemented using a Python code which interacts with ABAQUS.

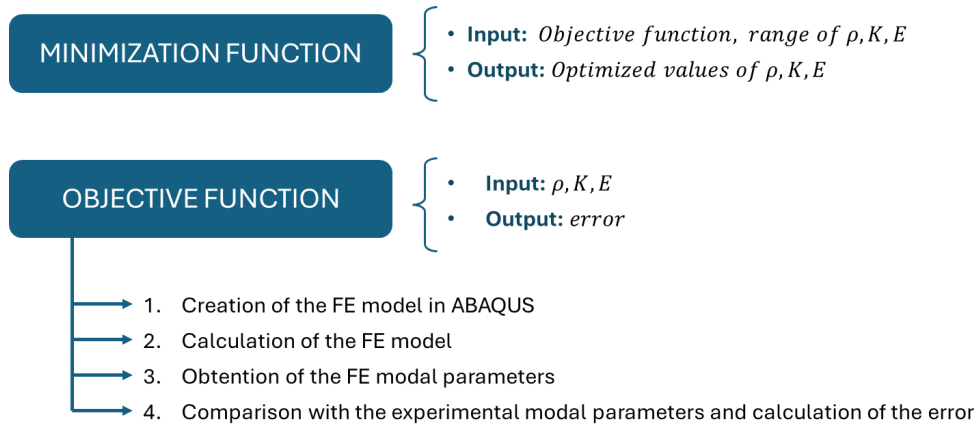


Figure 5: Functions and workflow implemented in Python.

Regarding the minimization function, the subpackage *optimize* of the *SciPy* library was utilized. The differential evolution method is used. This function minimizes the objective function, giving as output the optimum values of the considered parameters ( $E, \rho, K$ ).

The objective function is a function whose inputs are the considered parameters ( $E, \rho, K$ ) and whose output is the error calculated as seen before (eq. (11-14)). Each time this function is evaluated for a certain value of  $E, \rho$  and  $K$ , the following steps are performed (see Fig. 5). The FE model is created in Abaqus with the selected parameters through the command window. The model is solved and the numerical modal parameters (frequencies and mode shapes are obtained). Then the numerical modal parameters are compared with the experimental ones (Mac and T-Stiffness are calculated if required). A scalar value for the error is obtained using the equations previously described.



## 5 RESULTS

### 5.1 Sensitivity Analysis Results

Through a sensitivity analysis, the impact of the model parameters ( $E, \rho, K$ ) in the error values for the different error functions ( $\mathbf{O}_A, \mathbf{O}_B, \mathbf{O}_C, \mathbf{O}_D$ ) was study. The Elementary Effects Test indices were calculated, and the results are shown in Fig. 4, where the mean value of the indices (x-axis) indicates the overall importance of the input factor on the model output and the standard deviation (y-axis) evaluates the interactions.

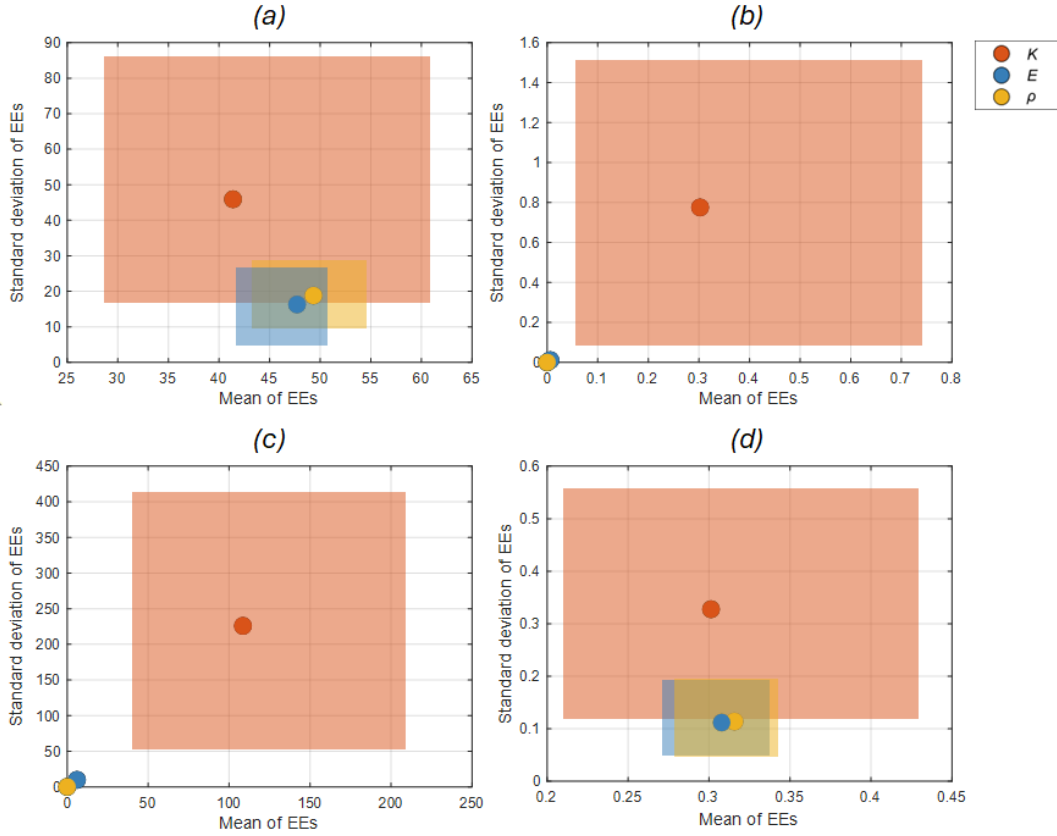


Figure 6: Sensitivity analysis of the parameters:  $K, E, \rho$ : (a) with objective function  $\mathbf{O}_A$ ; (b) with objective function  $\mathbf{O}_B$ ; (c) with objective function  $\mathbf{O}_C$ , (d) with objective function  $\mathbf{O}_D$ .

As previously seen, in the objective function  $\mathbf{O}_A$  only natural frequencies were considered (mode shapes were not included). As seen in Figure 6 (a), the impact of the mass-density and Young's modulus is higher than the impact of the spring stiffness, however the interaction of  $K$  is much higher.

For the objective function  $\mathbf{O}_B$  the natural frequencies were not considered. With respect to  $\mathbf{O}_C$ , in the T-Stiffness a combination of mode shapes and natural frequencies were used. With these techniques, the spring stiffness is the most important variable, both in terms of mean values of indices and standard deviations.

Finally, when the objective function considers the modal assurance criteria (MAC) and the natural frequencies ( $\mathbf{O}_D$ ). The parameters ( $E, \rho, K$ ) are similar in importance, although the interaction of the spring stiffness is higher.

If the samples considered in the sensitivity analysis are plotted with the calculated error ( $\mathbf{O}_A$ ,  $\mathbf{O}_B$ ,  $\mathbf{O}_C$  and  $\mathbf{O}_D$ ), it can be clearly observed how the distribution of the errors (color bar) changes for the same inputs. As it can be seen in Figure 7, a different behavior of the error is observed when natural frequencies are not directly included in the error function ( $\mathbf{O}_B$  and  $\mathbf{O}_C$ ) compared to when the natural frequencies are considered in the error function ( $\mathbf{O}_A$  and  $\mathbf{O}_D$ ).

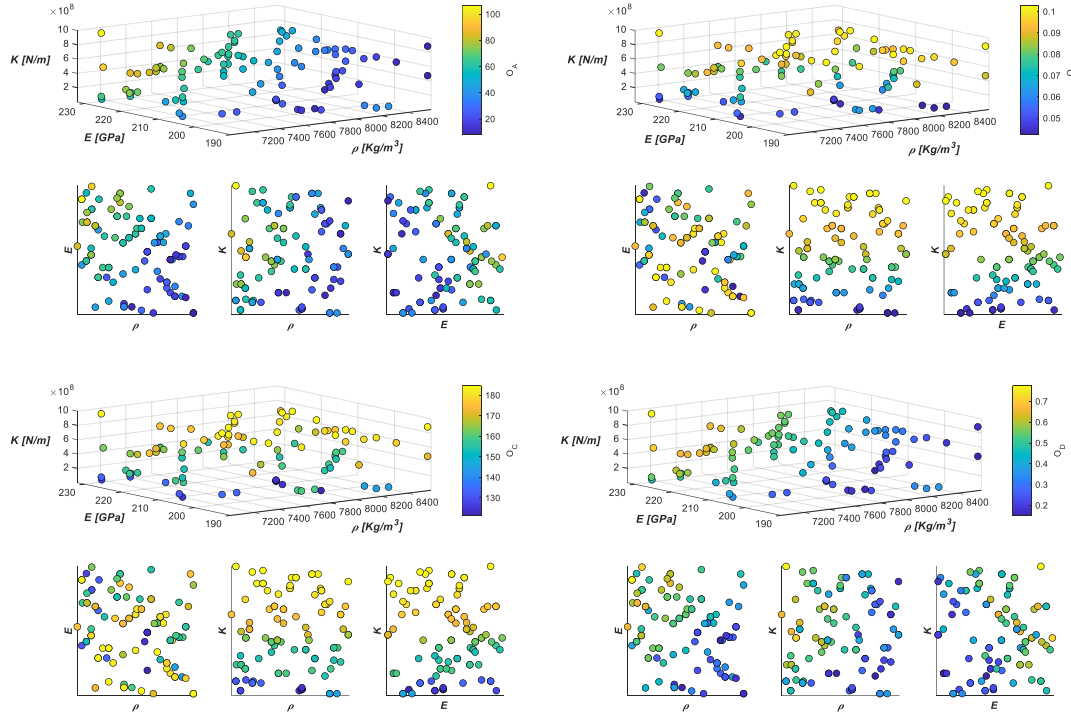


Figure 7: Sensitivity analysis for objective functions  $O_A$  (upper left),  $O_B$  (upper right),  $O_C$  (lower left) and  $O_D$  (lower right).

Considering these results and in order to compare the different objective functions, the three parameters ( $E, \rho, K$ ) will always be considered in the updating process.

## 5.2 Correlation before updating

Before doing any updating procedure, the correlation between an initial FE model and the experimental results, is studied. The initial properties considered for the three parameters ( $E, \rho, K$ ) are shown in Table 1.

$E$ [GPa]	$\rho$ [Kg/m <sup>3</sup> ]	$K$ [N/m]
211	7800	500000

Table 1: Initial FE model properties.

The errors in the natural frequencies, the modal assurance criteria (MAC), and the T-Stiffness, are shown in Tables 2, 3, and 4, respectively.

$f_{EXP}$ [Hz]	$f_{NUM}$ [Hz]	Error [%]
11.34	8.80	22.43
76.39	73.47	3.83
216.84	220.09	1.50
417.56	434.57	4.07
647.60	696.27	7.52

Table 2: Errors in the natural frequencies for the initial FE model.

MAC				
0.999	0.062	0.052	0.058	0.060
0.030	0.998	0.069	0.062	0.069
0.044	0.046	0.999	0.067	0.074
0.047	0.052	0.072	0.998	0.063
0.047	0.075	0.040	0.151	0.966

Table 3: MAC for the initial FE model.

T-Stiffness				
	88.39	89.78	89.84	89.92
79.40		88.74	89.72	89.64
78.95	80.46		89.49	89.81
58.18	81.76	88.01		87.46
46.79	62.18	88.12	83.60	

Table 4: T-Stiffness for the initial FE model.

As it can be observed, despite good results in terms of MAC are obtained, the error in the first natural frequency is significantly high.

### 5.3 Updating Procedure A

The first automated updating procedure (denoted as *A*) was performed using the objective function  $\mathbf{O}_A$ . Table 5 shows the optimum values for the parameters ( $E, \rho, K$ ) obtained after the updating process.

$E$ [GPa]	$\rho$ [Kg/m <sup>3</sup> ]	$K$ [N/m]
193.4	8146.3	194580739.3

Table 5: Optimum values for procedure A.

Tables 6, 7 and 8 show the errors obtained in the natural frequencies, the MAC values, and the T-Stiffness values, after the updating procedure. It can be observed in Table 6 that the errors in the natural frequencies are below 1% for the first four modes and around 2% for the fifth

mode. On the other hand, a very good MAC (see Table 7) has been obtained for the first four modes. With respect to the T-stiffness (Table 8), no significant improvements can be seen after the updating process.

$f_{EXP}$ [Hz]	$f_{NUM}$ [Hz]	<i>Error</i> [%]
11.34	11.34	0.00
76.39	75.86	0.70
216.84	216.00	0.39
417.56	417.59	0.01
647.60	662.17	2.25

Table 6: Errors in the natural frequencies for procedure A.

<b>MAC</b>				
1.000	0.044	0.056	0.057	0.060
0.048	0.999	0.049	0.069	0.065
0.044	0.064	0.997	0.050	0.082
0.052	0.047	0.092	0.991	0.048
0.051	0.075	0.036	0.177	0.946

Table 7: MAC for procedure A.

<b>T-Stiffness</b>				
---	89.28	89.61	89.93	89.99
79.14	---	88.58	89.32	89.93
39.66	79.11	---	88.57	89.65
60.66	70.97	84.79	---	88.15
76.41	85.01	86.90	85.49	---

Table 8: T-Stiffness for procedure A.

The results of the model evaluations performed during the updating process are shown in Fig 8.

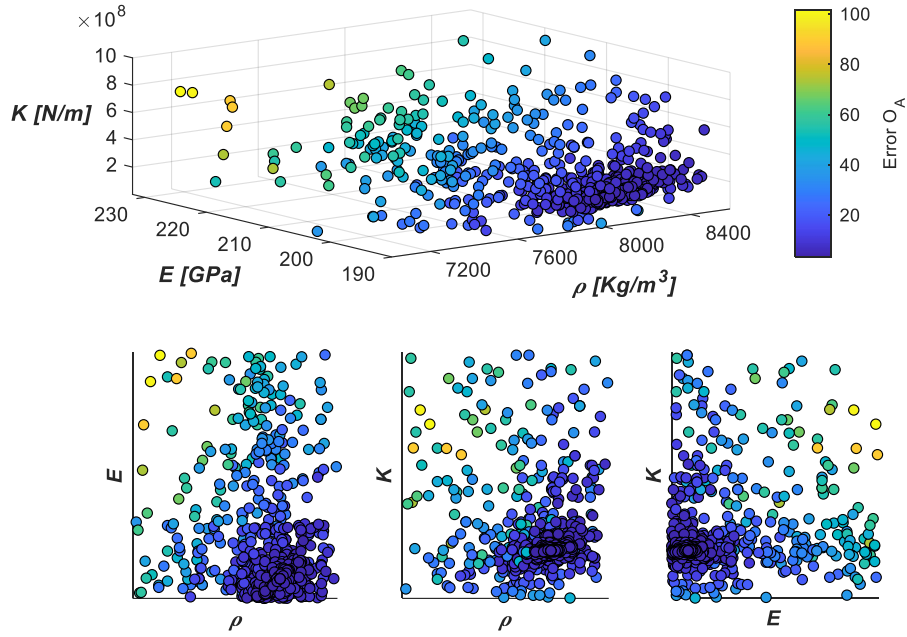


Figure 8: Iterations of procedure A

#### 5.4 Updating Procedure B Results

The updating procedure *B* was performed using the objective function  $\mathbf{O}_B$  and the optimum values for the parameters ( $E, \rho, K$ ) are shown in Table 9.

$E$ [GPa]	$\rho$ [Kg/m <sup>3</sup> ]	$K$ [N/m]
202.4	7223.9	163174.9

Table 9: Optimum values for procedure *B*.

Tables 10, 11 and 12 show the errors obtained in the natural frequencies, the MAC values, and the T-Stiffness values, after the updating procedure. Large errors in the natural frequencies have been obtained, which is expected because they have not been considered in the updating process. With respect to the MAC, the correlation is very good, except for mode 5. No changes can be observed in the T-stiffness.

$f_{EXP}$ [Hz]	$f_{NUM}$ [Hz]	Error [%]
11.34	8.94	21.20
76.39	74.75	2.16
216.84	223.97	3.29
417.56	442.26	5.92
647.60	708.60	9.42

Table 10: Errors in the natural frequencies for procedure *B*.

MAC				
0.999	0.062	0.052	0.058	0.060
0.030	0.997	0.069	0.062	0.069
0.044	0.046	0.999	0.067	0.074
0.047	0.052	0.072	0.998	0.063
0.047	0.075	0.040	0.151	0.966

Table 11: MAC for procedure *B*.

T-Stiffness				
---	88.38	89.77	89.84	89.92
79.39	---	88.73	89.72	89.64
78.89	80.40	---	89.48	89.81
58.15	81.69	87.99	---	87.46
46.84	62.13	88.11	83.60	---

Table 12: T-Stiffness for procedure *B*.

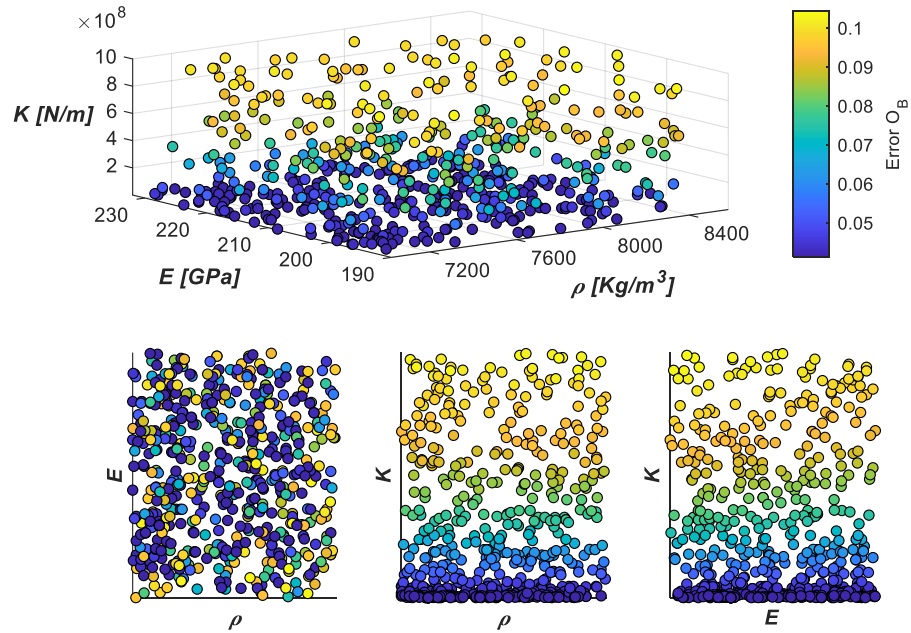


Figure 9: Iterations of procedure *B*

The results of the model evaluations performed during the updating process are shown in Fig 9.

### 5.5 Updating Procedure C Results

The updating procedure performed using the objective function  $\mathbf{O}_C$ , provides the optimum values for the parameters  $(E, \rho, K)$  shown in Table 13.

$E$ [GPa]	$\rho$ [Kg/m <sup>3</sup> ]	$K$ [N/m]
213.9	8513.2	48117464.6

Table 13: Optimum values for procedure C.

Tables 14, 15 and 16 show the errors obtained in the natural frequencies, the MAC values, and the T-Stiffness values, after the updating procedure. The errors in the natural frequencies have diminished but are still large, the MAC has not been modified, and the T-stiffness has slightly improved.

$f_{EXP}$ [Hz]	$f_{NUM}$ [Hz]	Error [%]
11.34	9.95	12.23%
76.39	73.61	3.64%
216.84	215.73	0.51%
417.56	422.51	1.19%
647.60	674.42	4.14%

Table 14: Errors in the natural frequencies for procedure C.

MAC				
1.000	0.054	0.054	0.058	0.060
0.037	0.999	0.061	0.065	0.067
0.044	0.052	0.999	0.061	0.077
0.049	0.050	0.078	0.996	0.058
0.049	0.075	0.039	0.159	0.960

Table 15: MAC for procedure C.

T-Stiffness				
	89.18	90.00	89.92	89.94
81.55		89.73	89.94	89.74
89.96	87.77		89.82	90.00
64.31	88.21	89.33		87.71
37.67	69.44	90.00	84.29	

Table 16: T-Stiffness for procedure C.

The results of the model evaluations performed during the updating process are shown in Fig 10.

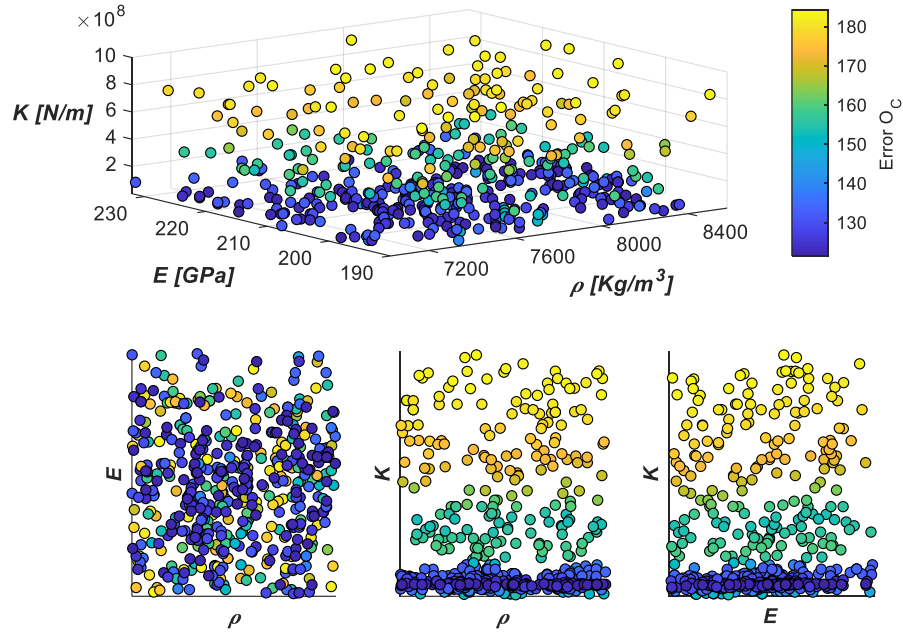


Figure 10: Iterations of procedure *C*

### 5.6 Updating Procedure *D* Results

The updating procedure performed using the objective function  $\mathbf{O}_D$ , provides the optimum values for the parameters  $(E, \rho, K)$  shown in Table 17.

$E$ [GPa]	$\rho$ [Kg/m³]	$K$ [N/m]
195.2	8223.7	196420199.9

Table 17: Optimum values for procedure *D*.

Tables 18, 19 and 20 show the errors obtained in the natural frequencies, the MAC values, and the T-Stiffness values, after the updating procedure. The errors in the natural frequencies have significantly diminished, but the technique is not able to improve the MAC. The T-stiffness has not been improved either.

$f_{EXP}$ [Hz]	$f_{NUM}$ [Hz]	Error [%]
11.34	11.34	0.01%
76.39	75.86	0.70%
216.84	215.98	0.39%
417.56	417.56	0.00%
647.60	662.13	2.24%

Table 18: Errors in the natural frequencies for procedure *D*.



MAC				
1.000	0.044	0.056	0.057	0.060
0.048	0.999	0.049	0.069	0.065
0.044	0.064	0.997	0.050	0.082
0.052	0.047	0.092	0.991	0.048
0.051	0.075	0.036	0.177	0.946

Table 19: MAC for procedure *D*.

T-Stiffness				
	89.28	89.61	89.93	89.99
79.14		88.58	89.32	89.93
39.66	79.11		88.57	89.65
60.66	70.97	84.79		88.15
76.42	85.01	86.90	85.49	

Table 20: T-Stiffness for procedure *D*.

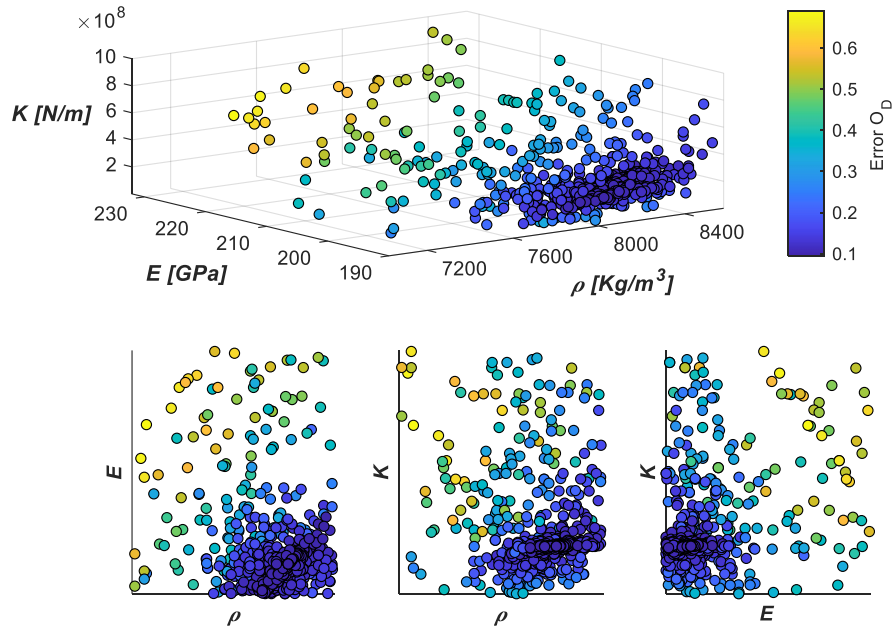


Figure 11: Iterations of procedure *D*

The results of the model evaluations performed during the updating process are shown Fig 11.

## 6 DISCUSSION

A summary of the parameters ( $E, \rho, K$ ) obtained after the updating process are presented in Table 21, whereas the total errors in natural frequencies, MAC, and T-Stiffness are shown in Table 22.

	<i>Initial</i>	<i>A</i>	<i>B</i>	<i>C</i>	<i>D</i>
$E$ [GPa]	211	193.4	202.4	213.9	195.2
$\rho$ [Kg/m <sup>3</sup> ]	7800	8146.3	7223.9	8513.2	8223.7
$K$ [N/m]	0.5e6	194.6 e6	0.16 e6	48.1 e6	196.4 e6

Table 21: Optimum values of the parameters for each updating procedure

	<i>Initial</i>	<i>A</i>	<i>B</i>	<i>C</i>	<i>D</i>
Error in freq. [%]	39.35	3.34	41.93	21.74	3.35
Error in MAC [-]	0.040	0.066	0.041	0.046	0.066
Error in T-Stiffness [°]	159.76	158.85	160.06	121.49	158.85

Table 22: Error values obtained for each updating procedure.

From these tables it can be inferred that the minimum error in natural frequencies is obtained with techniques *A* and *D*, all the techniques provide similar values of MAC, and the T-stiffness is only improved with technique *C*.

## 7 CONCLUSIONS AND FUTURE WORKS

In summary, the following conclusions can be drawn:

- An updating methodology was successfully implemented, consisting of a sensitivity analysis and an automated updating of a FE Abaqus model. The methodology was validated updating a numerical model of a cantilever beam, where the experimental modal parameters estimated by operational modal analysis, were used.
- Different objective functions were implemented and compared, both from the sensitivity analysis point of view and by comparing the results of the updating process. An objective function based on the use of a new correlation parameter, T-Stiffness, was proposed.
- When only mode shapes are considered in the optimization functions, high errors in the natural frequencies were obtained.
- When natural frequencies and MAC were considered in the objective function, small improvements in the MAC values were obtained. Therefore, weighting factors could be used to increase the importance of the MAC in the updating process.
- Future work includes the development of an objective function that combines the T-Stiffness and the natural frequencies.
- The selection of the parameters to be updated and their ranges, along with the chosen objective function, significantly influences the updating results. Therefore, engineering expertise is essential in the updating process.

- A limitation of this methodology lies in its high computational demands. When computational time is critical in the updating process, surrogate modeling emerges as a valuable strategy.

## ACKNOWLEDGEMENTS

This work was supported by the Spanish Ministry of Science and Innovation [MCI-20-PID2019-105593 GB-I00/AEI/10.13039/501100011033 and MCI-21-PRE2020-094923].

## REFERENCES

- [1] S. Ereiz, I. Duvnjak, J. Fernando Jiménez-Alonso, Review of finite element model updating methods for structural applications, *Structures*. 41 (2022) 684–723. doi: 10.1016/j.istruc.2022.05.041.
- [2] B. Barros, B. Conde, M. Cabaleiro, and B. Riveiro, Deterministic and probabilistic-based model updating of aging steel bridges, *Structures*. 54 (2023) 89–105. doi: 10.1016/j.istruc.2023.05.020.
- [3] M. Girardi, C. Padovani, D. Pellegrini, and L. Robol, A finite element model updating method based on global optimization, *Mech. Syst. Signal Process.*, 152 (2021) 107372. doi: 10.1016/j.ymssp.2020.107372.
- [4] Avitabile P, Twenty years of structural dynamic modification - A review., *Sound and Vibration*. (2003).
- [5] F. Sarrazin, T. Wagener, A Matlab toolbox for Global Sensitivity Analysis, *Environmental Modelling & Software*, 70, 80-85, doi: 10.1016/j.envsoft.2015.04.009, 2015.
- [6] D. Arezzo, N. Vanni, S. Carbonari, F. Gara, Optimal sensor placement for the dynamic monitoring of a historical masonry church in central Italy, *Proceedings of 9th IOMAC International Operational Modal Analysis Conference*, 311 – 320, 2022.

## DEVELOPING A MODAL IDENTIFICATION TECHNIQUE TO PERFORM AN EXPERIMENTAL MODAL ANALYSIS BASED ON CNN AND DEEP LEARNING

Álvaro Iglesias-Pordomingo<sup>1\*</sup>, César Peláez-Rodríguez<sup>2</sup>, Guillermo Fernández<sup>1</sup>,  
José María García-Terán<sup>1</sup> and Álvaro Magdaleno<sup>1</sup>

<sup>1</sup>ITAP. Universidad de Valladolid  
Paseo del Cauce 59, 47011 Valladolid, Spain  
e-mail: alvaro.iglesias@uva.es / guillermo.fernandez.ordonez@uva.es  
josemaria.gteran@uva.es / alvaro.magdaleno@uva.es

<sup>2</sup> Department of Signal Processing and Communications. Universidad de Alcalá  
Ctra. Madrid-Barcelona, km 33.600, 28805 Alcalá de Henares  
e-mail: cesar.pelaez@uah.es

**Keywords:** modal identification, deep learning, structure vibration, CNN, EMA

**Abstract.** Vibration problems are usually a source of uncertainty in slender structures such as footbridges, buildings or wind-turbines. When studying the dynamic behavior of these physical systems, there are several approaches for which the final aim is to identify the modal parameters of the structure: natural frequencies, mode shapes and damping ratios. In most cases, an inverse problem should be solved as it is not possible to set out the eigenvalue problem based on physical properties. Experimental approaches are based on the vibration of the structure measurement: forces, displacements and accelerations. One of the most used methods to extract the modal properties throughout synchronized signals is the experimental modal analysis (EMA), in which both excitation and response of the vibratory system are monitored. The frequency domain representation of the resulting transfer function is the frequency response function (FRF). Modal identification techniques, such as peak-peaking and curve fitting, implement optimization algorithms to obtain the modal parameters. Nevertheless, as the structures grow in complexity, the computational effort increases as well.

Nowadays, data-driven techniques and artificial neural networks are increasing their application to civil engineering and dynamics as they offer a different way of solving the differential equations in which modal parameters are involved, as well as approaching non-linear effects in structures. The potential of deep learning relies on a change of paradigm when solving complex cases: a set of labelled data is automatically processed through a neural network model which is trained until its output matches the labelled data. After the model is tested with new data, it is able to give the solution to an input which was not in the training set, according to some accuracy criteria. The restraint of knowing the searched features of the model is overtaken by a “generic” black box where the forward-backpropagation method adjusts the weight values of the corresponding neural architecture, finding itself the relevant features that link the input data with their ground-truth.

Deep learning has been applied to structural issues in the last years. The field of work has been wide due to the versatility of data-driven tools: prediction of vibration signals and ambient conditions, characterization of loads on structures [1], etc. Structural health monitoring is one of the most explored applications [2]: the classification problem is especially adequate for damage detection. Neural networks have also been applied to modelling the dynamic behavior of structures by predicting their response in the time domain, or to carrying out directly a modal identification of the structure. Liu et al. [3] used a neural network to process vibration time series in order to extract modal information from the weight values. However, other studies focus on the FRFs with a data-driven black-box model based on encoder-decoder neural networks [4].

The aim of this study is to approach modal identification from FRFs through deep-learning techniques. The complex values of the FRF in a delimited range of frequency were processed to input the neural network, which should output the modal parameters of a system with a low number of degrees of freedom (DOF). As the dimension of the output vector depends on the number of DOFs, several neural architectures were studied to optimize the identification, so that convolutional neural networks (CNN) were used. CNN is a specific architecture that processes data in a different way to dense neural networks: instead of making data flow through several dense layers, there are some “moving” filters containing the weights that sweep the input vectors reducing the data dimension at each convolutional layer until the output dimension is reached. The network was trained with synthetic labelled data that was generated according to the mode superposition equation for vibratory systems:

$$h_{ik}(\omega) = \sum_{r=1}^n \frac{V_{r,ik}}{-\omega^2 + j2\zeta_r\omega_r\omega + \omega_r^2}$$

where  $\omega$  is the frequency vector,  $n$  is the number of modes and  $V_r$ ,  $\zeta_r$  and  $\omega_r$  were the modal parameters to reach (mode shape amplitude, damping ratio and natural frequency of each mode evaluated on a particular point of the structure, respectively). Finally, an EMA was carried out on a simple building-like structure to evaluate the performance of the tool.

**Acknowledgments:** The authors wish to acknowledge to the AEI, Spanish Government (10.13039/501100011033), and to “ERDF A way of making Europe”, for the partial support through the grant PID2022- 140117NB-I00.

## References:

- [1] C. Peláez-Rodríguez, Á. Magdaleno, S. Salcedo-Sanz, and A. Lorenzana, “Human-induced force reconstruction using a non-linear electrodynamic shaker applying an iterative neural network algorithm,” *Bulletin of the Polish Academy of Sciences Technical Sciences*, pp. 144615–144615, Feb. 2023, doi: 10.24425/bpasts.2023.144615.
- [2] X. W. Ye, T. Jin, and C. B. Yun, “A review on deep learning-based structural health monitoring of civil infrastructures,” *Smart Structures and Systems*, vol. 24, no. 5. Techno-Press, pp. 567–585, Nov. 01, 2019. doi: 10.12989/sss.2019.24.5.567.
- [3] D. Liu, Z. Tang, Y. Bao, and H. Li, “Machine-learning-based methods for output-only structural modal identification,” *Struct Control Health Monit*, vol. 28, no. 12, Dec. 2021, doi: 10.1002/stc.2843.
- [4] Y. Qu, G. W. Vogl, and Z. Wang, “MSEC2021-XXXX A DEEP NEURAL NETWORK MODEL FOR LEARNING RUNTIME FREQUENCY RESPONSE FUNCTION USING SENSOR MEASUREMENTS.”

## APPROACHES FOR DAMAGE DETECTION AND QUANTIFICATION IN BEAMS USING WAVELET ANALYSIS OF INCREMENTAL MODE SHAPES

Mario Solís<sup>1\*</sup>, Qiaoyu Ma<sup>1</sup>, Pedro Galvín<sup>1</sup>

<sup>1</sup>Escuela Técnica Superior de Ingeniería, Universidad de Sevilla  
Camino de los Descubrimientos s/n, 41092, Sevilla, Spain  
e-mail: msolis@us.es, qma1@us.es, pedrogalvin@us.es

**Keywords:** damage detection; beams; wavelet analysis

**Abstract.** *Vibration-based damage detection is a traditional approach for Structural Health Monitoring. It relies on identifying changes in the dynamic response of a structure caused by damage. This paper summarizes techniques utilizing the wavelet transform to detect variations in the mode shapes of a beam due to local damage. Wavelet analysis is applied to the differences between reference and potentially damaged states. To detect and locate damage, wavelet coefficients are normalized, allowing consistent singularity identification across wavelet scales. Additionally, a weighted combination of wavelet coefficients for each identified mode shape is performed, resulting in a single scalogram for damage localization. The weighting coefficients are based on natural frequency variations to emphasize modes most affected by damage. The 'wavelet ridge' concept, based on counting local extreme values in the scalogram across all scales, can also predict damage locations. For damage quantification, a Damage Severity Index (DSI) based on the Lipschitz exponent inequality is used. The DSI is developed using the estimated modal bending moment, making it independent of mode order, location, and boundary conditions. Numerical values are used as reference. Illustration examples based on experimental results are included for both localization and quantification approaches. Artificially induced damage in steel beams serves as benchmark scenarios. Despite robust theoretical results from numerical simulations, the sensitivity of the techniques to damage depends on the accuracy of the modal identification process and the measurement grid density. Nonetheless, experimental results indicate that practical useful results can be obtained with a relatively small number of sensors.*

## 1 INTRODUCTION

Vibration-based Structural Health Monitoring (SHM) is appealing due to its ability to monitor and detect damage through global testing of a structure. It is based on the premise that damage-induced stiffness loss affects the structure's dynamic response, influencing natural frequencies, mode shapes, and damping ratios. Structural damage, defined over a local region, results in a sudden change in the slope of the modal displacement field. Detection, localization, and quantification can be achieved by analyzing abnormalities between the post-damage and reference structural responses. The wavelet transform is a powerful mathematical tool for detecting changes in mode shapes induced by damage. Damage effects result in local peak values of wavelet coefficients [1, 2, 3, 4, 5, 6].

This paper presents two wavelet-based damage detection methods combining modal parameters and wavelet analysis. The first method [1] analyzes and adds the coefficients of the continuous wavelet transform of mode shape differences between reference and damaged states. Natural frequency changes are used to weight the addition of the wavelet coefficients of each mode. The second method [7] introduces a Combined Damage Locating Index (CDLI) and a Damage Severity Index (DSI) [8], based on the Continuous Wavelet Transform (CWT) and Lipschitz exponent of the experimental mode shapes of a damaged beam. Unlike related approaches [9, 10, 11], the proposed DSI is independent of damage location, mode order, and boundary conditions.

## 2 WAVELET ANALYSIS OF INCREMENTAL MODE SHAPES

The Continuous Wavelet Transform (CWT) of a signal is the convolution of a wavelet function and the signal. The wavelet function can be shifted by the translation parameter  $v$  and stretched or shrunk by the scale parameter  $s$  in the CWT. The primary step of the damage identification process involves the continuous wavelet transform of mode shape differences (Eq. 1):

$$Wf_{\phi_{I,j}}(v, s) = \frac{1}{\sqrt{s}} \int_{-\infty}^{+\infty} \phi_{I,j}(x) \psi^* \left( \frac{x-v}{s} \right) dx \quad (1)$$

where  $\phi_{I,j}(x)$  represents the difference between the  $j^{th}$  mode shapes of the reference and damaged states of the beam,  $\psi^*(x)$  is the complex conjugate of the wavelet function, and  $Wf$  denotes the wavelet coefficient at position  $v$  for a specific scale  $s$  of the wavelet function. Asymmetric padding is applied to eliminate the well-known edge effect at both extreme coordinates of the mode shapes. Further insights into wavelet transform definitions and fundamentals are beyond this paper's scope but can be found elsewhere [1, 12].

## 3 DAMAGE LOCALIZATION APPROACHES

### 3.1 Normalized Weighted Addition of Wavelet Coefficients

To create an overall scalogram that includes information from all mode shapes for damage detection, the CWT coefficients of each mode shape are summed (Equation 2). Combining the results from all mode shapes may reduce noise in a specific mode shape while accumulating the damage effect for all mode shapes. To detect singularities more precisely, the absolute values of the wavelet coefficients are combined and analyzed. Additionally, the coefficients for each mode shape are weighted according to changes in their natural frequencies:

$$Wf_{sum}(v, s) = \sum_{j=1}^N |Wf_j(v, s)_{\phi_{I,j}}(v, s)| \cdot \left(1 - \frac{\omega_R^j}{\omega_D^j}\right)^2 \quad (2)$$

where  $\omega_R^j$  and  $\omega_D^j$  represent the natural frequencies of mode shape  $j$  for the reference and damaged states, respectively.

Weighting the mode shape differences by their natural frequency ratios emphasizes the most damage-sensitive mode shapes. Modes exhibiting significant frequency changes are more sensitive to damage, making changes in these mode shapes more significant. Conversely, modes with unchanged natural frequencies are almost disregarded, as they likely introduce noise into the final combined result.

Finally, the weighted addition of CWT coefficients is normalized to unity for each scale:

$$Wf_{sum-norm}(v, s) = \frac{Wf_{sum}(v, s)}{\max[Wf_{sum}(v, s)]_s} \quad (3)$$

Normalized coefficients provide clearer results, enabling the analysis of information across all scales. Due to the wavelet transform's mathematical properties, the induced abnormality in the modal displacement field at the damage location results in a local peak value of wavelet coefficients. Potential damage locations are identified where normalized weighted coefficients exhibit peak values across all scales.

### 3.2 Wavelet Ridge

Considering the previous idea, more precise damage locations can be identified by analyzing the wavelet ridge. This ridge is defined as the line connecting local extreme values across scales. Utilizing this property, a Combined Damage Locating Index (CDLI) is proposed, based on counting the local extreme values of wavelet coefficients at each position:

$$CDLI_p = \sum_{m=1}^M \sum_{l=1}^L \text{Count}_{p,m,l} \quad (4)$$

$$\text{Count}_{p,m,l} = \begin{cases} 1 & \text{if } Wf_{\phi_{I,m}}(x_p, s_l) \text{ is a local maximum or minimum;} \\ 0 & \text{everywhere else.} \end{cases} \quad (5)$$

where  $p = 1, 2, \dots, P$ ,  $m = 1, 2, \dots, M$ , and  $l = 1, 2, \dots, L$ , with  $P$  representing the number of measurement points,  $M$  the number of identified modes, and  $L$  the number of scales used in the wavelet transform. In theory, damage is located at points where the absolute value of DLI equals  $R$ .

## 4 DAMAGE QUANTIFICATION APPROACH

For severity quantification, another wavelet transform property at identified discontinuity locations is used. At each location  $(x_0)$ , the wavelet coefficients for each mode  $j$  satisfy:

$$|Wf_{\phi_{I,j}}(x_p, s)| \leq As^{\alpha+1/2}, \quad \text{where } p = 1, 2, \dots, P \quad (6)$$

where  $A$  is a constant, and  $\alpha$  is the Lipschitz exponent of the signal at  $x_p$ . Constant  $A$  relates to the discontinuity magnitude, and  $\alpha$  relates to the discontinuity order [8, 10, 11, 13]. Dividing



both sides of Eq. (6) by the modal bending moment at the damage location in the damaged state ( $m_{D,j}(x_p)$ ) and taking logarithms yields:

$$\log_2(W f'_{\phi_{I,j}}(x_p, s)) \leq A' + (\alpha + 1/2) \log_2 s \quad (7)$$

$$W f'_{\phi_{I,j}}(x_p, s) = \left| \frac{W f_j(x_p, s)}{m_{D,j}(x_p)} \right| \quad \text{and} \quad A' = \log_2 \left( \frac{A}{|m_{D,j}(x_p)|} \right) \quad (8)$$

$W f'_{\phi_{I,j}}(x_p, s)$  are the normalized wavelet coefficients at  $x_p$ , and  $A'$  is the Damage Severity Index (DSI) for location  $x_p$  of mode  $j$ . It can be demonstrated [7, 14, 15] that the difference between the  $j^{th}$  mode shapes of the reference and damaged states of the beams ( $\phi_{I,j}(x)$ ) corresponds to the operational deflection shape obtained when the beam is subjected to a pair of self-equilibrated harmonic bending moments acting at the damage location, of an amplitude equal to the modal bending moment at that location in the Reference state and with a frequency equal to the  $j$ th natural frequency. The resulting operational deflection ( $\phi_{I,j}(x)$ ) equals the mode shape difference ( $\phi_{I,j}(x)$ ), and the resulting internal bending moment at the damage location equals the modal bending moment at that location in the Damaged state ( $m_{D,j}(x_p)$ ).

Thus, if damage is considered a local physical discontinuity (traditionally represented by a lumped spring model), the local singularity in the beam's response is defined solely by the damage severity and the bending moment at the damaged section. Based on this assumption, the discontinuity at  $x_p$  is proportional to the modal bending moment  $m_{D,j}(x_p)$ . Thus, the proposed normalization procedure with  $m_{D,j}(x_p)$  makes the DSI dependent only on the damage severity, independent of the damage location.

The DSI can be obtained for all available measurement points along the beam. The damage severity can then be estimated at each point by comparing the DSI value with reference values obtained from a numerical model of the beam.

## 5 EXPERIMENTAL RESULTS

### 5.1 Experimental Tests

The experimental program involved dynamic characterization of specimens by modal analysis. An impact force was applied using an instrumented impact hammer, and the response was measured by piezoelectric accelerometers with nominal sensitivity of 100 mV/g.

#### 5.1.1 Experimental Modal Analysis of I-beams with Progressive Single Damage

Standard steel I-beams were tested to apply the proposed methodology. The beams, with length  $L = 1280$  mm, height  $h = 100$  mm, width  $b = 50$  mm, web thickness  $h_w = 4.5$  mm, flange thickness  $h_f = 6.8$  mm, and mass per unit length  $m = 8.1$  kg/m, were damaged by saw cuts in the scenarios described in Table 1 and Figures 1.(a-b). Two damage severities and two different locations were considered. The beams were hung on two soft springs approximating a free-free boundary condition (Figure 1 (c)). The modal response was determined at 65 measurement points distributed uniformly along the beam.

Table 2 presents the first three natural frequencies identified for each damage scenario.

For the damage identification process, the mode shapes are smoothed through a quadratic regression process to mitigate the effect of noisy modal amplitudes (see [1] for details).

Table 1: Damage scenarios.

Scenario	Cutting Location	Cut Depth
0.5-30	0.5 L	30 mm
0.5-20	0.5 L	20 mm
0.25-30	0.25 L	30 mm
0.25-20	0.25 L	20 mm

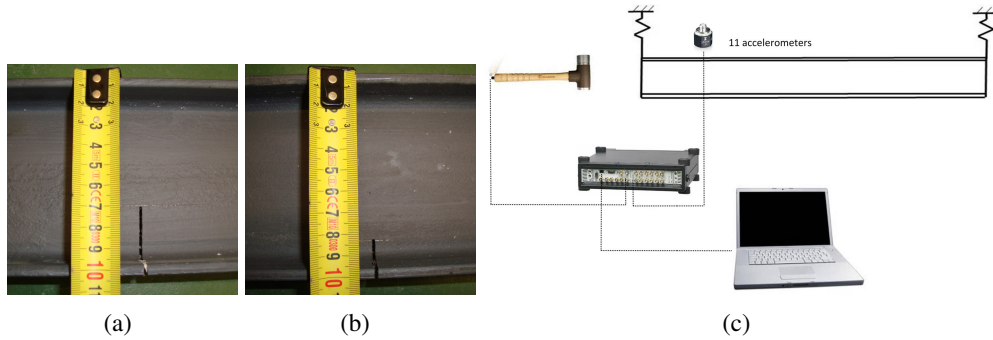


Figure 1: (a) 30mm and (b) 20mm depth induced saw cut damage for the steel I-beams. (c) Experimental set-up

Table 2: Experimental natural frequencies [Hz] for each damage scenario.

Mode\Scenario	Reference	0.5-30	0.5-20	0.25-30	0.25-20
1	415.65	300.96	362.28	364.75	397.27
2 1032.7	1027.35	1030.15	949.64	822.99	932.71
3	1786.75	1473.96	1634.17	1557.21	1663.19

### 5.1.2 Experimental Modal Analysis of Rectangular Cross-Section Beams with Progressive Multiple Damage

A steel beam with a rectangular cross-section (length 700 mm, width 80 mm, and height 20 mm) was tested. 35 measurement points were considered, and two artificial notches were introduced as damage at locations 170 mm and 470 mm (Figure 2). Two damage scenarios (S1 and S2) included notches of depth 25% and 50% of the beam height at those two locations.

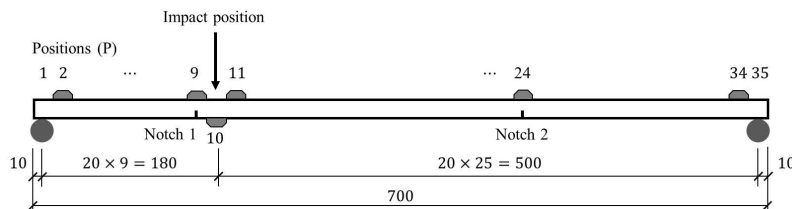


Figure 2: Configuration of the positions on the test beam (unit: mm).

A procedure based on noise evaluation through a normalized standard deviation index related

to a spline fit of each mode shape was applied for selecting the most suitable mode shapes. As a result, modes 2 and 3 were selected for the damage identification process. Details can be found in [7].

## 5.2 Damage Localization Results

Figure 3 shows the normalized weighted addition of wavelet coefficients for the damage scenarios 1-4 defined for the experimental tests from Section 5.1.1. It illustrates how localized unity values of wavelet coefficients are obtained at the damage locations.

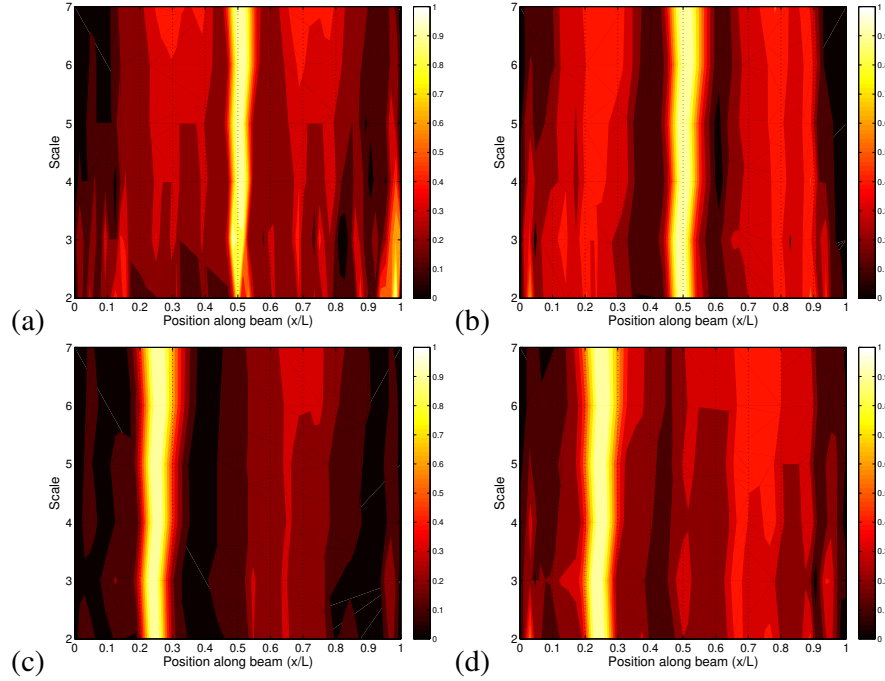


Figure 3: Normalized weighted addition of wavelet coefficients of tested I-beams for damage scenarios 1 to 4 (figures (a)-(d) respectively).

Applying the proposed CDLI to the damage scenarios S1 and S2 of the rectangular cross-section beam provides the results presented in Figure 4. Due to the oscillatory nature of the wavelet function, wavelet extreme values may appear at adjacent locations for different scales and modes. Thus, the theoretical absolute value of the CDLI at a damage location is either 3 (the maximum number of scales considered) with no CDLI of the same sign at its adjacent locations, or 2 with one of the two adjacent points having a CDLI of value 1 of the same sign [7]. Therefore, potential damage is determined at locations with a  $CDLI_i$  equal to 5 or at adjacent locations with both CDLI values equaling 3. Consequently, Figure 4 indicates that the predicted damage locations are 170 mm, 470 mm, and 550 mm for scenario S1, and 170 mm and 470 mm for S2.

## 5.3 Damage Quantification Results

Figure 5 shows the reference values of the DSI for the tested rectangular cross-section beam under three different boundary conditions obtained from a finite element model. The corresponding DSI for the tested beam at identified potentially damaged locations is obtained from

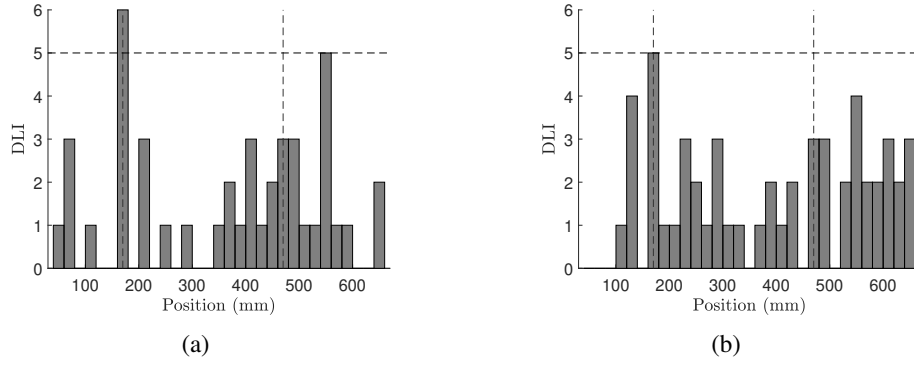


Figure 4: The Combined Damage Locating Index (CDLI) of scenarios (a) S1 and (b) S2.

Eq. 8 for each mode. The required value of the modal bending moment is obtained from a curve fitting process of the modal curvature along the beam to avoid the effect of noisy peaks in the second derivative of the mode shapes. The estimated crack depths are obtained by comparing the experimental DSI values with the reference DSI values from the reference map. Since the actual structure's boundary conditions are none of the three perfect types applied in the numerical models, and the measurement sparsity may affect the DSI definition, it is recommended to use DSI Reference Maps of different boundary types for severity assessment. The estimated notch depths using the DSI Reference Maps from Figure 5 are shown in Figure 6. In S1, both damages are underestimated from Mode 2, and D1 is overestimated while D2 is underestimated from Mode 3. The absolute error for estimating D1 ranges from  $-1.5$  mm to  $1.5$  mm, and for D2, it ranges from  $-1.2$  mm to  $-0.8$  mm. In S2, both Mode 2 and Mode 3 underestimate both damages. The prediction error for D1 ranges from  $-2$  mm to  $-0.5$  mm, and for D2, it ranges from  $-3.0$  mm to  $-0.5$  mm.

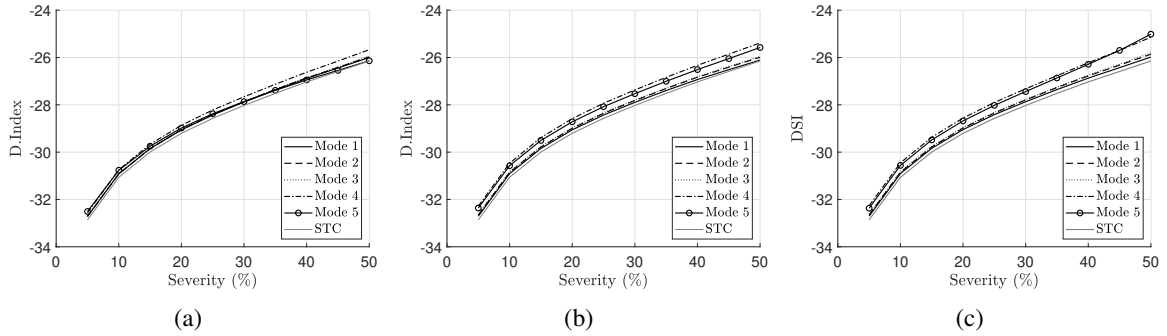


Figure 5: The DSI reference maps for different boundary conditions (Set-20): (a) simply-supported, (b) fixed-fixed, (c) free-free.

Experimental results demonstrate that the proposed method successfully identifies double-damage locations and estimates severity with a certain accuracy level. The experimental case study illustrates the practical limits of the proposed methodology.

## 6 CONCLUSIONS

This paper summarizes the application of different wavelet transform-based approaches for damage identification in beams. The wavelet transform is proven to be a powerful mathematical tool for identifying damage-induced singularities. The presented results show that damage can

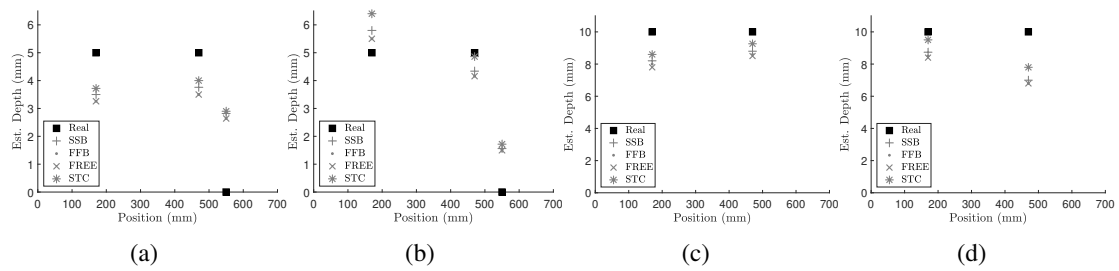


Figure 6: The estimated damage depth from Reference Maps of simply-supported (SSB), fixed-fixed (FFB), free-free (FREE) modal analysis and static (STC) analysis: (a) S1 Mode 2; (b) S1 Mode 3; (c) S2 Mode 2; (d) S2 Mode 3.

be successfully localized and quantified in practical applications. The accuracy of the identification results is influenced by the quality of the experimental data. Identifying more modes and obtaining less noisy (smooth) mode shapes lead to more accurate results. The number of measurement points also affects the quality of the damage identification process. Higher spatial resolution can reduce deviations from the estimated damage identification process and the actual values.

## ACKNOWLEDGMENTS

The authors acknowledge the financial support provided by the Spanish Ministry of Science and Innovation and Universities (research project PID2022-138674OB-C21) and the Regional Ministry of Economic Transformation, Industry, Knowledge, and Universities of Andalusia (research project PROYEXCEL\_00659).

## REFERENCES

- [1] M. Solís, M. Algaba, P. Galvín, Continuous wavelet analysis of mode shapes differences for damage detection, *Mechanical Systems and Signal Processing* 40 (2) (2013) 645–666. doi:10.1016/j.ymssp.2013.06.006.
- [2] M. S. Cao, W. Xu, W. X. Ren, W. Ostachowicz, G. G. Sha, L. X. Pan, A concept of complex-wavelet modal curvature for detecting multiple cracks in beams under noisy conditions, *Mechanical Systems and Signal Processing* 76-77 (2016) 555–575. doi:10.1016/j.ymssp.2016.01.012.
- [3] R. Janeliukstis, S. Rucevskis, M. Wesolowski, A. Chate, Experimental structural damage localization in beam structure using spatial continuous wavelet transform and mode shape curvature methods, *Measurement: Journal of the International Measurement Confederation* 102 (2017) 253–270. doi:10.1016/j.measurement.2017.02.005. URL <http://dx.doi.org/10.1016/j.measurement.2017.02.005>
- [4] V. Shahsavari, L. Chouinard, J. Bastien, Wavelet-based analysis of mode shapes for statistical detection and localization of damage in beams using likelihood ratio test, *Engineering Structures* 132 (2017) 494–507. doi:10.1016/j.engstruct.2016.11.056. URL <http://dx.doi.org/10.1016/j.engstruct.2016.11.056>
- [5] A. Ghanbari Mardasi, N. Wu, C. Wu, Experimental study on the crack detection with optimized spatial wavelet analysis and windowing, *Mechanical Systems and Signal Pro-*

- cessing 104 (2018) 619–630. doi:10.1016/j.ymssp.2017.11.039.  
URL <https://doi.org/10.1016/j.ymssp.2017.11.039>
- [6] A. Deng, M. Cao, Q. Lu, W. Xu, Identification of multiple cracks in composite laminated beams using perturbation to dynamic equilibrium, *Sensors* 21 (18) (2021). doi:10.3390/s21186171.
- [7] Q. Ma, M. Solís, J. D. Rodríguez-Mariscal, P. Galvín, Wavelet and lipschitz exponent based damage identification method for beams using mode shapes, *Measurement* 205 (2022) 112201. doi:<https://doi.org/10.1016/j.measurement.2022.112201>.  
URL <https://www.sciencedirect.com/science/article/pii/S0263224122013975>
- [8] Q. Ma, M. Solís, P. Galvín, Wavelet analysis of static deflections for multiple damage identification in beams, *Mechanical Systems and Signal Processing* 147 (2021) 107103. doi:10.1016/j.ymssp.2020.107103.  
URL <https://doi.org/10.1016/j.ymssp.2020.107103>
- [9] L. F. Zhu, L. L. Ke, X. Q. Zhu, Y. Xiang, Y. S. Wang, Crack identification of functionally graded beams using continuous wavelet transform, *Composite Structures* 210 (November 2018) (2019) 473–485. doi:10.1016/j.compstruct.2018.11.042.  
URL <https://doi.org/10.1016/j.compstruct.2018.11.042>
- [10] E. Douka, S. Loutridis, A. Trochidis, Crack identification in beams using wavelet analysis, *International Journal of Solids and Structures* 40 (13-14) (2003) 3557–3569. doi:10.1016/S0020-7683(03)00147-1.
- [11] S. Loutridis, E. Douka, A. Trochidis, Crack identification in double-cracked beams using wavelet analysis, *Journal of Sound and Vibration* 277 (4-5) (2004) 1025–1039. doi:10.1016/j.jsv.2003.09.035.
- [12] G. Strang, N. Truong, *Wavelets and Filter Banks*, Wellesley College Press, Cambridge, 1996.
- [13] J. C. Hong, Y. Y. Kim, H. C. Lee, Y. W. Lee, Damage detection using the Lipschitz exponent estimated by the wavelet transform: Applications to vibration modes of a beam, *International Journal of Solids and Structures* 39 (7) (2002) 1803–1816. doi:10.1016/S0020-7683(01)00279-7.
- [14] Q. Ma, M. Solís, Damage localization and quantification in beams from slope discontinuities in static deflections, *Smart structures and systems* 22 (3) (2018) 291–302.
- [15] Multiple damage identification in beams from full-field digital photogrammetry, *Journal of Engineering Mechanics* 145 (8) (2019) 1–12. doi:10.1061/(ASCE)EM.1943-7889.0001629.

## FATIGUE DAMAGE ON A FLOATING BREAKWATER – A CASE STUDY

Cebada-Relea, Alejandro<sup>1\*</sup>, López Gallego, Mario<sup>1</sup>, and Aenlle López, Manuel<sup>1</sup>

<sup>1</sup> DyMAST research group and Department of Construction and Manufacturing Engineering,  
Univertisty of Oviedo, Polytechnic School of Mieres, 33600 Mieres-Asturias, Spain

\*cebadaalejandro@uniovi.es

**Keywords:** Marine structure; floating pontoon, numerical modelling, spectral fatigue damage.

**Abstract.** *The fatigue life of a structure is a topic of great interest within the engineering community. Specifically, this matter becomes even more critical when it comes to floating structures placed in the sea, where the climatic conditions they must withstand are more adverse and their maintenance is more complex. Modular floating breakwaters are commonly deployed in ports and coastal areas with mild wave conditions to shelter vessels from waves. Although they generally perform satisfactorily, frequent structural failures have been reported. Commonly, these failures are related to their weakest elements: the connections between modules.*

*This study is focused on analyzing the fatigue damage endured by connections on a generic floating breakwater of the pontoon subtype. Initially, the dynamic wave-structure interaction was numerically modeled using the code ANSYS Aqwa under different white noise wave spectra and heading directions. Subsequently, the stress power spectral density on each connection was obtained from the corresponding stress time history. Combining the incident wave spectra with the resulting stress spectrum, a characteristic stress transfer function was obtained for each wave heading direction and connection.*

*Finally, the local wave conditions of the Ria of Vigo were used asses the fatigue life of the structure. The local time histories of heights, periods and directions were used to define both swell and sea wave conditions. The wave spectrum for each sea state was then obtained by applying a predefined parametric wave spectral model. Once obtained the spectra for each sea state, the transfer functions were applied to obtain the corresponding stress spectra at the different connections in the array. Finally, the Wirsching-Light spectral model was applied to estimate the fatigue damage on each connection for the different sea states, which allowed predicting the fatigue life of the structure.*

*In sum, a complete methodology to address the fatigue life of, not only of floating structures, but also other floating marine structures, is applied and demonstrated through a case study. The results reveal that the wave heading directions is paramount to the fatigue damage on the connections of floating breakwaters. Therefore, the alignment of a floating breakwater to the dominant wave directions should be carefully analyzed for a precise fatigue assessment.*

## THE CONCEPT OF ROTMAC IN STRUCTURAL DYNAMICS

N. García-Fernández<sup>1</sup>, F. Pelayo<sup>2</sup>, M. Aenlle<sup>2\*</sup>

<sup>1</sup> Dept. Construction and Manufacturing Engineering  
Campus de Gijón. s/n. Universidad de Oviedo, Gijón. 33203  
e-mail: [garciafnatalia@uniovi.es](mailto:garciafnatalia@uniovi.es)

<sup>2</sup> Dept. Construction and Manufacturing Engineering  
Campus de Gijón. s/n. Universidad de Oviedo, Gijón. 33203  
{ F. Pelayo } e-mail: [fernandezpelayo@uniovi.es](mailto:fernandezpelayo@uniovi.es)  
{ M. Aenlle } e-mail: [aenlle@uniovi.es](mailto:aenlle@uniovi.es)

**Keywords:** structural dynamic modification, polar decomposition, QR decomposition, rotation of mode shapes, scaling, shear.

**Abstract.** *In model correlation and model updating methods, the experimental model is typically considered a dynamic modification of a numerical model. The eigenvalue problem derived from the structural dynamic modification theory provides the natural frequencies of the perturbed system and a transformation matrix  $T$ , which relates the modal matrices of both systems. The eigenvectors of the perturbed system can be expressed as a linear combination of the eigenvectors of the unmodified system. The Modal Assurance Criterion (MAC) is the most widely used technique to compare two sets of eigenvectors. In this paper, a novel and physically meaningful version of the modal assurance criterion, known as rotated MAC or ROTMAC, is used to correlate the mode shapes of two systems. With this new definition, the mode shapes of the numerical model must be rotated, and then correlated with the mode shapes of the experimental model. Moreover, the ROTMAC is combined with the inner product  $T^T T$  to detect differences in terms of mass between two models.*

### 1 INTRODUCTION

Structural dynamic modification (SDM) is a technique to study the effects of structural modifications (material, supports, geometry, etc.) on the dynamic behavior of a structural system [1,2,3]. According to SDM, when a model A can be considered a dynamic modification of a model B, the eigenvectors of model A can be expressed as a linear combination of the eigenvectors of the model B through a transformation matrix (in this paper denoted as matrix  $T$ ) [1,2,3].



The normalized relative frequency difference (NRFD) [4] and the Modal Assurance Criterion (MAC) [4,5] are the most widely used techniques to compare the eigenvalues and eigenvectors, respectively, of two models. However, the modal assurance criterion (MAC) is not a good technique to compare eigenvectors of two systems with repeated or closely-spaced modes, and low MAC values can be obtained although a good correlation in terms of mass and stiffness exist between both models.

In [6,7], it was demonstrated that matrix  $\mathbf{T}$  is a pure rotation matrix when there are only stiffness discrepancies (no differences in stiffness) between models A and B. The rotation can affect to the full set of modes or be restricted to a local subspace. This rotation is small for systems with well separated modes and it increases as decreasing the separation between modes.

In the case of a mass discrepancies, matrix  $\mathbf{T}$  can be decomposed into three effects: rotation of mode shapes, changes in scaling, and shear (change of the relative angle between mode shapes). There are various techniques available for the matrix factorization and in this paper the QR decomposition is used to decompose the transformation matrix  $\mathbf{T}$  [8,9,10,11].

In [7], a new version of the modal assurance criteria (MAC), denoted rotated MAC or ROTMAC, was proposed to correlate the mode shapes of two models. The rotated MAC or ROTMAC correlates the mode shapes of two systems A and B. With this new technique, the mode shapes of model B must be previously rotated, and then correlated with the mode shapes of system A.

## 2 STRUCTURAL DYNAMIC MODIFICATION

In the case of no damping, the equation of motion of a structure subjected to a force  $\mathbf{p}$  is given by [12,13]:

$$\mathbf{M}_B \cdot \ddot{\mathbf{u}} + \mathbf{K}_B \cdot \mathbf{u} = \mathbf{p} \quad (1)$$

where  $\mathbf{K}_B$  and  $\mathbf{M}_B$  are the stiffness and the mass matrices, respectively. The homogeneous differential equation derived from Eq. (1) provides the following eigenvalue equation [12,13]:

$$(\mathbf{K}_B - \omega_{bi}^2 \mathbf{M}_B) \cdot \mathbf{b}_i = 0 \quad (2)$$

where  $\omega_{bi}^2$  and  $\mathbf{b}_i$  are the i-th eigenvalue and eigenvector, respectively. This eigenvalue problem is known in numerical mathematics as generalized eigenvalue problem.

If a dynamic modification given by the mass change  $\Delta \mathbf{M}$  and stiffness change  $\Delta \mathbf{K}$  matrices, is applied to system B, the following eigenvalue equation for the i-th mode of the perturbed system is derived [1,2,3]:

$$(\mathbf{M}_B + \Delta \mathbf{M}) \cdot \mathbf{a}_i \cdot \omega_{ai}^2 = (\mathbf{K}_B + \Delta \mathbf{K}) \cdot \mathbf{a}_i \quad (3)$$

where  $\omega_{ai}$  and  $\mathbf{a}_i$  are the natural frequency and the eigenvector, respectively, of the i-th mode.

The modal shape matrix  $\mathbf{A}$  (containing the mode shapes  $\mathbf{a}_i$  as column vectors) of the perturbed structure can be expressed as a linear combination of the modal shape matrix of system B as:

$$\mathbf{A} = \mathbf{B} \cdot \mathbf{T} \quad (4)$$

where  $\mathbf{T}$  is a transformation matrix and  $\mathbf{B}$  is the modal shape matrix of system B.

If system B is only perturbed with a stiffness change given by the matrix  $\Delta\mathbf{K}$ , matrix  $\mathbf{T}$  must be a rotation matrix (if both matrices  $\mathbf{B}$  and  $\mathbf{A}$  are mass normalized), i.e:

$$\mathbf{T}_K = \mathbf{R} \quad (5)$$

Where  $\mathbf{T}_K$  is the matrix  $\mathbf{T}$  when the system is only perturbed with a stiffness change, and:

$$\mathbf{T}_K^T \mathbf{T}_K = \mathbf{I} \quad (6)$$

On the other hand, if there are no discrepancies in terms of stiffness between systems A and B, Eq. (3) results in:

$$\omega_A^2 = \mathbf{T}_M^T \omega_B^2 \mathbf{T}_M \quad (7)$$

where  $\omega_A^2$  is a diagonal matrix containing the natural frequencies (squared) of system A and  $\mathbf{T}_M$  is the matrix  $\mathbf{T}$  when the system is only perturbed with a mass change.

From Eq. (10) it is inferred that the inner product  $\mathbf{T}_M^T \mathbf{T}_M$  is given by:

$$\mathbf{T}_M^T \mathbf{T}_M = \mathbf{I} - \mathbf{A}^T \Delta \mathbf{M} \mathbf{A} \quad (8)$$

which demonstrates that  $\mathbf{T}_M$  cannot be a pure rotation, but it approximates a rotation matrix for small mass changes, the changes in scaling and shear being negligible. In the case of repeated modes [7], the inner product  $\mathbf{T}_M^T \mathbf{T}_M$  must be a diagonal matrix, and the effect of a mass change is mainly a rotation of the mode shapes and a change in scaling.

The transformation matrix  $\mathbf{T}_M$  can be factorized using the QR decomposition [8,9,10,11] as:

$$\mathbf{T}_M = \mathbf{R}_M \mathbf{T}_{ch} \quad (9)$$

Where  $\mathbf{R}_M$  is a rotation matrix and  $\mathbf{T}_{ch}$  is an upper triangular matrix which contains the changes in scaling and shear, i.e. the inner product  $\mathbf{T}_M^T \mathbf{T}_M$  is given by:

$$\mathbf{T}_M^T \mathbf{T}_M = \mathbf{T}_{ch}^T \mathbf{T}_{ch} \quad (10)$$

In the case of simultaneous stiffness and mass changes, matrix  $\mathbf{T}$  can be expressed as:

$$\mathbf{T} = \mathbf{R} \mathbf{T}_{ch} \quad (11)$$

Where matrix  $\mathbf{R}$  contains the rotation due to the stiffness change and due to the mass change. The inner product  $\mathbf{T}^T \mathbf{T}$  is also given by:

$$\mathbf{T}^T \mathbf{T} = \mathbf{T}_{ch}^T \mathbf{T}_{ch} \quad (12)$$

All these properties have been summarized in Table 1.

MODES	STIFFNES CHANGE	MASS CHANGE
	<i><b>T is a pure rotation matrix</b></i>	<i><b>T is not a pure rotation matrix</b></i>
REPEATED	<ul style="list-style-type: none"> <li>• Large rotations</li> <li>• No changes in scaling</li> <li>• No shear</li> </ul>	<ul style="list-style-type: none"> <li>• Large rotations</li> <li>• Changes in scaling</li> <li>• No shear</li> </ul>
CLOSELY SPACED	<ul style="list-style-type: none"> <li>• Transition from large to small rotations</li> <li>• No changes in scaling</li> <li>• No shear</li> </ul>	<ul style="list-style-type: none"> <li>• Transition from large to small rotations</li> <li>• Changes in scaling</li> <li>• Shear</li> </ul>
WELL SEPARATED	<ul style="list-style-type: none"> <li>• Small rotations</li> <li>• No changes in scaling</li> <li>• No shear</li> </ul>	<ul style="list-style-type: none"> <li>• Small rotations</li> <li>• Changes in scaling</li> <li>• Shear</li> </ul>

Table 1: Effects of mass and stiffness changes in the case of repeated, closely-spaced and separated modes.

### 3 THE CONCEPT OF ROTMAC

From the previous section it can be inferred that a rotation is always involved when an undamped system is perturbed with a mass or a stiffness change. The rotation is small for systems with well separated modes and large for repeated or closely-spaced modes. This rotation explains why low MAC (Modal Assurance Criterion) values are obtained with systems which present repeated or closely-spaced modes.

A novel version of Modal Assurance Criterion, denoted ROTMAC or rotated MAC, was proposed in [5], where the classical expression of MAC:

$$MAC(\mathbf{b}_i, \mathbf{a}_j) = \frac{|\mathbf{b}_i^T \mathbf{a}_j|^2}{(\mathbf{b}_i^T \mathbf{b}_i)(\mathbf{a}_j^T \mathbf{a}_j)} \quad (13)$$

is calculated using the rotated the mode shapes of system B, i.e:

$$ROTMAC(\mathbf{b}_{Ri}, \mathbf{a}_j) = \frac{|\mathbf{b}_{Ri}^T \mathbf{a}_j|^2}{(\mathbf{b}_{Ri}^T \mathbf{b}_{Ri})(\mathbf{a}_j^T \mathbf{a}_j)} \quad (14)$$

In eq (14)  $\mathbf{b}_{Ri}$  is a column vector of matrix  $\mathbf{B}_R$ , obtained rotating the matrix  $\mathbf{B}$  as:

$$\mathbf{B}_R = \mathbf{B}\mathbf{R} \quad (15)$$

The rotation matrix  $\mathbf{R}$  can be obtained factorizing matrix  $\mathbf{T}$  into a product of two matrices, using the QR factorization [7].

When using eq. (14) the effect of the rotation is removed, because the mode shapes of system  $\mathbf{B}$  were previously rotated using eq. (15). On the other hand, MAC is calculated with mode shapes normalized to the unit length, so the ROTMAC cannot provide information of changes in scaling.

Thus, the ROTMAC can only detect the effect of shear in the mode shapes, and this shear only exists if there are mass discrepancies between systems B and A. However, the ROTMAC can be used in combination with the inner product  $\mathbf{T}^T \mathbf{T}$  to know if there are changes in scaling.

If mass normalized mode shapes are used, the ROTMAC must be an identity matrix in the following cases:

- The system A is a stiffness perturbation of system B. In this case, the rotated mode shapes  $\mathbf{B}_R$  coincide with mode shapes  $\mathbf{A}$ .
- The system has repeated modes. This is because there is not shear effect if the modes are repeated. Moreover, the ROTMAC will be very close to unity for closely spaced modes.

#### 4 EXAMPLE OF APPLICATION. A 3D SYMMETRIC BEAM STRUCTURE

A 3D beam structure composed of a steel vertical column with height  $H = 1500$  mm and four horizontal steel beams with a length  $L = 500$  mm (Fig. 1), both with a square hollow section  $50 \times 4$  mm, was assembled in ABAQUS [14]. The structure was meshed with S4R shell elements and the following material properties were considered for the steel:  $E = 211$  GPa,  $\nu = 0.3$ ,  $\rho = 7800$  Kg/m<sup>3</sup>.

This structure was modified adding a lumped mass of 0.463 kg, at the location indicated in Fig 1c.

The first 10 natural frequencies of both unperturbed and perturbed systems are shown in Table 2, and the corresponding mode shapes in Fig. 2. It can be observed in Table 2, that there are 3 sets of repeated modes.

Mode	Natural frequencies [Hz]	
	Unperturbed	Perturbed (with added mass)
1	10.30	10.10
2	10.30	10.14
3	24.13	22.97
4	70.39	65.02
5	70.39	70.39
6	81.21	77.19
7	173.74	157.57
8	173.93	172.29
9	173.93	173.83
10	184.66	181.31

Table 2: Natural frequencies of the unperturbed and perturbed structures.

When the frequency shift  $\left(\frac{\Delta\omega}{\omega}\right)$  between two modes is larger than  $10^{-1}$  [6], it can be considered that the modes are well separated. If  $\frac{\Delta\omega}{\omega} = 0$  the modes are repeated and when the frequency shift is in the range  $0 < \frac{\Delta\omega}{\omega} < 10^{-1}$ , the modes are closely-spaced. Based on these frequency ranges, the classification shown in Table 3 can be established.

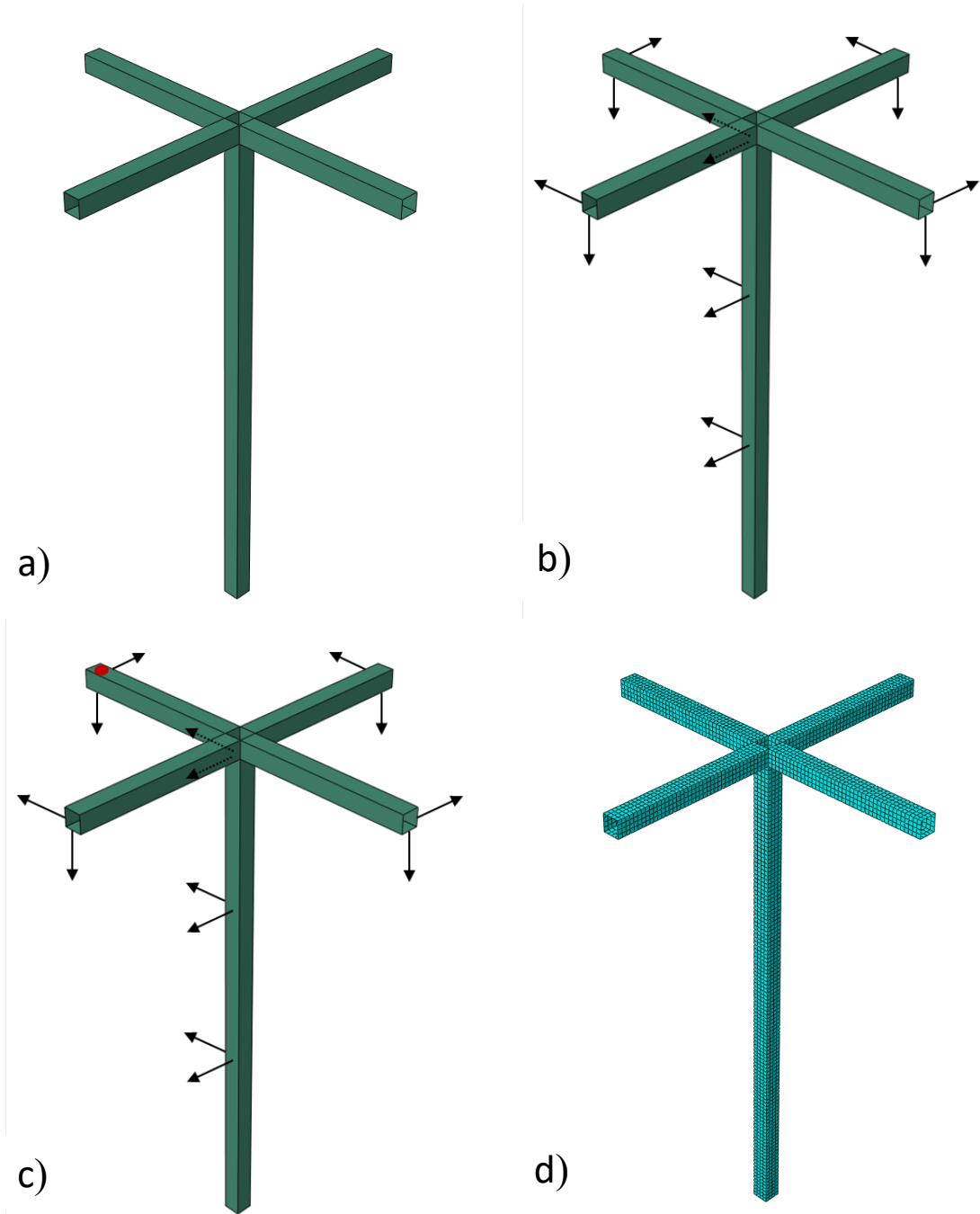


Figure 1: a) Numerical model of the steel beam structure. b) DOF's considered to estimate matrix T. c) Location of the attached mass. d) Mesh of the structure.

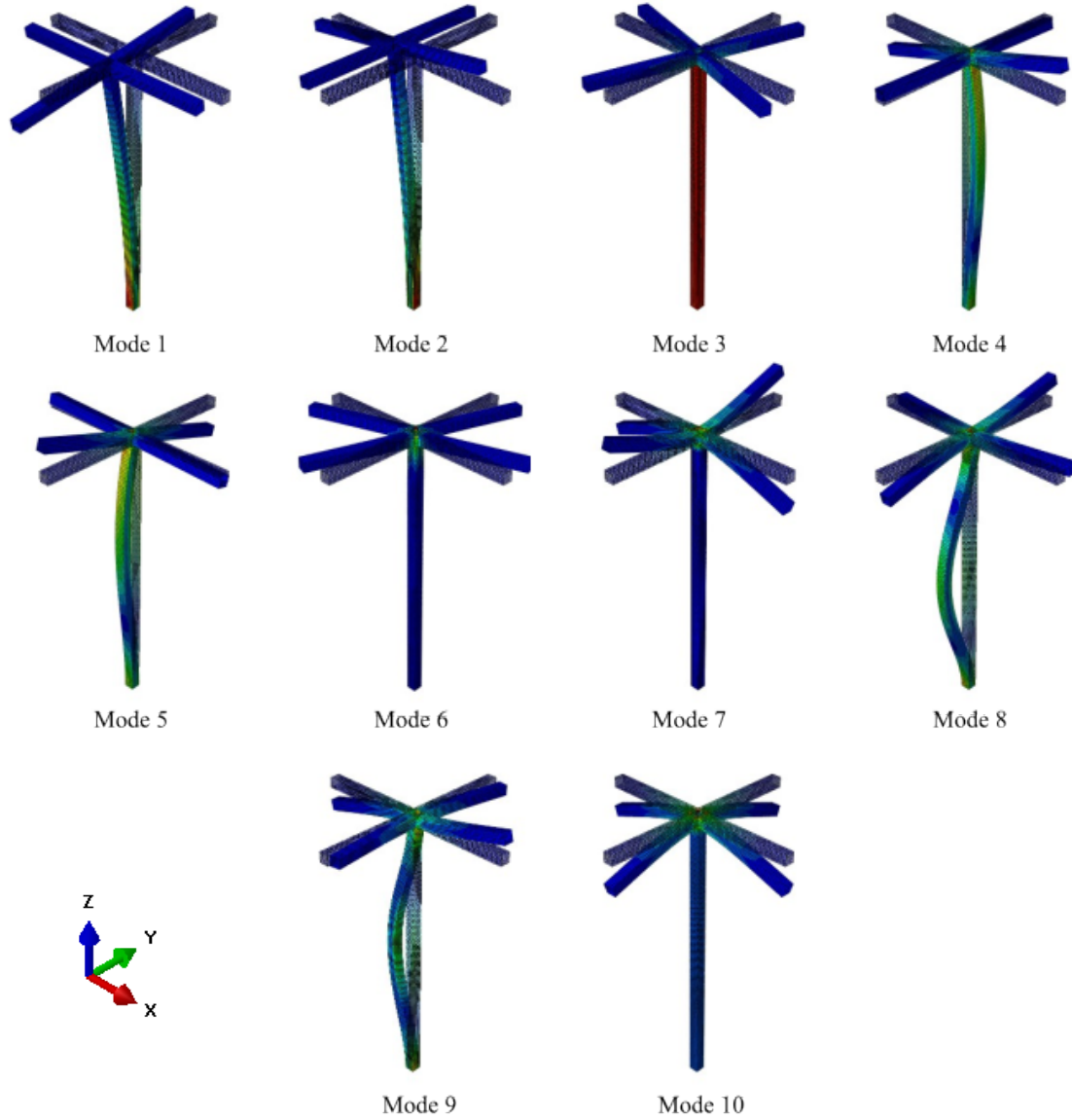


Figure 2: Mode shapes of the unperturbed structure.

Fourteen degrees freedom (indicated in Fig. 1b) and 11 modes were considered to estimate the matrix  $\hat{T}$  by:

$$\hat{T} = B^+ A \quad (4)$$

Where superindex ‘+’ indicates pseudoinverse. Matrix  $\hat{T}$  is shown in Table 4, where mass normalized mode shapes have been used. Due to the effect of truncation, the last columns of matrix  $\hat{T}$  are always estimated with less accuracy, and a matrix  $10 \times 10$  is shown in Table 4.

The inner product  $\hat{T}^T \hat{T}$  is shown in Table 5.  $\hat{T}^T \hat{T}$  is different than an identity matrix, which indicates that there are mass discrepancies between both models. This matrix confirms that there is a significant change in scaling in modes 3, 4, 6 and 7 (diagonal values quite below unity).

Mode	Natural frequencies [Hz]	Classification	Mode	Natural frequencies [Hz]	Classification
1	10.30	Repeated	2	10.30	Well separated
2	10.30		3	24.13	
3	24.13	Well separated	4	70.39	Repeated
4	70.39		5	70.39	
5	70.39	Well separated	6	81.21	Well separated
6	81.21		7	173.74	
7	173.74	Closely spaced	8	173.93	Repeated
8	173.93		9	173.93	
9	173.93	Closely spaced			
10	184.66				

Table 3: Classification of the modes.

0.976	-0.092	-0.006	0.037	0.000	0.004	0.033	0.000	-0.004	0.009
-0.091	-0.980	-0.065	-0.004	0.001	0.030	-0.008	0.063	0.001	-0.002
0.000	-0.013	0.951	0.000	0.004	0.105	-0.003	-0.042	0.000	-0.001
0.000	0.000	0.000	0.092	-0.995	0.013	-0.020	-0.003	0.000	-0.004
-0.001	0.000	0.000	0.916	0.100	-0.001	-0.200	0.000	-0.001	-0.042
0.000	-0.001	0.009	0.000	-0.010	-0.949	-0.002	-0.057	0.000	-0.001
0.000	0.000	0.000	0.023	0.000	0.000	0.688	0.000	-0.517	-0.408
0.000	0.000	0.000	-0.014	0.000	0.002	-0.409	-0.136	-0.848	0.248
0.000	0.000	-0.001	0.002	0.000	0.017	0.058	-1.004	0.116	-0.034
0.000	0.000	0.000	-0.020	0.000	0.000	-0.390	0.000	-0.004	-0.873

Table 4:  $\hat{\mathbf{T}}$  matrix.

0.961	-0.001	0.000	0.036	0.000	0.001	0.033	-0.006	-0.004	0.009
-0.001	0.969	0.052	0.001	-0.001	-0.030	0.005	-0.061	-0.001	0.001
0.000	0.052	0.909	0.000	0.004	0.089	-0.003	-0.044	0.000	-0.001
0.036	0.001	0.000	0.850	0.000	0.000	-0.154	-0.001	-0.001	-0.034
0.000	-0.001	0.004	0.000	1.000	-0.003	0.000	0.003	0.000	0.000
0.001	-0.030	0.089	0.000	-0.003	0.913	0.002	0.034	0.000	0.001
0.033	0.005	-0.003	-0.154	0.000	0.002	0.838	-0.003	0.000	-0.035
-0.006	-0.061	-0.044	-0.001	0.003	0.034	-0.003	1.036	-0.001	0.000
-0.004	-0.001	0.000	-0.001	0.000	0.000	0.000	-0.001	1.000	0.000
0.009	0.001	-0.001	-0.034	0.000	0.001	-0.035	0.000	0.000	0.993

Table 5:  $\hat{\mathbf{T}}^T \hat{\mathbf{T}}$  matrix.

The inner product  $\mathbf{T}^T \boldsymbol{\omega}_b^2 \mathbf{T}$  is presented in Table 6. It can be observed that the off-diagonal terms are very close to zero, and diagonal terms are very close to  $\boldsymbol{\omega}_a^2$  (Table 7), which indicates that there are no discrepancies in stiffness between these models.

Using the QR decomposition, matrix  $\hat{T}$  has been decomposed as:

$$\hat{T} = R \cdot Q \quad (4)$$

Where  $R$  is a rotation matrix (Table 8) and  $Q$  (Table 9) is a matrix containing the effect of the scaling and shear. From the rotation matrix is inferred that the first two modes are rotated in their local subspace an angle  $\theta = -5.3344^\circ$ . Modes 4 and 5 are not well paired but they also rotate an angle  $\theta = 5.7448^\circ$ . Modes 7 to 10 are a set of closely spaced and repeated modes mainly rotating on the subspace spanned by these four modes.

From matrix  $Q$  it is derived that the scaling of most of the modes (diagonal terms less than unity) are modified by the mass perturbation, the modes 3,4, 6 and 7 being the most affected [8]. The non-zero off-diagonal terms of matrix  $Q$  indicate that the mass perturbation produces shear in some of the modes [8].

4026.2	0.0	0.1	-2.1	0.0	-0.5	-10.8	0.8	0.2	-6.0
0.0	4055.9	0.1	1.5	-0.3	-2.5	9.1	15.4	0.1	2.7
0.1	0.1	20832.1	-10.3	2.7	16.0	-64.3	-120.3	-1.1	-19.0
-2.1	1.5	-10.3	167029.8	-1.9	100.3	454.7	-187.9	51.1	478.0
0.0	-0.3	2.7	-1.9	195579.4	-34.2	-11.4	106.6	0.1	-3.5
-0.5	-2.5	16.0	100.3	-34.2	234909.8	624.3	1729.8	11.8	184.2
-10.8	9.1	-64.3	454.7	-11.4	624.3	981066.4	-1181.3	354.7	2536.0
0.8	15.4	-120.3	-187.9	106.6	1729.8	-1181.3	1164213.4	-33.9	-346.1
0.2	0.1	-1.1	51.1	0.1	11.8	354.7	-33.9	1192900.4	88.3
-6.0	2.7	-19.0	478.0	-3.5	184.2	2536.0	-346.1	88.3	1299229.3

Table 6: Inner product  $T^T \omega_b^2 T$ .

Mode	1	2	3	4	5	6	7	8	9	10
Diagonal of $\sqrt{T^T \omega_b^2 T}$ (rd/s)	63.5	63.7	144.3	408.7	442.2	484.7	990.5	1079.0	1092.2	1139.8
$\omega_a$ (rd/s)	63.5	63.7	144.3	408.5	442.2	485.0	990.0	1082.5	1092.2	1139.2
Error [%]	0.00	0.00	0.00	-0.07	0.00	0.14	-0.09	0.65	0.00	-0.12

Table 7: Comparison of  $\omega_a$  and  $\sqrt{T^T \omega_b^2 T}$

However, although the structure has been perturbed with a mass change, the structural dynamic modification [1,2] establishes that there is no shear in the case of repeated modes. This can be seen in the zero values obtained for the terms  $Q(1,2)$ ,  $Q(3,4)$  and  $Q(8,9)$ , which are zero or approximately zero (for example  $Q(8,9)$  is approximately zero due to the effect of truncation). The same effect can be seen in  $\hat{T}^T \hat{T}$ .

When a set of repeated or closely spaced modes is well separated from the rest of the modes, the mode shapes are mainly rotating in the subspace spanned by the repeated or closely spaced modes. This means that the matrix can be accurately obtained using a reduced number of modes. In Table 10 it is presented the matrix  $\hat{T}$  obtained with the first three modes, which shows that the local  $\hat{T}$  matrix corresponding to modes 1 and 2 has been estimated with a good precision.



In order to reduce the effect of truncation, it is recommended to consider at least one mode below and another mode over the set of modes for which matrix  $\hat{T}$  is estimated. The matrices  $R$  and  $Q$  obtained with the QR decomposition are also shown in this table.

-0.996	-0.093	0.001	-0.001	0.000	0.000	0.000	0.000	0.000	0.000
0.093	-0.996	0.013	0.000	0.000	0.001	0.000	0.000	0.000	0.000
0.000	-0.013	-1.000	0.000	0.000	0.010	0.000	-0.001	0.000	0.000
0.000	0.000	0.000	-0.100	0.995	0.010	0.004	0.000	0.000	-0.001
0.001	0.000	0.000	-0.994	-0.100	-0.001	0.036	0.000	0.000	-0.007
0.000	-0.001	-0.010	0.000	0.010	-1.000	0.000	-0.018	0.000	0.000
0.000	0.000	0.000	-0.025	0.000	0.000	-0.770	0.002	0.517	-0.374
0.000	0.000	0.000	0.015	0.000	0.002	0.458	-0.136	0.848	0.228
0.000	0.000	0.001	-0.002	0.000	0.018	-0.065	-0.991	-0.115	-0.031
0.000	0.000	0.000	0.022	0.000	0.000	0.438	-0.002	0.005	-0.899

Table 8: Matrix  $R$ .

-0.981	0.000	0.000	-0.037	0.000	-0.001	-0.034	0.006	0.004	-0.009
0.000	0.984	0.053	0.001	-0.001	-0.031	0.005	-0.062	0.000	0.002
0.000	0.000	-0.952	0.000	-0.003	-0.095	0.003	0.042	0.000	0.001
0.000	0.000	0.000	-0.921	0.000	0.000	0.168	0.001	0.001	0.037
0.000	0.000	0.000	0.000	-1.000	0.004	0.000	-0.003	0.000	0.000
0.000	0.000	0.000	0.000	0.000	0.950	0.003	0.038	0.000	0.001
0.000	0.000	0.000	0.000	0.000	0.000	-0.899	0.003	0.001	0.046
0.000	0.000	0.000	0.000	0.000	0.000	0.000	1.014	-0.001	0.000
0.000	0.000	0.000	0.000	0.000	0.000	0.000	0.000	-1.000	0.000
0.000	0.000	0.000	0.000	0.000	0.000	0.000	0.000	0.000	0.995

Table 9: Matrix  $Q$ .

The results obtained considering modes 3, 4, 5 and 6 are presented in Table 11.

Matrix $\hat{T}$			Matrix $R$			Matrix $Q$		
0.977	-0.092	-0.006	-0.996	-0.093	-0.001	-0.981	0.000	0.000
-0.091	-0.980	-0.065	0.093	-0.996	-0.013	0.000	0.984	0.053
0.000	-0.013	0.951	0.000	-0.013	1.000	0.000	0.000	0.952

Table 10:  $T$ ,  $R$  and  $Q$  matrices estimated with modes 1,2 and 3.

The matrices  $\hat{T}$ ,  $R$  and  $Q$  estimated with modes 3,4,5 and 6 are shown in Table 11.

The MAC between the first ten perturbed and unperturbed mode shapes are shown in Table 12. It can be seen that there is a good agreement between the mode shapes except for modes 7, 8, 9 and 10. Table 12 also shows that modes 4 and 5 are not well paired.

Matrix $\hat{T}$				Matrix $R$				Matrix $Q$			
0.951	0.000	0.004	0.105	-1.000	0.000	0.010	0.010	-0.951	0.000	-0.013	-0.095
-0.009	0.092	-0.995	0.023	0.010	-0.100	0.995	0.010	0.000	-0.920	0.000	0.000
0.001	0.915	0.100	-0.002	-0.001	-0.995	-0.100	-0.001	0.000	0.000	-1.000	0.015
0.009	0.000	-0.010	-0.949	-0.010	0.000	0.010	-1.000	0.000	0.000	0.000	0.950

Table 11:  $\hat{T}$ ,  $R$  and  $Q$  matrices estimated with modes 3,4,5 and 6.

0.991	0.009	0.000	0.052	0.001	0.000	0.002	0.000	0.004	0.001
0.009	0.991	0.001	0.000	0.062	0.000	0.000	0.001	0.000	0.000
0.000	0.001	0.999	0.000	0.000	0.011	0.000	0.003	0.000	0.000
0.001	0.063	0.000	0.010	0.990	0.000	0.000	0.153	0.001	0.000
0.063	0.001	0.000	0.988	0.010	0.000	0.005	0.002	0.090	0.012
0.000	0.000	0.000	0.000	0.000	0.988	0.000	0.006	0.000	0.000
0.000	0.000	0.000	0.001	0.000	0.000	0.687	0.000	0.434	0.180
0.005	0.000	0.000	0.167	0.003	0.000	0.066	0.018	0.555	0.037
0.000	0.005	0.000	0.003	0.158	0.000	0.001	0.968	0.011	0.001
0.000	0.000	0.000	0.001	0.000	0.000	0.210	0.000	0.000	0.781

Table 12: **MAC** matrix with 10 modes.

Using the rotation matrix presented in Table 8, the mode shapes of the unperturbed system were rotated and the ROTMAC was calculated with eq. (15), the results being presented in Table 13. In the case of no mass discrepancies, the ROTMAC must be an identity matrix. Moreover, the ROTMAC only provides information of the shear [8].

1.000	0.000	0.000	0.053	0.000	0.000	0.002	0.000	0.004	0.001
0.000	1.000	0.000	0.000	0.063	0.000	0.000	0.001	0.000	0.000
0.000	0.000	0.999	0.000	0.000	0.009	0.000	0.003	0.000	0.000
0.064	0.000	0.000	1.000	0.000	0.000	0.001	0.000	0.084	0.010
0.000	0.063	0.000	0.000	1.000	0.000	0.000	0.155	0.000	0.000
0.000	0.000	0.000	0.000	0.000	0.991	0.000	0.004	0.000	0.000
0.000	0.000	0.000	0.021	0.000	0.000	0.970	0.000	0.087	0.000
0.000	0.005	0.000	0.000	0.162	0.000	0.000	0.990	0.000	0.000
0.003	0.000	0.000	0.085	0.000	0.000	0.121	0.000	1.000	0.019
0.000	0.000	0.000	0.004	0.000	0.000	0.003	0.000	0.018	0.996

Table 13: ROTMAC matrix with 10 modes.

According to the structural dynamic modification, the ROTMAC between repeated modes must be unity [8], effect which can be observed in Table 13. Moreover, the rest of the diagonal terms are very close to unity (except mode 7), which indicates that the effect of shear is low. With respect to the off-diagonal terms, there are some components in the range [0.05-0.16] which are also indicators of mass discrepancies between both models.

## 5 CONCLUSIONS

- In this paper, a steel beam structure has been assembled and ABAQUS and the natural frequencies and the mode shapes has been extracted with a frequency analysis. This model has been modified adding a lumped mass.
- The transformation matrix  $T$ , which relates the modal matrices of both the unperturbed and the perturbed systems, has been factorized with the QR decomposition. The diagonal terms of matrix  $Q$  provide information of changes in scaling, whereas the off-diagonal terms contain information about the shear.
- The inner product  $T^T \omega_b^2 T$  has been used to confirm that there are no stiffness discrepancies between both models.
- The matrix  $Q$  obtained is not diagonal, which indicates that there is effect of shear. However, the numerical results confirm that there is no shear in the case of repeated modes. This can be seen in the zero values obtained for the terms  $Q(1,2)$ ,  $Q(3,4)$  and  $Q(8,9)$ , which are zero or approximately zero.
- Several diagonal terms of matrix  $Q$  are not unity, which indicate that the scaling of the mode shapes have been modified.
- The concept of ROTMAC, together with the inner product  $T^T T$  (which was different to an identity matrix) and the inner product  $T^T \omega_b^2 T$ , confirms that the discrepancies in natural frequencies and mode shapes can be attributed to mass discrepancies.

## ACKNOWLEDGEMENTS

The authors would like to express their gratitude to the Spanish Ministry of Science and Innovation for the financial support through the projects MCI-20-PID2019-105593 GB-00/AEI/10.13039/501100011033 and MCI-21-PRE2020-094923.

## REFERENCES

- [1] A. Sestieri, "Structural dynamic modification," *Sadhana*, vol. 25, no. 3, pp. 247–259, Jun. 2000, doi: 10.1007/BF02703543
- [2] A. Sestieri and W. D'Ambrogio, "A modification method for vibration control of structures," *Mech. Syst. Signal Process.*, vol. 3, no. 3, pp. 229–253, Jul. 1989, doi: 10.1016/0888-3270(89)90051-4
- [3] M. Nad, "Structural dynamic modification of vibrating systems," *Appl. Comput. Mech.*, vol. 1, no. 1, pp. 203–214, 2007.
- [4] C. Lein and M. Beitelschmidt, "Comparative study of model correlation methods with application to model order reduction," 2014.
- [5] R. J. Allemang and D. Brown, "Correlation Coefficient for Modal Vector Analysis," in *Proceedings of the 1st International Modal Analysis Conference*, 1982, pp. 110–116.
- [6] M. Aenlle, Josué Pacheco-Chérrez and R. Brincker, "Sensitivity analysis of a system with two closely spaced modes using structural dynamic modification," *Mechanical Systems and Signal Processing*, vol. 206, pp. 110894, 2024, doi: 10.1016/j.ymssp.2023.110894

- [7] M. Aenlle, N. García-Fernández and F. Pelayo, “Rotation of mode shapes in structural dynamics due to mass and stiffness perturbations,” *Mechanical Systems and Signal Processing*, vol. 212, pp. 111269, 2024, doi: 10.1016/j.ymssp.2024.111269
- [8] T. Lyche, *Numerical Linear Algebra and Matrix Factorizations*, vol. 22. Cham: Springer International Publishing, 2020.
- [9] G. Golub and C. Van Loan, *Matrix Computations*, 4th ed. Johns Hopkins University Press, 2013.
- [10] C. R. Goodall, “Computation using the QR decomposition,” in *Handbook of Statistics*, 1993, pp. 467–508.
- [11] W. Gander, “Algorithms for the QR-Decomposition,” Zürich, Apr. 1980.
- [12] R. Clough and J. Penzien, *Dynamics of structures*. New York: McGraw-Hill, 1993.
- [13] W. Heylen, S. Lammens, and P. Sas, *Modal analysis theory and testing*. Belgium: Katholieke Universiteit Leuven, 2007.
- [14] M. Smith, “ABAQUS/Standard User's Manual,” Dassault Systemes Simulia Corp. United States, 2009.

## DYNAMIC BEHAVIOUR OF TRANSMISSION TOWERS THROUGH EXPERIMENTAL TESTING AND NUMERICAL MODELLING

Aitor Baldomir<sup>\*1</sup>, Arturo N. Fontán<sup>1</sup>, Luis E. Romera<sup>1</sup>, Marta Pérez<sup>2</sup>, Carlos J. Bajo<sup>2</sup>

<sup>1</sup> Grupo de Mecánica de Estructuras, Universidade da Coruña  
ETS de Ingeniería de Caminos, Canales y Puertos, CITEEC  
e-mail: aitor.baldomir@udc.es

<sup>2</sup> Ferrovial Construcción  
c/Ribera del Loira 42, 28042 Madrid  
mpescacho@ferrovial.com, carlos.bajo@ferrovial.com

**Keywords:** transmission tower, modal identification, free vibration test, numerical modelling

**Abstract.** *Transmission towers are usually steel lattice structures that support a power line covering long distances. Due to the large number of units required, they must be assembled quickly and reliably. One of the most important concerns is the correct assembly of all the parts that make up the tower. There are different procedures for detecting possible assembly faults, such as regular inspections, static tests or dynamic tests. Nowadays, the instrumentation of such a structure is relatively easy to carry out thanks to high-precision wireless devices. It is therefore possible to obtain real-time data from dynamic tests without the need for a major deployment of resources.*

*Modal identification through free vibration testing of electrical towers allows the detection of major assembly errors. In order to extrapolate the results to different tower designs, it is necessary to have reliable numerical models that allow the expected vibration modes and frequencies to be known in advance. In this study, dynamic tests were conducted on two types of towers: tower 1 (68.5 m in height) and tower 2 (46.9 m in height) and the results were compared with those obtained in numerical frame models. Eight wireless accelerometers were strategically placed to identify the global modes of the structure. Then experimental tests were conducted by applying an impulsive load at different heights of the tower. After recording acceleration data, FFTs were computed to obtain natural frequencies of the structure (Figure 1).*

*Once the experimental results are available, the goal is to compare them with those obtained from a numerical model. If the results are consistent, numerical models can be used to determine the structural response in the event of faulty assembly and even to foresee the structural behaviour in advance. The main purpose of this accurate modeling is to exchange the structural load testing by numerical model results, which can be tested on site just after tower erection. In this case, modal analyses were performed after creating 3D bar models for both towers. Before performing dynamic analyses, the models were checked with static loading assumptions.*

Although the two towers under study have different foundations types, it was accepted for this global dynamic analysis the use of embedment conditions at the base.

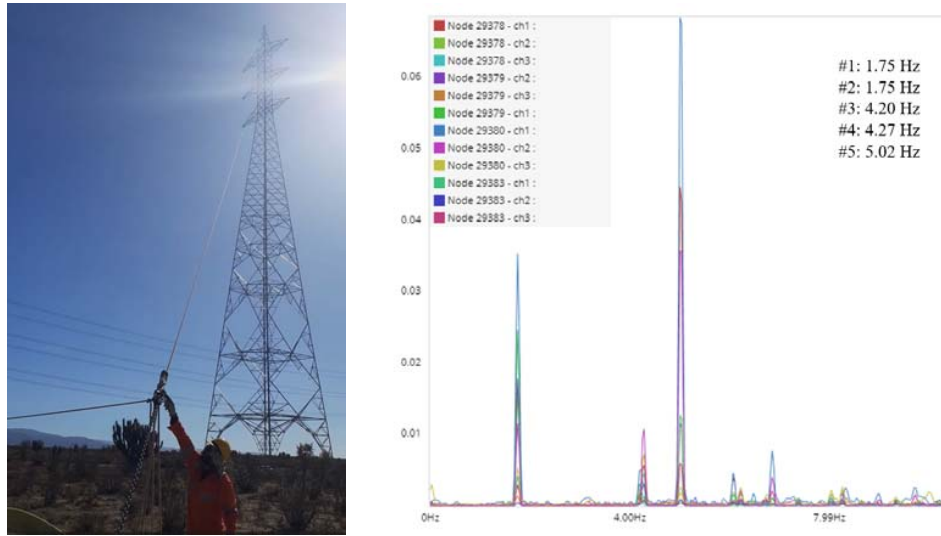


Figure 1: Tower 1 ( $h=68.5$  m). Application of impulsive load for the free vibration test (left). FFT from experimental data (right).

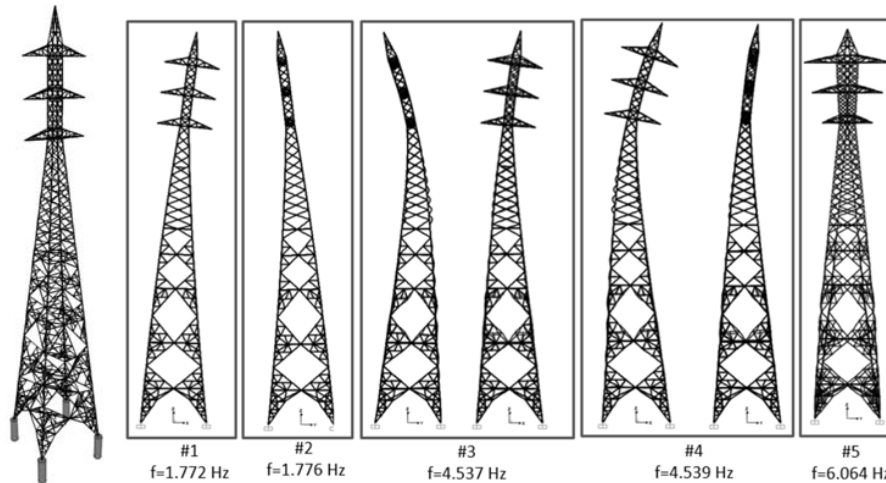


Figure 2: Tower 1 including actual foundation (left). Results of numerical modal analysis with embedded foundation (right).

The numerical models revealed discrepancies with the experimental results. In tower 1, differences of approximately 1.5% were observed in frequency values of the first two bending modes, and 8% in bending modes 3 and 4. These differences increased in tower 2 to 7.5% and 16%, respectively. The largest discrepancy was found in the first torsional mode, with errors of 32% for tower 1 and 49% for tower 2. From these results, we sought possible causes for the observed differences and made modifications to the numerical models. Firstly, we decided to accurately model the foundations of each tower based on the available project data, including mechanical properties of the soil at the tower locations. After this update, the results were significantly improved, particularly in tower 2. The associated error with the first 2 bending modes decreased from 8% to 1.4%, while the error associated with bending modes 3 and 4 was halved.

Additionally, the torsional mode setting improved, with an error of 19.5% in tower 1 and 16.2% in tower 2.

Therefore, it was confirmed that including the behaviour of the foundations in the model had an influence on the main vibration modes, but it was not sufficient to correctly adjust the torsional mode. We then assumed that slippage in bolted joints might be related to this effect. It was determined that the frames bracing main legs had an initial slip at their ends before they start to transmit forces. Non-linear springs were included in the numerical model and the dynamic tests carried out on the towers were replicated with a non-linear dynamic analysis in the time domain. Table 1 shows the results of all the hypotheses discussed above. It can be observed that the errors associated with the first torsional mode are reduced to 0.4% for tower 1 and 3.3% for tower 2 in the last case studied.

It is concluded that in order to achieve a reliable numerical model for the detection of assembly failures in transmission towers, two fundamental aspects must be taken into account: the correct modelling of the foundation properties of the structure and the consideration of slippage in bolted joints.

Tower 1 ( $h=68.5$ m)					
	1st bending	2nd bending	3rd bending	4th bending	1st torsional
Embedbed foundation	1.772	1.776	4.537	4.539	6.604
Model with foundation properties	1.769	1.772	4.490	4.510	6.000
Model considering slippage at joints	1.762	1.767	4.410	4.450	4.999
Experimental test	1.750	1.750	4.200	4.270	5.020
Tower 2 ( $h=46.9$ m)					
	1st bending	2nd bending	3rd bending	4th bending	1st torsional
Embedbed foundation	2.734	2.753	7.736	7.829	8.820
Model with foundation properties	2.576	2.591	6.624	6.721	7.119
Model considering slippage at joints	2.539	2.564	6.447	6.503	5.925
Experimental test	2.540	2.570	6.640	6.850	6.125

Table 1: Natural frequencies from numerical models and experimental tests.

## OPERATION OF AN INTERACTIVE VIBRATION MONITORING SYSTEM AD-HOC DESIGNED FOR TRACKING HISTORIC FAÇADES DURING CONSERVATION WORKS.

Antolin Lorenzana<sup>\*1</sup>, Juan Jose Villacorta<sup>1</sup>, Roberto D. Martinez<sup>2</sup>, Mariano Cacho<sup>1</sup> and Alberto Izquierdo<sup>1</sup>

<sup>1</sup>ITAP. Universidad de Valladolid  
Paseo del Cauce, 59, 47011 Valladolid  
e-mail: ali@eii.uva.es/juanjose.villacorta@uva.es/mariano.cacho@uva.es/alberto.izquierdo@uva.es

<sup>2</sup> Dpto. IAF. Universidad de Valladolid  
Avenida de Madrid, 57, 34004 Palencia  
e-mail: robertodiego.martinez@uva.es

**Keywords:** Heritage buildings, Structural Health Monitoring, Alert System

**Abstract.** *Heritage-listed façades may require relocation when the supporting building is at serious risk of collapse. Such is the case described in this paper, where entire façades must be cut into large sections of up to 200 m<sup>2</sup> and 150 tonnes in weight. Various engineering works must be carried out to ensure the structural integrity. Each section, which must be able to be handled by heavy-lift autocranes, is reinforced by a temporary steel structure prior to the disengagement from the supporting building structure. These operations demand heavy cutting tools which can induce potentially damaging vibrations. Likewise, the handling of the detached section, if not done carefully, can lead to catastrophic shocks. It is necessary to install a system that, in real time, acquire and process acceleration recordings and draw out commands that can alert to the operators, about the level of vibration. In the event of levels considered to be excessive, signals will advise workers to proceed more carefully. This brief report describes the specifically designed monitoring system, its electronic parts and how they operate. Two different applications are described. Firstly, at laboratory level, the vibrations of a scaled section, with well identified dynamic behaviour, are tracked from its original vertical position to its horizontal one. Subsequently (not shown in this abstract), it is applied to the case of an actual large section, correlating the recordings with the different on-site works and the corresponding alarms generated for each case.*

The acquisition system [1] is based on the ADXL355 digital MEMS triaxial accelerometers from Analog Devices, with a noise density of  $25 \mu\text{g}/\sqrt{\text{Hz}}$  and sensitivity set to  $3.9 \mu\text{g}/\text{LSB}$  in the range  $\pm 2\text{g}$ , bandwidth from 0 Hz (can measure the acceleration due to gravity) to 1500 Hz and capable to sample up to 4 kHz with 20 bit per sample. Up to six of them are connected to a microcontroller and microprocessor unit based on a myRIO device (hardware based on a Xilinx Zynq 7010 chip, incorporating a FPGA and a dual-core ARM® Cortex™-A9 processor) from National Instruments. Once a certain time increment is selected (set to 10 s), the recordings are processed in order to extract physical parameters such as acceleration amplitudes, prevalent



frequencies and rate of change of the Euler angles. If the adjusted thresholds are exceeded, the system generates different codified alarm outputs ranging from light signals of different colours to sounds with different tones and intensities.

In order to understand the conceptual records shown in figure 1, the typical process of detachment of a façade section is described below. In the case under study, sections up to  $10 \times 20 \text{ m}^2$  are identified to be separated from the rest of the façade by means of straight cuts. As the sections are fragile, they must be reinforced by steel structures on both sides, connected to each other through holes bored in the façade itself. The section, together with its protective steel structure, forming a rigid sandwich, is still connected to the rest of the building through the heads of the floor slabs. On-site works are required to release the sandwich assembly from the building structure. During these works, for safety reasons, the sandwich is held in place by the slings of the autocrane. The works consist of cutting (using wire saws), demolition (using jack-hammers and air breakers) and the use of flame-cutting systems for the metal parts. This kind of equipment induces vibrations (area highlighted in yellow). Once the section has been released, it is hung from the crane, which then moves it away from the building by means of translation and rotation movements. Assuming that the façade is in the X (vertical) Y (horizontal) plane, figure shows a  $90^\circ$  turn with respect to the X-axis (area indicated in green). The work continues with the tilt ( $90^\circ$  turn with respect to the Y-axis) after which the section will lie flat on the ground. The tilting is carried out with the help of a second crane and is shown in the band indicated in blue. Vibrations may occur during all the process due to the necessary movements of the cranes, possible impacts with the building, the ground support manoeuvre or the readjustment of the slings during the tilting.

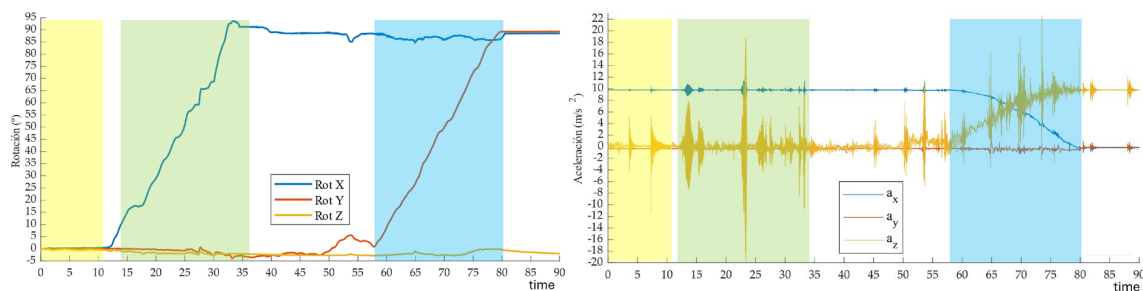


Figure 1: Euler angles (left) and accelerations (right)

Figure 1 shows the rotation and acceleration recordings of the conceptual test carried out at laboratory scale (1:10), where the whole process was carried out in 90 s and vibrations up to 2 g were intentionally induced. The case study to be shown consists of a section of  $20 \times 10 \text{ m}^2$  and 136 t, handled by 2 cranes of 700 t and 500 t, where 26 hours were used for its releasing and overturning, where the maximum acceleration did not exceed  $3.8 \text{ m/s}^2$ .

**Acknowledgments:** The authors wish would like to thank the company CAV Diseño e Ingeniería and to Fundación Santa Maria la Real p.h. for their cooperative work. Also the authors wish to acknowledge to the AEI, Spanish Government (10.13039/501100011033), and to “ERDF A way of making Europe”, for the partial support through the grant PID2022- 140117NB-I00.

#### Reference:

- [1] Magdaleno A.; Villacorta JJ.; delVal L.; Izquierdo A.; Lorenzana A., (2021) Measurement of acceleration response functions with scalable low-cost devices. An application to the experimental modal analysis. *Sensors*, 21, pp.6637. DOI: 10.3390/s21196637

## FATIGUE MONITORING OF STRUCTURES AS A SHM TECHNIQUE

F. Pelayo<sup>1</sup>, Natalia García-Fernández<sup>1</sup> Miguel Muñoz Calvente<sup>1</sup> and Manuel Aenlle-López<sup>1</sup>

<sup>1</sup> Department of Construction and Building Engineering. University of Oviedo. Spain

[fernandezpelayo@uniovi.es](mailto:fernandezpelayo@uniovi.es)  
{garciafnatalia, munizcmiguel, aenlle}@uniovi.es

**Keywords:** Dynamic Analysis, OMA, Numerical Models, Model-Updating.

**Abstract.** *The fatigue phenomenon can produce failure in structural and mechanical components when they are subjected to dynamic cyclic loadings. One of the most commonly used methodologies in fatigue design consists of determining the stresses time histories from variable amplitude load models, calculating the stress spectrum using the rainflow technique, and evaluating the total fatigue damage using Miner's rule [1].*

*Although Structural Health Monitoring techniques (SHM) [2] have used during recent times. The data used, i.e. accelerations, are mainly used for modal parameters identification. However, this data can be used in combination with a finite element modal of the structure in order to obtain the stresses time histories during the structure service conditions.*

*If stresses are estimated in real time, it is possible to perform fatigue monitoring of the structure, i.e. to calculate the accumulated damage over time, providing valuable information for estimating the remaining life of structures in service. This methodology also has the advantage of being combinable with other damage detection techniques based on operational modal analysis (OMA) and in Structural Health Monitoring processes.*

### 1. METHODOLOGY

The proposed methodology is developed in two phases. In the first one, the modal parameters of the structure must be identified using modal analysis and a finite element model (FEM) of the structure has to be assembled as well as updated [3], if necessary (see Fig. 1). In this phase, the experimental mode shapes ( $\phi_x$ ) and the displacement ( $\phi_{FE}$ ) and stresses numerical ( $\phi_{\sigma_{FE}}$ ) mode shapes have to be determined.

With the previous data, it would start the Fatigue-Monitoring Phase. This second phase can be divided into 4 steps as presented in Fig. 1.

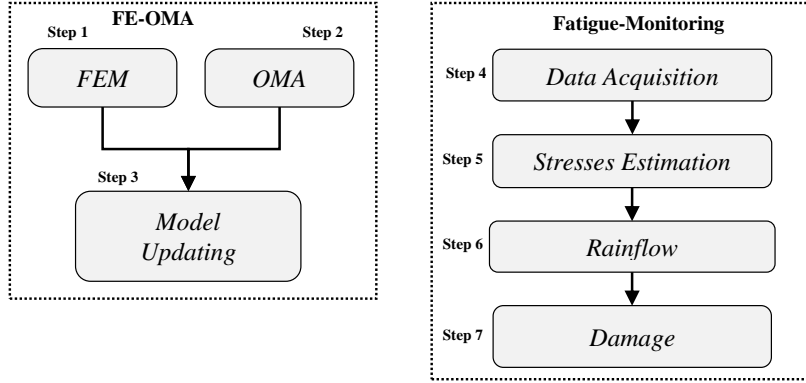


Figure 1. Phases and Steps for developing the proposed methodology.

The step 4 is common to SHM processes and data would be registered (i.e. accelerations). The next step is to estimated the stresses:

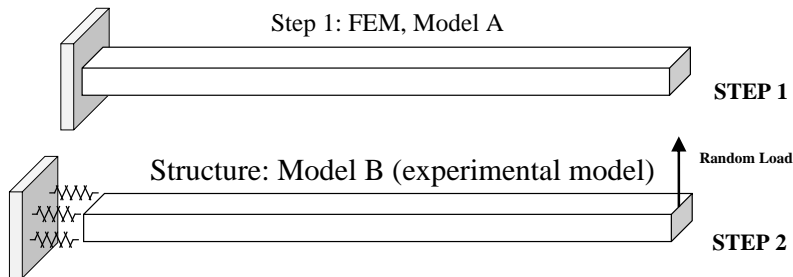
$$\sigma(t) = \phi_{\sigma_x} \cdot q_x(t) \quad (1)$$

Where  $\phi_{\sigma_x}$  are the experimental stress modes obtained from the numerical stress modes ( $\phi_{\sigma_{FE}}$ ) and expanded to those points where stresses will be of interest using the transformation matrix  $T$  ( $\phi_x = \phi_{FE} \cdot T$ ) [4]. Finally,  $q_x(t)$  are the displacement modal coordinates obtained with data from Step 4.

Steps 6 and 7 are related with the damage induced by fatigue in the structure. Firstly, from the stresses obtained from Eq. (1), stress ranges and cycles are obtained using counting techniques such as the Rainflow. After, using the corresponding standards and codes, the fatigue can be estimated, i.e. with the Miner's Rule.

## 2. EXAMPLE

In this section, all phases of the methodology are applied using a simulated example. A steel cantilever beam with a rectangular solid section was modeled in ABAQUS CAE. In the model, 3D quadratic elements with reduced integration (C3D20R) were used. The length of the beam was 1.8 meters, with a section of 80 x 40 mm. Linear elastic behavior was assumed for the steel. A fixed support boundary condition was used for the numerical model A (Step 1), whereas a flexible support boundary condition was used for the experimental model B (Step 2). In the experimental model B, a random load was applied to the free end of the beam to simulate a real load. Both models are presented in Figure 2. The figure also shows the points used as “measured points” for Step 4 and the “unknown point” where Step 5 is applied to estimate the stresses.



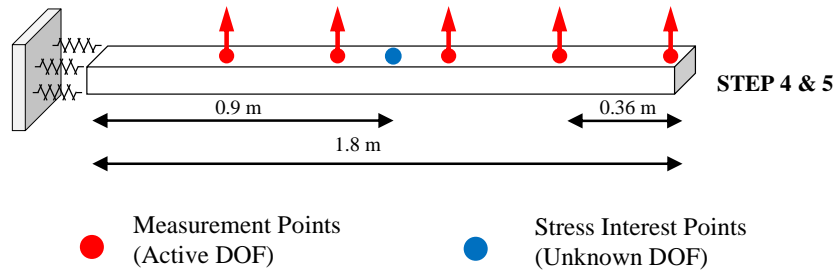


Figure 2. Models used in the different steps.

## 2.1 FE-OMA PHASE

From both Models A and B, the modal analysis was carried out, with the natural frequencies presented in Table 1. The MAC was also obtained, showing a good correlation between the first four bending modes used in this example. Although the errors in natural frequencies are about 11%, no further model updating was performed. It is important to note that only a good correlation in terms of mode shapes is needed with this methodology, because the information corresponding to the natural frequencies and damping ratios is contained in the experimental modal coordinates (Step 5).

Model A	Model B	Error [%]
10.07	8.96	11.03
62.94	57.16	9.18
175.61	161.78	7.88
342.33	319.06	6.80

Table 1. Natural frequencies [Hz] of models A and B.

## 2.2 FATIGUE-MONITORING.

With the data obtained from the FE-OMA phase (see Section 1), Step 5 can be applied to obtain the stresses at the points of interest (see Figure 2) using Eq. (1). The stresses obtained are presented in Figure 3, where a good correlation can be observed.

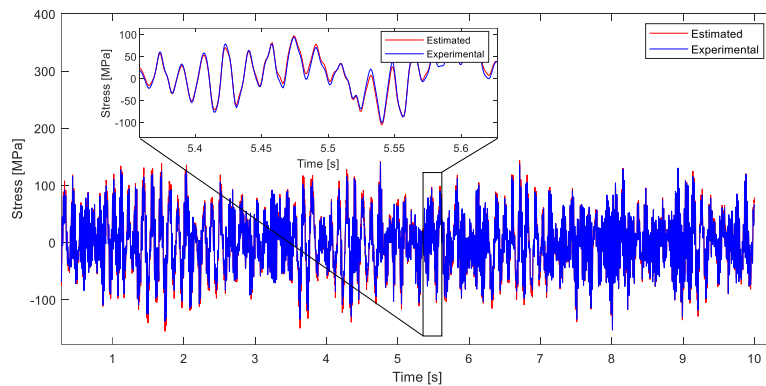


Figure 3. Stresses estimated with Eq. (1) and those obtained directly from the numerical simulation (experimental).

Once the stresses are estimated in Step 5, the Rainflow counting method (Step 6) can be applied using MATLAB to obtain the cycles at different stress ranges. Finally, the accumulated fatigue damage is estimated using Miner's Rule (Step 7). An S-N curve from Eurocode 3 [5], corresponding to a category 80 (a plate welded to the beam at the point where the stresses are estimated), was assumed. Using a strength reduction coefficient  $\gamma_{mf}=1.15$  [5], a damage index  $D=0.4$  was estimated.

### 3. CONCLUSIONS

- A methodology to estimate stresses at any point of a real structure, using experimental data of the structure and the modal parameters of a numerical model, is proposed.
- The stresses estimated with this methodology allow a real time fatigue calculation.
- This fatigue monitoring technique is fully compatible with other vibration-based monitoring techniques.
- The proposed methodology for stress estimation and fatigue calculation has been validated through numerical simulations in a cantilever beam example.

### ACKNOWLEDGEMENTS

The authors would like to thank the Ministry of Science and Innovation of Spain for the financial support received in the project “Real-time fatigue monitoring and calculation of civil and industrial structures” (MCI-20-PID2019-105593GB-I00/AEI/10.13039/501100011033).

### REFERENCES

- [1] Miner MA (1945) Cumulative Damage in Fatigue. *J. Appl. Mech.* 12(3):A159–A164.
- [2] Rytter A, Kirkegaard PHP (1994) Vibration based inspection of civil engineering structures, Aalborg University.
- [3] Friswell MI, Mottershead JE (1995) Finite Element Model Updating in Structural Dynamics. Dordrecht: Springer Netherlands.
- [4] Pelayo F, Skaftø A, Aenlle ML, Brincker R (2015) Modal Analysis Based Stress Estimation for Structural Elements Subjected to Operational Dynamic Loadings. *Experimental Mechanics* 55(9):1791–1802.
- [5] AENOR, “Eurocode 3: UNE-EN 1993-1-9.” 2013.

## AUTONOMOUS MONITORING SYSTEMS FOR LONG-TERM PREDICTIVE MAINTENANCE OF A METRO BRIDGE

A. Romero<sup>1</sup>, J.D. Clavijo-Vázquez<sup>1</sup>, R. Velázquez-Mata<sup>1</sup>, J. Cámara-Molina<sup>1</sup>,  
M.A. Mengual-Pintos<sup>2</sup> and P. Galvín<sup>1</sup>

<sup>1</sup>Escuela Técnica Superior de Ingeniería, Universidad de Sevilla,  
Camino de los Descubrimientos, ES-41092, Spain  
e-mail: {rvmata, aro, jcamara, pedro galvin}@us.es

<sup>2</sup>Metro de Sevilla, Carmen Vendrell, 2, ES-41006, Spain  
e-mail: mamengual@metrodesevilla.es

**Keywords:** long-term monitoring, bridge, tram, low-cost sensor.

**Abstract.** *This work presents the deployment of a long-term monitoring system in a bridge belonging to the tram system of Seville. The location of the sensors is shown in Figure 1.*

*The commercial sensors are Willow AX-3D triaxial MEMS accelerometers manufactured by BeanAir with a measuring range of  $\pm 2g$ , a sensitivity of 660 mV/g and a maximum sampling rate (in streaming mode) of 2 kHz per axis. Their power consumption is between 20 and 30 mA (@3.3 V) during data acquisition, about 250 mA during radio transmission and less than 100  $\mu A$  during sleep mode. The external power supply is provided by solar energy harvesting. Communication with the monitoring system is via a gateway with WIFI and 3G/4G/LTE connectivity. Remote acquisition using the MQTT (Message Queuing Telemetry Transport) protocol is used for the communication between the devices. It is particularly suitable for IoT and remote monitoring scenarios. The remote management system is provided as a cloud service, enabling acquisition, analysis, metrics monitoring, and alarm management (Figure 2).*

*The system should anticipate system failures to prevent downtime. This is achieved by monitoring system health, analysing data trends (in time and frequency domains), and predicting maintenance needs, particularly for critical components. Failure detection algorithms include automated operational modal analysis methods, the use of surrogate models in digital twins, and supervised learning techniques.*

*We are presenting this work in DinEst2024 to discuss with colleagues our experience in this case study, including the problems we encountered during the deployment of the sensors, the power supply, the communication, and the data transmission, and to stimulate the exchange of experiences on this topic.*

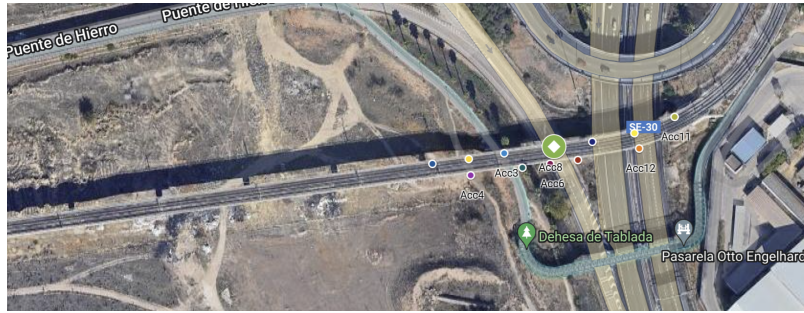


Figure 1: Location of the sensors.

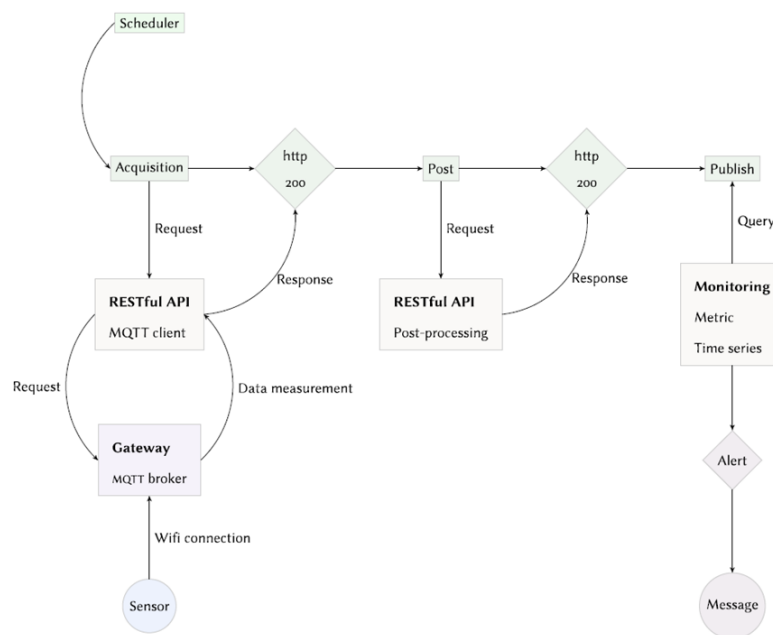


Figure 2: Monitoring system description.

## THERMAL DIGITAL TWIN FOR MONITORING AN ASPHALT ROAD ACCORDING TO AN UPDATED PHYSICS-BASED MODEL

Javier Álvarez<sup>1\*</sup>, Blas González<sup>2</sup>, Lucija Barišić<sup>3</sup>, Javier Fernando Jiménez-Alonso<sup>4</sup>  
and Andrés Sáez<sup>5</sup>

<sup>1</sup> University of Seville  
e-mail: [javalvpoz@alum.us.es](mailto:javalvpoz@alum.us.es)

<sup>2</sup> University of Seville  
e-mail: [bgonzalez@us.es](mailto:bgonzalez@us.es)

<sup>3</sup> University of Denmark  
e-mail: [lbar@ramboll.dk](mailto:lbar@ramboll.dk)

<sup>4</sup> University of Seville  
e-mail: [jfjimenez@us.es](mailto:jfjimenez@us.es)

<sup>5</sup> University of Seville  
e-mail: [andres@us.es](mailto:andres@us.es)

**Keywords:** : digital-twin, internet-of-things, pavement, long-term monitoring, physics-based-method

**Abstract.** *In this paper, a Thermal Digital Twin applicated to pavement is tested using two physic models: 1-Dimensional Difference Finite Model and 3-Dimensional Finite Element Model. Grade of adjustment and computational efficiency are discussed running the Digital Twin on data collected by a near climate station a contrasting with the measures takes by sensors embedded in the pavement. To update the Digital Twin, control theory is employed. Finally best option for building a Thermal Digital Twin is established.*



## 1 INTRODUCTION

Digital Twin (DT) concept, which appeared for first time in 2002, can be understood like a virtual mirror of a certain product [1]. It is considered as an important asset of Construction 4.0 applied to the predictive maintenance, as well as, Internet of Things (IoT) [2]. Focused on a civil infrastructure, the DT model makes possible to monitor the state of an infra-structure through time real simulation of the physical model. This physical model is continuously updated with information collected from the infrastructure. For instance, this technique has been applied successfully both in the performance prediction of pavements and in the health monitoring of pavements from their thermal response [3].

Updating of the Digital Twin model needs to be made properly to guarantee its well performance. In ref[4], three main approaches are exposed to make this task:

- Control techniques. Based on control theory, they are about the study of the model physics and representation in mathematical laws (transfer functions). This function relates each input signal with the corresponding output signal.
- Data-Dependent models. They are based on black box model using structures composed of a number of variables to describe the system according to a level of abstraction.
- Hybrid Control- Data Models.

In this study, physics-based models, considered as black box, are used in combination with control theory to update the physics' input parameters. Otherwise, two opposite physics models are used in this research: One-dimensional transient difference finite method (DFM) and Tree dimensional transient finite element method (3D-FEM). The implementation is made in a thermal problem in pavement, whose goal is monitoring the asphalt temperatures contrasting field temperatures through sensors with calculated temperatures.

## 2 THERMAL MODEL USED TO BUILD THE DIGITAL TWIN

### 2.1 Boundary conditions

Environmental conditions need to be included in both models. This is made estimating the heat flux based on energy balance equation. The mains effects to keep in mind is the radiation, convection, and conduction[5]:

- i) Radiation. Energy that comes from the sun. It's affected by the diffusion in the sky by the atmosphere and clouds. It's divided into two types: shortwave radiation and longwave radiation.
- ii) Convection. Transference of energy between fluids. In this case is between air and the pavement surface.
- iii) Conduction. It occurs inside of the pavement.

As is described in the literature, the heat flux is calculated as follow[3]:

$$q(t) = -k \left. \frac{\partial T(z,t)}{\partial z} \right|_{z=0} = \underbrace{f_s(t)}_{\text{Shortwave}} + \underbrace{h_c(t)(T_{air}(t) - T(0,t))}_{\text{Convection}} + \underbrace{(f_D(t) - \sigma \varepsilon_s (T(0,t) + 273,15)^4)}_{\text{Longwave radiation}} \quad (1)$$

Where,  $q$  = heat flux ( $W/m^2$ );  $f_s(t)$  = shortwave radiation ( $W/m^2$ );  $h_c(t)$  = convection coefficient ( $1/W^2 K$ );  $T_{air}(t)$  = temperature of air ( $^{\circ}C$ );  $T(0, t)$  = bulk temperature ( $^{\circ}C$ );  $f_D(t)$  = downwelling long wave radiation from the atmosphere ( $W/m^2$ );  $\sigma$  = Stefan-Boltzmann constant ( $5,670 \cdot 10^{-8} W/m K^4$ );  $\varepsilon_s$  = surface emittance (non dimensional)

As second boundary condition, a constant equilibrium temperature is considered at equilibrium depth.

## 2.2 Difference finite method applied to the differential heat equation

Difference finite method (DFM) is the first method employed in the research. The continuous solution of the partial differential equation is approximated with a discretization of the spatial model. The approach is obtained in each node, which can be selected by the user. Accuracy and resolution of the results is related with the number of nodes selected. [6]

Discretization is realized as[6]:

$$\frac{\partial \phi}{\partial x} \approx \frac{\phi_{i+1} - \phi_i}{\Delta x} \quad (2)$$

Being the Fourier's one-dimensional differential heat equation the following expression [3]:

$$\frac{\partial^2 T}{\partial z^2} + \frac{\dot{q}}{k} = \frac{1}{\alpha} \frac{\partial T}{\partial t} \quad (3)$$

where:

$T$ = temperature ( $^{\circ}K$ );  $\dot{q}$ = heat generation;  $k$ = thermal conductivity ( $W/m K$ );  $\alpha$ = diffusion coefficient ( $m^2/s$ );  $z$  = depth (m)

Applying the equation (2) to the expression (3) and setting  $\dot{q}=0$  the discretization is as follows [3]:

$$\frac{\partial T}{\partial t} \approx \frac{T(z, t + \Delta t) - T(z, t)}{\Delta t} \quad (4)$$

$$\frac{\partial^2 T}{\partial z^2} \approx \frac{T(z + \Delta z, t) - 2T(z, t) + T(z - \Delta z, t)}{\Delta z^2} \quad (5)$$

Inserting equations (4) and (5) into equation (3), we get the expression to solve in each node [3]:

$$T(z, t + \Delta t) = \left(1 - \frac{2\alpha}{\Delta z^2}\right) T(z, t) + \frac{\alpha \Delta t}{\Delta z^2} (T(z + \Delta z, t) + T(z - \Delta z, t)) \quad (6)$$

This methodology was studied and implemented in a study case in the literature's reference in ref[3],

### 2.3 Finite element method

Third-dimensional finite element method is the other methodology to study to performance the digital twin. In this case, it is necessary to use the Fourier's differential heat equation, in three dimensions[7]:

$$\nabla^2 T + \frac{\dot{q}}{k} = \frac{1}{\alpha} \frac{\partial T}{\partial t} \quad (7)$$

$$\text{where: } \nabla^2 = \frac{\partial}{\partial x^2} + \frac{\partial}{\partial y^2} + \frac{\partial}{\partial z^2}$$

Phenomenon considered are the same than employed with the difference finite method. Radiation and convection are introduced as boundary conditions on the top layer elements. Conduction represents the heat flow across the section and  $k$  is considered equal in any direction.

For solving the thermal analysis, a general finite element source code is used as is employed in ref [7]. Specifically, Mechanical ANSYS, version 2024.1.0 is connected to the digital twin and run with the same data that difference element method. Pavement is meshing using the SOLID70 3D thermal element.

### 3 MODEL UPDATION USING CONTROL THEORY

Input parameters of the previous physics models needs to be updated properly to performance the Digital Twin correctly. To make this task, a proportional controller (based on PID controllers) is used. However, first it's necessary set the parameter to update. In single input – single output (SISO) system only one parameter can be selected.

In this study, shortwave radiation and downwelling long wave radiation are measured directly from a near weather station. Nevertheless, convection is not possible measured directly, and it is necessary to estimates it through empirical correlations. [5] So, remembering equation (1), heat flux due to convection is obtained as:

$$q_c(t) = h_c(t)(T_{air}(t) - T(0,t)) \quad (8)$$

where:  $q_c(t)$  = heat flux due to convection

Being  $T_{air}(t)$  measured from a near climate station and  $T(0,t)$  the bulk temperature obtained from the physic model,  $h_c(t)$  is fixed as the parameter to control. The way to update the parameter selected is while a proportional controller. Hence, applying the P-controller expression [8], the parameter updated is obtained with the next expression:

$$h_c(t) = K_p e(t) \quad (9)$$

Where:  $h(t)$  is the convection coefficient;  $e(t)$  is the error signal of the system; and  $K_p$  is the controller's gain.

Selecting an appropriate gain  $K_p$  is not a trivial decision, cause the stability of the system depends on it. Therefore, the closed loop system features are studied.

To get mathematically the closed loop equation of this system, the control theory[9] is applied to the Fourier's one-dimensional heat flow equation (3). First, using the discretization exposed in direction  $Z$  (5):

$$\frac{1}{\alpha} \frac{\partial T}{\partial t} \approx \frac{T(z + \Delta z, t) - 2T(z, t) + T(z - \Delta z, t)}{\Delta z^2} \quad (10)$$

Applying the Laplace Transformation to this expression:

$$T(z, s) = \alpha \frac{T(z + \Delta z, s) - 2T(z, s) + T(z - \Delta z, s)}{s \Delta z^2} \quad (11)$$

Newly using the Laplace Transformation in the boundary condition (1), the next equation is obtained:

$$-k \frac{T(\Delta z, s) - T(-\Delta z, s)}{2\Delta z} = \underbrace{H_c(s)(T_{air}(s) - T(0, s))}_{U(s)} + \underbrace{F_s(s) + (F_D(s) - \sigma \varepsilon_s(T(0, s) + 273, 15)^4)}_{W(s)} \quad (12)$$

$F(s)$

Introducing the equation (12) into equation (11) and taking  $z = \Delta z$ , the response of the system at top of surface is:

$$T(0, s) = C(s) = \underbrace{\frac{2\alpha T(\Delta z, s)}{s\Delta z^2 - 2\alpha}}_{T_k(s)} + \underbrace{\frac{2\alpha}{k \left( s\Delta z - \frac{2\alpha}{\Delta z} \right)}}_{Q(s)} F(s) \quad (13)$$

The closed loop system is showed in the next block diagram:

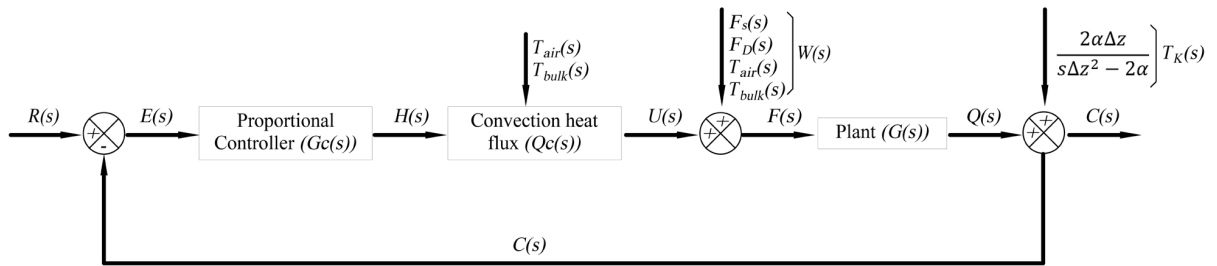


Figure 1. Closes loop system

Where:  $R(s)$ ,  $E(s)$ ,  $H(s)$ ,  $U(s)$ ,  $F(s)$ ,  $C(s)$  corresponding to the Fourier's transform of functions  $r(z, t)$ ,  $e(t)$ ,  $h_c(t)$ ,  $q_c(t)$ ,  $q(t)$ ,  $T(\Delta z, t)$  being:  $r(\Delta z, t)$  the signal reference defined as temperature in sensor at depth  $\Delta z$ ;  $e(t)$  is the error signal at depth  $\Delta z$  defined as  $e(t) = r(\Delta z, t) - T(\Delta z, t)$ ,  $tk(\Delta z, t)$  is the independent term of the plant

Setting  $T_k = 0$ , the transfer function has the following expression:

$$G(s) = \frac{C(s)}{F(s)} = \frac{2\alpha}{k \left( s\Delta z - \frac{2\alpha}{\Delta z} \right)} F(s) \quad (14)$$

Finally, setting  $T_k = 0$  and  $W_s = 0$  the closed loop equation is expressed as:

$$\frac{C(s)}{R(s)} = \frac{G_c(s)Q_c(s)G(s)}{1 + G_c(s)Q_c(s)G(s)} \quad (15)$$

Applying the Routh's stability criterion [9] to the previous relation, the next condition is obtained about the controller's tuning:

$$K_p \geq \frac{k}{\Delta z(T_{air} - T_{bulk})} \quad (16)$$

## 4 CASE STUDY: UPDATING DIGITAL TWIN OF A STREET PAVEMENT

### 4.1 Model data

The case study is a pavement of a street located in the campus of Technical University of Denmark (DTU), at coordinates 55°47'26.9"N 12°31'39.0"E. The street is straight and there are some buildings and tree shorts around. The pavement is composed with two layers of Stone Mastic Asphalt (SMA) with maximum aggregate size of 9 mm at top with 4cm thick each one, and one base layer of SMA with maximum aggregate size of 11 mm and thickness between 1,5 and 4 cm. There are embedded six temperatures sensors located at 1 cm depth under pavement surface. The reference signal is the average of temperature from sensors measures. [3]

The climate data are collected from a near climate station whose data are published at DTU webpage and can be inquired freely. The performance encompasses data since 23/03/2020 7.32 am to 15/07/2020 10:30 am. The step of the simulation is set in 60 seconds, corresponding it to amount 164338 steps.

The spatial domain of DFM is set through  $\Delta z$  set in 0,01 meters up to a depth of 10 meters. 3D-FEM model needs also set the element size, fixed 0,01 x 0,01 x 0,01 meters, composing a column of 10 meters with a base of 0,01 x 0,01 meters. This is selected of this way due to computational efficiency criterions and limitations of educational software used. Nevertheless, this assumption has no effect because the boundary conditions are the same for the whole surface, being the results independent of the size of the base.

On the other hand, parameters of physics model are set as:  $k = 1 \frac{W}{m^2 \text{ } ^\circ K}$ ;  $c = 4000 \frac{J}{kg \text{ } ^\circ K}$ ;  $\varepsilon$  (non dimensional) = 0,9;  $\rho = 2200 \frac{kg}{m^3}$

The DT model is implemented through a source code using language Python 3.11. The script has four (4) parts: i) data reading and model definition; ii) updating the model; iii) running the simulation using DFM or FEM methods alternately, iv) saving and exporting results. DFM model was written in the source code meanwhile FEM model is powered in ANSYS using the module named PyAnsys. All simulations are run in laptop.

The P-Controller's gain is tuned before final simulation. First, equation (16) is used. The system is stable and well approaches are obtained. However, soon it is noted that multiplying the equation (16) by ten, the accuracy improves slightly. In tests made, it has been seen that gains greater than 100 may do the system instable. Hence, the values of gain have been limited between 0 and 100, using the equation (16) multiplied by ten in intermediate values.

## 4.2 Physics-based models results

The Digital Twin was run first using the difference finite method, spending a total of 380.44 seconds to be completed. It means that each simulation spent about 0,0023149 seconds. On the other hand, in the case of 3D-FEM model computational efficiency is a key to keep in mind. The fact is that the simulation spent about 600 hours to be completed. It means that in average, 13.14 seconds are necessary to run the 3D FEM in each time step. This cost is much greater than employed by DFM. Therefore, the cost computational is acceptable compared to time step of 60 seconds in this Digital Twin in a real time simulation. Nevertheless, its implantation in other applications with a shorter time step would be unviable.

Differences between calculated temperatures are exposed following:

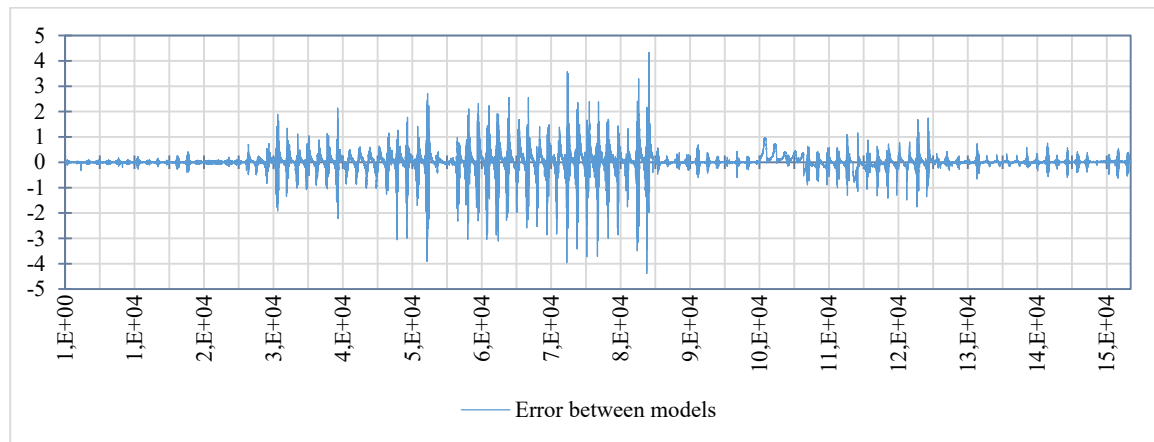


Figure 2. Errors between models in °C

Charting the physics-based models results with temperatures measured, the values are very similar. The mains differences occur mainly in low temperatures of the day:

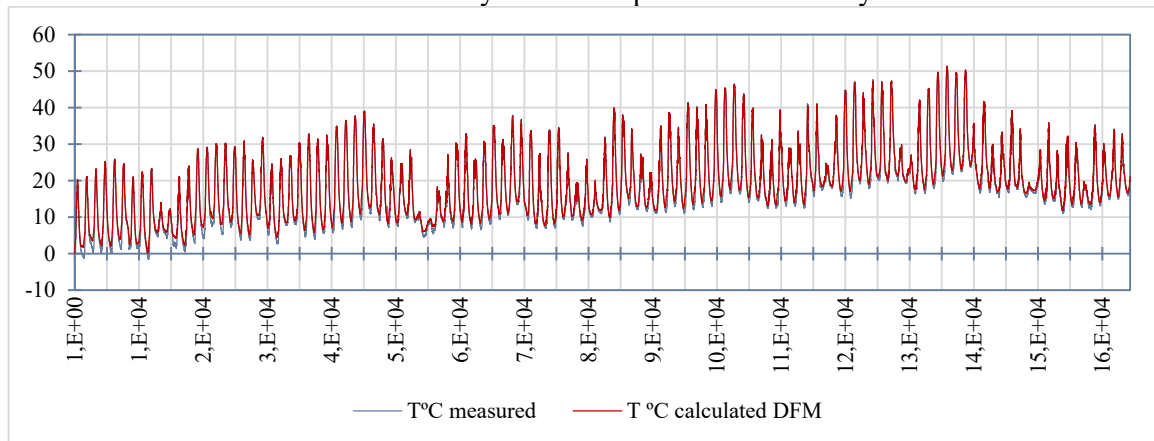


Figure 3. Comparative between measured and calculated temperatures (°C) by DFM. Full series.

The average error obtained is 0,65°C in DFM versus 0,711°C in 3D FEM. Differences between calculated and measured temperatures could be related with variations of other parameters not updated, or even with phenomenon no included in the model as rain.

## 5 CONCLUSIONS

In this research has been tested a Thermal Digital Twin running with 2 physics-based model updated using a proportional controller. How as have seen before, models based on FEM are a higher cost computational than DFM models. Hence, it is necessary analyze in each case the requirements, verifying that step time is greater than computational time.

On the other hand, both models offer similar results, however occasionally values of error grow up to 4 ° C. Anyway, in this case DFM provides a slight better adjustment to measured sensors than FEM models. Therefore, employ of DFM seems best option to use in pavements thermal Digital Twin, depending always of the requirements.

The proportional controller offers a great adjustment that no like be affected by the method employed. However, differences between temperatures calculated and measured could be affected by other parameters not updated or phenomenon not included. In addition, the quality of adjusted parameters should be studied deeper.

## REFERENCES

- [1] I. Errandonea, S. Beltrán, and S. Arrizabalaga, “Digital Twin for maintenance: A literature review,” *Computers in Industry*, vol. 123. Elsevier B.V., Dec. 01, 2020. doi: 10.1016/j.compind.2020.103316.
- [2] H. Naderi and A. Shojaei, “Digital twinning of civil infrastructures: Current state of model architectures, interoperability solutions, and future prospects,” *Automation in Construction*, vol. 149. Elsevier B.V., May 01, 2023. doi: 10.1016/j.autcon.2023.104785.
- [3] L. Barisic, E. Levenberg, A. Skar, A. Boyd, and P. Zoulis, “A thermal digital twin for condition monitoring of asphalt roads,” *Green and Intelligent Technologies for Sustainable and Smart Asphalt Pavements - Proceedings of the 5th International Symposium on Frontiers of Road and Airport Engineering, IFRAE 2021*, no. November, pp. 709–713, 2022, doi: 10.1201/9781003251125-113.
- [4] M. Segovia and J. Garcia-Alfaro, “Design, Modeling and Implementation of Digital Twins,” *Sensors*, vol. 22, no. 14, 2022, doi: 10.3390/s22145396.
- [5] C. Yavuzturk, K. Ksaibati, and A. D. Chiasson, “Assessment of Temperature Fluctuations in Asphalt Pavements Due to Thermal Environmental Conditions Using a Two-Dimensional, Transient Finite-Difference Approach,” *Journal of Materials in Civil Engineering*, vol. 17, no. 4, pp. 465–475, Aug. 2005, doi: 10.1061/(asce)0899-1561(2005)17:4(465).
- [6] G. W. Recktenwald, “Finite-Difference Approximations to the Heat Equation,” 2004.
- [7] M. J. C. Minhoto, J. C. Pais, P. A. A. Pereira, and L. G. Picado-Santos, “Predicting asphalt pavement temperature with a three-dimensional finite element method,” in *Transportation Research Record*, National Research Council, 2005, pp. 96–110. doi: 10.3141/1919-11.
- [8] Liuping Wang, *PID Control System Design and Automatic Tuning using MATLAB/Simulink*. RMIT University, 2020.
- [9] Katsuhiko Ogata, *Ingeniería de control moderna*, vol. 5th. Pearson Educación, 2010.

## OPERATIONAL MODAL ANALYSIS OF AN ENTIRE WIND FARM

Asier Legaz<sup>1</sup>, Íñigo Vilella<sup>2</sup>, Miroslav Zivanovic<sup>1,3</sup>, \*Xabier Iriarte<sup>3,4</sup>, Aitor Plaza<sup>4</sup> and Alfonso Carlosena<sup>1,3</sup>

<sup>1</sup> Dept. of Electrical, Electronics and Communications Engineering.  
Public University of Navarre  
e-mail: {asier.legaz, miro, alfonso.carlosena}@unavarra.es

<sup>2</sup> IED Electronics, Polígono Industrial Plazaola E-6, E-31195, Aizoain, Spain  
e-mail: ivilella@iedgreenpower.com

<sup>3</sup> Institute of Smart Cities. Public University of Navarre

<sup>4</sup> Dept. of Engineering  
Public University of Navarre  
e-mail: {xabier.iriarte, aitor.plaza}@unavarra.es

**Keywords:** Wind turbines, Wind Farm, Harmonic Removal, Modal Analysis, OMA

**Abstract.** *The estimation of modal frequencies, and sometimes damping too, is proposed in the literature as a means to assess the condition of a mechanical structure and therefore to measure possible damages and even to estimate the remaining life-time. In the case of big structures such as bridges, buildings and high-rise towers where a well-controlled excitation is not possible, proposed methods to obtain the modal parameters resort on OMA (Operational Modal Analysis) techniques which rely on natural excitation. They routinely assume that such natural excitation (wind, waves, ...) can be modelled as white Gaussian noise. Regardless of the OMA method used on measured acceleration data, modal frequencies are usually easy to estimate with acceptable errors, whereas damping is subjected to large deviations.*

*In the case of Wind Turbines (WT) the situation is more complicated, since the rotating nature of the structure induces harmonic excitations which contaminate the accelerations measured, violating the basic assumptions for the applicability of OMA methods. The frequencies of these harmonics, originated mainly from the tower shadow effect and imbalances in the rotor, may be close to the frequencies of the turbine modes, making it impossible to determine both natural frequencies and damping. The most relevant harmonics are named as 1P (rotating frequency), 3P (blade passing) and their higher orders: 2P, 6P and 9P remarkably. There are in the literature several methods to avoid or mitigate the influence of the harmonic excitations in the modal analysis. In the time domain, for example, it is worth mentioning the Time Synchronous Averaging (TSA), Self-Adaptive Noise Cancellation (SANC). Other methods perform both in the frequency and the cepstral domains.*

*In a previous paper published by the authors (Instantaneous amplitude and phase signal modeling for harmonic removal in wind turbines) we proposed a method to estimate the har-*



monics and remove them from the raw acceleration signal. The method builds on the idea that a harmonic can be modelled as a frequency and amplitude modulated (FM-AM) sinusoid. Then, a conventional and well-known Covariance Driven Stochastic Subspace Identification (SSI-COV) is applied to obtain the true system modes over a signal supposedly free from harmonics. We demonstrated, over a number of changing operating conditions, that the algorithm provides an better estimation of the natural modes, comparing the algorithm to the plain application of SSI-COV.

In an attempt to improve this harmonic removal technique, particularly when the frequencies of the harmonics are close to those of the natural modes, we realized that the estimated harmonics contain part of the power due to the response of modes, resulting in notches in the signal spectrum (once the harmonics are removed) and thus in errors in the estimation of the natural frequency and particularly the estimation of the damping ratio. This is the reason why we came up with the idea of simultaneously modelling harmonics and natural modes, to extract the modal parameters from the isolated natural modes. An interesting side effect of this procedure is that it results in a much more computationally efficient method for modal analysis than those found in the literature, enabling the possibility to use methods as the RANDOMDEC for the estimation of the modal damping ratios.

In this paper the data from a number of wind turbines of the same wind farm has been used. The analysed turbines are of the same model and generate a nominal power of 3MW. The data is acquired twice a day, from a triaxial accelerometer located at the nacelle. Typically, the registers contains 30.000 samples per channel at 50 Hz (10 minutes). Each register is tagged automatically with a number from 1 to 6, depending on the state of the machine. In addition to the acceleration, the signal from a tachometer is also available with a phase resolution around 5°. Giving the geographical configuration of the wind farm, all the turbines operate typically under the same state, enabling the simultaneous comparison of all machines under similar conditions.

In this study we have applied the harmonic removal technique and the modal parameter estimation techniques to a all the WT of the farm under different operating conditions, meaning a different relation between modes and harmonics, and even no harmonics (no wind). One of the results is that the method has to be tuned to the operating mode for optimum results, though the process can be automated. The obtained results only correspond to the operation at nominal power, which happens in a wide range of wind speeds (between approximately 10 and 20 m/s). This is, to the best of our knowledge, the first study showing results combining a number of wind turbines, for a long period of time (4.5 months) with all turbines in operation.

The preliminary results show that the presented method gives estimations of modal frequencies which allow a discrimination of the behavior of the different wind turbines. The results of 1<sup>st</sup> and 2<sup>nd</sup> modes in both side-side and fore-aft directions are coherent, with likely a higher discrimination capability of side-side modes. Regarding the estimated of damping, the results are not conclusive. More data under different operating conditions, and longer periods, surely in combination with other information (wind, power,..) need to be analyzed to come up with more conclusive results.

## FATIGUE LIFE CYCLE ASSESSMENT OF EXTERNAL POST-TENSIONING SYSTEMS CONSIDERING CORROSION EFFECTS

Javier Naranjo-Pérez<sup>1</sup>, Javier F. Jiménez-Alonso<sup>1</sup>, José M. Soria<sup>2</sup>, and Iván M. Díaz<sup>2</sup>

<sup>1</sup>Department of Continuum Mechanics and Structural Analysis, ETSI, Universidad de Sevilla  
Camino de los descubrimientos, Seville, Spain  
e-mail: {jnaranjo3,jfjimenez}@us.es

<sup>2</sup> Department of Continuum Mechanics and Theory of Structures, ETSI Caminos, Canales y Puertos,  
Universidad Politécnica de Madrid  
Calle Profesor Aranguren 3, Madrid, 28040, Spain  
e-mail: {jm.soria,ivan.munoz}@upm.es

**Keywords:** External post-tensioning tendons, Fatigue analysis, Corrosion phenomenon, Cable dynamics.

**Abstract.** *External tendons in road and railway bridges are expected to reach 100 years. Nevertheless, failure cases of external post-tensioning tendons, well before they reach their lifespan, have increased in recent years. Among the main causes that have triggered partial or total breakage of these tendons are: i) grout disaggregation, ii) steel strand corrosion and iii) fatigue associated with stress cycles. Structural Health Monitoring (SHM) based on non-destructive testing has demonstrated its reliability as a tool to assist structural engineers in the prediction and prevention of this phenomenon which severely threatens the safety of the structure. The data, obtained during the short/long term monitoring, are processed to estimate experimentally both the modal properties and the tension force of the tendons. The estimation of these parameters allows checking the structural integrity of the existing structure.*

*Despite its goodness, the abovementioned method has a clear limitation, it cannot be addressed during the design stage of a new structure. Thus, numerical techniques must be developed to cope with this problem. In order to shed light on this problem, a new methodology is proposed in this study to assess the structural behaviour of external post-tensioning tendons during their overall life cycle analysing in detail the joint effect of the fatigue and the corrosion phenomena.*

*As benchmark structure, a railway bridge with a length of 48m and six external post-tensioning tendons has been considered. The natural frequencies obtained from a numerical modal analysis have been used to build an equivalent modal state-space model. This model has been used to predict the dynamic response of the bridge when subjected to the moving train loads. The strain and the stress of the tendon are calculated from the dynamic response at midspan and deviators.*

*The method is based on the linking between two behavioural models previously reported in the literature: i) a corrosion model and ii) a fatigue assessment model.*

*The corrosion model, based on the method proposed by Eurocodes, can be implemented as follows. First, the presence of chlorides must be studied. Initially, there is a chloride content in the concrete which starts to penetrate. When this chloride concentration is higher than a threshold, a localised breakdown which triggers corrosion arises. The depth at which the chlorides threshold is reached is given by a diffusion law that depends on numerous factors, such as environment, exposure or diffusion coefficient. If the chlorides have reached the surrounding area of the steel strands, corrosion begins, and a loss of steel section is produced. Otherwise, corrosion does not appear. Loss of section is produced by two different corrosion processes: uniform and pitting corrosion. The former assumes a concentric uniform loss of diameter of the steel strand. On the other hand, the later produces a localised loss of diameter. Both pitting and uniform corrosion are characterised by the corrosion parameter and corrosion rate (velocity at which corrosion propagates). Loss of section results in an increase of strand stress which may cause plastic strain up to its failure and a stress redistribution to the adjacent strands.*

*The fatigue assessment model is based on the current cumulative damage method reported in Eurocodes. According to this, the fatigue analysis is carried out considering the actual section of the tendon at each year of its service life. Computation of stress cycle counts is performed via the rainflow counting method. After this, the theoretical number of cycles are derived from the SN curve and the damage is assessed as the relationship between actual long-term cycles and the theoretical one.*

*It can be noticed the large amount of influencing variables that must be considered in the study. Hence, a sensitivity analysis has been included to compute the influence of these variables on the life cycle of the tendons. To do this, these variables have been considered as fuzzy variables: i) trains and their velocities, ii) exposures, iii) corrosion parameters and iv) traffic flow. As result of this study, a numerical tool is developed. This numerical technique allows predicting the long-term dynamic behaviour of the external post-tensioning tendons and preventing possible failures before the structure is built (during its design stage).*

## CURRENT CHALLENGES ON VIBRATION-BASED NDT AND CONTINUOUS MONITORING OF EXTERNAL POST-TENSIONING TENDONS IN BRIDGES

Carlos M. C. Renedo<sup>1</sup>, Iván M. Díaz<sup>1</sup>, Luis Chillitupa<sup>1</sup>, Belén Vecino<sup>1</sup> and Jaime H. García Palacios<sup>2</sup>

<sup>1</sup> Department of Continuum Mechanics and Theory of Structures, ETSI Caminos, Canales y Puertos, Universidad Politécnica de Madrid, Madrid, Spain.  
Calle Profesor Aranguren 3, 28040, Madrid, Spain  
e-mail: [carlos.martindelaconcha@upm.es](mailto:carlos.martindelaconcha@upm.es), [ivan.munoz@upm.es](mailto:ivan.munoz@upm.es), [belen.vecino@alumnos.upm.es](mailto:belen.vecino@alumnos.upm.es), [luis.cpalomino@upm.es](mailto:luis.cpalomino@upm.es)

<sup>2</sup> Department of Hydraulics, Energy and Environmental Engineering, ETSI Caminos, Canales y Puertos, Universidad Politécnica de Madrid, Madrid, Spain.  
Calle Profesor Aranguren 3, 28040, Madrid, Spain  
e-mail: [jaime.garcia.palacios@upm.es](mailto:jaime.garcia.palacios@upm.es)

**Keywords:** Vibration-based NDT, External Tendons, SHM, Bridges, Damage Detection.

**Abstract.** *External post-tensioning tendons are key vulnerable elements of modern bridges, as corrosion and fatigue have a big impact on their health state. For this reason and due to their important role in structural stability, currently, there is a clear demand of: i) NDT systems able to detect anomalies on their performance, and ii) cost effective continuous monitoring systems. The use of vibration-based techniques can be used nowadays to track the natural frequencies of these structural elements. These data can be then used to wisely estimate the tension force of the tendon, and its bending stiffness, which can be assumed to be reasonable performance indicators of the tendon health state. For this purpose, many different models and estimation strategies can be used, and often, knowing which one is more adequate in each case is something that up today is not clear. Additionally, the frequency tracking itself is a challenging task due to the contamination of the measured signals with the vibration of near tendons, and due to the complexity of the boundary conditions of the tendons. Both problems are commented along this paper, presenting the different alternatives and their main benefits and drawbacks.*

*In recent years, machine learning-based clustering and regression have proved to offer interesting tools to tackle most of the difficulties aforementioned on the SHM of external tendons: i) spectral doublets (due to different moment of inertia depending on the direction, the frequency coupling from adjacent tendons and the presence of bracing systems), ii) significant frequency variation due to temperature changes that may mask potential damage, iii) selection of principal/significant performance indicators to be tracked, iv) automatic detection of abnormal tendons in multi-span bridges with a huge number of tendon segments, and v) detection of abnormal tendon segments within a multi-span tendon considering friction losses and anchor sets.*



 DinEst 2024  
12-13 SEPTIEMBRE  
SEVILLA

